

# ASIAEM 2015

## Conference Proceedings

**August 2-7, 2015, ICC, Jeju Island, Republic of Korea**

**Conference General Chair:** *Prof. Yanzhao Xie*, Xi'an Jiaotong University, China

**Co-Chair:** *Prof. Chang Su Huh*, Inha University, Republic of Korea

**Technical Program Committee Chair:** *Dr. Dave Giri*, Pro-Tech, U.S.A.

**Co-Chair:** *Dr. William Radasky*, Metatech, U.S.A.

**Co-Chair:** *Prof. Lihua Shi*, Key Lab. on E3OE, China

**Organized by:**



Xi'an Jiaotong University (XJTU)



The Korean Institute of Electrical and Electronic Material Engineers (KIEEME)

**Supported by:**



State Key Laboratory of Electrical Insulation and Power Equipment



Inha University



The SUMMA Foundation

**Co-Organized by:**

- ✦ State Key Laboratory of Intense Pulsed Radiation Simulation and Effect, China
- ✦ State Laboratory on Environmental Electromagnetic Effects and Electro-optic Engineering, China
- ✦ Science and Technology on High Power Microwave Laboratory, China
- ✦ State Key Laboratory of Applied Physics-Chemistry Research, China
- ✦ Agency for Defense Development(ADD), Republic of Korea

**The Media Partner:**



# Contents

<b>I. TC01 Sources, Antennas and Facilities.....</b>	<b>1</b>
<b>A. The Effect of Conductor Size on Helical Antennas, <i>D. V. Giri, F. M. Tesche</i>.....</b>	<b>1</b>
<b>B. Optimization of a Virtual Cathode Oscillator Using NSGA-II Evolutionary Algorithm, <i>E. Neira, F. Vega, J.J. Pantoja</i>.....</b>	<b>3</b>
<b>C. High-power sources of ultra-wideband radiation pulses with elliptic polarization, <i>V. I. Koshelev, Yu. A. Andreev, A. M. Efremov, B. M. Kovalchuk, A. A. Petkun, V. V. Plisko, K. N. Sukhushin, M. Yu. Zorkaltseva</i>.....</b>	<b>6</b>
<b>D. UWB HPEM generator with changeable pulse waveform for IEMI testing, <i>Jin-Ho Shin, Young-Kyung Jeong, Dong-Gi Youn</i>.....</b>	<b>8</b>
<b>E. Design of a Portable Rectangular Generator Based on MOSFET and Avalanche Transistor, <i>QIAO Bing-bing, GUO Jie, LI Ke-lun</i>.....</b>	<b>9</b>
<b>F. Frequency, Time, and Thermal Domain Analysis of Planar Bi-Directional Log-Periodic Antenna, <i>J. Ha, M.A. Elmansouri, D.S. Filipovic</i>.....</b>	<b>12</b>
<b>G. A Compact Relativistic Magnetron with an Axial Output of TE<sub>11</sub> Mode, <i>Di-Fu Shi, Bao-Liang Qian, Yi Yin, Hong-Gang Wang, Wei Li</i>.....</b>	<b>15</b>
<b>H. A Miniature Pulse Generator, <i>Xing Zhou, Min Zhao, Qingxi Yang</i>.....</b>	<b>18</b>
<b>I. Comparative analysis of directivity and gain in according to Antenna's dielectric-shape, <i>Ruck-Woan Kim, Jin-Wook Park, Seung-Moon Han, Chang-su Huh</i>.....</b>	<b>20</b>
<b>J. Design Consideration of Marx Generator for a Continuous Operation at a High Repetition Rate, <i>Jeong-Hyeon Kuk, Dong-Woo Yim, Jin-Soo Choi, Sun-Mook Hwang, Tae-Hyun Lim</i>.....</b>	<b>21</b>
<b>K. Design of a smart phased array antenna for IEMI applications, <i>Jinwoo Shin, Junho Choi, Woosang Lee, Joonho So</i>.....</b>	<b>24</b>
<b>L. Effects of the Earth Ground on the Radiation Performance of Log-Periodic Dipole Antennas, <i>Xiang Gao, Zhongxiang Shen</i>.....</b>	<b>26</b>
<b>M. E-shaped Patch Antennas Fed with Ultra-short Pulses for Radiating High-power Mesoband Pulses, <i>Kiho Kim, Jiheon Ryu, Jin Soo Choi</i>.....</b>	<b>28</b>
<b>N. Experiment of a Ku-band Gyro-BWO on Square waveguide, <i>K. H. Jang, J. J. Choi, S. W. Jung</i>.....</b>	<b>30</b>
<b>II. TC02 Applications of Coupling to Structures and Cables .....</b>	<b>32</b>
<b>A. HEMP Conducted Environment Analysis for Cable Lying on Ground, <i>Sun Beiyun, Yang Jing</i>.....</b>	<b>32</b>
<b>B. Nonlinear and Short-Orbit Time-Reversal in a Wave Chaotic System, <i>Bo Xiao, Thomas Antonsen, Edward Ott, Steven M. Anlage</i>.....</b>	<b>35</b>
<b>C. A study for the effect of external incident wave on the simplified vehicle model, <i>Wonjune Kang, Junho Choi, Joonho So, Kangin Lee, Youngseek Chung</i>.....</b>	<b>37</b>

D. Analysis of the Compromising Electromagnetic Emanations of PS/2 Keyboards, <i>Ho Seong Lee, Dong-Joo Sim, Kyuhong Sim, Jong-Gwan Yook</i> .....	39
E. Ultra-wideband Electromagnetic Band-gap Structure with Multi-slot for Simultaneous Switching Noise Suppression, <i>J. H. Choi, J. W Shin, J. H. So</i> .....	41
<b>III. TC03 Measurement Techniques</b> .....	<b>43</b>
A. Design of a compact free-field sensor with fiber-optic link for EMP measurement, <i>Lihua Shi, Rongen Si, Yinghui Zhou</i> .....	43
B. Determination of Q-value of an Avionics Bay or Other Multi-resonant Cavity by Measurements in Time and Frequency Domain, with One or Two Antennas, <i>B. Vallhagen, C. Samuelsson, M. Bäckström</i> .....	45
C. Experimental comparison of mode-stirrer geometries for EMC, <i>V. Houchouas, C. Kasmi, J. Lopes Esteves, D. Coiffard</i> .....	48
D. Destructive High-Power Microwave Testing of Electronic Circuits using a Reverberation Chamber, <i>Tomas Hurtig, Leif Adelöw, Mose Akyuz, Mattias Elfsberg, Anders Larsson, Sten E. Nyholm</i> .....	51
E. Effect of Different Factors on Parameters in Noncontacted Electrostatic Discharge, <i>Fangming Ruan, Wenjun Xiao, Hu Shengbo, Xiaohong Yang</i> .....	54
F. Vectorial analysis of intense electromagnetic field using a noninvasive optical probe, <i>G. Gaborit, L. Gillette, P. Jarrige, J. Dahdah, T. Trève, L. Duvillaret</i> .....	57
G. Cutting-off Coupling Effects caused by Coaxial Cables while measuring Electric Field with ROD Antennas, <i>Michele Zingarelli, Roberto Grego</i> .....	59
<b>IV. TC04 IEMI Threats, Effects and Protection</b> .....	<b>62</b>
A. The detector of dangerous pulse electromagnetic interferences: conception of creation, <i>Yury V. Parfenov, Boris A. Titov, Leonid N. Zdoukhov, Xie Yanzhao</i> .....	62
B. Breakdown Characteristics of Si Bipolar Junction Transistor Injected with Microwave Pulses, <i>Cunbo Zhang, Honggang Wang, Jiande Zhang, Baoliang Qian, Guangxing Du</i> .....	65
C. Frequency Response Analysis of IEMI in Different Types of Electrical Networks, <i>Bing Li, Daniel Månsson</i> .....	68
D. Analysis of Transmission Characteristic of Composite Material with Wire Mesh and Honeycomb Core in Aircraft, <i>Se-Young Hyun, Ic-Pyo Hong, Chilsung Jung, Eung-Jo Kim, Jong-Gwan Yook</i> .....	71
E. On the Applicability of the Transmission Line Theory for the Analysis of Common-Mode IEMI-Induced Signals, <i>G. Lugrin, N. Mora, F. Rachidi, M. Nyffeler, P. Bertholet, M. Rubinstein, S. Tkachenko</i> .....	73
F. Test of Surge Protective Devices to Mitigate Intentional Electromagnetic Interferences (IEMI), <i>G. Lugrin, N. Mora, F. Rachidi, P. Bertholet, M. Nyffeler, A. Kålin, S. Sliman, M. Rubinstein</i> .....	75
G. High Power Microwave Effects on Coated Window Panes, <i>P. Ångskog, M. Bäckström, B. Vallhagen</i> .....	77
H. IEMI and Smartphone Security: a smart use of front door coupling for remote	

	<b>command execution, C. Kasmi, J. Lopes-Esteves.....</b>	<b>80</b>
<b>I.</b>	<b>A survey of typical sudden commencement geomagnetic storm environments, W. A. Radasky, E. B. Savage.....</b>	<b>83</b>
<b>J.</b>	<b>Failure Rate Analysis of Solid State Device Caused by Repeated Pulse Characteristics, Ki-Hoon Park, Kwan-Sik Kim, Chang-Su Huh, Jin-Soo Choi, Jong-Won Lee.....</b>	<b>85</b>
<b>K.</b>	<b>Destruction Characteristic of CMOS AND gate by Variable Pulse repetition rate, Jeong-Ju Bang, Sun-Ho Choi, Chang-Su Huh, Jin-Soo Choi, Jong-Won Lee.....</b>	<b>86</b>
<b>L.</b>	<b>A Method to Design a New Kind Active Frequency Selective Surface which has the Ability of HPM Protection, Deng Feng, Wang Dongdong, Ding Fan.....</b>	<b>87</b>
<b>M.</b>	<b>Reflection and transmission of microwaves by a modern glass window, P. Ragulis, Ž. Kancleris, R. Simniškis, M. Dagys.....</b>	<b>90</b>
<b>N.</b>	<b>Coupling Effects According to the Orientations of Multi-layered PCB and Aperture inside a Metallic Enclosure, Jin-Kyoung Du, Yuna Kim, Jongwon Lee, Jin Soo Choi, Jong-Gwan Yook.....</b>	<b>93</b>
<b>V.</b>	<b>TC05 System Level Protection and Testing.....</b>	<b>95</b>
<b>A.</b>	<b>Assessment of HEMP-survivability of Photovoltaic Generators, Markus Nyffeler, Armin W. Kaelin.....</b>	<b>95</b>
<b>B.</b>	<b>Threat-level HEMP-tests of Photovoltaic Panels and Components, Markus Nyffeler, Armin W. Kaelin, Alex Hauser.....</b>	<b>98</b>
<b>C.</b>	<b>Experiment research on response of typical SPD to different EMP, Zhou Ying-hui, Du Mingxin, Shi Lihua, Zeng Jie.....</b>	<b>101</b>
<b>D.</b>	<b>Frequency Domain Analysis of Penetrated Ultra Wideband Signal in Large Scale Structure, Jongwon Lee, Seungho Han, Jin Soo Choi.....</b>	<b>103</b>
<b>VI.</b>	<b>TC06 Lightning EM Effects.....</b>	<b>105</b>
<b>A.</b>	<b>FDTD simulation of lightning-induced currents on a buried cable with a shield wire, Hiroki Tanaka, Yoshihiro Baba, Celio Fonseca Barbosa.....</b>	<b>105</b>
<b>B.</b>	<b>Lightning occurrence data observed with lightning location systems of electric power companies in Japan: 2009-2013, Takatoshi Shindo, Hideki Motoyama, Toru Miki, Mikihisa Saito, Akiyori Matsueda, Noriyasu Honma, Akira Matsumoto, Kazuo Shinjo, Kiyotaka Hayashi, Hayato Awazu, Katsuhisa Makabe, Masato Fujikawa, Satoshi Kurihara, Masashi Sato.....</b>	<b>107</b>
<b>C.</b>	<b>Influence of Grounding Device Models on Lightning Protection Characteristics of Transmission lines with Different Rated Voltages, Jinliang He, Jinpeng Wu, Bo Zhang.....</b>	<b>110</b>
<b>D.</b>	<b>Correlation between air surface temperature and lightning events in Colombia during the last 15 years, F. Diaz, F. Roman.....</b>	<b>112</b>
<b>E.</b>	<b>Effect of Nearby Building on Horizontal Electric Field from Lightning Return Strokes, Fei Guo, Zhi-dong Jiang, Bi-hua Zhou.....</b>	<b>115</b>
<b>F.</b>	<b>On the Classification of Tower Flashes as Self-Initiated and Other-Triggered, M. Rubinstein, Alexander Smorgonskiy, F. Rachidi, J. Zuber.....</b>	<b>118</b>

<b>G. Lightning Protection Design Based on Energy Calculation</b> , <i>John J. Pantoja, Francisco Roman, Francisco Amórtegui</i> .....	<b>120</b>
<b>VII. TC07 Analytical and Numerical Modeling</b> .....	<b>123</b>
<b>A. On the Unconditionally Stable FDTD Method Based on Associated Hermite Functions</b> , <i>Huang Zhengyu, Shi Lihua, Zhang Zhixin</i> .....	<b>123</b>
<b>B. Transient response prediction using minimum phase method based on system simulation</b> , <i>Chen Peng, Sun Dongyang, Wu Gang, Chen Weiqing</i> .....	<b>126</b>
<b>C. Shielding Effect Analysis to Square Waves of Slotted Cavity Based on Shielding Effectiveness Curves</b> , <i>HU Xiao-feng, Liu Weidong, Chen Xiang, Wei Ming</i> .....	<b>129</b>
<b>D. Fourier-Collocation Method for the Surface Current Distribution On the Thin Antenna</b> , <i>H. K. Lin, J. S. Luo, L. Sun, W. X. Hou</i> .....	<b>132</b>
<b>E. Transient Voltage Responses of Multilayered PCBs in Metallic Enclosure Illuminated by Periodic Electromagnetic Pulse</b> , <i>Yuna Kim, Jin-Kyoung Du, Se-Young Hyun, Jong-Gwan Yook, Jongwon Lee, Jin Soo Choi</i> .....	<b>135</b>
<b>F. Parallelization of QR Decomposition Algorithm in Multi-conductor Transmission Line Equation Based on CUDA</b> , <i>Yao Liu, Min Zhou, Yang Cai</i> .....	<b>138</b>
<b>G. A methodology for numerical calculation of isotropic aperture transmission cross section</b> , <i>R. Gunnarsson, M. Bäckström</i> .....	<b>140</b>
<b>H. Time Marching Method Instability: a Deconvolution Approach</b> , <i>Juan Miguel David Becerra Tobar, Jose Félix Vega Stravo, John Jairo Pantoja Acosta</i> .....	<b>143</b>
<b>I. Development of the HEMP Propagation Analysis and Optimal Hardening Shelter Design, Simulation Tool "KTI HEMP CORD"</b> , <i>GyungChan, Min, YeongKwan, Jung</i> .....	<b>146</b>
<b>J. Electromagnetic Simulation Models for Wideband Pulse Generators Driven By a High-voltage Spark-gap Switch</b> , <i>Jiheon Ryu, Jaimin Lee, Jin Soo Choi, Sung-Hyun Baek, Jin Kyung Jung</i> .....	<b>149</b>
<b>K. Particle Simulation of Coaxial VIRCATOR</b> , <i>S. H. Han, J. S. Choi, S. H. Baek, T. Hurtig</i> .....	<b>151</b>
<b>L. Prediction of EMP Coupling to Multi-conductor Transmission Lines by Using Different Iteration Methods</b> , <i>Jun Guo, Yan-zhao Xie</i> .....	<b>152</b>
<b>M. Propagation Characteristics of the UWB EM Wave in Soil Media and its Influence on the Detection of Buried Unexploded Ordnance</b> , <i>S. Vijayakumar, M. Joy Thomas</i> .....	<b>154</b>
<b>VIII. TC08 Bio Effects and Medical Applications</b> .....	<b>157</b>
<b>A. Recent Research Activities to Investigate the Interaction of Electromagnetic Waves and Cells of the Haematopoietic System</b> , <i>Lars Ole Fichte, Marcus Stiemer</i> .....	<b>157</b>
<b>B. The effect of standard cell culture environment on cellular electromagnetic effects study</b> , <i>Wen-yu Peng, Jian-gang Ma, Xiao-yun LU, Yan-zhao XIE</i> .....	<b>159</b>
<b>IX. TC09 Antenna Design, Radiation and Propagation</b> .....	<b>161</b>

<b>A. Examples of the Power Wave Theory of Antennas, E. G. Farr.....</b>	<b>161</b>
<b>B. Radiation characteristics of a high-power ultra-wideband pulse radiating antenna, Jae Sik Kim, Young Joong Yoon, Jiheon Ryu, Jin Soo Choi.....</b>	<b>164</b>
<b>C. On the characteristic impedance of parallel-plate transmission line with plates of unequal breadths, Wang Shaofei, Xie Yanzhao, Du Leiming, Li Kejie.....</b>	<b>166</b>
<b>D. Modified two-element TEM horn array for radiating UWB electromagnetic pulses, Chunming Tian, Peiwu Qiao, Yanzhao Xie and Juan Chen.....</b>	<b>168</b>
<b>E. Optimization of HEMP Simulator Antenna for Improving Test Area Field Distribution, Zheng Sheng-quan, Deng Feng, Wang Dong-dong, Hou Dong-yun....</b>	<b>170</b>
<b>F. Miniaturized COBRA for HPEM System, Jihwan Ahn, Young Joong Yoon.....</b>	<b>173</b>
<b>G. Optimization of Offset Parabolic Antennas based on Genetic Algorithm, Junggeun Park, Young-seek Chung, Wonjune Kang, Kang-in Lee, Hojun Yoon.....</b>	<b>175</b>
<b>H. Experimental Verification of a Wideband Patch Antenna for Application to High-power Wideband Radiators, Taehyun Lim, Haeok Kwon, Jiheon Ryu, Dong Woo Yim, Jin Soo Choi.....</b>	<b>178</b>
<b>I. Low-Frequency-Compensated Horn Antenna: for the Simulation of HEMP, Shaofei Wang, Yanzhao Xie.....</b>	<b>180</b>
<b>J. Analysis of the Induced Electromagnetic Field in the Surroundings of a NEMP Simulator, B. Daout, N. Mora, M. Sallin, C. Romero, F. Vega, F. Rachidi.....</b>	<b>182</b>
<b>X. TC11 Target Detection, Discrimination and Imaging.....</b>	<b>184</b>
<b>A. Detection of metal objects by ultra-wideband pulses with different polarization, V. I. Koshelev, E. V. Balzovsky, Yu. I. Buyanov, E. S. Nekrasov, A. A. Petkun, V. M. Tarnovsky.....</b>	<b>184</b>
<b>B. Pulse Compression for OFDM based Ground Penetrating Radar, Shi Zheng, Wen Huang, Xuehan Pan, Anxue Zhang.....</b>	<b>187</b>
<b>C. A Valentine Antenna Working in 150 MHz – 350 MHz Band for UWB Application, Xuehan Pan, Shi Zheng, Anxue Zhang.....</b>	<b>189</b>
<b>D. A new design of TEM UWB antenna for ISAR imaging, Shitao Zhu, Anxue Zhang, Zhuo Xu, Xiaoli Dong.....</b>	<b>191</b>
<b>E. Active Detection of Fissile Materials via Laser-Induced Ionization-Seeded Plasmas, Geehyun Kim, Mark Hammig.....</b>	<b>194</b>
<b>XI. TC12 Landmine &amp; IED Detection and Neutralization.....</b>	<b>196</b>
<b>A. The effect of ANFO on the Complex Resonance Frequencies of an IED, S. A. Gutierrez, E. Neira, J. J. Pantoja, F. Vega.....</b>	<b>196</b>
<b>XII. TC13 Electromagnetic Transients in UHV/EHV Transmission Lines and Substations .....</b>	<b>199</b>
<b>A. Study on Statistical Characteristic of Transient Disturbances and Correlation with Immunity Waveform, Zhang Weidong, Zhang Xiaoli, Luo Guangxiao.....</b>	<b>199</b>
<b>B. Modelling and analyzing of HEMP coupling to overhead multi-conductor transmission lines, Ni LI, Jun GUO, Jian-gong ZHANG, Qing LIU, Yan-zhao</b>	

	<i>XIE</i> .....	201
<b>C.</b>	<b>Simulation Research of Offshore Wind Farm Lightning Intruding Overvoltage Based on ATP/EMTP, <i>XU Yang, LIU Wenbo, WANG Yu, LAN Lei, ZHU Sheng</i>.....</b>	<b>204</b>
<b>D.</b>	<b>Calculation and Analysis on Transient Induced Voltage of Multiple Parallel UHV Transmission Lines, <i>ZHANG Gongda, ZHOU Peihong, ZHANG Xiaoqing, YUE Lingping</i>.....</b>	<b>207</b>
<b>E.</b>	<b>Study of Influence Factors of Transient Enclosure Voltages in GIS, <i>CHEN Shu, GUO Jie , LI Kelun</i>.....</b>	<b>210</b>
<b>F.</b>	<b>Characteristics Analysis of Metal Oxide Arresters in GIS Excited by Very Fast Impulse, <i>Jie Chen, Jie Guo, Ai-ci Qiu</i>.....</b>	<b>213</b>
<b>G.</b>	<b>Influence of Ground Wires on Ion Flow Field around HVDC Transmission Lines, <i>Bo Zhang, Jinliang He</i>.....</b>	<b>216</b>
<b>H.</b>	<b>Transient Electric Field Caused by High-voltage Circuit Breaker's Switching Operation, <i>Xu Kong, Yan-zhao Xie, Qing Liu, Shao-Fei Wang, Xue-mei Sun, Yu-Hao Chen</i>.....</b>	<b>219</b>
<b>XIII.</b>	<b>SS01 Design of Protective Devices and Test Methods.....</b>	<b>222</b>
<b>A.</b>	<b>Characterization of Limiters for HPM and UWB Front-Door Protection, <i>T. Nilsson, M. Bäckström</i>.....</b>	<b>222</b>
<b>B.</b>	<b>Low Insertion Loss Energy Sensitive Bandpass Filter to Protect Ku-Band Receivers from HPEM Threats, <i>W. A. Arriola, T. H. Jang, J. Y. Ahn, I. S. Kim</i>.....</b>	<b>224</b>
<b>C.</b>	<b>Reliable HEMP Protective Devices for the Power Line, <i>Joon-Hyuck Kwon, Ki-Hwan Song, Jong-Gwan Yook</i>.....</b>	<b>227</b>
<b>D.</b>	<b>Key Design Technologies of RF Front-end Protection Module with Ultra-low Limited Output Power, <i>Dongdong Wang, Lan Gao, Shengquan Zheng, Feng Deng, Dongyun Hou</i>.....</b>	<b>229</b>
<b>E.</b>	<b>Simple printed structures for low-cost and effective protection against UWB pulses, <i>A.T. Gazizov</i>.....</b>	<b>232</b>
<b>F.</b>	<b>Overview of test methods for HEMP protective filters in Korea, <i>Tae Heon Jang, Hyo Sik Choi, Won Seo Cho</i>.....</b>	<b>235</b>
<b>XIV.</b>	<b>SS02 HPEM Impacts on Critical Infrastructure.....</b>	<b>237</b>
<b>A.</b>	<b>Laboratory test of the IEMI vulnerability of a security surveillance camera, <i>E. B. Savage, W. A. Radasky</i>.....</b>	<b>237</b>
<b>B.</b>	<b>Laboratory tests of the IEMI/HEMP vulnerability of some low power switched-mode power supplies (SMPS), <i>E. B. Savage, W. A. Radasky</i>.....</b>	<b>239</b>
<b>C.</b>	<b>IEMI laboratory tests of network line protectors: vulnerability and protection ability, <i>E. B. Savage, W. A. Radasky</i>.....</b>	<b>241</b>
<b>D.</b>	<b>Study of the Propagation of IEMI Signals along Power and Communication Lines, <i>N. Mora, G. Lugrin, F. Rachidi, M. Nyffeler, P. Bertholet, M. Rubinstein</i>.....</b>	<b>243</b>
<b>E.</b>	<b>Effect of the Penetration through a Concrete Wall on the Propagation of Common Mode IEMI Signals, <i>N. Mora, G. Lugrin, F. Rachidi, M. Nyffeler, P. Bertholet, M. Rubinstein</i>.....</b>	<b>245</b>

<b>XV. SS03 Explosive Devices Effects and Protection for HPEM.....</b>	<b>248</b>
<b>A. Application of varistor for RF protection of semiconductor bridge, Bin Zhou, Jun Wang, Pei-kang Du, Yong Li.....</b>	<b>248</b>
<b>B. Simulation of protective effect of several protective devices to sensitive EED under extreme ESD environment, Zhixing Lv, Nan Yan, Wei Ren, Yingwei Bai.....</b>	<b>252</b>
<b>C. Wideband Differential Technique to Measure the Input Impedance of Electro-Explosive Devices, John J. Pantoja, Néstor Peña, Ernesto Neira, Félix Vega, Francisco Roman.....</b>	<b>255</b>
<b>D. Research on Induction Current of Bridge Wire of Industrial Electric Caps using FDTD Arithmetic, DU Bin, Luan Ying.....</b>	<b>258</b>
<b>XVI. SS04 Statistical Tools in HPEM.....</b>	<b>261</b>
<b>A. Application of the Random Coupling Model to Statistical Properties of Complex Enclosures, Bo Xiao, Thomas Antonsen, Edward Ott, Steven M. Anlage.....</b>	<b>261</b>
<b>B. Real-Time Radiated tests optimization using a bootstrap module, C. Kasmi, S. Lall éch ère, S. Girard, P. Bonnet, F. Paladian.....</b>	<b>263</b>
<b>C. Threshold Probability Model for EMP Effects Evaluation, Kejie LI, Yanzhao XIE, Yury V. Parfenov.....</b>	<b>266</b>
<b>D. On the Statistical Validity of HPEM Field Tests, Lars Ole Fichte, Sven Knoth, Marcus Stiemer.....</b>	<b>268</b>
<b>XVII. SS05 HPEM Standards.....</b>	<b>271</b>
<b>A. Some standardization problems of high power electromagnetic pulses, formed by test facilities, Yury V. Parfenov, Boris A. Titov, Leonid N. Zdoukhov, William A. Radasky.....</b>	<b>271</b>
<b>B. Overview of HPEM Standards Produced by IEC SC 77C, Richard Hoad, William A. Radasky.....</b>	<b>272</b>
<b>C. An overview of two recent IEMI publications: IEEE Std 1642 and Cigr é Technical Brochure 600, W. A. Radasky.....</b>	<b>274</b>
<b>D. Field uniformity area assessment using a hyper-band HIRA, Tae Heon Jang, Jae Han Cho, Won Seo Cho.....</b>	<b>276</b>
<b>E. A brief review of the root action norm for waveform analysis, E. Schamiloglu.....</b>	<b>278</b>
<b>XVIII. SS06 Vulnerability of Aircraft to EM Threats.....</b>	<b>280</b>
<b>A. The Discrete Method of BLT Equation on Non-parallel Two-Wire Transmission Line, Mengshi Zhang, Guyan Ni, Min Zhou.....</b>	<b>280</b>
<b>B. The tensor field equation of systematic electromagnetism and its exterior form representation, Shaorong Chen, Xiang Li, Xishun Liu, Jianshu Luo, Zhuangzhuang Tian, Jun Zhang.....</b>	<b>283</b>
<b>C. Measurement result and analysis of aeronautical cables at high frequency range, Z. L. Tong, J. S. Luo, H. Lei, Y. F. Liu, X. S. Liu, C. X. Tang.....</b>	<b>286</b>

D. Crosstalk analysis of PCB traces based on BLT equations and equivalent multi-conductor transmission line mode, <i>Y. Li, G. Y. Ni, X. D. Chen</i> .....	289
E. Electromagnetic topology analysis and Simulation of electromagnetic coupling of cable bundle of aircraft platform system, <i>J. S. Luo, H. Wang</i> .....	292
F. Iterative QR Method for Multi-conductor Transmission Line Equation, <i>H. Wang, J. S. Luo</i> .....	295
<b>XIX. SS07 Pulse Power for Electromagnetic Launch</b> .....	<b>298</b>
A. Experimental Research on Rod-shaped Triggered Gas Switch, <i>Chen Jingliang, Lei Wanglong, Yao Xueling</i> .....	298
B. An automatic fragmenting and triggering method for capacitive pulse forming units of the electromagnetic railgun, <i>Xukun Liu, Xinjie Yu, Xiucheng Liu, ZANJI Wang</i> .....	301
C. Transient Analysis Method of Pulsed Power Circuit, <i>Seong-Ho Kim, Young-Hyun Lee, Byungha Lee, Jin Hyuk Chung, Sanghyuk An</i> .....	305
D. Development of small electromagnetic railgun launch device for inductive pulsed power supply, <i>Rui Ban, Xinjie Yu, Zhen Li, ZANJI Wang</i> .....	308
E. Performance Evaluation of an Experimental Railgun, <i>Young-Hyun Lee, Seong-Ho Kim, Byungha Lee, Jin Hyuk Chung, Sanghyuk An</i> .....	310
F. Saturation of Amorphous-Core Tesla Transformer Applied to Pulsed High-Voltage Generator, <i>C. H. Kim, H. O. Kwon, J. S. Choi</i> .....	312
G. Parametric analysis of STRETCH meat grinder circuit based on equivalent induction theory, <i>Jianmin Ding, Xinjie Yu, ZANJI Wang</i> .....	314

# The Effect of Conductor Size on Helical Antennas

*D. V. Giri\* and F. M. Tesche †*

\*Pro-Tech, 11-C Orchard Court, Alamo, CA 94507-1541, † EM Consultant, 1519 Miller Mountain Road, Saluda, NC 28773

## Abstract

In this paper, we consider the effect of the conductor diameter on the performance of a helical antenna. The helical antenna considered here is an axial-beam type working in the frequency range of 300 to 500 MHz. We find that the conductor size has a significant effect on the gain of the antenna. Results of a numerical analysis of the antenna with varying conductor diameters are presented and compared with some available measurement data.

**Keywords:** Helical antennas, Gain, Axial ratio, Phase velocity

## 1 Introduction

Krauss, the inventor of helical antennas has considered an axial beam helical antenna with three different conductor sizes [1 and 2] as shown in Figure 1.

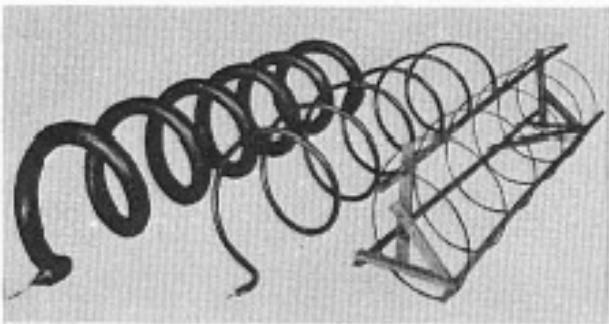


**Figure 1. Helical antenna with varying wire radii**

The three antennas in the accompanying figure have conductor diameters of 0.317cm, 1.27cm and 4.13 cm, with a variation of 13 to 1. The antenna parameters [2] are major diameter  $D = 21.9$  cm, pitch angle  $\alpha = 14^\circ$  and a spacing between turns  $S = 17.15$  cm. The ground plane is a square 1.5 m x 1.5 m copper plate. The antenna is designed to work in the frequency range of 300 to 500 MHz.

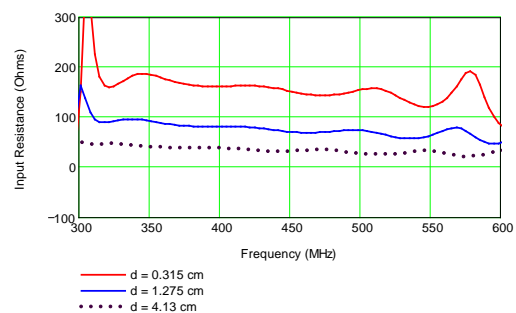
We find that the length of one turn

$L_1 = \sqrt{(\pi D)^2 + S^2} = 70.89$  cm which is a wavelength at 423 MHz. Tice and Krauss (Ref 2) consider the performance of these three antennas at a frequency of 400 MHz, and come to the following 5 conclusions.

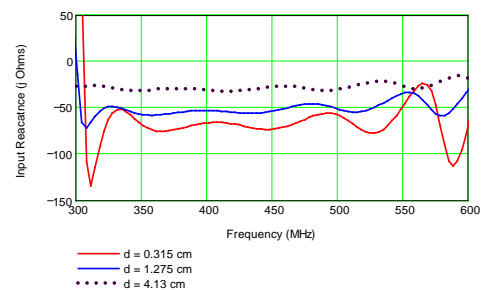
- 1) The half power beam width varies only a few %
- 2) Ratio of the maximum main lobe to maximum side lobe varies only 8 %,
- 3) The axial ratio is nearly the same for all three cases and within  $\pm 4\%$ ,
- 4) The terminal impedance is nearly resistive and the variation is  $\pm 25$  % and
- 5) Phase velocity is unaffected by conductor size.

## 2 WIPL-D Numerical Analysis

We have analyzed the above three antennas using WIPL-D ([http:// www.wipl-d.com](http://www.wipl-d.com)) and the results are presented in Figures 2 and 3.



**a. Real part**



**b. Reactive part**

**Figure 2. Real and Imaginary Parts of the terminal Impedance**

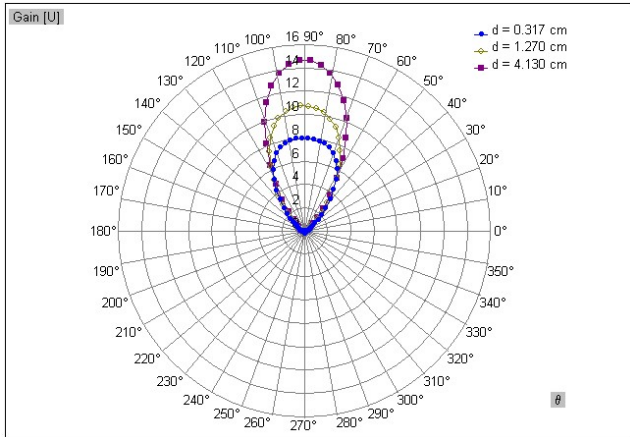


**Figure 3. Effect of the conductor diameter on the Gain of the Helical Antenna at 400 MHz (WIPL-D calculations)**

We compare and contrast our findings with that of Tice and Kraus [2], in a tabular form.

the antenna goes up and hence more radiation. Since Tice and Kraus (Ref 2) also found almost exactly the same the resistance variation, it is curious why they did not look at or comment about the antenna gain. Their results are based on measurements and our results described above are purely based on numerical computations.

Furthermore, some measurements [3] validate the increased gain with increased conductor radius. Using a 1 GHz helical antenna, 1/2" tubing produced 35% higher output than 1/4" tubing. No further improvement was seen with ~ 1" tubing. It is entirely possible that there is an optimal conductor radius that matches the source impedance to the antenna impedance. WE will discuss the computational and measured data in this presentation.

Performance Parameter	Conclusions from Ref 2	Our findings
Half-power beam width	varies only a few percent	same as [2]
Ratio of maximum main lobe to maximum side lobe	varies only 8 %	did not investigate
Axial ratio	varies only $\pm 4$ %	did not investigate
Terminal impedance	nearly resistive, no reactance mentioned resistance varies $\pm 25$ %	Resistive variation is about $\pm 50$ % however, we do see a reactive component shown in Figure 3
Phase velocity	unaffected by conductor size	did not investigate
Gain	<b>No mention is made</b>	<b>Significant Effect</b> Numerical Gains 8, 10.8 and 14.6 Gain (in dB) 9.03,10.33,11.64 Fatter wire has higher gain

## References

- [1] J. D. Kraus and R. J. Marhefka, Antennas for all Applications, McGraw Hill Publication, 3rd edition.
- [2] T. E. Tice and J. D. Kraus, "The Influence of Conductor Size on the Properties of Helical Beam Antennas," Proceedings of IRE, Volume 37, No. 11, November 1949.
- [3] Dr. Jerrold Levine, L3 Communications, San Leandro, CA, Private Communication, 2015.

From Figure 3 above, it is evident that there is a significant improvement in the antenna gain as one increases the conductor diameter. This can also be correlated to the fact that the terminal resistance is going down with the conductor size. As the terminal resistance goes down (from about 150 to 100 to 50 Ohms, which is a variation of  $\pm 25$  %), the current on

# Optimization of a Virtual Cathode Oscillator Using NSGA-II Evolutionary Algorithm

E. Neira\*, F. Vega† J.J. Pantoja‡

Electromagnetic Compatibility Group, Universidad Nacional de Colombia, \*[eneric@unal.edu.co](mailto:eneric@unal.edu.co) †[jfvegas@unal.edu.co](mailto:jfvegas@unal.edu.co) ‡[jjpantojaa@unal.edu.co](mailto:jjpantojaa@unal.edu.co)

## Abstract

This paper presents an optimization of a virtual cathode oscillator (Vircator) with axial extraction using the multi-objective Non-dominated Sorting Genetic Algorithm II (NSGA-II) evolutionary algorithm. The optimization was implemented with two objective functions to maximize the radiated energy and to tune the resonance frequency at 5GHz. The simulations were made on CST Particle Studio. The evolutionary algorithm was programmed in Matlab. An interface between CST and Matlab was implemented. At the end, the algorithm produced a set of the best individuals.

**Keywords:** Optimization, Vircator, NSGA-II, Matlab – CST PS interface.

## 1 Introduction

A Vircator is a High Power Microwave Source (HPMS). Vircators are able to generate microwaves power above 1 GW during tens or hundreds of ns and their typical radiation frequencies are between 1 GHz to 10 GHz. Vircator can be constructed with different geometries and the most used are [1,2]. Vircator of axial extraction (Fig. 1), Vircator with transverse extraction, Reditron, Reflex Triode and the Vircator Coaxial. Some applications of Vircators are experimentation, electronic warfare, particle accelerators and breakdown experiment. The most relevant advantages are easy construction, low maintaining prices, low cost, relative small size, [1,3]. On the other side, the main constrain is the low efficiency. The Vircator operation theory can be consulted in [2,4].

The design of HPMS can be oriented to achieve different optimization objectives as: energy, power, power efficiency, energy efficiency, specific frequency response, and sizes. Depending on the application, a multi-objective optimization is required. For example, an application that requires a small size Vircator, a specific frequency response and a determined power level.

A lot of experimental and numerical optimization efforts have been made to improve the Vircator response in some specific objectives. Research oriented to the optimization of cathode and anode materials can be consulted in [5]–[7]. In these studies, the behaviour of a set of different materials on the electron emission has been studied. A work about the cathode

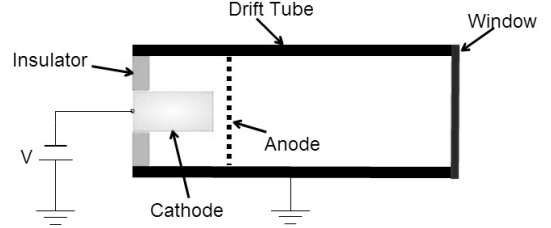


Fig 1. Axially extracted Vircator

sizes and anode-cathode distance variation have been reported in [8]. In [9], a study of the anode-cathode distance effect over the frequency response and the energy efficiency is presented. In [10], the anode-cathode distance variation is studied in order to improve the power efficiency on a Reflex Triode.

Most of the previous works have been focused on the study of effects on just one response due to the variation of one or two parameters. Due to the variety of objectives that can be required in Vircators design, optimal parameters for an objective can impair the response to another important objective.

In this paper, we present the implementation of the multiobjective algorithm NSGA-II [11] in order to find a way to design a Vircator with a specific frequency response, while is maximized the radiated energy. This implementation was developed in Matlab. FDTD-PIC simulations were performed using CST-PS. An interface between Matlab and CST-PS was developed using the methodology presented in [12]. Next chapter presents simulation details and the method to calculate the radiated energy.

## 2 Simulations

Figure 1 shows a diagram of the Vircator modelled on CST-PS. The feed voltage between anode and cathode was configured to follow the behaviour of a Marx Generator of low energy feeding a Vircator. The voltage wave equation, used in the simulations, is presented in (1) with time in ns. The time simulation was setup on 50ns. Fixed size parameters of simulation are shown in Table 1.

$$v(t) = V \left( -0.4789e^{-\left(\frac{t+9.05}{14.43}\right)^2} + 1.148 \times 10^6 e^{-\left(\frac{t+296.8}{82.7}\right)^2} - 8767e^{-\left(\frac{t+67.67}{23.75}\right)^2} \right) \quad (1)$$

**Table 1: Simulation fixed parameters.**

Parameter	Value
Drift Tube Length(L) [cm]	45
Drift Tube Material	PEC
Isolator width(iL)[cm]	1
Isolator Material	Teflon (PTFE)
Cathode material	PEC
Anode material	PEC
Particle Source emission model	Explosive
Explosive - Rise time [ns]	0.5
Explosive -Threshold Field[kV/m]	20
Number of emission points	Adjusted to mesh
Frequency range [GHz]	0.5-8
Cells per wavelength	10
Cell per max model box edge	20
Cathode form	Circular

The electric and the magnetic fields over the extraction surface (A) were used to measure the Vircator energy response. It was performed with 61 magnetic field probes and 61 electric field probes distributed over the extraction surface. Each probe point coordinates was calculated to represent the center of a surface of same sizes (dA) given by  $dA=A/61$  (see Fig. 2).

The complex power leaving the extraction surface is define by [13] as:

$$P_f = \iint_S \mathbf{S} \cdot d\mathbf{s} = \iint_S \mathbf{E} \times \mathbf{H}' \cdot d\mathbf{s} \quad (2)$$

where the time-average power flow is the real part of  $P_f$ . The energy can be obtained by integrating the time-average power over the frequency of interest. We are interested only in the energy flowing in a direction normal to the extraction surface.

Next section present the optimization problem and the solution way.

### 3 Optimization Process

Problem definition:

$$\begin{aligned} & \text{Minimize} && f_1, f_2 \\ & f_1 = && |f_{\max} - 5GHz| \\ & f_2 = 1 / \int_{4.95GHz}^{5.05GHz} \left( \iint_S \text{Re}\{E \times H'\} \cdot d\mathbf{s} \right) df \end{aligned}$$

where  $f_{\max}$ , E and H are function of: voltage V, anode transparency T, cathode length  $K_1$ , Drift Tube radius  $R_b$ , anode-cathode distance  $ak_d$ , cathode radius  $K_r$

$$\begin{aligned} 100kV \leq V \leq 400kV, & \quad 10\% \leq T \leq 90\%, \quad 0.3cm \leq ak_d \leq 4cm, \\ 3cm \leq R_b \leq 10cm, & \quad 0.5cm \leq K_r \leq R_b - 0.5cm \end{aligned}$$

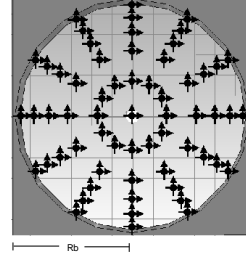


Fig 2. Field probes over the extraction surface

The main problem in the optimization is the lack of equations describing the behavior of the Vircator for some interest responses. As consequences: first, a limited number of optimization techniques can be used; second, the evaluation time is very long due to the need to use of numerical simulation. Therefore, it is necessary to use an optimization technique that allows using a low number of evaluations and presents rapid convergence.

We selected the multiobjective genetic algorithms to make a first approach to the optimization problem. It was performed by checking the use of metaheuristic algorithms to solve the problem. First, we considered the Vector Evaluated Genetic Algorithm (VEGA) [14]. After, we studied the MultiObjective Genetic Algorithm(MOGA) [15]. Two previous algorithms were not implemented since the evaluations are not oriented to use the Pareto Front. The NSGA-II [11] was selected despite the problems which may be presented by the use of non-dominance criteria in the parents selection [16].

Due to the longtime of simulation, the initial population was established to 28 individuals. The selection step was made using the first Pareto fronts needed to complete 14 individuals. If number of individuals needed to complete the parents was less that the individuals in to the last selected front, it is used the crowded-comparison approach described in [11]. To produce new gens on the next generation, the mating step was implemented using 2 procedures. The first procedure was one-point crossover. The second implemented procedure was a blending method. It recombines one gen, with a random value between the genes of the parents. The other genes are copy from one parent[17]. The two methods were intercalated between generations. The mutation was established to the 5% of the population.

### 4 Results

Figure 3 shows a comparison of behavior regard to objective functions, between individuals in the first generation (Blue dot) and individuals in the tenth generation (Black Diamond). We can interpret an improvement on the energy radiated in 5GHz, but the progress is not same in the frequency tune.

After 30 generations, the algorithm found a single individual with the best performance. The characteristics of this individual are shown in the table 2. The power response in the frequency domain is shown in figure 4.

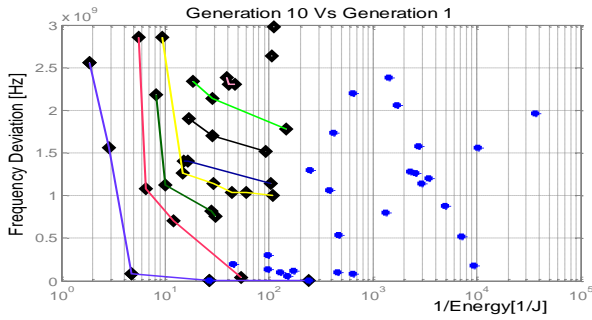


Fig 3. Comparison between two generations.

Table 2: Best individual parameters.

Inputs	Value	Outputs	Value
$AK_d$ [cm]	0.5	Energy in 5GHz	0.937Juls
$K_r$ [cm]	2.5	$F_{max}$	5 GHz
$K_l$ [cm]	12.9	Median impedance	13 $\Omega$
$R_p$ [cm]	5.7	Input Energy	112.4 Juls
$T$ [%]	63	Energy Efficiency in 5 GHz $\pm$ 50 MHz	0.8336%
V	288kV		

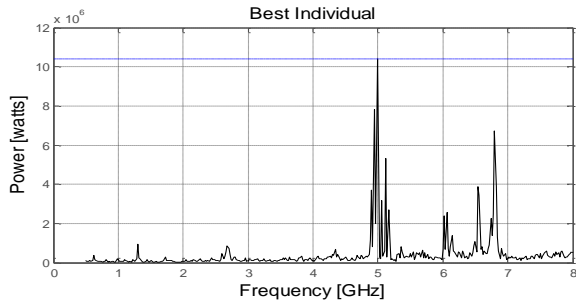


Fig 4. Best individual

## 5 Conclusions

Metaheuristics as NSGA-II can be used in the design of Vircators. The main constrain identified in the use of GA to optimize Vircators is the simulation time to evaluate each new candidate solution. We saw that the exploration of the parameters using GA is not efficient for our problem. So, the convergence of the algorithm is slow. Finally, we suggest using an optimization algorithm that allows fewer evaluations.

## References

[1] K. Scott, "High-Power, Coaxial Vircator Geometries," Texas Tech University, 1998.  
 [2] J. Benford, J. Swegle, and E. Schamiloglu, *High power microwaves*. 2007.  
 [3] W. Jiang, K. Woolverton, J. Dickens, and M. Kristiansen, "High power microwave generation by a coaxial virtual cathode oscillator," *Plasma Science, IEEE Transactions on*, vol. 27, no. 5. pp. 1538–1542, 1999.

[4] C. Möller, *High Power Microwave Sources : Design and Experiments*. Licentiate Thesis Stockholm, Sweden 2011, 2011.  
 [5] Y. Chen, J. Mankowski, J. Walter, M. Kristiansen, and R. Gale, "Cathode and Anode Optimization in a Virtual Cathode Oscillator," *Dielectrics and Electrical Insulation, IEEE Transactions on*, vol. 14, no. 4. pp. 1037–1044, 2007.  
 [6] M. Elfsberg, T. Hurtig, A. Larsson, C. Moller, and S. E. Nyholm, "Experimental Studies of Anode and Cathode Materials in a Repetitive Driven Axial Vircator," *IEEE Trans. Plasma Sci.*, vol. 36, no. 3, pp. 688–693, Jun. 2008.  
 [7] J. Walter, J. Vara, C. Lynn, J. Dickens, A. Neuber, and M. Kristiansen, "Initial anode optimization for a compact sealed tube vircator," *Pulsed Power Conference (PPC), 2011 IEEE*. pp. 807–810, 2011.  
 [8] P. Appelgren, M. Akyuz, M. Elfsberg, T. Hurtig, A. Larsson, S. E. Nyholm, and C. Moller, "Study of a Compact HPM System With a Reflex Triode and a Marx Generator," *Plasma Science, IEEE Transactions on*, vol. 34, no. 5. pp. 1796–1805, 2006.  
 [9] H. Sze, J. Benford, T. Young, D. Bromley, and B. Harteneck, "A Radially and Axially Extracted Virtual-Cathode Oscillator (Vircator)," *Plasma Science, IEEE Transactions on*, vol. 13, no. 6. pp. 492–497, 1985.  
 [10] J. J. Mankowski, X. Chen, J. C. Dickens, and M. Kristiansen, "Experimental optimization of a Reflex Triode Virtual Cathode Oscillator," *High-Power Particle Beams (BEAMS 2004), 2004 International Conference on*. pp. 426–429, 2004.  
 [11] K. Deb, A. Pratap, S. Agarwal, and T. Meyarivan, "A fast and elitist multiobjective genetic algorithm: NSGA-II," *Evolutionary Computation, IEEE Transactions on*, vol. 6, no. 2. pp. 182–197, 2002.  
 [12] R. L. Haupt, "Using MATLAB to Control Commercial Computational Electromagnetics Software," *Aces J.*, vol. 23, no. 1, pp. 98–102, 2008.  
 [13] R. F. Harrington, *Time-Harmonic Electromagnetic Fields*. 2001.  
 [14] J. D. Schaffer, "Multiple Objective Optimization with Vector Evaluated Genetic Algorithms," in *1st International Conference on Genetic Algorithms*, 1985, pp. 93–100.  
 [15] C. M. Fonseca and P. J. Fleming, "Multiobjective genetic algorithms," *Genetic Algorithms for Control Systems Engineering, IEE Colloquium on*. pp. 6/1–6/5, 1993.  
 [16] K. Ikeda, H. Kita, and S. Kobayashi, "Failure of Pareto-based MOEAs: does non-dominated really mean near to optimal?," *Evolutionary Computation, 2001. Proceedings of the 2001 Congress on*, vol. 2. pp. 957–962 vol. 2, 2001.  
 [17] R. L. Haupt and S. E. Haupt, *Practical Genetic Algorithms*. 2004, pp. 57–60.

# High-power sources of ultrawideband radiation pulses with elliptic polarization

*V. I. Koshelev, Yu. A. Andreev, A. M. Efremov, B. M. Kovalchuk, A. A. Petkun,*

*V. V. Plisko, K. N. Sukhushin, M. Yu. Zorkaltseva*

*Institute of High Current Electronics SB RAS  
2/3, Akademichesky Ave., Tomsk 634055, Russia  
[koshelev@lhfe.hcei.tsc.ru](mailto:koshelev@lhfe.hcei.tsc.ru)*

## Abstract

The paper generalizes the results of investigations of high-power sources of ultrawideband (UWB) radiation with elliptical polarization developed at the Institute of High Current Electronics. In the UWB sources, both single cylindrical and conical helical antennas and a 2×2 array were used. To increase the energy efficiency of the sources, the radiators were excited by bipolar voltage pulses. In the experiments, the bipolar voltage pulses of the amplitude 200 kV and length of 1 and 2 ns were used. At the pulse rate of 100 Hz, radiation pulses with effective potential of up to 300 kV and 440 kV were obtained for the sources with a single antenna and antenna array, respectively. Methods for estimation of the radiation center and the far-field boundary of the elliptically polarized electromagnetic field were suggested.

**Keywords:** Ultrawideband radiation, helical antennas, elliptic polarization, bipolar pulses.

## 1 Introduction

In recent years, intensive investigations and development of high-power UWB radiation sources with linear and elliptical polarization for solution of various problems have been carried out. Previously, at the Institute of High Current Electronics, we realized a program on the development of high-power UWB radiation sources with linear polarization based on the excitation of single combined antennas and multielement arrays (2×2, 4×4, and 8×8) by bipolar voltage pulses of the amplitude up to 200 kV and length of 0.25-3 ns. These experiments resulted in obtaining radiation pulses with the effective potential (the product of the peak electric field strength  $E_p$  by the distance  $r$  in the far-field zone) of 0.4-4.3 MV at the pulse rate of 100 Hz [1].

At the present time, our research team realizes the program on the development of high-power UWB radiation sources with elliptic polarization [2] based on the excitation of single helical antennas and antenna arrays by nanosecond bipolar pulses of the amplitude up to 200 kV. In all the experiments, a bipolar pulse generator consisting of the SINUS-160 monopolar pulse generator and open-circuit bipolar pulse former firstly suggested in [3] were used. The output impedance of the bipolar pulse generator was equal to 50 Ohm.

Helical antennas were used in the axial mode of radiation. The number of turns  $N$  in the antennas varied in the limits of 4-7. The antennas were made of a copper tube. To prevent the electrical breakdown, the antennas were placed into radiotransparent containers filled with SF<sub>6</sub>-gas at a gauge pressure of up to 2 atm. The performed investigations have shown that dielectric containers practically have no influence on the radiation characteristics.

To measure the radiation characteristics, it is necessary to know the position of the radiation center and the boundary of the far-field zone. To estimate the position of the radiation center, we suggested to use a criterium  $rE_p = \text{const}$ , and to estimate the boundary of the far-field zone, a criterium  $p = \text{const}$  is used, where  $p$  is the ellipticity coefficient or for its inverse value (axial ratio)  $AR = \text{const}$ .

## 2 UWB radiation sources with single antennas

Three high-power sources of UWB radiation based on the excitation of cylindrical helical antennas ( $N = 4$  and 4.5) by bipolar voltage pulses of the length

1 ns and 2 ns as well as of a conical helical antenna ( $N = 7$ ) excited by a bipolar voltage pulse of the length 1 ns have been developed and investigated. The amplitude of the bipolar pulses reached 200 kV. The energy efficiency of the radiators reached 0.8. The ellipticity coefficient of radiation was of 0.75-0.8 ( $AR = 1.3$ ). In the experiments, at a pulse repetition rate of 100 Hz, the radiation pulses with the effective potential of 250-300 kV were obtained at a continuous operation during 1 hour. The root-mean-square deviation of the field amplitude per 100 pulses was  $\sigma = 0.03-0.06$ . The boundary of the far-field zone determined by the suggested criteria was shown to be located at larger distances than at the evaluations using standard approaches.

### 3 Ultrawideband radiation source with a 4-element array

A high-power source of UWB radiation has been developed and investigated. The scheme of the source is the following: a monopolar pulse generator – a bipolar pulse former – a wave impedance transformer (50/12.5) – a 4-channel power divider – coaxial 50 Ohm cables with cord insulation filled with SF<sub>6</sub> gas at a gauge pressure of up to 4 atm – a square 2×2 array of cylindrical helical antennas ( $N=4.5$ ). The antennas were located on a metal plate at a 21-cm distance from each other. Bipolar voltage pulses of the length 1 ns and amplitude of 225 kV were applied to the input of the wave transformer. In the experiments, the radiation pulses with the effective potential of 440 kV and high stability ( $\sigma = 0.02-0.05$ ) at the pulse repetition rate of 100 Hz were obtained at a continuous operation during 1 hour. The ellipticity coefficient is 0.7 ( $AR = 1.4$ ). FWHM of the pattern by peak power is 30°. Using the suggested methods, the location of the array radiation center and the boundary of the far-field zone of the elliptically polarized radiation were estimated.

### Acknowledgements

The work was supported by the Basic Research Program of the Presidium of Russian Academy of Sciences “Fundamental problems of pulsed high-current electronics”.

### References

- [1] A. M. Efremov, V. I. Koshelev, B. M. Kovalchuk, V. V. Plisko, and K. N. Sukhushin. “Generation and radiation of ultra-wideband electromagnetic pulses with high stability and effective potential”, *Laser Part. Beams*, **32**, pp. 413-418, (2014).
- [2] Yu. A. Andreev, A. M. Efremov, V. I. Koshelev, B. M. Kovalchuk, A. A. Petkun, K. N. Sukhushin, and M. Yu. Zorkaltseva. “A source of high-power pulses of elliptically polarized ultrawideband radiation”, *Rev. Sci. Instrum.*, **85**, 104703, (2014).
- [3] Yu. A. Andreev, V. P. Gubanov, A. M. Efremov, V. I. Koshelev, S. D. Korovin, B. M. Kovalchuk, V. V. Kremnev, V. V. Plisko, A. S. Stepchenko, and K. N. Sukhushin. “High-power ultrawideband radiation source”, *Laser Part. Beams*, **21**, pp. 211-217, (2003).

# UWB HPEM generator with changeable pulse waveform for IEMI testing

Jin-Ho Shin\*, Young-Kyung Jeong\*, Dong-Gi Youn\*

\* Replex Co., Ltd, Republic of Korea and [hpett@replex.co.kr](mailto:hpett@replex.co.kr), [ykj@replex.co.kr](mailto:ykj@replex.co.kr), [ceo@replex.co.kr](mailto:ceo@replex.co.kr)

## Abstract

This paper presents UWB HPEM generator with changeable waveform for IEMI testing. Generally, for wide bandwidth and high power requirements, the systems use high voltage monopolar or bipolar pulse as antenna input. In order to satisfy various pulse waveform requirements above, the proposed pulse generator can produce  $338\text{kV}_p$  monopolar pulse or  $504\text{kV}_{p-p}$  bipolar pulse with controlling knob simply.

**Keywords:** UWB HPEM, High-power electromagnetic, Pulse forming, Tesla transformer

## 1 Introduction

UWB HPEM systems have bandwidth from several hundreds of MHz to several GHz and high peak power to be capable of IEMI testing. The pulse waveform of these systems can be selected which antenna is adopted or what frequency content is preferable [1][2]. In the interest of various pulse waveforms like these, the designed pulse generator has changeable pulse waveform function by mechanical structure. Pulse waveform can change easily by external control knob without depressurizing. This UWB HPEM generator with changeable pulse waveform can apply various types of antenna also investigate IEMI effect for different bandwidth or frequency content.

## 2 Measurement results

The UWB HPEM generator consists of power supply, high voltage (HV) generator and pulse forming line (PFL) and is shown in Fig. 1.

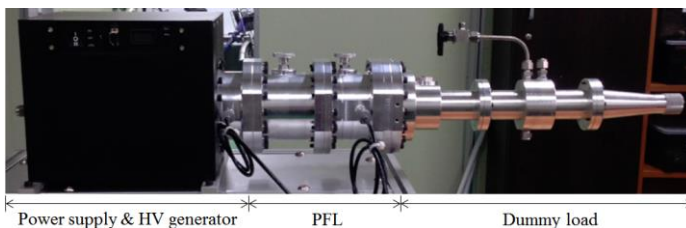


Figure 1. UWB HPEM generator.

Fig. 2 shows voltage spectral density versus frequency. Monopolar pulse has dominant voltage spectral density than

bipolar pulse below 800MHz. But bipolar pulse have more voltage spectral density than monopolar pulse from 800MHz to 5GHz.

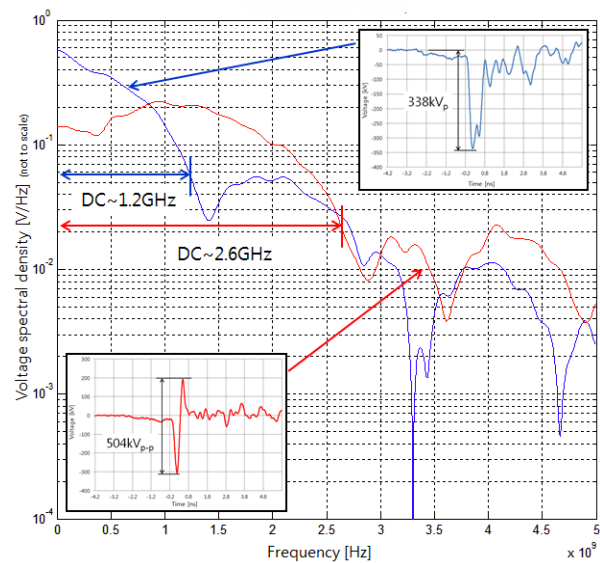


Figure 2. Frequency spectrum of pulses.

## 3 Conclusions

In this paper, the UWB HPEM generator with the proposed changeable pulse former was built. The generator can produce  $338\text{kV}_p$  monopolar or  $504\text{kV}_{p-p}$  bipolar pulse with compact size of  $53\text{cm} \times 23\text{cm} \times 20\text{cm}$  and  $21\text{kg}$  in weight. It is useful to develop UWB HPEM systems with various antenna and IEMI testing.

## References

- [1] Carl E. Baum et al. "JOLT: A Highly Directive, Very Intensive, Impulse-Like Radiator", AFRL-DE-PS-TR-2006-1073, pp. 32-33, (2006)
- [2] A.M. Efremov, V.I. Koshelev, B.M. Kovalchuk, V.V. Plisko, and K.N. Sukhushin. "Generation and radiation of ultra-wideband electromagnetic pulses with high stability and effective potential", Laser and Particle Beams, 32, pp. 413-418, (2014)

# Design of a Portable Rectangular Generator Based on MOSFET and Avalanche Transistor

QIAO Bing-bing, GUO Jie, LI Ke-lun

School of Electrical Engineering, Xi'an Jiaotong University, Xi'an, China  
binqiao1225@163.com

## Abstract

This paper describes a portable rectangular impulse generator based on MOSFET and serial connection of avalanche transistors. The characteristics of power MOSFET and avalanche transistor, and co-operation between them are studied. Then the compact circuit is designed. A rectangular impulse with amplitude over 1kV is acquired, with a few hundreds of nanoseconds rising time and less than 8ns fall time. The device is tested on capacitive load less than 300pF and resistive load greater than 3kΩ.

**Keywords:** rectangular impulse generator, electronic circuit; power MOSFET; avalanche transistor; nanosecond fall time

## 1 Introduction

With the development of electromagnetic pulse technology, impulse bandwidth concerned recently is much wider, such as nuclear electromagnetic pulse, electro-static discharge and electromagnetic pulse caused by lightning or switching operation [1-2]. Voltage transducer is used to measure the voltage impulse. The transducer should have a good high-frequency response characteristics to insure the measurement results are accurate and reliable. Thus it is necessary to calibrate high-frequency response characteristics of the transducer, and other capacitive or resistive load. Rectangular impulse voltage generator is used widely to calibrate high-frequency response characteristics of transducers [3-4].

There are kinds of impulse voltage generators like spark gap rectangular impulse generator which can output rectangular impulse with high amplitude and fast rising time, but the device is often ponderous and operated complicatedly. Recently many scholars do some research on impulse generator based on solid-state switch mainly include power MOSFET, IGBT and avalanche transistor, instead of spark gap switch. The rectangular impulse generated by MOSFET and IGBT impulse generator has slow slope, because of its relatively slow switching speed compared with avalanche transistor. Impulse generator based on only avalanche transistor can only output narrow-width rectangular impulse, restricted by its current capacity. The portable rectangular impulse generator proposed in this paper, fully integrating power MOSFET's heavy current capacity and avalanche transistor's fast switching speed [5-6]. So that the generator can output rectangular impulse with amplitude over 1kV and less than 8ns fall time. The generator can be used to calibrate

high-frequency response characteristics of voltage transducer, and other capacitive load, resistive load and RC load (parallel connect).

## 2 The Circuit Design and Implementation

Figure 1 shows the design scheme of the rectangular impulse generator based on power MOSFET and serial connection of avalanche transistors. It consists of the following several parts: 1) high voltage direct current source and energy storage capacitor; 2) the trigger and pulse width regulating circuit; 3) the rectangular impulse rising edge circuit, consisting of power MOSFET and its optical isolation drive circuit; 4) the rectangular impulse falling edge circuit, consisting of power MOSFET and serial connection of avalanche transistors circuit. We make the MOSFET  $T_b$  and serial connection of avalanche transistors be triggered and turned on synchronously by using the same trigger circuit. The pulse width can be changed from hundreds of nanoseconds to hundreds of microseconds continuously, and the fall time is several nanoseconds.

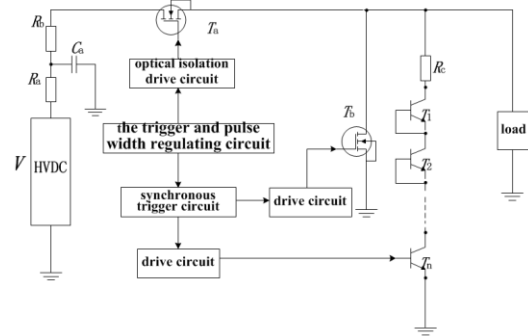


Figure 1 Design scheme of the rectangular impulse generator

In the figure:  $V$  - high voltage direct current source;  
 $R_a$  - charging resistance;  
 $C_a$  - energy storage capacitor;  
 $R_b, R_c$  - damping resistance;  
 $T_a, T_b$  - MOSFET in the rising edge circuit and falling edge circuit;  
 $T_1, T_2, \dots, T_n$  - avalanche transistor;

The rectangular impulse rise and fall time are usually several tens or hundreds of nanoseconds from generator only based on MOSFET, and the pulse width is more than the load's response stability time. At the fall time, the serial connection of avalanche transistors truncates the fall time of MOSFET circuit. Thus, the fall time is shorted from  $t_{f2}$  (several tens or hundreds of nanoseconds) to  $t_{f1}$  (several nanoseconds). Figure 2 shows the rectangular impulse fall

time shorten from  $t_{f2}$  to  $t_{f1}$ . The circuit can solve the problem of MOSFET's slow switching speed and deficiency of avalanche transistor's current capacity. Meanwhile the MOSFET  $T_b$  keeps on continuously to stabilize the voltage at about 0V after the rectangular falling edge.

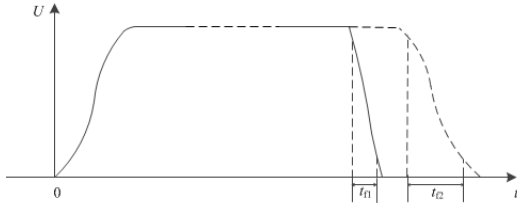


Figure 2 Schematic drawing of rectangular impulse

### 2.1 The Rising Edge Circuit

The damping resistance  $R_b$  can restrain oscillation at the rising edge. Meanwhile it can prevent the storage capacitor from recharging the load after the impulse, as the MOSFET  $T_a$  can't be turned off within several nanoseconds. Figure 3 shows the actual measured rising edge impulse, with RC load parallel connected with a resistor 5 kΩ and a capacitor 100pF. The rising time is several hundreds of nanoseconds read from the figure.

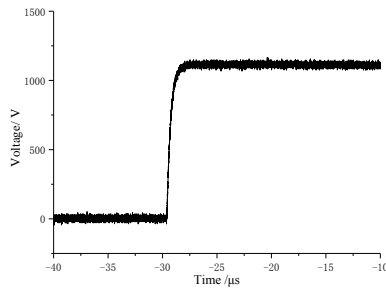


Figure 3 Actual measured rising edge impulse

### 2.2 The Falling Edge Circuit

#### a) Avalanche transistor

The circuit chooses ZETEX FM417 NPN silicon planar bipolar transistors. FM417 has small volume in SOT23-package, with low collector-emitter inductance of 2.5nH. Its second breakdown region is wide, from 100V to 320V, and current capacity is relatively heavy. It is found that the dispersion of breakdown voltage between different transistors is large, by testing each transistor in the laboratory. We choose those in the same batch showing good consistency and wide breakdown region, collector-base breakdown voltage  $V_{CBO}>320V$  and collector-emitter breakdown voltage  $V_{CEO}<160V$ , to insure all the transistors turn to second breakdown state synchronously.

#### b) Voltage sharing of the series connected transistors

There are three avalanche operating modes, triggered, overvoltage and fast rising voltage between collector and emitter [7]. Due to the fast rising edge of rectangular impulse depended by the power MOSFET's switching time, the shortest rising time on the load is within a hundred

nanoseconds. The voltage impulse steepness on avalanche transistor collector-emitter is large enough to cause it to turn on. Besides, there exists difference between collector-emitter impedance of different transistors and stray capacitance in the circuit. Under much steeper voltage than rated value some avalanche transistors, and even the whole transistors will turn. It can make the rectangular impulse fail and even burn out the transistors.

To solve the problem, there are two following aspects. One is placing the damping resistance  $R_b$  introduced above, to lengthen the rising time. It can decrease the current and prevent transistors from damaged when the circuit failed. Another is placing equalizing capacitors and resistances to balance the voltage on each transistor showed as Figure 4. Equalizing capacitors and resistances are surface mounted devices and use compactly layout structure to reduce the circuit volume and stray parameters. Theoretical Analysis and experimental results show that in the rise time of rectangular impulse, the voltage value on each avalanche is related to collector-emitter capacitance and affected by stray capacitance. When the rectangular impulse voltage is stable, the voltage value on each avalanche depends on the equalizing resistances. Figure 5 shows the rising edge waveform of each transistor after choosing suitable equalizing capacitors and resistances.

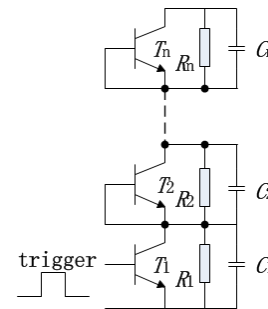


Figure 4 Schematic of equalizing circuit

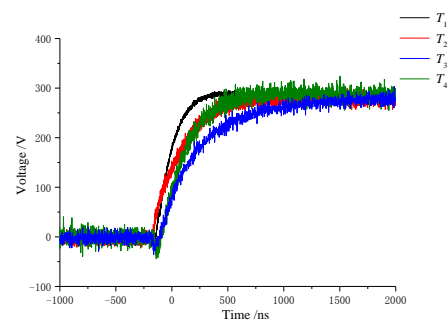


Figure 5 Rising edge waveform of each transistor

#### c) Test results

Figure 6 shows the falling edge waveform of rectangular impulse at the output terminal when the RC load is parallel connected with a resistor and a capacitor (capacitance 100pF and resistance 10kΩ ). The measuring instruments are Tektronix DPO4032 oscilloscope with 350MHz bandwidth and Lecroy PPE4kV high voltage probe with 400MHz bandwidth. It indicates the rectangular impulse with amplitude over 1kV and falling time of 5.9ns.

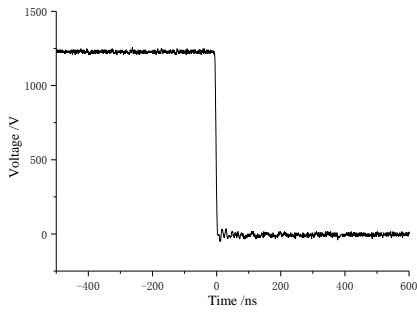


Figure 6 Actual measured falling edge at the output terminal

### 3 Results

The voltage can keep at 0V stably after falling edge through controlling avalanche transistors and power MOSFET  $T_b$  to operate synchronously, and turning off the MOSFET  $T_a$  in the rising edge circuit timely. Pulse waveforms are measured with different loads. The results show that fall time (10%~90%) is less than 8ns and amplitude is over 1kV, with a RC load parallel connected with the resistor and capacitor (capacitance less than 300pF, and resistance load greater than 3k $\Omega$ ), or a single capacitive load or resistive load. The rise time is hundreds of nanoseconds, and the pulse width can range from hundreds of nanoseconds to hundreds of microseconds continuously.

Figure 7 shows an actual measured waveform of rectangular impulse at the output terminal, with capacitive load 200pF. It can be seen that fall time is 7.2ns.

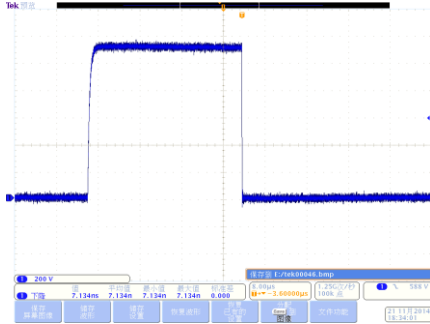


Figure 7 Actual measured waveform of rectangular impulse at the output terminal

### 4. Conclusion

By designing a portable rectangular impulse generator based on MOSFET and serial connection of avalanche transistors, the following conclusion can be drawn.

1) Solid-state switch avalanche transistor and power MOSFET is used to replace the spark gap switch to design a compact and portable rectangle impulse generator with all devices electronic;

2) In the synchronous trigger circuit, the MOSFET and serial connection of avalanche transistors can be triggered and switch on synchronously. The circuit can solve the problem of MOSFET's slow switching speed and deficiency of avalanche transistor's current capacity. Thus, it can output rectangle

impulse with several nanoseconds fall time.

3) Use compactly layout structure to reduce the circuit volume and stray parameters, and choose suitable equalizing capacitors and resistances. Voltage on each avalanche transistor is basically identical at the rising edge of the rectangle impulse, which can avoid avalanche transistors operating incorrectly.

### Acknowledgements

We are grateful to professor Ding Wei-dong for guidance and many suggestions. We also express gratitude to Zhong Xu for providing the high-voltage attenuator probe and advice in the electronic circuit design. Thank you for your instructions and help.

### References

- [1] ZHOU Bi-hua, CHEN Bin, SHI Li-hua et al. EMP and EMP Protection[M]. Beijing, National Defence Industry Press, 2003, pp. 99-104.
- [2] Tesche F M, Barnes P R. A multi-conductor model for determining the response of power transmission and distribution lines to a high altitude electromagnetic pulse (HEMP)[J]. Power Engineering Review, IEEE, 1989, 9(7): 82-82.
- [3] MA Guo-ming, LI Cheng-rong, QUAN Jiang-tao et al. Portable High Voltage Square Generator for Calibrating Voltage Divider[J], High Voltage and Insulation Technology, 2008 pp, 1479-1484
- [4] ZHANG Ren-yu, CHEN Chang-yu, WANG Chang-chang et al. High-voltage Testing Technology[M], Beijing, Tsinghua University Press, 2003, pp 131-166.
- [5] Chakera J A, Naik P A, Kumbhare S R, et al. A VARIABLE NANO-SECOND PULSE DURATION LASER PULSE SLICER BASED ON HIGH-VOLTAGE AVALANCHE TRANSISTOR SWITCH[J]. Journal of the Indian Institute of Sciences, 1996, 76(2): pp 273-278.
- [6] Davis S.J, Murray J.E, Downs D.C, et al. High performance avalanche transistor switch out for external pulse selection at 1.06  $\mu\text{m}$ [J]. Applied Optics, 1978, 17(19), pp 3184-3186.
- [7] Oldham W G, Samuelson R R, Antognetti P. Triggering Phenomena in Avalanche Diodes[J]. IEEE Transactions on Electron Devices, 1972, 19 (9), pp 1056-1060.

# Frequency, Time, and Thermal Domain Analysis of Planar Bi-Directional Log-Periodic Antenna

J. Ha, M.A. Elmansouri, and D.S. Filipovic

Department of Electrical, Computer, and Energy Engineering  
University of Colorado, Boulder  
Boulder, CO, USA

{Jaegeun.Ha, Mohamed.Elmansouri, Dejan.Filipovic}@Colorado.EDU

## Abstract

Planar bi-directional log-periodic (LP) antennas with different design parameters are analysed in frequency, time, and thermal domains to assess their possible use in high power short pulse applications. The boom of an LP arm is widened by moving its virtual apex into the next arm. This modification provides wide-enough ground plane for the microstrip feed line and results in improved impedance match and gain. The effect of the boom width is also analysed in thermal domain using linked electro-thermal multiphysics simulation. Results show that the widened boom reduces the maximum temperature developed on the antenna. The effect of LP growth rate is also studied. In time domain, the small growth rate mitigates the inherent dispersive characteristic of the LP antenna, while frequency domain performance is somewhat sacrificed. Moreover, the small growth rate can relieve the undesirable temperature peaks in thermal domain, thus making the planar LP antenna an attractive candidate for high power short pulse applications requiring a bi-directional radiator.

**Keywords:** Electro-thermal multiphysics, log-periodic antennas, time domain antennas

## 1 Introduction

It is a commonly accepted belief that the log-periodic (LP) antennas are highly dispersive, therefore they are usually not considered for short pulse systems despite the good frequency domain (FD) performance. To mitigate the dispersion, pre-distortion of the input pulse [1], metamaterial phase shifter between radiating elements [2], and a small growth rate [3] have been considered. Small growth rate offers the simplest method, though the gain and pattern are somewhat compromised. In addition, the power handling capability of planar LP antennas is generally low, but more importantly, there is a lack of understanding of their thermal behaviour. Recent developments of multiphysics simulation tools enable engineers to reliably analyse electromagnetic, thermal, and mechanical characteristics of antennas and other components.

In this paper, a planar bi-directional LP antenna fed by a microstrip impedance transformer is analysed in frequency, time, and thermal domain. A modification of a conventional

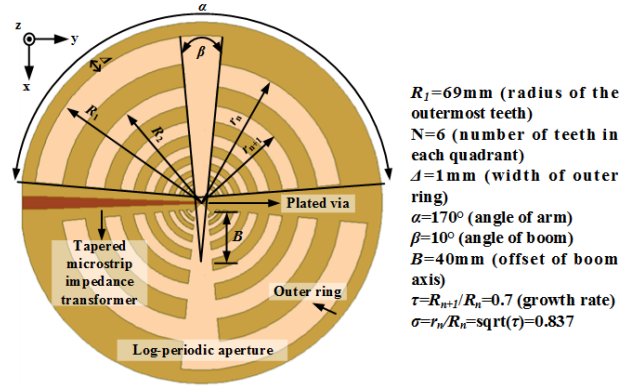


Figure 1. Geometry of the wide-boom log-periodic aperture and its parameters.

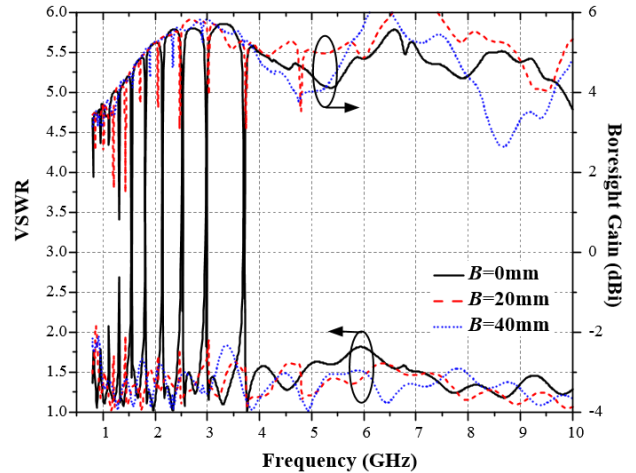


Figure 2. VSWR and gain for various values of  $B$ .

planar LP aperture is proposed and effects on impedance, gain, and temperature are determined. To improve the time domain (TD) performance, the growth rate is reduced resulting in a significant improvement in thermal domain.

## 2 Effect of Boom Width

Fig. 1 shows the proposed wide-boom LP antenna implemented on a 1.524 mm RO3003 substrate ( $\epsilon_r = 3$ ,  $\tan\delta = 0.001$ ). The planar LP aperture is printed on top and the linearly tapered (3.79 mm to 0.4 mm) microstrip impedance

Table 1: Thermal characteristics of used materials.

	Rogers3003	Copper
Conductivity $K_T$ (W/°K/m)	0.5	401.0
Specific Heat $C_p$ (J/°K/kg)	900	390
Diffusivity $a$ (m <sup>2</sup> /s)	2.65e-7	1.15e-4
Density $\rho$ (kg/m <sup>3</sup> )	2100	8930
Thickness (mm)	1.524	0.07

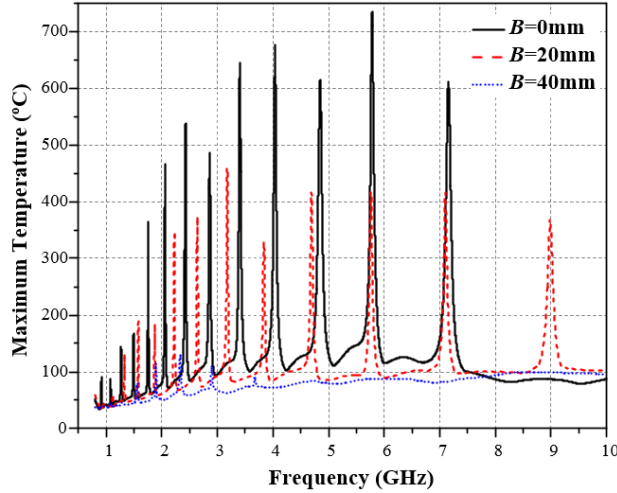


Figure 3. Maximum temperature rise of the antenna fed by 100 W CW input for various  $B$ .

transformer is on the bottom of the substrate. The feeding microstrip line is connected to the right arm of the LP aperture through a plated via. The boom of the left arm functions as a ground plane for the microstrip line. The boom angle  $\beta$  is fixed at  $10^\circ$  in order to lower the turn-on frequency [3]. However, the smaller boom angle gives rise to a narrow ground plane for the microstrip line, especially around the centre, in which the line impedance becomes higher than it is designed for. To provide wide ground plane while keeping small boom angle, axis of the boom (fan-shaped) is offset by 20 mm. Fig. 2 shows the effect of the offset distance  $B$  in impedance match and gain. The simulation is performed in Ansys HFSS 2014. As seen, VSWR of the microstrip-fed LP antenna is improved as  $B$  increases because the wider boom enables stable characteristic impedance. Not only the impedance match is improved, but also the gain and overall pattern performances are enhanced with the wider boom. This is because the widening reduces the radiation loss associated with the leaking the guided wave on the transmission line into the teeth before the feed via.

The simulated field data in HFSS are used to calculate the RF heat generation in the antenna that are mainly composed of conduction and dielectric losses as given in Equation (1).

$$Q = \frac{1}{2\sigma} |\vec{J}_s|^2 + \frac{\omega}{2} \epsilon'' |\vec{E}|^2. \quad (1)$$

The generated RF heat is imported into Ansys Mechanics thermal solver and the temperature distribution of the antenna

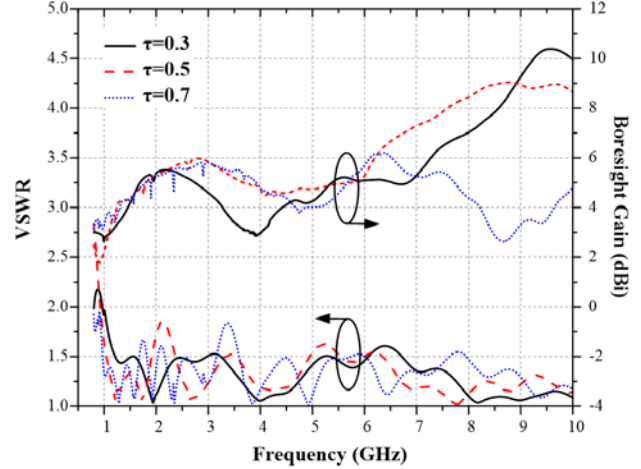


Figure 4. VSWR and boresight gain of the LP antenna for different growth rate  $\tau$ .

is obtained based on the Fourier heat conduction equation and the Newton's law of cooling as given in Equations (2) and (3), respectively.

$$\frac{\partial T}{\partial t} = \alpha \nabla^2 T + Q / \rho C_p. \quad (2)$$

$$Q_s = hA(T - T_0). \quad (3)$$

The ambient temperature  $T_0$  and the convection coefficient  $h$  are assumed to be  $20^\circ\text{C}$  and  $10 \text{ W/m}^2 \cdot ^\circ\text{C}$ , respectively. The thermal properties of the used substrate and metallic trace are summarised in Table 1. Fig. 3 shows the maximum steady-state temperature in the antenna structure for various  $B$  for RF source power of 100 W CW at each frequency. As seen, the maximum temperature is decreased as  $B$  increases because wider boom provides larger area for efficient heat transfer through convection and conduction. In addition, it is interesting to note that there are multiple temperature peaks that follow the LP growth of the antenna. In fact, these temperature peaks coincide with resonant frequencies of each LP teeth pair (not shown here). At the resonant frequencies, strong electric field and current density are formed at the active teeth which brings about higher dielectric and conduction losses to cause hot spots in the active region. The effect of the boom width on the TD performance is insignificant.

### 3 Effect of Growth Rate

Although the frequency domain and thermal domain performances improved by increasing the boom width, the LP antenna shown in Fig. 1 is not appropriate for short pulse applications due to the highly dispersive characteristic. Thus, simply decreasing the growth rate of LP antenna is considered to alleviate the TD dispersion. VSWR and boresight gain of the antenna with  $B = 40 \text{ mm}$  and growth rate  $\tau = 0.3, 0.5$ , and  $0.7$  are shown in Fig. 4. The number of teeth in each quadrant  $N$  is 2, 3, and 6, respectively. VSWR is not much affected, but gain at high frequencies is decreased as growth rate decreases.

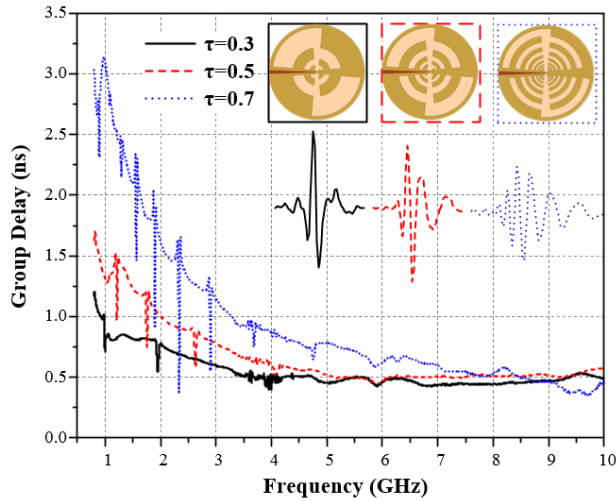


**Figure 5. Group delay and boresight radiated pulse shape in time domain for different growth rate.**

In addition, the antenna performance in TD for various growth rates is studied. To perform the TD analysis, the transfer function of the antenna is synthesized using the simulated field data [4]. The calculated transfer function is used to obtain output pulse spectrum by multiplying with input pulse spectrum. Then the pulse spectrums in FD are used to obtain the TD pulse response by applying the inverse fast Fourier transform. The group delay is obtained from the derivative of the unwrapped phase of the transfer function. The group delay and output pulse shape in TD are computed for the LP antennas having growth rates of 0.3, 0.5, and 0.7. Obtained results are shown in Fig. 5. The second derivative of Gaussian pulse with 10dB spectrum from 0.9 GHz to 10 GHz is used as input pulse. As clearly seen, the group delay of the LP antenna is improved by decreasing the growth rate since the effective path lengths of the travelling currents to the radiating region are decreased especially at low frequencies. Consequently, the output pulse shape shown in the insets is improved as growth rate decreases. The fidelity factors of each radiated pulse are 91%, 79%, and 70% for the corresponding growth rates of 0.3, 0.5, and 0.7.

The thermal performance of the antenna for each growth rate is also evaluated. Fig. 6 shows the maximum temperature of the LP antenna for various growth rates. It is demonstrated that the small growth rate can improve the thermal performance as well and the high peak temperature is removed. This is because the smaller growth rate provides wider radiating teeth, thus increased surface area for the efficient cooling through convection and conduction.

#### 4 Conclusion

In this paper, frequency, time, and thermal domain analysis on a microstrip-fed log-periodic antenna was performed. The offset of boom axis gives wider boom and stable ground plane for the feed line, so that the impedance match and gain characteristics of antenna in FD are improved. Additionally, maximum temperature of the LP antenna is decreased owing

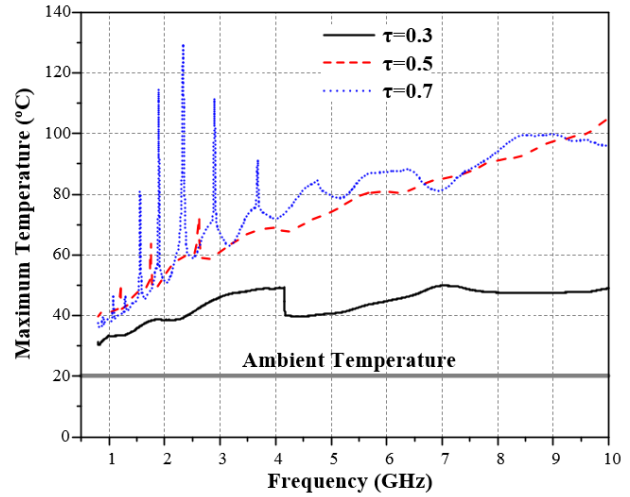


**Figure 6. Maximum temperature of the antenna fed by 100 W CW source for various LP growth rate  $\tau$ .**

to the wider area for efficient heat convection and conduction. To improve the TD performance, study on the growth rate was carried out. In FD, the gain at high frequencies is compromised for smaller growth rate; however, improved time and thermal domain performances are achieved. Therefore, the planar LP antenna with wide-boom and small growth rate may be used as a bi-directional radiator for electronic warfare and/or long distance relay communication link using high power short pulse signal.

#### Acknowledgements

This work was funded by the Office of Naval Research Award #N00014-13-1-0537.

#### References

- [1] S. Gupta and C. Caloz, "Dispersion-Compensation Technique for Log-Periodic Antennas using C-section All-Pass Dispersive Delay Structures," in *Proc. IEEE Int. Symp. Antennas Propag. (ISAP)*, Jeju, Rep. Korea, (2011).
- [2] R.W. Ziolkowski and P. Jin, "Metamaterial-Based Dispersion Engineering to Achieve High Fidelity Output Pulses From a Log-Periodic Dipole Array," *IEEE Trans. Antennas Propag.*, vol. 56, pp. 3619-3629, (2008).
- [3] M.A. Elmansouri, R. Sammeta, and D.S. Filipović, "Joint Frequency- and Time-Domain Characterization of Planar Log-Periodic Antennas," in *Proc. IEEE Antennas Propag. Soc. Int. Symp. (APSURSI)*, Memphis, TN, (2014).
- [4] C. Roblin, "Representation, Characterization, and Modelling of Ultra Wide Band Antennas," *Ultra Wide Band Antennas*, NJ: John Wiley, (2011).

# A Compact Relativistic Magnetron with an Axial Output of TE<sub>11</sub> Mode

Di-Fu Shi, Bao-Liang Qian\*, Yi Yin, Hong-Gang Wang, and Wei Li

College of Optoelectric Science and Engineering, National University of Defense Technology, Changsha, Hunan 410073, P. R. China (\*Corresponding author, email: blqian@163.com)

## Abstract

A compact relativistic magnetron with an axial output of TE<sub>11</sub> mode is proposed, and the magnetron operating in the  $\pi$ -mode can radiate axially with a TE<sub>11</sub> mode through a cylindrical waveguide which is designed to match with the anode. This design, on one hand, makes both the diameter and the axial length of the magnetron minimized, so that the volume and weight of the coils of the applied magnetic field and the distance between the electron dump and the anode block can be reduced. On the other hand, it provides a much purer radiated mode in the output waveguide as a result of the limit to the dimension of the output waveguide for a certain frequency. In three-dimensional particle-in-cell (PIC) simulation, the power conversion efficiency can reach 21.9%, corresponding to the output power of 247.0 MW and the resonant frequency of 4.18 GHz, under the condition of the applied voltage of 280 kV and the applied magnetic field of 0.5 T.

**Keywords:** high power microwave; relativistic magnetron; compactness; axial output; TE<sub>11</sub> mode.

## 1 Introduction

High power microwave (HPM) sources with a Gaussian radiation pattern are required for many commercial and military applications for example, in high power radar systems, super interference machine, excitation of gas lasers, heating of plasmas in fusion reactors and so on. And at present, with the development of the HPM sources, reducing size and weight of a system and improving its performances have become one of the development directions for future HPM sources. Thus, it is of great realistic significance to investigating the compact HPM sources with the TE<sub>11</sub> radiated mode for high efficient radiation antenna. The relativistic magnetron (RM), for its simple structure, high-power capability, suitable application for long pulse, and high pulse repetition rate, as well as its tunability, has become one of the most promising devices of high power microwave sources [1]. In recent years, The RMs have been explored extensively, including transparent cathode [2-4], electric or magnetic priming [5-9], axial diffraction output [10-14], compactness [15-17], and so on. And more and more attention also has been attracted to a compact RM radiating with the TE<sub>11</sub> radiated mode. In 2012, a compact A6 RM was proposed which operated in the  $\pi$ -mode and whose radiation

was extracted axially as a TE<sub>11</sub> mode through a cylindrical waveguide with the same cross section as that of the anode block, although with reduced efficiency (approximately 14%) [15].

In this paper, we describe a compact A6 RM with an axial output of TE<sub>11</sub> mode and an acceptable efficiency (about 21.9 %). The magnetron operates in the  $\pi$ -mode, and its radiation can be extracted as a TE<sub>11</sub> mode axially through a cylindrical waveguide which is designed to match radially with the anode. This configuration has several advantages. Firstly, the magnetron of this structure can reduce both the diameter and the axial length of the magnetron, and therefore reduce the volume and weight of the coils of the applied magnetic field and the distance between the electron dump and the anode block. Secondly, the axial magnetic field created by the Helmholtz coils proposed in this paper can be distributed more uniformly in the interaction space, so that the beam-wave interaction can proceed more sufficiently and effectively. Thirdly, as a result of the limit to the dimension of the output waveguide for a certain frequency, such a simple output structure can provide a much purer radiated mode.

## 2 Simulation Model

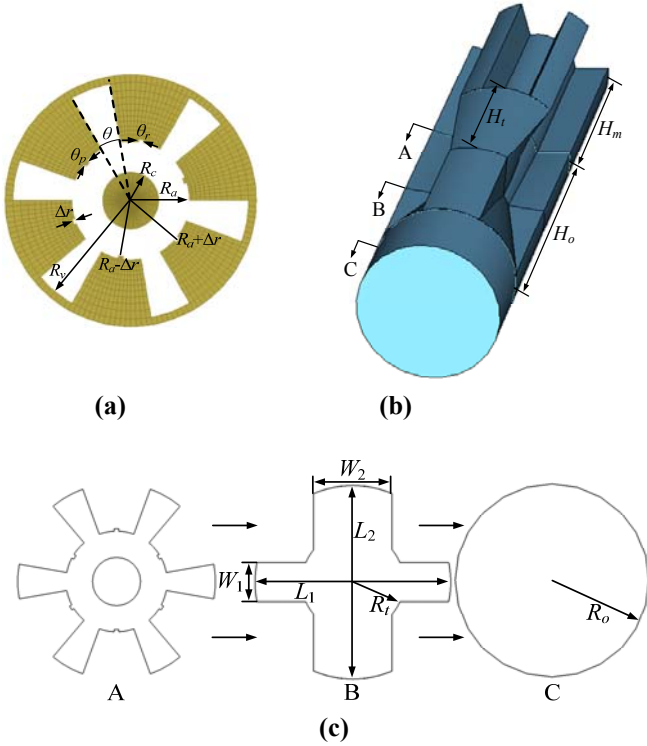
The software of three-dimensional fully electromagnetic and particle-in-cell (PIC) code CHIPIC and the software of CST Studio Suite are both utilized to investigate the model of the compact relativistic magnetron with an axial output of TE<sub>11</sub> mode, as shown in Fig.1. In addition, the modified structure of the well-known A6 magnetron [19] and the structure of protrusions and recessions on the inner surface of anode vanes [5] for reducing the start-up time are adopted in the simulation, as seen in Fig.1(a).

Figure 1(a) shows the schematic diagram of the horizontal cross section of the A6 magnetron with three protrusions, alternating with three recessions. The structure of the magnetron consists of 6 sectorial cavities with height  $H_m=72.0$  mm and angle  $\theta=20^\circ$ . The radii of the cathode, the anode, and the cavities are  $R_c=5.0$  mm,  $R_a=13.0$  mm, and  $R_v=25.0$  mm, respectively. The angular width of the protrusions and recessions are  $\theta_p=5^\circ$  and  $\theta_r=5^\circ$ , respectively. The protrusion and recession radii are  $(R_a - \Delta r)=12.0$  mm and  $(R_a + \Delta r)=14.0$  mm, respectively, where the radial variation  $\Delta r=1.0$  mm is the same as that if the protrusion and the recession.

Figure 1(b) shows the 3D view of the model. Figure 1(c) shows the conversion of the horizontal cross section of the

device along the axial direction. At the end of the A6 magnetron along the axial direction, two diametrically opposite cavities are gradually changed to an approximately rectangular waveguide with length  $L_1=50.0$  mm and width  $W_1=10.0$  mm. In the rest of the cavities, every two neighbouring cavities are gradually changed to an approximately rectangular waveguide with length  $L_2=50.0$  mm and width  $W_2=20.0$  mm. And the interaction space of the magnetron is gradually changed to a cylindrical waveguide with radius  $R_i=13.0$  mm. In addition, all the three transition sections mentioned above are of the same height  $H_i=50.0$  mm. Then the cylindrical waveguide with radius  $R_i=13.0$  mm is gradually changed to the next cylindrical waveguide with radius  $R_o=25.0$  mm, while the other two approximately rectangular waveguides keep their shape and size along the axial direction. The distance between the A6 magnetron and the cylindrical waveguide with radius  $R_o=25.0$  mm is  $H_o=100.0$  mm.

In our simulations, the applied voltage has a rise time of 3 ns after which it maintained a constant amplitude of 280 kV for a duration of 40 ns, and the applied axial magnetic field created by Helmholtz coils for interaction region is 0.5 T.



**Figure 1. (a) Schematic diagram of the horizontal cross section of the A6 magnetron with three protrusions alternating and three recessions. (b) 3D view of the whole inner space of the device. (c) Conversion of the horizontal cross section of the device along the axial direction.**

### 3 Simulation Results

According to the model described in Section 2, the performance of the compact relativistic magnetron with an axial output of  $TE_{11}$  mode is investigated by the software of

3D PIC, CHIPIC, and Fig.2 and Fig.3 give the simulation results.

Figure 2(a) indicates that the input electron beam power maintains a constant amplitude of 1.13 GW after 20 ns. Figure 2(b) indicates that the output microwave power of 247.0 MW reaches to saturation at 20 ns, corresponding to a power conversion efficiency of 21.9%. It takes a little long time for both the input power and output power to start up, because the electron spokes in the A6 magnetron have three azimuthally symmetric periods while the  $TE_{11}$  radiated mode in the cylindrical waveguide has one azimuthally symmetric period, and this contradiction is not helpful to reduce the start-up time. However, we believe that further design and optimization could reduce the start-up time and increase the power conversion efficiency.

Figure 2(c) shows the spectrum of the electric field in the resonant cavity from 0 to 40 ns, and at least it consists of the frequency of the fundamental harmonic of  $\pi$  mode,  $f_\pi$ , and the frequency of the 2nd harmonic of  $\pi$  mode,  $2f_\pi$ . The frequency of fundamental harmonic of  $\pi$  mode,  $f_\pi$ , as the main operating frequency is 4.18 GHz, which is higher than the cutoff frequency (3.52 GHz) of the  $TE_{11}$  mode in the cylindrical waveguide. This condition guarantees that the microwave of 4.18 GHz could propagate in this device. In addition, higher order harmonics with competing modes may cause the impurity of the radiated mode in the cylindrical waveguide, but the fundamental harmonic of  $\pi$  mode with the largest growth rate can eventually dominate. It indicates that the resonant system of the magnetron could operate in the  $\pi$  mode properly as expected, and better results may be obtained by further optimization. Figure 2(d) indicates that the radiated mode in the output port is  $TE_{11}$  mode, which is the lowest order mode in the cylindrical waveguide.

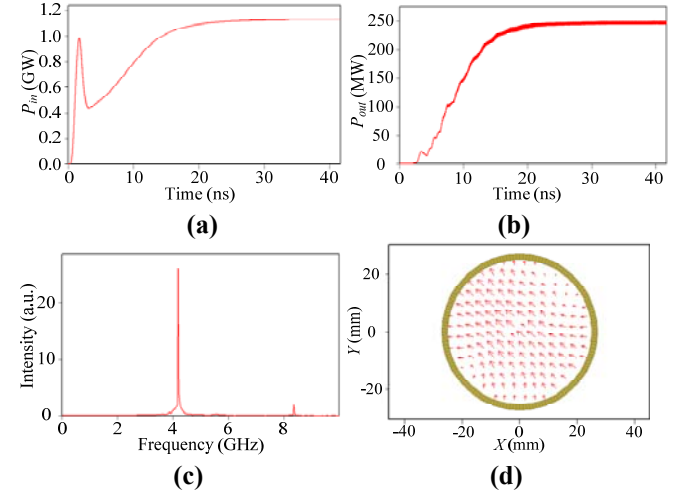


**Figure 2. (a) Input electron beam power versus time. (b) Output microwave power versus time. (c) Spectrum of electric field in resonant cavity from 0 to 40 ns. (d) Radiated mode  $TE_{11}$  in the output port.**

Compared with the magnetron of diffraction output (MDO), the magnetron of this paper can reduce the dimension of the output port, and therefore reduce the volume and weight of the coils of the applied magnetic field, and also reduce the distance between the electron dump and the anode block, so

that both the diameter and the axial length of the magnetron can be minimized. In addition, since the output structure of this compact magnetron has a cylindrical shell with the same cross section as that of the anode block, it is more convenient for the Helmholtz coils to wrap around the body of the magnetron and the axial magnetic field created by this kind of Helmholtz coils can be distributed more uniformly in the interaction region, so that the beam-wave interaction can proceed more sufficiently and effectively. Such a simple output structure investigated in this paper is able to guarantee that only the  $TE_{11}$  mode can propagate in the cylindrical waveguide for the dominant frequency of fundamental harmonic of  $\pi$  mode ( $f_{\pi}=4.18$  GHz), although higher order harmonics of  $\pi$  mode may have some influence on the purity of the radiated mode.

#### 4 Conclusion

In conclusion, a compact relativistic magnetron with an axial output of  $TE_{11}$  mode is proposed in this paper. The magnetron operating in the  $\pi$ -mode can radiate axially with a  $TE_{11}$  mode through a cylindrical waveguide which is designed to match with the anode. This design not only makes both the diameter and the axial length of the magnetron minimized, but also provides a much purer radiated mode in the output waveguide, and the magnetron can operate with acceptable efficiency (about 21.9%), although we think some performances of the magnetron need to be further improved, such as reducing the start-up time of microwave, reducing the leakage electrons from the interaction region, suppressing the undesired modes and increasing the power conversion efficiency.

#### References

- [1] J. Benford, J. Swegle, and E. Schamiloglu, "High-Power Microwaves 2nd ed." (*Artech House, Norwood, MA*, 2006), Chap. 7, pp. 259-320.
- [2] M. Fuks, S. Prasad, and E. Schamiloglu, "Increased efficiency and faster turn-on in magnetrons using the transparent cathode," in *Proc. Int. Conf. CAVMAG*, 2010, pp. 76–81.
- [3] E. Schamiloglu and M. I. Fuks, "The transparent cathode: Rejuvenator of magnetrons and inspiration for new RF sources," in *Proc. IET Conf. High Power RF Technol.*, 2009, pp. 1–5.
- [4] M. I. Fuks and E. Schamiloglu, "70% efficient relativistic magnetron with axial extraction of radiation through a horn antenna," *IEEE Trans. Plasma Sci.*, vol. **38**, no. 6, pp. 1302–1312, Jun. 2010.
- [5] J. I. Kim, J. H. Won, and G. S. Park, "Electron prebunching in microwave magnetron by electric priming using anode shape modification," *Appl. Phys. Lett.*, vol. **86**, no. 17, pp. 171501-1–171501-3, Apr. 2005.
- [6] V. B. Baiburin and K. V. Kaminskii, "Effect of an azimuthally varying magnetic field on the noise level in a multicavity magnetron," *Tech. Phys. Lett.*, vol. **35**, no. 6, pp. 582–584, Jun. 2009.
- [7] V. B. Neculaes, M. C. Jones, R. M. Gilgenbach, Y. Y. Lau, J. W. Luginsland, B. W. Hoff, W. M. White, N. M. Jordan, P. Pengvanich, Y. Hidaka, and H. L. Bosman, "Magnetic priming effects on noise, startup, and mode competition in magnetrons," *IEEE Trans. Plasma Sci.*, vol. **33**, no. 1, pp. 94–101, Feb. 2005.
- [8] B. W. Hoff, R. M. Gilgenbach, N. M. Jordan, Y. Y. Lau, E. J. Cruz, D. M. French, M. R. Gomez, J. C. Zier, T. A. Spencer, and D. Price, "Magnetic priming at the cathode of a relativistic magnetron," *IEEE Trans. Plasma Sci.*, vol. **36**, no. 3, pp. 710–717, Jun. 2008.
- [9] Shivendra Maurya, V. V. P. Singh, and P. K. Jain, "Three-Dimensional Particle-in-Cell Simulation of Fast Oscillation Startup and Efficiency Improvement in a Relativistic Magnetron With Electric Priming," *IEEE Trans. Plasma Sci.*, vol. **40**, no. 10, pp. 2686–2692, Oct. 2012.
- [10] M. I. Fuks, N. F. Kovalev, A. D. Andreev, and E. Schamiloglu, "Mode conversion in a magnetron with axial extraction of radiation," *IEEE Trans. Plasma Sci.*, vol. **34**, no. 3, pp. 620–626, Jun. 2006.
- [11] M. Daimon and W. Jiang, "Modified configuration of relativistic magnetron with diffraction output for efficiency improvement," *Appl. Phys. Lett.*, vol. **91**, no. 19, pp. 191 503-1–191 503-3, Nov. 2007.
- [12] M. Daimon, K. Itoh, G. Imada, and W. Jiang, "Experimental demonstration of relativistic magnetron with modified output configuration," *Appl. Phys. Lett.*, vol. **92**, no. 19, pp. 191 504-1–191 504-3, May 2008.
- [13] W. Li and Y.-G. Liu, "An efficient mode conversion configuration in relativistic magnetron with axial diffraction output," *J. Appl. Phys.*, vol. **106**, no. 5, pp. 053 303-1–053 303-3, Sep. 2009.
- [14] Wei Li, Yong-gui Liu, Jun Zhang, Di-fu Shi, and Wei-qi Zhang, "Experimental investigations on the relations between configurations and radiation patterns of a relativistic magnetron with diffraction output," *J. Appl. Phys.*, vol. **113**, no. 2, pp. 023 304-1–023 304-4, Jan. 2013.
- [15] C. Leach, S. Prasad, M. Fuks, and E. Schamiloglu, "Compact relativistic magnetron with Gaussian radiation pattern," *IEEE Trans. Plasma Sci.*, vol. **40**, no. 11, pp. 3116–3120, Nov. 2012.
- [16] Wei Li, Yong-gui Liu, Ting Shu, Han-wu Yang, Yu-wei Fan et al, "Experimental demonstration of a compact high efficient relativistic magnetron with directly axial radiation," *Phys. Plasmas*, vol. **19**, no. 1, pp. 013 105-1–013 105-4, Jan. 2012.
- [17] W. Li and Y. G. Liu, "Modified magnetic field distribution in relativistic magnetron with diffraction output for compact operation," *Phys. Plasmas*, vol. **18**, no. 2, pp. 023103-1–023103-4, Feb. 2011.
- [18] J. Zhou, D. Liu, C. Liao, and Z. Li, "CHIPIC: An Efficient Code for Electromagnetic PIC Modeling and Simulation," *IEEE Trans. Plasma Sci.*, vol. **37**, no. 10, pp. 2002–2011, Oct. 2009.
- [19] A. Palevsky and G. Bekefi, "Microwave emission from pulsed, relativistic e-beam diodes. II. The multiresonator magnetron," *Phys. Fluids*, vol. **22**, no. 5, pp. 986–996, May 1979.

# A Miniature Pulse Generator

Xing Zhou\*, Min Zhao, Qingxi Yang

\*Shijiazhuang Mechanical Engineering College, Shijiazhuang, Hebei, China, zxlwbh@126.com

**Abstract:** A miniature Marx generator based on avalanche transistors is developed. The avalanche transistors, which exceed traditional gas-gap switches in stability, size and repetition rate, are used as high-speed switches in the Marx circuit. Meanwhile, the wide-band power combiner is designed, and the combiner can increase the output voltage for 1.4 times. The test results show that the miniature EMP generator have the virtue of high stability and high repetition rate.

**Keywords:** high stability; high repetition rate; avalanche transistor; pulse generator

## 1 Introduction

Marx generator is a classical pulse-generation circuit, which can obtain the multiples of charging voltage using parallel charging and serial discharging of its capacitances. The discharge of the Marx circuit is controlled by high-speed switches. Conventional switches are the gas-gap switches. Because the breakdown of gas is random and the recovery time is long, the stability and the repetition frequency of gas-gap switches are not very good. Solid high-speed switches, such as MOSFET (metallic oxide semiconductor field effect transistor), IGBT (Insulated Gate Bipolar Transistor), have higher stability, higher speed, longer lifetime and smaller size.

There are three switching means of the avalanche transistors. One is the external triggered switching. Another is the avalanche-mode switching when the voltage of the collector-emitter ( $U_{ce}$ ) exceeds  $U_{(BR)CEO}$ . The third is the fast rise time switching when the slope rate of  $U_{ce}$  ( $dU_{ce}/dt$ ) is sharp enough.

## 2 Avalanche Transistors

The working characteristic of a general transistor has four regions: cut-off region, linear region, saturation region, and avalanche region [11-12], as shown in Fig.1. The NPN transistor operates in the cut-off region when the base current is negative and the base-emitter is reverse biased. Its working mode turns to the avalanche region if  $U_{CE}$  increases gradually, and the collector current rapidly changes with  $U_{CE}$  and  $I_B$ . In the avalanche mode, the switch is operated at a voltage which is close to the breakdown voltage of its reversed biased PN junction. If the voltage exceeds this limit value, the impact ionization and carrier multiplication lead to an avalanche breakdown of the junction [2]. Since new carriers are

generated within the junction itself, the switching time is effectively reduced by the rate of the new carriers are created, which is the ionization rate. The switching time in this case is less than 1 ns.

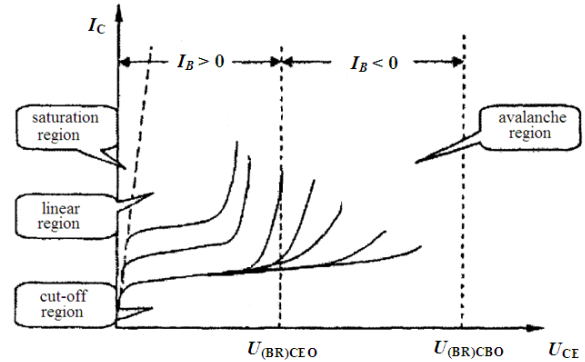


Fig.1 Working characteristic of transistors

## 3 Miniature Marx Circuit

Pulse generator consists of DC charger, trigger circuit, and Marx circuit. All the switches of Marx circuit use FM417 transistors. The avalanche transistor of the first stage works in the external triggering mode, and others work in the avalanche mode. The five stages monopole circuit of the Marx generator is shown in Fig. 2.

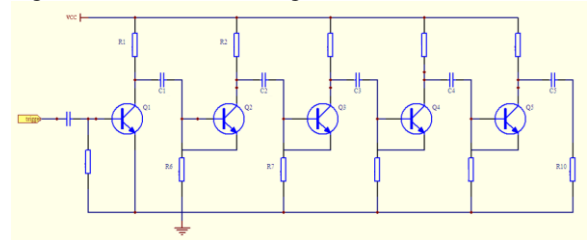


Fig. 2 Five stages monopole Marx circuit

## 4 Trigger Circuit

The trigger circuit consists of the 555 timer and the 74LS123 reshaping circuit. The 555 timer and peripheral components form the monostable circuit or the multivibrator type oscillator, which generates a single pulse or repetition pulses. Fig.3 shows a single pulse trigger circuit. When the switch  $S_1$  is turned on, the third pin of the 555 timer can produce a pulse with the pulse width determined as

$$t_{w1} = R_2 C_2 \ln \frac{U_{CC}}{U_{CC} - 2/3 U_{CC}} = 1.1 R_2 C_2 \quad (1)$$

The 555 timer can produce the pulses with the pulse

width ( $t_{w1}$ ) varies from tens of us to several minutes.

If the  $t_{w1}$  is longer than the charging time of capacitors ( $C_1 \sim C_5$  in Fig.2), the capacitors are charged again after discharging. When voltage at the capacitors exceed  $U_{(BR)CEO}$ , it causes transistors to switch on again. The result is that several pulses are produced by once trigger. In order to avoid this, the 74LS123 circuit is applied to reduce the pulse width of trigger.

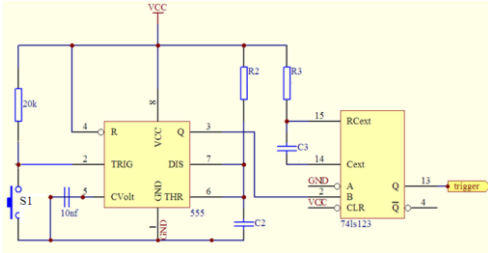


Fig. 3 Trigger circuit

### 5 Power Combiner

To increase the output power/voltage, a wide-band power combiner is designed, which is shown in Fig.4. it can enhance the power/voltage by 2/1.4 times.

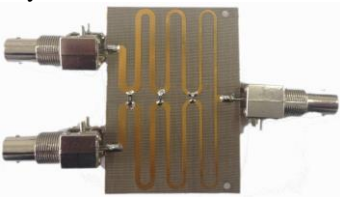


Fig. 4 Power combiner

### 6 Experimental Results

According to above principles, a 50-stage generator is designed, which is shown in Fig.5. Its output voltage is 5500 volts, and repetition rate is 10kHz. The output voltage wave is shown in Fig. 5.



Fig. 4 Pulse circuit



Fig. 5 Output voltage wave

### References

[1] ZHANG Renyu, CHEN Changyu, WANG Changchang. High voltage test technology[M]. Beijing,China: Tsinghua University,2003:25-50.  
 [2] Streetman B G , Banerjee S. Solid state electronic devices[M]. Englewood Cliffs, USA: Prentice Hall, 2000:90-110.  
 [3] ZHANG Xianglong, WANG Yi, TIAN Fuqiang, *et al.* Design and characteristic comparison of bipolar and unipolar high voltage nanosecond pulsers[J]. High Voltage Engineering, 2012, 38(1):963-970.  
 [4]Van Bezooijen An, van Straten F, Mahmoudi R.. Avalanche breakdown protection by adaptive output power control[C]. 2006 IEEE Radio and Wireless Symposium. [s.l.]:IEEE,2006:519-52.

# Comparative analysis of directivity and gain in according to Antenna's dielectric- shape

**Ruck-Woan Kim\***, **Jin-Wook Park\***, **Seung-Moon Han\***, **Chang-su Huh\*** †

\*Department of Electrical Engineering, Inha University, Incheon 402-751

## Abstract

This paper compares the results by executing the simulation in order to analyse the antenna characteristics depending on the shape of dielectric to be applied to the opening of the TEM horn antenna. Dielectric of opening of the antenna is two type of Fresnel and hemispherical. Fresnel and hemispherical lens are made with Teflon. Directivity and radiation efficiency at the central frequency is not much difference. However, it is confirmed that a Fresnel lens is more efficient in total efficiency.

**Keywords:** Dielectric antenna, Fresnel lens, Hemispherical lens, TEM antenna.

## 1 Introduction

According to the shape of the opening antenna, Lens antennas can change characteristics of directivity and gain of antenna. Dielectric lenses have been suggested as an alternative solution to offset dual reflector system for scientific space applications. [1] To optimize Directivity and gain of a TEM antenna used for EMP radiation experiments, this paper compares with a Fresnel lens and a hemispherical lens and analyses the results.

## 2 Manuscript preparation

Unlike normal horn antenna, TEM horn antenna is fed to the two separating conductive plates. when electromagnetic waves are generated from the power of the two parallel conductive plates, they are copied into the air via the antenna aperture. Current flowed through a coaxial line is transformed to the energy because of impedance match between the inner conductor of the coaxial line and the antenna conductor plate.[2] The generated electromagnetic wave will have a TEM characteristics by flowing current and the voltage difference in the two conductive plates and proceeds between the two conductive plates. The directivity and gain of the electromagnetic wave emitted through the Fresnel type and hemispherical type was analyzed by simulation.

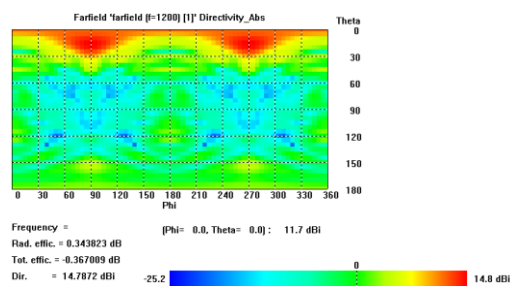


Figure 1. Directivity of hemispherical lens

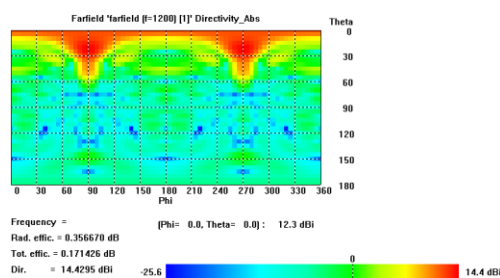


Figure 2. Directivity of Fresnel lens

dB value of the hemispheric and Fresnel type as shown in the figure above does not show much of a difference but shows greater overall efficiency in fresnel lens than in hemispherical lens. In addition, Fresnel lens are more easily manufactured because the amount of the material reduced.

## References

- [1] P. C. Hargrave, G. Savini, N. Trappe, A. Challinor, S. B. Sørensen, P. A. R. Ade, R. V. Sudiwala, I. K. Walker, M. Gradziel, N. Tynan, and M. van der Vorst, "Coated dielectric lens design, modeling and measurements for future CMB polarimetry missions," in Proc. EuCAP, Gothenburg, Sweden, 2013.
- [2] J. Wang, C. Tian, G. Luo and Y. Chen, D. Ge, "Four-element TEM horn array for radiating ultra-wideband electromagnetic pulses", *Microwave and Optical Technology Letters*, vol. 31, no. 3, pp. 190-194, Nov. 5 2001.

# Design Consideration of Marx Generator for a Continuous Operation at a High Repetition Rate

Jeong-Hyeon Kuk<sup>†</sup>, Dong-Woo Yim\*, Jin-Soo Choi\*, Sun-Mook Hwang\*\*, Tae-Hyun Lim\*\*

\*Agency for Defense Development, Korea, \*\*Hanwha Corporation, Korea

## Abstract

In order to develop a compact and repetitive pulse power supply by using a Marx generator, variations of temperature and resistance of all the resistors installed in a Marx generator were measured and investigated during a continuous operation at a high repetition rate. In the experiments, two kinds of resistors were attached to and detached from the Marx generator fabricated previously, respectively. The repetition rate of the Marx generator's operation was 100 Hz and the continuous working time was arbitrarily determined under consideration of the resistor's heating. The experimental results were analysed in comparison with the simulation results of the Marx generator. These analyses will be applied to design and manufacture of a compact and high repetitive Marx generator.

**Keywords:** Marx Generator, Repetition Rate, Resistor

## 1. Introduction

A Marx generator is a capacitive energy storage circuit which consists of resistors, capacitors and spark gap switches. In the circuit, resistors control the charging and the discharging current of capacitors and capacitors are charged to a given voltage level in parallel and then quickly discharged in series by triggering spark gap switches. When the spark gap switches are triggered, the energies stored in the capacitors are delivered to a load at a very high power level. If a Marx generator is made up of  $N$  capacitors charged to a voltage  $V$  in parallel through resistors, the voltage pulse delivered to a load by triggering spark gap switches is theoretically  $N \times V$  [1].

This study has been carried out because several resistors of Marx circuit were heated and then deformed due to the breakdown between two terminals of the resistors when the Marx generator fabricated previously [2] was repetitively operated. In this study, high repetition tests of the Marx generator fabricated previously were continuously performed and the temperature and the resistance of each resistor were measured while the resistors of the Marx circuit were changed in two kinds of resistors. The analyses of the test results will be applied to design and manufacture of a compact and high repetitive Marx generator.

## 2. Experimental Setup

The Marx generator fabricated previously and the setup for high repetition test in succession are illustrated in Figure 1 and Figure 2, respectively. The attached power supply in Figure 1 was replaced

with a portable power supply for the convenience of the test. The resistors applied to the test are 3RLab's model HTE44C-BC 10 k $\Omega$  used in the Marx generator fabricated previously and TKK's model ER5AS 1 k $\Omega$ . In the test, the resistors were selected in three types of one 10 k $\Omega$ , two 10 k $\Omega$  in parallel and one 1 k $\Omega$ . The Marx generator was charged to 50 kV by using power supply in all the tests and then its output pulse power was discharged into the load resistor of 100  $\Omega$  when a resistor was 10 k  $\Omega$  and the load resistor of 25  $\Omega$  when 1 k  $\Omega$ . The repetition rate was 100 Hz and the continuous operating time was gradually increased under consideration of the resistor's heating. There was pausing time of one minute to measure the temperature and the resistance of every resistor whenever a continuous operating time was increased. The resistance and the temperature of all the resistors were measured by using commercial resistance tester and Raytec Company's model MX-6 that is an untouched IR thermometer, respectively.

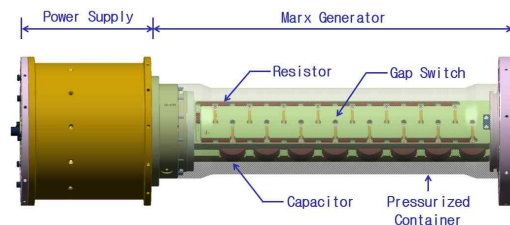


Figure. Marx generator fabricated previously.

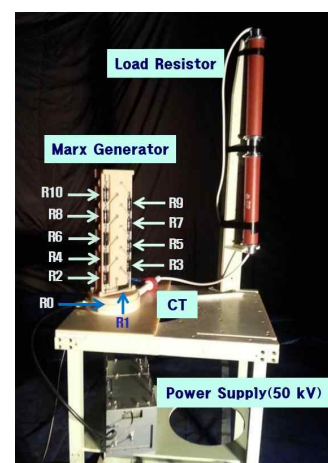


Figure 2. Setup for high repetition test.

In order to measure and analyse a resistance and a temperature of a test resistor when a Marx generator is charged in a high repetition rate, a simple test setup comprised of a power supply to flow a constant current into a resistor, an oscilloscope and a high voltage

<sup>†</sup> Corresponding author; jhkuk7@gmail.com

probe to measure the voltage of a resistor was used in the test. The test procedure was the same as that of the high repetition test.

### 3. Experimental Results

The results of the high repetition charging tests are shown in Figure 3. As shown in Figure 3, the resistance variations of 3Rlab's resistors are very small though their temperatures are considerably high.

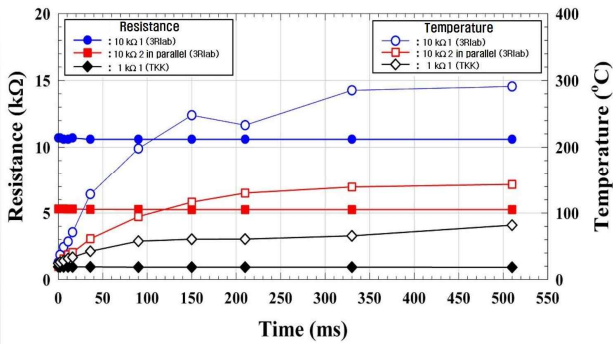


Figure 3. Resistance and temperature variations of resistors in high repetition charging test.

The results of the high repetition test in succession are drawn in Figure 4 and 5. In the Figure 4, the surface of the 3Rlab's resistor mounted at the R10 location showed dark coloured marks by burning and current flowing traces in deep indentation form caused by the breakdown. In the Figure 5, the coating of the TKK's resistor mounted at the R10 location burned but there were no current flowing traces on its surface.

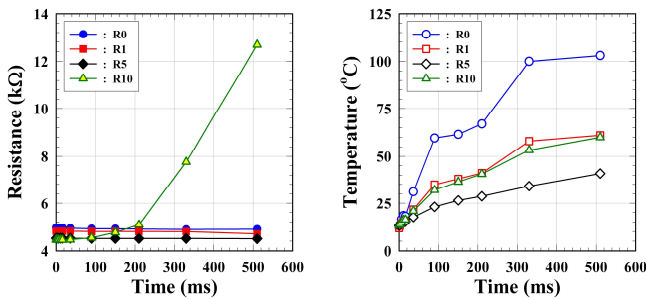


Figure 4. Resistance and temperature variations of two 10 kΩ resistors in parallel.

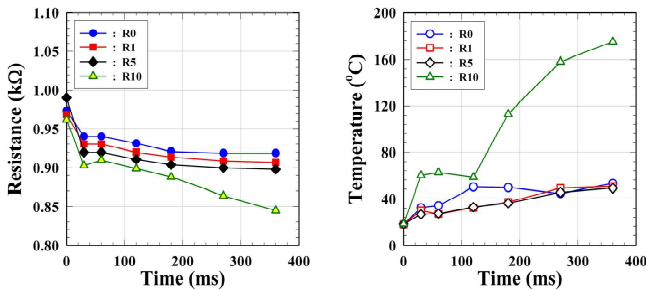


Figure 5. Resistance and temperature variations of one 1 kΩ resistors.

To analyse the test results, an output characteristics of the Marx generator was simulated by using P-spice circuit model seen in Figure 6. The simulation results are drawn in Figure 7 to Figure 9.

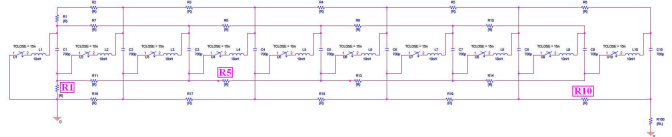


Figure 6. P-spice modelling of the Marx generator.

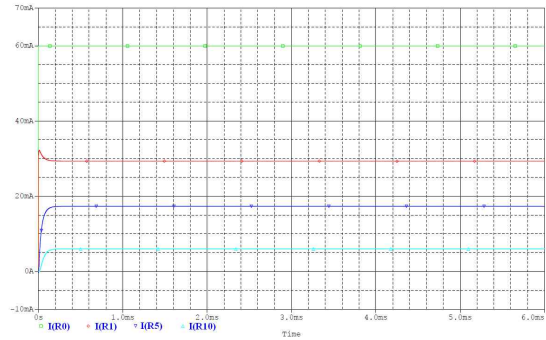


Figure 7. Current flowing through the resistors when charged.

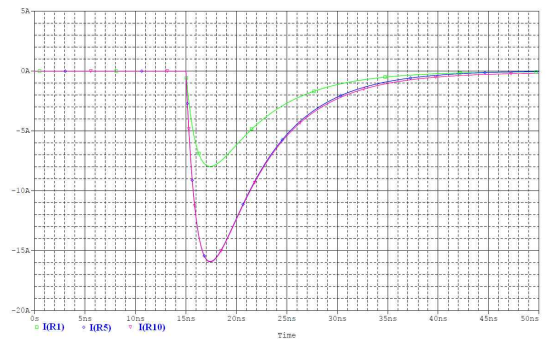


Figure 8. Current flowing through the resistors when discharged in the use of two parallel 10 kΩ.

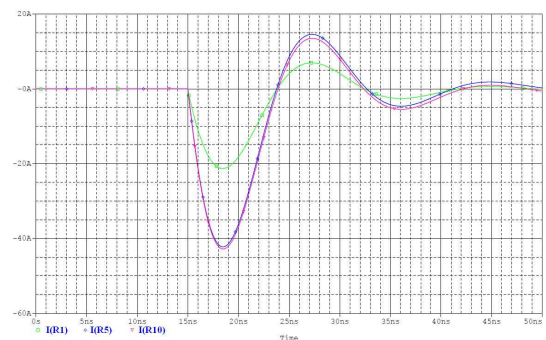
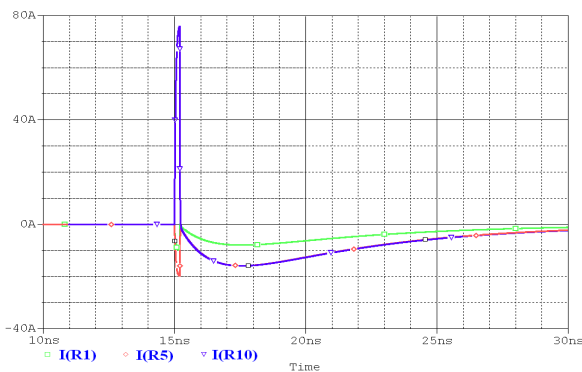


Figure 9. Current flowing through the resistors when discharged in the use of one 1 kΩ.

### 4. Discussion

The resistance variations of TKK's resistors below 100 °C and 3Rlab's resistors below 300 °C in the range of test are very small as shown in Figure 3. The reason for the

temperature of the R0 resistor to be the highest in Figure 4 is that the charging current is the highest in Figure 7 and the time for the capacitors to be charged into 50 kV is approximately required 6 ms. The current flowing through the R5 resistor is higher than the R10 resistor in Figure 7 and 8, however the temperature of the R5 resistor is lower than the R10 resistor in Figure 4. To understand the phenomena, the P-spice circuit modelling to put the trigger time of the tenth spark gap switch off 0.2 ns was carried out. The simulation result is shown in Figure 10. As shown in Figure 10, the reason why the temperature of the R10 resistor is higher than the R5 resistor seems to be an excessive current caused by the trigger time discrepancies of the spark gap switches. The resistance of the R10 resistor in comparison with the R0 resistor is rapidly increased though the temperature of the R0 resistor is higher than the R10 resistor in Figure 4. That is why the surface of the R10 resistor melted or burned due to a high temperature and was repetitively damaged by the breakdown as mentioned in the experimental results. The voltage of the R10 resistor is about 80 kV when discharged. The temperature of the R10 resistor in Figure 5 is the highest unlike Figure 4. That seems to be why the current flowing through the R10 resistor is very high of about 43 A when discharged as shown in Figure 9. The resistance of TKK's R10 resistor in Figure 5 is not increased unlike 3Rlab's R10 resistor in Figure 4 though the temperature of TKK's R10 resistor is three times as high as 3Rlab's R10 resistor. On the contrary, the resistance of TKK's R10 resistor is decreased in small amounts. That seems to be why there was no physical damage by the breakdown on the surface of TKK's R10 resistor and the coating of TKK's R10 resistor was carbonized by burning. The voltage of 3Rlab's R10 resistor is about 80 kV, but the voltage of TKK's R10 resistor is about 43 kV.



**Figure 10. Current flowing through the resistors when the trigger time of the tenth spark gap switch is delayed 0.2 ns unlike the other switches.**

From the test results, the voltages between two terminals of resistors are more considered than temperatures for a high repetitive and continuous operation of Marx generator in a stable state. The allowed voltages of resistors used in manufacture of Marx generator should be determined in the early design stage in consideration of resistor's working properties. According to the situation, a new resistor should be designed and manufactured on the basis of the experimental results. The 3Rlab's 10 kΩ resistor can be

possibly used in manufacture of Marx generator for a high repetitive and continuous operation in a stable state if the voltage below 50 kV is applied to the resistor. A new type of resistor should be designed and fabricated in the way to lengthen the distance between two terminals of resistor if the voltage of 80 kV is applied to a resistor as this experiment.

## 5. Conclusion

In order to fabricate a compact and repetitive pulse power supply by using a Marx generator, not only numerical analyses but also operating characteristics of circuit elements should be analysed on the basis of experiment. From the test and the simulation results, the Marx generator fabricated previously was improved and its operating condition was determined for a continuous operation at a high repetition rate in a stable state.

## References

- [1] W. J. Carey and J. R. Mayes, "Marx Generator Design and Performance", *IEEE Power Modulator Symposium 2002*, pp. 625-628, (2002).
- [2] D. Yim, C. Kim and J. Choi, "Design of a Compact and Repetitive Pulse Generator", Agency for Defense Development Report, ADDR-410-091771, 2009.

# Design of a smart phased array antenna for IEMI applications

Jinwoo Shin\*, Junho Choi\*, Woosang Lee\* and Joonho So\*

\*Agency for Defense Development, Korea, sjinu@add.re.kr

## Abstract

In this paper, we present the design procedures and the numerical performances of a smart phased array antenna for IEMI system and applications. We also present the beam focusing algorithm using the smart array antenna in order to concentrate the microwave energy on the desired point which is applicable in the small anechoic chamber for checking the effectiveness by the IEMI system.

**Keywords:** Smart Array Antenna, Beam Focusing, IEMI

## 1 Introduction

Smart array antenna is applicable to various areas and applications to identify spatial signal and to form the beam toward the signal source [1-3]. If we use a smart array antenna for the IEMI(Intended Electro-magnetic Interference) system, we can track the direction of arrival from the target and then focus the narrow beam on the desired target with the capability of rejecting interfering signals. Smart array antenna also provides multiple access due to the phased array antenna so it would be possible to track the multi-beam from several targets. In this paper, we present the design procedure for optimizing the unit radiator of the smart array antenna system for IEMI applications and propose a beam focusing algorithm using smart array antenna system for investigating the effectiveness of IEMI by the high power source.

## 2 Design of Smart Array Antenna

In general, the configuration of the smart array antenna system is composed of TRMs(transmitting & receiving modules) and radiating elements. We assume the tile-typed TRM as a source module and design the interface between the module and the radiator in order to design a compact smart array antenna. We've optimized the antenna structure and the characteristics of a unit radiator by dividing the radiating elements into two parts; tapered slot antenna and balun. We've fixed the gap size of the tapered slot because of impedance matching with the wideband balun and optimized the tapered slot shape of a unit antenna to change the length and width of the single antenna ridge. The balun has been designed with shorted open stub whose diameter is 4.4mm. After connecting the optimized slot antenna to the balun, the performance of the whole unit antenna is checked. And then, we've considered grating lobe within scanning angles with the array distance as  $0.8 \lambda_h$  which is a wavelength at highest operating frequency and also investigate the synthesized

beam pattern for the linear array including mutual coupling between radiators. We've got the wideband result about the return loss under -15 dB over 3:1 frequency bandwidth.

## 3 Beam Focused Array for IEMI application

Sometimes, we need to focus the microwave energy on the target in the near distance for the IEMI application using high power phased array antenna system based on semiconductor amplifier. So, we've considered a beam focusing algorithm between the arrayed high power source and the target. Figure 1 shows the normalized power density and focused energy diagram at the distance of 1500 mm from phased array source.

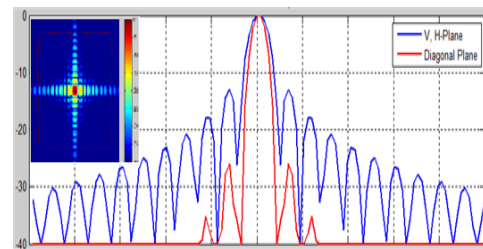


Figure 1. Normalized power density by focused beam

Beam focusing is accomplished by calculating the phase difference between a focused point and each radiating element of phased array antenna. After each radiating element is assigned time delay according to the calculated phase differences, the focused beam is concentrated on the desired point.

## 4 Conclusion

We present the design results and numerical performances of the smart adaptive array antenna system for IEMI application and electronic warfare as a countermeasure to electronic jamming as well. We also present the focusing algorithm for illuminating microwave energy into the desired point. With the developed beam focused array antenna, it is possible to perform the test and evaluation for the IEMI system including the effectiveness at various targets in a small space.

## References

- [1] J. H. Winters, "Smart antenna for wireless systems", *IEEE Personal Com. Magazine*, pp. 23-27, (1998).
- [2] M. Chryssomallis, "Smart antennas", *IEEE Mag. On Antenna Propag.*, vol. 42, pp. 129-136, (2000).

- [3] M. Rivas, S. Xie, D. Su, "A review of adaptive beamforming techniques for wideband smart antennas", *6<sup>th</sup> Intl. Conference on WiCOM*, pp. 1-7, (2010).

# Effects of the Earth Ground on the Radiation Performance of Log-Periodic Dipole Antennas

Xiang Gao and Zhongxiang Shen  
 School of Electrical and Electronic Engineering  
 Nanyang Technological University  
 50 Nanyang Avenue, Singapore 639798  
 Email: xgao@ntu.edu.sg; ezxshen@ntu.edu.sg

**Abstract**—A theoretical analysis elaborating the ground effects on log-periodic dipole antenna (LPDA) is presented. Based on image theory, analytical expressions are derived to describe the radiation fields of LPDA placed over an infinite ground plane. Moreover, the variations of a typical LPDA's overall performance are also carefully examined using commercial electromagnetic software, when the antenna is located at different heights from soil ground and sea surface, respectively. The simulated results are in well agreement with the ones obtained with analytical formulas, which demonstrates that the LPDA should be installed at a reasonable height to make a good compromise between radiation efficiency and patterns.

**Keywords**—log-periodic dipole antenna (LPDA); ground effects.

## I. INTRODUCTION

Log-periodic dipole antenna (LPDA) has been widely applied in VHF and UHF wireless communication systems, for its low fabrication cost as well as its good performance such as ultra-wide bandwidth, high directivity and low cross-polarization ratio [1]-[2]. Considering the LPDAs are often used for long range communication, it is very necessary to examine the effects of earth ground (e. g., soil ground and sea surface) on their radiation performance, including the variations of input impedance, voltage standing wave ratio (VSWR), efficiency and radiation patterns for different installation heights.

This paper presents a detailed theoretical analysis to clarify the ground effects on LPDA, which not only provides the analytic radiation field formulas of LPDA in presence of an infinite lossy ground, but also give a full analysis of the overall performance of a typical LPDA respectively placed over soil ground and sea surface using ANSYS High Frequency Structure Simulator (HFSS). The simulated radiation patterns are in well agreement with the one obtained with analytic field formulas, which validates the effectiveness of theoretical derivation and indicates a reasonable installation height to ensure radiation efficiency and patterns.

## II. THEORETICAL FORMULAS OF RADIATION FIELDS

The schematic of a LPDA horizontally placed over an infinite lossy ground is shown in Fig. 1. Due to the presence of ground plane, there appears a reflected wave which interferes with the directly radiated wave from the LPDA itself. The

final radiation total field can be obtained by using image theory. To be different from the perfect ground case, the strength of the image here should be weighted with reflection coefficients of the real earth. Considering the reflection coefficient depends on the specific polarization with regard to the incidence plane, polarization decomposition is conducted in the derivation to obtain the radiation total field. To make it brief, the total field formula is derived as

$$\hat{E} = E_{\text{free}} \left\{ \frac{[1 + R_v \exp(-j4\pi h \sin \theta \cos \varphi / \lambda)] \cos \theta}{\sqrt{\cos^2 \theta + \sin^4 \theta \sin^2 \varphi \cos^2 \varphi}} \hat{e}_v + \frac{[1 + R_p \exp(-j4\pi h \sin \theta \cos \varphi / \lambda)] \sin^2 \theta \sin \varphi \cos \varphi}{\sqrt{\cos^2 \theta + \sin^4 \theta \sin^2 \varphi \cos^2 \varphi}} \hat{e}_p \right\} \quad (1)$$

where  $\lambda$  is the operating wavelength,  $h$  is the height of LPDA from ground plane,  $R_v$  and  $R_p$  are the reflection coefficient of lossy ground for vertical and parallel polarization, respectively.  $E_{\text{free}}$  is the radiation field of LPDA in the free space, which can be denoted as [3]

$$E_{\text{free}} = \frac{\cos[(N\pi R_n / \lambda)(1 - \tau)(\cos \theta - 1)]}{\cos[(\pi R_n / \lambda)(1 - \tau)(\cos \theta - 1)]} \cdot \sin \left[ \frac{\pi R_n}{\lambda} \left( \frac{1}{\tau} - 1 \right) \cos \theta \right] \frac{\cos(\pi \sin \theta \sin \varphi / 2)}{\sqrt{1 - \sin^2 \theta \sin^2 \varphi}} \quad (2)$$

where  $N$  is the number of dipoles in the active region,  $R_n$  is the distance between the resonant dipole and apex of LPDA, and  $\tau$  is the scaling factor.

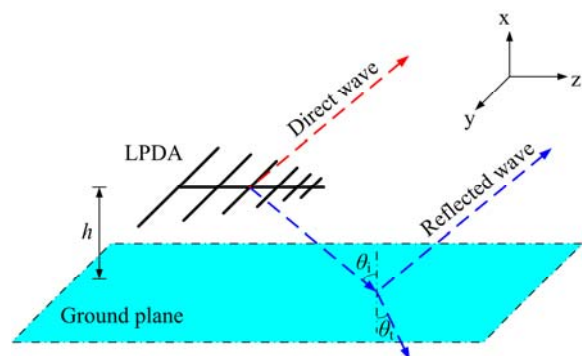


Fig. 1. Schematic of a LPDA over an infinite ground.

### III. ANALYSIS OF A LPDA OVER AN INFINITE SOIL GROUND AND SEA SURFACE

In order to investigate the overall performance of LPDA placed over a lossy ground, a typical LPDA operates from 300 MHz to 900 MHz is designed, and thoroughly analyzed for two typical application environments (above soil ground and sea surface). As shown in Fig. 2 and Fig. 3, the VSWR keeps relatively stable for heights larger than a quarter of wavelength, while the radiation efficiency degrades rapidly as the height decreases, resulting from the low conductivity of soil. Fig. 4 shows the calculated and simulated radiation patterns, which are in very well agreement with each other. It can be clearly seen that there appears more sidelobes on H-plane as the height increases. In comparison, the radiation pattern on E-plane is relatively nice and stable. Figs. 5-7 also give similar results, corresponding to an infinite sea surface.

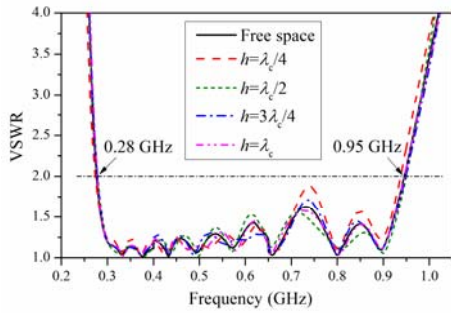


Fig. 2. Simulated VSWR of a LPDA over an infinite soil ground using HFSS.

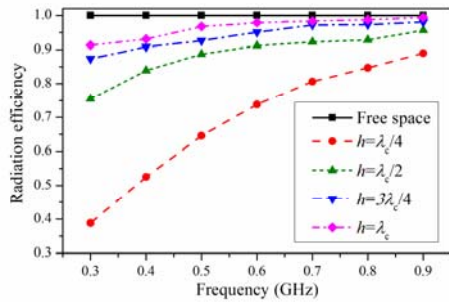


Fig. 3. Simulated radiation efficiency of a LPDA over an infinite soil ground using HFSS.

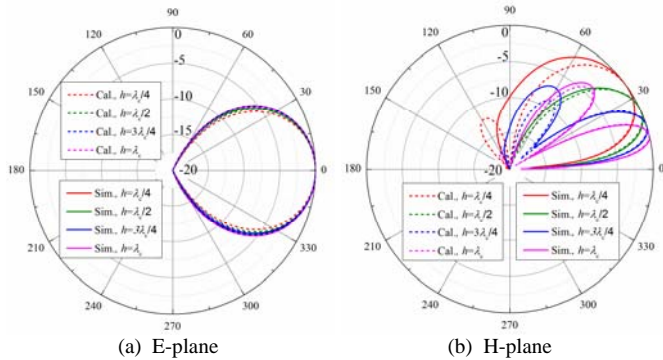


Fig. 4. Calculated and simulated radiation patterns of a LPDA over an infinite soil ground (H-plane:  $xz$ -plane; E-plane: a plane comprised of  $y$  axis and maximum radiation direction)

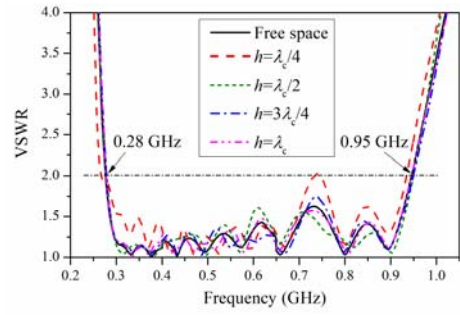


Fig. 5. Simulated VSWR of a LPDA over an infinite sea surface using HFSS.

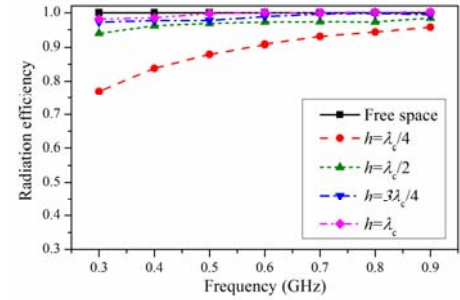


Fig. 6. Simulated radiation efficiency of a LPDA over an infinite sea surface using HFSS

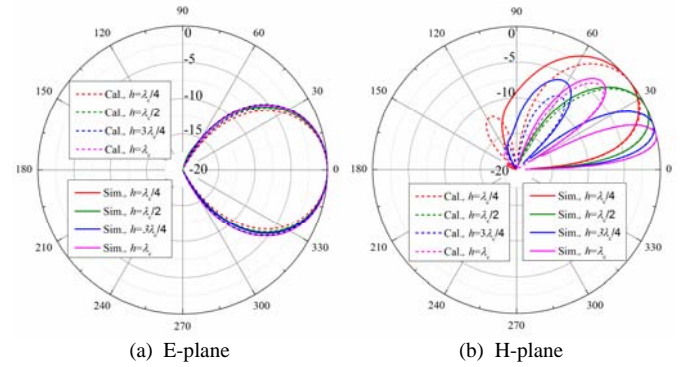


Fig. 7. Calculated and simulated radiation patterns of a LPDA over an infinite sea surface (H-plane:  $xz$ -plane; E-plane: a plane comprised of  $y$  axis and maximum radiation direction).

### IV. CONCLUSION

A theoretical analysis regarding the effects of lossy ground on LPDA is presented. By using the proposed theoretical formulas based on image theory and ANSYS HFSS, detailed analysis results are obtained and discussed for a typical UHF LPDA placed over an infinite soil ground and sea surface.

### REFERENCES

- [1] C. A. Balanis, *Antenna Theory: Analysis and Design*. New York: Wiley, 1992.
- [2] R. L. Carrel, *Analysis and Design of the Log-Periodic Dipole Antenna*. Urbana, Illinois, USA: University of Illinois, 1961.
- [3] S. P. Kosta, "A theory of the log-periodic dipole antenna", *International Journal of Electronics*, vol. 23, no. 5, pp. 473-483, 1967.

# E-shaped Patch Antennas Fed with Ultra-short Pulses for Radiating High-power Mesoband Pulses

Kiho Kim\*, Jiheon Ryu\*, Jin Soo Choi\*

\*Agency for Defense Development, Daejeon, Republic of Korea.

## Abstract

In this paper, we present a simple method to build a mesoband pulse radiator by using a wideband patch antenna fed with ultra-short pulses generator. Because E-shaped patch antennas have a wide bandwidth, they filter the mesoband pulses out of the ultra-short pulses in addition to radiate the mesoband pulses. We designed, manufactured and tested an E-shaped patch antenna with a center frequency of 1GHz. This antenna radiates mesoband pulses with an electric field strength of 6kV/m and a pulse width of 5ns at a distance of 3m when it is fed with a 0.5ns ultra-short pulse generator.

**Keywords:** Ultra-short pulse, Mesoband pulse, Patch antenna, Electromagnetic pulse.

## 1 Introduction

High-power mesoband radiators with many different frequency bands are useful to study high-power electromagnetic (HPEM) effects [1]. A high-power microwave system that converts the range of 200MHz to 6GHz in nine frequency bands has been developed [2].

Here, we propose wideband patch antenna modules that have several tuned frequencies and are fed with a single ultra-short pulse (USP) generator to study HPEM effects depending on frequency. The USP has an ultra-wide-band (UWB) spectrum. As shown in Fig. 1, we can obtain the mesoband pulses by feeding the wideband patch antenna modules of several tuned frequency bands with a USB generator.

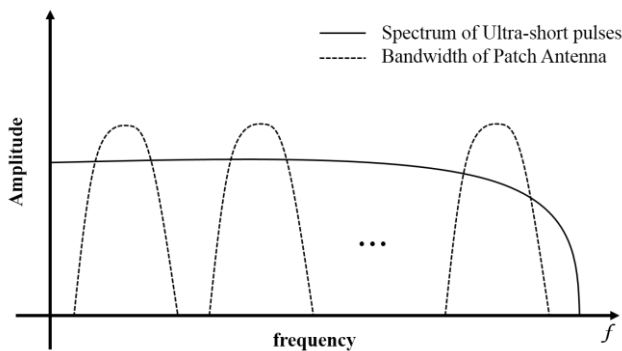


Figure 1. UWB frequency characteristic.

## 2 Simulation and Experiment Results

We designed an E-shaped patch antenna because this has a wide bandwidth among many patch antennas and a compact structure [3]. Separation between the ground plane and the E-shape allows high-voltage pulses to be fed without breakdown.

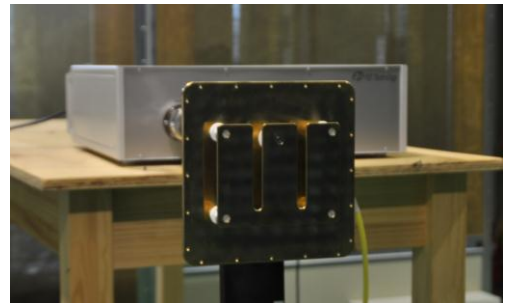


Figure 2. Configuration E-shaped antenna fed with USP generator.

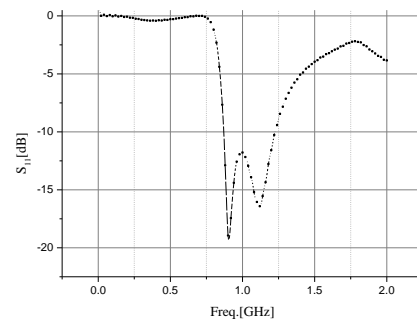
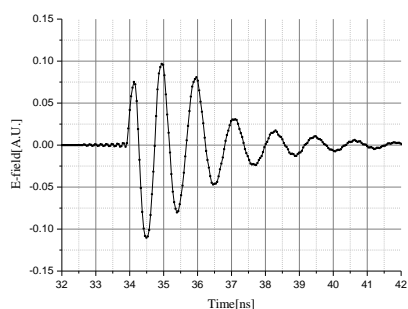
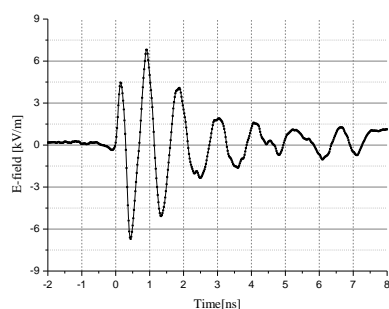


Figure 3. Reflection coefficient of the E-shaped patch antenna.

Fig. 2 shows the manufactured patch antenna. The reflection coefficient of the antenna is the same as Fig. 3. The center frequency is 1GHz. The fractional bandwidth is 30% at the center frequency. A radiated field waveform is calculated by CST simulation, as shown in Fig. 4. Fig. 5 shows the measurement result of waveform radiated from the patch antenna. This antenna radiates mesoband pulses with an electric field strength of 6kV/m and a pulse width of 5ns at a distance of 3m when it is fed with a 0.5ns ultra-short pulse generator.



**Figure 4. E-field waveform of CST simulation.**



**Figure 5. Mesoband pulse radiated from antenna.**

### 3 Conclusion

In this paper, we present a simple method to build a mesoband pulse radiator by using a wideband patch antenna fed with USP generator. We fabricated an E-shaped patch antenna with the center frequency of 1GHz. This antenna radiates mesoband pulses with an electric field strength of 6kV/m and a pulse width of 5ns at a distance of 3m when it is fed with a 0.5ns USP generator.

### References

- [1] Jiheon Ryu, Dong Woo Yim and Jaimin Lee. "Analysis and Design of Switched Transmission Line Circuits for High-Power Wide-band Radiation", *Journal of the Korean Physical Society*, **volume 59**, No. 6, pp. 3567-3572, (2011).
- [2] D. Morton, J. Banister, T. Dasilva, J. Levine, T. Naff, I. Smith, H. Sze, T. Warren, D. V. Giri, C. Mora, J. Pavlinko, J. Schleher, and C. E. Baum. "HPM WBTS, A Transportable High-Power Wide-Band Microwave Source", *Power Modulation and High Voltage Conference, IEEE International*, pp. 186-189, (2010).
- [3] Kin-Lu Wong and Wen-Hsiu Hsu. "A Broad-Band Rectangular Patch Antenna With a Pair of Wide Slits", *Antennas and Propagation IEEE Transaction on*, **volume 49**, No. 9, pp. 1345-1347, (2001).

# Experiment of a Ku-band Gyro-BWO on Square waveguide

*K. H. Jang\**, *J. J. Choi\** and *S. W. Jung<sup>†</sup>*

*\*Kwangwoon university, Korea and High Power Microwave Engineering Laboratory,*

*<sup>†</sup>National Fusion Research Institute, Korea*

## Abstract

**A Ku-band gyrotron backward wave oscillator (gyro-BWO) operating in the TE<sub>10</sub> square waveguide mode at the fundamental cyclotron frequency was designed. The circuit performance was predicted by MAGIC code. Initial experiments operating condition at -18.9kV and 1A have demonstrated output power of 316W and efficiency of 2%. In the future, we will proceed with the detail study of experiment.**

**Keywords:** Square waveguide, Gyro-BWO, Ku-band, BWO.

## 1 Introduction

Vacuum electron devices are important sources of high power microwave radiation for use in industrial heating, plasma heating in magnetic confinement fusion experiments radar, communications, driving accelerators and many other applications [1]. There are many high power microwave devices, [2], [3] (such as twts, vircator, extended interaction klystron-EIKS, gyrotrons, free electron lasers-FELS etc.) which are capable to produce the frequency in Ku-band but the requirement of a proper combination of frequency, power, efficiency and compactness of the device is the problem of research [4].

In this paper, we designed a Ku-band gyro-BWO as interaction circuit of square waveguide. The characteristic of interaction circuit predict by MAGIC code. The designed circuit was manufactured. The fabricated circuit composed experiment setup and we performed experiments of gyro-BWO.

## 2 The gyro-BWO setup

Figure 1 shows the layout of a Gyro-BWO. It consists of a double anode MIG (Magnetron-Injection-Gun), a beam tunnel, an interaction circuit, a collector, a window and an electro magnet. The MIG has been performed the simulation that it could to operate in Ku-band by controlling magnetic field, a beam voltage and the modulating anode voltage. The beam tunnel is designed circular type. Its cut off frequency is 12.87GHz at TE<sub>11</sub> mode. The beam tunnel protects the MIG by the oscillation power. Next part is interaction circuit. The circuit of square waveguide was designed to operate the output power more than 300W in TE<sub>10</sub> mode. The operating conditions are the velocity ratio of 0.6 to 0.8, a cathode voltage

of -18kV and magnetic field of 4.3kG. Its performance predict by the MAGIC code. The dimension of square waveguide width and height is respectively 13.7mm. Also a length of the circuit is 550mm. The electron beam passing through the interaction circuit is collected in the collector. The collector structure is a tapered rectangular waveguide which changes to the WR-62 in the square waveguide. Next, the vacuum window was designed with a ceramic of stepped alumina for the broad band performance. Finally, the electromagnet used a solenoid coil type.

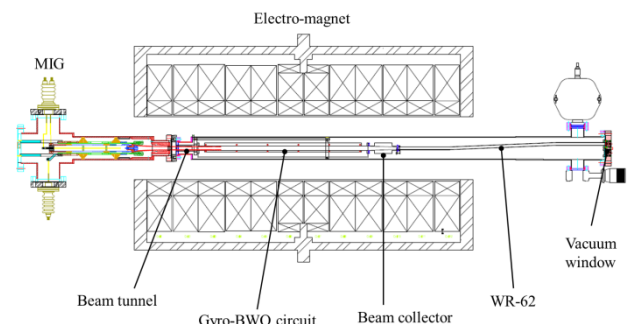


**Figure 1. The gyro-BWO experiment setup**

## 3 Experimental

The test of gyro-BWO is performed using the solenoid coil and a high voltage modulator. Diagnostic apparatus was used for a detector, a spectrum analyzer, a power meter. The detector and the spectrum analyzer is finding of oscillated signal and frequency respectively. The output power was measured by the power meter.

The operating conditions of the gyro-BWO are cathode voltage of -18.9kV, a mod-anode voltage of -5.66kV and the beam current 1A. The initial magnetic field is flat field of 4.3kG. However, this condition was not occurred the oscillation. So we found the optimization of the oscillation condition by adjusting the magnetic field. As a result, the output power is 316W at 11.69GHz and the magnetic field profile has a slop of 4.3kG to 4.7kG in interaction circuit region. At this time, the efficiency is 2%. Figure 2 is signal of appeared oscillation by spectrum analyzer.

The next experiment is finding of a starting oscillation condition. The test conditions were the same as previous. Only the variable parameter is beam current. Figure 3 appear the

starting oscillation condition in beam current of 1A. As shown in the graph at the current can see that power is growing rapidly.

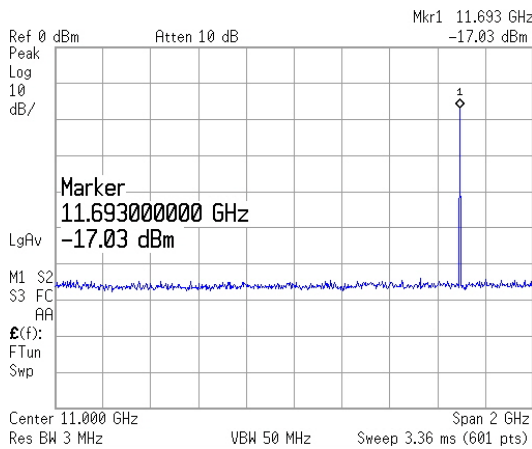


**Figure 2. Onset of oscillation signal**

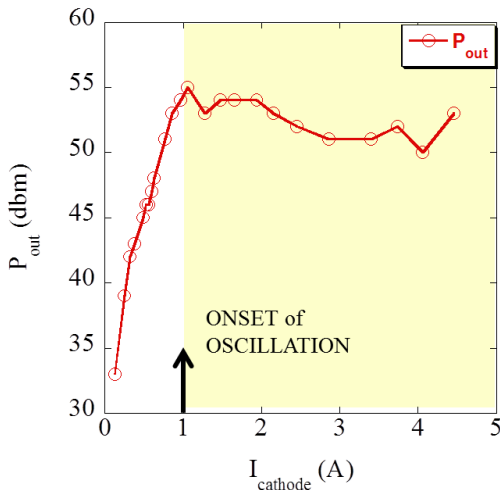


**Figure 3. Condition of starting oscillation.**

## 4 Conclusions

The Ku-band gyro-BWO has been designed and tested. Experiments have demonstrated the output power of 316W, maximum efficiency of 2% and operating frequency 11.69GHz. The operating condition is a cathode voltage of -18.9kV, a mod-anode voltage of -5.66kV and the magnetic field profile has a slop of 4.3kG to 4.7kG in interaction circuit region. The onset of oscillation is appeared at beam current of 1A. In future, we will analyze through additional experiments of gyro-BWO.

## References

[1] K. Felch, B. G. Danly, H. R. Jory, K. E. Kreishcher, W. Lawson, B. Levush, and R. J. Temkin, "Characteristics

and Applications of Fast-Wave Gyro-devices", Proc. Of the IEEE, vol. 87, no. 5, pp. 752-781, (1999).  
 [2] J. H. Booske, R. J. Dobbs, C. D. Joye, C. L. Kory, G. R. Neil, G. S. Park, J. H. Park and R. J. Temkin, "Vacuum Electronic High Power Terahertz Sources", *IEEE Transactions on terahertz science and technology*, vol. 1, no. 1, pp. 54-75, (2011).  
 [3] M. Sattorov, E. Khutorvan, K. Lukin, O. J. Kwon and G. S. Park, "Improved Efficiency of Backward-Wave Oscillator With an Inclined Electron Beam, *IEEE Transactions on terahertz science and technology*, vol. 60, no. 1, pp. 458-463, (2013).  
 [4] Y. N. Pchelnikov, "BWO with an amplifying section", *International Vacuum Electronics Conference, Monterey, California*, pp. 73-74, April 27-29, (2004).

# HEMP Conducted Environment Analysis for Cable Lying on Ground

Sun Beiyun, Yang Jing

Northwest Institute of Nuclear Technology, China, 710024

## Abstract

The induced current for cable lying on ground illuminated by four kinds of HEMP radiation environment is investigated. By analyzing the calculated results, the relationship between the HEMP radiated environment prescribed in IEC61000-2-9 and the HEMP conducted environment prescribed in MIL-STD-188-125-2 is shown.

**Keywords:** HEMP, radiated environment, conducted environment, cable, induced current

## 1 Introduction

As we well known, radiated disturbance protection and conducted disturbance protection are necessary to ensure the HEMP survivability of weapons. Before a weapon with HEMP protection is designed, the designer needs to know the HEMP radiated environment and the HEMP conducted environment. MIL-STD-2169 and MIL-STD-188-125-1/2([1], [2]) prescribe the HEMP radiated environment and the HEMP conducted environment for the U.S. military systems. For MIL-STD-2169 is classified, we do not know how the HEMP conducted environment in MIL-STD-188-125-1/2 is deduced. However, MIL-STD-464 [3] indicates if the HEMP radiated environment is not defined, the IEC HEMP radiated environment [4] can be used. Then there is a problem that if the HEMP conducted environment in MIL-STD-188-125-1/2 can be used under the IEC HEMP radiated environment.

The definition of an intrasite cable can be found in MIL-STD-188-125-2. The HEMP conducted environment for the intrasite cable is expressed by an induced current whose waveform is double exponential wave with 1000A amplitude, less than 20ns rise time and 500~550ns pulse width. In order to show the relationship between the IEC HEMP radiated environment and the HEMP conducted environment in MIL-STD-188-125-2, the induced current for a cable with length of 200m lying on ground illuminated by four kinds of radiated HEMP environment is calculated.

## 2 Computational model

In fig.1, a cable is illuminated by HEMP, where  $y$  is incident angle, and  $f$  is azimuth angle. The induced current along the cable can be calculated by transmission line equations

presented in reference[5], which is closely relative to the HEMP radiated environment, the structure of cable and the electrical parameter of the ground.

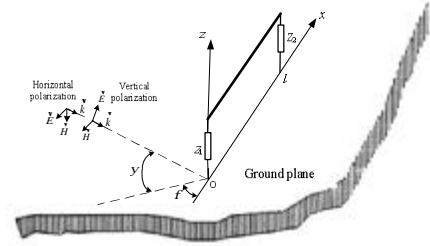


Fig.1 A cable illuminated by HEMP

The HEMP radiated environment can be expressed by double exponential wave:

$$E(t) = kE_0 (e^{-at} - e^{-bt}) \quad t > 0 \quad (1)$$

The values of  $k$ ,  $E_0$ ,  $a$  and  $b$  are given in table.1 for four kinds of HEMP with 23ns, 50ns, 75ns and 184ns pulse width respectively, and the time-domain waveforms can be seen in fig.2, where the first is IEC HEMP environment, the second and the third are assumed HEMP environment, and the fourth is Bell Laboratory environment.

Table 1: The parameters of HEMP environment

HEMP	$E_0$	$k$	$a$	$b$
1	50kV/m	1.30	$4.00 \times 10^7$	$6.00 \times 10^8$
2	50kV/m	1.12	$1.58 \times 10^7$	$6.98 \times 10^8$
3	50kV/m	1.08	$1.02 \times 10^7$	$7.36 \times 10^8$
4	50kV/m	1.05	$4.00 \times 10^6$	$4.76 \times 10^8$

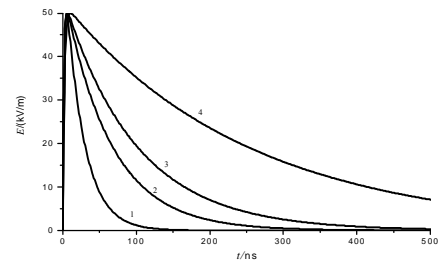


Fig.2 The four kinds of HEMP

The ground parameters are chosen as: relative permittivity  $\epsilon_g=10$  and conductivity  $s_g=0.01, 0.001, 0.0001$ S/m.

The cable parameters are chosen as: length  $l=200$ m, height  $h=0.1$ m, cable radius  $a=1$ cm and terminal impedance  $Z_1=Z_2=0\Omega$ .

### 3 Computational results

Fig.3 illustrates the calculated current in the cable at  $x=l$  for different ground conductivities for horizontal polarization wave at  $y=90^\circ$ , where the maximum value of peak current is obtained. It can be seen that as the ground conductivity decreases, the peak current value, rise time and pulse width of the current increase accordingly.

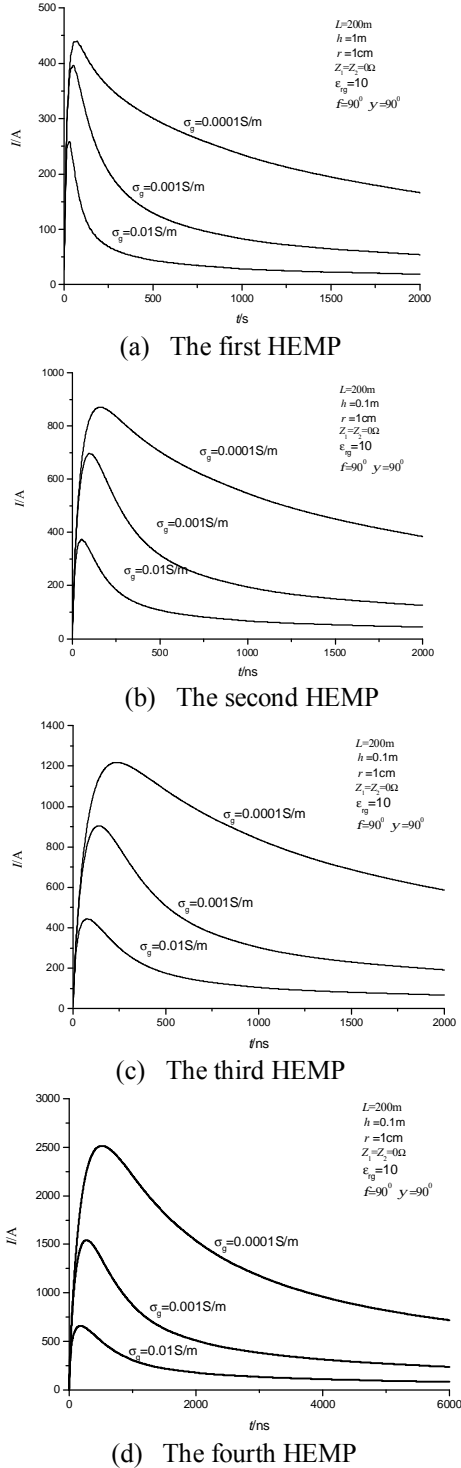


Fig.3 Induced current for horizontal polarization

Fig.4 illustrates the calculated current in the cable at  $x=l$  for different ground conductivities for vertical polarization wave at  $y=30^\circ$  and  $f=0^\circ$ , where the maximum value of peak current is obtained. It also can be seen that as the ground conductivity decreases, the peak current value, rise time and pulse width of the current increase accordingly. However, the peak current value is larger than that for the horizontal polarization wave, and pulse width is less than that for horizontal polarization wave.

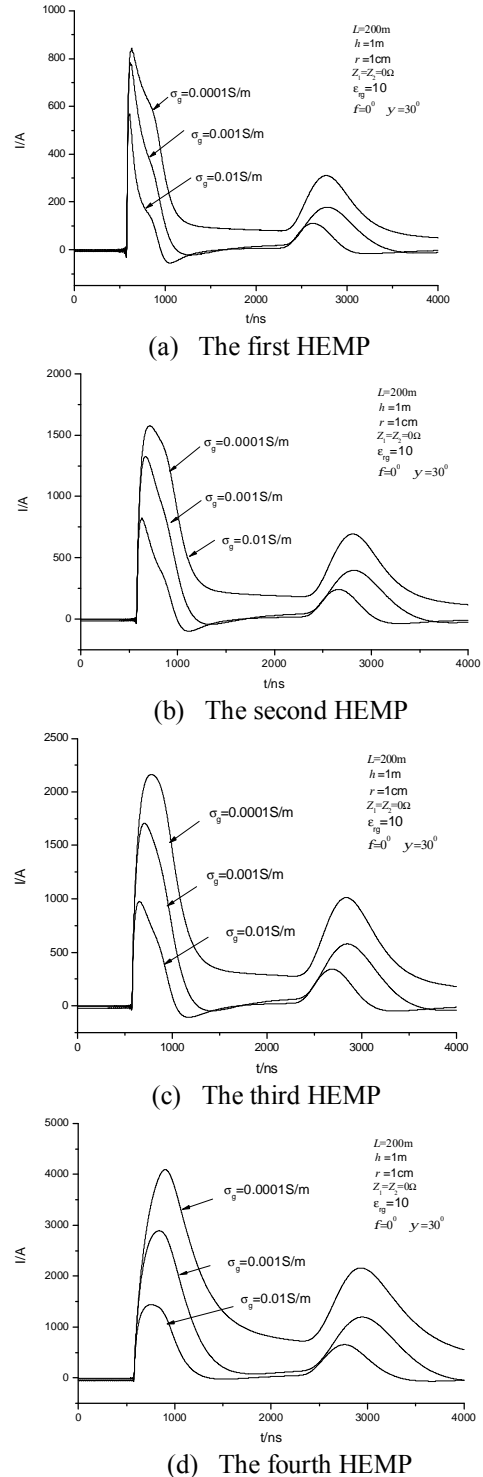


Fig.4 Induced current for vertical polarization

## 4 HEMP conducted environment analysis

Some typical ground conductivities can be found in the reference [6]. The HEMP conducted environment can be obtained according to the calculated current with  $s_g=0.001\text{S/m}$ .

The HEMP conducted environment is expressed by double exponential wave. However, the calculated results are some different from double exponential wave. Therefore, the calculated results are needed to be fitted to double exponential wave. According to calculated results, the pulse width is larger than the rise time, so the fitted pulse width can be estimated by single exponential wave. The fitting ruler is that the whole energy of calculated wave is the same value as that of fitted wave, indicated by the following equation:

$$\int_0^{\infty} i(t)^2 dt = \int_0^{\infty} \left( e^{-\frac{t}{\tau}} \right)^2 dt \quad (2)$$

Where  $i(t)$  is united current,  $\tau$  is the time constant of single exponential wave.

In table.2, the calculated pulse width and the fitted pulse width of the induced current for the four kinds of HEMP for both horizontal polarization and vertical polarization are given. It can be seen that the fitted pulse width of horizontal polarization is larger than that of vertical polarization, and the fitted result of horizontal polarization for the first HEMP is similar to the conducted HEMP environment in MIL-STD-188-125-2. Fig.5 illustrates the calculated current wave and the fitted current wave for the first HEMP. The curve of the pulse width of fitted current vs. that of HEMP is illustrated in Fig.6.

Table 2: Fitted induced current waveform

HEMP	I/A		Calculated $t_w/\text{ns}$		Fitted $t_w/\text{ns}$	
	H	V	H	V	H	V
1	397	781	258	229	439	274
2	697	1328	419	333	691	433
3	905	1700	555	377	887	535
4	1543	2892	1118	500	1647	797

The combination of maximum peak current value, maximum ratio of rise time and maximum pulse width forms the conducted HEMP environment for weapons. If the IEC HEMP radiated environment is used, according to calculated results, the HEMP conducted environment may be chosen as: peak current 800A and pulse width 450ns. In addition, the maximum ratio of rise time is about  $35 \times 10^9 \text{A/s}$  as  $s_g=0.01\text{S/m}$ . Thus, if peak current is 800A, the rise time is 18ns. Considering the fact that the rise time value of the truly vertical polarization wave may be larger than that of IEC HEMP radiated environment, it is practicable to choose the rise time value as not larger than 20ns. For the intrasite cable defined in MIL-STD-188-125-2 may have elevated parts, 1000A may be chosen for it, and 800A may be chosen for buried cable.

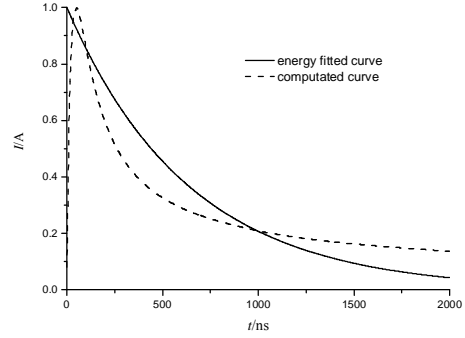


Fig.5 The calculated waveform and the fitted waveform

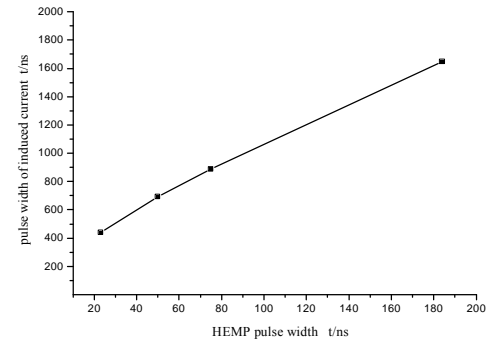


Fig.6 Pulse width of fitted current vs. pulse width of HEMP

## 5 Conclusion

The induced current for cable lying on ground illuminated by four kinds of HEMP radiation environments is calculated. The results show that the peak current value for vertical polarization is larger than that for horizontal polarization, and the rise time and pulsed width of induced current increase as ground conductivity decreases. By analyzing the calculated results, the relationship between the HEMP radiated environment in IEC61000-2-9 and the HEMP conducted environment in MIL-STD-188-125-1/2 has been shown.

## References

- [1] *High-Altitude Electromagnetic Pulse (NEMP) Protection for Ground-Based C<sup>4</sup>I Facilities Performing Critical, Time-Urgent Missions Part 1- Fixed Facilities*. MIL-STD-188-125-1, Jul.17, 1998
- [2] *High-Altitude Electromagnetic Pulse (NEMP) Protection for Ground-Based C<sup>4</sup>I Facilities Performing Critical, Time-Urgent Missions - Part 2 - Transportable Systems*. MIL-STD-188-125-2, Mar.3,1999
- [3] *Electromagnetic environmental effects requirements for systems*. MIL-STD-464, Mar.18, 1997
- [4] *Description of HEMP environment-radiation disturbance*. IEC61000-2-9, 1996
- [5] F.M.Tesche, M.Ianoz, T.Karlsson. *EMC Analysis methods and computational models*. New York: Wiley, 1997.
- [6] E.F.vance. *Coupling to shield cable*. New York: Wiley, 1978.

# Nonlinear and Short-Orbit Time-Reversal in a Wave Chaotic System

*Bo Xiao\**, *Thomas Antonsen\**, *Edward Ott\**, *Steven M. Anlage\**

\* *Department of Physics and Department of Electrical and Computer Engineering at the University of Maryland, College Park, MD, USA 20742-4111, [anlage@umd.edu](mailto:anlage@umd.edu), <http://anlage.umd.edu>*

## Abstract

Time reversal mirrors have been widely used to achieve wave focusing in acoustics and electromagnetics. A typical time reversal experiment requires that a transmitter be initially present at the target focusing point, which limits the application of this technique. In this contribution, we propose two methods to focus waves at an arbitrary location inside a complex enclosure using either a passive nonlinear object or a numerically calculated wave excitation signal. In the latter case we use a semi-classical ray algorithm to calculate the signal that would be received at a transceiver port resulting from the injection of a short pulse at the desired target location. The quality of the pulse reconstruction is quantified in three different ways and the values of these metrics can be predicted by the statistics of the scattering-parameter  $|S_{21}|^2$  between the transceiver and target points in the enclosure. We experimentally demonstrate the method using a microwave billiard and quantify the reconstruction quality as a function of enclosure loss, port coupling and other considerations.

**Keywords:** Time-reversed wave focusing, semiclassical treatment, nonlinear time-reversal mirror, synthetic sona.

## 1 Introduction

Exploiting the time-reversal invariance and reciprocal properties of the lossless wave equation enables elegantly simple solutions to complex wave-scattering problems and is embodied in the time-reversal mirror [1]. In previous work, we extended the concepts of Loschmidt Echo and Fidelity to classical waves, such as acoustic and electromagnetic waves, to realize a new sensor paradigm [2-4]. Here we demonstrate the implementation of an electromagnetic time-reversal mirror in a wave chaotic system containing a discrete nonlinearity [5]. We demonstrate that the time-reversed nonlinear excitations reconstruct exclusively upon the source of the nonlinearity. As an example of its utility, we demonstrate a new form of secure communication and point out other applications.

A typical time reversal experiment requires that a transmitter be initially present at the target focusing point, which limits the application of time-reversal techniques. We propose a method to focus waves at an arbitrary location inside a complex enclosure using a numerically calculated wave signal [6]. We use a semi-classical ray algorithm to calculate the signal that would be received at a transceiver port resulting from the injection of a short pulse at the desired target location. The quality of the reconstruction is quantified in three different ways and the values of these metrics can be predicted by the statistics of the scattering-parameter  $|S_{21}|^2$  between the transceiver and target points in the enclosure.

## 2 Experiment

We experimentally demonstrate the two methods using both a flat microwave billiard (enclosure with reflecting interior boundaries) and three-dimensional complex enclosure (Fig. 1), and quantify the reconstruction quality as a function of enclosure loss, port coupling and other considerations.

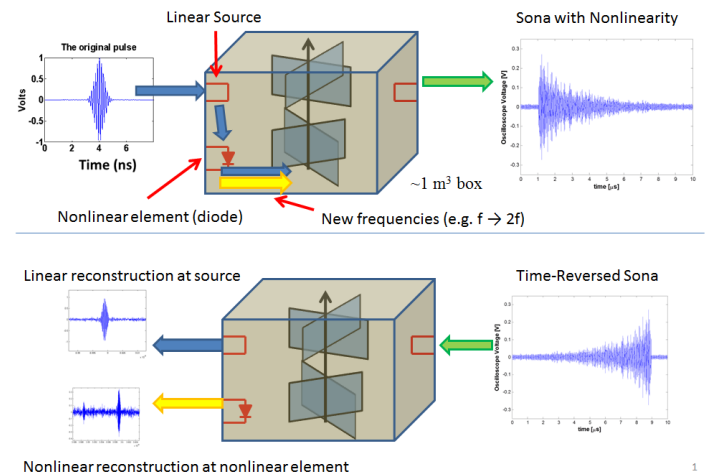


**Figure 1.** (Top) time-forward step in which a brief Gaussian pulse is injected into a complex over-moded enclosure, modulated on a multi-GHz carrier, and produces a complex sona signal. (Bottom) Time-reversed step in which the time-reversed sonas are injected into the enclosure and reconstruct as time-reversed replicas.

The first experiment is schematically illustrated in Fig. 1. We utilize a passive nonlinear source (a diode in this case) to respond to an interrogation pulse ( $\sim$  few ns duration Gaussian of a microwave carrier signal) by creating a second harmonic sona signal. (We use the word ‘sona’ to represent the entire waveform produced by the complex enclosure, as opposed to ‘coda’ which refers to just the end of the waveform.) Both the linear and nonlinear sona signals are collected at a third port. In the second step, the two sonas are time-reversed and injected into the same port in which they were measured. The linear sona reconstructs as a time-reversed replica of the original pulse at the linear source. The nonlinear sona reconstructs as a time-reversed replica of the up-converted interrogation pulse, and a few of its echoes, at the nonlinear element. This demonstrates a selective reconstruction at an arbitrary location in the enclosure, and requires only the initial presence of a passive nonlinear object [5, 7].

Applications include exclusive communications and wireless power transfer. As discussed in detail elsewhere [7] we have sent images from the third port to either the linear or nonlinear port. The image sent to one port is not visible at the other port, demonstrating the exclusivity of the information transfer.

A second experiment utilizes the synthetic sona technique to create a purely theoretical waveform that, when time-reversed and injected into a physical two-dimensional microwave billiard, will reconstruct as a short pulse at a precise (and arbitrarily chosen) location in the billiard. This method exploits ‘short orbits’ [8, 9] between the injection point and reconstruction point to perform a semi-classical calculation of the synthetic sona [6]. The experimental reconstructions are successful for billiards in which the interior geometry is known. We find that the quality of the synthetic sona reconstructions correlates strongly with the transmission S-parameter over the bandwidth of the pulse.

## Acknowledgements

This work was funded by the AFOSR (No. FA95500710049), the Office of Naval Research (contract No. N00014130474), and the Center for Nanophysics and Advanced Materials (CNAM).

## References

- [1] S. M. Anlage, J. Rodgers, S. Hemmady, J. Hart, T. M. Antonsen, E. Ott, *Acta Physica Polonica A* vol. 112, pp. 569-574, 2007.
- [2] B. T. Taddese, J. Hart, T. M. Antonsen, E. Ott, and S. M. Anlage, *Applied Physics Letters* vol. 95, 114103, 2009.
- [3] B. T. Taddese, T. M. Antonsen, E. Ott, and S. M. Anlage, *Journal of Applied Physics* vol. 108, 114911, 2010.
- [4] B. T. Taddese, G. Gradoni, F. Moglie, T. M. Antonsen, E. Ott, S. M. Anlage, *New Journal of Physics* vol. 15, 023025, 2013.
- [5] M. Frazier, B. Taddese, T. Antonsen, S. M. Anlage, *Physical Review Letters* vol. 110, 063902, 2013. See "Alice and Bob Go Nonlinear" Synopsis on Physics.APS.org (<http://physics.aps.org/synopsis-for/10.1103/PhysRevLett.110.063902>).
- [6] Bo Xiao, Thomas M. Antonsen, Edward Ott, Steven M. Anlage, *Focusing Waves at Arbitrary Locations in a Ray-Chaotic Enclosure Using Time-Reversed Synthetic Sonas*, <http://arxiv.org/abs/1409.3850>.
- [7] Matthew Frazier, Biniyam Taddese, Bo Xiao, Thomas Antonsen, Edward Ott, Steven M. Anlage, "Nonlinear Time-Reversal of Classical Waves: Experiment and Model," *Phys. Rev. E* vol. 88, 062910, 2013.
- [8] James A. Hart, T. M. Antonsen, E. Ott, "The effect of short ray trajectories on the scattering statistics of wave chaotic systems," *Phys. Rev. E* vol. 80, 041109, 2009.
- [9] Jen-Hao Yeh, James Hart, Elliott Bradshaw, Thomas Antonsen, Edward Ott, Steven M. Anlage, "Experimental Examination of the Effect of Short Ray Trajectories in Two-port Wave-Chaotic Scattering Systems," *Phys. Rev. E* vol. 82, 041114, 2010.

# A study for the effect of external incident wave on the simplified vehicle model

Wonjune Kang\*, Junho Choi<sup>†</sup>, Joonho So<sup>†</sup>, Kangin Lee\* and Youngseek Chung\*

\* Department of Wireless Communications Engineering,  
Kwangwoon University, Seoul, Korea  
astin1983@naver.com,

<sup>†</sup>Agency for Defence Development, Daejeon, Korea

## Abstract

In this paper, we present a study on the analysis of EMI(Electro-magnetic Interference) effects on the vehicle model which is directly exposed to an external incident wave. The electronic devices in a vehicle are required to prepare for unwanted electromagnetic coupling effects. To effectively anticipate and respond to the problem, the analysis of the internal structure is essential by the external electromagnetic wave.

**Keywords:** Vehicle, EMI, EMC, Shielding Effectiveness

## 1 Introduction

Modern electronic systems have become smaller and more complex. For this reason, EMC (Electromagnetic Compatibility) problem has become more important. Furthermore, the possibility of malfunction is increased according to the power consumption of the system is reduced. These problems are particularly important in areas which can be life-threatening for people when causing a malfunction as a vehicle. Especially in the case of a vehicle that the external frame is made to the metal, the penetrated electromagnetic wave from small apertures can cause resonance inside the structure. It can be fatal to the internal electronic systems of the vehicle. To effectively anticipate and respond to the problem, the analysis of EMI effects on the vehicle is essential by the external electromagnetic wave. Full wave methods such as FDTD(Finite-difference time-domain) method and FEM(Finite element method) are very strong to analyse the effects of EMI[1,2]. However, full wave analysis methods will be difficult to apply large models as target size increase because of limited computer performance. In this paper, we analyse the effect of EMI inside the vehicle model using mode matching method[3,4].

## 2 Analysis of EMI effects on the simplified vehicle model using mode matching

The simplified vehicle model is shown in Fig. 1. This model consists of two cavities with apertures. The sizes of vehicle model are shown in Table. 1. It is illuminated by an external

plane wave polarized in x-direction, as shown in Fig. 1. The coupled fields on each aperture affect the interior of vehicle model.

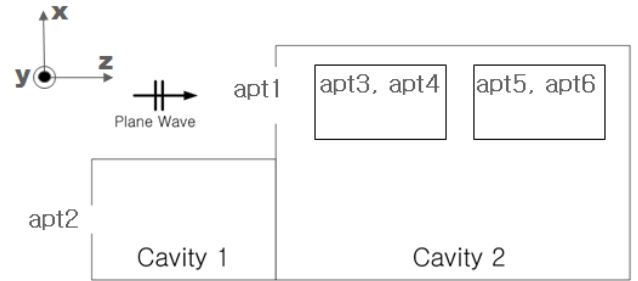


Figure 1. Simplified vehicle model

Table 1: Sizes of the vehicle model

Item	x [mm]	y [mm]	z [mm]
Cavity 1	600	300	500
Cavity 2	600	500	1000
Apt 1	400	-	100
Apt 2	200	-	45
Apt3~Apt6	-	250	120

Based on mode matching method, equations on apertures can be written as

$$\left( \mathbf{H}^{inc, apt1} + \mathbf{H}^{ref, apt1} \right) \Big|_{y=apt1} = \left( \mathbf{H}_{cav2}^{apt1} + \mathbf{H}_{cav2}^{apt3-apt6} \right) \Big|_{y=apt1} \quad (1)$$

$$\left( \mathbf{H}^{inc, apt2} + \mathbf{H}^{ref, apt2} \right) \Big|_{y=apt2} = \left( \mathbf{H}_{cav1}^{apt2} \right) \Big|_{y=apt2} \quad (2)$$

$$\left( \mathbf{H}^{ref, apt3} \right) \Big|_{z=apt3} = \left( \mathbf{H}_{cav2}^{apt1} + \mathbf{H}_{cav2}^{apt3-apt6} \right) \Big|_{z=apt3} \quad (3)$$

$$\left( \mathbf{H}^{ref, apt4} \right) \Big|_{z=apt4} = \left( \mathbf{H}_{cav2}^{apt1} + \mathbf{H}_{cav2}^{apt3-apt6} \right) \Big|_{z=apt4} \quad (4)$$

$$\left( \mathbf{H}^{ref, apt5} \right) \Big|_{z=apt5} = \left( \mathbf{H}_{cav2}^{apt1} + \mathbf{H}_{cav2}^{apt3-apt6} \right) \Big|_{z=apt5} \quad (5)$$

$$\left( \mathbf{H}^{ref, apt6} \right) \Big|_{z=apt6} = \left( \mathbf{H}_{cav2}^{apt1} + \mathbf{H}_{cav2}^{apt3-apt6} \right) \Big|_{z=apt6} \quad (6)$$

$\mathbf{H}^{inc,apt1}$  is the incident magnetic field to aperture 1 and  $\mathbf{H}^{ref,apt1}$  is the reflected field from aperture 1.  $\mathbf{H}^{apt1}_{cav2}$  means that the magnetic field by aperture1 inside cavity 2. In similar way,  $\mathbf{H}^{apt3-apt6}_{cav2}$  indicates magnetic field by side apertures inside cavity 2.

We introduce the shielding effectiveness [5] to compare how much fields are penetrated. Shielding effectiveness is defined as a following equation.

$$\text{Shielding Effectiveness (dB)} = 20 \log \left( \frac{|\mathbf{E}_{Ext}|}{|\mathbf{E}_{Center}|} \right) \quad (7)$$

$E_{Ext}$  is the incident E-field from source and  $E_{Center}$  is the E-field in the center point of the cavity.

We compare the simulation results using mode matching method with FDTD method.

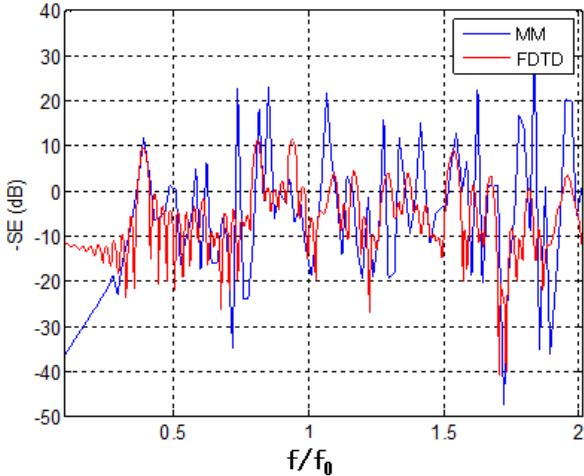


Figure 2. Shielding effectiveness of Cavity 1 (center)

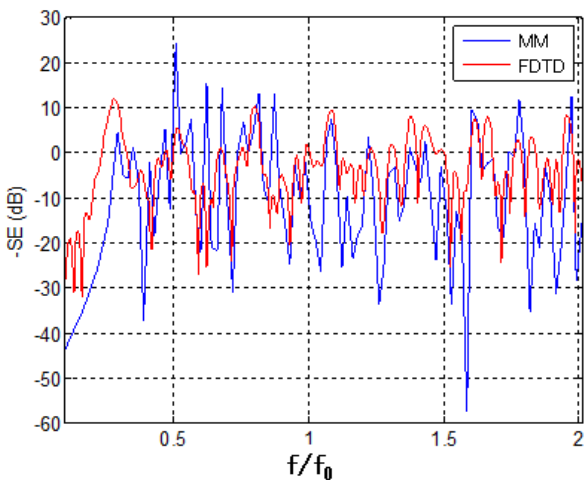


Figure 3. Shielding effectiveness of Cavity 2 (center)

### 3 Conclusions

In the paper, we analyse the effect of EMI inside the vehicle model using mode matching method. Furthermore, we compare the simulation results of mode matching method with FDTD method. The results are in good agreement except a difference of magnitude on resonance frequencies.

### Acknowledgements

This research was supported by Basic Science Research Program through the National Research Foundation of Korea(NRF) funded by the Ministry of Education, Science and Technology(2013R1A1A2011054).

The authors gratefully acknowledge the financial support provided by Agency for Defense Development.

### References

- [1] A. Taflove, Computational Electrodynamics: The Finite-Difference Time-Domain Method, Artech House, 1995
- [2] J. M. Jin, The Finite Element Method in Electromagnetics., Wiley, 1993
- [3] R. F. Harrington, Time-Harmonic Electromagnetic Fields, McGraw-Hill, New York, 1961.
- [4] Deshpande, M. D. 2000. Electromagnetic field penetration studies. Report No. CR-2000-210297, National Aeronautics and Space Administration, June 2000.
- [5] Ott, H. W., Noise reduction techniques in electronic systems. New York: Wiley., 1988.

# Analysis of the Compromising Electromagnetic Emanations of PS/2 Keyboards

Ho Seong Lee\*, Dong-Joo Sim\*, Kyuhong Sim<sup>†</sup>, and Jong-Gwan Yook\*

\*Dept. Electrical and Electronic Engineering, Yonsei University, Seoul, Republic of Korea

<sup>†</sup>Electronic Warfare R&D Lab, LIG Nex1, Seongnam, Republic of Korea

jgyook@yonsei.ac.kr

## Abstract

The compromising electromagnetic emanations of personal system/2 (PS/2) keyboards are generated by electric signal on the cable between the computer and the keyboard. They include key stroke information so that there is risk of information leakage, because significant key information such as passwords are eavesdropped. In this paper, the compromising electromagnetic emanations are detected and analyzed for verifying the possibility of electromagnetic eavesdropping. The leakage signals received by wideband antenna are reconstructed by designed algorithm. Analysis on the compromising electromagnetic emanations of PS/2 keyboard is conducted for the 36 key strokes and all the key strokes are reconstructed.

**Keywords:** eavesdropping; TEMPEST; electromagnetic interference (EMI); compromising electromagnetic emanations.

## 1 Introduction

It has been reported that the compromising electromagnetic emanations from the peripherals such as the monitor and the keyboard contain information of the computer [1]. The researches for the compromising electromagnetic emanations have been conducted consistently from discovery of van eck phreaking in 1985 [2]. Also, the study on the electromagnetic emanations of keyboards has been performed until now. In 2010, the research for analyzing the electromagnetic emanations of PS/2, USB, and wireless keyboards was carried out [3]. It was suggested that the leakage electromagnetic signals of PS/2 keyboards are analyzed and reconstructed with high accuracy but those of USB and wireless keyboards are insufficient.

In this paper, it is verified that the research on the analysis of the compromising electromagnetic emanations of PS/2 keyboards. The leakage signal of PS/2 keyboards was measured at the short distance, and algorithm of analysis the compromising electromagnetic emanations was supposed.

## 2 Measurement Results

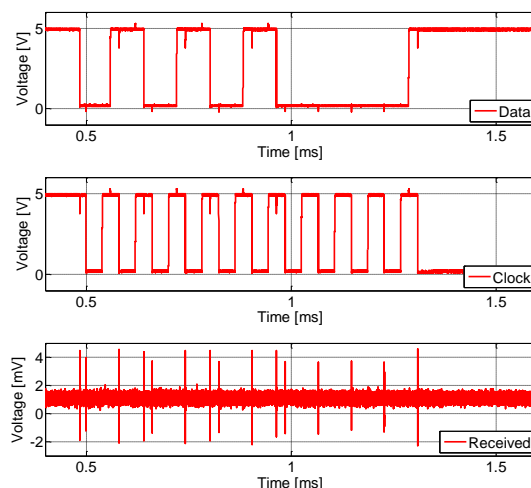


Figure 1. Measurement signals of PS/2 keyboard for data, clock, and received the compromising electromagnetic emanations.

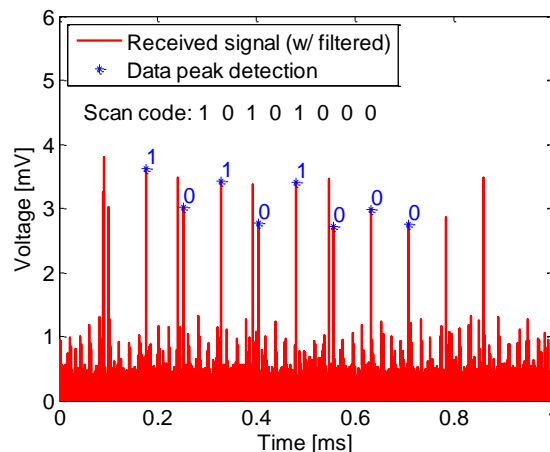


Figure 2. Reconstruction the compromising electromagnetic emanations of PS/2 keyboards when the key 'Q' is pressed.

The compromising electromagnetic emanations of PS/2 keyboards are measured by using the wideband antenna which has frequency range from 25 to 3000 MHz. The leakage signals are generated when the key is pressed. Fig. 1 shows the measured signals of PS/2 keyboard for data, clock, and received compromising electromagnetic emanations. The format of data and clock signal are related to the PS/2 protocol. The peaks of received signal are generated by

falling edge of data and clock signal. It is possible to infer transmitted data between computer and keyboard through the compromising electromagnetic emanations.

Measured data of the leakage signals in keyboard is input to the designed algorithm for analysis of key stroke data. The designed algorithm accomplishes some signal processing techniques which are band pass filtering, envelope, and peak detection. Band pass filtering operates on frequency domain and return to time domain signal using fast Fourier transform (FFT) and inverse fast Fourier transform (IFFT). Fig.2 shows the analysis result of compromising electromagnetic emanations of PS/2 keyboard when the key 'Q' is pressed. Each key of PS/2 keyboard has the scan code which is identification hexadecimal number. The state of pressed key data is distinguished by peak level of leakage signals. It is verified that analysis data of compromising electromagnetic emanations when the 'Q' key is pressed is equal to the scan code of the same key as shown in Fig. 2. In addition, analysis for other key stroke is conducted and all the keys are analyzed perfectly with designed algorithm.

### 3 Summary and Conclusion

In this paper, the compromising electromagnetic emanations of PS/2 keyboard are analyzed. The leakage signals from keyboard when the key is pressed are measured by wideband antenna and digital oscilloscope. The algorithm of analysis the compromising electromagnetic emanations is designed by using some signal processing technique. The number of key under the analysis is 36 (A to Z and 0 to 9), and all the keys are analyzed identically with their own scan code.

### Acknowledgements

"This work has been supported by the Agency for Defence Development (ADD) and LIG Nex1 under the contract UC140011ED"

### References

- [1] Kuhn, Markus G., and Ross J. Anderson. "Soft tempest: Hidden data transmission using electromagnetic emanations." *Information Hiding*. Springer Berlin Heidelberg, 1998.
- [2] Van Eck, Wim. "Electromagnetic radiation from video display units: an eavesdropping risk?." *Computers & Security* 4.4 (1985): 269-286.
- [2] Vuagnoux, M. and Pasini, S., "An improved technique to discover compromising electromagnetic emanations," *Electromagnetic Compatibility (EMC), 2010 IEEE International Symposium on*, pp.121-126, July 2010

# Ultra-wideband Electromagnetic Bandgap Structure with Multi-slot for Simultaneous Switching Noise Suppression

*J. H. Choi\*, J. W Shin\* and J. H. So\**

*\*Agency for Defense Development, Koea and email: junhochoi@add.re.kr*

## Abstract

**A compact and cost-effective electromagnetic bandgap (EBG) structure for noise suppression in ultra-wideband applications is designed and simulated. The structure is a hybrid EBG structure with multi-slot in a unit cell to provide excellent noise suppression up to 20 GHz. This type of hybrid EBG structure shows a high noise isolation and suppression capability of -55 dB on average in an ultra-wide stopband range of 3 GHz-20 GHz.**

**Keywords:** Ultra-wideband, electromagnetic bandgap (EBG), simultaneous switching noise (SSN).

## 1 Introduction

Electromagnetic bangap (EBG) structures embedded in power/ground planes have been widely studied as an efficient solution to suppress the power/ground noise in a high speed board and mixed-signal systems [1]-[4]. As system operating frequency increases more and more, simultaneous switching noise (SSN), also known as delta-I noise has become one of the major concerns in the development of high speed mixed-signal systems. To mitigate the effect of SSN in ultra-wideband, many noise suppression techniques have been developed, such as the mushroom-type EBG structure [2], L-bridge EBG structure [3] and AI-EBG structure [1]. However, the mushroom-type EBG structure requires additional metal layer with via connections, it presents an expensive solution for printed circuit board (PCB) applications. L-bridge EBG structure and AI-EBG structure are only made up of two metal layers of a periodic patterned power plane and solid ground plane. It provides a cheap fabrication and wide bandwidth as well as deep noise suppression. Based on the AI-EBG structure, we have presented a hybrid EBG structure with multi-slot which is inserted into each of unit cells to improve the noise suppression in an ultra-wideband. This hybrid EBG structure shows excellent noise isolation of -55 dB over 17 GHz.

## 2 Design and numerical simulation

The multi-slot EBG structure is a metallic-dielectric EBG structure consisting of two metal layers separated by a thin dielectric material, as shown in Fig. 1. In the EBG structure, only one metal layer has a periodic pattern which is a two-dimensional rectangular lattice with each element consisting

of a metal patch with multi-slot and connecting metal branches. The multi-slot and metal branches form multi distributed LC networks. In this structure, a metal branch introduces additional inductance while the metal patch with multi-slot forms a different capacitance corresponding to the solid planes isolated by a slot. This periodic pattern in a unit cell provides multi cutoff frequencies, which results in excellent noise isolation characteristics in a wide stopband range. The cutoff frequency of the unit metal patch is obtained as [4]:

$$f_{cutoff} = \frac{1}{\pi \sqrt{(L_{branch} + L_{patch}) \times C_{patch}}} \quad (1)$$

The numerical simulation is carried out by using a commercial electromagnetic simulator, Ansoft HFSS to evaluate the performance of the designed multi-slot EBG structure depicted in Fig. 1. The simulated result shows that the multi-slot embedded structure achieves an ultrawide SSN suppression characteristic over 3 GHz-20 GHz, as shown in Fig. 2.

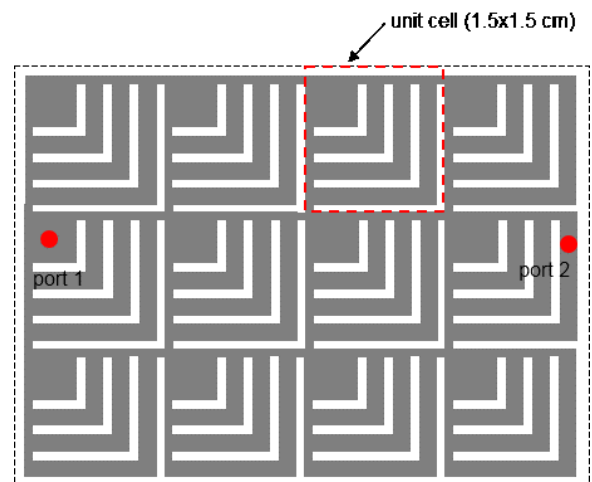


**Figure 1. Schematic diagram of multi-slot EBG structure based on AI-EBG.**

## 3 Conclusion

This paper presents embedded multi-slot technique to enhance the suppression against SSN based on the periodic planar AI-EBG structure. This hybrid EBG structure shows excellent noise suppression over 17 GHz. In addition, it can be easily designed and fabricated using a standard PCB

process because it is not necessary for blind via and an additional metal layer.

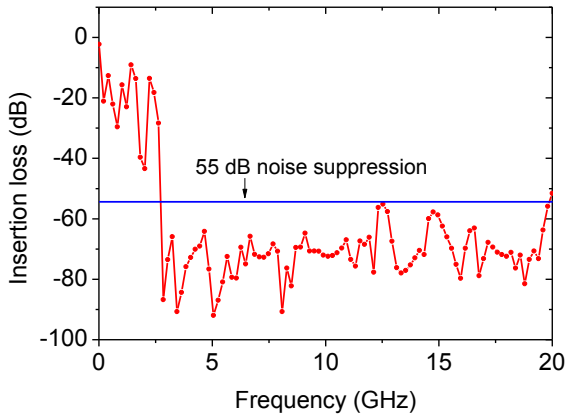


**Figure 2. Simulated result of multi-slot EBG structure based on AI-EBG.**

## References

- [1] J. W. Choi, "Alternative impedance electromagnetic bandgap structure for noise isolation in ultra-wideband", *Electron. Lett.*, volume 42, pp. 467-468, (2006).
- [2] J. Li, J. Mao, and M. Tang, "Mushroom-type ground plane structure for wideband SSN suppression in high-speed circuits", *IEEE. Microw. Wireless Compon. Lett.*, volume 21, pp. 646-648, (2011).
- [3] T. L. Wu, C. C. Wang, Y. H. Lin, T. K. Wang, and G. Chang, "A novel power plane with super-wideband elimination of ground bounce noise on high speed circuits", *IEEE. Microw. Wireless Compon. Lett.*, volume 15, pp. 174-176, (2005).
- [4] J. W. Choi, D. G. Kam, D. H. Chung, K. Srinivasan, V. Govind, J. H. Kim, and M. Swaminthan, "Near-field and far-field analyses of alternating impedance electromagnetic bandgap (AI-EBG) structure for mixed-signal applications", *IEEE Trans. Advan. Packaging*, volume 30, pp. 180-190, 2007.

# Design of a compact free-field sensor with fiber-optic link for EMP measurement

Lihua Shi, Rongen Si, Yinghui Zhou

National Key Laboratory on Electromagnetic Environmental Effects and Electro-optical Engineering,  
No.1 Haifuxiang, Nanjing, China

## Abstract

A small size dipole antenna with built-in fiber-optic transmitting circuit is developed for the measurement of free-field electromagnetic field. The response to and the influence on the tested field are investigated by numerical analysis. Design parameters are defined based on these analysis results. A prototype probe with length of 8cm and radius of 1.2cm is fabricated. A compact electro-optical transform circuit is designed and built in the hollow space of the antenna cylinder. The responses of the measurement system are tested in a parallel-plate electromagnetic pulse(EMP) simulator under input of high-altitude EMP(HEMP) and lightning EMP(LEMP). A rise-time of 2.8ns is obtained and the output has no obvious low-frequency distortion in measuring LEMP fields. This kind of sensor is suitable for measurement of wide-band electric field from 1kV/m to 15kV/m.

**Keywords:** Electric field sensor, EMP, dipole antenna, fiber-optic transmission, calibration.

## 1 Introduction

Wide-band frequency response, broad dynamic range and good anti-interference capability are the basic requirements for measurement of EMP. The design and features of various EMP sensors have been summarized by Baum *et al* in [1]. To avoid the disturbance from the external high-intensity field, EMP sensors usually use fiber-optic(FO) transmission system. Most of the market-available FO systems are provided as separate devices to be incorporated with the sensing system. As a result, both the size and the complicity of the measurement system will be increased. For an example, the differential type free-field sensor needs to use a balun first to transfer the balance output to the unbalance input of FO system, then the electric signal is transformed by the electro-optic(EO) transforming device. At the receiving end, one also needs to use a passive integrator for recovering the true shape of the measured field[2]. For measurement of EMP field inside a small cavity, traditional electric/magnetic field sensor and FO transmission system need to be integrated so as to minimized size and the influence of the measurement system to the field.

Gassmann and Furrer have designed a 3-D vector sensor consisting of three double-loaded orthogonal loops and built-in EO device[3]. To minimize the power consumption and the size, a RF-multiplexer was used to switch the 6-channel signals to only one amplifier. The analog signal is digitized within the sensor circuits and transferred by digital FO system to a computer. However, in measurement of EMP field which occurs as a very fast single pulse, it is better to use parallel transmission instead of the multiplexer. Xu *et al* has developed a 3-D pulsed electric field sensor using built-in 3-channel FO system[4], the circuit system was fixed in a 10cm metallic cubic.

The aim of this paper is to further reduce the size of the measurement device and provide a low-cost sensor for measurement of pulsed electric field. A compact circuit for balun and EO transforming was designed and the whole circuit can be fit in the hollow cylinder which is used as an antenna. The design process and tested results are introduced in the following parts.

## 2 Structure of the measurement system

As shown in Fig.1, two hollow cylinders are used as the main structure of the sensor. To minimize the influence of the sensor structure on the measured field, the field distribution in vicinity of the antenna is analyzed numerically under different situations. Fig.2 is an example of the field distribution for the antenna with semi-sphere caps. The equivalent RC load of the measurement circuit is also considered in the simulation. Parameters of the geometry and the input impedance are finally selected according to the response waveforms on the load and the influence of the antenna on the measured field.

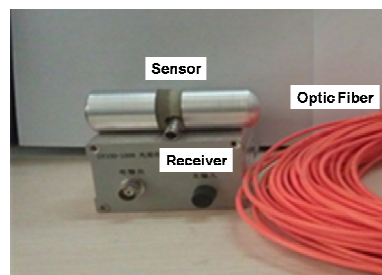


Fig. 1 Photo of the measurement system

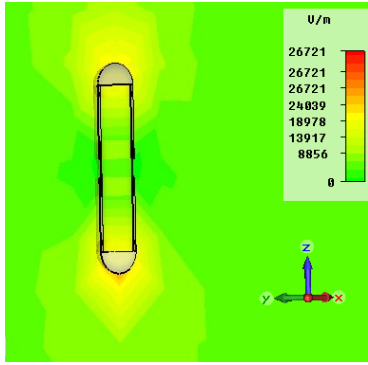


Fig. 2 Field distribution in vicinity of the antenna

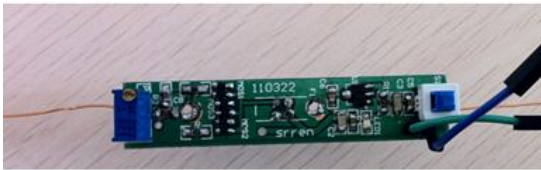


Fig. 3 Circuit board for use within antenna

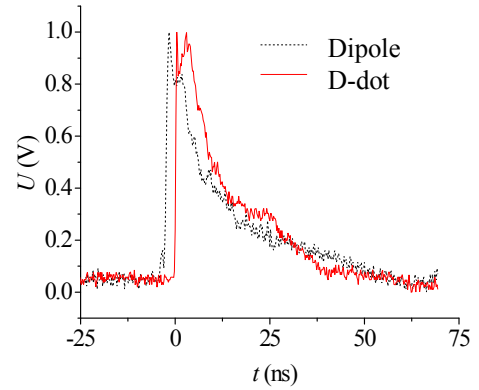
A compact circuit board was designed to be built in the antenna, which is shown in Fig.3. Three MOSFETs connected in parallel are used to provide driven current to the laser emitter. By adjusting the DC bias of the MOSFETs, 26mA steady state working current was set and it enables a dynamic range of 54dB. The sensitivity and lower cut-off frequency of the sensor can be adjusted by changing the load capacitance. For the antenna with full length of 8cm and radius of 1.2cm, the sensitivity to HEMP field is 19kV/m per volt when the load capacitance is 50pF.

### 3 Test results

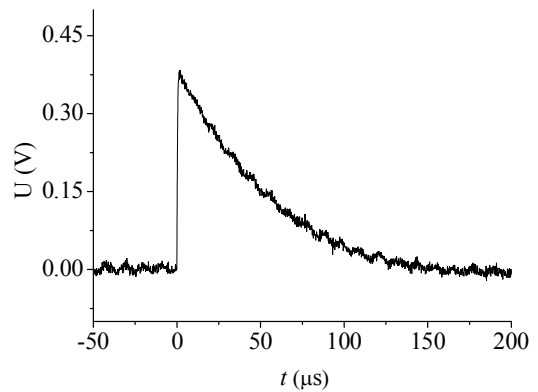
A parallel plate electromagnetic pulse simulator is used to verify the characteristics of the developed sensor. Fig.4 is the responses of the antenna to HEMP (2.3/25ns) and LEMP (1.2/50μs). The rise-time of the waveform for the dipole is 2.8ns. The response to HEMP is also compared with the measured waveform obtained by D-dot sensor on the ground plane of the simulator. The results show that the measurement device developed in this paper has good response for both HEMP and LEMP. However, the reference D-dot sensor fails to measure LEMP field because its extremely low sensitivity in lower frequency band.

### 4 Conclusion

The designed free-field EMP sensor has less perturbation to the measured field. Compared to the market available D-dot sensor, its output is the true waveform of the electric field. Experimental research in the EMP simulator has verified that the sensor can be used for both HEMP and LEMP measurement. Presently, the proto-type sensor is only for one dimensional measurement, a three-dimensional sensor in a spherical structure is under development.



(a) Response to HEMP



(b) Response to LEMP

Fig.4 Measurement results of the system

### Acknowledgements

This research was supported by National Science Foundation of China under Grant No. 51477183.

### References

- [1] C.E.Baum, E.L.Breen, J.C.Giles, J. O'Neill, G.D.Sower. "Sensors for Electromagnetic Pulse Measurements Both Inside and Away from Nuclear Source Regions", *IEEE Trans. on Electromagnetic Compatibility*, vol.20, no.1, pp.22-35,(1978).
- [2] IEC 61000-4-33, "Testing and measurement techniques-measurement methods for high-power transient parameters", pp9-10,(2005).
- [3] F.Gassmann, J.Furrer. "An isotropic broadband electric and magnetic field sensor for radiation hazard measurements", *Proc. IEEE International Symp. on Electromagnetic Compatibility*, 9-13 Aug, pp.105-109,(1993).
- [4] Yuan-zhe Xu, Cheng Gao. "Development of Three-dimensional Wideband Sensor for Pulse Electric Field Measurement", *High Voltage Engineering*, vol. 34, no. 3, (2008).
- [5] Bihua Zhou, Bin Chen, Lihua Shi, "EMP and EMP Protection", Beijing: National Defence Industry Press, (2003).

# Determination of Q-value of an Avionics Bay or Other Multiresonant Cavity by Measurements in Time- and Frequency-Domain, with One or Two Antennas

*B Vallhagen\*, C Samuelsson\*, M Bäckström\**

*\*SAAB Aeronautics, SAAB AB, Linköping, Sweden, bengt.vallhagen@saabgroup.com*

## Abstract

A study consisting of several experimental measurement campaigns have been performed, with aim to verify a way of determining the Q-value of multiresonant cavities, such as avionic bays in aircraft. Measurements have been performed in two reverberation chambers of difference size – of which one with approximate volume as an avionics bay – as well as in avionics bays of an aircraft. Besides the relatively well-known methods of measurements in frequency-domain, refined methods of measurements in time-domain have been verified, including a technique with only one antenna – operating in both transmitting and receiving mode. Use of a single antenna may be crucial for measurements in bays of small volume.

**Keywords:** Q-value, multiresonant, avionic bays, measurements, time-domain.

## 1 Introduction

It is vitally important in the design of modern aircraft to protect its equipment against High Intensity Radiated Fields (HIRF), i.e. man-made electromagnetic fields in the radio and microwave frequency range, from transmitters such as radio or radar. Vulnerable aircraft electronics – avionics – may be placed in well-shielded bays as part of this protection. The average Shielding Effectiveness (SE) of such a bay can be expressed [1,2] as:

$$\langle SE \rangle = \frac{2\pi V}{\sigma_a \lambda Q} \quad (1)$$

... where  $V$  is the cavity volume,  $\lambda$  is wavelength. Equation (1) also clearly shows that  $\sigma_a$  (the aperture transmission cross section) and  $Q$  (the cavity quality factor) have impact on the SE. Thus; it is important to know  $Q$ .

The main scope for the actual measurement campaign(s) has been to verify a useful method of determining the Q-value in multiresonant rooms such as avionics bays. Parts of this main scope has been to:

- Reproduce and possibly refine lab measurements performed by other labs [1,4]
- Qualitatively compare measurements in time- and frequency-domain

- Perform and evaluate measurements with a single antenna
- Perform and evaluate measurements in time-domain, with frequency stirring
- ... and finally
  - Compare said lab measurements with measurements performed on a “real” test object, i.e. aircraft.

This paper includes brief descriptions of the test methods used and extracts from the measured results from time-domain measurements in the lab and on the aircraft.

## 2 Laboratory Measurements

Laboratory measurements were performed in two different reverberation chambers (RC), one “main” which measure 35 m<sup>3</sup>, and one smaller (nicknamed “Akilles”) which measure 1 m<sup>3</sup>. Basic setup with two antennas is shown in Fig. 1:

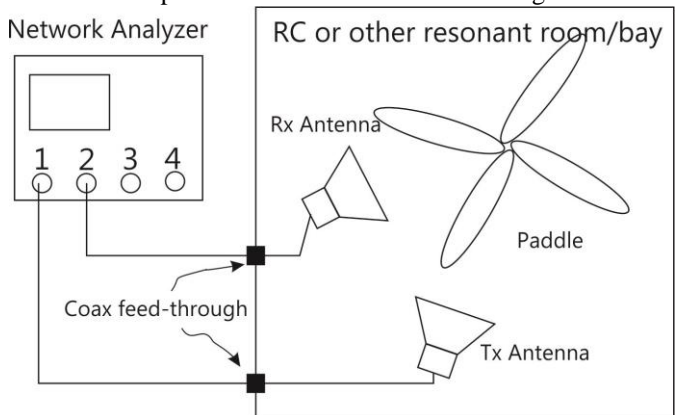


**Figure 1. Principle test setup in RC, frequency-domain measurements shown. For two-antenna measurements in time-domain, the network analyser (NA) is replaced by a signal generator feeding the Tx antenna, and a digital oscilloscope connected to the Rx antenna. The setup is also valid for measurements in avionics bays, though with no paddle present.**

### 2.1 Frequency-Domain

In frequency-domain, the Q-value is determined by measuring the  $S_{21}$ -parameter:

$$Q = \frac{16\pi^2 V}{\lambda^3} \left( \frac{P_{Rx}}{P_{Tx}} \right) \frac{1}{\eta_{Rx} \eta_{Tx} q_{Rx} q_{Tx}} \quad (2)$$

$$\left( \frac{P_{Rx}}{P_{Tx}} \right) = \langle |S_{21}|^2 \rangle \quad (2')$$

...where  $S_{21}$  is measured complex data from the NA,  $\eta$  represents the ohmic losses and  $q$  is the impedance mismatch factor. The brackets in Equation (2, 2') indicates averaging over a number of uncorrelated paddle positions in an isotropic environment. The method is well established, see e.g. [1,2]. The disadvantage of the method is the uncertainty in mentioned antenna parameters;  $q$  can be derived from  $S_{11}$ -measurements, but  $\eta$  has to be assumed (usually – as for actual measurements – set to 0.9 for horn antennas, cf. [3]).

## 2.2 Time-Domain

For measurements in time-domain, the resonant cavity is excited by a pulse modulated signal. Ideally, the pulse decay shall be decided by [1]:

$$U = U_s e^{-t/\tau} \quad (3)$$

...where  $t$  is time (set to  $t_0=0$  at the start of the decay),  $\tau$  is the time constant and  $U_s$  is the steady state energy in the cavity.  $t=\tau$  will occur when  $U = e^{-1}U_s \approx 0.37U_s$ , and with  $\tau$  measured,  $Q$  can be decided from the relation

$$Q = \omega\tau \quad (4)$$

... where  $\omega$  is angular frequency. For each frequency, data is measured and averaged over a large number of uncorrelated paddle positions or adjacent frequencies – mechanical or frequency stirring – where the latter is preferred in small cavities. Time-domain measurements are time-consuming. It is practically impossible to include as many frequency-points as with frequency-domain measurements.

## 2.3 The Circulator Method

An innovative method for measurements in time-domain is to use only a single antenna and add a circulator to the measurement setup, see Fig. 2.

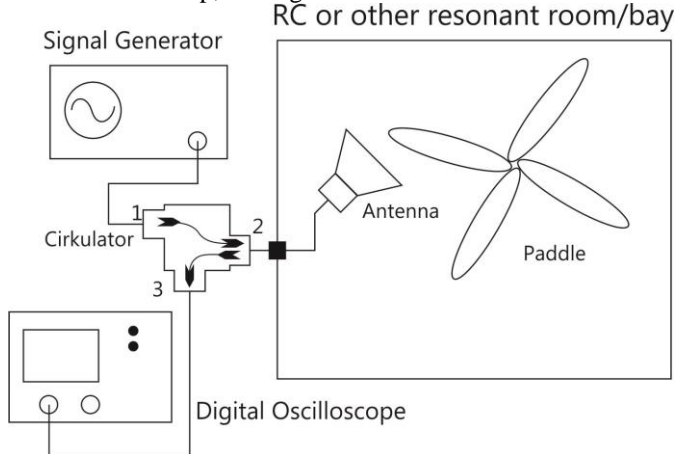


**Figure 2. Principle test setup for time-domain measurements with the “Circulator Method”, in RC or avionic bay (though without paddle).**

Here the antenna acts as both a receiver and transmitter; during the generator pulse time, both the incident and the reflected pulse will be present at port 3 of the circulator; but as the pulse shuts off ( $t=0$  in Equation (3)), only the reflected decay will remain on the circulator port 3.

Practically, all time-domain measurements were performed with continuous (frequency or mechanical) stirring and

continuous sampling oscilloscope sweeps. With a fast modern digital oscilloscope with built-in average function this is a convenient (and also reliable, see results further down) way to collect and process a large amount of data, guaranteeing enough uncorrelated stirrer positions. As a comparison, in [1] average were taken over 200 fixed paddle positions, while we average over 1024 or 4096 oscilloscope sweeps with the paddle in continuous movement (or frequency saw-tooth swept in a narrow band surrounding the frequency of interest). A snapshot example is shown in Fig. 3:

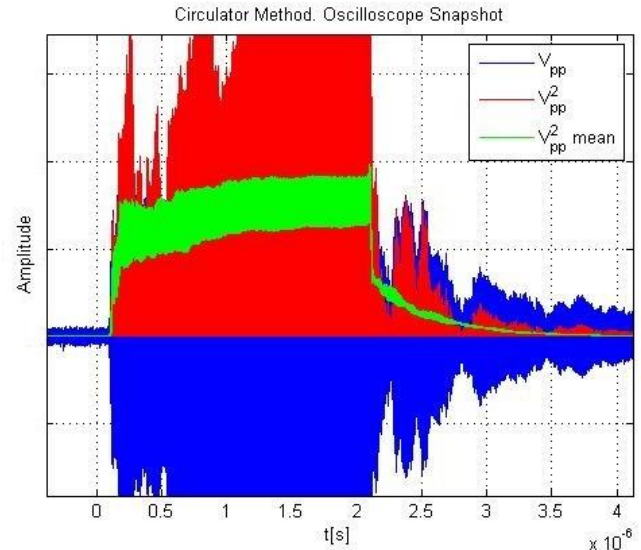


**Figure 3. Recreated oscilloscope snapshot from measurements with the circulator method, paddle stirring in Akilles. Blue curve is raw data (voltage), red curve is voltage squared (corresponding to the measured energy). Green curve corresponds to continuous averaging. Note the striking visual irregularity in the raw data, which is smoothed out nicely with averaging. Note also that the decay of interest starts about  $t=2.2\mu s$ ,  $ampl=0.7$  div. With the used oscilloscope, it takes roughly a minute to collect an average over 1024 sample sweeps, each consisting of 20000 points.**

## 3 Results in Time-domain

To verify the reliability of the measurements, comparison between measurements performed with the slightly different methods (two antennas vs the circulator method, frequency vs paddle stirring, and also time- vs frequency-domain measurements) shall have good correlation. Also, time-domain measured data shall have good correlation with a fitted exponential function (cf. Equation (3)). Fig. 4 shows examples from the RC, and similar results can be shown from measurements in Akilles. It may be noted that in the examples shown,  $\tau$  is in the  $\mu s$  range, corresponding to fairly high  $Q$ -values (Equation (4)) in – the  $10^3$ – $10^4$  range; Avionic bays have magnitudes lower  $Q$ -values.

Well-correlated comparisons between measurements in time- and frequency-domain can also be shown, but is left out of this paper.

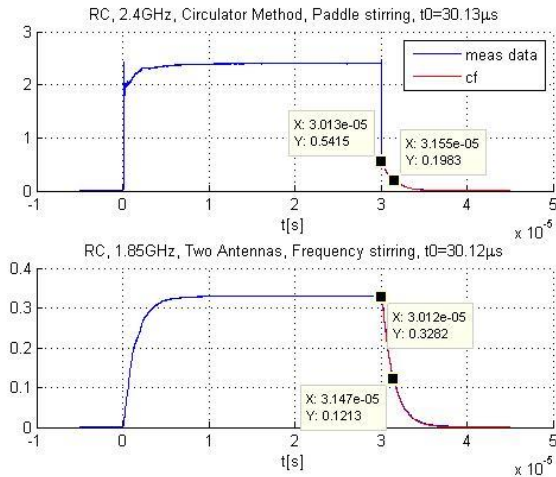


**Figure 4.** Blue curves is time-domain measurements from the RC. Red curves show curve-fitted exponential functions. The upper graph shows Circulator method results with paddle stirring. Note the characteristic “vertical drop” in amplitude preceding the decay of interest. The lower graph shows two antenna results with frequency stirring.  $\tau$  can be calculated from the markers on the blue curve, e.g. the lower graph gives  $1.35\mu\text{s}$  (from the corresponding fitted curve,  $\tau$  is in this case  $1.38\mu\text{s}$ ).

#### 4 Avionic Bay Measurements

In a similar manner as described above (Fig. 1, 2), measurements have also been performed in empty avionic bays on an aircraft; an example of antenna placement in Fig. 5. Holes were drilled in hatches for coaxial cable feed-throughs.

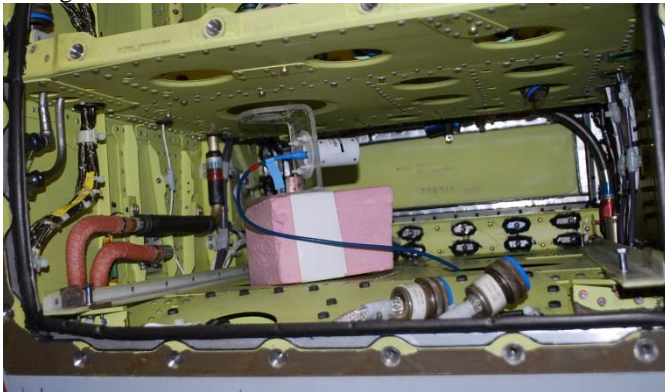


**Figure 5.** Bi-conical antenna inside small avionic bay.

Due to low Q-values (and also  $\tau$ ), interpretation of the test results is challenging. The signal time loss in the coaxial cables has to be taken into account (especially when using the circulator method), and a single-exponential function fits less perfect. In Fig. 6 time-domain measurements yield  $\tau \approx 10\text{ ns}$ , i.e.  $Q \approx 135$ . In [5], the following requirement is set up for an effective chamber, as a lower limit for exponential behaviour:

$$Q \gg Q_{thr} = \left(\frac{4\pi}{3}\right)^{\frac{2}{3}} \frac{3V^{\frac{1}{3}}}{2\lambda} \quad (5)$$

For the avionics bay we get  $Q_{thr} = 27$ . Since  $Q \approx 135$  we regard Equation (5) to be fulfilled. Similar results (though not shown in this paper) can be achieved in Akilles with added absorbers.

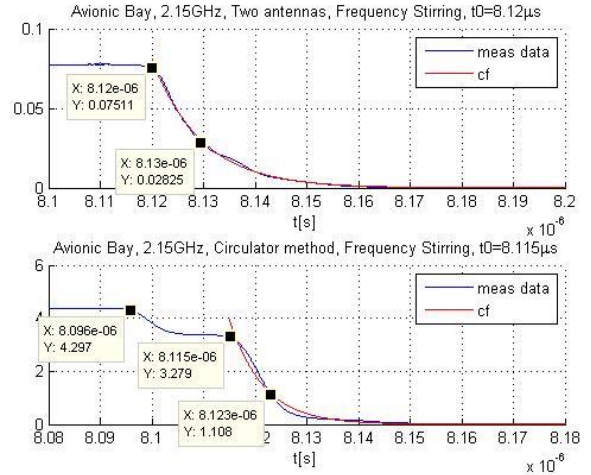


**Figure 6.** Time-domain measurements in avionic bay. Blue curves is measured data, red is curve-fitted. Note the three markers in the lower graph (circulator method), highlighting the coax cable delay ( $17.2\text{ns}$ ), and the decay of interest. Here the measured  $\tau \approx 10\text{ns}$ .

#### 5 Conclusion

Measurements of the Q-value (via  $\tau$ ) have been performed with slightly different methods in time- and frequency-domain, showing well-correlated results as long as Q (and  $\tau$ ) is comparatively high. With lower Q-values – where the bay of interest is on its limit of being overmoded, the results are harder to interpret, but correlation between the measurement methods remains good. The circulator method – time-domain measurements with only one antenna – is together with frequency stirring an attractive choice for measurement in small cavities such as avionic bays.

#### References

- [1] D. A. Hill et al. ”Aperture Excitation of Electrically Large, Lossy Cavities”, *NIST Technical Note 1361*, National Institute of Standards and Technology, USA (Sep 1993)
- [2] M. Bäckström et al. “Guideline for HPM Protection and Verification Based on the Method of Power Balance”, *EMC Europe 2014*, Gothenburg Sweden (Sep 2014)
- [3] “RTCA/DO-160G, Environmental Conditions and Test Procedures for Airborne Equipment, Section 20, Radio Frequency Susceptibility (Radiated and Conducted)”, RTCA, Inc, USA (Dec 2010)
- [4] M. Bäckström, O. Lundén. “Absorber Loading Study in FOI 36.7 m<sup>3</sup> Mode Stirred Reverberation Chamber for Pulsed Power Measurements”, *2008 IEEE Symposium*, Detroit USA (Aug 2008)
- [5] C. L. Holloway et al. “Requirements for an Effective Reverberation Chamber: Unloaded or Loaded”, *IEEE trans. on EMC, vol 48, No 1*, (Feb 2006)

# Experimental comparison of mode-stirrer geometries for EMC

V. Houchouas\*, C. Kasmi\*, J. Lopes Esteves\*, D. Coiffard\*

\*Wireless Security Lab, French Network and Information Security Agency, 51 bvd de la Tour Maubourg, 75007 Paris, France

## Abstract

During the last decades, the EMC community has shown a high interest in the use of reverberating chambers for the immunity testing of electronic devices. Standards have been published so that the compliance of test facilities can be checked. One of the remaining open questions is the efficiency of a mode-stirrer depending on the used material, its shape and its location within the cavity. In this paper, a description of the three main geometries found in the literature is given. A practical comparison of the mode-stirrers is proposed based on the Pearson correlation coefficient, the electric field distribution inside a computer and the results of the immunity testing of the same device.

**Keywords:** Reverberating chambers, Mode-stirrer, Statistics, Immunity.

## 1 Introduction

The immunity testing of electronic devices used in critical infrastructures is of fundamental interest to define adequate protections to be inserted in the facilities in order to improve the availability of services provided to users. The EMC community has shown a high interest for reverberation chambers (RC) for performing radiated immunity tests. One can consider the possible electromagnetic (EM) attack scenarios and apply them by generating an EM field with well-known magnitude, direction and polarization and moving the device under test (DUT) relative to the fixed source. Another way for performing immunity testing is the use of a RC where the DUT is placed in a fixed position in the working volume. For overmoded RC equipped with a moving mode-stirrer, the statistic of the field is supposed to be uniform. Thus, a quick statistic estimation of the susceptibility of the DUT can be performed. One of the remaining open questions, as far as we know, is the definition of an efficient geometry of the mode-stirrer for a given facility. Based on the last remark, a large review of the published academic and technical papers as well as the pictures available on the web has been conducted. Considering the most commonly used geometries; it has been decided to design and build the three most used mode-stirrers and to compare their stirring efficiency for a given Faraday cage thanks to the statistical tools recommended by standards. A comparison of the stirring efficiency is proposed in this paper.

Recently, a health monitoring software was proposed in [1] to characterize the effects of intentional electromagnetic

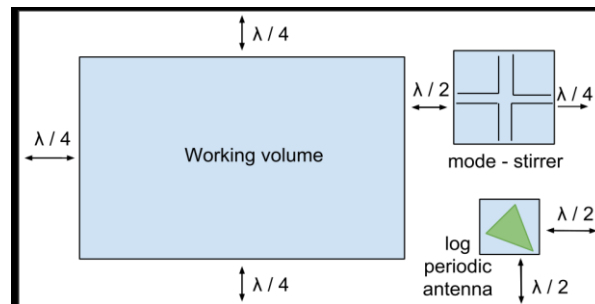


Figure 1: Schematic representing the RC

interference (IEMI) on a DUT by analysing drivers and operating system logs, in real-time operation. Thus, such a software is used in order to validate the statistical analysis of the stirring efficiency of the three mode-stirrers.

The paper is organized as follows: in Section 2, the procedure for characterizing the efficiency of mode-stirrers in reverberation chambers is summarized. In Section 3, the benefits of the immunity testing of a commercial off the shelf (COTS) computer using the mode-stirrers is discussed.

## 2 Analysis of mode-stirrers

The aim of mode-stirring is to produce inside a RC a statistically uniform electromagnetic field in terms of field homogeneity and isotropy [2]. This property directly depends on the number of significantly excited modes (bounded to the mode density at the considered frequency of operation), their quality factor  $Q$  (often estimated as a composite  $Q$  factor) which quantifies the amount of energy stored in the RC, their bandwidth  $BW_Q = f/Q$  and finally the stirred efficiency  $\tau_N$  (see Section 3). While setting up a RC with a mode-stirrer, one has to choose its shape. Unfortunately there is no theory, but only general guidelines [3], which provide an optimal geometry for an optimal stirring efficiency. First of all we determine the location and the maximum dimensions of the stirring volume given a required working volume (a computer 45.3 cm x 20.3 cm x 45.7 cm in what follows) in the RC. The RC we are working with is 43 cm high, 72 cm wide and 92 cm long. The lowest usable frequency LUF as defined by [3] is included in  $[3 f_{TE011}, 7 f_{TE011}]$ , in our case  $LUF \in [794 \text{ MHz}, 1.85 \text{ GHz}]$ . Another estimation from [4] links the LUF to the volume  $V$  of the RC as follows  $LUF = c(90/(4\pi V))^{1/3} = 879 \text{ MHz}$ . Therefore we fixed the minimum frequency of operation  $f_{\text{MIN}} = 2 \text{ GHz}$  (which corresponds to a maximum wavelength  $\lambda_{\text{MAX}} = 15 \text{ cm}$ ), i.e. well above these estimations of the LUF. It is commonly admitted that the working volume must be  $\lambda_{\text{MAX}}/4 = 3.75 \text{ cm}$  apart from the

enclosure walls, and  $\lambda_{\text{MAX}}/2 = 7.5$  cm apart from the emitting antenna to ensure a uniform distribution of the field around the DUT. Finally we get the stirrer's volume dimensions of 30 cm wide, 30 cm long and 34 cm high. The environment (Fig. 1) is composed of a working volume, a stirring volume and an excitation volume.

## 2.1 Review of the proposed geometries

To find the adequate shape of the mode-stirrer one can simulate different shapes [5-7], or design a stirrer by trial and error, minimising the symmetries and then choose the more appropriate, based on their characterization. Due to the large open literature on RCs and mode-stirrers, it could be also possible to rely on the existing shapes. In this work, it has been decided to select shapes from a review of commonly chosen ones in the literature (see for example [2, 7, 8, 9]). The three shapes (quoted as  $S_1$ ,  $S_2$  then  $S_3$ ) depicted in Fig. 2 have been selected from an analysis of more than 200 references. Note that even though we selected common stirrer shapes, this does not ensure that those are the most efficient ones.

## 2.2 Statistical tools

The stirred efficiency is commonly [9, 3] characterised by the Pearson correlation coefficient defined as:

$$r_N = \frac{\frac{1}{N} \sum_{i=1}^N (x_i - \mu_x)(y_i - \mu_y)}{\sqrt{\frac{\sum_{i=1}^N (x_i - \mu_x)^2}{N-1}} \sqrt{\frac{\sum_{i=1}^N (y_i - \mu_y)^2}{N-1}}} \quad (1)$$

where  $X = [x_0, \dots, x_{N-1}]$  is a series of measurements at a fixed frequency, for  $N$  consecutive mode-stirrer positions.  $Y$  is the same series rotated from one position i.e.:  $Y = [x_{N-1}, x_0, \dots, x_{N-2}]$ .  $\mu_x$  is the  $X$  series mean.

In our case,  $X$  is a series of magnitude of scattering parameters  $|S_{21}|$  measurements between ports 1 and 2 of a VNA connected to the transmitting and receiving antennas respectively.  $r_N$  reveals the capacity of the stirrer to lead to a non-correlated field distribution in the RC for different stirrer positions. A high number of positions  $N$  is likely to create highly correlated distributions, as the angle between two positions is small. According to [3], for uncorrelated data the estimated  $r_N$  should be lower than the threshold  $\rho$  ( $\rho = 1/e \approx 0.37$  for  $N = 30$ ). This assumption is not relevant for  $N \neq 30$  as highlighted in [10].

## 2.3 Measurement description and results

The stirring efficiency of each tested mode-stirrer shape is depicted in Fig. 2. The transmission parameter  $|S_{21}|$  is aggregated along a full rotation of the stirrer with  $N = 30$  steps in a bandwidth of [2 GHz, 6 GHz] with a resolution of 150 kHz using a vector network analyser (VNA). A resolution bandwidth slightly greater than  $\text{BW}_Q$  has been chosen while minimizing the noise floor. For graph readability, the mean, the first and the third quartiles have

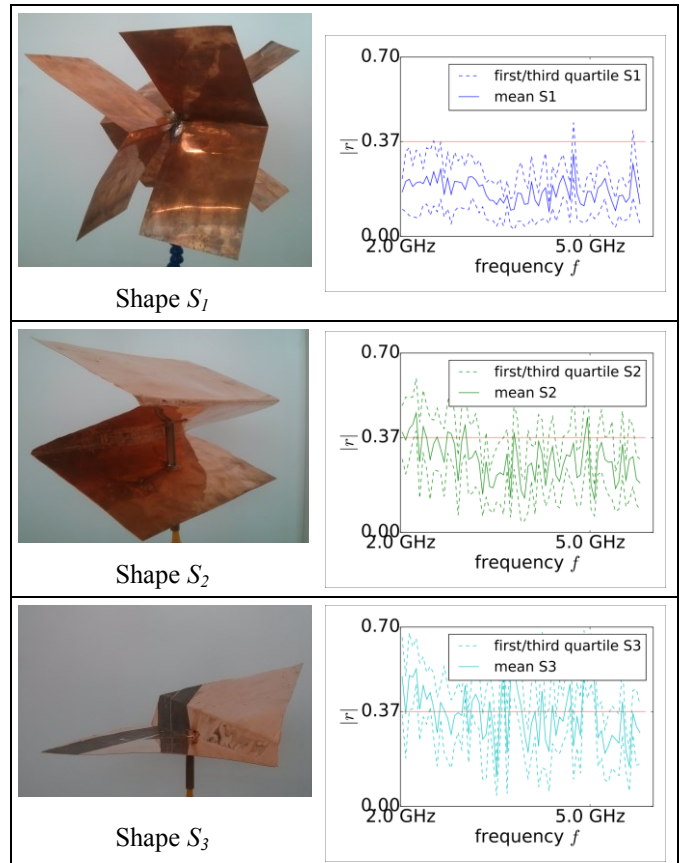


**Figure 2: Comparison of the three selected stirrers**

been estimated from the obtained  $r_N$  on blocks of 300 consecutive points of frequency. As highlighted by Fig. 2, the ranking based on  $r_N$  of mode-stirrers is:  $S_1$ ,  $S_2$  then  $S_3$ . According to this autocorrelation function criterion  $S_1$  appears to be much more efficient than the two others as its associated  $r_N$  is (mostly) below the threshold  $\rho$ . For shapes  $S_2$  and  $S_3$ , it can be mentioned that  $r_N$  decreases with the frequency at least in the half lower bandwidth under investigation, unlike  $S_1$  which seems to be less sensitive to the working wavelength. This tends to prove that this stirrer provides uncorrelated realizations almost all over the considered bandwidth.

## 3 Immunity testing of electronic device

RCs are well-suited for immunity testing of information systems (IS) for EMC or security. Indeed, in one measurement it is theoretically possible to simulate a large number of different aggressions due to the statistic of the field: uniform distribution of the EM wave direction and polarization. Doing so, using a stirrer in an RC can lead to a simple, cheap and fast method for the immunity testing of an IS. To evaluate the immunity of IS, different techniques can be applied. One can either measure the field inside a computer, measure induced voltages in circuits, or record the number of faults on a running system. In this Section, the electric field distributions at the points of interest in the computer are discussed. Then, a brief overview of observable

faults induced on the computer by parasitic fields is presented.

### 3.1 Mode-stirrers classification thanks to the induced electric field

The three positions, depicted in Fig. 3, are of high interest as susceptible components [1] are placed in these parts of the computer (P1: hard-disk drive, P2: CD player and P3: CPU cooling fan). In order to analyse the contribution of the different mode-stirrers, the distribution of the electric field along  $x$ ,  $y$  and  $z$  in the computer has been compared for the three mode-stirrers. While the homogeneity of the field inside the computer is not guaranteed, it has been observed that  $S_3$  allows a better excitation of the field along the three axes inside the computer in contrary to  $S_1$  and  $S_2$  which don't stimulate the component along  $y$ .

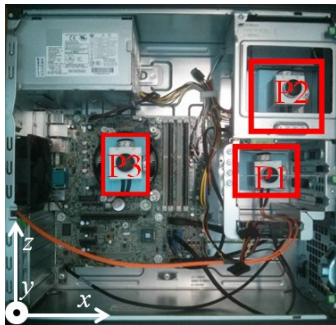


**Figure 3: Electric field probe inside the computer box at the three chosen positions**

### 3.2 Mode-stirrers classification based on fault detection and analysis

Linux has been installed on the computer in order to gain easy access to drivers and operating system logs. Faults [1] (ex. USB, PS2 and temperature sensors) induced by IEMI can be detected. The computer was tested using the described approach and, as for example, it has been observed that the I7 CPU clock balancing was highly deteriorated. Moreover, it has been observed that the effects (ex. clock balancing deterioration, temperature sensors errors) were induced at different levels of criticality depending on the mode-stirrer and the frequency. It can be mentioned that the mode-stirrers  $S_1$  and  $S_2$  don't stimulate the electric field along the  $y$  axis. In this case, the criticality of the induced errors is higher while the number of type of errors is small. On the contrary, the mode-stirrer  $S_3$  excites the three components of the field in the computer. In this case, it induces faults with less criticality levels but broadens the type of perturbations.

## 4 Conclusion

An exhaustive review of mode-stirrers geometry has been performed leading to the study of more than 100 conference and journal papers, 25 PhD theses and a large number of pictures available on the Internet. The three most common shapes have been designed and tested in order to have a clue on their stirring efficiency for a given reverberating chamber.

It has been observed that for three positions of interest in the computer, using a mode-stirrer allows to better evaluate the susceptibility of the critical components. During the presentation, the faults induced by parasitic fields will be presented. The contribution of mode-stirrers for information systems immunity testing will be discussed.

## Acknowledgements

The present work results from the MS Degree training period of Valentin Houchouas, student at the National Institute for Applied Science (INSA) Rennes, at the Wireless Security Lab of the French Network and Information Security (ANSSI). The authors would like to thank Dr. Philippe Besnier from IETR/INSA and Dr. Benoit Martin from Nuclétudes for their valuable advices.

## References

- [1] C. Kasmi, J. Lopes Esteves, and M. Renard. Automation of the immunity testing of COTS computers by the instrumentation of the internal sensors and involving the operating system logs - technical report. *System Design and assessment Note 44*, Nov 2014.
- [2] J.-I. Hong and C.-S. Huh. Optimization of stirrer with various parameters in reverberation chamber. *Progress In Electromagnetics Research*, 104:15-30, (2010).
- [3] IEC 61000-4-21, Electromagnetic Compatibility (EMC) — Part 4-21: Testing and Measurement Techniques Reverberation Chamber Test Methods, (2003).
- [4] IEEE 299.1, IEEE standard method for measuring the shielding effectiveness of enclosures and boxes having all dimensions between 0.1 m and 2 m. (2013).
- [5] K. Selemani, J.-B. Gros, E. Richalot, et al. Comparison of reverberation chamber shapes inspired from chaotic cavities. *IEEE Transactions on EMC*, (2014).
- [6] J.-S. Kim and R. Mittra. Numerical study of stirring effects in a mode-stirred reverberation chamber by using the finite difference time domain simulation. *Forum for Electromagnetic Research Methods and Application Technologies (FERMAT)*.
- [7] J. Clegg, A. Marvin, J. Dawson, et al. Optimization of stirrer designs in a reverberation chamber. *IEEE Transactions on EMC*, 47(4):824-832, (Nov 2005).
- [8] Y. Huang, N. Abumustafa, Q. Wang, et al. Comparison of two stirrer designs for a new reverberation chamber. In *Environmental Electromagnetics, The 2006 4th Asia-Pacific Conference*, pp. 450-453, (Aug 2006).
- [9] N. Wellander, O. Lundén, M. Bäckström, "Experimental Investigation and Mathematical Modeling of Design Parameters for Efficient Stirrers in Mode Stirred Reverberation Chambers", *IEEE Transactions on EMC*, Vol. 49, No. 1, February 2007, pp. 94 – 103
- [10] C. Lemoine. Contribution to the statistical analysis of measurements data in mode-stirred reverberation chamber. Applications for the evaluation of stirring efficiency and measurements uncertainty in the context of radiofrequencies and EMC. *Theses, INSA de Rennes*, (Jul. 2008).

# Destructive High-Power Microwave Testing of Electronic Circuits using a Reverberation Chamber

*Tomas Hurtig, Leif Adelöw, Mose Akyuz, Mattias Elfsberg, Anders Larsson and Sten E Nyholm*

*Division of Defence & Security, Systems and Technology*

*FOI – Swedish Defence Research Agency*

*Norra Sorunda, Sweden*

## Abstract

FOI is establishing a facility for destructive high-power microwave (HPM) testing and is developing an envisaged test methodology for such tests. The methodology consists of two test phases: (1) Determine the lowest electric field level required to destroy an object within a frequency range, using a reverberation chamber (RC). (2) At this frequency, determine the most sensitive direction of attack using an HPM generator. As a part of the development of the test method, destructive testing has been performed in an RC. The hypothesis of the tests was that the formula presented by Tasca for destructive testing of individual components subjected to direct injection is also applicable for to an electronic circuit consisting of many integrated circuits and other components when subjected to an incoming electro-magnetic wave. To check this hypothesis, a simple battery-powered electronic circuit has been extensively tested, and the electromagnetic energy density required to permanently destroy the functionality of the circuit was measured as a function of pulse length. The results follow the shape of the Tasca curve, and the adiabatic, Wunch-Bell and equilibrium regimes are identifiable.

**Keywords:** Destructive testing, Electronic circuit. High-Power Microwave (HPM), Reverberation chamber.

## 1 Introduction

Powerful high-power microwave (HPM) radiation can be used to destroy electronic equipment [1]. When mitigating effects from EMI and jamming, low-level tests can be performed since the system responses are linear. However, when studying destructive effects, the system response becomes non-linear and scaling from low-level tests will not be possible. To be able to perform tests in the destructive, non-linear regime, FOI is developing a relevant test methodology and appropriate facilities [2][3]. To find out the susceptibility of a device under test (DUT) to narrow band HPM-pulses it is necessary to irradiate at many discrete frequencies in a wide frequency band from many angles-of-attack and at least two polarizations. This is very time-consuming and will require an extensive range of HPM-sources. To make the procedure more efficient, the testing can be simplified by dividing it into two stages [3].

1. A reverberation chamber (RC) can be used to gain insight into at what field levels the DUT breaks at different frequencies. The RC must have a small time constant and be driven by a high-power pulsed amplifier.
2. Information on directivity can be obtained by tuning a high-power source to the critical frequency found in the RC-test. The source must be tuneable and have a well-defined polarization but does not need to be a true HPM-source.

This method is similar to the one suggested in IEC61000-5-9 [4]. As a part of developing this test methodology, an extensive test campaign has been conducted where destructive testing has been performed in a reverberation chamber.

## 2 Problem definition

Destructive testing of individual components by direct injection of electromagnetic energy has been reported in the literature [5][6], where Tasca [6] offers a three-dimensional model with a continuous time derivative for the energy as a function of pulse length required for the permanent damage of an isolated integrated circuit:

$$W_{tp} = \left( \frac{4}{3} \pi r^3 \rho C_p + 4 \pi r^2 \sqrt{\rho C_p \kappa t_p} + \frac{8}{3} \pi r \kappa t_p \right) \Delta T \quad (1)$$

where, in the experiments reported here,  $\Delta T = 475$  K,  $\rho = 5.32 \cdot 10^3$  kg/m<sup>3</sup>,  $\kappa = 55$  W/Km,  $C_p = 330$  J/kgK and  $r = 1.16 \cdot 10^{-5}$  m, and  $t_p$  is the pulse length.

The Tasca curve, valid for an isolated semiconductor device, should be applicable to an electronic circuit or system consisting of many integrated circuits and other components when subjected to an incoming electromagnetic pulse. In this context however the energy given by the Tasca curve needs to be multiplied with a factor that expresses the coupling between the energy density in the pulse and the energy needed for destruction of a circuit. That is, the energy density,  $W_{sys}$ , required to destroy an electronic system follows the formula

$$W_{sys} = C_f W_{tp} \quad (2)$$

where  $C_f = C_f(f)$  is a frequency-dependent geometrical factor that corresponds to the coupling of energy in the electromagnetic field to energy deposited inside the integrated

circuit. To test this hypothesis, a simple battery-powered electronic circuit was subjected to destructive testing in a reverberation chamber.

### 3 Experimental setup and test procedure

The reverberation chamber (RC) used was designed and delivered by Siepel and has an internal volume of  $1.24 \times 0.98 \times 0.82 \text{ m}^3$ , a working volume of  $0.72 \times 0.56 \times 0.40 \text{ m}^3$  and a lowest usable frequency (LUF) of 1 GHz. The time constant of the RC allows for testing down to a pulse length of  $2 \text{ }\mu\text{s}$  without loading the chamber while still complying with the DO-160 standard [7]. A photograph of the RC is given in Fig. 1. The amplifier used can deliver about 5 kW in the S-band (2-4 GHz) with a pulse length 200 ns – 50  $\mu\text{s}$ . Each test uses 18 paddle positions. To rationalize testing four circuits at a time are tested. General performance in terms of normalized electric field strength in, and time constant of, the RC are found elsewhere [3].



**Figure 1. Photograph showing the reverberating chamber (RC) with transmit and receive antennas. The chamber internal volume is  $1.24 \times 0.98 \times 0.82 \text{ m}^3$  and the lowest usable frequency (LUF) is 1 GHz.**

The DUT used was a simple battery-powered electronic circuit with one integrated circuit and three other semiconductors. All semiconductors were mounted in sockets so that they could be replaced between individual tests. The objective of the test is to find electric field level necessary to permanently destroy the DUT, with the pulse length and the microwave frequency as parameters that were varied. The test procedure was as follows: For a given pulse length and microwave frequency, the electric field strength was increased stepwise by 1 dB and after each application, the functionality of the circuits was examined. The electric field was increased until all individual DUTs were destroyed. In the experiments reported here it was always the same component, the integrated circuit, which was destroyed.

## 4 Results and discussion

### 4.1 Tasca curve comparison

Fig. 2 shows the electric field strength required for permanent destruction of circuit functionality at 2.0 GHz as a function of pulse length. The figure gives the field strength where the first of the four circuits is destroyed and the field strength where the last of the four circuits is destroyed. At the pulse length of 3  $\mu\text{s}$ , we could not achieve sufficiently high field strength to destroy all circuits. Fig. 3 shows the same data as in Fig. 2, but expressed in the form of energy density instead of electric field strength. The figure also includes a Tasca curve fitted according to equation (2) with  $C_{2,0}=3.15 \times 10^4 \text{ m}^{-2}$ , showing good general agreement.

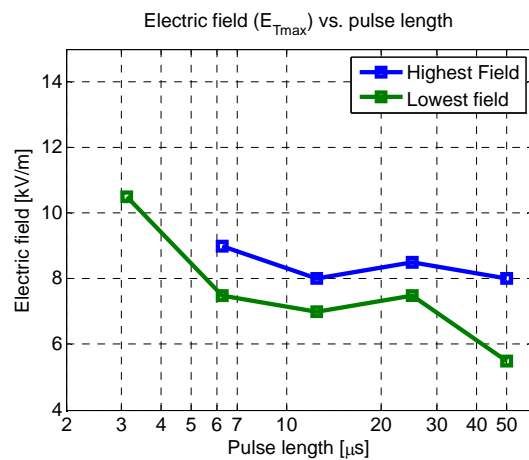


**Figure 2. Electric field strength required for permanent destruction of circuit functionality at 2.0 GHz. The green line shows the field strength required to destroy one of the four circuits. The blue line shows the field strength required to destroy all of the four circuits.**

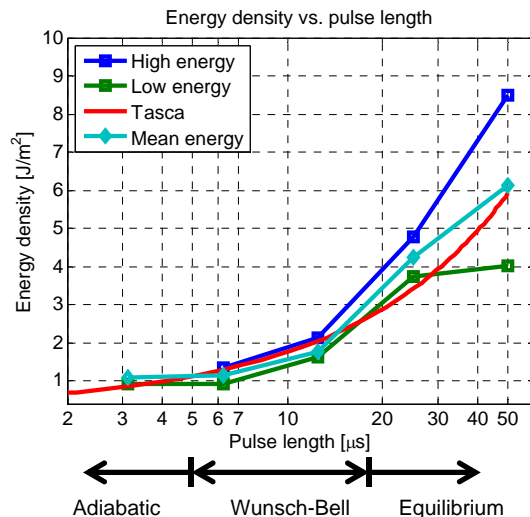


**Figure 3. Same data as in Fig. 2, but plotted in terms of energy density. Included is also the mean energy density required for destruction. In addition, the fitted Tasca curve (equation (2)) is added with  $C_{2,0}=3.15 \times 10^4 \text{ m}^{-2}$ . The**

approximate regions of adiabatic, Wunsch-Bell and equilibrium regimes are indicated in the figure.

Approximate extensions of the regions of adiabatic, Wunsch-Bell and equilibrium regimes are indicated in Fig. 3. It is seen that for the shortest pulse lengths (3 and 6  $\mu\text{s}$ ) the energy density levels out. This is an indication that the adiabatic region for this particular circuit is reached at about 6  $\mu\text{s}$ . More experiments are needed to confirm this but reaching the adiabatic regime means that the results can be extrapolated down to the often very short pulses, of the order of 10's or a few 100's of nanoseconds emitted by real HPM-generators.

#### 4.2 Cumulative distribution function

Several tests were performed at each electric field level for a pulse length of 50  $\mu\text{s}$ , and the experimental cumulative distribution function (CDF) is plotted (Fig. 5). Ten circuits were tested at each electric field level. The data shows that no circuits were destroyed at an electric field level of 5 kV/m and that all circuits tested were destroyed at 10 kV/m. The detailed shape of the curve might be interesting from an academic point of view, but is not really relevant for an HPM-perspective. This is because the data in the middle is not really relevant since no-one is interested in 50% survivability. Instead, when protecting a device, one is interested in the protection, or survivability, level  $P_p$ , which is the region where no circuit is destroyed (left of the vertical green line in Fig. 5). On the other hand, when designing an HPM-weapon, one is interested in the high kill-probability level  $P_w$ , which is the region where all circuits are destroyed (right of the vertical red line in Fig. 5). Note that although the exact shape of the curve might not be relevant, the distance between  $P_w$  and  $P_p$  (in V/m or W/m<sup>2</sup>) is relevant since it is a measure of how narrow the margin is.

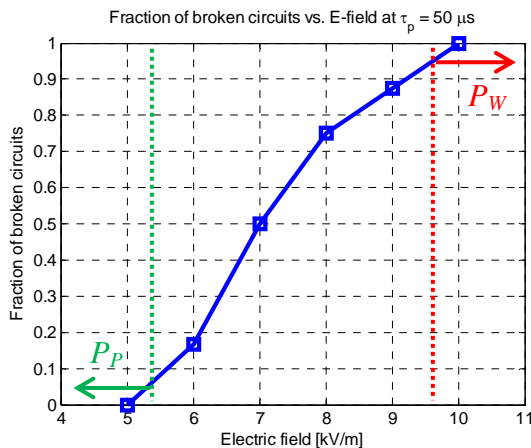


Figure 4. The experimentally measured cumulative distribution function (CDF) of the required electric field strength required for permanent destruction of circuit functionality, for a pulse length of 50  $\mu\text{s}$  and a frequency of 2.0 GHz. The vertical lines indicate the regions of interest for protection of the device,  $P_p$ , and for destruction of the device  $P_w$ . Lines in the picture are just examples where it is assumed that the desired protection

level results in  $P_p > 95\%$  survivability and the probability for a kill when designing a HPM-weapon is  $P_w > 95\%$ .

#### 5 Concluding remark

The energy density needed to permanently destroy the functionality of an electronic circuit at a certain frequency is shown to follow the Tasca curve together with a frequency-dependent geometrical factor accounting for the coupling efficiency between the field and the circuit. The results presented here are based on a small number of individual experiments; in order to obtain a better fit between experimental data and theory many more tests at each pulse length are needed.

In the cumulative distribution function (CDF) of the required electric field strength required for permanent destruction of circuit functionality, in general only the left-hand side (high survivability probability) and the right-hand side (high kill-probability) are of interest.

If RC-testing can be performed in the adiabatic regime where energy required for destruction is constant, the results can be extrapolated to realistic HPM-pulse lengths. Future studies will include destructive testing using an HPM-source.

#### References

- [1] D. V. Giri, High-power electromagnetic radiators, Cambridge: Harvard University Press (2004)
- [2] T. Hurtig, M. Akyuz, M. Elfsberg, A. Larsson and S. E. Nyholm, "Equipment and Methodology for Destructive High-Power Microwave Testing", AMEREM 2014, Albuquerque, USA, 27 July – 1 August 2014
- [3] T. Hurtig, M. Akyuz, M. Elfsberg, A. Larsson and S. E. Nyholm, "Methodology and Equipment for Destructive High-Power Microwave Testing", EMC Europe 2014, Gothenburg, Sweden, 1-4 September 2014
- [4] IEC/TS 61000-5-9, "Electromagnetic compatibility (EMC) - Part 5-9: Installation and mitigation guidelines – System-level susceptibility assessments for HEMP and HPEM", International Electrotechnical Commission, Switzerland (2009)
- [5] D. C. Wunsch and R. R. Bell, "Determination of Threshold Failure Levels of Semiconductor Diodes and Transistors Due to Pulse Voltages", IEEE Transactions on Nuclear Science, vol. 15, pp. 244-259, 1968.
- [6] D. M. Tasca, "Pulse Power Failure Modes in Semiconductors", IEEE Transactions on Nuclear Science, vol. 17, pp. 364-372, 1970.
- [7] RTCA, "Environmental Conditions and Test Procedures for Airborne Equipment", Document number DO-160F, Issue date 12/6/2007

# Effect of Different Factors on Parameters in Non-contacted Electrostatic Discharge

Fangming Ruan<sup>1</sup>, Wenjun Xiao<sup>2</sup>, Hu Shengbo<sup>3</sup>, Xiaohong Yang<sup>4</sup>

1,2,3: Dept. of Electronic and Information Engineering, Guizhou Normal University, Guiyang, China, ruan200145@yahoo.com

4: Guizhou Aerospace Institute of Metrology and Testing, Guiyang, China

**Abstract**—Forceful collision between moving electrode and the target due to large approach speed will result in deformation or damage when discussing discharge parameters variation with approach speed. Simultaneous impact of surroundings factors on discharge process made non-repeatability of discharge measurement. A novel electrostatic discharge(ESD) test system(China invention patent No. ZL201310017269.6) is created for detecting effect on discharge parameter of electrode moving to the target, after analysis of problem existed in test devices of electrostatic discharge(ESD) by previous research. The new system avoid possible instrument damage whereas keep straight line high velocity motion of ESD generator to the target. For the situation of multiple environmental factors impacting on discharge process, the new system can be used to measure every single factor effect in non-contacted ESD. Verification examples were provided in experiment. The variation of discharge current peak value reached  $\Delta I_p=0.56$  A for velocity change  $\Delta v=0.1276$  m/s. Fast velocity has two peak values in 1ns discharge current whereas only one peak value in 1ns discharge current for slow velocity.

**Index Terms**—velocity; multiple factor; discharge parameter; gap; noncontacted discharge

## I. INTRODUCTION

Detecting effect on discharge parameters of electrode movement at high velocity to the target and avoiding damage of experiment setup has been a hot problem in ESD research for long time since 1987, when B. Daout, H. Ryser et al<sup>[1]</sup>. pointed out that approach speed has influence on discharge result. Vehement collision for straight line motion between high velocity moving electrode and the target may cause serious damage of measurement system. The Swiss researchers used a rotating body with circular motion to replace directive line motion, getting equivalent straight line motion. One end of the arm rotating circular motion closed to the discharge target to be equivalent into linear motion. In this way, researchers intend to examine the influence on discharge result due to the equivalent linear motion between a charged body and the electricity body. Researchers in the China state key laboratory of electromagnetic circumstances protection<sup>[2]</sup>, made another experiment setup for approach action on ESD parameters. The discharge gun fastened on rigid body makes free fall rotary motion in the vertical plane. Discharge takes place when the ESD gun tip (discharge head) rotated to the position closest to the horizontal position (location of the discharge target fixed). Both experiment setups above mentioned have similar feature, no straight line motion between charged body and victim but with circular motion to equivalent linear straight motion. ESD

gun head speed, in the second place, at the position of perpendicular to the ground (closest to discharge target) speed value was got through energy transferring process calculation from gravitational potential energy into kinetic energy on the basis of the law of conservation of mechanical energy. D. Pommerenke<sup>[3]</sup> proposed method detecting approach speed, arc length.

No public job report, till now, has resolved the problem of electrode or the target possible deformation or damage, due to strong collision between them when electrode moves at large speed to the target along straight line. The accuracy and credibility of the research results are hence still needed to be improved much.

Based on comparative long time research our team creates a new detection system (China invention patent No. ZL201310017269.6) of electrode movement speed effect on parameters in ESD event, providing completed problem resolution of contradiction between large speed of moving electrode and serious damage due to strong collision between electrode and the target. Multiple factors of gas pressure, temperature, relative humidity, approach velocity, sorts of gas can be quantitatively measured with the new system.

## II. EQUIVALENT CIRCUIT OF ESD GENERATOR

A type of equivalent circuits of ESD generator is shown in Fig.1, describing two models of air discharge and contact discharge. All elements in the equivalent circuit are given with their symbols in frequency domain. The flat ground cable is 2m

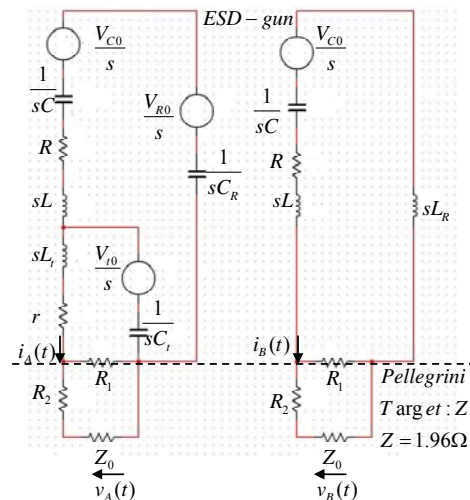


Fig1 Equivalent circuit of ESD generator discharge in two modes

This work was supported by National Nature Science Foundation of China (No. 60971078), by Guizhou Provincial Fund for International Collaborative Science and Technology Research(No. G [2012]7019), by Nature Science & Technology Foundation of Guiyang Baiyun District (No. [2014]10).

long. The current detector (discharge target) has  $2\Omega$  effective resistance. For contacted discharge model, seen the right half part in Fig.1, electrode tip has no effect discharge action to be considered, but in air discharge model (shown in the left half part in Fig.1) electrode tip capacitance play an important role in the entire discharge current process. Two large peaks for air discharge event can usually be seen in discharge current waveform in experiment measurement with electrostatic discharge generator.

For discharge current waveform the area under curve, accordance with relationship between current and electrical charge, refers to corresponding amount of charge. The first large current peak in discharge current waveform is caused by stray capacitor on the electrode tip, while the second large current peak is the discharge from cluster capacitor in electrostatic discharge simulator (ESD generator). Discharge Mode A and Mode B described in Fig2 are two types of ESD, providing equivalent circuit of electrostatic discharge generator. For two discharge modes in experiment with ESD generator, mode A correspond air discharge while Mode B represents contacted discharge.

### III. FEATURES OF NEW MEASUREMENT SYSTEM

In order to research influence on discharge parameters from multiple factors a new measurement system has been developed by our team. The new developed measurement system has been awarded patent with No. ZL201310017269.6. Electrode has high velocity to the target whereas avoid successfully instrument damage resulted from much strong collision between the electrode and the target, an difficult problem confused international researcher in EMC since 1987, has been resolved thoroughly through excellent machinery-electrical design. The second important feature of new system is to detect multiple factor effect on discharge parameters. The main factors impacted on discharge parameters include gas pressure, velocity of electrode moving to the target, temperature, relative humidity, and different sort of gas. The new developed ESD measurement system provides new means for researchers to implement deeper and more extensive investigation on electrostatic discharge properties.

In non-contacted air electrostatic discharge events discrete and much low repeatability of measurement results are the typical features of parameters measured. Mechanism investigation on low repeatability of measured discharge parameters has important theoretical significance for ESD research. We performed initially experiment research with our new ESD measurement system. The temperature and relative humidity in experiment are  $T=20\text{ }^{\circ}\text{C}$ ,  $\text{RH}=56$ , respectively. Discharge gap variation can be controlled through step motor serve circuit. High performance digital oscilloscope, DPO7254(BW2.5GHz, sampling rate 40GS/s), was employed to records discharge current data. The discharge target is set in the centre of right wall of the aluminium system body, connected through cable with digital input terminal of the digital oscilloscope. Electrostatic discharge generator is EMPEK ESD-2020G, which has specifications meeting with IEC standard IEC61000-4-2.

### IV. SIMPLE APPLICATION EXAMPLES OF NEW SYSTEM

The novel ESD measurement system was employed to detect velocity effect on parameters of discharge current. The setup is shown in Fig.2. The voltage in experiment applied on electrostatic discharge generator is 1kV. For driving motor,  $f=7000\text{Hz}$  refer to comparatively high velocity (corresponding



Fig.2 new measurement system of ESD(China invention patent No. ZL201310017269.6)

to  $\sim 0.2146\text{m/s}$ ) of electrode moving to the target,  $f=3000\text{kHz}$  refer to comparatively low velocity (corresponding to  $0.087\text{m/s}$ ). The result of measurement corresponding the two velocities shows notable difference on their peak value, rise time, waveform. Discharge result for the same charge voltage and same gap, usually seem to be identical too. The real measurement result of discharge currents for the same voltage and gap, however, give drastic difference. The result of measurement imply that there may be other factors, in addition to charge voltage and gap, which impact on discharge process and cause the distinct variation of current peak, rise time, waveform. Circumstances temperatures, relative humidity, air pressure, velocity of electrode to the target are important factors affecting discharge parameters.

As shown in figure3 is discharge current measured for the electrostatic discharge generator moves at low speed ( $0.087\text{m/s}$ ) to the discharge target. The frequency for motor is  $3000\text{Hz}$  (corresponding low velocity  $0.087\text{m/s}$ ), voltage supplied to electrostatic discharge generator is  $1.0\text{ kV}$ , air pressure within the experiment box is  $-0.008\text{MPa}$  ( $0.92\text{atm}$ ), temperature is  $10\text{ }^{\circ}\text{C}$ , relative humidity is  $65\%$  while the gas type is air.

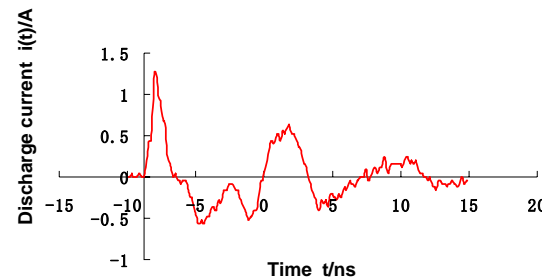


Fig. 3 discharge current for electrode moving at low speed

In figure 4 is given measurement example2 with new system, shown the discharge current for electrostatic discharge generator moves at comparatively high velocity ( $0.2146\text{m/s}$ ) to the discharge target, voltage supplied to electrostatic discharge generator is  $1.0\text{ kV}$ , pressure within the sealed experiment box

is  $-0.008\text{MPa}(0.92\text{atm})$ , frequency for motor is  $7000\text{ Hz}$ , temperature is  $10^\circ\text{C}$ , relative humidity is  $65\%$  and the gas species is air.

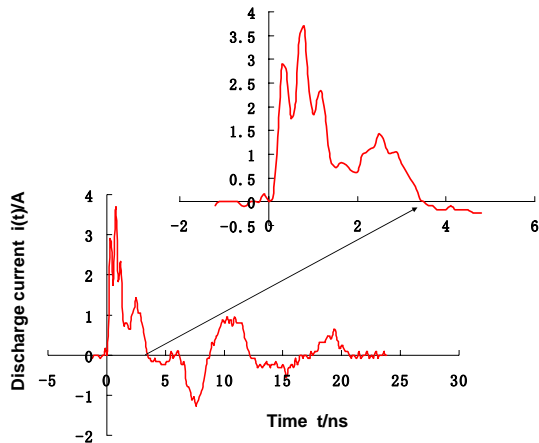


Fig.4 discharge current for electrode moving at high speed

Discharge current peak value, rise time, waveform, seen from Fig.3 and Fig.4, have distinct change with velocity of electrode (ESD gun) moving to the target. Seen from the two figures, one can observe that, the lower the electrode velocity to the target, the smaller the discharge peak value and the blunter rise time(Fig.3); the larger the velocity of electrode moving to the discharge target, the higher the current peak value and the steeper the rise time slope(Fig.4).

In  $1\text{ns}$  time range, seen in Fig.3 and Fig.4, fast velocity of electrode resulted in two current peaks but slow velocity corresponding only one peak current value. Difference of the largest peak current values between fast velocity and slow velocity reached  $\Delta I_p=0.56\text{A}$  for velocity change  $\Delta v=0.1276\text{m/s}$ . The first large peak current in the waveform of discharge, according to the equivalent circuit of ESD generator discharge shown in Fig.1, refers to discharge from distributive stray capacitor of the electrode tip. The second largest peak value in discharge current waveform corresponds to the discharge from the cluster capacitor(energy storing capacitor).

## V. CONCLUSION

The new test system of ESD can be used to investigate the effect of electrode velocity to target, gas pressure variation on discharge parameters in non-contacted ESD, and has strong potential function to research more factors effect on parameters in electrostatic discharge. The problem needing large velocity of electrode moving to the target and avoiding possible instrument damage due to strong collision has been resolved completely with the new ESD measurement system, which also provides a potential new approach or platform for extensive problems investigation of ESD.

## REFERENCES

[1] B. Daout, H. Ryser et al. The Correlation of Rising Slope and Speed of Approach in ESD Tests[C]. Proceedings of the 12<sup>th</sup> Int. Zurich Symp., 1987, pp.467-474.

[2] S.H. Liu. Electrostatic Related Standards[R]. 2012 Electrostatic Protection and Standardization Seminar, Beijing, Nov.12,2012: pp35-56.

[3] D. Pommerenke. On influence of speed of approach, humidity and arc length on ESD breakdown. Proc. The 3<sup>rd</sup> ESD Forum, Grainau, Germany, pp.103-111, 1993.

[4] S. Bonish, D. Pommerenke, W. Kalkner. Broadband measurement of ESD risetimes to distinguish between different discharge mechanisms. J. Electrostatics, vol56(3), pp. 363-383, 2002.

[5] D. Pommerenke. ESD: transient fields, arc simulation and rise time limit. Journal of Electrostatics, vol 36, pp.31-54, 1995.

[6] Meek and Craggs. Electrical breakdown of gases. Oxford Univ. Press, Oxford, 1953, and Wiley, New York, 1978.

[7] S. I. Bragiski. Theory of the development of a spark discharge. Sov. Phys, JETP(7), pp. 1068-1074, 1958.

[8] R.G. Renninger. Mechanisms of charged-device electrostatic discharge. Proc. EOS/ESD Symp.,1991.

[9] Mesyats. Physics of pulse breakdown in gases[M]. Nauka Publishers, Russia, 1991(in Russian)

[10] L. Lind and T. L. Welsher. From lightning to charged-device model electrostatic discharges. Proc. EOS/ESD Symp., pp.67-75, 1992.

[11] J.C. Martin. Multichannel gaps. Switching Notes, Note 10, 1970.

[12] V. M. Ristic and G. R. Dubois. Time dependent spark-gap resistance in short duration arcs with semimetallic cathodes. IEEE Trans. Plasma Sci., PS-6(4),1978.

[13] RC O'Rourke. Investigation of the resistive phase in high power gas switching[R]. Lawrence Livermore Laboratories, University of California, 1977.

[14] HM Hyatt. The resistive phase of an air discharge and the formation of fast rise time ESD pulse[C]. Proc. EOS/ESD Symp. (1992).

[15] Y Taka and O Fujiwara. Verification of spark-resistance formulae for micro-gap ESD. IEICE Transactions on Communication, E93-B(7), pp.1801-1806.

[16] I Mori, Y Taka, O Fujiwara. Current calculation model for contact discharge of charged human body. EMCJ2004-108, pp.35-40 (in Japanese).

[17] I Mori, O Fujiwara. Characteristics measurement of discharge current in air model discharge with ESD gun. Electricity B,122(11).

[18] F Ruan, D Shi, Y Shen, Y Gao. Investigation of discharge parameters relying on charge voltage in human-metal ESD event. Chinese J. Radio Science, vol 24, pp. 979-982, Octable 2009.

[19] F Ruan, Y Gao, D Shi. Analysis on electrode speed correlation of discharge parameters applying short-gap electrostatic discharge model. Proc. IEEE International Conference on EMC, WED-AM-4-4, Detroit, Michigan, U.S., Aug19-Aug23, 2008.

[20] F Ruan, Y Gao, D Shi. Mechanism analysis of correlation between electrode moving speed and discharge parameters. Chinese J. Radio Science, vol 23, pp.977-981,Octable 2008.

[21] F Ruan, Y Gao, D Shi. Analysis with Bernoulli theorem on speed moving effect of electrode in short-gap ESD. Chinese J. Radio Science, vol24, pp.551-555, June 2009.

[22] A Sumida, T Yoshida, N Masui. Effects of the relative humidity on ESD from the charged metal. Seidenki Gakkai Koen Ronbunshu, Vol.2006, pp.43-44 (in Japanese)

[23] Z Xue and D Wu. Electronic Emission and Electronic Spectrum. Beijing: Press of Beijing University,1993, pp.68-75.(in Chinese)

# Vectorial analysis of intense electromagnetic field using a non-invasive optical probe

G. Gaborit<sup>\*†</sup>, L. Gillette<sup>\*†</sup>, P. Jarrige<sup>†</sup>, J. Dahdah<sup>†</sup>, T. Trève<sup>†</sup> and L. Duvillaret<sup>†</sup>

<sup>\*</sup>IMEP-LAHC, Université Savoie Mont Blanc,  
73 376 Le Bourget-du-Lac, France;

<sup>†</sup>Kapteos, Alpespace, bât. Cleanpsace, 354 voie Magellan,  
F-73800 Sainte-Hélène du Lac, France

## Abstract

We here present our latest developments concerning electro-optic sensors dedicated to ultra-wide band (>9 decades of frequency) and high dynamics range (130 dB) characterization of electric fields. Such dielectric probes act as fully uncoupled and orthogonal to each other receiving dipole antennas; they allow to perform a vectorial analysis of the transient evolution of each electric field component. Furthermore, they present a very low invasiveness due to their low permittivity (<4), their very small size (measurement volume <1 cm<sup>3</sup>), and their practically unlimited optical fiber link (>100 m). These sensors give access to metrologic measurements (absolute strength of electric field) in harsh environments as the measurements are fully independent of temperature variations, fiber link mechanical vibrations, EMI, magnetic field and pressure variations.

**Keywords:** Electromagnetic measurement, Optical probe, Electro-optic effect, Electric field, Fiber optic sensor.

## 1 Introduction

Among the numerous solutions to characterize radiated and evanescent electric (E) fields, the use of antennas remains the most widespread experimental technique. In the case of guided E-field, contact probe are mainly used. The main drawback of such sensors lies in their metallic structure that could induce strong perturbation of the field to be measured. Moreover, their size is linked to the lower bound of their frequency bandwidth, this latter being intrinsically limited. Finally, while their measurement dynamics is rather large, the experimental analysis of intense field may lead to partial or even total discharges, which are critical for the downstream instrumentation. In this context, we here propose fully dielectric pigtailed optical sensors as an alternative for the non-invasive and ultra wide band vectorial electric field characterization.

## 2 Electric field sensor principle

These optical sensors are based on the linear electro-optic (EO) effect (also Pockels effect). This effect occurs in non-

linear optical crystals for which the eigen refractive indices are modified by the applied electric field vector to be measured. Experimentally, a laser beam is used to probe the EO crystal which acts as a phase, amplitude or polarization state [1] modulator. Then, the phase, amplitude or polarization state of the laser carries out the real time evolution of a given component of the field vector [2].

## 3 Optical probe description

The structure of the sensors consists in an optical arrangement involving micro-lenses to collimate the laser beam inside the EO crystal transducer and wave plates to control its polarization state. The packaging of the probe is based on a multi-layered dielectric coating ensuring both mechanical probe integrity and permittivity matching between the ambient medium in which the measurement is carried out (air, water, plasmas, ...) and the EO crystal transducer. The field characterization can be remoted up to several tens meters thanks to an optical fibre. This fibre links the sensors to an optoelectronic unit which includes both laser feeding and optical treatment. This unit delivers finally an electrical signal directly proportional to each of the three components of the E-field vector.

## 4 Electro-optic probe features and potentialities

The whole system has been exhaustively characterized and its intrinsic performances are summarized in Table 1.

Table 1: Performances of the EO system.

Minimum detectable field	< 1 V.m <sup>-1</sup> .Hz <sup>-1/2</sup>
Maximum measurable field	> 3 MV.m <sup>-1</sup>
Measurement dynamics	> 130 dB
Vectorial selectivity	> 40 dB
Freq. bandwidth (EO probe)	30 Hz → 10 or 50 GHz
Spatial resolution	< 3 x 3 x 5 mm <sup>3</sup>

Thanks to their above-mentioned features, to their millimetric size, the EO probes are suitable for metrological E-field assessment either in free-space or for guided waves. The potentialities of such a technique has already been

demonstrated for various applications: vectorial near field mapping [3], E-field assessment in liquids (water, biological media, ...) [4], high power microwave, electromagnetic interference, intense field analysis, electric discharge or plasma studies [5,6], and energy diagnostic [7]. As an example, Fig.1 presents the transient response of one component of the E field in the reactive region of an ultra wideband antenna fed by nanosecond pulses.

limitations of the EO technique will be also presented together with a benchmark of other available metrological techniques. Additionally, experimental electric field characterizations, in various conditions, will be presented and compared to theoretical and/or numerical simulation.

## Acknowledgements

The authors would like to acknowledge ANR (French National Research Agency) for the funded CHIC (program EESI 2010), the DGA (French Military Programs Management and Procurement Agency) for the funded SNIFER project (program RAPID), DGCIS for financial support. They also would like to thank the French National Research Program for Environmental and Occupational Health of Anses (2013/2/20). Finally, the authors would like to thanks the CEA Gramat for the experimental collaborations.

## References

- [1] L. Duvillaret, S. Riolland, and J.-L. Coutaz, "Electro-optic sensors for electric field measurements. I. Theoretical comparison among different modulation techniques", *JOSA B*, Vol. 19, 11, pp. 2692-2703, 2002.
- [2] G. Gaborit, J.-L. Coutaz, and L. Duvillaret, "Vectorial electric field measurement using isotropic electro-optic crystals", *Appl. Phys. Lett.*, Vol. 90, pp. 241118-1-3, 2007.
- [3] K. Yang, G. David, J.-G. Yook, I. Papapolymerou, L. P. B. Katehi, and J. F. Whitaker, "Electrooptic mapping and finite-element modeling of the near-field pattern of a microstrip patch antenna", *IEEE Trans. Microwave Theory Tech.*, Vol. 48, pp. 288-294, 2000.
- [4] N. Ticaud, S. Kohler, P. Jarrige, L. Duvillaret, G. Gaborit, R. P O'Connor, D. Arnaud-Cormos, and P. Leveque, "Specific absorption rate assessment using simultaneous electric field and temperature measurements", *IEEE Antennas Wireless Propag. Lett.*, Vol. 11, pp. 252-255, 2012.
- [5] G. Gaborit, J. Dahdah, F. Lecoche, P. Jarrige, Y. Gaeremyneck, E. Duraz, and L. Duvillaret, "Nonperturbative electro-optic sensor for in-situ electric discharge characterization", *IEEE Trans. Plasm. Sci.*, Vol. 41, pp. 2851-2857, 2013.
- [6] G. Gaborit, P. Jarrige, F. Lecoche, J. Dahdah, E. Duraz, C. Volat, and L. Duvillaret, "Single shot and vectorial characterization of intense electric field in various environments with pigtailed electrooptic probe", *IEEE Trans. Plasm. Sci.*, Vol. 42, pp. 1265-1273, 2014.
- [7] J. E. Toney, A. T. Tarditi, P. Pontius and A. Pollick, "Detection of energized structures with an electro-optic electric field sensor", *IEEE Sens. Journal*, Vol. 14, pp. 1364-1369, 2014.

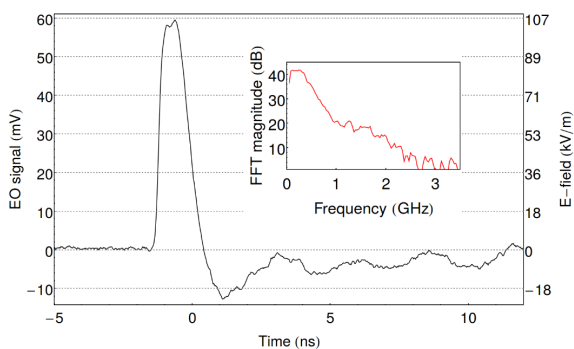
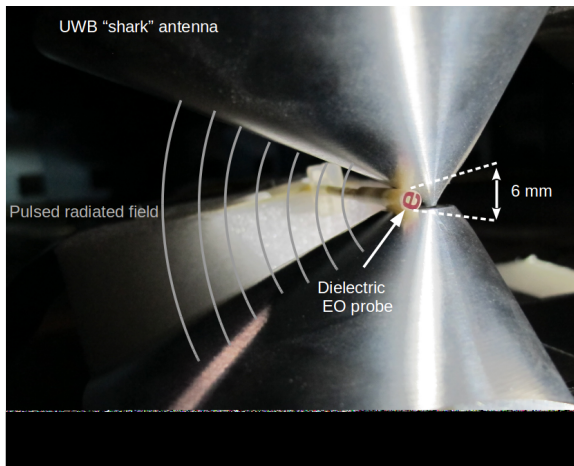


**Figure 1. Top: Photography of the EO probe located in the vicinity of a shark antenna. The antenna is fed by a Kentech generator delivering nanosecond pulses (5 kV peak volatge). The probe is orientated to measure the vertical component of the field. Bottom: absolute measurement (left scale) of the vertical E field component and associated spectrum.**

## 5 Conclusion

The EO technique allows to measured electric field in harsh environments, and leads to a comprehensive analysis of the spatio-temporal distribution of the E field in almost any configuration, wherever measurements performed in air, gases, vacuum or liquids. The associated performances make them suitable for many applications, and fulfill very well the requirements for non invasive and remoted intense field measurements. Basic principles of the EO technique will be explained during the conference. The advantages and

# Cutting-off Coupling Effects caused by Coaxial Cables while measuring Electric Field with ROD Antennas

**Michele Zingarelli**

EMC Division  
Narda Safety Test Solutions – Milano (Italy)  
[Michele.Zingarelli@L-3Com.com](mailto:Michele.Zingarelli@L-3Com.com)

**Roberto Grego**

EMC & EMF Division  
Narda Safety Test Solutions – Milano (Italy)  
[Roberto.Grego@L-3Com.com](mailto:Roberto.Grego@L-3Com.com)

## Abstract

It's commonly known that the Coaxial Cable connecting a Rod Antenna to a receiver does provide coupling effects fatally increasing E-field measurement uncertainty. The scope of this article is to introduce an alternative and innovative solution adopting the benefits of both Fiber Optic technology and Integrated Digital Receiver Design for exactly eliminating those effects caused by Coaxial Cables in all Civil, Military and Automotive applications adopting the Rod Antennas for measuring the Electric Field in the range of 9 kHz ÷ 30 MHz.

**Keywords:** Rod Antenna, Fiber Optic, Embedded Receiver.

## 1 Introduction

The Rod Antenna is a widely used type of antenna for measuring the E-field in the range of VLF and HF frequencies, where the main purpose is that of detecting the vertical component of this field generated by various kinds of EUTs (Equipment Under Test), like vehicles for civil and military use, subsystems and components.

These tests are performed in ALSE (Absorber Lined Shielded Enclosure) for compliance assessment to the EMC requirements according to CISPR 25 [1], MIL-STD-461F [2] and other Standards.

As the Rod Antenna must be positioned typically at 1 m distance (CISPR 25) from the EUT inside an ALSE, the length of the Coaxial Cable normally used to connect the measuring receiver outside the chamber can easily trespass the length of 3 meters, what is already relevant for the coupling effects in subject.

The counterpoise metal plate should be ideally infinite for providing the required “electrical length” of this monopole antenna, what is not possible to achieve in an ALSE.

Some bonding techniques are then used to optimize the test set-up in the best possible way (see Fig.1 below from CISPR 25).

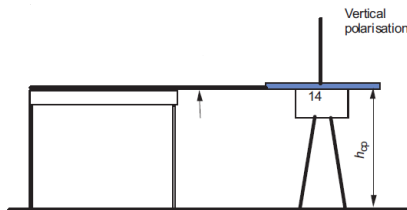


Figure 1. CISPR 25: “The rod antenna ground plane shall be bonded to the test bench ground plane” – Side view

A “Bonding” to floor of Coax Cable’s Shield, together with a Ferrite, is required in some cases (MIL-STD-461F as for Fig. 2) to reduce the effect of this cable on the total impedance.

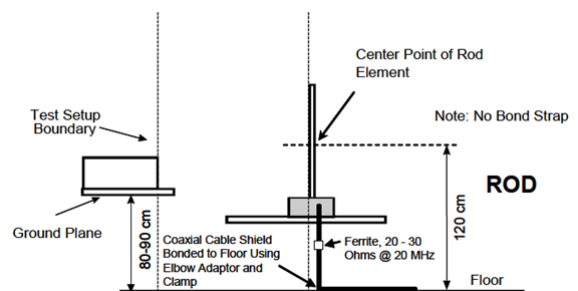


Figure 2. MIL-STD 461F: “RE102-6 Antenna Positioning”

This phenomenon has been studied and well documented by Mr. H.W. Gaul in his IEEE 2013 article [3], where he was also showing how a Rod Antenna with a “floating counterpoise”, with respect to the GP, could represent the best possible solution by using a Fiber Optic connection to collect the detected signal and send it to a measuring equipment; with this solution the measured E-field can definitely approach the theoretical expected value (i.e. with the lowest possible uncertainty), as showed in Fig. 3.

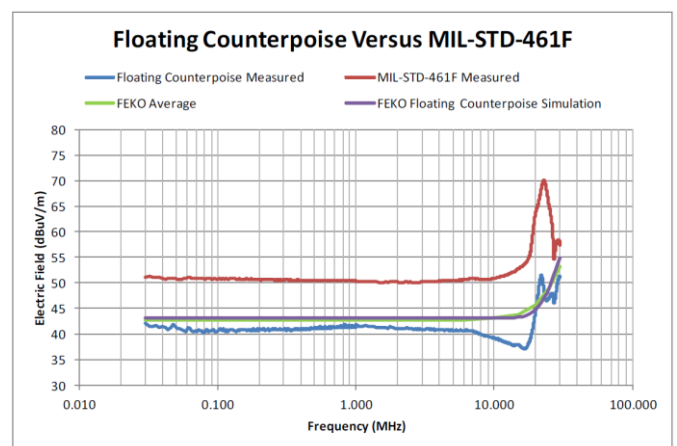


Figure 3. Theoretical E field found by Mr. H.W. Gaul [3] with FEKO simulation vs. measured values for Fiber Optic and MIL-STD-461F test setups

We will then concentrate onto the effects of the measuring Coaxial Cable only, just having a look to the equivalent circuit once connected to the monopole antenna.

After some considerations and simulation about physical effects, we will reach the conclusion that is definitely possible to cut-off all those troublesome effects coming from a Coaxial Cable just by including a fully-CISPR 16-1-1-compliant digital EMI Receiver in the same Rod Antenna body.

The adoption of a Fiber Optical Cable connecting straight to a personal computer or to another optically linked receiver will fix all remaining issues.

## 2 The Physical Effect

The circuit representing the Rod Antenna is that of the Short Monopole below (Fig. 4), where  $V_E$  is the equivalent voltage induced by the incident E-field, while  $C_{STYLUS}$  is the capacity of the Rod Antenna mainly depending from its dimensions (for 1 m Rod with 8 mm diameter  $\rightarrow C_{STYLUS} \approx 12.5$  pF above an ideal infinite GP) [CISPR 25 Annex E.3].

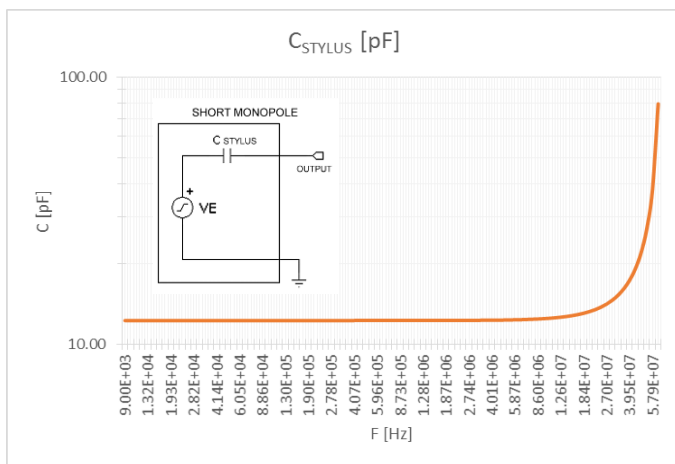


Figure 4. Theoretical Capacitance of 1 m length Ø 8 mm Rod Antenna above an ideally infinite Ground Plane

When a counterpoise 60 x 60 cm is mounted at the lower edge of the Rod Antenna and a Coax Cable is connected to the Receiver for the signal detection, the external conductor of this cable appears electrically connected to the counterpoise, so acting as an additional metal element of the antenna itself.

The result is a more complex structure to analyse in terms of equivalent Capacity C, considering the series of  $C_{STYLUS}$  and the additional impedance  $Z_C$  of the Coax Cable's shielding conductor, as for the following equivalent circuit (Fig. 5).

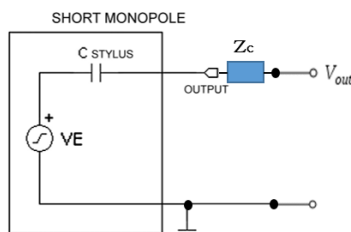


Figure 5. Rod Antenna equivalent circuit including the impedance  $Z_C$  due to the Coax Cable's shielding effects

This model brings to a resonating circuit, as for the influence of the inductive and capacitive components' variations of the cable with frequency.

A simulation has been performed considering only those phenomenon directly affecting the antenna geometry and its related self-capacitance, the latter being the reference parameter for the antenna calibration; therefore the Coax Cable has been considered floating at a certain distance (45 cm) from the GP.

Limiting the analysis in the frequency range far from resonance and focusing on the new total C capacitive component, the simulation can bring to those expected interesting results.

The reference configuration is then showed in Fig. 6, where the counterpoise has been assumed positioned at 90 cm over the GP (i.e. at a suitable height for both CISPR 25 and MIL-STD-461F) while the cable's shielding path has been divided in two vertical and one horizontal segments.

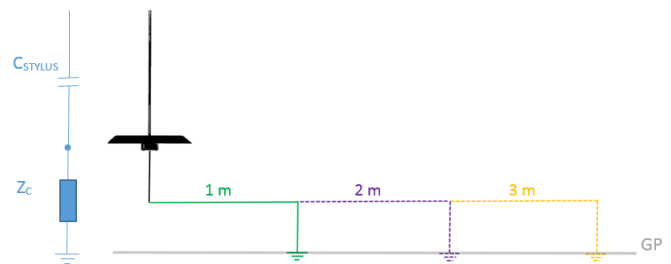


Figure 6. Test configuration with equivalent circuit for 1 m, 2 m and 3 m Coax Cable lengths respectively

While the two vertical segments have been considered of 45 cm each, the horizontal element of the cable has been simulated for three different lengths (1m, 2m and 3m respectively) to investigate about their influence on the total capacity.

The result is resumed in Fig. 7, where several resonances can be observed in frequency.

It appears immediately clear that a longer length of the Coax Cable does reduce the max applicable frequency, due to the fast increase of total capacity C, acting as an "open circuit" toward the measuring equipment much earlier than reaching the nominal 30 MHz upper operating frequency for these applications.

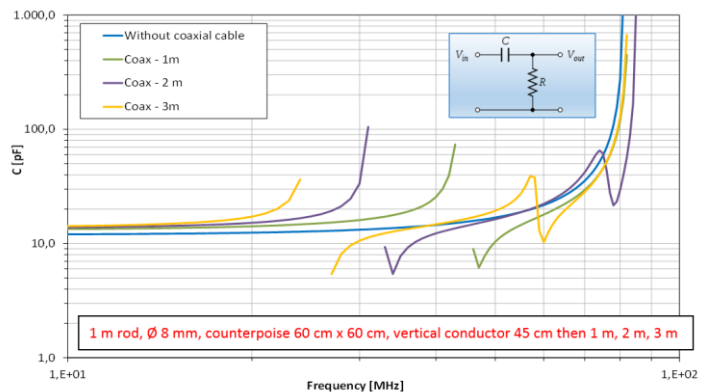


Figure 7. Total Capacity variation vs Frequency for 1 m, 2 m and 3 m length of Coax Cable's Shield connected to the Receiver, compared to the theoretical "floating" set-up

On the contrary, the “floating condition without the Coaxial Cable” does show exactly the same behaviour of the pure C<sub>STYLUS</sub> capacity, therefore the usage of a Fiber Optical connection appears extremely helpful in reducing differences between the various Labs, i.e. reducing the uncertainty just related to the test set-up.

### 3 Innovative “Embedded Receiver” Solution

As aforementioned, an embedded fully-CISPR 16-1-1-compliant receiver would represent the best solution to detect and adapt the signal received from the Rod Antenna immediately at the monopole output, with the additional benefits we’ll describe in this section, hence transferring the measured output directly through a Fiber Optic Cable to a personal computer or to the optical input of a perfectly matched receiver.

The embedded receiving part can definitely help in overcoming the following usual limitations of a classical Rod Antenna:

- easy Saturation of the broadband active input stage;
- weakness of the FET-based high-impedance stage;
- missing of automatic variable Attenuators;
- limited Sensitivity due to the high noise figure of input stage;
- “Antenna Factor” variation due to the C<sub>STYLUS</sub> changes with the set-up (grounding).

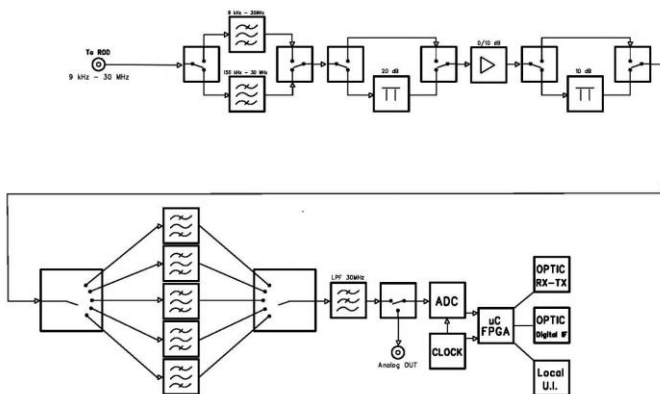


Figure 8. Block diagram of the “Embedded Receiver” solution

The innovative concept briefly sketched in Fig. 8 shows the meaningful blocks defined for the scope and detailed hereinafter:

- a. the first stage connected to the Rod element provides a High-Impedance Band-Pass Filtering divided in the two commonly used ranges of 9 kHz ÷ 30 MHz and 150 kHz ÷ 30 MHz, exactly to reduce potential saturation caused by broadband input signals;
- b. a selectable 20 dB Attenuator is then inserted before the usual high-impedance FET stage to protect it by possible saturation or damage;
- c. another 10 dB selectable attenuator can play a relevant role in the delicate balance between prevention of saturation after the FET, maximum sensitivity and highest achievable dynamic range; for instance, a Sensitivity of at least -22 dB $\mu$ V/m @ 1 MHz with 200 Hz RBW and a Dynamic

Range of up to 175 dB are considered match able;

- d. the following five Preselector Filters can guarantee the Full-Compliance to CISPR 16-1-1 requirements for low PRF signals at the EMI receiving section:

- 9 kHz ÷ 5.67 MHz
- 5.67 MHz ÷ 11.19 MHz
- 11.19 MHz ÷ 16.71 MHz
- 16.71 MHz ÷ 22.23 MHz
- 22.23 MHz ÷ 30.00 MHz

- e. finally a 30 MHz Low-Pass Filter cuts-off any possible inter-modulated out-of-band signal contribution before accessing the digital detecting part of the embedded EMI Receiver or the standard 50  $\Omega$  Analog Output (Fig. 9);
- f. the Optical Digital Output of the embedded receiver does provide all those relevant benefits in completely cutting-off both “coupling to GP” and “Coax Cable resonances” extensively described before.

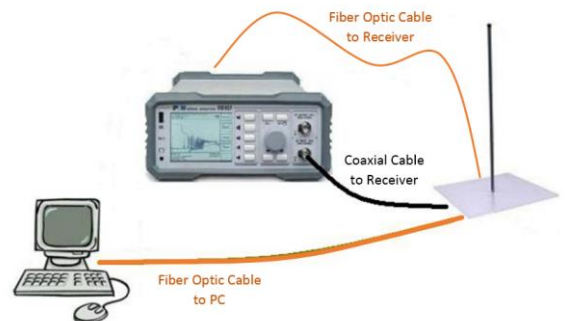


Figure 9. Possible connections for the Rod Antenna with “embedded receiver” (Coax and Fiber Optic)

### 4 Conclusions

The evidence of all the advantages offered by this innovative approach, matching the ideal achievement of a “Floating Counterpoise” (previously studied by Mr. Gaul [3]) to the Cut-Off of Coax Cables Coupling Effects, should definitely pose a thread for including it in the most relevant Standards adopting the Rod Antenna as a “sensing probe” for E-field in the VLF and HF ranges.

A prototype of “Field Receiving Rod Antenna” is being actually tested to provide practical demonstration of its effectiveness in the field.

### References

- [1] CISPR 25 Ed.3 (2008) – “Vehicles, boats and internal combustion engines - Radio disturbance characteristics - Limits and methods of measurement for the protection of on-board receivers”
- [2] MIL-STD-461F (2007) – “DEPARTMENT OF DEFENSE INTERFACE STANDARD – Requirements for the control of electromagnetic interference characteristics of subsystems and equipment”
- [3] Harry W. Gaul (2013) – “Electromagnetic Modeling and Measurements of the 104 cm Rod and Biconical Antenna for Radiated Emissions Testing Below 30 MHz” – [978-1-4799-0409-9/13/\\$31.00@2013](https://doi.org/10.1109/EMFT.2013.6504099) IEEE

# The detector of dangerous pulse electromagnetic interferences: conception of creation

Yury V. Parfenov<sup>1</sup>, Boris A. Titov<sup>1</sup>, Leonid N. Zdoukhov<sup>1</sup>, Xie Yanzhao<sup>2</sup>

<sup>1</sup>Russian Academy of Sciences, Joint Institute for High Temperatures, 125412 Moscow, Izhorskaya 13, bld.2, Russia, e-mail: [parfenov@ihed.ras.ru](mailto:parfenov@ihed.ras.ru)

<sup>2</sup>School of Electrical Engineering, Xi'an Jiaotong University, West Xianning Road No.28, Shaanxi Province, 710049, China, e-mail: [yzxie@mail.xjtu.edu.cn](mailto:yzxie@mail.xjtu.edu.cn)

## Abstract

The new approach to the creation of the devices, providing the detection of dangerous IEMI is introduced. This approach bases on registration of so called key parameters of pulse electric disturbances induced in the circuits of electronic systems. The dangerous IEMI registration system must determine the amplitude, the Joule integral, the energy and the repetition rate of electric pulse disturbances induced in device circuits. The detector functional diagram includes the following component parts: simulator of device critical circuit; signal processing module; fiber-optic communication link; computer interface unit. The detector can be used for defining the key parameters conditioning degree of danger of pulse interferences for equipment inside and outside the premises and for calculating screening factor with their help.

**Keywords:** intentional electromagnetic interferences (IEMI), pulse electric disturbances, key parameters, detector, screening factor.

## 1 Introduction

Permanent (damage) and temporary (upset) failures might occur in electronic systems under the influence of pulse electromagnetic interferences (EMI). Practically they do not differ from usual failures of systems. Special devices providing detection of dangerous EMI being absent, operating personnel would search the reason of occurred failures first of all in hardware and software facilities defects. It could lead to the retardation in making correct decisions on restoration of system's capacity for work. For increasing the electronic systems immunity it is necessary to have facilities capable to detect in proper time dangerous interferences and estimate their characteristics, thus providing the fulfillment of measures on preventing the undesirable effects of these interferences influence.

In [1] the device permitting to register the peak value of powerful electromagnetic pulses (EMP), which constitute potential danger for modern electronic systems is described (Fig. 1). The standard forms of high-altitude nuclear EMP

(HEMP) as well as intentional electromagnetic interferences of non-nuclear origin (IEMI) are embedded in this device [2,3]. It was developed in Great Britain.

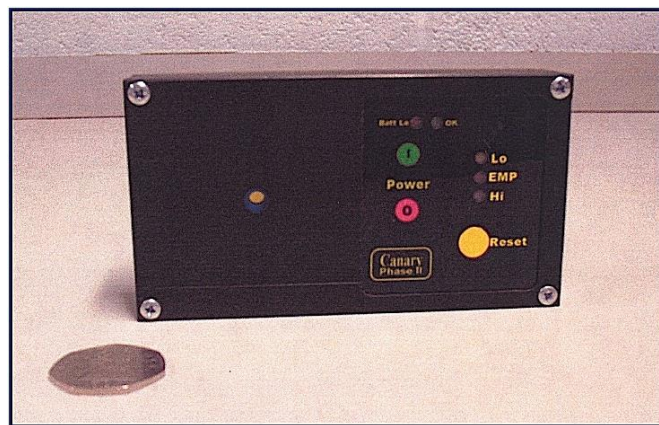


Figure 1 – IEMI hand-held mobile detector

In [4] the Russian analogous device permitting to register the IEMI peak values (Fig. 2) is described. The given device is calibrated with the aid of its designer's source of ultrawideband (UWB) electromagnetic pulses.



Figure 2 - Self-contained UWB-EMP amplitude meter

It should be noted that EMP forms, created by real sources, differ from above mentioned recommended standard forms [2,3]. Moreover, pulses forms, radiated by different sources, differ from each other. For these reasons the results of IEMI registration with the use of devices shown on fig. 1, 2, apparently, are not exactly correct. We should add one more disadvantage to the mentioned above one. In this case amplitude values of pulse disturbances registration results do not permit to estimate the real danger of registered pulses, as the IEMI danger for electronic systems depends not only on influencing these systems pulses amplitude, but also on timing data (spectral range) and repetition rate. In many practical cases, small-amplitude pulses, repeating with high frequency, will more seriously affect the devices' functioning than higher amplitude pulses of small repetition rate. In absence of criteria of dangerous IEMI it is necessary to adjust detectors to EMPs' minimum level, only slightly exceeding the electromagnetic environment. But in such a case detectors will produce frequent unfounded alarm signals. Therefore, the only one reasonable sphere of applying the device under consideration, is the registration of amplitude values of standard pulses formed by test simulators.

Below, the new approach to the creation of the devices, providing the detection of dangerous IEMI is introduced. This approach bases on registration of so called key parameters of pulse electric disturbances induced in the circuits of electronic systems.

## 2 Key parameters of pulse electric disturbances

The mechanism of powerful electromagnetic pulses influence on electronic devices is in forming in circuits of these devices pulse electric disturbances, which cause different failures (breakdowns) of their operating capacity. Such failures, which are sometimes called universal, might be as follows: irreversible (permanent) failure of some elements; transition of active elements to the saturation mode; incorrect transfer of data between digital devices. The possibility of failures occurrence depends on disturbances key parameters. The list of key parameters stipulating the possibility of the occurrence of frequently observed electronic devices failures is given below.

The condition of electronic device element irreversible failure is the simultaneous performing of the following conditions (criteria):  $U_{in} > U_{el.br}$ ;  $J_{in} > J_{therm.br}$ . Here  $U_{ex}$   $U_{in}$  is the amplitude of pulse voltage induced at the input of the given element.  $U_{el.br}$  is the voltage value of electric breakdown initiation;  $J_{in} = \int_0^T I_{in}^2(t)dt$  is the Joule integral;  $I_{in}(t)$  is the pulse of current, flowing through the element after electric breakdown occurrence,  $T$  is the duration of this pulse;  $J_{therm.br}$  is the Joule integral minimum value providing thermal breakdown.

For stable transition of active elements to saturation mode the performing of the following conditions is necessary:  $f > \frac{1}{\Delta T}$ .

$U_{in} > U_{sat}$ ;  $J_{in} > J_{sat}$ ;  $f > \frac{1}{\Delta T}$ . Here:  $U_{sat}$ ,  $J_{sat}$  and  $\Delta T$  are respectively, the minimum voltage value under reaching which the transition of active elements to saturation mode

makes start, Joule integral minimum value, providing stable elements transition to this mode and duration of process of going out from saturation mode after cut off current flow through elements.

As the criteria of digital devices failure caused by occurrences of errors in data packets transmission, the following inequalities can be accepted:  $N_{err} > N_{err.crit}$ ;  $R < R_{crit}$ ;  $P_{err} > P_{err.crit}$ . Here:  $N_{err}$  and  $R$  are the numbers of data packets containing errors, and data transmission rate under conditions of repeated pulse disturbance influence,  $P_{err}$  is the probability of errors occurrence in data packets transmission as a result of disturbance influence,  $N_{err.crit}$ ,  $R_{crit}$  and  $P_{err.crit}$  are critical values of these parameters. In turn,  $N_{err.crit}$ ,  $R_{crit}$  and  $P_{err.crit}$  depend on such parameters of induced pulse disturbance as pulse energy and its repetition rate.

Listed above parameters of the induced pulse disturbance are key parameters and their values characterize danger of the electromagnetic influence.

It should be said that the induced electric disturbance energy is not definitely connected with the energy of electromagnetic pulse influencing electronic device. Of course, it depends on amplitude-time characteristics of EMP, but it also depends on geometric and electric characteristics of influenced device electric circuits. In addition, under real conditions of electromagnetic wave propagation, for example, in the building as a result of pulse reflection from the walls, it is being transformed into complex pulse signal, the duration of which can considerably exceed the duration of initial signal. Correspondingly, the energy of the induced electric disturbance is being changed.

Thus, the dangerous IEMI registration system must determine the amplitude, the Joule integral, the energy and the repetition rate of electric pulse disturbances induced in device circuits. Sometimes, it is convenient to accept as the key parameter of the pulse electric disturbance average power, which is equal to pulse energy and its repetition rate product .

## 3 Dangerous IEMI detector structure

As it was mentioned before, under influence of EMPs pulse electric disturbances are being induced on communication and power supply lines of electronic device and are capable to obstruct its normal functioning. In this connection the simulator of typical communication or electric power supply line could be one of the detector elements. As the simulator of the typical circuit for defining the IEMI key parameters one of the paths in printed circuit boards could be taken [Fig. 3]. Electric dipole could also be the convenient simulator. Simulator design and characteristics depend on the features of the device under influence of EMPs, but this is the subject of separate justification and goes beyond the theme of this paper. The detector functional diagram includes the following component parts: simulator of device critical circuit; signal processing module; fiber-optic communication link; computer interface unit. The detector functions in the following way. Simulator of device critical circuit senses influencing EMP, transforms it into pulse voltage and delivers the latest on signal processing unit.

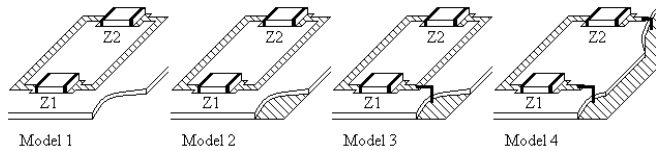


**Figure 3 - Models of the paths in Printed Circuit Boards, which are influenced by the pulse electromagnetic field**

The unit transforms analog signals into digital form, performs the calculation of key parameters values and sends this data over the fiber-optic communication link to the computer interface unit, which analyses the IEMI danger.

It should be noted that the detector does not require the detuning of reflected pulses, inherent in real electromagnetic situation. The thing is that the reflected pulses amplify influence and, undoubtedly, should be taken into consideration at IEMI danger estimation.

#### 4 Algorithm of detector operation

The list of parameters registered by the detector includes:

- the voltage pulse amplitude on the load of the device critical circuit simulator ( $U_i$ );
- an energy emitted in the load of simulator of the critical circuit ( $W_i$ );
- Joule integral of current running through the load simulating input resistance of the device element after electrical breakdown occurrence ( $J_i$ );
- repetition rate of influencing pulses ( $f$ ).

$N_{err}$ ,  $R$  and  $P_{err}$  parameters calculation is being performed after listed key parameters registration. For the last parameter calculation the following formula can be used:

$$P_{err} = 1 - (1 - P_e(z))^{f \frac{N}{R}}, \quad (1)$$

where:

$$P_e(z) = 0.5 \cdot \left( 1 - \operatorname{erf} \left( \frac{z}{\sqrt{2}} \right) \right);$$

$$z = \sqrt{\frac{W_{sign}}{W_{dist}}};$$

$W_{sign}$  is average energy of data bits being transmitted;

$W_{dist}$  is pulse disturbance energy;

$f$  is pulse disturbance repetition rate;

$N$  is quantity of bits in data packets;

$R$  is data transmission rate.

After performing the above listed operations the computer compares the received key parameters values with their critical levels and makes the conclusion about the possibility of one or another device failure occurrence. In accordance with the criteria, formulated in p.2,  $U_i$  and  $J_i$  parameters values characterize the possibility of the occurrence of device elements irreversible failures or reversible failures, stipulated by active elements transition to the saturation mode, and  $W_i$ ,  $R$  and  $P_{err}$  – the possibility of errors occurrence in data being transmitted between digital devices.

Key parameters critical levels are being defined by electronic systems testing or estimated by expertise and are being kept in computer data base.

## 5 Possible fields of application of the dangerous IEMI detector

As it was noted before, the detector can be used for detecting disturbances, for defining their key parameters and for preventing undesirable consequences of these disturbances influence on vital electronic systems. But it does not exhaust all possible fields of application of given device. Another field of application is the evaluation of suitability of premises intended for the placement of vital radio electronic apparatus, which can be influenced by powerful nanosecond and subnanosecond EMPs. At present such evaluation is performed by the defining the screening factor of premises' walls. Usually the amplitude of electromagnetic pulse outside of premises – to – the amplitude of pulse registered inside this premises ratio is being taken as the screening factor. In case if the defined in this way screening factor value exceeds the specified level, the premises is considered to be suitable for the placement of electronic apparatuses. If not, the measures should be taken to increase the screening factor.

It is absolutely evident that such approach suffers of certain incorrectness, because it is based on the comparison of amplitude values of two pulses (external and interior), which have different forms and by this reason they possess different influence efficiency on electronic apparatuses even under equal amplitude values. This can be accepted in cases when it is a question of inexpensive apparatuses. But such approach is unsuitable for the evaluation of suitability of premises intended for the placement of unique and expensive apparatus, malfunctioning of which could bring to serious consequences. More complicated approach which consists in measuring harmonic coefficient of screening in broad frequency band is used in such situations. However, it isn't also free from disadvantages. High cost and the risk of omission of "critical" frequencies, at which screening effect of premises walls sharply decreases, can be referred to its. It also contains the fundamental disadvantage conditioned by absence of rigid relationship between concrete values of harmonic screening factor and degree of influence of pulse electromagnetic field on the quality of performance of electronic apparatuses placed in the premises. It could be interesting to use the detector for defining the key parameters conditioning degree of danger of pulse interferences for equipment inside and outside the premises and for calculating screening factor with their help.

## References

- [1] Hoad R., et al. "Trends in EM susceptibility of IT Equipment", *IEEE Trans. on EMC*, Vol. 46, No.3, (2004).
- [2] IEC 61000-2-9: Environment - Description of HEMP environment - Radiated disturbances.
- [3] IEC 61000-2-13: Environment – High-power electromagnetic (HPERM) environments – radiated and conducted.
- [4] Sakharov K.Yu. "Ultrashort electromagnetic pulses radiators and methods of their parameters measurement", *M., Moscow State Institute of Electronics and Mathematics*, (2006).

# Breakdown Characteristics of Si Bipolar Junction Transistor Injected with Microwave Pulses

Cunbo Zhang, Honggang Wang, Jiande Zhang, Baoliang Qian, and Guangxing Du

College of Optoelectronic Science and Engineering, National University of Defense Technology, Changsha 410073, P. R. China

## Abstract

The damage effect experiment on the low noise amplifier based on Si bipolar junction transistor is carried out by the platform of microwave pulses injection experiment. In the failure analysis of low noise amplifier based on Si bipolar junction transistor, the transistor is permanently damaged when the gain of low-noise amplifier decreases more than 10 dB. The breakdown characteristic of the Si bipolar junction transistor is measured before and after its damage and the micro-characteristic of the damaged transistor is observed by scanning electron microscope. The results show that when the Si bipolar junction transistor is damaged with microwave pulses, the Si material in the base region is burned which causes short circuit of emitter junction and collector junction, such two junctions lose the PN junction characteristics and the device is damaged.

**Keywords:** Si bipolar junction transistor; microwave pulses; breakdown; failure analysis.

## 1 Introduction

With the wide application of electronic equipment, the current electromagnetic environment becomes more and more complicated. As a result, the threat to different kinds of communication and radio detection system increases and the vulnerability of radio frequency front end intensifies with intense electromagnetic pulse. The vulnerability experimental research of European electrified railway traffic management system is reported under microwave pulse radiation in the reference [1]. The results show that the low noise amplifier (LNA) is the vulnerable device in the system and it's of great significance to study the damage effect of LNA with microwave pulses [2-3]. Since Si bipolar junction transistor (BJT) is widely used in LNA, it's of great significance to study the damage properties of Si BJT injected with microwave pulses. The damage effect and mechanism of Si BJT injected with microwave pulses and step pulses are researched through analysis of electric field, current density and temperature distribution inside BJT by semiconductor simulation software in reference [4]. The experiment of LNA based on BJT injected with microwave pulses is reported in reference [5-6], in which the damage characteristics of transistor are presented with different microwave pulses parameters and injection pins. The purpose of experimental research lies in the obtaining of effect data and principles, however, the damage mechanism is rarely analyzed. The damage mechanism can be analyzed by numerical simulation, but the results of numerical simulation have not been verified

by experiment. To further research on the damage mechanism of Si BJT with microwave pulses, the breakdown characteristics of the damaged transistor is analyzed from macroscopic perspective and the damage part of the transistor is observed from microcosmic perspective to provide powerful experimental evidence for the research on damage mechanism.

In this paper, the breakdown characteristics of Si BJT are studied injected with microwave pulses from base, the PN junction breakdown performance of Si BJT is measured before and after damage, and failure positioning and damage part are observed with Optical Beam Induced Resistance Change (OBIRCH) technology and scanning electron microscope (SEM) to conclude the damage mechanism of device.

## 2 Damage Effect Experiment

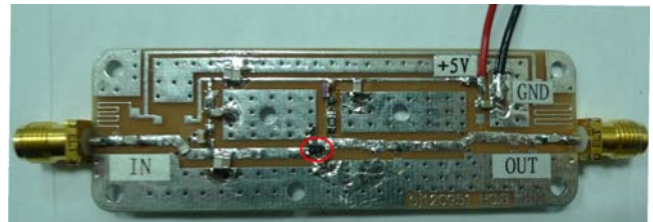


Figure 1. Picture of LNA integrated circuit.

The structure of an LNA based on the BJT is presented as follows. Fig. 1 is the picture of LNA. The core part of the LNA is BJT which is marked with a red circle in Fig. 1. The peripheral circuit includes the static biasing circuit of transistor and the input and output match circuits. The LNA is the common emitter circuit. The base of BJT connects with the input terminal of the amplifier, the collector connects with the output terminal and the emitter connects with the ground. The DC supply voltage of the LNA is 5 V. The quiescent operating point is that the collector-emitter bias voltage is 2.5 V and the collector current is 20 mA. The operating frequency is 1~2 GHz. At  $f=1.5$  GHz, the gain of the LNA is about 15 dB and the noise figure is about 2.4 dB.

The injection experiment equipment is shown in Fig. 2. The microwave pulses are injected from the input terminal of LNA are studied. The frequency of microwave pulses is 1.5 GHz and the pulse width is 50 ns. Only one microwave pulse is injected each time. The gain is measured by vector network analyzer after each injection. The device is considered to be damaged when the gain is reduced over 10 dB. The injection power is gradually increased until the LNA is damaged. The

gain of the amplifier can be recovered to normal status by replacing BJT of LNA, so it implies that the essence of LNA damage with microwave pulses is the damage to BJT.

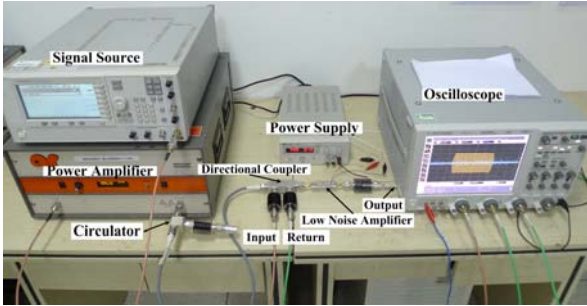


Figure 2. Testing system.

### 3 Failure Analysis

To analyze the damage properties of BJT with microwave pulses, 8 damaged BJTs were randomly selected for electric characteristics test and failure positioning analysis. The electric characteristics are measured before and after BJT damage for comparison. The failure positioning and damage part of damaged BJT are observed with OBIRCH technology and SEM.

#### 3.1 Electric characteristics test

The purpose of electric characteristics test is to determine the PN junction performance before and after damage by measuring the avalanche breakdown voltage  $V_{CBO}$  of collector junction in common base circuit and  $V_{CEO}$  in common emitter circuit and breakdown voltage  $V_{EBO}$  of emitter junction [7].

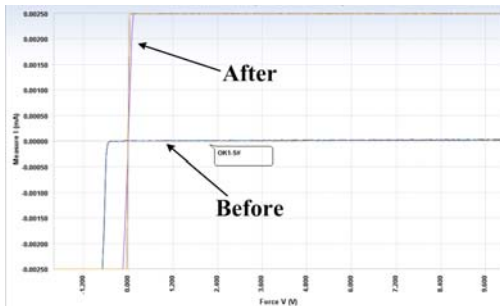


Figure 3. Breakdown characteristics of collector junction in common base.

The common base reverse cut-off current ( $I_{CBO}$ ) refers to the collector current when the emitter is open circuit ( $I_E=0$ ) and the collector junction is reversed ( $V_{CB}>0$ ). When the emitter is open circuit and the  $I_{CBO}$  tends to be infinite, the reverse voltage  $V_{CB}$  of collector junction is called as  $V_{CBO}$ . The  $V_{CBO}$  before and after BJT damage is shown in Fig. 3, among which the horizontal coordinate shows the collector junction voltage  $V_{CB}$  when the emitter is open circuit and the vertical coordinate shows the collector current. When  $V_{CB}>0$ , the collector junction is reversely biased; when  $V_{CB}<0$ , the collector junction is positively biased. From Fig. 3, the collector junction of good transistor has normal PN junction properties such as breakover in positively biased state and cut-off in reversely biased state. The  $V_{CBO}$  is more than 10 V.

The  $V_{CBO}$  of damaged transistor approximates to 0V. The collector junction is short circuit and loses PN junction properties.

The common emitter reverse cut-off current ( $I_{CEO}$ ) refers to the current penetrating from emitter to collector when the base is open circuit ( $I_B=0$ ) and the collector junction is reversed ( $V_{CB}>0$ ). When the base is open circuit and the  $I_{CEO}$  tends to be infinite, the voltage  $V_{CE}$  between the collector and emitter is called as  $V_{CEO}$ . The  $V_{CEO}$  is much lower than  $V_{CBO}$ . The  $V_{CEO}$  before and after BJT damage is shown in Fig. 4, among which the horizontal coordinate shows the voltage  $V_{CE}$  between the collector and emitter when the base is open circuit and the vertical coordinate shows the collector current. When  $V_{CE}>0$ , the collector junction is reversely biased; when  $V_{CE}<0$ , the collector junction is positively biased. From Fig. 4, the  $V_{CEO}$  of good transistor is more than 4.5 V and the  $V_{CEO}$  of damaged transistor approximates to 0 V. We can get the same results as mentioned above: the collector junction is short circuit and loses PN junction properties as well.

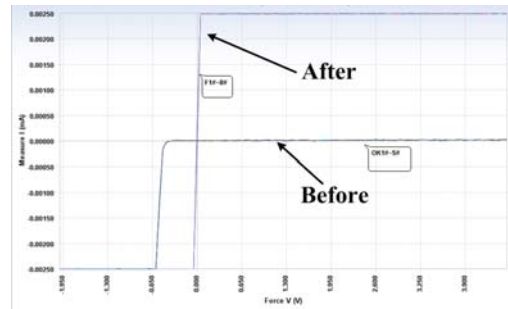


Figure 4. Breakdown characteristics of collector junction in common emitter.



Figure 5. Breakdown characteristics of emitter junction

$I_{EBO}$  refers to the emitter current when the collector is open circuit ( $I_C=0$ ) and the emitter junction is reversed ( $V_{EB}>0$ ). When the  $I_{EBO}$  tends to be infinite, the reverse voltage of emitter junction is called as  $V_{EBO}$ . The  $V_{EBO}$  before and after BJT damage is shown in Fig. 5, among which the horizontal coordinate shows the voltage  $V_{EB}$  of emitter junction when the collector is open circuit and the vertical coordinate shows the emitter current. When  $V_{EB}>0$ , the emitter junction is reversely biased; when  $V_{EB}<0$ , the emitter junction is positively biased. From Fig. 5, the emitter junction of good transistor has normal PN junction properties. The  $V_{EBO}$  is more than 1 V. The emitter junction of damaged 1#~7# transistors is short circuit and

that of 8# transistor presents resistance properties, so all the emitter junction loses PN junction properties.

The emitter junction and collector junction of damaged BJT present short circuit or resistance properties and lose PN junction properties by measuring  $V_{CBO}$ ,  $V_{CEO}$  and  $V_{EBO}$ , which causes permanent afuction of transistor.

### 3.2 Inspection of damage part

After decapping of transistor, the inspection is carried out on transistor surface by SEM to further determine the damage part and explore the damage mechanism. There is no obvious damage to the surface and metal electrode of transistor.

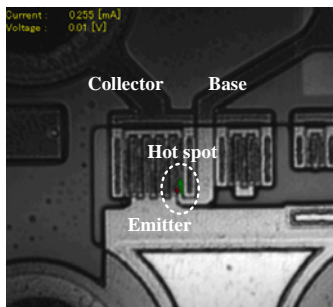


**Figure 6. Micrograph of fault location.**

The damage part is positioned by OBIRCH technology. For the measurement results of BJT, see Fig. 6. The red zone shows that the current density is big while the green zone shows the contrary circumstance during scanning in Fig. 6. It implies that the physical damage exists in silicon below the electrode at above zones. The damaged BJT is decapped and the surface passivation layer and top metal layer are removed; the typical microscopic damage image is observed by SEM, as indicated in Fig. 7. From Fig. 7, obvious corrosion is observed in a place where corresponds to the hot spot of Fig. 6. Thermal breakdown appears in silicon of base region in the corrosion place which causes short circuit and PN junction properties loss of emitter junction and collector junction; therefore, the transistor is permanently damaged.

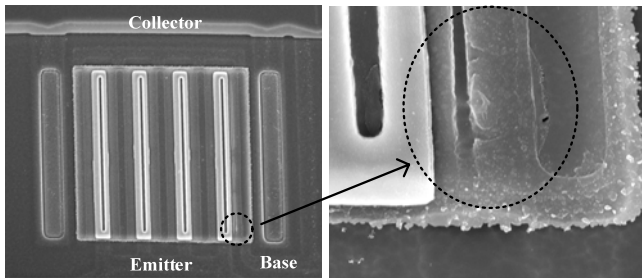


**Figure 7. Micrograph of damaged transistor.**

The damage mechanism of PN junction can be explained as follows. With microwave pulses, when the positive voltage of base is high, both the emitter junction and collector junction are positively biased; the current of PN junction is in exponential increase as voltage increases. When the negative voltage of base is high, both the emitter junction and collector

junction are reversely biased. Due to reverse breakdown of PN junction, the reverse current will abruptly increase when the negative voltage increases to a certain value. The bias voltage in the PN junction is mainly applied in the depletion region. The carriers are accelerated by the electrical field in the depletion region. The energy is transferred from the carrier to the lattice by impact, causing increase of the lattice energy and temperature rise of the PN junction. Both the positive and reverse currents of PN junction are in direct proportion to temperature. The current is increased in the PN junction by temperature rise and then positive feedback is formed between the current and temperature. The increased current by temperature rise will cause increase of the power loss and the further increase of temperature, so that the current is further increased. The process is an unlimited recycling, which causes increase of the current and temperature unlimitedly and burning to the PN junction finally.

## 4 Conclusion

The damage mechanism of BJT injected with microwave pulses is that the emitter junction and collector junction are in short circuit and lose PN junction properties due to the ablation of local silicon in base region. The electric characteristics, damage part and damage image of damaged BJT are presented in this paper which provides powerful experimental evidence for studying on the damage mechanism and serves as a reference for the prevention and hardening design of BJT against microwave pulses.

## References

- [1] Mansson D, Thottappillil R, Backstrom M, Lunden O. Vulnerability of European Rail Traffic Management System to Radiated Intentional EMI[J]. *IEEE Trans. Electromagn. Compat.* 2008, **50**(1): 101-109.
- [2] Zhang Cunbo, Wang Honggang, Zhang Jiande. Simulation and Experiment Research on High Electron Mobility Transistor Microwave Damage. *High Power Laser Part. Beam* 2014 **26**(6): 063014. (in Chinese)
- [3] Cunbo Zhang, Honggang Wang, Jiande Zhang, et al. Failure Analysis on Damaged GaAs HEMT MMIC Caused by Microwave Pulse[J]. *IEEE Trans. Electromagn. Compat.* 2014, DOI: 10.1109.
- [4] Ma Z Y, Chai C C, Ren X R, Yang Y T, Chen B. The damage effect and mechanism of the bipolar transistor caused by microwaves. *Acta Phys. Sin.* 2012, **61**(7):078501. (in Chinese)
- [5] Fan J P, Zhang L, Jia X Z HPM damage mechanism on bipolar transistors. *High Power Laser Part. Beam* 2010 **22**(6): 1319-1322. (in Chinese)
- [6] Chai C C, Zhang B, Ren X R, Leng P. Injection damage of the integrated silicon low-noise amplifier. *J. Xidian Univ.* 2010 **37**(5): 898-903. (in Chinese)
- [7] X. B. Chen, Q. Z. Zhang. Principle and Design of Transistor. (Publishing House of Electronics Industry, The Second Edition, 2006), P54-55. (in Chinese)

# Frequency Response Analysis of IEMI in Different Types of Electrical Networks

Bing Li and Daniel Månsson

KTH Royal Institute of Technology, School of Electrical Engineering  
 Department of Electromagnetic Engineering  
 Stockholm, Sweden  
[libing@kth.se](mailto:libing@kth.se), [manssond@kth.se](mailto:manssond@kth.se)

## Abstract

In this paper, the frequency responses of the loads in different types of electrical networks subjected to intentional electromagnetic interference (IEMI), are analysed with a method based on the Baum-Liu-Tesche (BLT) equation. The networks can be multi-conductor systems with multiple junctions and branches. To verify the calculation results, a commercial electromagnetic simulator based on electromagnetic topology was used. The calculation results agree well with the numerical simulations.

**Keywords:** Electrical network, multiple junctions, intentional electromagnetic interference (IEMI), frequency responses.

## 1 Introduction

Recently, in modern society, intentional electromagnetic interference (IEMI) appears more frequently in threat analyses. Because of the sophistication of electrotechnical and electronic systems the harmfulness of malicious manipulation should be easily understood. Different groups and scholars have contributed in the past to this field (e.g. [1, 2]). Here, in this paper, we investigate the effects on the frequency response characteristics of different loads in networks with different structures as they are subjected to intentional electromagnetic interference (IEMI).

## 2 The BLT Equation

For a simple electrical network, as shown in Fig. 1, to solve the frequency responses for each load, the BLT approach [3, 4] is applied. In this simple network, we suppose that the length of the transmission line is  $L$ , with propagation constant  $\gamma$  and characteristic impedance  $Z_c$ . The load impedances are  $Z_{L1}$  and  $Z_{L2}$ , respectively. The excitation source consists of a lumped voltage ( $V_s$ ) and current ( $I_s$ ) source, located  $x_s$  from the left load.

The application of BLT equation is described as follows;

$$\begin{bmatrix} V_1^{inc} \\ V_2^{inc} \end{bmatrix} = \begin{bmatrix} 0 & e^{-\gamma L} \\ e^{-\gamma L} & 0 \end{bmatrix} \begin{bmatrix} V_1^{ref} \\ V_2^{ref} \end{bmatrix} + \begin{bmatrix} S_1 \\ S_2 \end{bmatrix}, \quad (1)$$

where the excitation vector is

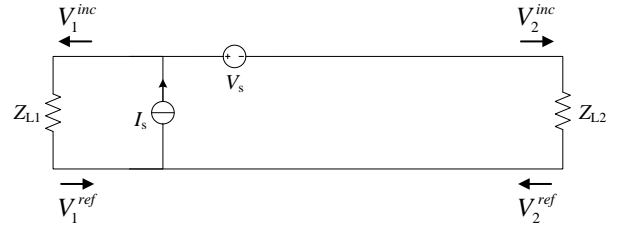


Figure 1. A simple electrical network.

$$\begin{bmatrix} S_1 \\ S_2 \end{bmatrix} = \begin{bmatrix} -\frac{1}{2}(V_s - Z_c I_s) e^{-\gamma x_s} \\ \frac{1}{2}(V_s + Z_c I_s) e^{-\gamma(L-x_s)} \end{bmatrix}.$$

At the terminals, the reflected voltage can be expressed as

$$\begin{bmatrix} V_1^{ref} \\ V_2^{ref} \end{bmatrix} = \begin{bmatrix} \rho_1 & 0 \\ 0 & \rho_2 \end{bmatrix} \begin{bmatrix} V_1^{inc} \\ V_2^{inc} \end{bmatrix}, \quad (2)$$

where  $\rho_1$  and  $\rho_2$  are the reflection coefficients, defined by

$$\rho_i = \frac{Z_{Li} - Z_c}{Z_{Li} + Z_c}, \quad (i = 1, 2).$$

Plugging (2) into (1), we obtain the vector of the incident voltages by

$$\begin{bmatrix} V_1^{inc} \\ V_2^{inc} \end{bmatrix} = \left[ \begin{bmatrix} 1 & 0 \\ 0 & 1 \end{bmatrix} - \begin{bmatrix} 0 & e^{-\gamma L} \\ e^{-\gamma L} & 0 \end{bmatrix} \cdot \begin{bmatrix} \rho_1 & 0 \\ 0 & \rho_2 \end{bmatrix} \right]^{-1} \cdot \begin{bmatrix} S_1 \\ S_2 \end{bmatrix}. \quad (3)$$

The frequency response at each load is the superposition of the incident and reflected voltages

$$\begin{bmatrix} V_1 \\ V_2 \end{bmatrix} = \begin{bmatrix} V_1^{inc} \\ V_2^{inc} \end{bmatrix} + \begin{bmatrix} V_1^{ref} \\ V_2^{ref} \end{bmatrix} = \begin{bmatrix} 1 + \rho_1 & 0 \\ 0 & 1 + \rho_2 \end{bmatrix} \cdot \begin{bmatrix} V_1^{inc} \\ V_2^{inc} \end{bmatrix} = \begin{bmatrix} 1 + \rho_1 & 0 \\ 0 & 1 + \rho_2 \end{bmatrix} \cdot \left[ \begin{bmatrix} 1 & 0 \\ 0 & 1 \end{bmatrix} - \begin{bmatrix} 0 & e^{-\gamma L} \\ e^{-\gamma L} & 0 \end{bmatrix} \cdot \begin{bmatrix} \rho_1 & 0 \\ 0 & \rho_2 \end{bmatrix} \right]^{-1} \cdot \begin{bmatrix} S_1 \\ S_2 \end{bmatrix}. \quad (4)$$

In addition, if TEM is the main mode of voltage wave propagation, then for any existing junctions in the electrical network, the reflection coefficients can be calculated according to the transmission line theory. If the transmission line parameters are the same for all branches of a junction (e.g. same type of cables used) and if the load connected to each branch is, electrically, far away from the junction, then the current is equally divided between the branches. For a

junction with  $N + 1$  branches, the reflection coefficient  $\rho^*$  and transmission coefficient  $T^*$  are respectively given by [5]

$$\rho^* = \frac{Z_c/N - Z_c}{Z_c/N + Z_c} = -\frac{(N-1)}{(N+1)} \quad (5)$$

$$T^* = 1 + \rho^* = \frac{2}{(N+1)} \quad (6)$$

### 3 Analysis of different types of network

To some extent, the complexity of an electrical network depends on the number of arbitrarily distributed junctions and branches. Besides, the characteristic impedances of the different transmission lines, branch lengths and load values are also factors. In this paper, we focus on the influence of the number of junctions and branches on the load voltages.

In Fig. 2, we enumerate seven types of electrical networks. In the analysis process, the commercial software EMEC [6] is applied to verify the calculation results. The line lengths, in meter, are given in the subfigures. All the transmission lines studied here were set to have the same characteristic impedance,  $Z_c = 45 \Omega$ , but a complex impedance could be given. The values of the load impedances vary from  $100 \Omega$  to  $600 \Omega$  ascendingly in accordance with the label (#1 ~ #6), and the increment is  $100 \Omega$ . The value of the lumped excitation source is chosen to be  $V_s = 100 \text{ V}$ ,  $I_s = 1 \text{ A}$ , and we sweep the frequency from  $1 \text{ Hz}$  to  $20 \text{ MHz}$ . (Even though the model can handle frequencies between quasi DC and very high frequencies and also more complex input parameters).

For the network shown in Fig. 2a), the calculation results are given in Fig. 3. The results marked with either a circle or a triangle are computed based on the BLT equation, while the solid lines are computed by EMEC. In Fig. 2b) ~ Fig. 2d), the results calculated based on the adapted BLT equation, and by EMEC are given in Fig. 4. Here, the colored red curve, blue curve and black curve represent the frequency responses of load #1, load #2 and load #3, respectively. The value of the curve is the mean value of the results for three networks, and at the same time, we also give the corresponding standard deviation. It is easy to see that, at high frequencies, increasing the number of branches significantly affects the frequency responses of the loads, which are not located on the same branch as the excitation source.

In Fig. 2e) ~ Fig. 2g), we observe the effects of the number of junctions and branches. The calculation results are given in Fig. 5. In this case, the colored cyan curve represents the frequency responses of load #4, while others remain the same meaning (as given above for Fig. 2b) ~ Fig. 2d)). In contrast to the one-junction networks, the overall standard deviation is smaller for the networks with multiple junctions. For load #1 (red curve), the voltage response changes a little after inserting the junction between the two junctions shown in Fig. 2e), while load #2 (blue curve), load #3 (black curve) and load #4 (cyan curve) suffer relatively more in different frequencies. Besides, the extent of the effects they experience

relies on the values of the loads, in other words, larger loads are more affected.

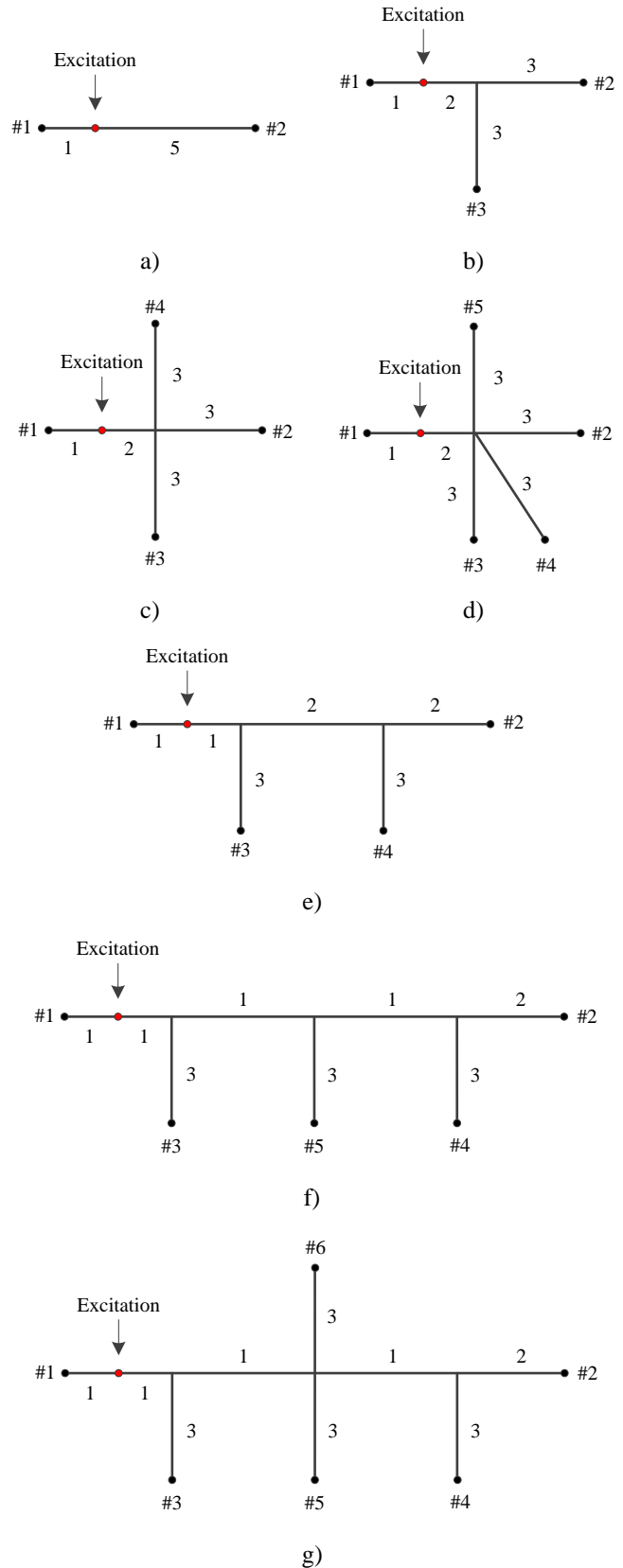


Figure 2. Different types of electrical networks.

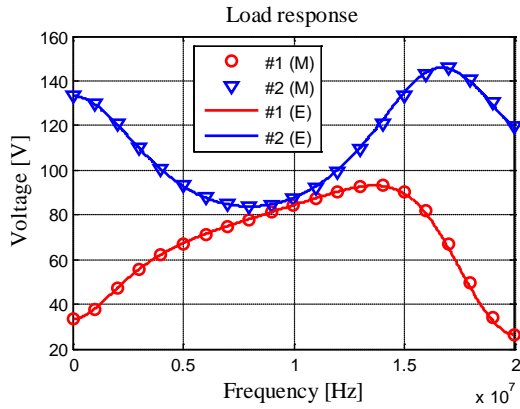


Figure 3. Results of the network shown in Fig. 2a).

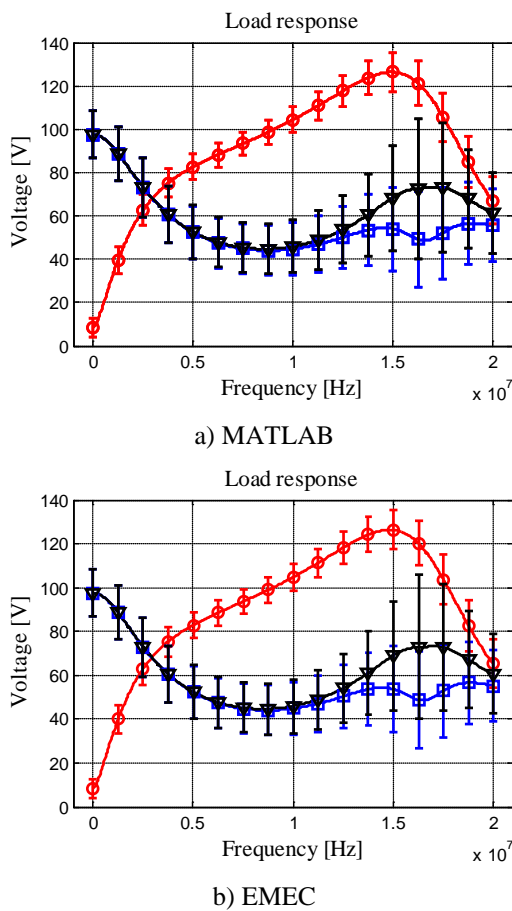


Figure 4. Results of one-junction networks.

## 4 Conclusions

In this paper, for the electrical networks that may suffer from IEMI attacks, we calculated the frequency responses of several different types of networks, and analyzed the effects of the number of junctions and branches. The results show that, increasing the number of branches at a junction has a great effect on the frequency responses of the loads connected to the different branches, while increasing the number of

junctions does not. The calculation results employed in the analysis were verified by the commercial software EMEC, and they agree well with each other.

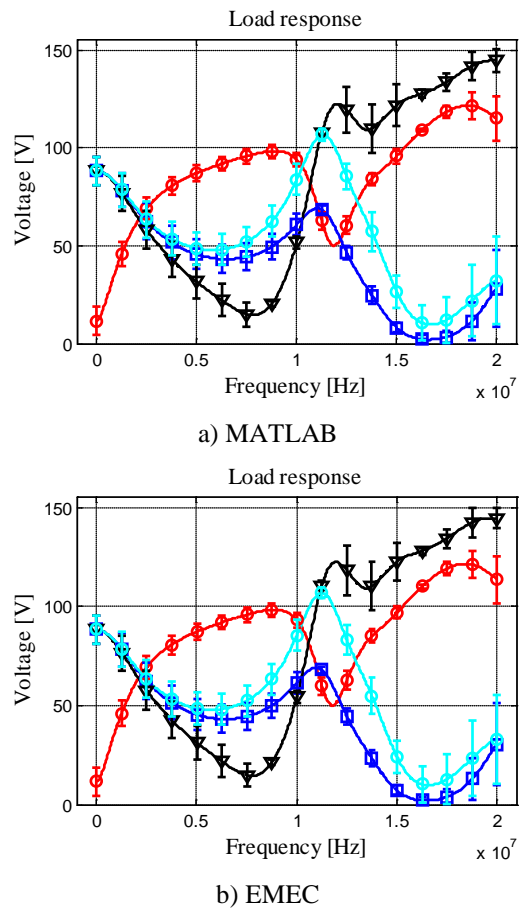


Figure 5. Results of multi-junction networks.

## References

- [1] D. V. Giri, F. M. Tesche. "Classification of intentional electromagnetic environments", *IEEE Trans. EMP*, vol. 46, pp. 322-328, (2004).
- [2] D. Månsson, R. Thottappillil, and M. Bäckström. "Methodology for classifying facilities with respect to Intentional EMI", *IEEE Trans. EMC*, vol. 51, pp. 46-52, (2009).
- [3] C. E. Baum. "Generalization of the BLT equation", *Proc. 13th Zurich EMC Symp.*, pp. 131-136, (1999).
- [4] F. M. Tesche. "Development and use of the BLT equation in the time domain as applied to a coaxial cable", *IEEE Trans. EMC*, vol. 49, pp. 3-11, (2007).
- [5] D. Månsson, R. Thottappillil, and M. Bäckström. "Propagation of UWB transients in low-voltage power installation networks", *IEEE Trans. EMC*, vol. 50, pp. 619-629, (2008).
- [6] J. Carlsson, T. Karlsson, and G. Undén. "EMEC—An EM Simulator Based on Topology", *IEEE Trans. EMC*, vol. 46, pp. 353-358, (2004).

# Analysis of Transmission Characteristic of Composite Material with Wire Mesh and Honeycomb Core in Aircraft

Se-Young Hyun\*, Ic-Pyo Hong\*\*, Chilsung Jung<sup>†</sup>, Eung-Jo Kim<sup>†</sup>, and Jong-Gwan Yook\*

\*Dept. of Electrical and Electronic Engineering Yonsei University, Seoul, Republic of Korea, jgyook@yonsei.ac.kr,

\*\*Dept. of Inf. and Comm. Engineering, Kongju National University, Seoul, Republic of Korea,

<sup>†</sup>The 7th R&D Institute Agency for Defense Development, Haemi Chungnam, Republic of Korea.

## Abstract

This paper focuses on the analysis of the transmission properties of the multi-layered composite material as well as enhanced analysis method, and the transmission coefficients of the multi-layered composite material with wire mesh and honeycomb under any of incidence have been analyzed below 16 GHz. The proposed method is based on boundary value solution of the analytic methods combined with homogenization method to better fit to multi-layered composite material with the wire mesh and honeycomb core.

**Keywords:** composite material, wire mesh, honeycomb

## 1 Introduction

Use of the composite materials has been expanded in aerospace industry to satisfy low weight, high strength, and low costs. In spite of the benefits of composite materials compare to the metallic structure, it is penetration path for unintended electromagnetic field because of their dielectric properties[1],[2]. Therefore, it is necessary to study the analysis of transmission characteristics for composite material in that aircraft electronic systems are required to be high reliability compared with the general ones. In order to apply to aircraft components, the composite materials are used in the form of a multi-layered structure which is combined with arbitrary structures such as a wire mesh and a honeycomb core. However, this structure is difficult to define its material properties and calculate the electromagnetic analysis for the complicated shape.

Therefore, this study is intended to analyse the transmission characteristics and to propose the method with efficient calculation time for the multi-layered composite material with the wire mesh and the honeycomb core.

## 2 Analysis of composite material

Figure 1. shows the simplified multi-layered composite material with the wire mesh and the honeycomb core. The wire mesh composed of conductor provides a shielding effectiveness for impinging lightning strike damage in aircraft

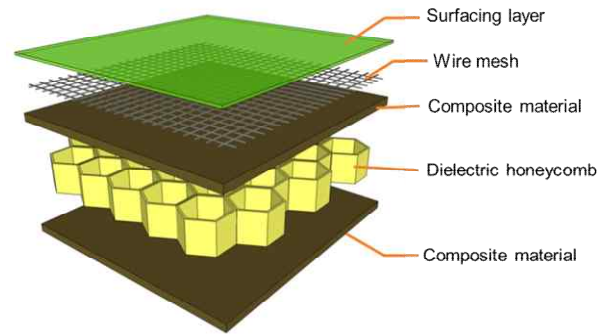


Figure 1. Composite material with wire mesh and honeycomb core.

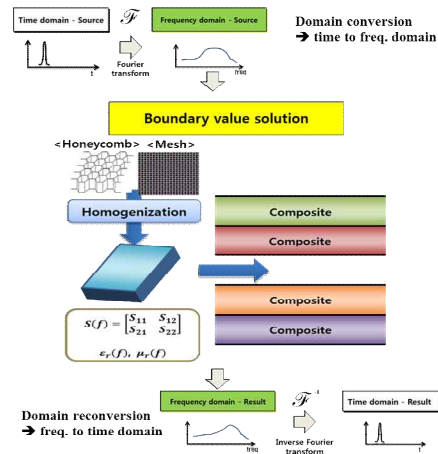
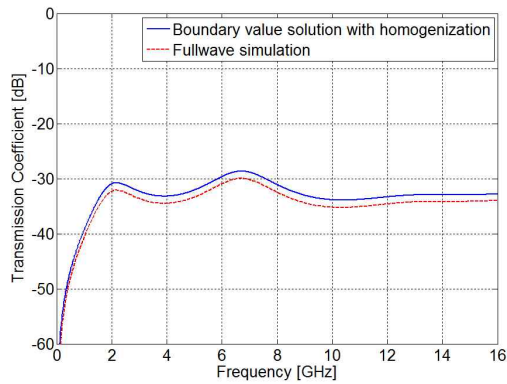


Figure 2. Procedure of boundary value solution with homogenization method.

and the dielectric honeycomb core is widely used for improving mechanical properties. The procedure of the boundary value solution with homogenization method proposed to analyze the multi-layered composite material is illustrated in Figure.2. The wire mesh and the honeycomb layer are replaced to the equivalent layer with effective electromagnetic properties and the transmission coefficient of



**Figure 3. Comparison of transmission coefficients between proposed method and full-wave simulation (perpendicular polarization,  $\theta = 60^\circ$ ).**

Table 1: Calculation time of proposed method and full-wave simulation.

Method	Frequency range (counts)	Calculation time (sec)
FEM (periodic boundary condition)	0.1~16 GHz (160)	269.00
Proposed method	0.1~16 GHz (160)	0.23

multi-layered composite material is calculated by the boundary value solution[3]. For the homogenization of wire mesh and honeycomb core, different method is performed to each structure[4]. Figure. 3 shows comparison of the transmission coefficients between proposed method and full-wave simulation as a function of the frequency, corresponding to  $\theta = 60^\circ$  incident angles with each polarization. As a result, a good agreement was obtained between boundary value solution with homogenization method and full-wave simulation. In Table 1, time consumption for entire structure is compared between the proposed method and full-wave simulation. The full-wave simulation which is FEM with periodic boundary condition (PBC) is used to compute the periodic and multi-layered structure. The frequency range and count are same for these methods that maximum frequency is 16 GHz and 160 counts are computed. Using the proposed method, calculation time is reduced to 0.08% compared with the full-wave simulation for multi-layered structure. This result shows the boundary value solution with homogenization method is efficient method for multi-layered composite material with the wire mesh and the honeycomb core.

### 3 Conclusion

The transmission characteristics of the multi-layered composite material with the wire mesh and honeycomb core in aircraft have been analyzed and efficient method for this structure is proposed. The composite materials applied to aircraft component are employed to multi-layered structure combined with conductive wire mesh and honeycomb core. This structure is difficult to define its material properties and calculate the electromagnetic analysis for the complicated shape. The proposed method is handled to convert from conductive wire mesh to effective layer. For the dielectric honeycomb core, it can be directly calculated by obtaining effective permittivity different from the homogenization of wire mesh. Using proposed method, transmission coefficient of multi-layered composite material used in aircraft can be analyzed.

### Acknowledgements

“This work has been supported by Agency for Defense Development of Republic of Korea under the contract UD130028JD”.

### References

- [1] S. Y. Hyun, J. K. Du, H. J. Lee, K. W. Lee, J. H. Lee, C. Jung, E. J. Kim, W. Kim, and J. G. Yook, “Analysis of shielding effectiveness of reinforced concrete against high-altitude electromagnetic pulse”, *IEEE Tran. on electromagnetic compatibility*, vol.56, no. 6, (2014).
- [2] J. K. Du, S. M. Hwang, H. J. W. Ahn, and J. G. Yook, “Analysis of coupling effects to PCBs inside waveguide using the modified BLT equation and full-wave analysis”, *IEEE Tran. on microwave theory and techniques*, vol.61, no. 10, (2013).
- [3] Dennis J. Kozakoff, “Analysis of radome enclosed antennas”, Artech House, (1977).
- [4] C. Menzel, C. Rockstuhl, T. Paul, F. Lederer, and T. Pertsch. “Title of the article”, *Physical Review B*, **77(19)**, (2008).

# On the Applicability of the Transmission Line Theory for the Analysis of Common-Mode IEMI-Induced Signals

G. Lugin\*, N. Mora\*, F. Rachidi\*, M. Nyffeler†, P. Bertholet†, M. Rubinstein‡, S. Tkachenko+

\* EMC Laboratory, EPFL, Switzerland, contact: [gaspard.lugin@epfl.ch](mailto:gaspard.lugin@epfl.ch)

† HPE Laboratory, Federal Department of Defence – Armasuisse, Switzerland

‡ University of Applied Sciences of Western Switzerland, Yverdon, Switzerland.

+ Otto-von Guericke University, Magdeburg, Germany

## Abstract

In this work, we discuss the possibility of using the transmission line (TL) theory for solving the field-to-wire coupling and propagation problems in scenarios where the distances between the lines and the reference plane are not electrically small, with special reference to IEMI-induced signals. A canonical configuration of a wire above a ground plane is chosen for studying the common mode coupling, and the solution obtained with the TL theory are compared with results obtained using full wave approaches. We show that for moderate band sources, the TL theory can provide with results that can be considered as acceptable for engineering purposes, even beyond the validity limits of the TL theory. However, in the case of hypoband sources, MTL might fail to correctly predict the response if the validity conditions are not respected.

**Keywords:** high-frequency plane wave excitation, intentional electromagnetic interferences (IEMI), transverse electromagnetic (TEM), transmission line (TL) theory.

## 1 Introduction

The evaluation of susceptibility level of sensitive devices to an IEMI (intentional electromagnetic interferences) attack requires an accurate evaluation of voltages and currents at their terminals.

The evaluation of electromagnetic coupling and wave propagation along cables is usually made using the classical transmission line (TL) theory which applies to uniform transmission lines with electrically small cross-sectional dimensions, and where the dominant mode of propagation is transverse electromagnetic (TEM) [1]. The objective of this work is to assess the applicability of the TL theory to disturbance sources with high frequency content such as IEMI.

## 2 Analysis Method

The applicability of the TL theory for the analysis of the IEMI coupling to transmission lines is assessed by comparing the solutions provided by full wave methods and the classical TL theory.

We consider for the analysis a single-wire, lossless line above a perfectly conducting ground plane illuminated by an IEMI

interference represented by a plane wave. In a real scenario, ground and dielectric losses will further attenuate and distort the propagation of the induced signals (see companion paper [2]).

The considered line is composed of a 3-m long, 0.7-mm radius wire located at a height of 10 cm over the ground plane. It is terminated by an impedance of  $339 \Omega$  at its left terminal and short-circuited at its right terminal.

The induced currents are computed using the BLT (Baum-Liu-Tesche) equation [3] in the frequency domain and converted into the time domain using inverse Fourier transformation. The TL results are compared with full-wave solutions obtained using CST Microwave Studio®, which uses the finite integration technique (FIT) in the time domain.

## 3 Results

The upper plot of Figure 1 shows a 2.01 GHz hypoband incident field waveform that was used to illuminate the line with a  $45^\circ$  elevation angle (the azimuth angle was set to zero). The bottom plot of Figure 2 shows a comparison of the current waveform at the line left-end termination calculated with the TL theory and a full-wave method.

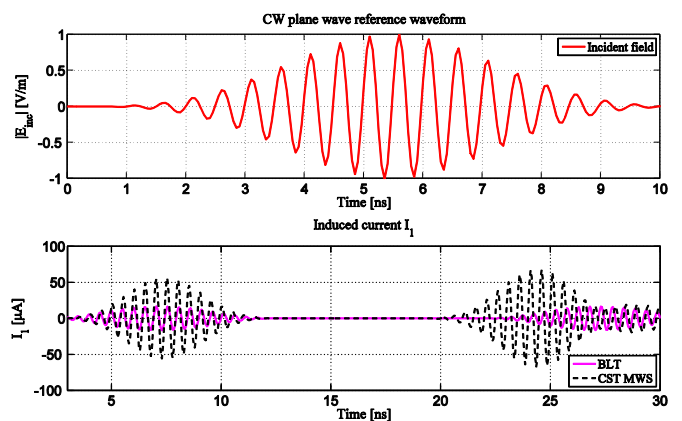


**Figure 1. Top: Incident electric field. Bottom: Induced current computed with the classical TL theory (BLT) and respectively a full-wave model (CST MWS).**

At this specific frequency, the classical TL theory underestimates by a factor of about 4 the peak amplitude of the induced currents.

Similar comparisons were carried out for hyperband and mesoband waveforms. In these cases, it was found that the TL theory can provide with results that are in reasonable agreement with full-wave simulations.

#### 4 Discussion and Conclusion

It was shown that, for hyperband and mesoband sources, the TL theory provides responses that are in fair agreement with the full wave codes even for cases where the distances between the wires are not electrically short. This is essentially because the energy density of these types of sources is typically concentrated in the low frequencies (below some GHz).

On the other hand, in the case of hypoband sources, TL theory might fail to correctly predict the response if the TL validity conditions are not respected.

#### Acknowledgements

This study was financed by the Armassuisse Science and Technology (Contract Nr. 8003504623).

#### References

- [1] F. Rachidi, "A Review of Field-to-Transmission Line Coupling Models with Special Emphasis to Lightning-Induced Voltages", *IEEE Trans. Electromagnetic Compatibility*, Vol 54, No. 4, pp. 898 - 911, 2012.
- [2] N. Mora, G. Lugrin, F. Rachidi, M. Nyffeler, P. Bertholet, M. Rubinstein, "Study of the Propagation of IEMI Signals along Power and Communication Lines", ASIAEM, Jeju, Republic of Korea, August 2-7, 2015.
- [3] F. M. Tesche, M. V. Ianoz, and T. Karlsson, *EMC analysis methods and computational models*. New York: Wiley, 1997.

# Test of Surge Protective Devices to Mitigate Intentional Electromagnetic Interferences (IEMI)

G. Lugrin<sup>1</sup>, N. Mora<sup>1</sup>, F. Rachidi<sup>1</sup>, P. Bertholet<sup>2</sup>, M. Nyffeler<sup>2</sup>, A. Kälin<sup>3</sup>, S. Sliman<sup>4</sup>, M. Rubinstein<sup>4</sup>

<sup>1</sup> EMC Laboratory, EPFL, Lausanne, Switzerland

<sup>2</sup>HPE Laboratory, Armasuisse, DDPS, Thun, Switzerland

<sup>3</sup>EMProtec, Hinwil, Switzerland

<sup>4</sup>IICT, University of Applied Sciences Yverdon, Switzerland

## Abstract

We report tests of feedthrough SPDs, designed to protect against lightning surges or HEMP, exposed to fast transients with a risetime in the order of a hundred picoseconds.

Two of the three tested SPDs limited well the disturbances under a safe threshold. One of them reduced effectively the low-frequency content of the pulse, while letting part of the high-frequency content go through.

**Keywords:** Intentional electromagnetic interference (IEMI), surge protective device (SPD).

## 1 Introduction

The performance of existing protection techniques, such as surge protective devices (SPDs) against conducted and radiated disturbances produced by intentional electromagnetic interferences (IEMI) is currently not well understood and constitutes the object of several recent studies (e.g., [1,2,3]). These protection measures are, at present, primarily designed to mitigate the effects of lightning, switching, electrostatic discharges and, to some extent, high altitude electromagnetic pulse.

In this study, we present experimental tests of a few commercially available lightning/HEMP SPDs against IEMI.

## 2 Test setup

The testing of SPDs against IEMI is challenging mainly because the expected disturbances are characterized by spectral components that extend to much higher frequencies, compared to lightning and HEMP. Furthermore, they can present significant variations in terms of their time-domain waveshape [4].

We used a transient high voltage generator providing pulses with a rise-time of about 100 ps with peak amplitudes ranging from 3 kV to 14 kV. It was connected to a specially designed adapter to make an impedance matching from 50  $\Omega$  to low impedance [5] (see Fig. 1). A current probe was placed between the adapter and the tested SPD to measure the current, which was placed on the wall of a metallic box.

Another setup, where the SPDs were placed inside the box, as described in a CISPR standard [6], was also tested. The SPDs were loaded through attenuators on a 50  $\Omega$ -input impedance.

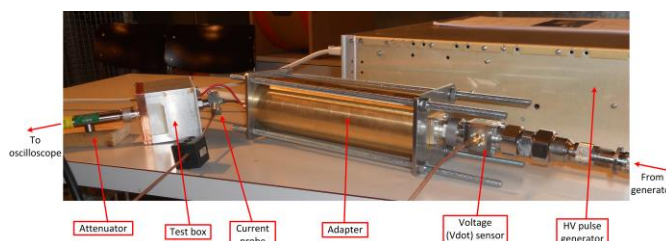


Figure 1. Picture of the test setup.

Three feed-through SPDs, designed to protect against HEMP/NEMP and lightning transients were tested.

## 3 Results and discussion

Two of the three tested SPDs limited well the disturbances under a safe threshold. The third one reduced partially the pulse (see Fig. 2). Results such as residuals currents will be shown and discussed during the presentation.

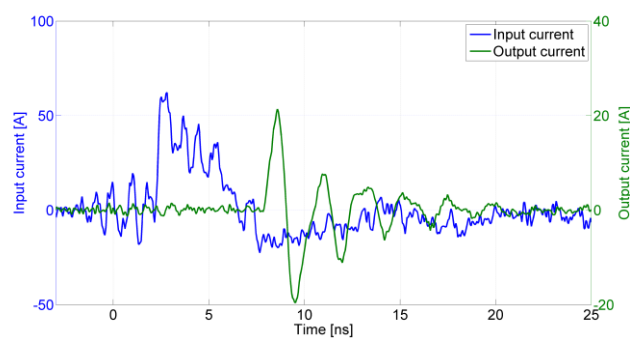


Figure 2. Injected current (in blue, left vertical scale) and residual current (in green, right vertical scale).

## Acknowledgements

This study was financially supported by the Swisselectric-Research.

## References

- [1] T. Nilsson, "Investigation of Limiters for HPM and UWB Front-door Protection," Master's thesis, Linköping University, 2006.
- [2] M. Nyffeler, A. Kaelin, D. Rolle, P.-F. Bertholet, and A. Jaquier, "Behavior of Combined Lightning- HEMP-Protection Devices to HPEM Overvoltage Input Signals," in ANTEM/AMEREM, July 2010.
- [3] W. Radaski et al., "Protection of the high voltage power network control electronics against intentional electromagnetic interference (IEMI)," Cigré, WG C4.206, Tech. Rep., 2013.
- [4] D. Giri and F. Tesche, "Classification of Intentional Electromagnetic Environments (IEME)," IEEE Transactions on Electromagnetic Compatibility, Vol. 46, pp. 322–328, August 2004.
- [5] P. Bertholet, A. Kälin, G. Lugrin, N. Mora, M. Nyffeler, F. Rachidi, and M. Rubinstein, "Design and realization of a high-voltage adapter for the testing of surge protective devices against intentional electromagnetic interferences," in American Electromagnetics International Symposium (AMEREM), Albuquerque, New Mexico, USA, 2014.
- [6] International Special Committee on Radio Interference (CISPR), Methods of measurement of the suppression characteristics of passive EMC filtering devices, 2011.

# High Power Microwave Effects on Coated Window Panes

P Ängskog<sup>\*†</sup>, M Bäckström<sup>\*#</sup>, B Vallhagen<sup>#</sup>

<sup>\*</sup>Electromagnetic Engineering Lab, KTH Royal Institute of Technology, Sweden, pangskog@kth.se,

<sup>†</sup>Department of Electronics, Mathematics and Natural Sciences, University of Gävle, Sweden

<sup>#</sup>SAAB Aeronautics, SAAB AB, Sweden, mats.backstrom@saabgroup.com

## Abstract

Today window panes are usually coated with at least one metal or metal oxide layer to prevent heat energy of the light spectrum from propagating to the other side. This has given problems regarding radio propagation through windows, which might be utilized as a part of a buildings IEMI protection. This paper reports the results from measurements of the shielding effectiveness of a selection of modern window panes before and after irradiation with high power electromagnetic waves. The shielding effectiveness measurements are made in a nested reverberation chamber covering the range 1 – 18 GHz; both before and after high power irradiation at 1.3 GHz. The results show that the shielding effectiveness of window panes may be severely impaired due to thermal stress effects on the coatings during the irradiation, depending of the type of coating.

**Keywords:** HPM; window panes; glass; transmission; propagation.

## 1 Introduction

Today window panes usually are coated with at least one layer of metal or metal oxide to prevent heat energy from propagating through a window. In cold climate the purpose is to contain the long-wave infra-red light inside a building while in hot climates the needs are similar; only the direction is opposite, the infra-red waves should be kept on the outside. Furthermore, the high-energy, short wavelength ultra-violet rays should preferably be blocked by the window preventing them from reaching objects on the inside and thus converting to heat.

The coatings of the panes are optimized with infra-red or ultra-violet radiation in mind while no attention is paid to the radio and microwave parts of the electromagnetic spectrum. This has proven to give problems in modern communication systems since radio signals are efficiently blocked by modern energy saving windows [1] - [5].

With the purpose to determine the effects from high power microwave (HPM) irradiation this paper examines the shielding effectiveness (SE) of single window panes with different coatings. A comparison of SE results before and after the high power exposure is presented.

## 2 Method

The high power effects are determined using a comparative method where first the SE is measured before high power irradiation, as a reference, and then re-measured to reveal any effects of the irradiation.

The SE measurements conducted to determine the shielding properties of the panes where made in a nested reverberation chamber (RC), Figure 1. In the RC a mode stirrer is employed to create a mode stirred incident field impinging on the sample mounted over an aperture in the nested chamber. Inside the nested chamber a second mode stirrer revolves to change the mode of the field incident on the receiver antenna. For each frequency 252 different combinations of stirrer positions are used when measuring the isotropic transmission cross section,  $\langle\sigma_a\rangle$ , of the test object. From  $\langle\sigma_a\rangle$  the SE is calculated [6]-[7].

In the present case the reference aperture is a square opening with an area, A, 300 x 300 mm<sup>2</sup>. For a reference aperture with such a simple geometry one may express the result above in terms of shielding effectiveness, i.e. in terms of a dimensionless quantity, simply by comparing the power transmitted through the unshielded opening (i.e. the square opening) with the power transmitted through the opening when the shielded structure is mounted on it, i.e.

$$\langle SE_{apert,iso} \rangle = \frac{A/4}{\langle\sigma_a\rangle}. \quad (1)$$

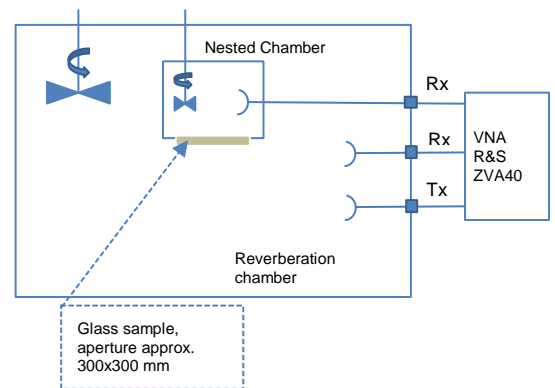


**Figure 1.** Simplified block diagram showing the reverberation chamber.

In (1) we approximate the transmission cross section of the unshielded opening by  $A/4$  which is exactly true only at frequencies where the opening is electrically large. For frequencies above 1 GHz the error is less than 1 dB.

The HPM exposure was carried out in the Microwave Test Facility (MTF) at SAAB Aeronautics in Sweden. The MTF was set to work in the L-band giving the field strength 28 kV/m in 5  $\mu$ s long pulses with a pulse repetition frequency of 390 Hz during a 10 s burst.

### 3 Measurement Samples

The measurement samples were four single window panes, as tabulated in Table 1. The specimen code found in the first column is an identifier for each sample; the second column explains of what specific glass type that specimen is.

Soft coated and hard coated low-emission glass are intended to reflect infrared light (i.e. heat) back while letting day-light pass through them. The difference between the two is the composition and method used for deposition of the coating layer.

Soft coating is deposited on pre-cut float glass in tens of nanometers thick layers using sputtering, a physical vapor deposition (PVD) where the layers consist of various metal oxides, typically tin-dioxide ( $\text{SnO}_2$ ), interleaved with one or more layers of silver. Other metal oxides such as ZnO and  $\text{TiO}_3$  may also be used. The more silver layers the lower emissivity and the better the reflection of ultra-violet rays.

Hard coating is applied on semi-molten glass in the production line using chemical vapor deposition (CVD) and typically consists of only one a few hundreds of nm thick layer of  $\text{SnO}_2$ .

Table 1. List of measurement samples – single window panes.

Single Panes, Standard Types	
Specimen Code	Specimen type
HC1-5	Solar Control, Soft Coated, Low-e glass; 1 Silver Layer
SC-5	Hard Coated, Low-e glass
Sp-5	Spandrel glass
2Ag-5	Solar Control, Soft Coated, Low-e glass; 2 Silver Layers

A spandrel pane is an opaque glass often placed as cladding element between clear-view windows to hide construction elements, insulation and building infrastructure installations. The opacity is achieved by adding coatings of metal, metal oxides or enamel on the rear (inner) side of the pane.

### 4 Results

#### 4.1 Visual Effects

A visual inspection of the samples after the HPM exposure gave at hand that the two silver coated samples, HC1-5 and 2Ag-5, exhibited visually clear cracks looking like Lichtenberg figures indicating an electrical breakdown process due to thermal stress from the very strong electric field, see Figure 2 and Figure 3. However, the other two samples, the hard coated (SC-5) and the spandrel (Sp-5) glasses showed no visual deterioration.

#### 4.2 Shielding Effectiveness Effects

Consequently, the SE measurements of the SC-5 and Sp-5 samples did not reveal any changes in SE at all. On the other hand, the two samples with cracked coatings the changes were evident.

The deterioration for the 2Ag-5 pane was approximately 5 dB between 1 and 1.8 GHz and from 6 GHz to 18 GHz while in the 2-5 GHz range there is no noticeable reduction in SE at all, cf. Figure 4. For the HC1-5 pane SE is on average

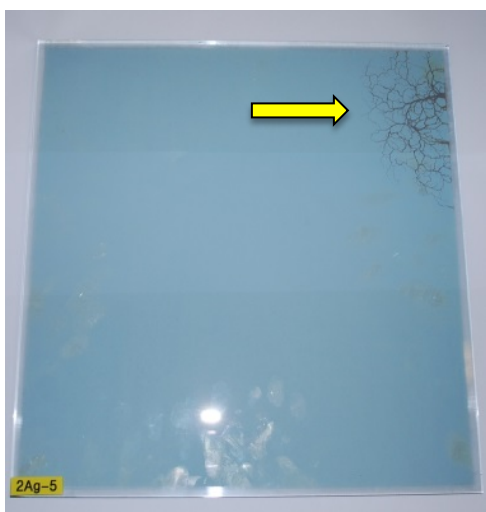


Figure 2. Cracks in the coating of the 2Ag pane resulting from HPM exposure.

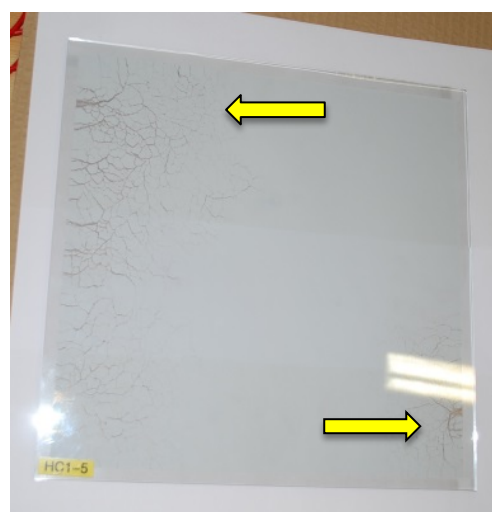
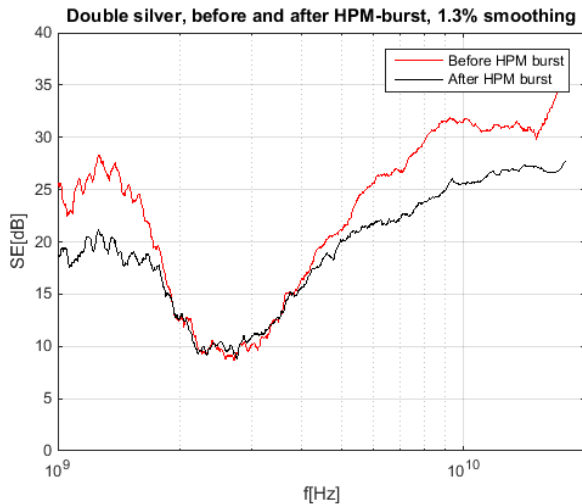


Figure 3. Cracks in the coating of the HC1 pane resulting from HPM exposure.



**Figure 4.** Comparing the shielding effectiveness measured on the double silver coated 2Ag sample before (upper) and after (lower) the HPM burst.

approximately 15 dB lower at 1 GHz decreasing to approximately 7 dB at 18 GHz, cf. Figure 5.

## 5 Discussion

Measurement results have been presented for a group of window panes intended for different window applications. The panes were subject to high power microwave irradiation after which the shielding effectiveness of the panes was measured and compared to the shielding effectiveness before the exposure.

An SE difference between panes with different coating was observed. Even though also the metal oxides are conductive, the main difference between unaffected and affected samples seems to be the metallic coating (silver) on the two affected panes while the unaffected samples were coated only with a metal oxide.

In this study we have shown that the potential of using window coatings as part of the protection against IEMI or unwanted electromagnetic emanations is not completely safe, depending on which type of coating the panes have – if it is possible to approach the facility with high power electromagnetic radiators.

## Acknowledgements

This work is a part of the project Protection against Electromagnetic Risks. Intentional Electromagnetic Interference (IEMI), funded by the Swedish Civil Contingencies Agency (MSB), the Swedish Fortifications Agency, The Swedish Post and Telecom Authority (PTS) and The National Food Agency (SLV). The authors also wish to emphasize the support from Mikael Ludvigsson and Maria Lang at the Swedish Glass Research Institute, Glafo, who were very helpful in the selection and acquisition of test samples.

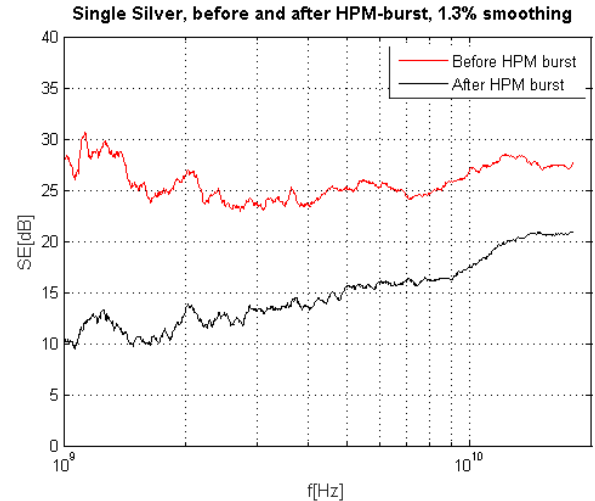


**Figure 5.** Comparing the shielding effectiveness measured on the single silver coated HC1 sample before (upper) and after (lower) the HPM burst.

## References

- [1] A. Asp et al, "Radio Signal Propagation and Attenuation Measurements for Modern Residential Buildings," in *Globecom Workshops (GC Wkshps), 2012 IEEE*, Anaheim, CA, USA, 2012.
- [2] E. Krogager and J. Godø, "Attenuation of Building used for HPM Testing," in *AMEREM-2014*, Albuquerque, NM, 2014.
- [3] P. Ragulis, Ž. Kancleris and R. Simniškis, "Transmission and Reflection of Microwave Radioation from Novel Window Panes," in *AMEREM-2014*, Albuquerque, NM, USA, 2014.
- [4] I. Rodriguez et al, "Radio Propagation into Modern Buildings: Attenuation Measurements in the Range from 800 MHz to 18 GHz," in *Vehicular Technology Conference (VTC Fall), 2014 IEEE 80th*, Vancouver, Canada, 2014.
- [5] G. I. Kiani et al, "Glass Characterization for Designing Frequency Selective Surfaces to Improve Transmission through Energy Saving Glass Windows," in *Microwave Conference, 2007. APMC 2007. Asia-Pacific*, Bangkok, Thailand, 2007.
- [6] M. Bäckström, T. Nilsson and B. Vallhagen, "Guideline for HPM protection and verification based on the method of power balance," in *Electromagnetic Compatibility (EMC Europe), 2014 International Symposium on*, Gothenburg, Sweden, 2014.
- [7] D. A. Hill et al, "Aperture Excitation of Electrically Large, Lossy Cavities," *IEEE Trans. Electromagn. Compat.*, vol. 36, no. 3, pp. 169-178, August 1994.

# IEMI and Smartphone Security: a smart use of front door coupling for remote command execution

C. Kasmi\*, J. Lopes-Esteves\*

\*Wireless Security Lab, French Network and Information Security Agency, 51 bvd de la Tour Maubourg, 75007 Paris, France

## Abstract

Many studies have been devoted to the analysis of the effects induced by IEMI on electronic devices. Some recent research was focused on the classification and the detection of those effects at both the hardware and software levels thanks to the analysis of operating systems and drivers event logs. Thanks to the last approach, it has been observed that the audio card is very responsive to IEMI. In this paper, a remote voice command injection technique on smartphones and desktop computers audio cards will be unveiled thanks to Smart RF signals.

**Keywords:** RF DEW, Cyber security, Voice command control.

## 1 Introduction

The use of RF DEW in military applications has been widely studied for a long time. The challenge of generating a large amount of power has slowly evolved to the definition of efficient waveforms to lower the level of emitted fields [1]. Recent research in the field of software defined radio [2] has provided the possibility of generating complex waveforms for a reduced budget [3]. The combination of low cost emitters with low cost amplifiers results in low cost RF DEW.

During the last decades, studies have been devoted to the fine-grain classification of effects induced by IEMI on information systems [4]. In the framework of the published experimentations, it has been shown that some parts of computers and smartphones react simultaneously to parasitic fields. One of these parts is the sound card. The parasitic signal envelop was recorded by the audio input interface [5]. In order to go deeper in the analysis, we have been working on RF pulses to check if audio signals (continuous wave modulated in amplitude with an audio file) can be automatically demodulated by the audio card thus allowing to remotely inject voice command on embedded systems providing voice command services. We propose here to consider the RF signal as smart RF DEW which could open a new area of vulnerability for cyber security.

The paper is organized as follows: in Section 2, the voice control features provided as a service in embedded systems are described. In Section 3, the conception of the so-called Smart RF DEW designed for the discussed voice control interface is provided. In Section 4, as for cyber security

requirements, the risks analysis and the counter-measures are given.

## 2 Voice control in smartphones

Voice command allows the hand-free use of a mobile device. This way of interacting with the mobile devices is spreading and will certainly be one of the main improvements in the upcoming UIs. It is being deployed in smartphones, extended by smart watches and wearables, in vehicle control systems and desktop computers. The features that can be accessed via voice commands are getting more and more critical from an information security and privacy point of view. Furthermore, mobile device manufacturers tend to enable voice interpreters by default, which exposes permanently the voice interface.

### 2.1 Hardware components

Most modern smartphones provide mainly two voice input interfaces, connected to a DSP stage which digitizes and filters the voice signal and forwards it to the application processor. The voice input interfaces are the built in microphone and the headphone's microphone. Generally, those interfaces are enabled alternatively, depending on the presence of microphone capable headphones (detected by the impedances on the 4-pin connector).

The headphones L and R audio outputs can also be used as an input antenna for FM radio signals in FM capable phones. Furthermore, microphone capable headphones provide a physical button interface. A button press changes the impedance of the microphone line, which is detected by the phone (Fig.1).

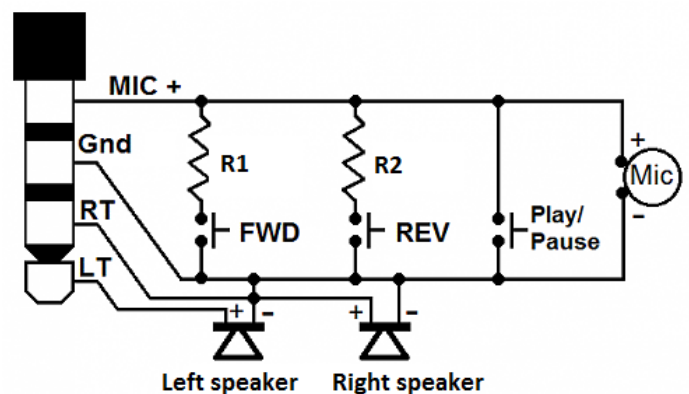


Figure 1. Wiring of a headset remote command.

## 2.2 Software services and features

Nowadays, a lot of features can be accessed by voice, depending on the device and the operating system. Some of them can be considered from a security point of view as critical. In this study, we focused on three cases: an Apple iPhone, a Google Nexus phone and a vendor customized Android phone (Samsung).

In the following, we shortly describe the voice services and the features exposed:

- *Samsung* [6]: Samsung voice control system is called *S-Voice*. It is a vendor software layer that is natively included in the Android core;
- *Apple* [7]: two services provide a voice command interface, namely *Voice Control* and *Siri*. On the latest versions of iOS, *Siri* completely replaced *Voice Control*;
- *Google* [8]: *Google Voice Search* is the original voice command interface and was merged to *Google Now* since Android Jelly Bean.

When the voice command interpreter is not enabled permanently, it is generally activated by a long hardware button press or by launching the aforementioned software applications. Then, the user must say a keyword followed by the voice command. The main features than can be accessed via the voice command interface are listed below:

- *Telephony services*: sending text messages, placing calls, answering calls;
- *Internet services*: visiting web pages, sending emails, posting on social networks, launching web searches, maps and positioning;
- *Local services*: launching applications, changing phone settings, creating calendar entries, notes, setting alarms...

The voice and speech recognition is generally performed on a remote server, except for the keyword. This means that voice command cannot be used without internet connectivity through Wi-Fi or mobile network.

## 3 RF DEW conception for data injection

The test phase aimed to validate the following hypothesis: as the headphones act as a FM antenna, it should be possible to use them as a front door coupling interface for voice command injection. To achieve this verification, the experimental setup consisted in placing the phones, with headphones plugged in, in a Faraday cage with a wireless access point relaying the IP traffic to a computer outside the cage via optical fibre. Additionally, an E-field probe was also installed next to the target so that we are able to link the trigger of the voice command controller and the required minimal field level. On the phones, we installed an application which records sound from the microphone. This application streams the recorded sound on the network in

real-time to the computer, which can store and play the sound samples.

For voice emission, we used a music player as a voice signal source which modulated a continuous wave produced by a RF synthesizer. During our experiments, the two following scenarios were considered:

1. The voice control command has been activated by default by the user: this means that the voice command service starts as soon as a key word was pronounced by the user. The experiments demonstrated that it is possible to trigger voice commands remotely by emitting an AM modulation of the keyword followed by some voice commands at FM radio frequencies. This signal is received by the headphone, as it is designed to act as an antenna for the FM radios. The resulting electric signal that is induced in the microphone cable of the headphones is really close to voice signal and is correctly interpreted by the voice command interface.
2. The voice command is not activated by default and a long hardware button press is required for launching the service: in this case, we have worked on injecting a specially crafted radio signal to trigger the activation of the voice command interpreter by emulating a headphone's command button press. It was shown that thanks to an FM modulated signal, we were able to launch the voice command service and to inject the voice command. To perform the emission of both the FM and AM modulated signals, we come up with the use of software defined radio tools [2-3].

It was observed that the minimal field required around the target was in the range of 25 – 30 V/m at 103 MHz, which is close to the limit accepted for human safety.

While voice command control becomes more and more powerful, we have shown that it also becomes a critical interface. In the next Section, we will provide a security analysis with the related countermeasures.

## 4 Security analysis

Being able to execute voice commands remotely on a system can be critical from an information security point of view. Furthermore, potentially all voice control capable systems can be vulnerable to this kind of attack. The attacker profile required for this attack can be considered as “proficient” (according to the Common Criteria), and involves publicly available RF equipment. A basic knowledge in software defined radio and some information about the target operating system and user settings is also necessary. The EM field levels required have a significant impact on the equipment needed by an attacker depending on the desired range he wants to operate from. The following table summarizes the attacker profile according to the range.

To understand the impact such an attack can have on a target, some attack scenarios have been considered:

- *Tracking and spying*: the attacker activates the wireless interfaces of the target for enabling mid-range tracking. He also can place a call to his own phone to capture the surrounding sounds;
- *Paid SMS services*: the attacker targets all the users in range and forces them to send a SMS to a paid service;
- *Drive-by malware download*: the attacker can force the target to visit a malicious web page which exploits a vulnerability to compromise the targets operating system.

In order to mitigate this attack vector, some countermeasures could be applied. Unfortunately, there is always a trade-off between security and usability:

- Some modifications on the audio front-end can be done in order to reduce the sensitivity of the input interface. This would force the attacker to reach higher EM field levels to achieve the attack. A better shielding of the headphones cable would also contribute to this mitigation.
- Voice and speech recognition improvements can also be part of the solution. Indeed, better recognizing the voice of the legit user would force the attacker to forge the commands with the user's voice signature. One could think of some techniques to detect if the voice has been digitized and replayed or if it comes from a physical speaker.
- A better granularity in the user settings could be a great improvement: letting the user choose his own keyword (already possible on most of devices but a few users are doing so), disabling the voice interface by default, allowing the user to choose the authorized actions via this interface would be interesting options.

## 7 Conclusion

In this paper we discussed the possibility to use low cost RF equipments and software defined radio to design an efficient low cost RF DEW. To demonstrate this, we introduced a new technique for remote voice command injection in smartphones. A security analysis has been performed and some possible countermeasures have been proposed.

The main contribution of this research is threefold: first, the reduction of the attacker costs for conceiving RF DEWs is illustrated. This should be taken into account in risks analysis. Secondly, a smart use of IEMI, which is not only focused on denial of service attacks or equipment disabling, is enlightened. Finally, we attract the attention of the vendors on the possibility to use the voice command interface as an attack vector, so that they can take it into account and improve the security of their products.

During the presentation, a set of videos showing the induction and the execution of voice commands on a set of targets will be displayed.

## Acknowledgements

The authors would like to thank the editors, the vendors and manufacturers of the devices that have been tested, namely Apple, Google and Samsung, for their reactivity after the responsible vulnerability disclosure process and for accepting the publication of this research.

## References

- [1] N. Mora, F. Vega, G. Lugrin, F. Rachidi, System Design & Assessment Note SDAN 41, "Study and Classification of Potential IEMI Sources", July 2014.
- [2] GNU Radio is a free & open-source software development toolkit, online: <http://gnuradio.org/redmine/projects/gnuradio/wiki>
- [3] Universal Software Radio Peripheral, online: <http://www.ettus.com/>
- [4] C. Kasmi, J. Lopes-Esteves, N. Picard, et al. "Event Logs Generated by an Operating System Running on a COTS Computer During HPEM Exposure," Electromagnetic Compatibility, IEEE Transactions on, vol., no.99, pp.1,4, 2014.
- [5] C. Kasmi, J. Lopes-Esteves, M. Renard, System Design & Assessment Note SDAN 44, "Automation of the Immunity testing of COTS computers by the instrumentation of the internal sensors and involving the operating system logs – Technical report", November 2014.
- [6] Samsung, "How do I Use Samsung S Voice", online description: [http://www.samsung.com/us/support/supportOwnersHowToGuidePopup.do?howto\\_guide\\_seq=7061&prd\\_ia\\_cd=N0000003&map\\_seq=54784](http://www.samsung.com/us/support/supportOwnersHowToGuidePopup.do?howto_guide_seq=7061&prd_ia_cd=N0000003&map_seq=54784)
- [7] Google, "Ok Google", online description: <https://support.google.com/websearch/answer/2940021?hl=en>
- [8] Apple, "Siri", online description: <https://www.apple.com/ios/siri/>

# A survey of typical sudden commencement geomagnetic storm environments

W A Radasky\*<sup>1</sup> and E B Savage\*<sup>2</sup>

\*Metatech Corporation, Goleta, California, USA, <sup>1</sup>wradasky@aol.com, <sup>2</sup>savagee@cox.net

## Abstract

In this paper we will consider a study of past geomagnetic sudden commencement events, which typically represent the beginning of a geomagnetic storm as it arrives at the Earth. These are of interest because of possible adverse geomagnetic storm effects on the long power transmission lines in a power grid at nearly any latitude.

**Keywords:** Sudden commencement, sudden impulse, geomagnetic storm.

## 1 Introduction

Geomagnetic storms, and their effects on our critical infrastructure, can be of interesting for several reasons. They are interesting in their own right, in efforts to try to understand the environments, their effects on the power grid, and in efforts to try to mitigate serious adverse effects. It is well known that geomagnetic storms can adversely affect power system, through generation of horizontal E fields in the ground, and the subsequent coupling of DC-like currents in long transmission lines. Storms are also of interest because of their similarities to E3 HEMP (MHD – magneto-hydrodynamics). Hardening against one might also apply to the other, and since we cannot really perform realistic E3 tests on a power grid, geomagnetic storms can provide useful E3 “simulations” instead. There is also the similarity of being rare, at least at the highest levels for geomagnetic storms. In fact, there are limited data on the extremes of geomagnetic storms, although considerable geomagnetic field data are being gathered at many stations located throughout the world.

Cigré (International Council on Large Electric Systems) has an interest in geomagnetic storms, because effects on power grids are one of the major manifestations of these storms. A Cigré working group (WG C4.32) is evaluating the different types of geomagnetic disturbances. One type is geomagnetic storm sudden commencement (SSC) or sudden impulse (SI). This is manifested as a sudden jump in the magnetic field, at the very start of a geomagnetic storm series. It is driven by the solar coronal mass ejection’s (CME’s) impact on the geomagnetic. The initial perturbations can be more than 100 nT (nanotesla), will usually have rise times of approximately 1 minute, and can generate E fields in the Earth of the order of volts per kilometer. The Cigré effort will look into magnetometer recordings of past SSC events, trying to understand the extreme cases, and looking for parameter

variations. Besides their possible adverse effects on power grids and the opportunity to use them for studying geomagnetic disturbance effects on the grid, they also might be useful because they are a precursor to a coming storm, as a warning and possible indication of the storm intensity. Ultimately the working group will produce a technical brochure on geomagnetic disturbances that may later become a standard. In this paper we will report on a study using magnetometer measurements of past sudden commencement events.

## 2 SSC Data Processing

Our study started with a time-of-arrival list of past SSCs from NOAA (Boulder, Colorado), and from these we selected a set to study, in the time period of 1997 to 2005. From our high-resolution private magnetometer (the first site listed below) and from two other working group members, we obtained magnetometer data for the selected events for the sites:

Forbes: lat<sub>geo</sub>: 57° (1 second data)

Brazil: lat<sub>geo</sub>: -13° (1 minute data)

Japan: lat<sub>geo</sub>: 27° (1 second data)

(lat<sub>geo</sub> is the geomagnetic latitude). Figs. 1 and 2 show the magnetic perturbations for two cases.

Consider Fig. 1. For all three cases the horizontal magnetic field suddenly (over a few minutes) increases – with very similar shapes, but reaching different amplitudes. (The dashed line is the vertical component). The Forbes jump (green line) is much higher than the other two, and the Japanese disturbance (blue line) is the lowest. Note that the Brazil data has only a 1-minute cadence (with data points marked by the asterisks), while the other two have 1-second

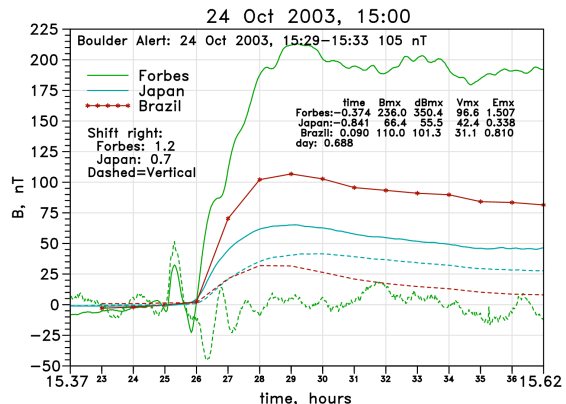


Figure 1. October 24, 2003, 15:29 SSC B waveforms.

data. Also, the Forbes data has higher frequency structure (or noise) not seen in the other two. We do not know the details of the data processing for the Japan and Brazil data (although a 1 minute cadence precludes the higher frequencies being observed); the Forbes data are the raw measurement values with averaging over a few points.

Fig. 2 shows a different behavior. In amplitude, the Brazil (red line) is the highest in its sustained amplitude, and shows little structure besides just an upward jump, while the other two cases are similar, in that they have an initial large spike, with more oscillations to follow, and then settling down to lower values.

Besides looking at the magnetic disturbances for all the SSC events studied, we are also interested in the resulting horizontal E field near ground interface, since these are what drive currents in high tension power transmission lines. Thus, we made 1-D (depth into ground) calculations for the E field driven by the horizontal B field disturbances, using several different layered profiles of ground conductivity. Figs. 3 and 4 show results for one ground profile for the SSC events in the previous figures. In Fig. 3 the E field amplitudes are in the same order as the B field peaks, however there is very much more structure in the Forbes (green line) result. In Fig. 4 the Forbes and Japan results are similar, but again with the highest oscillations in the Forbes results. Also, although the Brazil B field had a large jump, its E field is the smallest, and very short. These results are consistent with the E field generation process being both resistive and inductive.

### 3 Questions

Besides looking for extremes in the geomagnetic disturbances, and also considering the resulting E fields, which is partially influenced by the time derivative of the B field, there are other issues of interest, such as:

1. Are the effects worldwide and how well correlated are the disturbances over widely spread sites?
2. Are there systematic parameter effects, such as variation with geomagnetic latitude?
3. Are there variations with time-of-day (how well a site is pointed towards the sun)?

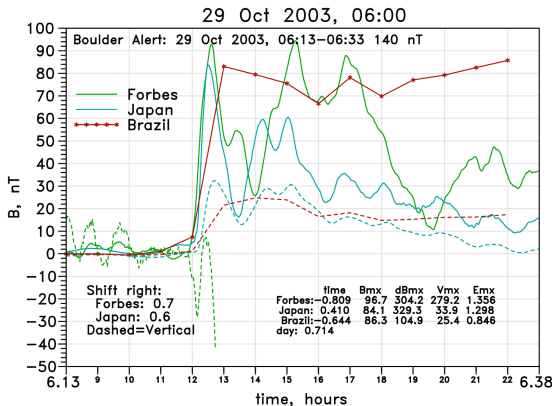


Figure 2. October 29, 2003, 06:00 SSC B waveforms.

4. Or time of year effects due to the orientation of the geomagnetic field?
5. Can anything be seen in the components of the fields, instead of just focusing on the amplitude?

Given that higher frequencies (faster derivatives) contribute more to the E field, there are additional issues:

6. Are the higher frequency variations also correlated over wide distances, or more localized (and so might average out over a power line run)?
7. Are there magnetometer data processing issues that adversely affect the calculation of the E field? We much prefer higher cadence data than the more common 1-minute data, but even for the higher resolution data are there data processing steps performed that might tend to filter out some of the higher frequencies?

In our study we also try to look at these issues.

### 4 Conclusions

We will be adding more sites to this study, especially with regard to examining some of the questions we have listed about sudden commencement storms and their variations.

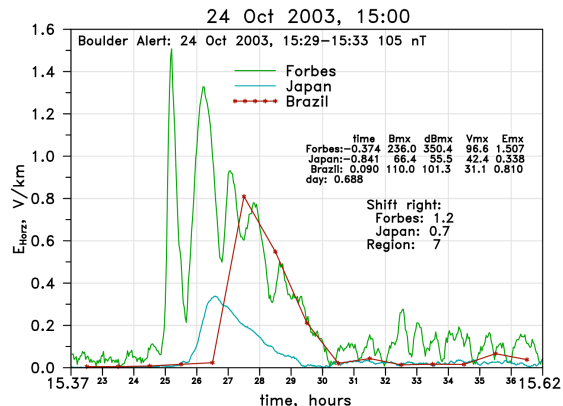


Figure 3. Sample E fields from Fig. 1 B fields.

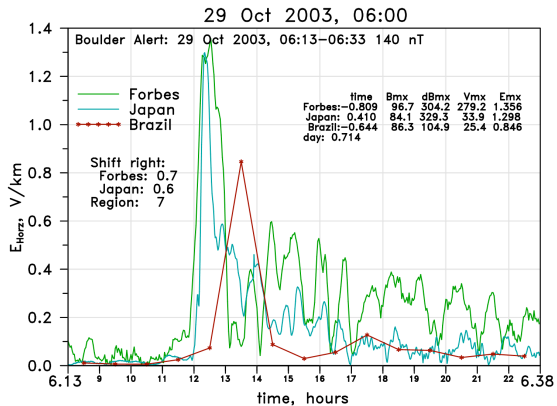


Figure 4. Sample E fields from Fig. 2 B fields.

# Failure Rate Analysis of Solid State Device Caused by Repeated Pulse Characteristics

Ki-Hoon Park\*, Kwan-Sik Kim\*, Chang-Su Huh\*<sup>†</sup>, Jin-Soo Choi\*\*, Jong-Won Lee\*\*

\*Department of Electrical Engineering, Inha University, Incheon 402-751, Korea

\*\*Agency for Defence Development, Dajeon 305-152, Korea

## Abstract

If the electronic systems are exposed to HPEM, the systems will be destroyed by the coupling effects of electromagnetic waves. The semiconductors are vulnerable to various pulse parameters such as frequency, voltage, and rise time of the pulse. Among those the parameters, the pulse repetition rate is a primary consideration about malfunction properties of the semiconductor. In this paper we designed an EUT for the pulse injection test in order to investigate destructive characteristics of semiconductor caused by pulse of 30, 60, 120 [Hz], and analyzed the destruction failure rate accordance with on/off-state of the general purpose IC. As a result, the injected pulses have changed to amplitude, duty ratio, and period of output generated by Timer IC. Also, they are susceptible to influence at the off-state IC. Finally, As the pulse repetition rate increases the breakdown threshold point of the Timer IC was reduced.

**Keywords:** Solid state device, HPEM, Pulse injection test, Electromagnetic waves, Failure rate

## 1 Introduction

Electronic systems consist of resistor, capacitor, inductor, and active devices. Among those the components, based on semiconductor is especially susceptible to a minimal change in electromagnetic waves. They often causes malfunction of system. However, It has not been enough research to solve problems such as Electromagnetic Interference (EMI). Therefore we discuss about malfunction mode and DFR (Destruction Failure Rate) of the semiconductor by amplitude and repetition rate of the pulse[1]. The pulses were injected into the VCC pin of general purpose IC. These pulses were produced by pulse generator and their characteristics are 2.1 [ns] of pulse width and 1.1 [ns] of pulse rise time.

## 2 Test setup

The Timer IC can work in monostable, bistable, and astable mode operations. It had wide range of applications like lamp dimmers and motor control. The astable multivibrator mode was used for the pulse injection test. The circuit generates a continuous pulse of rectangular. The Timer IC consists of eight pins as Ground, Trigger, Output, Reset, Control Voltage, Threshold, Discharge, V<sub>CC</sub>. The pulses inject into pins of IC

through a coaxial cable. Figure 1 shows the injected pulse. The pulses have repetition rate of 30, 60, 90 [Hz].

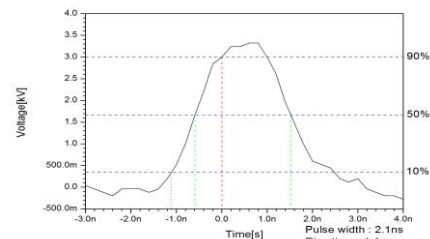
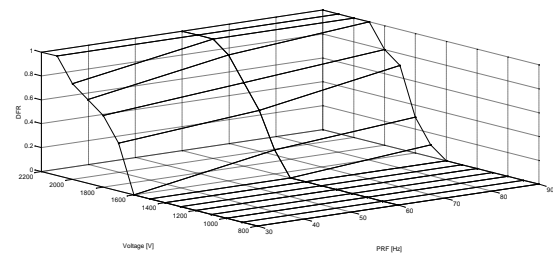


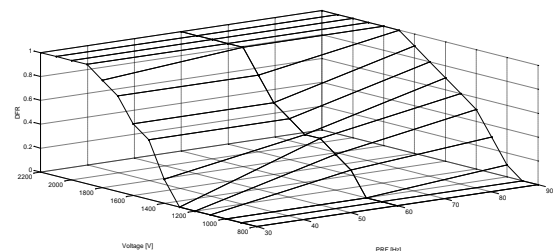
Figure 1. Injected pulse waveform of pulse generator.

## 3 Result

Figure 3-(a) and figure 3-(b) show on-state IC and off-state IC for Vcc pin with pulse injection. It shows the DFR due to the injected pulse of 30, 60, 120 [Hz] in accordance with on/off state. As a result, It can be noticed that the failure rate of the on-state IC is much sharper than the off-state IC. The on-state ICs will be destruction more than off-state ICs. Also, as the pulse repetition rate increases, it was reduced to breakdown threshold point of the timer IC



(a) On-state IC



(b) Off-state IC

Figure 3. DFR due to the change in the PRR and Voltage

## References

- [1] M. Camp, IEEE Trans. on EMC, Vol. 1, 87-92, (2002).

# Destruction Characteristic of CMOS AND gate by Variable Pulse repetition rate

Jeong-Ju Bang\*, Sun-Ho Choi\*, Chang-Su Huh\*<sup>†</sup>, Jin-Soo Choi\*\*, Jong-Won Lee\*\*

\* Department of Electrical Engineering, Inha University, Incheon, Korea

\*\*Agency for Defence Development, Dajeon 305-152, Korea

## Abstract

This study examined the destruction effect of CMOS AND gates by injecting repetitive pulses. Pulses are injected to the input pin of the AND gate. The pulse has a rise time of 1.0~2.1ns and a maximum peak voltage of 2 kV. In this study, destruction effect of semiconductor device by repetitive electromagnetic pulses was analyzed.

When AND gate is injected pulse, the AND gate destroyed. Because AND gate protection diode destroyed by injected pulses. The voltage of 50% destruction failure rate at which AND gate is destroyed decreases as the repetition rate of pulse increases.

**Keywords:** repetition pulse, CMOS, pulse injection,

## 1 Introduction

The modern electronic devices are very vulnerable to high power electromagnetic pulses because semiconductor elements are designed for low power and smaller size. Therefore, semiconductor elements become more susceptible to undesired noise. If high power electromagnetic waves pass through aperture of electronic device, the electromagnetic wave is coupled to the electronics device and generates a current in the circuit board. The coupled current causes a malfunction or failure of the electronic systems[1].

Research on effect analysis of high power electromagnetic on electronic devices and developing high power electromagnetic generators have been performed in the world.

Recently, repetitive electromagnetic pulse generators have been developed. Therefore, in this study, destruction effect of semiconductor device by repetitive electromagnetic pulses was analyzed.

## 2 Experimental Setup

In this study, three pulses are injected to the AND gate. Table 1 indicates that the injected pulses rise time and pulse width. The waveforms of the pulses are shown in Fig 1.

Table 1: Injected pulses

	Pulse1	Pulse2	Pulse3
Rise time(ns)	0.75	0.75	1.10
Pulse width(ns)	1.1	1.2	2.1

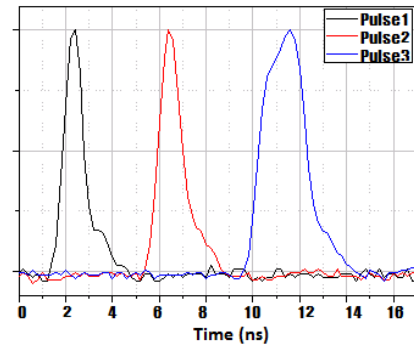


Figure 1. Waveforms of applied pulses

## 3 Result

Figure 2 show the destruction voltage of 50% destruction failure rate by different pulse repetitions. As shown in Figure 3, the destruction voltage of 50% destruction failure rate at which AND gate is destroyed decreases as the repetition rate of pulse increases.

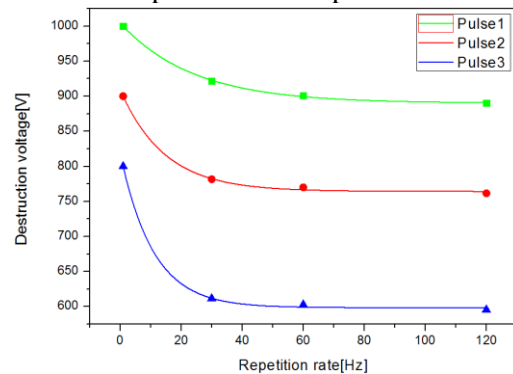


Figure 2. destruction voltage of 50% destruction failure rate

## References

[1] Hwang, S. M., J. I. Hong, S.-M. Han, C. S. Huh, and J.-S. Choi, "Susceptibility and coupled waveform of microcontroller device by impact of UWB-HPeM," Journal of Electromagnetic Waves and Applications, vol. 24, no.8-9, 1059-1067, 2010

# A Method to Design a New Kind Active Frequency Selective Surface which has the Ability of HPM Protection

Deng Feng Wang Dongdong Ding Fan

Science and Technology on Electromagnetic Compatibility Laboratory

**Abstract** — Conventional active frequency selective surfaces (AFSS) are designed with a DC biasing circuit to apply DC biasing voltage across active components. An innovative method to design AFSS is proposed in this paper to use an induced voltage across both ends of the surface loading components as the biasing signal to control FSS's transmission properties. The result from simulation proved that, a pass band exists on the AFSS at 3.5GHz when it is exposed to an electric field at a smaller intensity; at the electric field intensity (EFI) over 70 V/m, the insertion loss of the electromagnetic wave (EMW) increases at 3.5 GHz; in the case that the incident microwave's field intensity reaches 5000 V/m, the insertion loss is over 20 dB. This interesting phenomenon make the new AFSS has the ability of HPM protection, which mean that a pass band exists when EFI is week enough, along with increasing incident field intensity, the pass-band finally turns into a stop-band because of the break though of the diodes.

**Keywords:** Active; Frequency selective surface (FSS); microwave

## I Introduction

Nowadays, FSS has been widely used in devices such as including multiband reflecting antenna and radomes, and areas including communication and protections etc. [1][2]. In the above-mentioned applications, FSS functions at a fixed pass-band frequency. However, some applications require that FSS's pass-band frequency can be changed in some conditions and therefore have made study concerning AFSS become embraced enthusiastically [3]-[5].

Another applications of the AFSS is the HPM protection areas, when the incident field intensity of AFSS is small, a pass band exist on the AFSS, EM wave in the pass band can transmit through the AFSS; when the HPM exists, the original pass band turn into a stop band, then the HPM would be reflect from the AFSS. In spite of this, there is a key defect of conventional AFSS when it is used in above-mentioned application. It is known that a biasing circuit is commonly used in the conventional AFSSs to control the transmission properties, which means that the duration of the controlling procedure would not be short enough for the HPM protection[6][7].

A novel AFSS free of the biasing circuit is described in this paper: when the electromagnetic wave (EMW) is used to radiate AFSS, the induced voltage signal across the loading element is used as biasing voltage signal to control the impedance of the loading element and the whole AFSS's resonant frequency can be changed by changing the radiation field intensity. Doing so, AFSS's resonant frequency can be used to change at the time level of ns.

## II Working Principle

The AFSS described in this paper is devised with a Schottky diode as active component, with its structure as shown in Figure 1. The entire AFSS consists of the metallic grids, the square metallic sheets in the center of the grids and Schottky bilateral diodes loaded between the two corners. In this case, the AFSS may be considered as a FSS loaded with a lumped capacitance. In the case of exposure to a microwave at field intensity sufficient to make the semiconductor component at low impedance under the action of the induced signal, and its resonant frequency will be changed.

## III Design and Result from Simulation

To investigate the transmission properties of the above-mentioned AFSS, a typical AFSS is selected with the dimensions of the periodic unit shown in Table 1. The software CST MWS was used to simulate the nonlinear time-domain response properties of the AFSS exposed to microwaves at different frequencies and different field intensities and then based on the relation of the transmission field intensity versus the incident field intensity, the transmission characteristic of AFSS is calculated. The model is as shown in Figure 2.

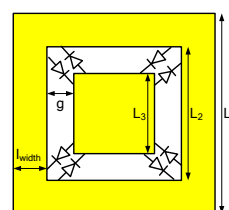


Figure 1 Sketch of the AFSS composition, the loading elements are bilateral diodes.

Table 1 Dimension of AFSS

Parameter	value
$L_1$	12.4mm
$L_2$	2mm
$L_3$	2mm
$l_{width}$	0.5mm
$g$	1mm
$H_{roger}$	1mm
$\epsilon_r$	3.66

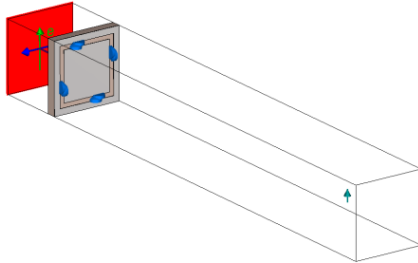


Figure 2 CST simulation model of AFSS

The transmission characteristics  $S_{21}$  of AFSS exposed at different field intensities from the above-described method is present in Figure 3. From it, it is observed that at a small field intensity of exposure, there exists a resonant pass-band at 3.5 GHz with the insertion loss of -0.9 dB; with increasing incident field intensity, the insertion loss increases around 3.5 GHz, and at the incident field intensity of 5000 V/m, the insertion loss is above -20 dB and the resonant frequency disappears totally.

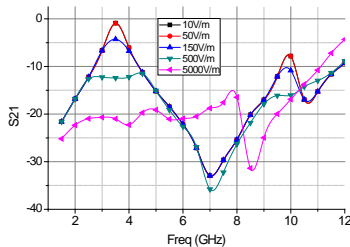


Figure 3 Transmission characteristic  $S_{21}$  of AFSS exposed to microwaves at different field intensities when the loaded diodes is bilateral.

Figure 4 is the 3.5 GHz Microwave's insertion loss on AFSS exposed at different field intensities. At the microwave's field intensity less than 70 V/m, microwave can transmit through the AFSS with no loss. With the incident field intensity getting higher, the insertion loss increase gradually when the microwave is passing through the AFSS. At the field intensity as large as 5000 V/m, the insertion loss can be as high as 20 dB.

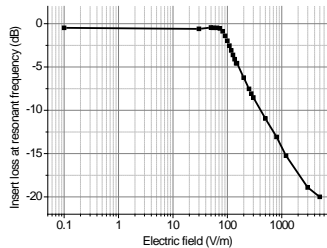


Figure 4 Insertion loss change versus the electric field intensity when a 3.5 GHz EMW is transmitting through the self-configurable AFSS at different field intensities

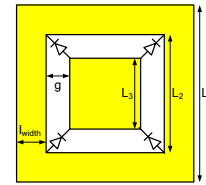


Figure 5 Sketch of the second AFSS, the loaded elements are unilateral diodes.

As mentioned earlier, the elements loaded in AFSS as fig.1 are bilateral diodes; we will discuss the transmission characteristic of AFSS loaded with unilateral schottky diodes at next.

Sketch of the first kind arrangement of unilateral diodes is as fig.5, the anode of the two diodes at the top of the unit cell is located in the metallic square, and the cathode of the two diodes at the bottom of the unit cell is located in the metallic square. The transmission characteristics of the AFSS at different incident electric field intensities are shown in fig.6. It can be found that the transmission characteristic has changed a lot when the field intensity is high enough. This AFSS has also the ability of HPM protection.

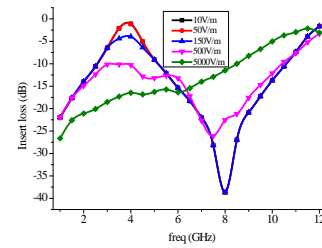


Figure 6 Transmission characteristic  $S_{21}$  of AFSS exposed to microwaves at different field intensities when the diodes arrangement is as fig.5

Sketch of the second kind arrangement of unilateral diodes is as fig.7, the cathode of the two diodes at the upper left and lower right of the unit cell is located in the metallic square, the anode of the two diodes at the upper right and lower left of the unit cell is located in the metallic square. The transmission characteristics of the AFSS at different incident electric field intensities are shown in fig.8. It can be found that the transmission characteristic has also changed a lot when the field intensity is high enough. But when the field intensity is 150V/m, the variation of transmission characteristics (as blue line infig.8) is much weaker than that in fig.6.

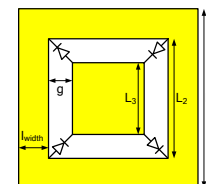


Figure 7 Sketch of the third AFSS

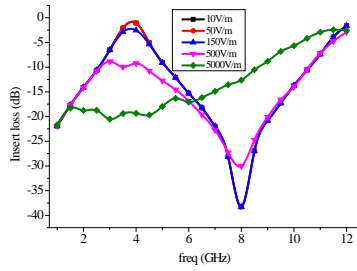


Figure 8 Transmission characteristic S21 of AFSS exposed to microwaves at different field intensities when the diodes arrangement is as fig.7

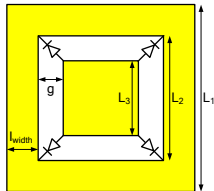


Figure 9 Sketch of the fourth AFSS

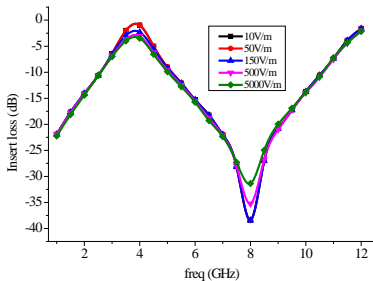


Figure 10 Transmission characteristic S21 of AFSS exposed to microwaves at different field intensities when the diodes arrangement is as fig.9

Sketch of the third kind arrangement of unilateral diodes is as fig.9, the cathode of the all diodes is located in the metallic square. The transmission characteristics of the AFSS at different incident electric field intensities are shown in Fig.10. It can be found that the transmission characteristic has not changed a lot when the field intensity is high enough. The arrangement of diodes as shown in Fig.9 can not be used in HPM protection.

## VI Result from Experiment

To verify the simulated result, samples of AFSS were developed in the dimensions of 220 \* 220 mm, housing 17 \* 17 periodic units each of which is loaded with 4 bilateral Schottky diodes, and the medium use on AFSS samples is Rogers4350B whose dielectric constant is 3.66. It is understood from the result from AFSS transmission characteristic that a pass-band exists on the AFSS at 3.5 GHz in the case of small electric field intensity, which is essentially consistent with the simulated result.

To compute AFSS's transmission coefficient, the signal strength received by the receiver antenna were measured at the opening before and after the prototype was covered on the opening. Figure 14 shows AFSS transmission coefficients at different exposure intensities at 4 different frequencies near the resonant frequency. It is found that the farther the EMW frequency is from the resonant frequency, the larger the insertion loss is in the case of

small field intensity; with increasing incident field intensity, the insertion loss increases, up to 23 dB, also coincident with the simulated result.

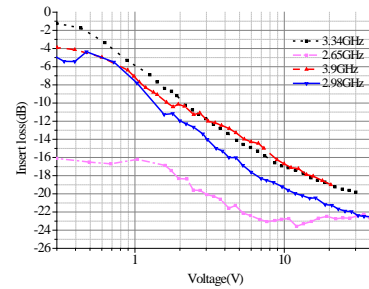


Figure 11 AFSS transmission coefficients at different exposure intensities at 4 different frequencies near the resonant frequency

## V Conclusion

This paper comes up with the method to design a novel AFSS which applies the microwave electromagnetic field, instead of the conventional DC biasing circuit, to load an induced voltage across the diodes as the biasing signal to control diode's impedance. The results from both the experiment and the simulation demonstrated that, at the incident field intensity less than 70 V/m, a pass-band exists on the AFSS at 3.5GHz and with increasing incident field intensity, the pass-band finally turns a stop-band because of increasing insertion loss therein. The new AFSS can be used in application of HPM protection.

## Reference

- [1] B.A MUNK, Kouyoumjian R.G., and PETERS, L.JR., "Reflection properties of periodic surfaces of loaded dipoles," *IEEE Trans Antennas Propagat.*, Vol. 19, pp. 612-617. 1971
- [2] R. A. Hill and B. A. Munk, "The effect of perturbing a frequency selective surface and its relation to the design of a dual-band surface," *IEEE Trans Antennas Propagat.*, Vol. 44, pp. 368-374, Mar. 1996.
- [3] L. Zhang; Q. Wu; T. A. Denidni, "Electronically Radiation Pattern Steerable Antennas Using Active Frequency Selective Surfaces," *IEEE Trans Antennas Propagat.*, Vol. 61, pp. 6000-6007, Dec. 2013
- [4] E. A. Parker, S. B. Savia, "Active frequency selective surfaces with ferroelectric substrates," *IEE Proc., Microw., Antennas Propag.*, Vol. 148, pp. 103-108, 2001
- [5] B. S. Izquierdo, E. A. Parker, J. C. Batchelor, "Switchable Frequency Selective Slot Arrays" *IEEE Trans Antennas Propagat.*, Vol. 59, pp. 2728 - 2731, July 2011
- [6] DENG Feng, ZHENG Shengquan, WANG Dongdong. Design of an active frequency selective surface without biasing grids[J]. *Chinese Journal of Ship Research*, Vol.10, pp.89-92, Feb 2015
- [7] ZHENG Shengquan, DENG Feng, WANG Dongdong, et al. Overview of the HPM field-circuit integrated protection methods for electronic equipment and system RF-channels [J]. *Chinese Journal of Ship Research*, Vol.10, pp. 7-14, Feb 2015

# Reflection and transmission of microwaves by a modern glass window

*P. Ragulis, Ž. Kancleris, R. Simniškis and M. Dagys*

*Microwave Laboratory of Physical Technology Department  
Centre for Physical Sciences and Technology  
Vilnius, Lithuania  
paulius.ragulis@ftmc.lt*

## Abstract

The reflection and transmission of a microwave by samples of the regular glass and multiple pane modern windows are investigated in a frequency range of 2.6-12.5 GHz. The influence of a surface conductivity of a metal layer on the reflection and transmission coefficients is considered for a single sheet of metalized glass. The shift and elimination of Fabry-Perot resonances are analyzed as a function of metal layer conductivity. Properties of a thin metal layer are accounted for when modeling the transmission and reflections coefficients of the windows under test. The experimental measurements of a shielding effectiveness of the modern multiple pane windows are performed.

**Keywords:** microwave transmission and reflection measurements; window panes; coated window glass.

## 1 Introduction

State of the art multiple pane windows uses high-performance heat reflected glass. This glass is usually flat sheet of soda-lime-silicate glass covered with a thin layer of electrically conductive film. This thin and transparent to a visible light coating effectively reflects far infrared radiation. In this way it protects a house from overheating by the solar radiation during summer and from cooling during winter [1]. The metallic layer appearing on a window glass should influence the transmission of microwave radiation through it, but we did not find detailed investigation of such phenomenon in a scientific literature. It is worth mentioning that the investigations presented here were motivated by the not planned measurement of attenuation during 2013 RAID trials at Horten, Norway. During them microwave attenuation of a newly installed double pane window in the building under test was measured. It was found that behind the window the microwave pulse at 5.7 GHz was attenuated by 23 dB.

Here we present a theoretical consideration of the influence of a thin metal coating of the glass on the transmission and reflection of microwaves. The transmission and reflection coefficients in a frequency range 2.6-12.5 GHz have been measured on a regular glass and glass coated with a thin metal

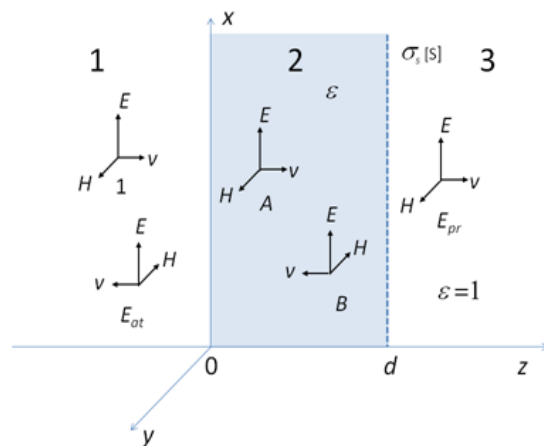


**Figure 1. Electromagnetic waves interacting with a dielectric plate. On the back surface of the plate a thin metal coating, characterized by the plate conductivity  $\sigma_s$ , is deposited.**

layer samples. Double and triple pane window samples were also investigated.

## 2 Calculation of reflection and transmission

To calculate the reflection and transmission coefficients we consider a plane electromagnetic wave impinging perpendicularly to the dielectric plate as it is shown in Figure 1. The plate is infinite in  $x$  and  $y$  directions. The width of the plate is  $d$  and relative dielectric constant is  $\epsilon$ . The back surface of the plate is coated with a thin metallic layer. A surface conductivity of this layer is denoted as  $\sigma_s$  and measured in units of [S]. As follows from the figure, there are falling and reflected waves before the plate. Two waves moving left and right appear inside the dielectric plate as well. Finally, behind the plate the only wave moving right remains. The interference of the waves moving left and right in the dielectric initiates so-called Fabry-Perot resonances or bleaching when the width of the plate becomes an integer number of half wavelengths in it.

The preceding theoretical consideration of the metalized layer deposited on the dielectric plate [2, 3] is based on the transmission line theory. The layer was treated as a finite length section of transmission line appearing as a shunt resistance. On the one hand, the conductivity of the line should

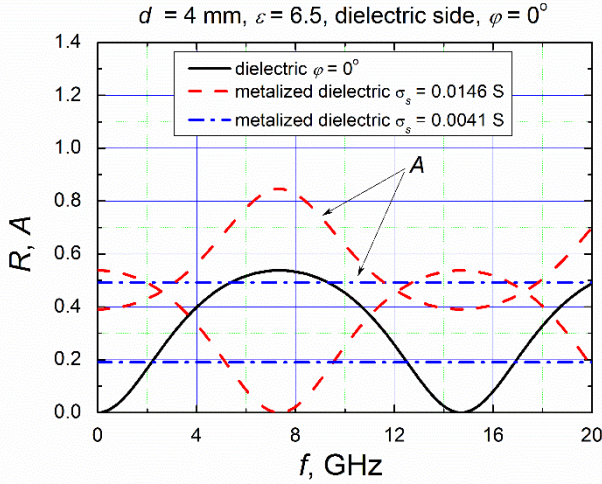


**Figure 2. The dependence of the reflectance and absorption on frequency for a metalized dielectric when a plane wave falls on the dielectric side. The letter A denotes the absorption coefficient.**

be high enough to govern the propagation of the electromagnetic wave in it. On the other hand, a skin depth of the layer should be much larger than its thickness. Only under these two conditions, one can represent the metalized layer as a shunt sheet resistance. The approach used in the present paper is free from assumptions mentioned above. The conductive layer on the back surface of the dielectric is very thin; its thickness is many times less than the wavelength of the electromagnetic oscillation. So we treated it as a boundary condition at the interface leading to the break of the tangential component of the magnetic field proportional to the surface current. This is the standard method accounting for the boundary conditions in classical electrodynamics [4]. Satisfying this and other boundary conditions on the both interfaces, one can get expressions describing the reflection and transmission coefficients of the dielectric coated with a thin metal layer. The expression of the reflection coefficient can be written down in the following way:

$$E^{(r)} = -\frac{\sigma_s \eta_0 \cos(kd) + i \left( \sqrt{\varepsilon} - \frac{1}{\sqrt{\varepsilon}} \pm \frac{\sigma_s \eta_0}{\sqrt{\varepsilon}} \right) \sin(kd)}{(2 + \sigma_s \eta_0) \cos(kd) + i \left( \sqrt{\varepsilon} + \frac{1}{\sqrt{\varepsilon}} + \frac{\sigma_s \eta_0}{\sqrt{\varepsilon}} \right) \sin(kd)}. \quad (1)$$

The transmission coefficient is expressed accordingly:

$$E^{(t)} = \frac{2}{(2 + \sigma_s \eta_0) \cos(kd) + i \left( \sqrt{\varepsilon} + \frac{1}{\sqrt{\varepsilon}} + \frac{\sigma_s \eta_0}{\sqrt{\varepsilon}} \right) \sin(kd)}. \quad (2)$$

Here  $\eta_0$  is a wave impedance of free space,  $k = 2\pi\sqrt{\varepsilon}/\lambda$ , where  $\lambda$  is a wavelength of microwaves in free space. The upper and lower signs in (1) correspond to the wave impinging on the metalized and dielectric side respectively. To get the expressions of the reflectance and transmittance, those are usually measured experimentally, the reflection and transmission coefficients should be multiplied by their conjugates.

On the one hand, from (1) it is seen that the reflection of the incident wave from the dielectric side can be equaled to zero

by choosing the appropriate value of the surface conductivity. Indeed assuming

$$\sigma_s = (\varepsilon - 1)/\eta_0, \quad (3)$$

one can get that the reflection disappears at the certain frequency. On the other hand, choosing the surface conductivity

$$\sigma_s = \sqrt{\varepsilon - 1}/\eta_0, \quad (4)$$

one can get that the Fabry-Perrot oscillations are absent in reflected from the dielectric side and transmitted waves.

The example of calculated dependences of the reflectance by the metalized dielectric when a plane wave falls on the dielectric side is shown in Figure 2. For the sake of comparison the reflectance from the uncoated dielectric is also shown in the figure by a solid line. It is seen that by choosing the value of the sheet conductivity in accordance with (3) the minimum of reflection appears at the frequency where the maximum of it is seen for the uncoated dielectric. The reason is that the wave reflected from the metallic surface gets the additional phase shift. Therefore in the metalized dielectric the reflection minimum appears at such conditions where the reflection maximum is found in a dielectric plate. When the sheet conductivity is set in accordance with (4), it is seen that Fabry-Perrot resonances disappear and the reflection coefficient is independent of frequency.

When considering a window consisting of a few glasses it is impossible to get a simple expression describing transmission or reflection from it. In this case, we used matrix method the details of which are published elsewhere [5].

### 3 Measurement setup and results

Measurements of reflected and transmitted waves by the metalized glass and multiple window panes have been performed in a frequency range 2.6-12.5 GHz in a semi-anechoic chamber. Horn antennas were used for the illumination of the sample and for the measurement of transmitted and reflected waves. Dimensions of the investigated samples were 20×30 cm<sup>2</sup>. A regular and metalized glass samples, as well as a few samples of double and triple pane windows from the Saint-Gobain company were tested. The sample under test is surrounded by absorber sheets preventing the diffracted wave directly get to the receiving antenna. As a microwave source Agilent PSG analog signal generator E8257D was used. Transmitted and reflected power was measured by Rohde & Schwarz average power sensors. In the case of multiple pane windows, measured transmittance is expressed as a shielding effectiveness

$$S = 10 \log \frac{P_t}{P_f}, \quad (5)$$

where  $P_t$  and  $P_f$  is the power transmitted through the window and falling on it, respectively.

Typical measurement results for a single sheet of metalized glass are shown in Figure 3. The dependences of the reflectance and transmittance are shown when the wave falls from the dielectric and metal sides. It is seen that the transmittance is independent of the side, from which the wave

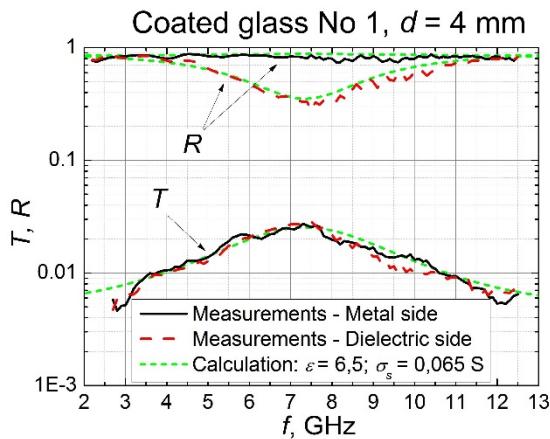


**Figure 3.** The dependence of the reflectance and transmission on frequency for a metalized glass. The solid lines show measurement results when wave falls on the metalized side, the dashed lines corresponds to the dielectric side and short dash lines demonstrate calculations results.

impinges on the metalized glass, whereas the reflectance differs significantly depending on the side, from which the metalized glass is illuminated. The short dash lines demonstrate calculation results using expressions (1) and (2). Relative dielectric constant  $\epsilon = 6.5$  was used in the calculations. The magnitude of the surface conductivity  $\sigma_s = 0.065$  S was chosen to get the best fit between the measured and calculated results. The value was close enough to that obtained from the measurement of the surface conductivity using four probe method ( $\sigma_s = 0.075$  S). It is worth mentioning that the surface conductivity of the metalized glass is roughly five times larger than required for the total cancelation of the reflection (ref. to Figure 2). The large difference between reflections from different sides of the metalized glass should be compensated by the absorption in the metal layer since the transmittance is independent of direction.

The typical measurement results of a shielding effectiveness of a double pane window from the Saint-Gobain company is shown in Figure 4. From the insert, it is seen that the investigated window consists of two 4 mm thickness glasses, the inner surface of one glass is covered with a thin metallic layer. The gap between glasses is 16 mm. It is seen that shielding effectiveness of the investigated window at some frequencies is more than -40 dB. There are two transmission maximums at frequencies around 2 and 9 GHz. Our investigations on other double pane windows have revealed that the position of the second maximum in a frequency scale depends on the gap between the glasses. It practically does not depend on the thickness of the metalized window. It is seen that calculated dependence of  $S$  on frequency using matrix method fits well measurement results. On the one hand, the investigated window exhibits a low transmittance at GSM frequencies (0.9 and 1.8 GHz) and at Wi-Fi frequency (2.4 GHz). These peculiarities of the state-of-the-art window panels should be taken into account when installing them in a public area. On the other hand, an installation of a new window should

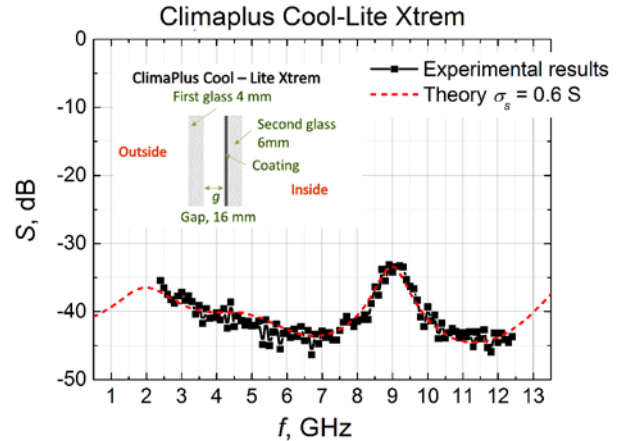


**Figure 4.** The dependence of the shielding effectiveness on frequency for a double pane window from the Saint Gobain company. The points show measurement results, the dashed line demonstrates calculation results using matrix method. The dimensions of the window are shown in the insert.

be a good opportunity to increase the protection of buildings against microwave threats.

Concluding it is worth mentioning that by choosing a surface conductivity of the metallization layer deposited on a dielectric the Fabry-Perot resonance might be shifted in a frequency scale or even suppressed. The measured shielding effectiveness of a few double and triple pane windows has revealed that the modern double pane windows, one glass of which is covered with a thin metal layer, demonstrate shielding effectiveness of microwaves in the range 25-45 dB, depending on a metallization surface conductivity. Triple pane windows with two outer glasses metalized demonstrate even larger attenuation at a lower surface conductivity of the metallization layers.

## Acknowledgement

This research was funded by EU project No 284802 "Protection of Critical Infrastructures against High Power Microwave Threats" (HIPOW).

## References

- [1] "Saint-Gobain home page: <http://uk.saint-gobain-glass.com/>."
- [2] P. Hui, E. Lim and H. Tan, IEEE Transactions on Microwave Theory and Techniques **48** (4), 615-618 (2000).
- [3] A. Thoman, A. Kern, H. Helm and M. Walther, Physical Review B **77** (19), 195405 (2008).
- [4] S. J. Orfanidis, *Electromagnetic waves and antennas*. (Rutgers University New Brunswick, NJ, 2002).
- [5] P. Ragulis, Ž. Kancleris and R. Simniškis (in press).

# Coupling Effects According to the Orientations of Multi-layered PCB and Aperture inside a Metallic Enclosure

Jin-Kyoungh Du\*, Yuna Kim\*, Jongwon Lee , Jin Soo Choi , and Jong-Gwan Yook\*

\*Dept. of Electrical and Electronic Engineering, Yonsei University, Seoul, Republic of Korea

†Agency of Defense Development, Daejeon, Republic of Korea

## Abstract

**In this paper, radiated coupling effects to a multi-layered PCB from incident electromagnetic fields are discussed investigated according to the orientations of the PCB and an aperture of a metallic enclosure. To reduce the radiated coupling effects, orientations of the multi-layered PCB and aperture can be adjusted effectively when the polarization characteristics of incident electromagnetic fields are predictable.**

**Keywords:** Aperture, metallic enclosure, multi-layered PCB, orientation, radiated coupling.

## 1 Introduction

For high-performance applications, multi-layered printed circuit boards (PCBs) are generally used, which have several signal layers as well as reference planes inside. Via-holes are also required for the multi-layered PCB to design signal traces running different layers, and PCB resonances between reference planes are coupled through these via-holes affecting signal traces at last [1-3]. The PCB resonance is usually excited from via-holes, but it can be also generated from incident electromagnetic fields [4-6]. Especially, the intentional electromagnetic interference (IEMI) might be dangerous because its power is extremely high.

To protect multi-layered PCBs against IEMI, they can be shielded by a metallic enclosure, but a perfect shielding is almost impossible because apertures should exist at the enclosure for providing power to the PCB or connecting data cables. The incident electromagnetic fields penetrate through the aperture and cause radiated coupling effects to multi-layered PCBs inside the metallic enclosure. To reduce radiated coupling effects, the orientations of multi-layered PCB and aperture can be adjusted because the incident angle and the polarization characteristic of incident electromagnetic fields occurs different PCB resonances [7-8]. In this paper, coupling effects to a multi-layered PCB from incident electromagnetic fields are investigated according to the orientations of the PCB and an aperture of a metallic enclosure.

## 2 Configurations

A six-layered PCB is designed which has a signal trace running the top and bottom layers of the PCB, as well as including a via-hole. The multi-layered PCB is placed inside a metallic enclosure which has an aperture. If the aperture has a shape of rectangular slot then penetrated fields will be affected accordance with the polarization characteristics of incident electromagnetic fields. Besides, coupling effects of the penetrated fields to the multi-layered PCB will be also influenced from the relationship between orientations of the PCB and the aperture.

## 3 Analysis Methodology

The coupling effects from incident electromagnetic fields to a multi-layered PCB inside a metallic enclosure including an aperture are simulated using the method of moments (MoM). The induced voltages at a target signal trace is calculated when the intensity of incident electric fields around the metallic enclosure is assumed to be 1 V/m. Each end of the target trace is terminated with 50 Ohm load.

## 4 Discussions

If the polarization characteristics of incident electromagnetic fields are predictable then apertures of the metallic enclosure should be designed to block the polarized fields effectively. As well, the orientation of multi-layered PCBs inside the metallic enclosure should be adjusted considering the polarization characteristics of the incident fields.

## Acknowledgements

This work was supported by Agency for Defense Development, Daejeon, Republic of Korea.

## References

- [1] J. Park, H. Kim, Y. Jeong, J. Kim, J. S. Pak, D. G. Kam, simultaneous switching noise coupling through signal *IEEE Transactions on Advanced Packaging*, vol. 29, no. 3, pp. 548-559, Aug. 2006.
- [2] J. H. Kwon, D. U. Sim, S. I. Kwak, and J.-G. Yook, electromagnetic bandgap array structure on power distribution network for suppressing simultaneous switching noise and minimizing effects on high-speed

- IEEE Transactions on Electromagnetic Compatibility*, vol. 52, no. 2, pp. 365–372, May 2010.
- [3] H.-D. Kang, H. Kim, S.-G. Kim, and J.-localized enhanced power plane topology for wideband  
*IEEE Transactions on Electromagnetic Compatibility*, vol. 52, no. 2, pp. 373–380, May 2010.
- [ power/ground plane edge radiation excited by high-frequency  
*Proceedings of International Symposium on Electromagnetic Compatibility*, vol. 1, pp. 197–202, Aug. 2004.
- [ coupling, isolation, and EM radiation in high-speed package  
*Proceedings of IEEE International Symposium on Circuits Systems*, vol. 6, pp. 5766–5769, May 2005.
- [ measurement of radiated field emission from a power/ground plane cavity edge excited by a through-hole signal via based on a balanced TLM and via coupling  
*IEEE Transactions on Advanced Packaging*, vol. 30, no. 1, pp. 73–85, Feb. 2007.
- [7] J.-K. Du, S.-Y. Hyun, J.-G. Yook, J. Lee, and J. S. Choi,  
“  
*Proceedings of American Electromagnetics*, vol. 1, p. 1 (ID 150), Jul. 2014.
- [8] J.-K. Du, *Analysis of Coupling Effects from IEMI to Multilayered PCBs in Metallic Enclosures*, Ph.D. thesis, Dept. of Electrical and Electronic Engineering, Yonsei University, Seoul, Republic of Korea, 2015.

# Assessment of HEMP-survivability of Photovoltaic Generators

Markus Nyffeler\*, Armin W. Kaelin †

\*armasuisse Science + Technology, Switzerland, [markus.nyffeler@armasuisse.ch](mailto:markus.nyffeler@armasuisse.ch),

†EMProtec GmbH, Switzerland, [armin.kaelin@emprotec.ch](mailto:armin.kaelin@emprotec.ch)

## Abstract

Renewable electricity generation by means of solar Photovoltaic (PV) modules become more and more cost effective in the recent years. As decentralized power plants PV-generators also have a potential to be used as emergency backup power sources when operated in off-grid mode.

Especially if used as backup power one would wish that PV-generators could survive also a HEMP-attack (High Altitude ElectroMagnetic Pulse). Since shielding of PV-modules seems not to be an attractive solution the question is, if HEMP-protection of a solar power plant is an option at all. This paper assesses the HEMP-coupling to typical PV-generators and the system survivability in the case of HEMP.

It is found that HEMP-protected solar power plants are feasible provided that some HEMP-protection measures are taken.

**Keywords:** PV-generator, HEMP-protection, off-grid backup power.

## 1 Introduction

The number of solar power plants increased quite rapidly in the recent years thanks to continuously improved cost efficiency of PV-modules. Two basic kinds of PV-generators exist: grid-connected and off-grid. Especially off-grid versions have a potential as backup-power together with battery-storage. Recently there have been proposals to EMP-protect roof-top solar power systems [1]. It was proposed to use wire mesh to cover solar modules in order to prevent HEMP-coupling to the modules. Unfortunately such a mesh is not only costly to install, it takes also about 10% or more of the power of the modules by the effect of shading the cells. Shielding of PV-modules is therefore definitely not a favourable option. However, by looking at the principle of solar modules we see that they basically consist of a series of extended flat diodes, which are sensitive to sunlight. How do diodes perform under surge current conditions?

It is well known that special Zener diodes called TVS (Transient Voltage Suppressors) are capable to clamp surge currents very fast to the Zener voltage. It is to be expected, that regular diodes or PV-cell diodes also clamp surges to their forward voltage in forward direction. However, the question remains, what happens to the diodes in reverse direction when they are operated in the avalanche region,

where their behaviour is not well defined? In most PV-modules bypass-diodes are used to prevent a reverse current to flow through the PV-cells in the case of partial shading. These bypass-diodes are electrically anti-parallel to the diodes of the PV-cell itself, therefore the cell-diodes and the bypass-diodes could protect each other against conducted surges. This means, that PV-modules could be HEMP-protected without shielding. HEMP-protection of the PV-generator could be simply achieved by protecting the attached cabling and the solar inverter or battery charging unit.

In this paper we look at the HEMP-coupling paths and possible damaging mechanisms as well as at possible protection concepts. In a further study the behaviour of PV-modules under threat-level HEMP-conditions will be measured.

## 2 Diode structure of PV-module

PV-modules, both monocrystalline and polycrystalline types, are typically made of 60 or 72 solar cells. Each solar-cell is electrically a light sensitive diode with a relatively large area of typically  $156 \times 156 \text{ mm}^2$ . Electrically these diodes are switched in series to receive a higher voltage at the output as shown in Figure 1. The junction box contains 3 bypass-diodes and the connection contacts to the next modules.

**Figure 1: Schematic diagram of a 60-cell PV-module with 3 bypass-diodes in the junction box**

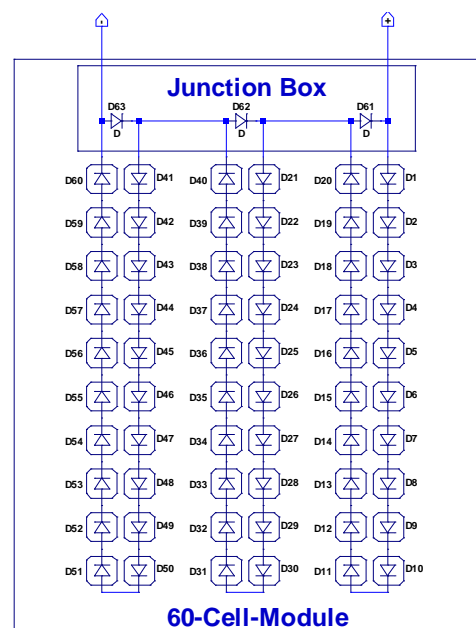
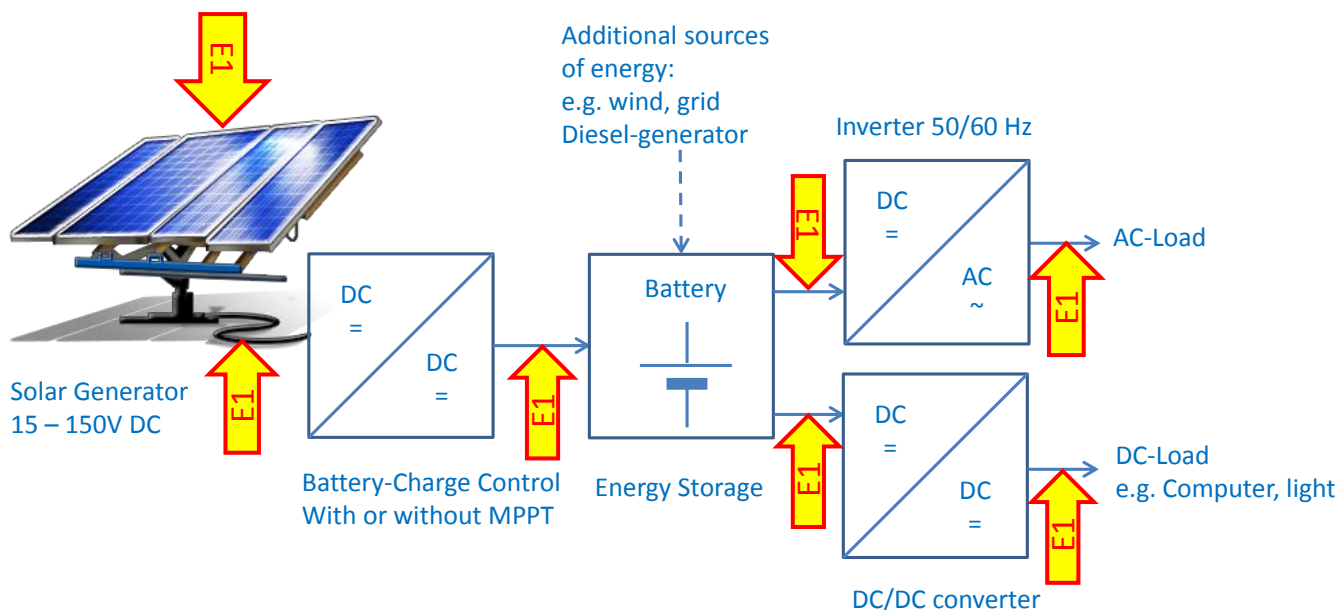


**Figure 2: Block diagram of an off-grid PV-generator with battery and DC/AC and DC/DC inverters. The arrows show possible HEMP-energy coupling paths. As all wiring is relatively short (<100m) only short-time EMP (E1) is relevant.**



The bypass-diodes are anti-parallel to the cell diodes and prevent a reverse current flow through the cells, in the case one or several cells are in shadow and do not generate solar current. In this case the current is bypassed through the corresponding bypass-diode. Fortunately these bypass-diodes have their benefit also in the case of transient surge currents induced in the module by external EM-fields such as nearby-lightning or HEMP. Depending on the surge polarity, the surge current always flows in forward direction of either the PV-cell diodes or the bypass-diode. Therefore it is to be expected, that the diodes are not stressed with reverse surge currents. This fact will be investigated in realistic threat-level HEMP-tests.

### 3 HEMP-Coupling Paths

In a first step we are interested to know, how HEMP-energy can couple to a PV-generator. We look at an off-grid PV-generator because this is most interesting as a HEMP-protected backup-power source. Of course grid-connected PV-generators can also be HEMP-protected. However in the case of HEMP it is to be expected, that the power grid collapses at least temporarily. In this case the grid-connected inverter would switch off also regardless of the HEMP-protection of the PV-generator and make this powerless.

Figure 2 shows a block diagram of a typical off-grid PV-generator. The arrows show the main HEMP-coupling paths. Coupling occurs directly to the modules, to the cables between modules and battery charging unit, cables to and from the battery and into the load cabling.

Since there is no connection to the power-grid, all cables are relatively short (<100m). Therefore only short-time or E1 [2] EMP currents are coupled to the system. Although E1 currents are very fast in risetime, their energy content is

relatively low. Nevertheless these fast transients must be kept off the electronics to prevent upset or damages.

Based on previous assumptions it is expected, that the PV-generator itself will survive HEMP-fields easily, provided that the conducted HEMP-currents coupled from the cable side are not higher than the surge capability of the PV-cells and bypass-diodes.

### 4 HEMP-Protection Concept

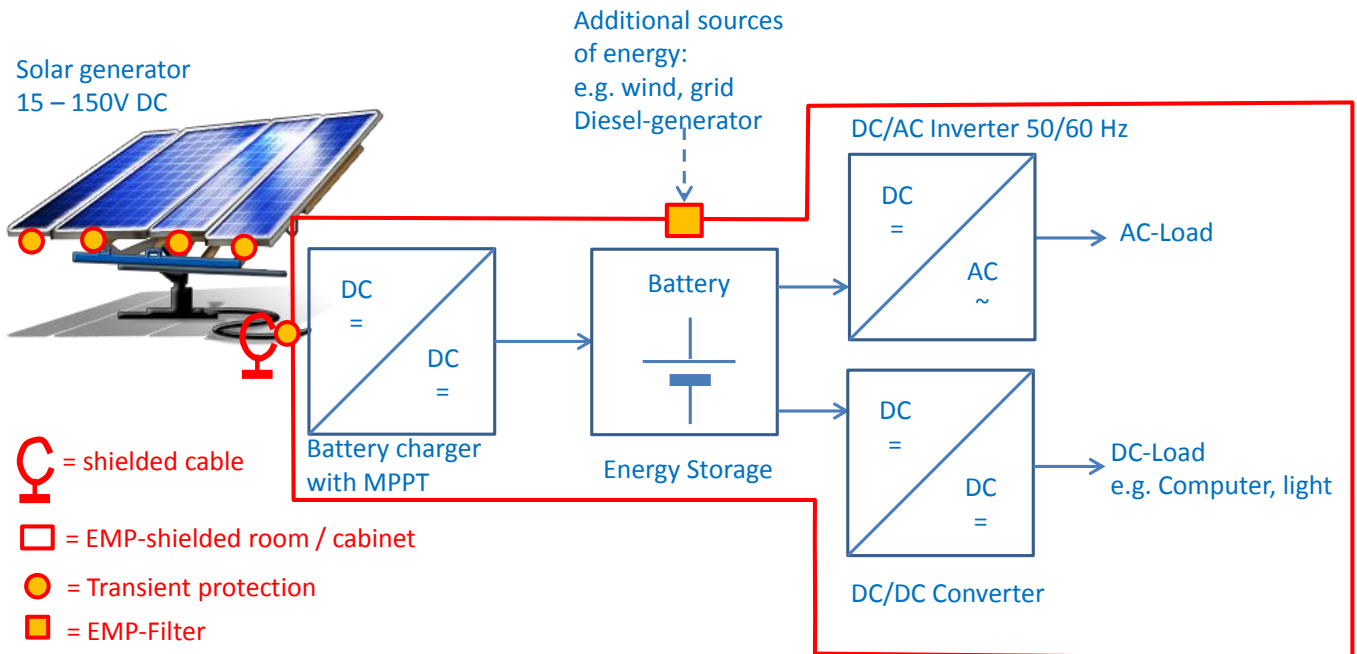
In a next step HEMP-coupling shall be minimized by shielding. This does not necessarily mean that a fully HEMP-protected room is required under all circumstances. Most cables can be shielded quite easily. Many electronics, such as DC/DC-converters or inverters, are housed in a metal box to prevent unwanted emissions. This metal box is also a good shield, provided that the entering cables are also shielded. Possible protection measures using a shielded room or a shielded cabinet are shown in Figure 3.

The PV-generator itself shall not be shielded to prevent loss of solar conversion efficiency. But due to the robustness of diodes the generator itself is capable to withstand direct HEMP-coupling fields easily as will be shown in threat-level tests. In order to give highest possible reliability, it is proposed to add some transient protection to the junction box of each module.

Alternatively to shielding the cables all electronics including the energy storage unit can be placed in a shielded room or in a shielded cabinet, such as an EMC cabinet. All penetrating wires are equipped with HEMP-filters. If the load is not placed in the shielded room, then the load cables are also to be protected by HEMP-filters.

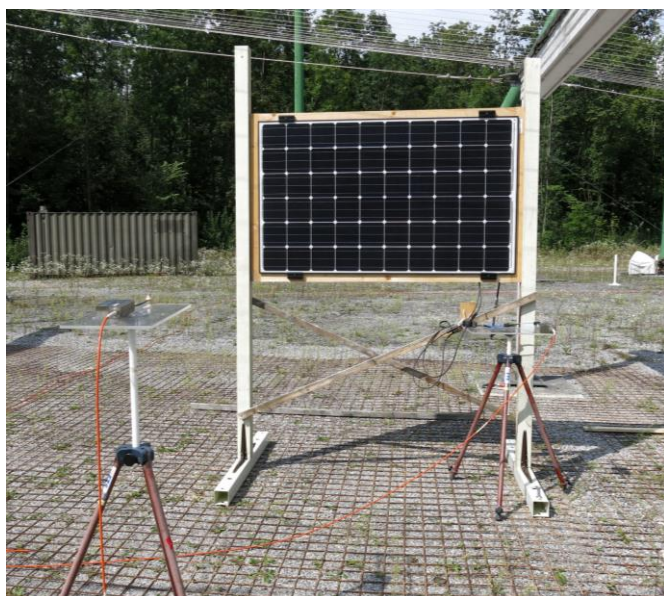
Which method is easier depends on the overall size and complexity of the PV-generator.

**Figure 3: HEMP-Protection measures for HEMP-protection of an off-grid PV-generator system**



In order to verify that unshielded PV-modules can survive HEMP-threats without damage, full threat-level HEMP-tests (see Figure 4) are conducted. It was found, that PV-modules easily survive HEMP-fields up to three times the expected threat-level [2] and that therefore no shielding of the modules is required. Together with transient protection measures in each junction box even very large generator arrays can be safely EMP-protected. Detailed results of these HEMP-tests are presented in a separate paper in this conference.

**Figure 4: PV-module test in HEMP-simulator VEPES. The modules are tested in six different directions.**



## 5 Conclusions

It has been shown that HEMP-protected Photovoltaic power plants are feasible. Due to the fact that PV-modules consist of a series of flat diodes combined with anti-parallel bypass-diodes, induced surge or HEMP-currents flow only in forward direction of the diodes. Therefore no damages to the cells occur even without shielding of the modules. Since no shield is required, the full solar conversion efficiency can be achieved. Detailed threat-level test results will be presented in another paper during this conference.

To protect also extended PV-generators the modules have to be equipped with transient protection, which can be installed in the junction box. Of course the subsequent electronics such as the inverter have to be protected adequately by known protection measures.

## References

- [1] Donald R. J. White. "EMP-Protect Family, Homes & Community", 5-Vol. EMP Encyclopedia Series, *Vol.1, Ed.2*, CreateSpace Independent Publishing Platform, 2013, ISBN-13: 978-1482349207,
- [2] MIL-STD-461F. "Requirements for the control of electromagnetic interference characteristics of subsystems and equipment", *Department of Defense Interface Standard*, 10 December 2007.

# Threat-level HEMP-tests of Photovoltaic Panels and Components

Markus Nyffeler\*, Armin W. Kaelin<sup>†</sup>, Alex Hauser<sup>§</sup>

\*armasuisse Science + Technology, Switzerland, [markus.nyffeler@armasuisse.ch](mailto:markus.nyffeler@armasuisse.ch),

<sup>†</sup>EMProtec GmbH, Switzerland, [armin.kaelin@emprotec.ch](mailto:armin.kaelin@emprotec.ch)

<sup>§</sup>Meyer Burger AG, Switzerland, [alex-hauser@web.de](mailto:alex-hauser@web.de)

## Abstract

Due to their working principle to collect solar light arrays of Photovoltaic (PV) modules cover a relatively large area of tens or even hundreds of meters square. This extension makes PV modules quite exposed to possible HEMP-radiation (High Altitude ElectroMagnetic Pulse) coupling. Shielding is not a favourable protection option as this would considerably lower the efficiency. However, since PV-modules consist of many diodes with large surface, similar as protection diodes, it is expected that PV-components have a quite good immunity against HEMP-disturbances. In this work we experimentally investigate the robustness of various Photovoltaic components against radiated and conducted HEMP-disturbances.

**Keywords:** Photovoltaic cell, bypass diode, HEMP-protection

## 1 Introduction

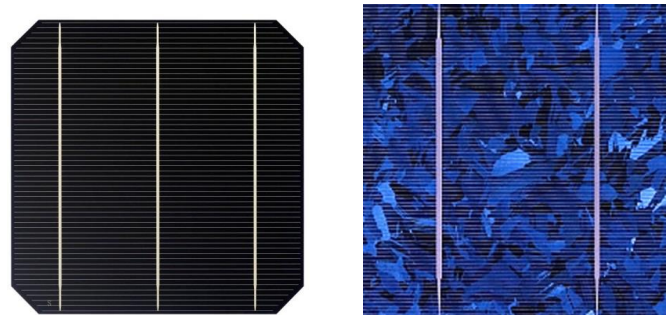
Photovoltaic (PV) modules became very popular during the past years, as they have a great potential for generating renewable electric energy by simply collecting sunlight. PV generators typically consist of ten to hundreds of PV modules, which are electrically wired to form one or several strings. These strings are attached to an inverter, which converts the DC into AC and feeds the power into the grid. Alternatively DC-power is stored in batteries by a battery charge control unit, preferably with MPPT (maximum power point tracking). So far the industry provides a lot of products for lightning protection of PV systems. Mostly these protection measures aim at the protection of the inverter or to prevent a fire in the building in the case of a direct lightning stroke. There is little known about the survivability of the generator modules in the case of lightning strike. Usually the protection strategy is to prevent a direct lightning strike into the modules [1]. There is only a very limited amount of literature available about the effects of nearby lightning currents to PV modules [2]. However, this is a good starting point for the assessment of HEMP-effects to PV-modules. We start with tests on cell level and continue then on module level.

## 2 Cell Level Tests

Since there is no literature available on the behaviour of photovoltaic cells under external electromagnetic stress (both

conducted and radiated), we started our investigations on cell level. Monocrystalline (mc) (Figure 1, left picture) and polycrystalline (pc) (Figure 1 right picture) solar cells were investigated. Different cell concepts use different technologies for contacting the cells. Usually the backside is fully metallized and the front side has typically 3 bus bars with small wires. One concept uses interdigitated back-contact fingers, so there is no shadow on the front side. A special cell concept is the HJT-cell (Hetero Junction Technology), which uses thin amorphous layers in addition to the monocrystalline structure.

**Figure 1: Monocrystalline (left) and polycrystalline PV-cell (right) with 3 or 2 bus bars on surface**



In a first step, we were looking for a criterion that allows noticing any changes in the PV-cell due to the EM-tests. We found that the V-I-diagram in all four quadrants is a good criterion to show any changes. In forward direction the PV-cell is conducting like a diode. In reverse direction it blocks the current like a diode up to the point, where an avalanche breakdown occurs. This breakdown voltage is relatively low; it is around -40V for monocrystalline and around -15V for polycrystalline PV-cells.

We stressed the PV-cells with the following radiated and conducted EM-disturbances: a) HEMP-fields according to RS105 with levels up to 150kV/m, b) 15kV Electrostatic discharge (ESD) directly to the cells, c) 8/20 $\mu$ s surge current up to 2kA in forward direction, d) 8/20 $\mu$ s surge current up to 2kA in reverse direction, e) HEMP-PCI-current up to 5kA in forward direction and f) HEMP-PCI-current up to 2.5kA in reverse direction.

It was found, that the PV-cells are quite robust and can easily withstand a) and b) without any alterations. Also c), which is relatively powerful and rich in energy, did not change the cells. Even the fast rising HEMP-current of e) did not affect the cells at all. However, tests d) and f) in reverse direction

showed changes in the VI-characteristic at surge current amplitudes around 500A. The cells were not damaged, but showed some resistive behaviour, although they continued to produce electricity in sunlight.

**Figure 2: VI-diagram of a new monocrystalline PV-cell: green is the applied voltage, magenta is the current and blue is the VI-diagram ( $V_{breakdown}$  approx. -40V)**

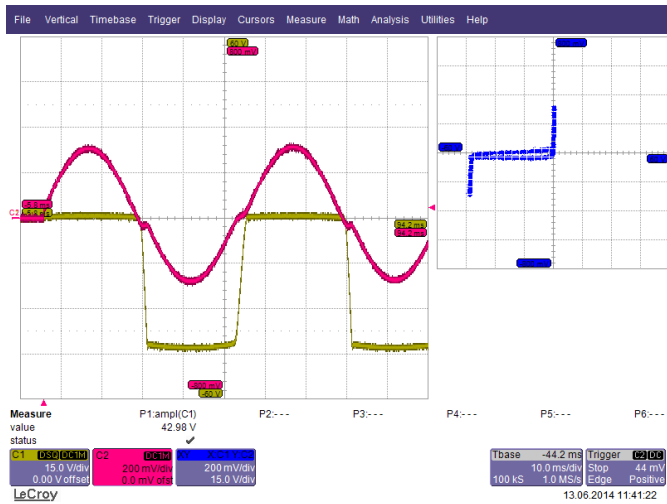
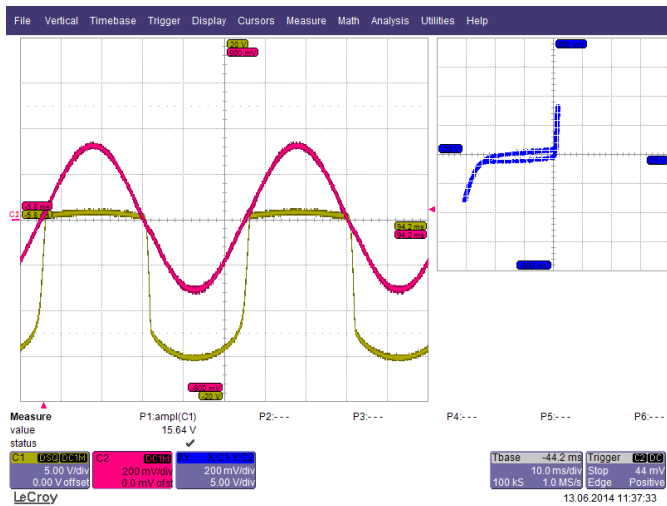


**Figure 3: VI-diagram of a new polycrystalline PV-cell: magenta is the applied voltage, green is the current and blue is the VI-diagram ( $V_{breakdown}$  approx. -15V)**



The results clearly show that PV-cells are quite robust to surges of various shapes in forward direction, while they are much more sensitive to surges in reverse direction. In normal operation in sunlight DC-cell-currents in reverse direction are highly unwanted. For this reason, solar modules are equipped with bypass-diodes, which are anti-parallel in an array of typically 20 cells in order to prevent reverse currents due to local shadow on a module. This bypass-diode helps to protect the PV-cells also against unwanted reverse surge currents.

Therefore we investigated also bypass-diodes and found that they are robust in forward direction, but not at all in reverse direction. However, the combination of PV-cells and anti-

parallel bypass-diodes protects the combination well against surges of both polarities.

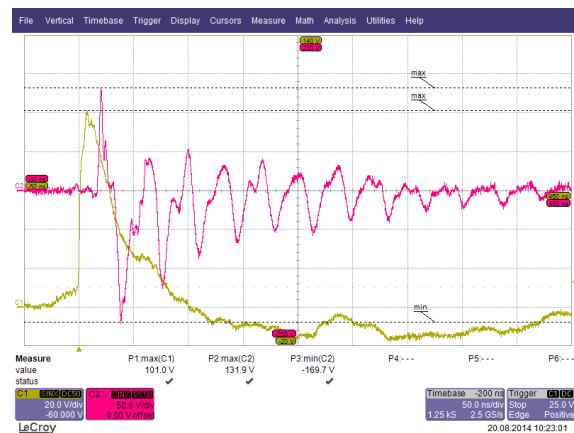
### 3 Module Level Tests

In a next step we conducted threat-level tests of PV-modules. A typical 60 cell module consists of 3 times 20 cells arranged in 3 arrays. Each string has an anti-parallel bypass diode located in the junction box to prevent reverse operating currents in the case of partial shading of a module. In order to assess the HEMP-induced currents a wire-model of a module in a wooden frame was built first (Figure 4). It was noticed, that the metallic frame that often surrounds PV-modules reduces HEMP-coupling somewhat, so we made the investigations under worst-case conditions and no metal-frame.

**Figure 4: Wire model of a PV-module with 3x20 arrays and junction box for studying and measuring the HEMP-coupled currents**



**Figure 5: HEMP-field (green, 20kV/m per div.) and HEMP-induced current in wire model (magenta, 50A/div.)**



We measured HEMP-induced currents in different orientations and found the amplitudes to be always  $<200\text{A}$  at incident field levels of  $100\text{kV/m}$  (twice the threat-level). A typical HEMP-induced current is shown in Figure 5 together with the recorded incident HEMP-field of the EMP-simulator VEPES.

In a next step complete PV-modules (Figure 6) were tested in HEMP-simulator VEPES. Again modules consisting of polycrystalline and monocrystalline cells were tested. In various orientations HEMP-fields according to RS105 of MIL-STD 461F [3] have been applied. The field strength was originally  $50\text{kV/m}$  and we increased the field levels to  $100\text{kV/m}$  and to  $150\text{kV/m}$ , which corresponds to 2 times and 3 times the HEMP-threat-level.

**Figure 6: PV-module in HEMP-simulator VEPES**



The modules were oriented in totally six directions: x, y and z plus the negative directions of these axes. The negative direction was chosen to test also with negative field levels, since the impulse of HEMP-simulator VEPES is positive only and the PV-cells are polarized by the cell-diodes.

First the tests with standard HEMP-level of  $50\text{kV/m}$  were performed. In each configuration at least 3 impulses were fired. The load of the solar cells was either open, short-circuited or an resistive load formed by 3 pieces  $30\text{W}$  each Halogen lamps.

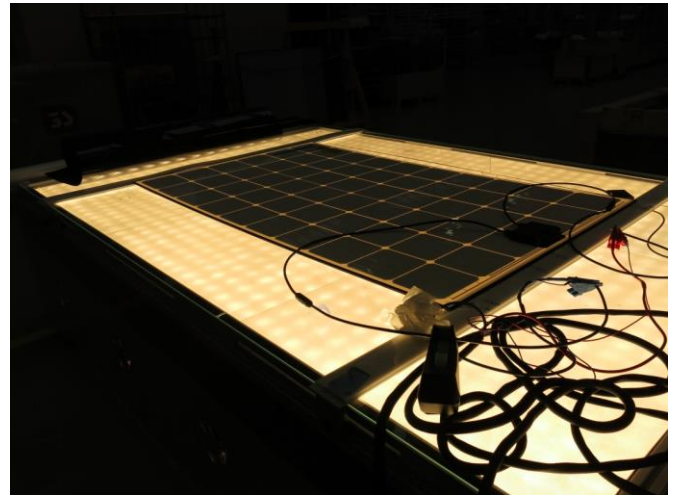
After the test series the modules were taken to the “Flasher”, a special illumination machine, which permits to characterize the solar power generation characteristic very precisely (Figure 7). Since the “Flasher” measurements clearly showed, that all cells and strings work properly, we repeated the HEMP-tests on the next level of  $100\text{kV/m}$ , again in all directions as before.

After the test series with double threat-level the modules were taken again to the “Flasher” and checked again for any changes in their behaviour. Absolutely no change was observed.

Finally the same modules were tested again in the HEMP-simulator, which was now operated at  $150\text{kV/m}$ . Again all directions were tested with at least 3 impulses per orientation.

After the test series on triple threat-level the modules were analysed again in the “Flasher”, which clearly showed, that all cells worked still properly and delivered the full power as they did before the HEMP-test series began.

**Figure 7: The power characterization of a PV-Module in the “Flasher” easily discovers any changes in efficiency**



### 3 Conclusions

It has been shown that PV-cells and bypass-diodes are very robust against surge currents in forward direction. They are much less robust in reverse direction. However, in a typical arrangement there are always PV-cells and bypass-diodes, which are electrically anti-parallel. This not only prevents reverse currents in the case of partial shadows on a module, but this also prevents unwanted surge currents to flow in the reverse direction. Therefore PV-modules easily survived HEMP-fields of up to 3 times the standard HEMP-threat level without shielding. HEMP-protected PV-generators become now feasible without any loss in power due to shielding.

In order to protect also extended arrays of PV-generators, it is recommended to protect the long lines according to known HEMP-protection methods. Of course also the inverter is to be protected accordingly.

### References

- [1] Nikolaos Kokkinos, Nicholas Christofides, Charalambos Charalambous. “Lightning Protection Practice for Large-Extended Photovoltaic Installations”, *ICLP 2012, Vienna, 2012 International Conference on Lightning Protection (ICLP)*, Vienna, Austria
- [2] Heinrich Haerberlin. “Damages at Bypass Diodes by Induced Voltages and Currents in PV Modules Caused by Nearby Lightning Currents in PV Modules”, *22nd European Photovoltaic Solar Energy Conference*, Milano, Italy, Sept. 2007.
- [3] MIL-STD-461F. “Requirements for the control of electromagnetic interference characteristics of subsystems and equipment”, *Department of Defense Interface Standard*, 10 December 2007.

# Experiment research on response of typical SPD to different EMP

Zhou Ying-hui \*, Du Mingxin †, Shi Lihua †, Zeng Jie \*

\*State Key Laboratory of Mechanics and Control of Mechanical Structures, NUAA, Nanjing 210007, China, †National Key Laboratory on Electromagnetic Environmental Effects and Electro-optical Engineering, Nanjing Jiangsu 210007, China

## Abstract

In this paper, the study of protection effectiveness of typical surge protective devices (SPD) to electromagnetic pulse is developed, an SPD test fixture is designed and the test setup is built based on a pulse generator. Different kinds of pulses have been injected to some typical SPDs respectively, test results show that the protection effectiveness is correlated with rise time of injected pulse. According to the test result, relationship of SPD's response character with injected pulse rise time can be fitted. Then, some benefit reference is given to choose protective device against EMP disturbance.

**Keywords:** Surge protective device (SPD); Electromagnetic Pulse (EMP); protected effect; rise time; experiment research.

## 1 Introduction

SPD includes of some kinds of device which protect the equipment by limiting the transient over voltage or surge current. They are always used for lightning protection in transmission line or conducted circuit, protective characteristics of these devices to EMP are still not sure. In order to discuss the protection effectiveness of typical SPD to injected EMP voltage, and the test setup is built according the renewed criterion -- IEC 61000-4-24. Effects of variable EMP voltage with different rise time and half width are tested and described in the following experiment research.

## 2 SPD test setup

A universal test fixture is designed to fix all kinds of two- and four-terminal SPDs in accordance with [1] (see Fig. 1). Insert attenuation of this fixture is measured by an Agilent-4396B analyzer, the result is about 9dB in range of 100k~1GHz and the transfer character is smooth in this frequency range.

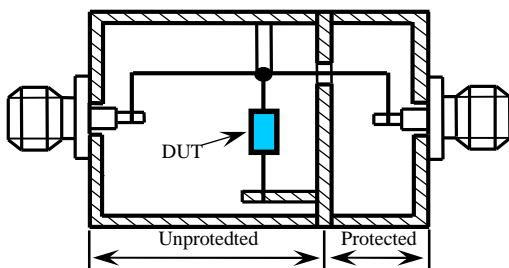


Figure 1. SPD test fixture

The test setup consists of pulse generators, launching lines, test fixture and oscilloscope. The two lightning surge generators can output three kinds of voltages waveform, the rise time/half width are (3/25) ns, (10/100) ns and (10/700)  $\mu$ s, respectively.

## 3 EMP Response of typical SPD

By the test setup mentioned above, several kinds of typical SPDs are tested to obtain their response characteristics. Wide pulse (10/700 $\mu$ s) and narrow pulse (3/25ns or 10/100ns) are injected to each kind of device under tested (DUT). Representative test results are shown in the follow.

### 3.1 Coaxial gas charge tube

According to IEC 61000-4-24, a kind of CMTZ-50 model coaxial gas tube is tested by the setup, the protection effectiveness to wide and narrow injected pulses is analyzed. Test results show that these devices start to response when the injected voltage enhanced to certain amplitude, and the response effect varied with scale-up injected pulse.

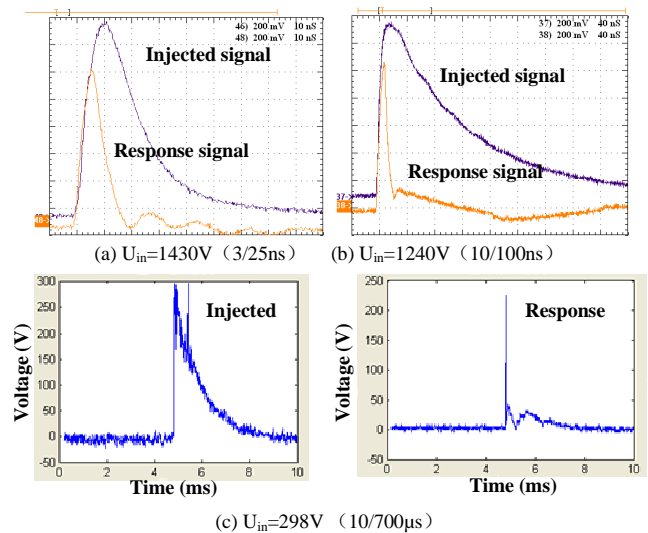


Figure 2. Response of coaxial gas charge tube to different injected pulse

Fig.2 shows response of the coaxial gas charge tubes to different injected pulse. It can be found that response voltage of this SPD is closely related to the rise time of injected pulse. The shorter rise time leads to the higher response voltage amplitude. In order to investigate the device response action to the rise time of injected pulse, the pulse generator impedances and inductances were adjusted to get output

signal with different rise time. The rise time of generator output is turned up from 3ns to about 30ns, and the response voltage is decrease from 1kV to 361V with the decline of injected pulse rise time. For sake of estimating the relationship of device response voltage level, the 1<sup>st</sup> order exponential fitting model is adopted here and the expression is shown as (1).

$$U=1127.6e^{-0.1915t_r} + 415 \quad (3\text{ns} \leq t_r \leq 30\text{ns}) \quad (1)$$

Here U is the device response voltage;  $t_r$  is the injected pulse rise time. Then, the coaxial gas tube response character can be estimated by (1) under different injected pulse, and the applicability to protected equipment can be estimated by this expression.

## 2.2 Metal oxide varistor (MOV)

MOV is tested by the setup and method mentioned above, test result indicated that MOV can clamp injected wide pulse obviously. But it cannot clamp the narrow injected pulse instead of decrease its peak value. Under wide pulse injected pulse, the highest clamp voltage value of MOV is about 1.6~1.8 times higher than its nominal value. While to narrow injected pulse, the constrained voltage value is about 1.4~2 times higher than its nominal value. The rise time of narrow pulse injected is about (3~10ns), which means it has abundant high frequency components. Then, MOV appear lower impedance under higher frequency pulse, the energy of injected pulse is absorbed and constrained by this way.

## 2.3 Transient voltage suppress (TVS) tube

Similar test has been done to TVS tube, and test results show its restrain ability to both wide and narrow injected pulse. The action character is comparable with MOV. The highest clamp voltage to wide injected pulse is about 1.2~1.6 times higher than its nominal value, and the constrained voltage is about 3~4 times higher than its nominal value.

## 3 Conclusions

In this paper, experimental research has been developed to several types of SPDs under injected pulse with different rise time. Test results indicate the common SPDs applied in lightning surge protection also have constrained ability to EMP in a certain extent. Because of the different rise time and half width between lightning and EMP waveform, the response characters have great distance with their nominal values. Although many SPD's components nominal values is in nano second, the test results show they barely response to injected pulse of 10ns (3ns) rise time waveform.

According to the tested protective character, the relationship of SPD's response voltage with injected pulse rise time can be fitted by mathematic functions. This research provides some benefit reference to choose of protective component against EMP disturbance.

## Acknowledgements

This work was supported by NSFC under Grant No. 51407198 and 51477183.

## References

- [1] Jinliang He; Zhiyong Yuan; Shunchao Wang, et. al., "Effective Protection Distances of Low-Voltage SPD With Different Voltage Protection Levels". IEEE Trans. on Power Delivery. 2010. vol.25 (1), 187-195.
- [2] Long duration impulse withstand capability of SPD. Zhang Nanfa; Kang Guoyao; Guo Yaping. Asia-Pacific Symposium on EMC. 2010. 1510 – 1513.
- [3] Analysis of additional tests for SPD's failure mode in IEC61643.11. Yang Guohua; Wang Chongling; Dai Dezhi; Wan Kaili. International Conference on Lightning Protection. 2014. 1083 - 1086
- [4] Overcurrent protection function for SPD disconnectors. Sato, A.; Morii, N.; Sato, H. The 7th Asia-Pacific International Conference on Lightning. 2011. 586 – 589.
- [5] IEC 61000-4-24: 2013, Testing and measurement techniques - Test methods for protective devices for HEMP conducted disturbance[S].

# Frequency Domain Analysis of Penetrated Ultra Wideband Signal in Large Scale Structure

Jongwon Lee, Seungho Han, and Jin Soo Choi

The 4th institute, Agency for Defense Development, Daejeon, Republic of Korea, [jwlee@add.re.kr](mailto:jwlee@add.re.kr)

## Abstract

In the effect of electromagnetic pulses, it is important to accurately analyse the electric fields in ultra wideband pulses. Electromagnetic coupling of the fields are analysed by observing the penetration effect. We experimentally measured the penetrated fields in a large scale structure in frequency domain. The measured data shows that the penetration ratio is significantly changed according to the material of wall and the frequency of fields.

**Keywords:** Electromagnetic pulse, Ultra wideband.

## 1 Introduction

It is critical to efficiently and accurately analyse the pattern of electric fields in ultra wideband (UWB) pulses to expect the effect of high power electromagnetics. However, in contrary to measurements of small electronic devices, the penetration experiment for a very large scale structure is influenced by environment variables. Therefore, due to the uncontrollable parameters and insufficient experimental data, it has been difficult to precisely expect the effect of penetrations and reflections of fields in large scale experiments. Recently, by using the state-of-art numerical electromagnetic techniques, we then easily validate the measured penetration data of large scale structure.

In this work, we first explain the design of experiments. A target large structure and the configuration of field measurement are introduced. We then analyse the measured data in frequency domain. The penetration characteristics at different frequency would be explained in detail.

## 2 Design

We first generate electromagnetic pulses outside the target building structure. The electric fields are then measured inside the structure. To verify the penetration effect of electric fields, we design the entire experiment as shown in Fig.1. It illustrates the floor plan of experimental configuration in the target structure. Since the signal source is sufficiently far from the structure, we assume the incident signal as a plane wave. To capture the penetrated electric fields, we install derivative (D-dot) sensors inside the building. The sensors are located in front room, corridor, and rear room in sequence. The radiated plane wave firstly passes through the glass window from outside to the front room. The wave then passes

through wooden door from the front room to the corridor. Finally, the wave reaches the rear room through concrete wall.

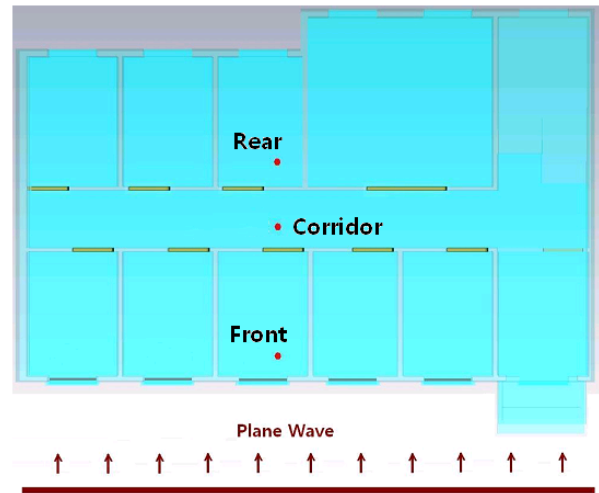


**Figure 1. Floor plan of experimental configuration**

In the propagation of fields, the attenuation factor  $\alpha$  is written as follows [1].

$$\alpha = \omega \sqrt{\left(\frac{\mu \varepsilon'}{2}\right)} \left[ \sqrt{1 + \left(\frac{\varepsilon''}{\varepsilon'}\right)^2} - 1 \right] \quad (1)$$

where  $\omega$ ,  $\mu$ , and  $\varepsilon$  denote angular frequency, permeability, and permittivity, respectively. Therefore, the attenuation factor depends on the dielectric losses and the conduction losses.

When the frequency of the wave is same as the resonance frequency of target object, the penetration rate of wave would be significantly reduced. Here the wave in the resonance frequency is contained inside the object. In other words, the wave cannot escape the object due to the very high reflection rate. Generally, the resonance frequency is influenced by electromagnetic characteristics of object. The characteristics such a permeability, and permittivity are determined from the type of material and the shape of object. However, in the real sturcutre, it is very expensive to accurately define the exact value of material characteristics  $\varepsilon'$  and  $\varepsilon''$  of objects such as glass, door, and wall. Therefore, we generally deteremine the physical parameters by using experimentally known values.

### 3 Measurement

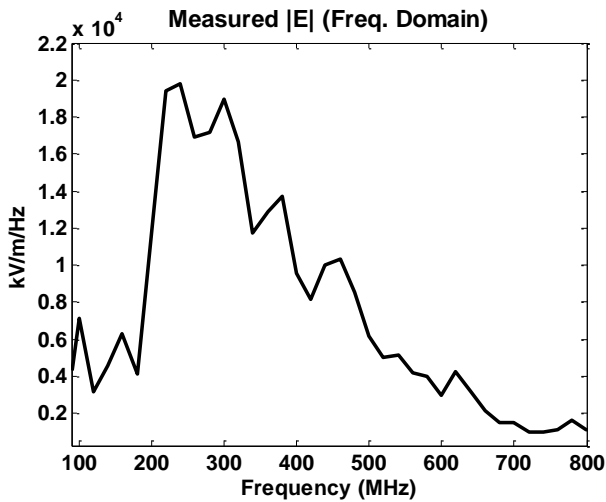


Figure 2. Radiated electric fields in frequency domain

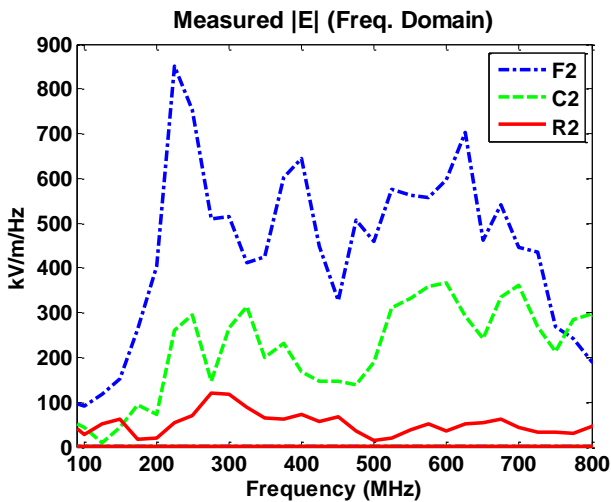


Figure 3. Penetrated electric fields in frequency domain

Table 1: Ratio of penetrated electric fields (%)

	Frequency (MHz)					
	200	300	400	500	600	700
<b>F2/ORI</b>	3.43	2.72	6.77	7.43	19.97	29.24
<b>C2/ORI</b>	0.61	1.41	1.76	3.07	12.24	23.63
<b>R2/ORI</b>	0.18	0.61	0.76	0.26	1.23	2.87

Fig.2 shows the electric fields in frequency domain captured in front of the signal source. In Fig.3, it shows the electric fields in frequency domain measured from the sensors in the large building structure [2]. F2, C2, and R2 represents the front room, corridor, and rear room, respectively. Since the distance between sensors is sufficiently small compared to the distance between the sensor and the signal source, we neglect the effect by the distance between sensors.

Firstly, we see the strength of electric fields. As shown in Fig.2, the range of center frequency bandwidth is from

200MHz to 600MHz. The corresponding wavelength is between 1.5m and 0.5m. It is also seen that the strength of fields in 200~400MHz is higher than that in 400~600MHz in the original signal. In Fig.2, the peak value of original signal is 22MV/m/Hz which appears at 250MHz. In Fig.3, this field strength is reduced by 25 times in the front room. The strength is 0.85MV/m/Hz. In the rear room, the peak strength of electric field decreases to around 0.1MV/m/Hz at 280MHz. Secondly, we observe which frequency bandwidth of signal remains or disappears after the field penetration. Table 1 lists the ratio of penetrated electric fields. The ratio is computed by dividing the electric field measured at sensors by the field at original source. F2, C2, and R2 are the front room, corridor, and rear room, respectively. In the front room, the fields of low frequency range are highly disappeared. Table 1 indicates that, in the front room, the electric field of 700MHz is penetrated higher than that of 200MHz by 8.5 times. Similar results are shown in the results of corridor. However, in the rear room, the penetration ratio of 500MHz is lower than the ratios of 300~400MHz.

As a result, from outside to the front room, the fields of 200~400MHz are mainly filtered out by the glass window. From the front room to the corridor, the effect of wooden door is similar to that of glass window. Fields of high frequency are penetrated more. From the corridor to the rear room, the fields around 500MHz are strongly blocked by the concrete wall. It is clearly seen that the fields of 400MHz and 600MHz penetrate the structure more than the field of 500MHz.

Measuring discrepancies possibly occur due to compositions inside wall and arbitrary wave reflections. For example, if metal meshes are installed inside the concrete wall, the glass window and wooden door behave like aperture. Then the dimension and shape of the aperture can be critical factors to determine the penetration ratio. If we ignore these outside effects, fields of 200~400MHz may be easily filtered out by glass and wood while the concrete wall intensely blocks the field around 500MHz.

### 4 Conclusions

The field penetration for large structure is experimentally analysed in frequency domain. Different penetration ratios are observed as the material and frequency bandwidth change.

### References

- [1] S.Ramo, J.R.Whinnery, T.V. Duzer, "Fields and Waves in Communication Electronics," 3<sup>rd</sup> Edition, Wiley, 1994
- [2] J. Lee, J.Choi, J.Ryu, and J. Lee, "A Computer Simulation for Penetration Effects of a Ultra Wide Band (UWB) Signal Source in a Large Structure," *Symposium on the Korea Institute of Military Science and Technology*, pp1-4, Jeju, Korea, June 2011

# FDTD simulation of lightning-induced currents on a buried cable with a shield wire

Hiroki Tanaka\*, Yoshihiro Baba\*, Celio Fonseca Barbosa†

\*Doshisha University, Kyoto-610-0321, Japan, ef8.circl@gmail.com, ybaba@mail.doshisha.ac.jp

†Centro de Pesquisa e Desenvolvimento em Telecomunicacoes (CPqD), Campinas, SP 13083060, Brazil, gcelio@cpqd.com.br

## Abstract

In this paper, currents on a 1-km long buried cable with a shield wire, induced by a lightning strike about 25 m away from the middle of the buried cable, are computed using the finite-difference time-domain (FDTD) method for solving discretized Maxwell's equations. FDTD-computed waveforms of lightning-induced currents on the buried cable and the shield wire agree reasonably well with the corresponding measured ones. The effect of shield wire is also studied.

**Keywords:** Finite-difference time-domain method, lightning, buried cable, shield wire.

## 1 Introduction

Evaluation of lightning-induced currents on cables in air and/or buried in a soil is of importance for their insulation design against overvoltages and for the protection of connected equipment. For this aim, computer simulations have been done [1-2].

In this paper, we apply the three-dimensional (3D) finite-difference time-domain (FDTD) method [3] for solving discretized Maxwell's equations to analyzing currents on a buried cable and its shield wire, induced by a nearby lightning strike, and compare the FDTD-computed waveforms with the corresponding measured ones.

## 2 Method

Figure 1 shows a cable with a shield wire buried in a homogeneous soil, to be analyzed using the 3D FDTD method. The working volume of 1010 m × 150 m × 150 m is divided nonuniformly, and surrounded by six planes of Liao's second-order absorbing boundary condition [4] to minimize unwanted reflections there. Cell sizes are not constant: 3 mm × 3 mm in the radial direction in the vicinity of the cables and 7 mm in the longitudinal direction in the vicinity of each junction between the cable and the shield wire, and they increase gradually. The thickness of the soil of resistivity 1850 Ωm and relative permittivity 10 (distance between the ground surface and the bottom absorbing boundary) is set to 110 m, while the height of the working volume is 150 m. The time increment is set to 7.03 ps. The length of the buried cable is 1 km, and that of its parallel shield wire is also 1 km. The former is buried at depth 0.6 m, and the latter is buried at

0.3 m. A vertical lightning return-stroke channel, represented by the transmission-line (TL) model [5], is located about 25 m from the middle of the buried cable. The return-stroke wavefront speed is set to 130 m/μs. The equivalent radius of the shield wire is 0.69 mm ( $\approx 0.23\Delta s = 0.23 \times 3$  mm, where  $\Delta s$  is the radial-direction cell dimension) [6]. This configuration represents part of experiments with rocket-triggered lightning carried out in Brazil [7]-[8].

Figure 2 shows the cross-section of the cable, which is represented by a single conductor covered by an insulating layer. The conductor is represented by a perfect conductor with cross-section of 18 mm × 18 mm (=6 cells × 6 cells), and

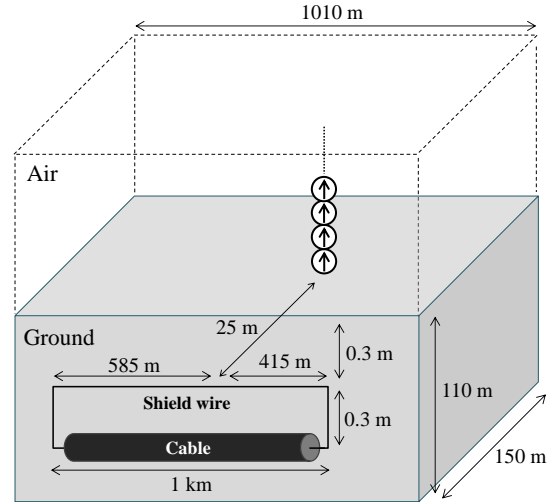


Figure 1. The cable, shield wire, and the vertical lightning channel used in the FDTD simulation.

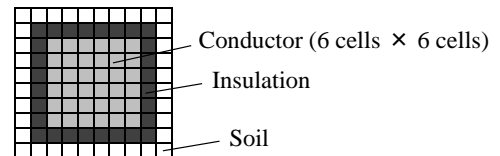


Figure 2. Cross-sectional view of the buried cable used in the FDTD method.

thickness of its insulation coat is set to 3 mm (=one cell). Since this insulation thickness is different from that of the cable in the experiment (2 mm), the relative permittivity  $\epsilon_{r,fld}$  of the model cable insulation is adjusted as follows:  $\epsilon_{r,fld} = \epsilon_r \ln(D_{i,fld}/D_{c,fld}) / \ln(D_i/D_c) = 3.7$ , where  $\epsilon_r$  (=2.9) is the

relative permittivity of the actual cable insulation,  $D_i$  ( $=20$  mm) is the cable diameter, and  $D_c$  ( $=16$  mm) is central conductor diameter,  $D_{i,fdtd}$  ( $=4 \times 24$  mm/ $\pi = 30.56$  mm) is the equivalent diameter of the cable, and  $D_{c,fdtd}$  ( $=4 \times 18$  mm/ $\pi = 22.92$  mm) is the equivalent diameter of the central conductor.

### 3 Analysis and results

Figure 3 shows the waveform of channel-base current, which simulates the one measured at a short tower due to rocket-triggered lightning and is used in the FDTD simulation.

Figure 4 shows FDTD-computed waveforms of lightning-induced currents on the buried cable and the shield wire and the corresponding ones measured at 20 m from the shortest distance between the tower and the cable. The FDTD-computed waveforms agree reasonably well with the measured ones. Note that the initial gradual increase observed in the measured waveforms is probably due to the leader that are not considered in the FDTD simulation.

Figure 5 shows FDTD-computed waveforms of lightning-induced current on the buried cable with and without the shield wire. The magnitude of current on the shield-wired cable is approximately 35% lower than that of current on the non-shielded cable.

### 4 Conclusions

In this paper, we have computed currents on a 1-km long buried cable with or without a shield wire, induced by a lightning strike about 25 m away from the middle of the buried cable, using the 3D-FDTD method. FDTD-computed waveforms of lightning-induced currents on the buried cable and the shield wire agree reasonably well with the corresponding measured ones. The accuracy of the results is similar to those presented in [1] using different calculation methods. Also, we have confirmed the effect of the shield wire against external fields.

### References

[1] M. Paolone, E. Petrache, F. Rachidi, C. A. Nucci, V. A. Rakov, M. A. Uman, D. Jordan, K. Rambo, J. Jerauld, M. Nyffeler, J. Schoene. "Lightning-induced voltages on buried cables -Part II: Experiment and model validation", *IEEE Trans. EMC*, **47** (3), pp. 509-520 (2005).

[2] J. O. S. Paulino, C. F. Barbosa, W. C. Boaventura. "Lightning-induced current in a cable buried in the first layer of a two-layer ground", *IEEE Trans. EMC*, **56** (4), pp. 956-963 (2014).

[3] K. S. Yee. "Numerical solution of initial boundary value problems involving Maxwell's equations in isotropic media", *IEEE Trans. AP*, **14** (4), pp. 302-197 (1966).

[4] Z. P. Liao, H. L. Wong, B. P. Yang, Y. F. Yuan. "A transmitting boundary for transient wave analysis", *Scientia Sinica*, **A27** (10), pp. 1063-1076 (1984).

[5] M. A. Uman, D. K. McLain. "The magnetic field of the lightning return stroke". *J. Geophys. Res.*, **74**, pp. 6899-6910 (1969).

[6] T. Noda, S. Yokoyama. "Thin wire representation in finite difference time domain surge simulation", *IEEE Trans. PWRD*, **17** (3), pp. 840-847 (2002).

[7] C. F. Barbosa, F. E. Nallin, S. Person, A. Zeddani. "Current distribution in a telecommunication tower struck by rocket-triggered lightning", Int. Symp. on Lightning Protection (SIPDA), Foz do Iguassu (2007).

[8] J. O. S. Paulino, C. F. Barbosa, I. J. S. Lopes, and G. C. Miranda, "Time-domain analysis of rocket-triggered lightning-induced surges on an overhead line," *IEEE Trans. EMC*, vol. 51, no. 3, pp. 725-732, Aug. 2009.

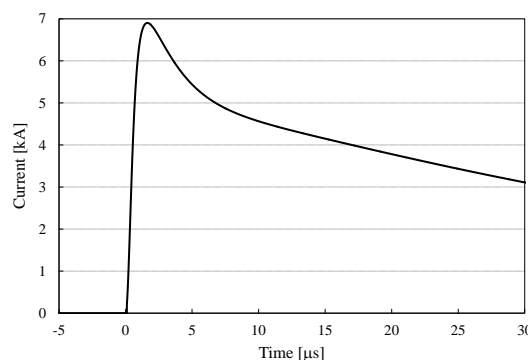


Figure 3. Waveform of lightning current, which simulates a measured waveform and is used in the FDTD simulation.

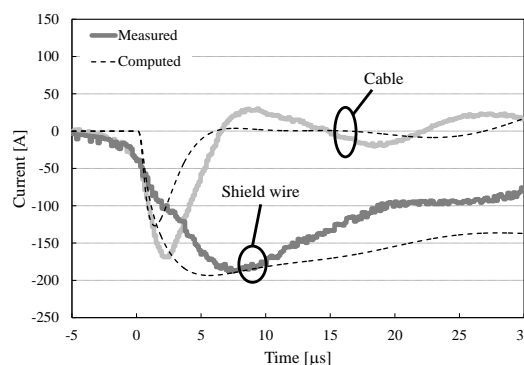


Figure 4. FDTD-computed waveforms of lightning-induced currents wire and the measured ones.

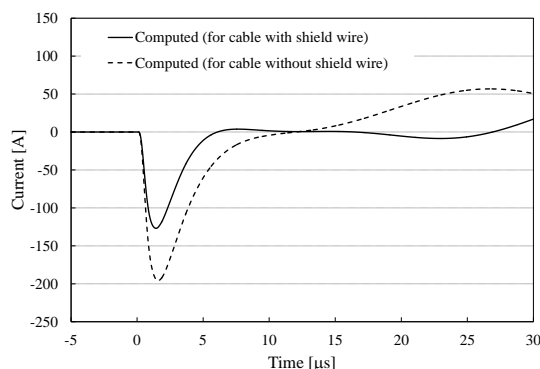


Figure 5. FDTD-computed waveforms of induced current on the buried cable with and without the shield wire.

# Lightning occurrence data observed with lightning location systems of electric power companies in Japan: 2009-2013

Takatoshi Shindo<sup>\*1</sup>, Hideki Motoyama<sup>\*1</sup>, Toru Miki<sup>\*1</sup>, Mikihisa Saito<sup>\*1</sup>, Akiyori Matsueda<sup>\*2</sup>, Noriyasu Honma<sup>\*3</sup>, Akira Matsumoto<sup>\*4</sup>, Kazuo Shinjo<sup>\*5</sup>, Kiyotaka Hayashi<sup>\*6</sup>, Hayato Awazu<sup>\*7</sup>, Katsuhisa Makabe<sup>\*8</sup>, Masato Fujikawa<sup>\*9</sup>, Satoshi Kurihara<sup>\*10</sup>, Masashi Sato<sup>\*11</sup>

<sup>\*1</sup>CRIEPI, 2-6-1, Nagasaka, Yokosuka-shi, Kanagawa-ken, Japan, shindo@criepi.denken.or.jp,

<sup>\*2</sup>Hokkaido Electric Power Company, Japan, <sup>\*3</sup>Tohoku Electric Power Company, Japan, <sup>\*4</sup>Tokyo Electric Power Company, Japan, <sup>\*5</sup>Hokuriku Electric Power Company, Japan, <sup>\*6</sup>Chubu Electric Power Company, Japan, <sup>\*7</sup>Kansai Electric Power Company, Japan, <sup>\*8</sup>Chugoku Electric Power Company, Japan, <sup>\*9</sup>Shikoku Electric Power Company, Japan, <sup>\*10</sup>Kyushu Electric Power Company, Japan, <sup>\*11</sup>J-Power, Japan

## Abstract

5 years of lightning data from 2009 to 2013 obtained with lightning location system of 9 electric power companies in Japan have been summarized and analyzed. The recent annual number of lightning flashes of which current is more than 10 kA in Japan is around one million. The variations of lightning occurrence characteristics by areas, seasons and so on are clarified.

**Keywords:** Lightning, Database, Lightning location system, Lightning current

## 1 Introduction

Cloud-to-ground lightning flash frequency is one of the important factors for rational insulation design of power transmission systems. Recently, lightning location system have been widely used and lightning data with such systems have been collected and summarized all over the world [1-9]. In Japan, nine electric power companies have their own lightning location systems and lightning data have been collected. The Central Research Institute of Electric Power Industry (CRIEPI) has carried out fundamental researches on the construction of a lightning frequency map in cooperation with electric power companies in Japan [10-12]. The lightning location systems of Japanese electric companies have been improved and most of them have introduced the LS 7000 or LS8000 version of lightning location systems at present. In this paper, based on the 5 years of lightning data from 2009 to 2013 observed with the lightning location systems, characteristics of lightning occurrence frequency and lightning currents have been summarized.

## 2 Lightning location systems of Japanese electric power companies

Fig. 1 shows the location of Direction Finders (DFs) of lightning location systems of the nine Japanese electric power companies as of 2013. In order to make a lightning frequency map in Japan, nine subdivisions were determined considering the service area of each electric power company as shown in Fig. 2. Lightning data in each subdivision were provided by the lightning location system of each electric power company located in the same subdivision and summarized in meshes of 0.25 degree (latitude) by 0.25 degree (longitude). The actual size of each mesh is not exactly same but it is about 23 km by 27 km. Lightning data are summarized as flash data and the data whose current is more than 10 kA are used in this analysis according to the previous analysis [10-12].

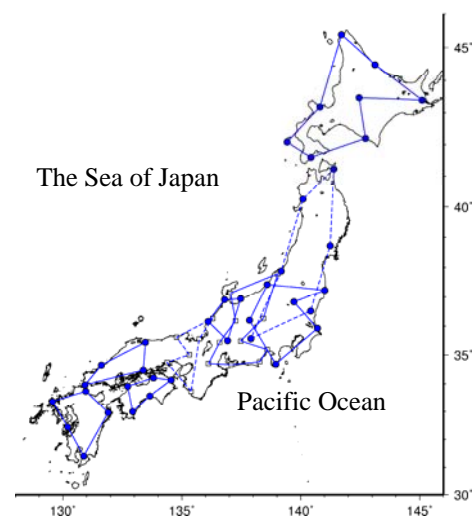


Figure 1 Locations of DFs of lightning location systems of Japanese electric power companies as of 2013.

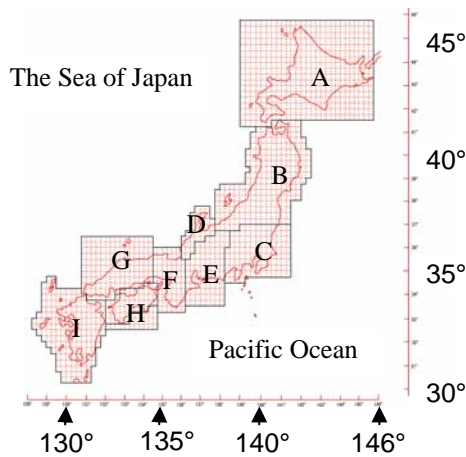


Figure 2 The subdivisions used in the analysis.

### 3 Lightning data

Basically lightning data are summarized in two seasons which are summer (from April to October) and winter (from November to March). The year shown hereafter is the fiscal year (from April to March of the next year) unless otherwise stated.

#### 3.1 Number of lightning occurrence

Fig. 3 shows the variation of annual number of lightning flashes in Japan. The variation of number of lightning flashes in winter is also shown in Fig. 4.

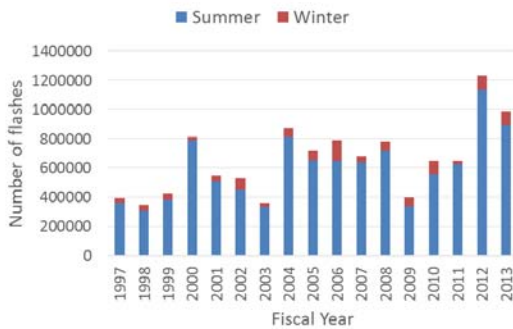


Figure 3 Annual number of lightning flashes.

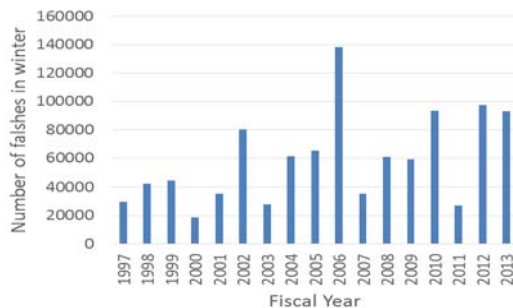


Figure 4 Number of flashes in winter season.

From Figs. 3 and 4, it seems that number of lightning occurrence is increasing. However we should note that the detection efficiency of lightning location systems may have been improved in recent systems.

#### 3.2 Lightning density map in Japan

Fig. 5 shows lightning flash density maps in summer and winter. Not only the 5-year average from 2009 to 2013 but 7-year average from 2002-2008 are shown for reference. In summer, we have lot of lightning flashes in the north part of Kanto plain (subdivision C in Fig. 2) and the central area of Japan. On the other hand, we have lightning flashes in the coastal area along the Sea of Japan in winter. The regional lightning occurrence characteristics stated above are almost same as those from 1992 to 2008, which was reported in [12].

#### 3.3 Lightning current

We summarized the 50% value and 5% value of the cumulative lightning current distribution in Table 1, assuming the log-normal distribution for lightning current. It seems that there is a tendency of decrease of current values recently.

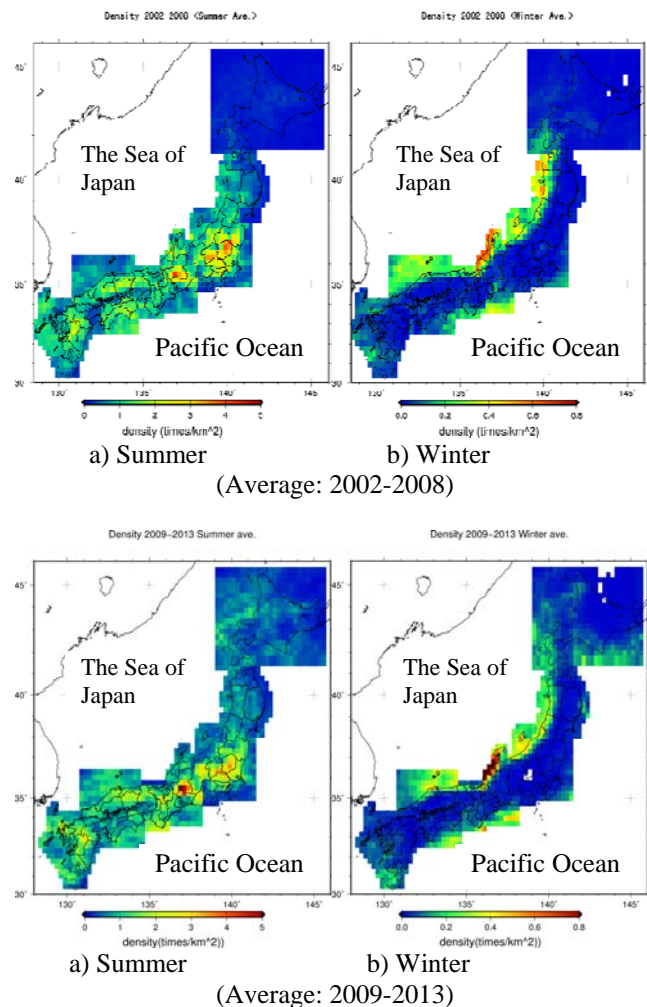


Figure 5 Lightning flash density map in summer and in winter.

Table 1: 50% Values and 5% values of the cumulative current distributions from 2002 to 2013.

FY	50% value (kA)		5% value (kA)	
	Summer	Winter	Summer	Winter
2002	22.6	27.4	58.6	88.2
2003	23.5	29.6	64.6	107.3
2004	22.8	27.1	60.2	83.3
2005	22.5	26.0	57.3	85.8
2006	23.5	24.6	62.9	71.6
2007	23.1	29.2	60.7	103.7
2008	23.9	27.2	63.5	86.9
2009	25.1	27.8	70.7	85.9
2010	22.8	24.7	59.3	76.7
2011	21.8	25.1	55.9	80.7
2012	20.6	23.1	51.8	72.8
2013	20.2	23.6	50.1	74.9

## Conclusions

Based on the lightning data obtained with the lightning location systems of the electric power companies in Japan, recent lightning occurrence characteristics are summarized.

We will analyse the lightning data in more detail and clarify lightning current characteristics and the effects of the climate on lightning characteristics.

## References

- [1] R. E. Orville, A. C. Silver, "Lightning ground flash density in the contiguous United States: 1992-1995", *Monthly Weather Review*, Vol. 125, pp. 631-638, 1991.
- [2] R. E. Orville, G. R. Huffines, "Lightning ground flash measurement over the contiguous United States: 1995-97", *Monthly Weather Review*, Vol. 127, pp. 2693 - 2702, 1999..
- [3] R. E. Orville et al., "The North American Lightning Detection Network (NALDN) -First Results: 1998-2000", *Monthly Weather Review*, Vol. 130, pp. 2098 - 2109, 2002.
- [4] W. Schulz et al., "Cloud-to ground lightning in Austria: A 10-year study using data from a lightning location system", *J. of Geophysical Research*, Vol. 110, No. D090101, 2005.
- [5] O. Pinto Jr., et al., "Cloud-to-ground lightning in southeastern Brazil in 1993 a. Geographical distribution", *J. of Geophysical Research*, Vol. 104, No. D24, pp. 31,369-31,379, 1999.
- [6] S. Hidayat, M. Ishii, "Spatial and temporal distribution of lightning activity around Java", *J. of Geophysical Research*, Vol. 103, No. D12, pp. 14,001-14,00931, 1998.
- [7] S. M. Chen, "Lightning data observed with lightning location system in Guang-Dong province, China", *IEEE Trans. on Power Delivery*, Vol. 19, No. 3, pp. 1148-1153, 2004.
- [8] S. K. Kar, Kyung-Ja Ha, "Characteristics differences of rainfall and cloud-to-ground lightning activity over South Korea during summer monsoon season", *Monthly Weather Review*, Vol. 131, pp. 2312-2323, 2003.
- [9] L. R. Soriano, F. Pablo, "Maritime cloud-to-ground lightning: The western Mediterranean sea", *J. of Geophysical Research*, Vol. 107, No. D21, ACL 15 1-15, 2002.
- [10] T. Shindo, S. Yokoyama, "Lightning occurrence data observed with lightning location systems in Japan: 1992-1995", *IEEE Trans. on Power Delivery*, Vol. 13, No. 4, pp. 1468-1474, 1998.
- [11] The Committee of Lightning Protection Design, Lightning Database Working Group, "Lightning occurrence data observed with lightning location systems of electric power utilities in Japan: 1992-2001", *IEEJ Trans. on PE*, Vol. 124, No. 10, pp. 1255 -1262, 2004.
- [12] T. Shindo, H. Motoyama, A. Sakai, N. Honma, J. Takami, M. Shimizu, K. Tamura, K. Shinjo, F. Ishikawa, Y. Ueno, M. Ikuta, D. Takahashi, "Lightning Occurrence Characteristics in Japan for 17 Years: Observation Results with Lightning Location Systems of Electric Power Utilities from 1992 to 2008", *IEEJ Trans. on Electrical and Electronic Engineering*, Vol.7 No.3, pp.251-257, 2012.

# Influence of Grounding Device Models on Lightning Protection Characteristics of Transmission lines with Different Rated Voltages

Jinliang He, Jinpeng Wu, Bo Zhang

State Key Lab of Power Systems, Dept. of Electrical Engineering, Tsinghua University, Beijing 100084, China

## Abstract

The design of grounding devices is one of the key issues in transmission tower design. The transient grounding resistance which can accurately reflect the characteristics of grounding device under lightning current is required in the numerical calculation. The constant resistance model or some other simplified models are usually applied in the lightning protection analysis. In order to evaluate the effect of different models on the simulation results of lightning protection, the lightning withstand levels are compared when applying different grounding device models, the influence of grounding devices on the lightning protection effects in transmission lines with different voltage classes is discussed, and the significance of grounding device in different voltage class is also presented.

**Keywords:** Lightning protection, grounding device model, transmission line, lightning withstand level.

## 1 Introduction

The lightning is the main cause of failure in the transmission system. Direct striking on the shielding wires is a frequent phenomenon which leads to lightning overvoltage [1]. For evaluating the direct striking protection effect of the transmission system, researchers usually establish the transient simulation models of the transmission system including the transmission line, the insulator string, the tower and the grounding device in the time-domain. It is very essential to determine a suitable model of the grounding device for transient analysis, which the proposed paper precisely aims at.

There are two kinds of models which are commonly applied to describe the performance of the grounding device: one is the constant resistance model, which is the most usual model applied in the lightning protection analysis; the other one is the dynamic resistance model recommended by IEEE [1] and CIGRE [2]:

$$R_t = \frac{R_0}{\sqrt{1 + \frac{I}{I_g}}} \quad (1)$$

$$I_g = \frac{E_0 \rho}{2\pi R_0^2} \quad (2)$$

where:

$R_t$ : Resistance of grounding device under impulse condition,  $\Omega$ ;

$R_0$ : Resistance of grounding device under power frequency condition,  $\Omega$ ;

$I$ : Lightning current through the tower footing, kA;

$I_g$ : Critical ionization current, kA;

$E_0$ : Soil ionization gradient, kV/m;

$\rho$ : Soil resistivity,  $\Omega \cdot m$ .

As a matter of fact, these two models cannot describe the transient performance well. The actual grounding resistance is time-dependent with the lightning current injecting, which can be described as [4]:

$$R_T = \frac{V(t)}{I(t)} \quad (3)$$

So a calculation method of the transient performance of grounding device is needed. In [3], a time-domain analysis method is obtained, which considers the soil ionization, frequency dependence and mutual coupling in the quasi-static process.

The proposed paper carries out a simulation to compare the three kinds of the grounding model at the conditions of four different voltage levels.

## 2 Parameters

The transmission tower configuration in simulation is illustrated in Fig. 1. It consists of a single-circuit three-phase line and two shield wires. TABLE I. gives the tower parameters for 110-kV, 220-kV, 500-kV and 1000-kV transmission lines.

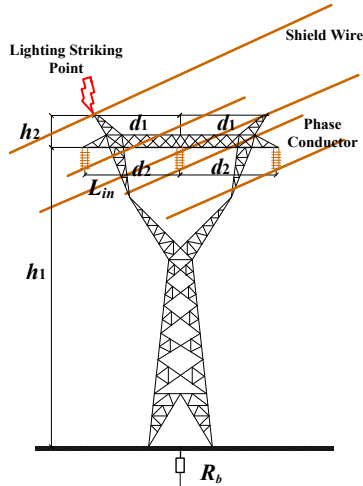


Fig. 1. The Configuration of Tower for Four Voltage Levels.

TABLE I. THE TOWER PARAMETERS FOR TRANSMISSION LINES WITH DIFFERENT RATED VOLTAGES

Rated Voltage (kV)	1000	500	220	110
$h_1$ (m)	63.0	45.0	24.14	20.0
$h_2$ (m)	5.0	5.5	3.26	3.0
$d_1$ (m)	28.8	12.0	5.5	4.9
$d_2$ (m)	26.8	13.9	7.0	6.5

The grounding device is taken as cross horizontal conductors made of steel with a diameter of 12 mm and a length of 40 m is buried in the soil with a depth of 1 m. The soil resistivity is 1000  $\Omega\text{m}$  and the critical breakdown electrical field is 300 kV/m. The power frequency resistance is 12  $\Omega$ , and the impulse resistance is 25  $\Omega$ . A lightning current with a waveform of 2.6/50  $\mu\text{s}$  is applied in the simulation.

### 3 Simulation Results

The simulation results are illustrated in Fig. 2. It is obvious that the lightning withstand level becomes high with the voltage level grows. As for the three kinds of grounding model, the dynamic model recommended by IEEE is higher than the real-time dynamic model, and the constant model is the lowest. As a matter of fact, this conclusion works in terms of various soil resistivity.

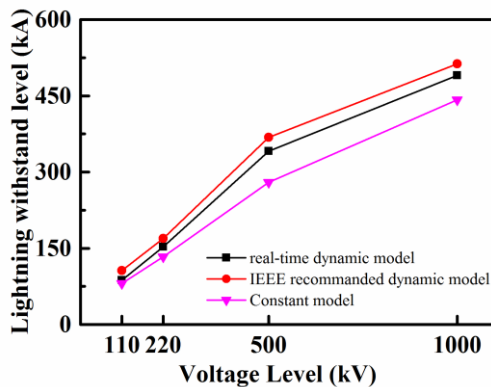


Fig. 2. The Configuration of Tower for Four Voltage Levels.

Compared with the real-time dynamic model, the IEEE recommended model considers the soil ionization effect but ignores the frequency dependence effect of the grounding device. This is the main cause of the difference between the two dynamic models.

### 4. Conclusion

The transient performance of the grounding device is a complex real-time dynamic model. However, it is usually simplified as a constant resistance. IEEE and CIGRE recommends a simple dynamic model. Compared with the two dynamic models, the recommended dynamic model results to a dangerous lightning withstand level.

### Acknowledgements

This work is supported by the National Natural Science Foundations of China under Grant No. 51277107.

### References

- [1] IEEE Std. 1243–1997, “IEEE design guide for improving the lightning performance of transmission lines”, Dec. 1997
- [2] CIGRE Working Group on Lightning, “Guide to procedures for estimating the lightning performance of transmission lines”, CIGRE Paris, France, Oct. 1991
- [3] J. P. Wu, B. Zhang, J. L. He, and R. Zeng, “A comprehensive approach for transient performance of grounding system in the time domain,” *IEEE Trans. Electromagn. Compat.*, vol. 57, no. 2, pp. 250-256, April 2015.
- [4] J. L. He, R. Zeng, and B. Zhang, “Methodology and technology for power system grounding,” Wiley & Sons, 2012.

# Correlation between air surface temperature and lightning events in Colombia during the last 15 years

F. Diaz, and F. Roman,

*Electromagnetic Compatibility Research Group (EMC-UN), Universidad Nacional de Colombia  
Ciudad Universitaria, Unidad Camilo Torres, B4 701, Bogotá, Colombia.  
feadiazor@unal.edu.co, fjromanc@unal.edu.co*

**Abstract**—A study considering both the 30 years air surface temperature data measured by 9 meteorological stations and the 15 years lightning events data recorded by the Tropical Rainfall Measuring Mission, suggest a positive correlation between the increase in air surface temperature and the Colombian lightning activity. This result is important to take preventive actions mainly because in the Colombias northern part is located a region with one of the world largest lightning activity and a large number of lightning victims.

**Index Terms**—Lightning, temperature effects, warming temperature trends

## I. INTRODUCTION

THE Tropical Rainfall Measuring Mission (TRMM), a joint collaborative study between the National Aeronautics and Space Administration (NASA) and the Japan Aerospace Agency (JAXA), shows that lightning is more likely to occur over land than over oceans [1]. Air over land heats faster than over oceans because land is not able to store as much energy as oceans do. Therefore, for this denser air, it is easier to rise up in the atmosphere very fast and to carry water droplets above the freezing levels, creating the necessary conditions for lightning [2]. The hydrological cycle is mainly driven by the heat available in a region [3]. Therefore, and if the right conditions are given, it is reasonable to affirm that a warmer climate will create the necessary conditions for an accelerated hydrological cycle which could increase the lightning activity. However, it is important to notice that some studies have shown that an increase in temperature seems to reduce the number of thunderstorms but could create more intense ones [4]. The reason is not simple to explain, but it includes the fact that in conjunction with other aspects like winds, topographical conditions, human intervention, etc., some regions of the world are turning drier and others wetter. In the context of weather, it is almost impossible to generalize because meteorological variables require a detail analysis which should be made in different scales such as from local to synoptic scale. All these studies evidence that Colombia is a country with a very high keraunic level. This is the reason why the present investigation's main interest is to show some

results of possible increase in both the local temperature and in the lightning activity in Colombia.

## II. RELATIONSHIP BETWEEN AIR SURFACE TEMPERATURE AND LIGHTNING

According to the Assessment Report of the Fourth and Fifth Intergovernmental Panels on Climate Change (IPCC), increases in carbon dioxide and other greenhouse gases have almost certainly played a major role in the observed temperature increases in the 20th century. Specifically, results from more than 20 different 3-D climate models presented in the 4th IPCC Assessment Report, show that with drier surface and warmer climate, lightning activity will increase [5]–[8]. Among others, the most important potential impacts of climate warming are changes in extreme weather events [1]. In some regions, global precipitation will decrease, but in others heaviest precipitation events will be more intense [9]. Several climate model simulations have indicated an approximated ten percent increase in global lightning activity for each degree of global warming, with the most increase occurring in the tropics [4]. This behavior seems to be related to one of the elements required to generate thunderstorms, which is the existence of warmer surface-air, which can rise quickly creating powerful updrafts. Updrafts carry water droplets at altitudes where the temperatures are considerably colder than freezing. At that altitude those water droplets quickly freeze and start to collide with ice crystals and graupel initiating charge transfer process [2].

## III. GEOPHYSICAL CHARACTERISTICS OF COLOMBIA

In the northern part of Colombia and according to [5]–[7], it is situated one of the world's largest lightning flash density rate areas. This is related to the seasonal variation of the trade winds associated with the oscillation of the Intertropical Convergence Zone (ITCZ) and its interaction with local mountains [10], [11].

## IV. AIR SURFACE TEMPERATURE AND LIGHTNING DATA IN COLOMBIA

This study uses air surface temperature data from meteorological stations around the world available at the Goddard Institute for Space Studies Surface Temperature Analysis (GIS-TEMP). In Colombia there are records of nineteen stations.

Unfortunately not all of them have complete data records sets, and most have only a few years. In this study two restrictions are considered: first, an observation window of at least thirty years and second, the most recent observation data is, at least, from year 2013. These restrictions reduce the available number of datasets to the ten stations mentioned in Table I.

TABLE I  
INFORMATION OF METEOROLOGICAL STATIONS USED FOR THIS STUDY.

Station Name	Long	Lat	ID	Period
Bucaramanga	7.1N	73.2W	305800940000	1977-2015
Barrancabermeja	7.0N	73.8W	305800910000	1973-2015
Medellín	6.2N	75.6W	305801100000	1941-2015
Barranquilla	10.9N	74.8W	305800280000	1966-2015
Cartagena	10.4N	75.5W	305800220000	1951-2015
Bogotá	4.7N	74.2W	305802220000	1961-2015
Santa Marta	11.1N	74.2W	305800090000	1975-2015
Villavicencio	4.2N	73.6W	305802340000	1961-2015
Cali	3.4N	76.4W	305802590000	1951-2014

The information of lightning occurrence data is available at the Tropical Rainfall Measuring Mission –TRMM–. On board of the satellite of this mission was installed an optical sensor named Lightning Imaging Sensor (LIS) which is able to observe any given point of the Earth’s surface for about 90 seconds. The sensor monitors continuously the background radiances to detect optical transients. LIS has a total field view of 500 x 500 km<sup>2</sup> with an efficiency between 90-95%. With these data the Lightning and Atmospheric Electricity Research at Global Hydrology Resource Center, delivers data by monthly average (including daytime and night-time) since 1998. Fig. 1 shows the Colombian total number of flash events during 2014.

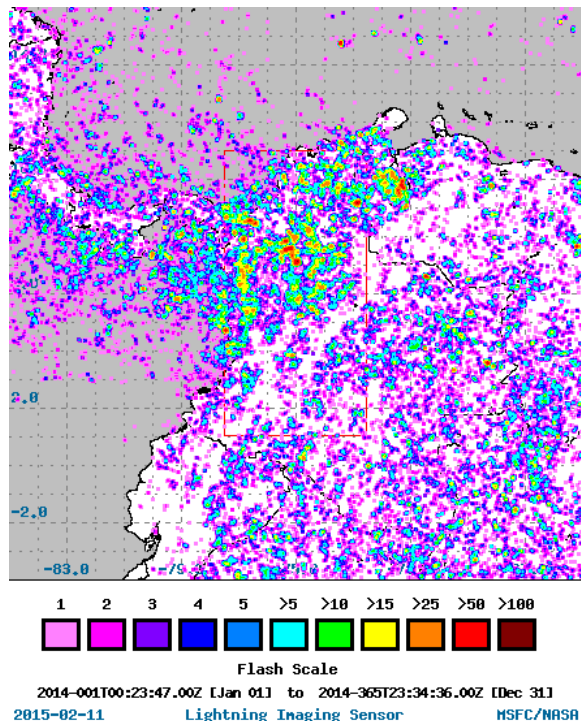


Fig. 1. Total lightning events detected by TRMM during 2014.

## V. DATA ANALYSIS AND DISCUSSION

The annual series of the total lightning events and the annual series of air surface temperature were computed from their monthly series. Correlation tests were used to assess if there is a linear relationship between the air surface temperature per year and total annual lightning events per year. To answer this question a Pearson correlation test with a 95% confidence interval was used to obtain a measure of the linear association between the two variables. After finding a positive correlation between the two variables, linear regression is used to test for linear trends. The t-test is used to demonstrate that the slope is statistically different from zero. The air surface temperature data is based on monthly measurements.

TABLE II  
RESULTS OF SOME STATISTICAL ANALYSIS OVER THE DATA.

Dataset	Pearson	p-value
Bucaramanga	0.3507	0.042
Barrancabermeja	0.5578	0.00031
Medellín	0.7047	2.70e-09
Barranquilla	0.5456	0.00015
Cartagena	0.6740	1.50e-07
Bogotá	0.8538	1.75e-13
Santa Marta	0.3331	0.04394
Villavicencio	0.7562	6.93e-09
Cali	0.3463	0.00671
Lightning	0.6235	0.00748

With this information the air surface temperature annual mean value is estimated. If the data of three or more months is missing, then the average temperature for the year is not calculated.

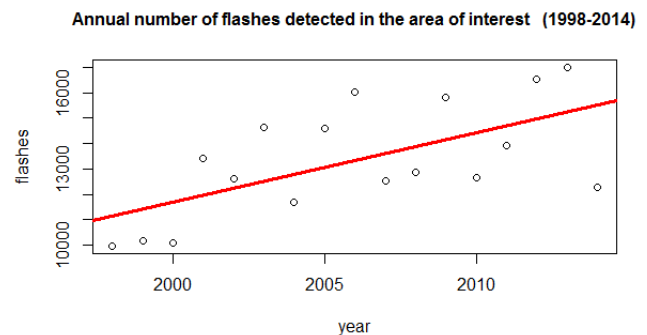


Fig. 2. Time series of total annual number of flashes detected from 1998 to 2014 over Colombia.

The apparent increase in temperature is very difficult to explain with the available data. Although, every city of this study has experimented a rapid increase in population and area in the last 50 years, so the phenomenon of heat island is a very plausible explanation of the increase in air surface temperature. Heat islands (due to the materials of the buildings, houses, and streets) store much more energy, reducing the changes in average temperature.

Another possible explanation is the change in the environmental conditions due to deforestation and exhausting of

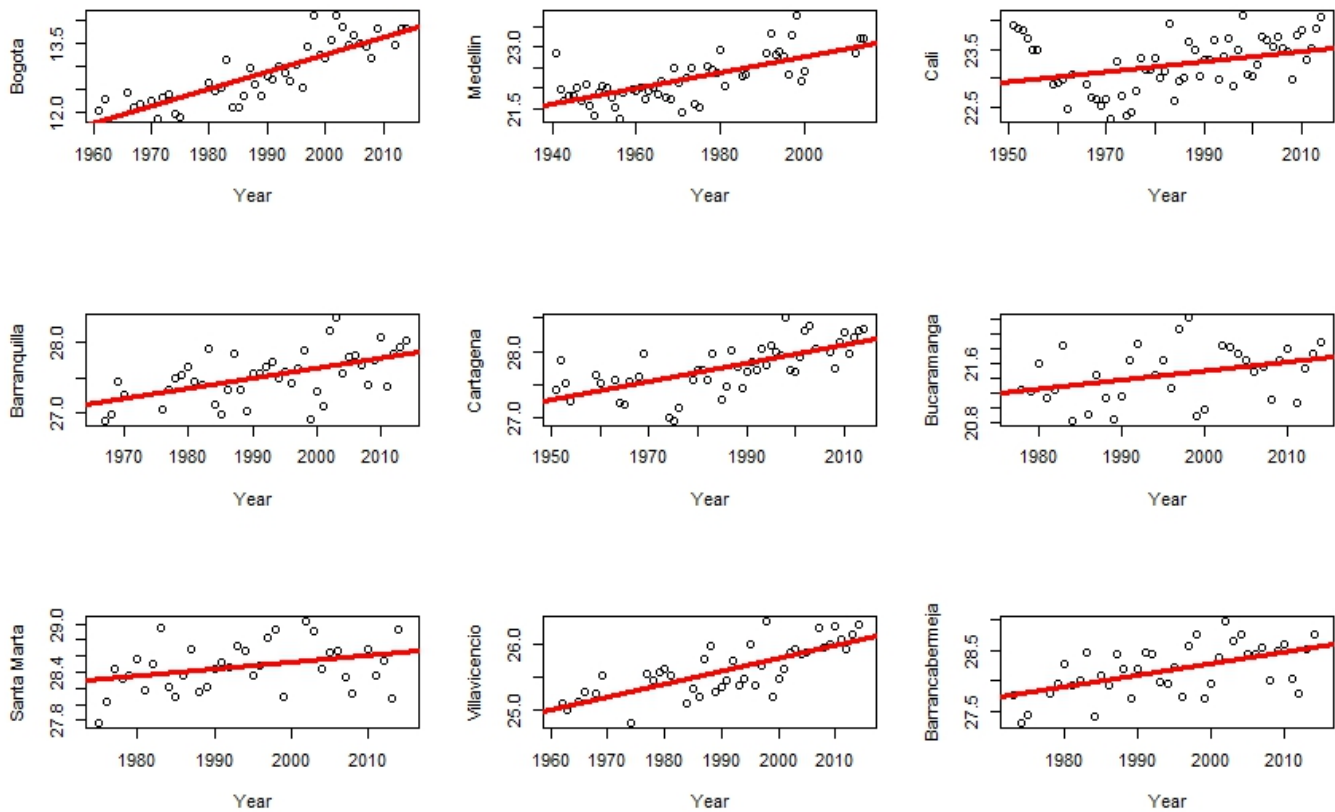


Fig. 3. Time series air surface temperature with its corresponding simple linear regression model.

water supplies, turning these areas in drier places. Therefore to have a general confirmation of the increase of air surface temperature it is necessary to consider data from small town and rural areas in order to confirm the hypothesis. The authors of this study are working now in this issue in order to get more reliable conclusions.

## VI. CONCLUSION

Results obtained suggest a warming process in the nine Colombia's largest cities [12], represented in an increase of about  $0.64^{\circ}\text{C}$  over the last 40 years. The causes and its implications will remain a topic for research and discussion. The apparent increase in lightning activity represents a threat for the potential lightning damages on human lives, facilities and infrastructure, especially in the Colombian regions with the highest density flash rate. In this context power lines, transformers, and other electric utility equipment are at high risk in Colombia, with its corresponding economic impact.

## REFERENCES

- [1] A. Del Genio. (2012) Will a warmer world be stormier? NASA, Goddard Institute for Space Studies. [Online]. Available: [www.giss.nasa.gov/research/briefs/delgenio](http://www.giss.nasa.gov/research/briefs/delgenio)
- [2] J. Dwyer and M. Uman, "The physics of lightning," *Physics Reports*, vol. 534, no. 4, pp. 147–241, 2014.
- [3] T. Oki and S. Kanae, "Global hydrological cycles and world water resources," *Scie*, vol. 313, no. 5790, pp. 1068–1072, 2006.
- [4] C. Price, "Will a drier climate result in more lightning?" *Atmospheric Research*, vol. 91, no. 2, pp. 479–484, 2009.
- [5] J. Grenfell, D. Shindell, and V. Grewe, "Sensitivity studies of oxidative changes in the troposphere in 2100 using giss gcm," *Atmospheric Chemistry and Physics*, vol. 3, no. 5, pp. 1267–1283, 2003.
- [6] C. Price and D. Rind, "A simple lightning parameterization for calculating global lightning distributions," *Journal of Geophysical Research: Atmospheres*, vol. 97, no. D9, pp. 9919–9933, 1992.
- [7] D. Shindell, G. Faluvegi, N. Unger, E. Aguilar, G. Koch, and D. Schmidt, "Simulations of preindustrial, present-day, and 2100 conditions in the nasa giss composition climate model g-puccini," *Atmospheric Chemistry and Physics*, vol. 6, no. 12, pp. 4427–4459, 2006.
- [8] C. Price, "Global surface temperatures and the atmospheric electric circuit," *Geophysical Research Letters*, vol. 20, no. 13, pp. 1363–1366, July 1993.
- [9] S. Min, X. Zhang, F. Zwiers, and G. Hegerl, "Human contribution to more-intense precipitation extremes," *Nature*, vol. 470, pp. 378–381, Feb 2011.
- [10] H. Christian and et al., "Global frequency and distribution of lightning as observed from space by the optical transient detector," *Journal of Geophysical Research: Atmospheres*, vol. 108, pp. ACL–4, 2003.
- [11] O. Pinto, I. Pinto, and K. Naccarato, "Maximum cloud to ground lightning flash densities observed by lightning location systems in the tropical region: A review," *Atmospheric Research*, vol. 84, no. 3, pp. 189–200, 2007.
- [12] DANE. (2013) Poblacin colombiana. Departamento Administrativo Nacional de Estadstica DANE. [Online]. Available: <http://www.banrep.gov.co/es/poblacion>

# Effect of Nearby Building on Horizontal Electric Field from Lightning Return Strokes

Fei Guo, Zhi-dong Jiang, Bi-hua Zhou

National Key laboratory on Electromagnetic Environment and Electro-optical Engineering, PLA University of Science and Technology, Nanjing, 210007, China

## Abstract

The effect of nearby building on the horizontal electric field radiated by lightning is discussed by a two-step finite-difference time-domain (FDTD) method. The enhancement or attenuation effect of the building on the horizontal electric field is analyzed as well. The horizontal electric field, which is located in front and behind the building, will be enhanced significantly, and the polarity is opposite for different sides of the building. The vertical electric field on the sides of the building will decrease, while the vertical electric field on the roof will be enhanced.

**Keywords:** horizontal electric field, FDTD, Lightning Return Strokes.

## 1 Introduction

In order to optimize lightning protection means of tall buildings, it is important to know the change of the electric field at the top of the building due to lightning strikes nearby. Further, lightning electric field measurement is often carried out on the roof of tall buildings [1-2], so the effect due to the presence of tall buildings is needed for guiding and interpreting the measurement of the electric field. Enhancement or attenuation effects caused by metallic beams and other conducting parts of the building on the vertical electric field and azimuthal magnetic field have been reported in previous studies [3-6]. To the best of our knowledge, those works have focused on the vertical electric field and magnetic field. The influence of the nearby building on the horizontal electric field has not been dealt with in previous studies. In [3] and [4], the ground and building were assumed to be perfectly conducting. However, the conductivity of the ground and building has a significant effect on the horizontal electric field. In addition, the velocities of the current propagation and corresponding lightning return stroke models cannot be considered and realized in the CST model [6]. The horizontal electric field due to lightning return strokes is related to the assessment of lightning induced overvoltages. However, there are many difficulties and restrictions for the measurement of the horizontal electric field [7-8]. So evaluation the effects of nearby buildings on the horizontal electric field will benefit for optimizing lightning protection means of nearby telecommunication and power distribution

lines. In this paper, we present a two-step FDTD method for the evaluation of the enhancement or attenuation effect introduced by a nearby building on the horizontal electric field. The proposed two-step FDTD method can greatly reduce the calculation scale, making the calculation time much less. For comparison purposes, the effect on the vertical electric field at the same field point is also presented. The horizontal electric field and vertical electric field are compared in the presence of building with their counterparts in the absence of the building, both investigated by the proposed two-step FDTD method.

## 2 Methodology

The configuration of the calculation model is presented in Fig. 1. The electromagnetic fields near the lightning channel are calculated in the 2-D cylindrical coordinates, and then the electromagnetic fields calculated in the former step can be added into the 3-D working volume at the total field-scattered field connecting boundary. In addition, a sub-grid technology is used in 2-D Cylindrical coordinate model for precision consideration of the building structure on the ground. The dimension of the building structure is smaller than the corresponding wavelength of the main spectra of cloud-to-ground lightning return stroke, which is below 1 MHz, the scatter radiation fields and fine structure of the building are ignored.

In this study, the TL model is adopted. In order to reproduce a typical return stroke current of a negative downward flash, the channel base current  $I(t)$  at the ground level is described by a double exponential functions as follows:

$$I(t) = 1.1 \times I_0 \times (e^{-3.0 \times 10^4 t} - e^{-1.0 \times 10^7 t}) \quad (1)$$

Where:

$I_0$  is the peak value of the first lightning current, and the return-stroke speed  $v$  is  $1.3 \times 10^8$  m/s.

The conductivity of the ground and building is  $1 \times 10^{-3}$  S/m and the relative permittivity is assumed to be equal to 10. To avoid reflections, the working volume is surrounded by absorbing boundary, and the convolutional perfect matched layer (CPML) is used in this paper.

The horizontal distance from the centre of the building to the lightning channel is set to 100 m. The point C is located at the centre point on the flat roof of the building having a plan area  $S_b = 20 \times 20$  m<sup>2</sup>, and the point C\* is located on the same location in the absence of building. The point A and B are located at ground level closer to or further from the lightning channel,

and the point A is in the front of the building, while the point B is on the other side of the building.

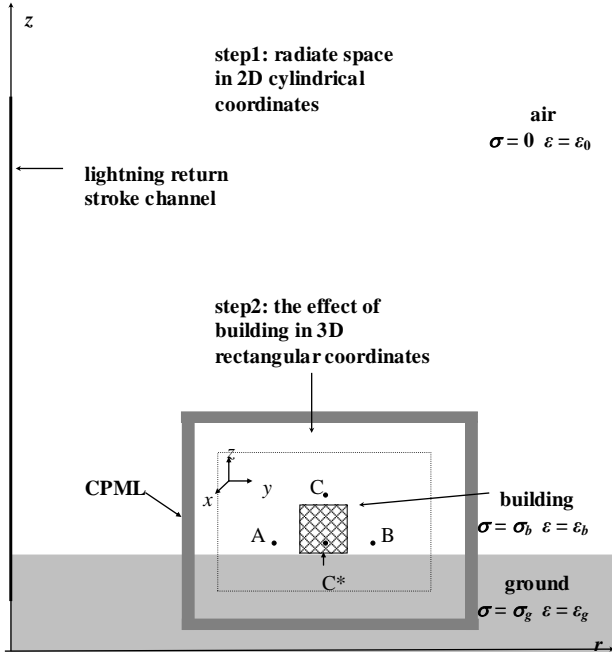


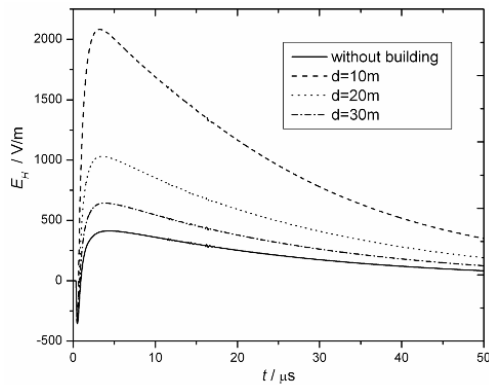
Figure.1 Configuration of the calculation model

### 3 Simulated Results and Analysis

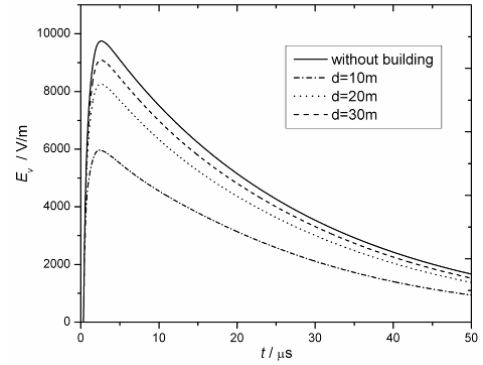
#### 3.1 The effect of the distance from the building to the field point on the electric field

In this section, the effects of different distance from the building on the electric fields are evaluated. The distance from the point A or B to the lightning channel remains unchanged, and the distance from the edge of the building to the point A or B is 10m, 20m and 30m, respectively.

Fig.2 show waveforms of  $E_H$  and  $E_V$  at Point A in the presence of the building, and the point A located at distance  $d=10, 20$  and  $30$ m from the building. It is clear that the magnitude of the horizontal electric field at ground level in the vicinity of the building are enhanced due to the presence of the building, while the vertical electric field at the same field point are attenuated due to the shielding effect of the presence of the building.



(a) Horizontal electrical field



(b) Vertical electrical field

Figure.2 The effects of the distance between building and point A on the electrical field

Table I shows the ratios of magnitudes of electric field at points A and B in the presence of the building located at distance  $d=10, 20, 30, 40$  or  $50$ m and those in the absence of the building. The enhancement factor of  $E_H$  at ground level become smaller as the horizontal distance increases from 10 to 50 m. As for the vertical electric field, the enhancement factor becomes larger. The variation of the vertical electric field at ground level due to the presence of building is negligible (less than 10%) when the horizontal distance from the building to the field point larger than 30 m.

Table I Ratios of magnitudes of electrical field with different distances

Enhancement factor		Horizontal distance (m)				
		10	20	30	40	50
A	$M_H$	5.04	2.49	1.56	1.25	1.13
	$M_V$	0.61	0.85	0.93	0.96	0.98
B	$M_H$	4.97	2.37	1.64	1.21	1.09
	$M_V$	0.46	0.71	0.84	0.88	0.95

#### 3.2 The effect of different building heights on the electric field at different field position

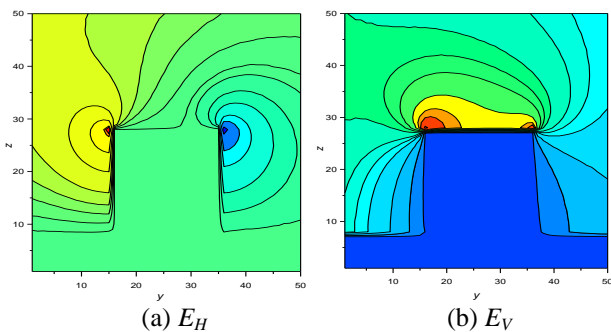
Table I presents the effects of the building height on the enhancement factor between the calculated fields in the presence of the building and those obtained without the building. The magnitude of  $E_H$  and  $E_V$  at ground level in the vicinity of the building (both point A and B) becomes smaller as the building height increases, while the magnitude of  $E_H$  and  $E_V$  on the roof of the building become larger. The results suggest that the simulated vertical electric field at the top of a 10-m tall building is enhanced by a factor of 1.56, which is consistent with Mosaddeghi's result in [5].

Table II Effects of the building height on the enhancement factor

Enhancement factor		The height of building (m)			
		10	20	30	50
A	$M_H$	6.47	4.32	3.91	3.43
	$M_V$	0.94	0.68	0.54	0.46
B	$M_H$	5.31	3.72	3.38	2.56
	$M_V$	0.87	0.57	0.39	0.30
C	$M_H$	0.28	0.42	0.57	0.80
	$M_V$	1.56	1.97	2.46	3.11

### 3.3 The distribution of the electric field

Fig.3 and 4 show the side view and the plan view of the distribution of the electric field (calculated at 6  $\mu$ s after the return stroke) nearby the building. It is clear from Fig.3 that the closer the building, the larger the horizontal electric field at ground level, while the vertical electric field just the opposite. The conclusions about the distribution of the electric field are consistent with those above obtained. Fig. 4 show that the magnitude of  $E_H$  on the roof of the building is largest at the edge of the roof near to or far away from the lightning channel, while the change of the magnitude of  $E_V$  on the roof is smallest at the centre of the roof.



**Figure.3** Side view of the distribution of the electrical field

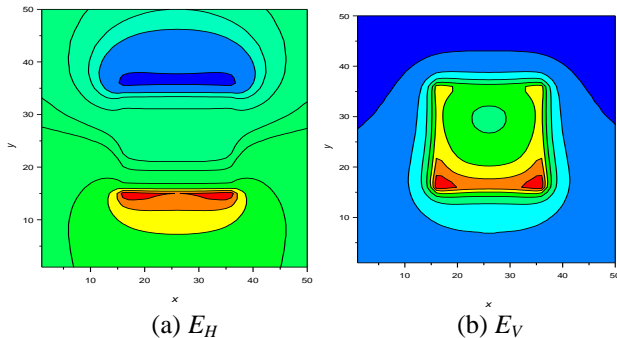


**Figure.4** Plan view of the distribution of the electrical field

The observed effects can be explained as follows. The building can be treated as a finitely conducting object above ground in the external electric field from the lightning, and a vertical component which can drive motion of electric charges to its upper extremity will be produced. The vertical field on vertical conducting surfaces (*e.g.* walls of a rectangular) requires that field in near zero on the surface and reduced in the vicinity [5]. As expected, vertical electric field will be reduced in the vicinity of the building. The effect will be reduced when the horizontal distance increases. As for the horizontal electric field, the scatter radiation fields from the building and ground are contributing to the enhancement of the magnitude of the horizontal field.

### 4 Conclusion

In this paper, we compared the horizontal electric field and vertical electric field from lightning return stroke in the presence of nearby building with their counterparts in the absence of the building. A two-step FDTD method is proposed for evaluating the effect of the building on the

horizontal electric field. The simulations have shown that the presence of nearby building has a significant effect on both magnitude and shape of the horizontal electric field, while the effect on the vertical electric field is mainly reflected in the magnitude changes of the peak. The horizontal electric field of the field point, which is located in front and behind the building, will be enhanced significantly, while the vertical electric field will decrease. The vertical electric field on the roof will be enhanced, so the field point located above the ground for LEMP measurement should be chosen as far away from tall buildings.

### Acknowledgements

The authors would like to thank the anonymous reviewers for their helpful remarks, and this work was supported by the Chinese National Science Foundation under Grant No. 61301063.

### References

- [1] Motoyama H., Janischewskij W., Hussein A., Rusan R., Chisholm W. A., and Chang J. S., "Electromagnetic field radiation model for lightning strokes to tall structures," *Power Delivery, IEEE Transactions on*, Vol. 11, No.3, pp. 1624-1632, (1996).
- [2] Rakov V. A., "Transient response of a tall object to lightning," *Electromagnetic Compatibility, IEEE Transactions on*, Vol. 43, No.4, pp. 654-661, (2001).
- [3] Mosaddeghi, A., Pavanello D., Rachidi F., and Zwiackner P., "Effect of Nearby Buildings on Electromagnetic Fields from Lightning," *Journal of Lightning Research*, Vol. 1, pp. 52-60, (2009).
- [4] Bonyadi-Ram S., Moini R., Sadeghi S. H. H., and Mahanfar A., "The effects of tall buildings on the measurement of electromagnetic fields due to lightning return strokes," *IEEE International Symposium on Electromagnetic Compatibility*, pp.1001-1004, Vol.2, (2001).
- [5] Baba Y. and Rakov V. A., "Electromagnetic Fields at the Top of a Tall Building Associated With Nearby Lightning Return Strokes," *Electromagnetic Compatibility, IEEE Transactions on*, Vol. 49, No.3, pp. 632-643, (2007).
- [6] Vieira M. S. and Janiszewski J. M., "Propagation of lightning electromagnetic fields in the presence of buildings," *Electric Power Systems Research*, Vol. 118, pp. 101-109, (2015).
- [7] Shoory A., Rachidi F., Rubinstein M., and Thottappillil R., "On the Measurement and Calculation of Horizontal Electric Fields From Lightning," *Electromagnetic Compatibility, IEEE Transactions on*, Vol. 53, No.3, pp. 792-801, (2011).
- [8] Mosaddeghi A., Shoory A., Rachidi F., Diendorfer G., Pichler H., Pavanello D., Rubinstein M., Zwiackner P., and Nyffeler M., "Lightning electromagnetic fields at very close distances associated with lightning strikes to the Gaisberg tower," *J. Geophys. Res.*, Vol. 115, pp. D17101, (2010).

# On the Classification of Tower Flashes as Self-Initiated and Other-Triggered

*M Rubinstein\**, *Alexander Smorgonskiy*<sup>†</sup>, *F Rachidi*<sup>†</sup>, *J Zuber\**

\* *University of Applied Sciences of Western Switzerland, Yverdon, Switzerland, marcos.rubinstein@heig-vd.ch*

<sup>†</sup> *EMC Laboratory, Swiss Federal Institute of Technology (EPFL), Switzerland, farhad.rachidi@epfl.ch*

## Abstract

Tower lightning has been classified into “other-triggered” and “self-initiated” lightning based on whether or not the tower flash is preceded by natural lightning activity in the vicinity of the tower location. The causality relation between other-triggered flashes and the preceding activity has not been established. In this paper, we use a probabilistic model to show that it is possible to explain at least some of the lightning activity prior to tower flashes as being the result of chance.

**Keywords:** Lightning, self-initiated, other-triggered.

## 1 Introduction

Lightning flashes to towers have been classified into “other-triggered” lightning and “self-initiated” lightning based, respectively, on the presence or the absence of other lightning activity in the geographical vicinity and within a temporal interval preceding the tower flash (e.g., [1,2,3]). Smorgonskiy et al. [4] remarked that the causality relation for other-triggered flashes has not been established. The name “other-triggered” could thus be misleading if the causality does not exist for any or for some of the flashes. In this paper, we study the so-called other-triggered flashes and show that it is possible to explain the occurrence of flashes shortly before tower lightning by way of a simple probabilistic model. It is important to note that this study shows that causality is not the only possible explanation for the succession of natural and tower flashes but it does not reject the possibility of causality. This paper is organized as follows: In Section 2, we present a probabilistic model based on a number of simplifying assumptions regarding the lightning flash density over the area of a storm and the lightning flash frequency over the duration of the storm. In Section 3, we use simulations to verify the model. Section 4 contains a discussion and conclusions.

## 2 Probabilistic Model

In this section, we propose a probabilistic model for the time and location of flashes in a storm over a tower. The model is

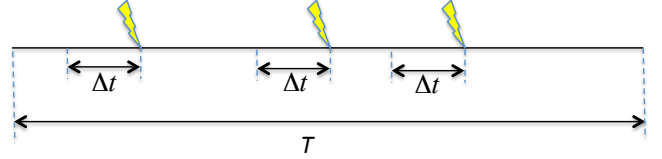


Figure 1. Time axis with three flashes striking a tower and  $\Delta t$  time bins before them. If at least one natural flash strikes within a given bin, the tower flash associated with that bin is classified as an “other-triggered” flash.

based on the following assumptions: 1. The storm is confined to an area  $A_s$  and the lightning flash density is uniform over it. 2. The storm area contains one tower. 3. The storm lasts  $T$  seconds, it has specific start and end times and the probability that a flash will occur at any time during the storm is the same. We also assume that a total of  $N_{tower} + N_{natural}$  flashes occur during the storm. Of these,  $N_{tower}$  flashes strike the tower and  $N_{natural}$  flashes strike in the area of the storm but not the tower. Note that we have called the flashes that do not strike the tower “natural flashes” to distinguish them from those striking the tower, which we call “tower flashes”. An example showing 3 tower flashes occurring over a time period  $T$  is shown for illustrative purposes in Figure 1. A time interval  $\Delta t$  immediately before each tower strike is also shown in the figure. Tower flashes for which there is at least one natural flash within its associated  $\Delta t$  and which strike within a radius “ $a$ ” of the tower are considered to belong to the other-triggered category. Under these assumptions, the expected value for the percentage of other-triggered flashes is given by

$$Other - triggered\% = 100 \left( 1 - \left( 1 - \frac{\Delta t}{T} \right)^{\frac{N_{natural} \pi a^2}{A_s}} \right) \quad (1)$$

where all the parameters have been defined in the text above.

## 3 Simulations

Using Matlab<sup>®</sup>, we calculated  $N_{tower}$  random real numbers from 0 to  $T$  with a uniform probability density function. This set of  $N_{tower}$  random numbers corresponds to the times of strikes to the tower. Using, again, a random number function in Matlab<sup>®</sup>, we generated a set of  $N_{natural}$  random real numbers from 0 to  $T$ , which represent random times at which the natural flashes occur according to the uniform-probability

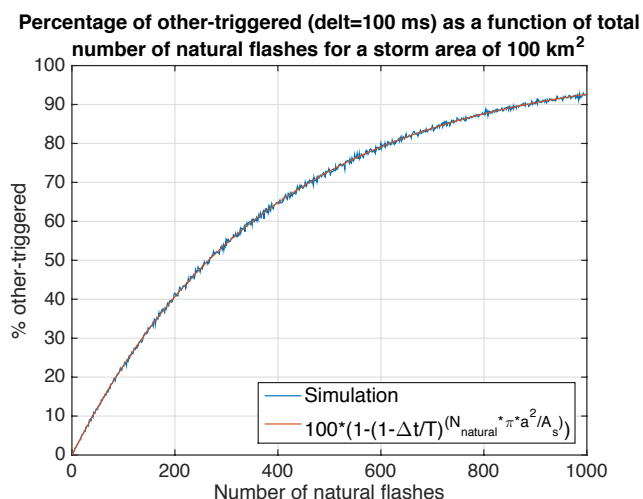


**Figure 2. Percentage of other-triggered flashes as a function of the number of natural flashes  $N_{natural}$  in the storm.**

function model. We then selected time intervals  $\Delta t$  prior to the tower strikes and counted the number of natural flash times that fall within these intervals. If at least one natural flash was found within  $\Delta t$  before any of the tower flashes, that tower flash was classified as other-triggered. We used the results to calculate the percentage of other-triggered flashes. The procedure was repeated independently several times and an average percentage of other-triggered flashes for the selected value of  $N_{natural}$  was calculated. The complete procedure was redone for other values of  $N_{natural}$  and, finally, a plot of the results was generated. This plot, along with the theoretical prediction from Equation (1) are shown in Fig. 2. The particular values used in Fig. 2 are  $T = 600$  s,  $\Delta t = 2$  s,  $A_s = 100$  km<sup>2</sup>, and  $a = 5$  km. An excellent agreement can be observed between the theoretical and the simulation results.

#### 4 Discussion and Conclusions

We have used a simple probabilistic model to estimate the percentage of lightning flashes that would be classified as other-triggered if they occurred by chance in the vicinity of a tower and within a specified time interval before the tower. The model used assumes that the flash density does not vary either with time during the storm or with the position in the area covered by the storm. The results show that the number of flashes in the storm is determinant. Under the model assumptions and the selected parameters, a storm with between some 50 and 100 flashes would lead to a percentage of other-triggered tower flashes somewhere between 10% and 20%. On the other hand, a storm with 400 flashes or more would exhibit a percentage of other-triggered flashes greater than 70%, although the exact values are dependent on the values selected for the parameters  $\Delta t$  and  $a$ , and on the

duration  $T$ , extension and intensity of the storm. It is thus important as future work to test the model presented here against data from real storms over a tower. We have shown that, under the assumptions of our model, it is possible that at least some of the flashes that have been considered as other-triggered are actually just happening at the right time and the right place by chance. However, this possibility does not prove that there is no causality relation.

Since the frequency of occurrence of lightning flashes during a storm may vary with time and since the ground flash density in a storm may vary with position (for instance from the center of the storm to the edges), a better model should be developed using more realistic statistical data.

If there is a causality relation between preceding lightning activity and tower flashes, then nearby lightning activity directly before tower flashes should be statistically different from lightning activity directly after tower flashes. This could be used as a further test of causality. Note that, although a statistical difference would strongly point to a causality relation, a statistical agreement would not directly negate the causality.

#### Acknowledgements

Financial support from the Swiss National Science Foundation (Projects No. 200021-122457 and 200021\_147058) and BKW Ecology Fund are acknowledged.

#### References

- [1] D. Wang, N. Takagi, T. Watanabe, H. Sakurano, and M. Hashimoto, "Observed characteristics of upward leaders that are initiated from a windmill and its lightning protection tower", *Geophys. Res. Lett.*, vol.35, L02803, doi:10.1029/2007GL032136, (2008).
- [2] D. Wang, N. Takagi, T. Watanabe and M. Hashimoto, "Observed characteristics of the lightning striking on a windmill and its lightning- protection tower", 29th Intern. Conf. on Lightning Protection, Uppsala University, Uppsala, Sweden, (2008).
- [3] F. Heidler, M. Manhardt, and K. Stimpfer, Self-Initiated and Other-Triggered Positive Upward Lightning Measured at the Peissenberg Tower, Germany, International Conference on Lightning Protection (ICLP), Shanghai, China (2014).
- [4] Alexander Smorgonskiy, Alaleh Tajalli, Farhad Rachidi, Marcos Rubinstein, Gerhard Diendorfer, and Hannes Pichler, Analysis of Lightning Events Preceding Upward Flashes from Gaisberg and Säntis Towers, International Conference on Lightning Protection (ICLP), Shanghai, China (2014).

# Lightning Protection Design Based on Energy Calculation

John J. Pantoja, Francisco Roman, Francisco Amórtegui

Electromagnetic Compatibility Group (EMC-UN), Universidad Nacional de Colombia, Bogotá, Colombia  
jjpantojaa@unal.edu.co

## Abstract

In this paper the methodology to calculate the energy transferred to the human body by a 100 kA, 10/350 lightning current impacting in a 30 m high earthed mast is presented. This calculation is performed to evaluate the lightning earthing system of a Corona current measuring station installed at the Universidad Nacional de Colombia in Bogotá. Calculations were performed using the electromagnetic program CST Microwave Studio.

**Keywords-** Transient Step- and Touch- voltages, transient earthing systems, Lightning simulations, Lightning current.

## 1 Introduction

The EMC-Group from the Universidad Nacional de Colombia is investigating Corona currents in high masts. To perform this investigation the 30 m high mast shown in Fig. 1 was installed in a quite deserted street at the university campus. The mast base is isolated by a 2 m high square fence, called here Metallic Enclosure, separated 2 m from the mast centre. However, due to its location and to protect people walking or staying in the neighbourhood of the metallic enclosure, lightning induced overvoltages around the structure are calculated. To design the earthing system, both, step- and touch-overvoltages generated by a 100 kA, 10/350 lightning current are calculated. Additionally and knowing that these transient overvoltages could affect persons, the induced energy in the human body is also calculated using the electromagnetic program CST Microwave Studio.

## 2 Earthing of the Lightning Protection System

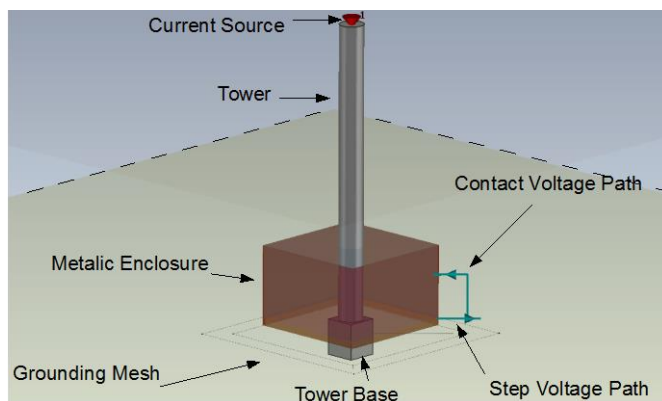
The lightning protection design consisted of two concentric squared earth loops around the tower, as shown in Fig. 2. The lightning protection system was assessed by simulating a direct lightning strike on the tower. A numerical simulation in CST Microwave Studio using a transient solver was performed. The lightning current is represented by an ideal current source at the tower top and the current parameters correspond to levels III or IV of the international standard IEC 62305-1. The required 100 kA double exponential current waveform suggested in the standard, with 10  $\mu$ s rise-time and 350  $\mu$ s time-to-mean-value respectively, is presented in Fig. 3.

Due to the metallic enclosure geometry, higher electric field intensities are presented at the metallic enclosure corners. For this reason, the protection assessment was based on calculating the step- and contact- induced voltages at the metallic enclosure corners. These voltages were calculated

by integrating the electric field in the paths shown in Fig. 2a; where the step length is 1 m and the touch path is formed by 2 straight lines, one horizontal and one vertical with respective lengths of 1 m and 1.5 m.



Figure 1. Installation of the 30 m high Corona current measuring mast in the campus of the Universidad Nacional de Colombia.



(a)

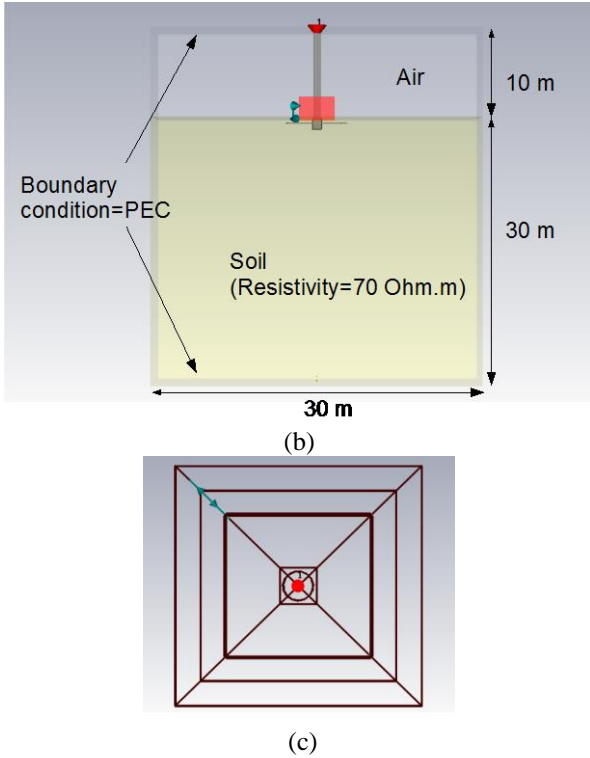


Figure 2. Simulation Setup. (a) Perspective, (b) lateral, and (c) top views. The boundary condition PEC is perfect electric conductor.

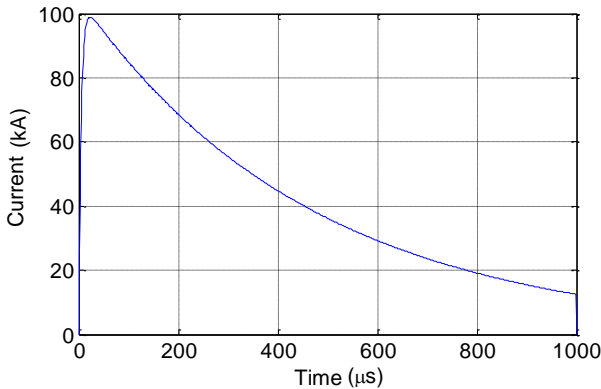


Figure 3. 100 kA, 10/350 lightning current waveform used in the CST simulations. The waveform is based in international standard IEC 62305-1.

### 3 Lightning Protection Assessment

The main purpose of the mast is to measure corona current and atmospheric conditions in its top. However, the mast is prone to be impacted by lightning and touch and step voltages could be expected in the metallic enclosure. Therefore, a special risk assessment was performed. Two possible situations of the metallic enclosure were considered: In the first one the metallic enclosure is electrically floating, while in the second the corners of the metallic enclosure are bounded to the earthing mesh.

Particularly, risks caused by transient electric signals in human beings are still being studied [1]. Here, the designed protection system is assessed using two parameters commonly used: the energy delivered to a person touching the tower and the step voltage.

#### A. Energy Calculation

The first estimated parameter is the amount of energy delivered to a person by a lightning induced overvoltage. The limit of the amount of energy  $W$  in Joules, which a person could withstand, is calculated by using both Dalziel curve shown in Fig. 4 and equation (1):

$$W = I^2 * R * t \quad (1)$$

where,  $I$  and  $t$  are the pair of current and time values along the Dalziel curve in Fig. 4 and  $R$  is the human body resistance estimated in  $1000 \Omega$ . When the energy that a person could withstand is calculated using Dalziel's characteristic curve, a constant energy value of 10 J is obtained. Although Fig. 4 is based on alternating currents below 100 Hz, its application to transient currents could be justified if the 10 J limit obtained with the Dalziel's curve is always lower than any calculated value in region 6.

To calculate the energy given by the lightning induced step and touch overvoltages, the methodology of the Thevenin equivalent circuit proposed in [2] and shown in Fig. 5 was used.

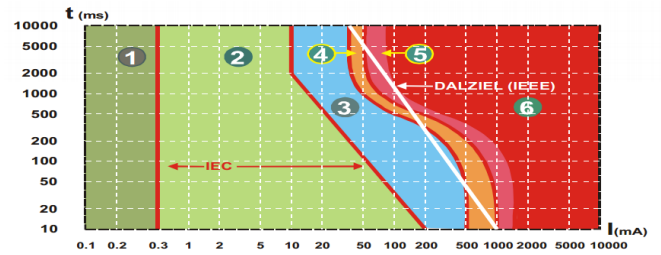


Figure 4. Classification of alternating currents of 15 Hz to 100 Hz in current-time areas according to their effects. Effects: 1-None, 2-None physiopathological effect, 3- Non fibrillation risk, 4- Fibrillation risk (5%), 5- Fibrillation risk (<50%), 6- Hearth attack, burns, fibrillation risk (>50%). Taken from [3] and based in the international standard IEC 60479-2.

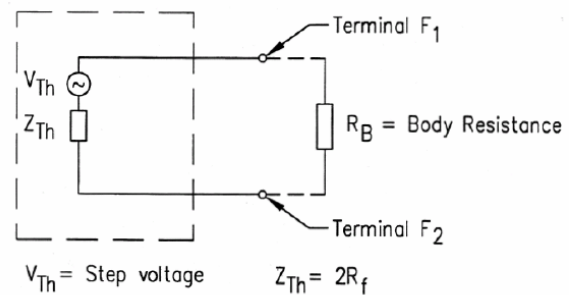


Figure 5. Thevenin equivalent circuit used to calculate the current and energy delivered to a human being. Taken from [2].

In the calculations, the Thevenin voltage,  $V_{Th}$ , corresponded to the step or touch voltage, the Thevenin impedance,  $Z_{Th}$ , was neglected, assuming that the feet contact resistance was zero, and the body resistance,  $R_b$ , was assumed to be  $1000 \Omega$ . Finally, the energy was calculated as

$$W = \int P(t) dt = \int \frac{V(t)^2}{R_b} dt \quad (2)$$

where,  $V(t)$  is the step or touch voltage calculated with CST as a function of the time and  $P(t)$  is the dissipated power as a function of the time.

The design energy levels were calculated applying (2) to the calculated voltages presented in Fig. 6. Table 1 shows that both alternatives, with floating and earthed metallic enclosure, are below the 10 J limit. In addition, Table 1 shows that the floating metallic enclosure design delivers less energy and presents lower levels than the suggested threshold of 0.25 J.

### B. Step Voltage Threshold

The second method used to assess the lightning protection system was comparing the induced step voltage with a voltage threshold calculated as [4]

$$U_{st} = \frac{(165 \sim 250) + \rho_g}{\sqrt{t}} \quad (3)$$

where,  $\rho_g$  is the soil resistivity and  $t$  is the lightning duration. Using  $\rho_g = 70 \Omega\text{m}$  and  $t = 1 \text{ ms}$ , a 10.12 kV threshold voltage is obtained. Peak step voltages are presented in Table 1, which shows that both designs have lower levels than the suggested threshold.

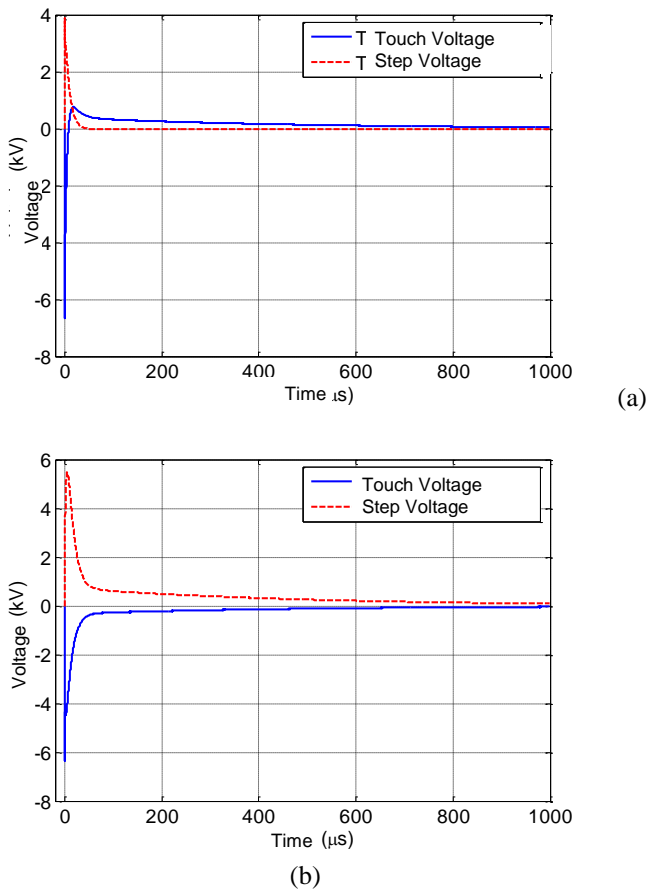


Figure 6. Voltages calculated at the corner's metallic enclosure considering (a) floating metallic enclosure and (b) earthed metallic enclosure.

Table 1: Energy levels obtained from simulated voltages.

Metallic Enclosure	Delivered Energy (J)		Step Voltage (kV)
	Touch	Step	
Floating	0.062	0.083	3.87
Grounded	0.240	0.567	5.48

## 4 Conclusion

Two techniques to assess the performance of a lightning protection system against transient currents, based in energy and voltage thresholds, were used to compare two earthing designs. By using both techniques similar results were obtained, since the considered designs are giving lower levels than the suggested thresholds for each technique. Particularly, it is shown that the metallic enclosure in the floating condition compared with the earthed one, produces lower energy and voltage levels to a person touching it.

## References

- [1] A. Sowa and J. Wiater, "Reduction of the Step Voltages Around Building During Direct Lightning Strike," presented at the IX International Symposium on Lightning Protection, Foz do Iguaçu, Brazil, 2007.
- [2] IEEE, "IEEE Std 80-2000: IEEE Guide for Safety in AC Substation Grounding," ed, 2000.
- [3] *Reglamento Técnico de Instalaciones Eléctricas RETIE 2013*: Ministerio de Minas y Energía, República de Colombia, 2013.
- [4] B. Zhou, H. Ren, L. Shi, and C. Gao, "Calculation of step voltage near lightning current," in *Radio Science Conference, 2004. Proceedings. 2004 Asia-Pacific*, 2004, pp. 646-649.

# On the Unconditionally Stable FDTD Method Based on Associated Hermite Functions

Huang Zhengyu, Shi Lihua, Zhang Zhixin

National Key Laboratory on Electromagnetic Environmental Effects and Electro-optical Engineering,  
No.1 Haifuxiang, Nanjing, China

## Abstract

This paper introduces developments of the unconditionally stable finite-difference time-domain (FDTD) method based on the Associated Hermite (AH) orthogonal functions. This method has renewed the category of orthogonal-functions-based unconditionally stable FDTD method, which is dominated by Weighted Laguerre Polynomials (WLP) FDTD method previously. Comparison of the proposed method with FDTD in analysing fine structures, as well as the application in dispersive medium are given in this paper.

**Keywords:** Associated Hermite functions, finite difference time domain (FDTD), and unconditional stability.

## 1 Introduction

The finite-difference time-domain (FDTD) method has been widely used to analyse transient electromagnetic scattering problems. In the cases of fine geometric structures, the time step should be limited by the Courant–Friedrich–Levy (CFL) stability condition. To deal with this problem, orthogonal decomposition of Maxwell’s equations by basis functions attracts attention in recent years. The dominated method in this area is Weighted Laguerre Polynomials (WLP) FDTD method [1], which shows relatively less numerical dispersion error when larger time step is used. Inspired by Weighted Laguerre Polynomials, we have explored Associated Hermite (AH) functions [2] as another possible orthogonal basis to incorporate with FDTD to form an unconditionally stable scheme [3]. Recently, two main progresses have been achieved. The one is its extension to the frequency-dependent dispersive problems and the other is the improvement of memory storage reduction by using the eigenvalue transformation.

## 2 Methodologies

Associated Hermite basis functions are an orthonormal set of basis functions

$$\phi_q(t) = \frac{1}{\sqrt{2^q q! \sqrt{\pi}}} e^{-t^2/2} H_q(t) \quad (q = 0, 1, \dots) \quad (1)$$

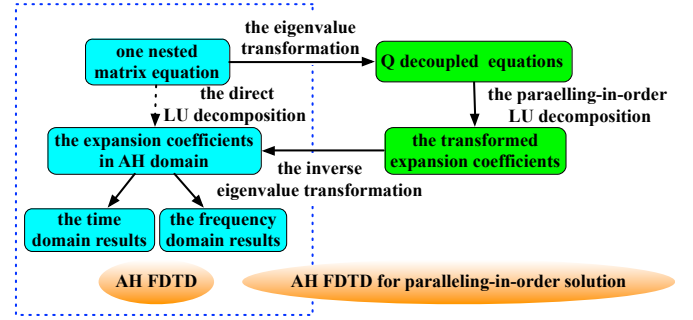


Figure 1. The framework of AH FDTD and its implementation of paralleling-in-order solution.

where  $H_q(t) = (-1)^q e^{t^2} \frac{d^q}{dt^q} (e^{-t^2})$  is Hermite polynomials. The time derivation of the  $q$ -th order AH function is

$$\frac{d}{dt} \phi_q(t) = \sqrt{\frac{q}{2}} \phi_{q-1}(t) - \sqrt{\frac{q+1}{2}} \phi_{q+1}(t) \quad (2)$$

The main ideal of AH-FDTD is to use a finite  $Q$ -dimensional AH expansion as temporal testing functions to span the time-domain Maxwell’s equations and calculate the expansion coefficients of electromagnetic fields in AH domain; the time-domain results can be reconstructed from these expansion coefficients. There are two main interesting properties for AH functions: the most compact time-frequency support (TFSs) and the unique isomorphism of the AH function with its Fourier transform. The former can expand the transient signals with less orders of polynomials, which means relative fewer unknowns to calculation for AH FDTD scheme and the latter can make the time or frequency domain results can both be directly reconstructed from the expansion coefficients in AH domain. The key step for its implementation is how to solve the implicit equations to obtain the EM filed expansion coefficients in order. For it cannot be calculated from the march-on-in-order scheme like the WLP method, instead, we establish a set of nested matrix equations with  $Q$ -tuple variables in whole computational domains to obtain the expansion coefficients.

$$[A]\{[P]\} = \{[J]\} \quad (3)$$

where  $\{[P]\}$  is an unknown  $Q$ -tuple field variable.  $\{[J]\}$  is a  $Q$ -tuple item included with excitation source coefficients.  $[A]$  is a nested banded coefficient matrix. A numerical experiment

with 2-D parallel plate waveguide is performed as shown in Figure 2.

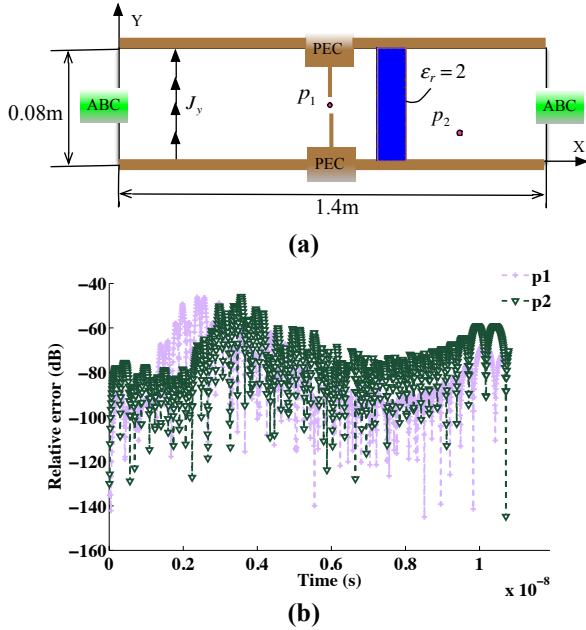


**Figure 2. (a) Computational domain of 2-D parallel plate waveguide with the thin PEC slot of the thickness 1.2 μm and the distance 0.9 cm, and the partly filled dielectric material of the thickness 0.04 m. (b) Comparison of the relative error at point  $p_1$  and  $p_2$ .**

The EM responses waves calculated are agreeable with the conventional FDTD solution very well, where the values of relative error are very small, almost below -40 dB. And the reduction ratio of the CPU time is 0.59% to conventional FDTD, which validated its high efficiency, but with much more memory storage about 80 times of conventional FDTD for trade off. The main part of consuming memory storage is the process of solving the banded nested matrix equation (3), for it involves a lower-upper (LU) decomposition of a large-scale nested coefficient matrix especially when it is with a relative bigger  $Q$  or number of unknown field variables. Although the decomposition is done for only once, it occupies 97.5% of the entire computing time.

In order to reduce the memory storage consuming, a significance improvement of paralleling-in-order solving scheme for original AH FDTD method is also investigated by using the eigenvalue transformation. An AH differential transformation matrix  $[\alpha]$  is introduced and incorporated into original AH FDTD formulations. By using the eigenvector matrix of  $[\alpha]$ , the eigenvalue transformation to the nested matrix equation (3) is performed and  $Q$  decoupled equations can be obtained. For example, the  $q$ -th equation is

$$A(\lambda_q)P^*|^q = J^*|^q \quad (4)$$

where  $A(\lambda_q)$  is a banded sparse coefficient matrix function of eigenvalue  $\lambda_q$ , and  $P^*|^q$  or  $J^*|^q$  are the transformed field

variables or excitation expansion coefficients items. For the coefficient matrixes of matrix equations are functions of eigenvalue, the solution can be achieved in parallel with different orders. The basic methodology and the framework of AH FDTD and its paralleling-in-order solution scheme are shown in Figure 1. Compared to the original AH-FDTD method in the same numerical example, the paralleling-in-order scheme shows less memory consumption and simultaneously much higher efficiency as shown in TABLE I. The memory storage is reduced by 4.24% and the CPU time is improved by 55.1%. More over, the improvement is slightly influenced with the increasing of the orders.

**TABLE I Comparison of the computational recourses.**

	$\Delta t$	Memory (Mb)	CPU times (s)
Conventional FDTD	1.98 fs	0.98	412.31
AH-FDTD	8.0 ps	77.8	2.43
Paralleling-in-order AH-FDTD	8.0 ps	3.30	1.34

By introducing the AH transformation matrix  $T$  [4], the method also shows its potential in solving frequency-dependent dispersive problems in AH domain. Take the liner dispersive medium with parameters  $\varepsilon(\omega)$  as example, using the AH transfer matrix  $T$ , the  $Q$ -tuple electric field  $[E]$  and  $[D]$  in AH domain can be represented by a matrix multiply form

$$[D] = T[E] \quad (5)$$

Then it can be well treated and incorporated with the AH FDTD formulations for the further calculation. So the time domain convolution operator of  $D(t) = \varepsilon(t) \otimes E(t)$  is avoided.

Generally,  $T = [t_{i,j}]_{1 \leq i,j \leq Q}$  is calculated by using the time domain data as  $t_{i,j} = \langle \phi_j(t) \otimes \varepsilon(t), \phi_i(t) \rangle$ , but it can also be obtained directly from the frequency domain  $\varepsilon(\omega)$  using the unique isomorphism property. A first-order Debye dispersive medium is analysed to calculate the reflection coefficients of an infinite planer. And a relative smaller numerical dispersive error is obtained when compared with ADI-FDTD method, which is shown in Figure 3.

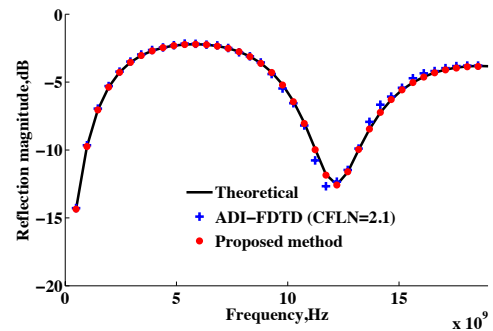


**Figure 3. Reflection magnitude.**

Currently, we are investigating the possibility of march-on-in-order scheme for other orthogonal basis functions.

Hermite-Rodriguez (HR) functions [2] might be a possible one. For clarity, we analysed a 1-D EM propagation through a lossy dielectric slab with the thickness of 0.09 m, relative permittivity of 2, and conductivity of 0.05 S/m. Both the spatial and the time domain numerical results computed by the conventional FDTD and HR FDTD method are agreeable very well with each other, which is shown in Figure 4. Some idea will be further discussed.

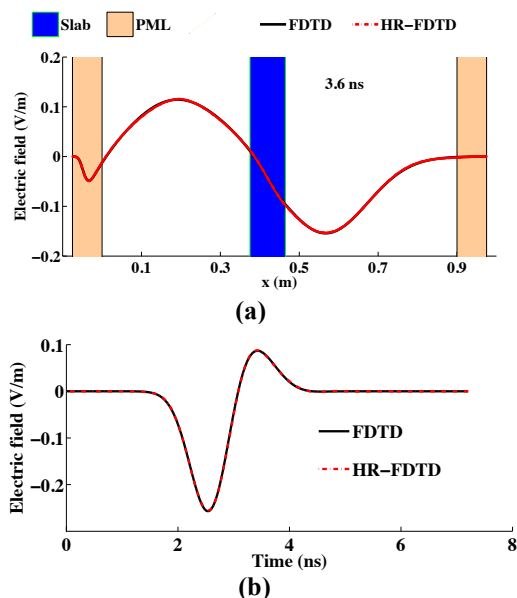


**Figure 4. (a) Electric field spatial distribution at  $t = 3.6$  ns, (b) Transient electric field at  $x = 0.3$  cm.**

## Acknowledgements

This research is supported by the National Natural Science Foundation of China under Grants 51477183 and 51407198.

## References

- [1] Chung Y.S., Sarkar T.K., Jung B.H., and Salazar-Palma M., "An unconditionally stable scheme for the finite-difference time-domain method", *IEEE Trans. Microw. Theory Tech.*, **vol.51**, **no.3**, pp. 697-704, (2003).
- [2] Loredana R. Lo Conte, Roberto Merletti and Guido V. Sandri, "Hermite Expansions of Compact Support Waveforms: Applications to Myoelectric Signals", *IEEE Trans. Biomed. Eng.*, **vol. 41**, **no.12**, pp.1147-1159, (1994).
- [3] Z. Y. Huang, L. H. Shi, Y. H. Zhou and B. Chen, "A new unconditionally stable scheme for FDTD Method Using Associated Hermite orthogonal functions", *IEEE Trans. Antennas Propagat.*, **vol. 62**, **no. 9**, pp. 4804-4809, (2014).
- [4] Shekoofeh, S., Behzad, K. "Time-Domain Distortion Analysis of Wideband Electromagnetic Field Sensors Using Hermite-Gauss Orthogonal Functions," *IEEE Trans. EMC.*, **vol. 54**, **no. 3**, pp. 511-521, (2012).

# Transient response prediction using minimum phase method based on system simulation

Chen Peng\*<sup>†</sup>, Sun Dongyang\*<sup>†</sup>, Wu Gang\*<sup>†</sup>, Chen Weiqing\*<sup>†</sup>

\*Northwest Institute of Nuclear Technology, P.O.Box 69-20, Xi'an, 710024, China

<sup>†</sup>State Key Laboratory of Intense Pulsed Radiation Simulation and Effect, Xi'an, ShanXi, 710024, China

## Abstract

In the area of electromagnetic pulse(EMP) technology, the transfer function is usually used to predict the transient response when a system is radiated by EMP. The complex spectrum is needed in the prediction while the measured continuous wave(CW) transfer function data is usually magnitude-only. If the system is a minimum phase system, its phase can be estimated by Hilbert transform, but it's difficult to judge whether a system is minimum phase in actual cases. In this paper, four types of systems which may exist in actual cases are simulated. The transient responses calculated by circuit software and predicted by minimum phase method are almost identical. The transient response in the center of a shielding box is calculated by an electromagnetic field software, and is predicted by minimum phase method. The predicted response is almost the same with that simulated by software.

**Keywords:** Minimum phase Transient response Prediction

## 1 Introduction

In the research of system-level susceptibility assessments for EMP, it is frequently desired to obtain a knowledge of the transient response of a system. Most data can be measured directly, but it is impossible to test every system in an EMP facility. An alternative way is to obtain the system transfer function and predict the transient response.

The minimum phase system, whose reverse system can be realized physically, is commonly used in system identification and deconvolution. The logarithm of spectral of a minimum phase system is analytical, so the real and imaginary parts are not independent. The two components are related by Hilbert transform which can be derived from an integral in the analytical complex frequency plane using the Cauchy residue theorem.[1][2]. Some research indicates that probes for measuring electric or magnetic field are minimum phase systems, and the transfer function can be reconstructed from magnitude only[3][4]. In another research, the double exponential waveform and damped oscillating waveform are reconstructed respectively using the cepstrum[5].

In this paper, the transient responses of lowpass, highpass, bandpass and bandstop systems are calculated and predicted, bas-

ed on the research above. In addition, a 3-D model of a shielding box with a circular hole is built in a computational electromagnetic software, and the transient response is calculated. The magnitude of the transfer function is obtained by minimum phase method, and the prediction of response is illustrated.

## 2 Transient response prediction based on circuit simulation

There are many different systems in the area of EMP. For example, a shielding cable excited by EMP field can be seen as a system. The response current is the output of the system and the field is the input. These various systems can be simulated in softwares or programmes.

### 2.1 Phase reconstruction from magnitude of a minimum phase system

Considering a minimum phase sequence  $x(n)$ , if the magnitude is known, then it can be reconstructed without the phase as follows[6]:

Firstly, get the natural logarithm of the magnitude  $|X(k)|$ , and symmetrise the sequence

$$X_{\ln}(k) = \ln|X(k)|, k = 1, 2, \dots, N/2. \quad (1)$$

$$X_{\ln}(N/2 + j) = \ln|X(N/2 - j)|, j = 1, 2, \dots, N/2 - 2 \quad (2)$$

where  $N = 2^n$ , and  $n$  is an integer. The IFFT of  $X_{\ln}$  can be written as

$$x_{\ln}(n) = \text{IFFT}(X_{\ln}) \quad (3)$$

then a new sequence  $x_{\text{new}}(n)$  can be set as

$$x_{\text{new}}(n) = \begin{cases} x_{\ln}(n) & n = 1, \dots, N/2 \\ 2x_{\ln}(n) & n = 2, \dots, N/2 - 1 \\ 0 & n = N/2 + 1, \dots, N - 2 \end{cases} \quad (4)$$

the minimum phase sequence is expressed as

$$x_{\min}(n) = \text{IFFT}(e^{\text{FFT}(x_{\text{new}}(n))}) \quad (5)$$

### 2.2 Results comparison between the circuit simulation and transfer function prediction

There are upper limits in frequency domain of the probes used in EMP measurement, so the similarity between probes and

lowpass filters is noticed. A lowpass system that may exist in actual cases is considered and simulated in circuit software. The frequency domain circuit for obtaining the magnitude of the system is shown in Fig.1

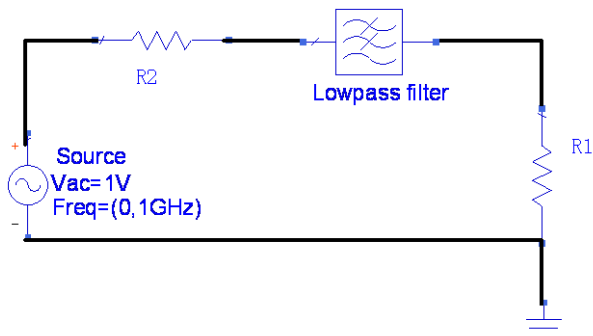


**Figure 1. Frequency domain circuit for obtaining the magnitude.**

The parameters of the lowpass filter in the circuit are set, and the source is set in frequency domain. The magnitude is obtained by circuit simulation and then the system transfer function is calculated by minimum phase method. The transient response is obtained by simulate the circuit in time domain, as shown in Fig.2.

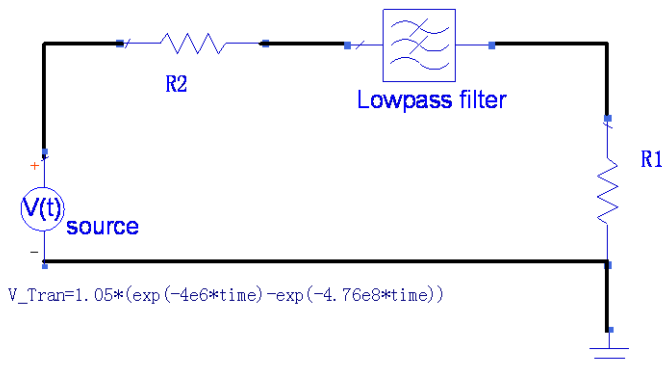


**Figure 2. The transient circuit excited by EMP waveform**

The transient responses of highpass system, bandpass system and bandstop system are obtained in the same way as introduced in Fig.1 and Fig.2. The results predicted and simulated are illustrated in Fig.3

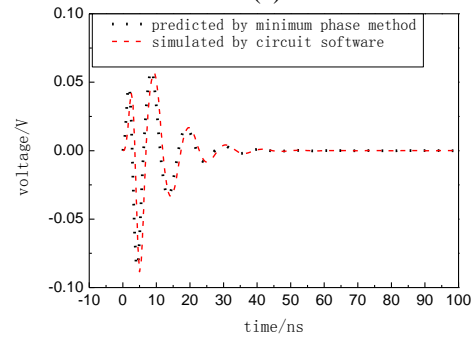
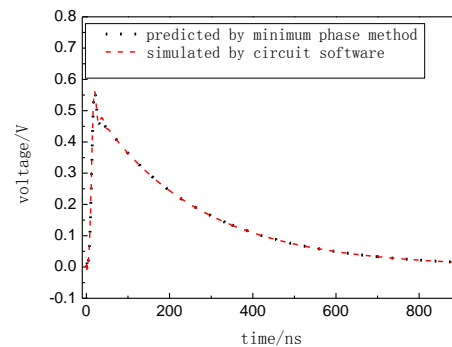
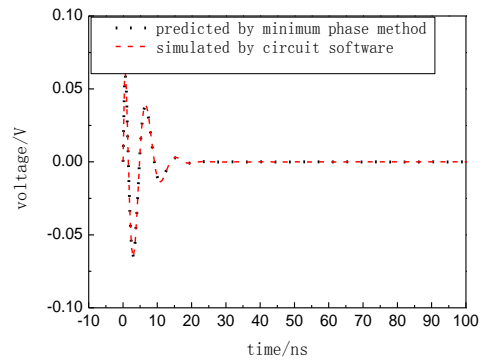
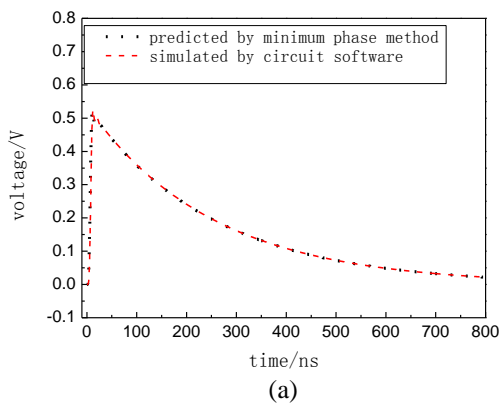


**Figure 3. Response predicted and simulated for different kind of systems.(a)lowpass system.(b)highpass system.(c)bandstop system.(d)bandpass system**

The results comparison indicate that in actual cases, transfer functions of lowpass, highpass, bandpass and bandstop system can be reconstructed by magnitude only, and the minimum phase method is validated in the response prediction process.

### 3 Transient response prediction based on 3-D electromagnetic field simulation

In the area of system-level susceptibility assessments and hardness validation, the system response excited by EMP is desired. So the research about the transient response in a shielding box is much more closer to reality. A shielding box

with a simple circular hole is built in the 3-D electromagnetic field simulation software, as shown in Fig.4.

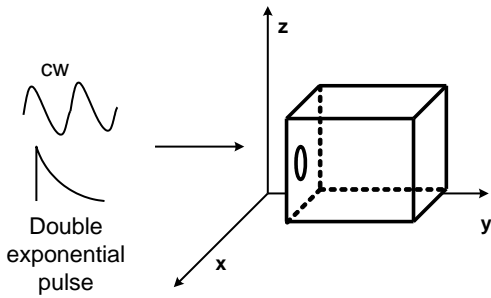


**Figure 4. 3-D model for electromagnetic field computation**

The model is a metal cubic box which side length is 40cm, and the diameter of the hole is 10cm. A field monitor is placed in the center of the box and the CW frequency swap range is set from 10kHz to 1GHz. The magnitude of transfer function about the inner response and the CW electric field is shown in Fig.5

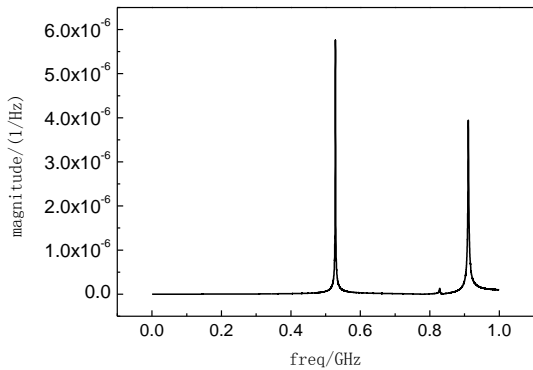


**Figure 5. Magnitude of the shielding box transfer function**

As shown in Fig.5, there are two resonant frequencies in the box, 528MHz and 911MHz. They are intrinsic frequencies and determined by the dimension of the box as follows[7]

$$\omega_{\text{mnp}} = \frac{\pi}{\sqrt{\mu\epsilon}} \sqrt{\left(\frac{m}{a}\right)^2 + \left(\frac{n}{b}\right)^2 + \left(\frac{p}{l}\right)^2} \quad (6)$$

The resonant frequencies derived from (6) are 529MHz and 917MHz, which are 0.19% and 0.66% higher than the results simulated, because of the circular hole.

The transient response excited by Bell lab. EMP waveform is shown in Fig.6.

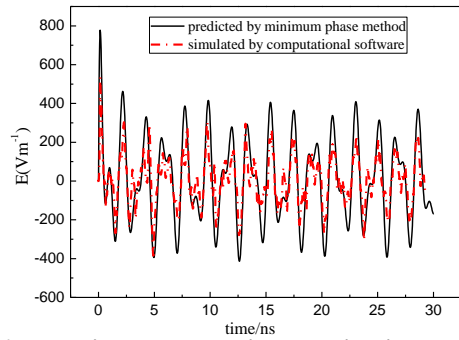


**Figure 6. Transient response in the shielding box excited by EMP.**

The dash line in Fig.6 is calculated by CST software. The dash dot line is predicted by minimum phase method. In this example, there is some difference between the peaks of the two waveforms, but the oscillation period is almost identical. The difference in peaks may be caused by the FFT transformation and the cut-off magnitude(>1GHz).

#### 4 Conclusion

In this paper the transient responses of different systems are simulated and the response prediction method is discussed. The waveforms predicted by minimum phase method are illustrated to compare with the simulated responses, and the predictions exactly show the characteristics of the simulated responses.

#### Acknowledgements

The author would like to acknowledgement helpful discussions with Dr. Cheng Yinhui about the minimum phase method and his advise on the circuit simulation.

#### References

- [1] Frederick M. Tesche. "On the use of Hilbert transform for processing measured cw data", *IEEE Trans on EMC*, **34(3)**, pp.259-266, (1992).
- [2] Hayes H M, Lim J S, Oppenheim A V. "Signal reconstruction from phase or magnitude", *IEEE Trans on Acoustics, Speech, and Signal Processing*, **28(6)**, pp.672-680, (1980).
- [3] Shi L H, Zhou B H. "Time domain characterization of a system based on the magnitude of its frequency response", *Chinese Journal of Radio Science*, **15(4)**, pp.467-471, (2000).
- [4] Cao J Y, Xie S G, "Application of minimum phase method in a pulse measurement", *Chinese Journal of Radio Science*, **26(6)**, pp.1103-1106, (2011).
- [5] Xie Y Z, Wang Z J, "Reconstruction of electromagnetic pulse waveform based on the amplitude spectrum data", *High Power Laser and Particle Beams*, **16(3)**, pp.320-324, (2004).
- [6] Oppenheim A V, Schaffer R. "Discrete-Time Signal Processing", *Englewood Cliffs, NJ: Prentice-Hall*, (1989).
- [7] Zhang K Q, Li D J. "Electromagnetic Theory for Microwaves and Optoelectronics", *Beijing: Publishing House of Electronics Industry*, pp. 250-252, (2001).

# Shielding Effect Analysis to Square Waves of Slotted Cavity Based on Shielding Effectiveness Curves

HU Xiao-feng, Liu Weidong, Chen Xiang, Wei Ming

(Institute of Electrostatic and Electromagnetic Protection, Mechanical Engineering College, Shijiazhuang 050003, China)

## Abstract

As we known that shielding effectiveness curves characterize the shielding effect of the shielded system to the electromagnetic waves in frequency domain, but for electromagnetic pulse waves, the curves have some disadvantages. For example, the rise time, pulse width and other information of the electromagnetic pulse cannot be analyzed. The frequency domain test system was built by using GTEM cell in this paper, and the frequency domain shielding effectiveness curves of the small cavity with different size slots were developed. Based on the curves, the time-domain waveform in the small cavity can be reconstructed with the minimum phase method. As can be seen from the reconstruction results, the waveform reconstruction method based on minimum phase can roughly calculate the time domain waveform of the square waves that passed through the slot, therefore it is suitable for estimation the time domain shielding effectiveness of the slotted cavity under square wave excitation.

**Keywords:** time-domain shielding effectiveness; square waves; waveform reconstruction; minimum phase systems.

## 1 Introduction

Shielding effectiveness of existing measurement standards are usually described in frequency domain by using continuous wave measurements. By measuring the amplitude response of a system at each frequency point, the shielding effectiveness can be represented by the amplitude-versus- frequency curve, and then the shielding ability of the shielded system to electromagnetic wave on the measured frequency point can be comprehensively understand. But with the research of high power electromagnetic pulse interference, people have found that the shielding effectiveness in frequency domain can not fully characterize the shielding effect of the shielded system to the electromagnetic pulse field in time domain.<sup>[1-7]</sup>

At present, the peak value of electromagnetic pulse is mostly used to calculate the shielding effectiveness of the pulse energy, which can not directly determined from the frequency domain measurement<sup>[8-10]</sup>. Meanwhile, the shielding effectiveness calculated only with the peak value can not fully meet the needs of the design for electromagnetic pulse protection because the rise time, pulse width and other information of the electromagnetic pulse is equally important with its peak value.

Based on the analysis of waveform reconstruction method, the flow chart of transfer function reconstruction and

waveform recovery with minimum phase method of the slotted cavity shielding effectiveness was proposed. The shielding effectiveness and transfer function in frequency domain of a small cavity can be obtained through simulation and experiment, and then the square waveform of square waves in the cavity can be reconstructed. By analyzing the shielding effectiveness of the cavity under square wave excitation, the method of transfer function reconstruction and waveform recovery based on minimum phase was verified correctly.

## 2. Experiment setup and results

The frequency domain test system was built by using GTEM cell as shown in Fig.1. In the experiment, the gain of power amplifier, which is a broadband power amplifier with 4000w and 80MHz-1000MHz, was set to 50%; the SML01 RF signal source was set to -5dBm; the EMR-200 E-field strength meter in the center place with a distance of 30cm from the slot, which can be used for 100kHz~3GHz and 0.6-800V/m, was connected to a notebook by using the optical fiber. slotted small cavity and the experiment setup is shown in Figure 2.

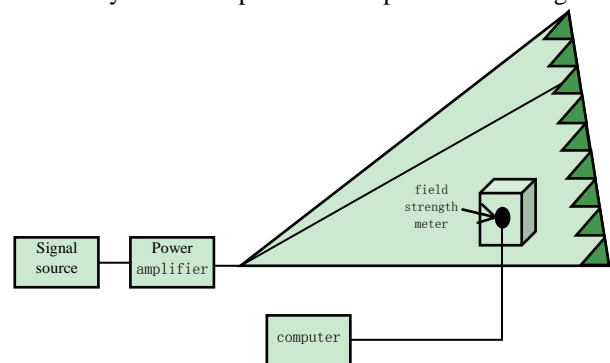


**Figure 1. Experiment configuration of the frequency domain test**

The frequency domain shielding effectiveness curves of the small cavity with different size slots were measured as shown in Figure 3. It can be seen that both shielding effectiveness curves have the same trend, and there are two resonance points in 400MHz and 700MHz, these results show that the small cavity with different size slots have the two main resonance frequency points because the resonance theory. Furthermore, the shielding effectiveness with the slot size of 50mm×40mm is higher than another slot size of

200mm×10mm, which is consistent with the simulation results.

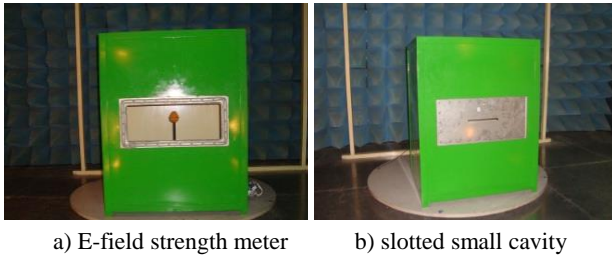


**Figure 2. Experiment setup and its physical equipment**

The frequency domain shielding effectiveness curves of the small cavity with different size slots were measured as shown in Figure 7. It can be seen that both shielding effectiveness curves have the same trend, and there are two resonance points in 400MHz and 700MHz, these results show that the small cavity with different size slots have the two main resonance frequency points because the resonance theory. Furthermore, the shielding effectiveness with the slot size of 50mm×40mm is higher than another slot size of 200mm×10mm, which is consistent with the simulation results.

Compared with Figure 3, The calculate results have more resonance points and higher shielding effectiveness than the measuring results. There are some reasons including the calculating model with no considering some other slots and holes of the cavity, the measuring work with the frequency steps of 50MHz and so on.

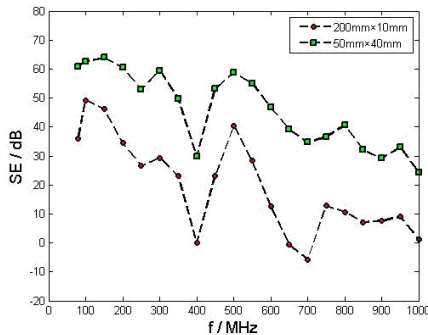


**Figure 3. Shielding effectiveness curves of two slotted small cavities**

### 3. Square waves shielding effectiveness analysis based on waveform reconstruction

Known to shield the frequency-domain curve of SE of body, will not shield the square wave excitation as the input of the system, shielding the body's response to the output of the system, the frequency-domain transfer function  $H(\omega)$  using the formula (1) to get. Then according to the frequency-domain transfer function, assuming that minimum phase systems to calculate the time-domain transfer function, and square wave time-domain waveform convolution unshielded, shielded by the shield, the time-domain waveform  $E_m(t)$ , and then estimated time-domain SE of the shield.<sup>[11]</sup>

$$SE = 20 * \log_{10} \frac{E_{unshielding}(\omega)}{E_{shielding}(\omega)}$$

$$H(\omega) = \frac{E_{shielding}(\omega)}{E_{unshielding}(\omega)} = 10^{-\frac{SE}{20}} \quad (1)$$

According to the frequency domain shielding effectiveness that measured, the time-domain waveform in the small cavity can be reconstructed with the minimum phase method. The square waveform measurement in GTEM cell was selected as the input pulse, and the reconstructed waveform can be seen in Figure 4.

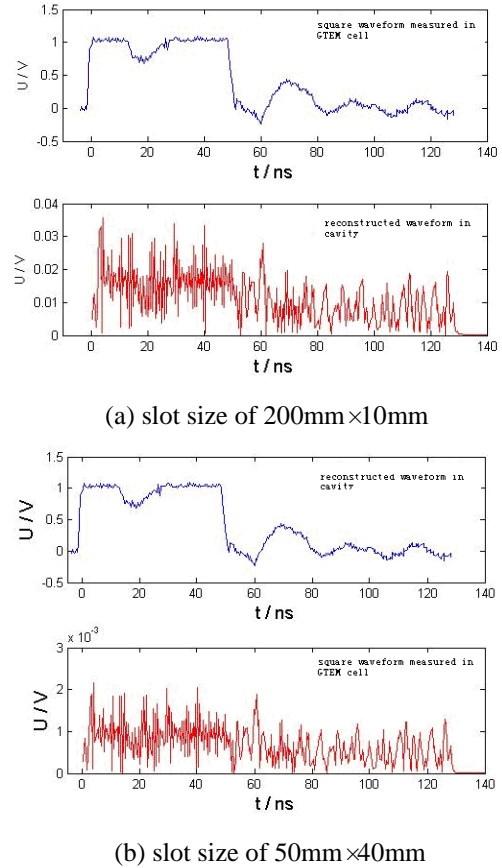


**Figure 4. Waveform reconstruction in two cavities with different slot size**

As can be seen from the reconstruction results, the waveform reconstruction method based on minimum phase can roughly calculate the time domain waveform of the square waves that passed through the slot, therefore it is suitable for estimation the time domain shielding effectiveness of the slotted cavity under square waves excitation. As shown in Figure 4, the shielding effectiveness, with the slot size of 200mm×10mm, calculated with the peak value is about 35dB while another is about 60dB with the slot size of 50mm×40mm. Those calculated results are only consistent with the low-frequency shielding effectiveness that measured in frequency domain, so it is not suitable to calculate the square waves shielding effectiveness only with the pulse peak, the rise time, pulse width and other parameters of the square waves can also be considered. In this experiment, it can be seen that the waveform of the square wave that reconstructed in the cavity

have some differences with the input square wave, which indicated that the rise time and pulse width of the pulse should be considered in the square waves shielding effectiveness calculation. In addition, the reconstruction algorithm used in this paper assumes the system is minimum phase systems, which is not suitable for every shielded system, and it is also unable to reconstruct the time domain waveform of the square waves in a slotted cavity with strong resonance.<sup>[12,13]</sup>

#### 4. Conclusions

Some conclusions are showed as follows: (1)The waveform reconstruction method based on minimum phase, can roughly calculate the time domain waveform of square waves through the slotted small cavity, and it is suitable to estimation the time domain shielding effectiveness of slotted small cavity with square waves excitation; (2)while it is not suitable to the slotted cavity with strong resonance; (3)the time domain response of the mixed-phase shielded system under pulse excitation should be researched in future. Meanwhile, by using the frequency domain transfer function fitting with rational function and the inverse Laplace transform, a new method to calculate the time domain impulse response can be studied based on the recursive convolution algorithm.

#### Acknowledgements

This work was financially supported by the National Natural Science Foundation of China. (61001050)

#### References

- [1] BAO Yongfang, LU Yinghua, ZHANG Hongxin, HAN Chunyuan. The Analysis of Shielding Effectiveness of Negative Permittivity Composite Materials to Different EMP. *IEEE International Symposium on Microwave, Propagation and EMC Technologies for Wireless Communications Proceedings*, pp.635-638(2005).
- [2] Special issue on high-power electromagnetic (HP EM) and intentional electromagnetic interference (IEMI). *IEEE Trans. EMC*, **46**, pp.314-496,(2004).
- [3] Andrew C. Marvin, John F. Dawson and Simon Ward, et al. A Proposed New Definition and Measurement of the Shielding Effect of Equipment Enclosures. *IEEE Trans. On Electromagnetic Compatibility*, **46**, pp. 459-468, (2004).
- [4] MICHEL AGUET, MIRCEA IANOVICI, and CHUNG-CHI LIN. Transient Electromagnetic Field Coupling to Long Shielded Cables. *IEEE Trans. On Electromagnetic Compatibility*, **22**, pp. 276-282, (1980).
- [5] M. P. Robinson, T.M.Benson and C. Christopoulos. Analytical formulation for the Shielding Effectiveness of Enclosures with Apertures. *IEEE Trans. on Electromagnetic Compatibility*, **40**, pp.240-248,(1998).
- [6] David W P Thomas. Alan C Demon. Tadeusz Konefal, et al. Model of the electromagnetic fields inside a cuboidal enclosure populated with conducting planes or printed circuit board. *IEEE Trans. on EMC*, **43**, pp.161-169,(2001).
- [7] LI MIN, James L Drewniak, Sergin Radu, et al. An EMI estimate for shielding-enclosure evaluation. *IEEE Trans. on EMC*, **43**, pp.295-304,(2001).
- [8] ZHOU Bihua, GAO Cheng, REN Heming. The Definition of EMP Shielding Effectiveness. *Asia-Pacific Conference on Environmental Electromagnetics*, pp.562-565,(2003).
- [9] ZHOU Bihua, GAO Cheng, CHEN Bin, CHEN Ziming. Experimental Investigation of EMP Shielding Effectiveness of Reinforced-Concrete Cell Model. *Asia-Pacific Conference on Environmental Electromagnetics*, pp.296-300,(2000).
- [10] J. P Bruhin. Shielding Effectiveness of Reinforcement Concrete against Electromagnetic Wave. *EMP 84 Parts 2*, pp.597-605.
- [11] HU Xiaofeng, CHEN xiang, WEI Ming. Time-Domain Simulation and Waveform Reconstruction for Shielding Effectiveness of Materials against Electromagnetic Pulse, *the 7th International conference on applied electrostatics*, Dalian,China,83-84,(2012)
- [12] SHI Lihua, ZHOU Bihua, CHEN Bin, GAO Cheng. Time domain characterization of a system based on the magnitude of its frequency reponse. *Chinese journal of radio science*, **15**, pp.467-471 (2000).
- [13] CHEN Xiang, CHEN Yongguang, WEI Ming, HU Xiaofeng. Time Domain Testing Methods of Material' s Shielding Effectiveness of Electromagnetic Pulse Using Flange Coaxial, *High Voltage Engineering*, **28**, pp.594-600, (2012).

HU Xiao-feng was born in Jixi city, Anhui Province, China, in 1977. He received the B.Sc, M.Sc and Ph.D. degree in Mechanical Engineering College. He is a vice-professor in Mechanical Engineering College now and studies electromagnetic pulse measurement and electromagnetic protection to electronic systems.

# Fourier-Collocation Method for the Surface Current Distribution On the Thin Antenna

H K Lin\*, J S Luo\*, L Sun\*, W X Hou†

\*College of Science, National University of Defense Technology, Changsha, China  
e-mail:linhekai10@163.com

†PLA 94452, Henan, China

## Abstract

Fourier-Collocation method for solving the current distribution on the cylindrical thin center-fed dipole antenna is applied in this paper. It needs less basis functions than NEC method and both of the current distributions are approximate. Comparisons of input impedance at the center of the antenna and the elapse time between Fourier-Collocation and Pulse-Collocation which was obtained with pulse base and Dirac- $\delta$  testing are made. Both current distributions of our method and approximate analysis method are presented in same figure. The accuracy and efficiency of numerical results clearly show the efficient application of our method on the numerical calculation for the integral equation.

**Keywords:** Fourier-Collocation, Current Distribution, Hallen Integral Equation.

## 1 Introduction

As the complex antennas are concerned, it is effective to analyze the electromagnetic properties of complex antennas by decomposing them into some simple antenna elements. Therefore, the significance of searching effective and fast methods for researching antenna elements is clear. After acquiring current distribution on antennas, their basic parameters and radiation fields can be obtained. Current distribution of integral equation can be used to simulate antenna model. To obtain current distribution on thin-wire antenna, Professor Jones presented valid methods based on Hallen integral equation [1,2]. Wang put forward a linear representation of the integral kernel based on Bessel function series [3]. However, its error is large as the variable approaches origin point. Correspondingly, Pearson proposed that the integral equation kernel could be separated from continuous function items and Logarithmic function item with singularity [4]. The error of his method is larger than Wang's when distant point is taken into consideration. At present, The Method of Moments has high accuracy without considering the regularity of solution.

In order to solve Hallen integral equation fast, we approximate the current distribution by a short sum of some continuous global basis functions based on MoM, which

contributes to reasonable continuous results with low computing resource. Our method is compared with NEC which uses local sinusoidal functions as basis functions, but both of current distributions are very similar.

## 2 Cylindrical Thin Dipole Antenna

### 2.1 Hallen Integral Equation

Dipole antenna is the most basic model. This paper is based on dipole antenna driven by incident field  $E_{in}$ . The antenna induces current by  $E_{in}$ , and current produces electric field. There is a cylindrical thin antenna, its length is  $l$ , radius is  $a$ , and cylindrical coordinate system is established, like figure 1 [5]. Supposing that current distribution function was  $I(z)$ .

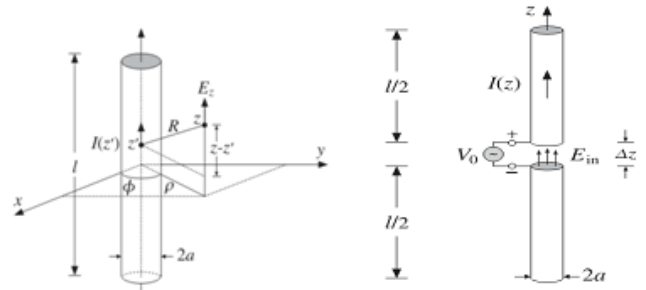


Figure 1. Cylindrical Antenna

According to work [5], Hallen integral equation was raised based on arbitrary incident field.

$$\frac{j\eta}{2\pi} \int_{-h}^h K(z-z') I(z') dz' = C_1 \cos kz + C_2 \sin kz + \int_{-h}^h G(z-z') E_{in}(z') dz' \quad (1)$$

Define  $h=l/2$ ,  $\eta = \sqrt{\mu/\epsilon}$  and  $c\omega\epsilon\mu = \omega/c = k$ . In free space,  $\eta$  is  $120\pi\Omega$ . The excitation is  $V_0\delta(z)$ .

The integral kernel is written as

$$K(z-z') = \frac{e^{-jkR}}{R}, R = \sqrt{(z-z')^2 + a^2}$$

The Green function  $G(z)=\sin(k|z|)$  can be used in this integral equation [5]. The boundary condition is  $I(h)=I(-h)=0$ , which

can ensure constant  $C_1$  and  $C_2$ . Since current distribution is symmetrical,  $C_2$  is equal to zero. A more simple Hallen integral equation is obtained.

$$\frac{j\eta}{2\pi} \int_{-h}^h K(z-z')I(z')dz' = C_1 \cos kz + V_0 \sin k|z| \quad (2)$$

## 2.2 The Determination of Parameter Matrix

In order to transform integral interval  $[-h, h]$  into  $[0, \pi]$ , it chooses transformation  $z=h \cos(t)$ . Then, the integral interval is divided into  $N$  equal parts, and the center point of each part is taken as the collocation point. Therefore It can be written as,  $t_i = (2i+1)\pi/2N$ ,  $i=0,1,2,\dots,N-1$ . As the model is symmetrical, the following cosine functions are chosen as basis functions.

$$e_j(y) = \begin{cases} \frac{1}{\sqrt{2\pi}} & j=0 \\ \frac{1}{\sqrt{2\pi}} \cos jy & j \neq 0 \end{cases}$$

A linear combination of basis functions of current distribution can be obtained.  $u(y) \approx u_N(y) = \sum_{j=0}^{N-1} a_j e_j(y)$ . Where  $u(y)$

is  $I(h \cos(y)) \sin(y)$ . All above are substituted into integral equation, and algebraic equation is presented.

$$KA = C_1 G + F \quad (3)$$

Finally, The Parameter Matrix can be written as.

$$A = C_1 K^{-1} G + K^{-1} F.$$

$$k_{ij} = \int_0^\pi K(h \cos t_j - h \cos y) e_i(y) dy$$

$$g_j = \frac{2\pi}{j\eta h} \cos(kh \cos t_j)$$

$$f_j = \frac{2\pi}{j\eta h} V_0 \sin k |h \cos t_j|$$

$$K = (k_{ij})_{N \times N}, G = (g_j)_{N \times 1},$$

$$F = (f_j)_{N \times 1}, A = (a_j)_{N \times 1}$$

According to boundary conditions, constant  $C_1$  can be ensured.

$$C_1 = -\frac{[E(0)]K^{-1}F}{[E(0)]K^{-1}G}$$

## 2.3 Numerical Simulation and Analyze

Calculate the current distribution on the center-fed antenna. The parameters are as follows: the antenna length  $l=0.5\lambda$ , the radius  $a=0.007\lambda$ , the feed voltage 1V. Figure 2 shows the results of current response, which is divided into real part and imaginary part.

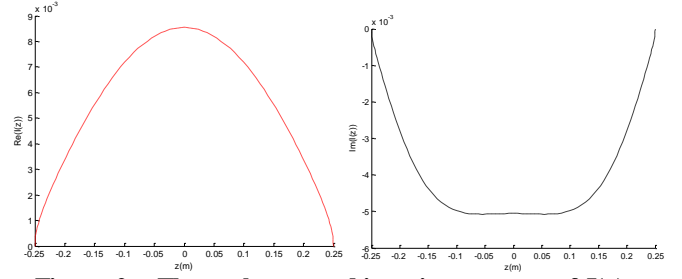


Figure 2. The real part and imaginary part of  $I(z)$ ,  $l=0.5\lambda$ ,  $a=0.007\lambda$ ,  $N=30$ .

We choose NEC method to compare the accuracy of result, figure 3 following.

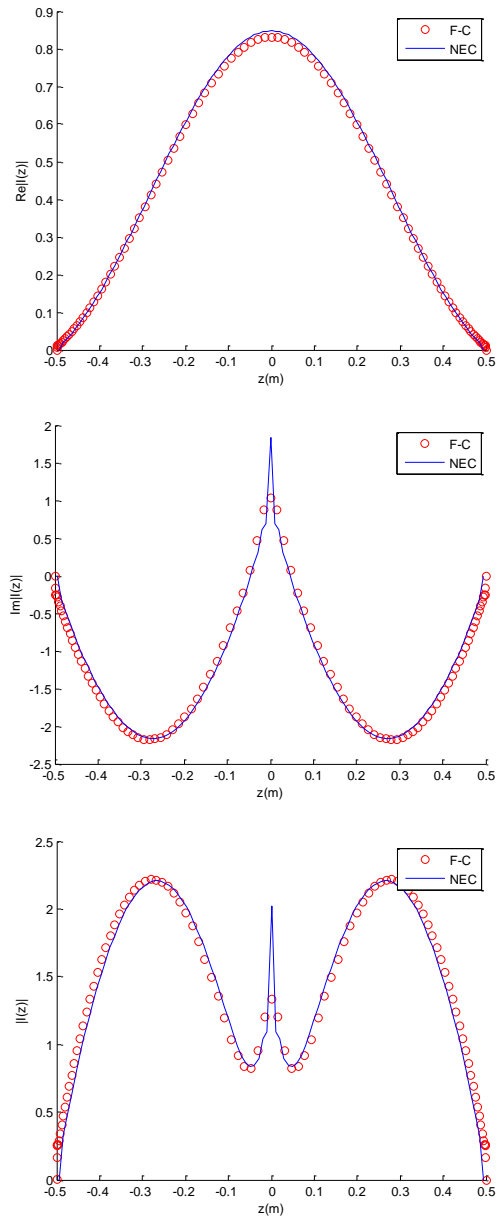


Figure 3. The real part, imaginary part and norm of  $I(z)$  for F\_C and NEC,  $l=\lambda$ ,  $a=0.005\lambda$ ,  $N=50$ .

In order to obtain effect of numerical simulation, Comparisons of input impedance and the elapsed time between Fourier-Collocation (F-C) and Pulse-Collocation (it use piecewise linear polynomials as basis functions, P-C) are adopted.

Table 1: Comparisons of impedance at  $z=0$  and elapsed time between P-C and F-C,  $l=0.4\lambda$ ,  $a=0.005\lambda$ .

P-C			F-C		
$N$	$I(0)/V_0$	t(s)	$N$	$I(0)/V_0$	t(s)
10	0.0111	0.327	10	0.0109	0.527
20	0.0116	1.525	20	0.0119	1.798
30	0.0117	4.283	30	0.0120	3.106
40	0.0118	8.569	40	0.0121	7.038
50	0.0118	13.384	50	0.0121	12.203

As the number of basis functions is increased, the impedance at  $z=0$  approximates  $0.012 \ 1/\Omega$ , but F-C is as fast as P-C. However, F-C needs less basis functions to decrease error than P-C at times. According to [5], the equation can be approximated by the following formula,

$$\frac{j\eta}{2\pi} \int_{-h}^h K(z-z')I(z')dz' \approx XI(z) \quad (4)$$

$$= C_1 \cos kz + V_0 \sin |z|$$

$X$  is the mean of  $j\eta K(z-z')/2\pi$  in integral interval. Then, it is an approximate analysis method and the current can be written as,

$$I(z) = I(0) \frac{\sin(k(h-|z|))}{\sin kh}, I(0) = -\frac{V_0 \sin kh}{X \cos kh} \quad (5)$$

Comparing their current distributions, their relative error is under 5%.

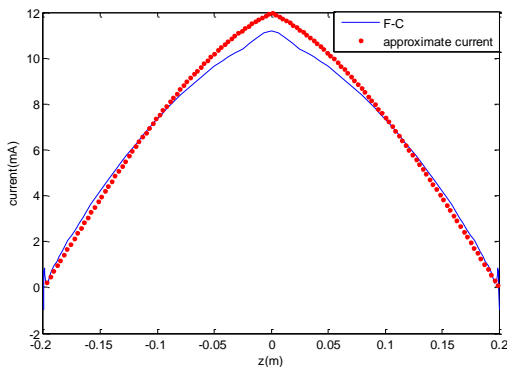


Figure 4. The real part and imaginary apart of  $I(z)$ ,  $l=0.5\lambda$ ,  $a=0.007\lambda$ ,  $N=30$ .

### 3 Conclusion

For the center-fed cylindrical thin antenna, this paper presents Fourier-Collocation method based on the Hallen integral

equation. Comparisons of results between F-C and P-C are made. It shows that F-C method can ensure both accuracy and calculation speed. However, Measures should be taken to settle integral kernel with singularity, and case that current appears volatility on both endpoints of the antenna.

### Acknowledgments

This work is supported by the National Natural Science Foundation of China (No.61171018).

### References

- [1] G. Fikioris, T. T. Wu. "On the Application of Numerical Methods to Hallen Equation", *IEEE Transactions on Antennas and Propagation*, **49(3)**, pp. 383-392, (2001).
- [2] D. S. Jones "Note on the integral equation for a straight wire antenna", *IEE Proceedings on Microwaves, Optics and Antennas*, **128(2)**, pp. 114-116, (1981).
- [3] W. X. Wang. "The exact kernel for cylindrical antenna", *IEEE Trans. Antennas Propagat*, pp. 434-435, (1991).
- [4] L. W. Pearson. "A separation of the logarithmic singularity in the exact kernel of the cylindrical antenna integral equation", *IEEE Trans. Antennas Propagat*, pp.256-258, (1975).
- [5] S. J. Orfanidis. "Electromagnetic Waves and Antennas", Rutgers University, pp. 801-859, (2004).
- [6] K. S. Yee. "Numerical Solution of Initial Boundary Value Problems Involving Maxwell's Equations in Isotropic Media", *IEEE Transactions on Antennas Propagation*, **14**, pp. 302-307, (1966).
- [7] G. FIKIORIS. "The approximate integral equation for a cylindrical scatterer has no solution", *Electromagnetic Waves*, pp. 1153-1159, (2001).

# Transient Voltage Responses of Multilayered PCBs in Metallic Enclosure Illuminated by Periodic Electromagnetic Pulse

Yuna Kim\*, Jin-Kyoung Du\*, Se-Young Hyun\*, Jong-Gwan Yook\*,  
Jongwon Lee†, and Jin Soo Choi †

\*Dept. Of Electrical and Electronic engineering, Yonsei University, Seoul, Republic of Korea, jgyook@yonsei.ac.kr  
†Agency of Defense Development, Daejeon, Republic of Korea, jwlee@add.re.kr, jschoi@add.re.kr

## Abstract

The impact of periodic electromagnetic pulse (EMP) is highly affected by enclosure and target PCB within it. As well as a property of pulse, resonant frequencies of metallic enclosure and PCB determine the transient voltage response of the signal trace on the PCB. Periodic EMP used in this paper is mainly distributed under 1 GHz. As the number of resonant frequencies in the range of 0 GHz – 1 GHz increases, the voltage coupling to the trace on PCB is intensified. Under the same periodic EMP, the maximum voltage coupling is 10 times higher than before as the length of the PCB quadruples.

**Keywords:** Electromagnetic transients; EMP radiation effects; Printed circuits; Electromagnetic pulse

## 1 Introduction

When target is illuminated by periodic electromagnetic pulse (EMP), it causes many undesirable electromagnetic phenomena. The enclosures which include PCBs within them are useful to protect the circuit boards from the harmful effect. Many studies demonstrate the shielding effectiveness especially for metallic enclosures [1-2]. When the PCB is placed in the enclosure, the coupling to PCB has totally different tendency. As well as the orientation of PCB [3], the resonant frequencies of enclosure and multi-layered PCB are dominant factors to decide how much the electromagnetic coupling occurs [4]. After the coupling from external EMP to PCB, unwanted results are observed ranging from malfunction to breakdown of the device [5-6]. These are the result of transient process which is a complex combination of thermal, mechanical, and electrical interactions. Thus, the coupling characteristics should be analysed in transient response. This study demonstrates the effect of PCB design on transient voltage response for various conditions.

## 2 Configuration

The metallic rectangular enclosure with aperture contains multilayered PCB as shown in figure 1. The aperture allows periodic EMP to go through and to have influence on the PCB. The permittivity of the board is considered as 4. Target PCB consists of 6 layers including two power and ground plane as

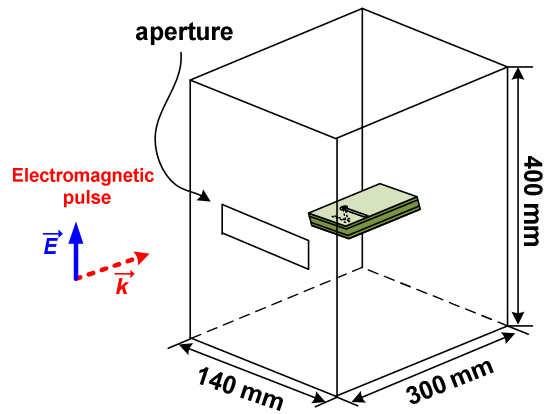


Figure 1. Multilayered PCB in metallic enclosure

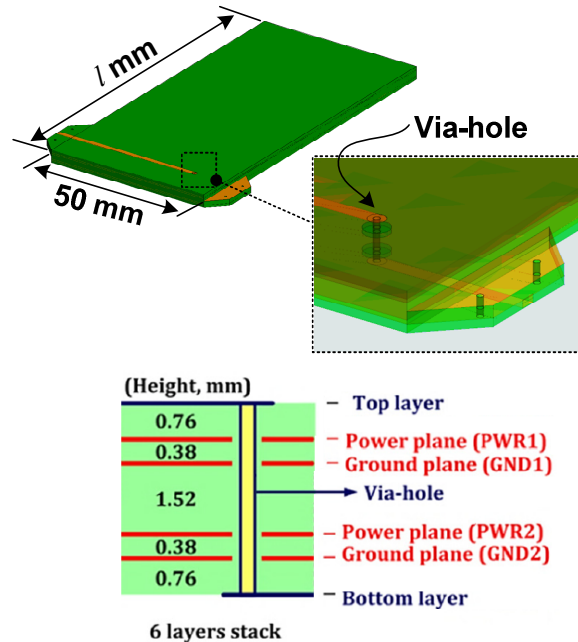
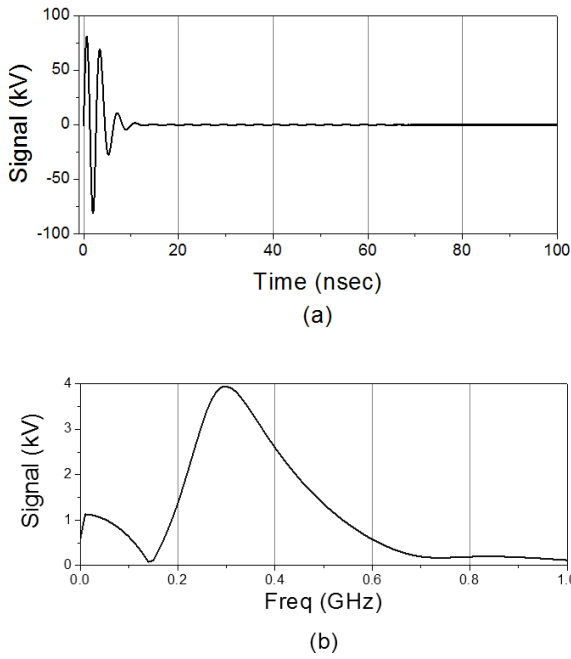


Figure 2. PCB structure with via-hole

shown in figure 2. Several via-holes on the board enhance the effect of resonance between power and ground plane.

## 3 Transient Voltage Response



**Figure 3. Incident electromagnetic pulse in (a) time domain and (b) frequency domain**

The radiated pulse is shown as figure 3. The pulse is generated in the experiment conducted in [7]. It is assumed to be vertically polarized. The number of repetition is 10 with the period of 0.1 seconds. In frequency domain shown in 3(b), the power of the pulse is mainly distributed under 1 GHz. Thus, the existence of resonant modes in that frequency range is one of the critical factors.

Figure 4 shows the transient voltage response for the cases with two different  $l$  in figure 2:  $l = 64$  mm and  $l = 250$  mm. The amplitude and shape are totally different from original radiated pulse. For both cases, the level of coupling voltage cannot reach one tenth of original pulse. Under the exposure to same periodic EMP, different PCB size causes dissimilar coupling characteristics on the signal traces. As well as the shape of pulse, the maximum voltage coupling for  $l = 250$  mm becomes ten times higher than PCB with  $l = 64$  mm as shown in the figure 4. As the multi-layered PCB lengthened, the impact of periodic EMP is intensified. The tendency can be observed in figure 5. The PCB with longer  $l$  allows more resonant frequencies to appear in the range of 0 GHz – 1GHz. Then it increases the coupling to signal trace.

#### 4 Conclusion

The transient voltage response is decided by two factors: property of input pulse and resonant characteristics of target structure. Although PCB is placed in the identical circumstances, the change of the length of PCB is able to increase the number of resonant modes. It leads higher voltage coupling to signal traces on the board. The result reveals that proper design is required to increase the

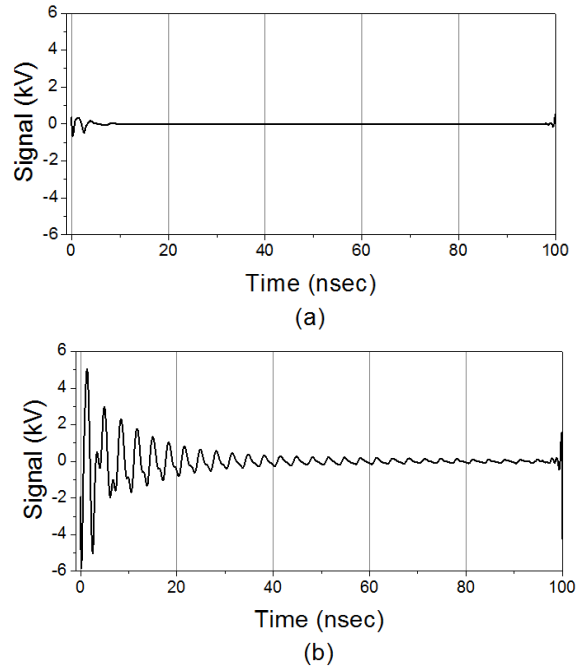


**Figure 4. Coupled voltage signals when (a)  $l = 64$  mm and (b)  $l = 250$  mm**

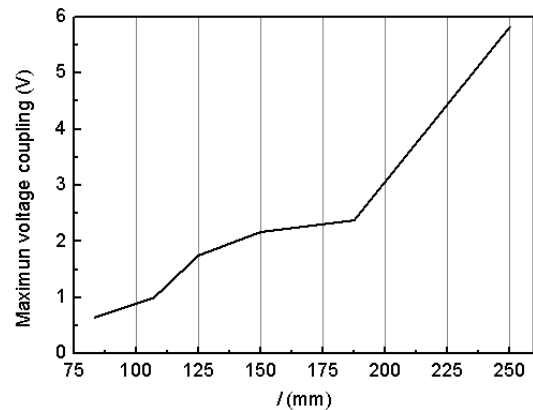


**Figure 5. Maximum voltage coupling as  $l$  is changed**

shielding effectiveness of a device. In the future work, succeeding analysis can provide us the guideline to design the enclosure and PCB arrangement in order to suppress the impact of periodic EMP.

#### Acknowledgements

This work was supported by Agency for Defense Development, Daejeon, Republic of Korea.

## References

- [1] T. Yang and J. L. Volakis, "Coupling onto wires enclosed in cavities with apertures," *Electromagnetics*, vol. 25, pp. 655-678, (2005).
- [2] B. -L. Nie, P. Du, Y. -T. Yu, and Z. Shi, "Study of the shielding properties of enclosures with apertures at higher frequencies using the transmission-line modelling method," *IEEE Trans. Electromagn. Compat.* vol. 53, no. 1, pp. 73-81, (2011).
- [3] J. -K. Du, S. -Y. Hyun, J. -G. Yook, J. Lee, and J. S. Choi, "Coupling effects according to PCB orientations," in *Proc. American Electromagnetics (AMEREM)*, vol. 1, pp. 1 (ID 150), Jul. (2014).
- [4] J. -K. Du, Y. Kim, J. -G. Yook, J. Lee, and J. S. Choi, "Coupling effects of incident electromagnetic waves to multi-layered PCBs in metallic enclosures," in *proc. International workshop on antenna technology (IWAT)*, Mar. (2015).
- [5] Z. Ren, W. -Y. Yin, Y. -B. Shi, and Q. H. Liu, "Thermal accumulation effects on the transient temperature responses in LDMOSFETs under the impact of a periodic electromagnetic pulse," *IEEE Trans. Electron Devices*, vol. 57, no. 1, (2010).
- [6] F. -Z. Kong, W. -Y. Yin, J. -F. Mao, Q.H. Liu, "Electro-Thermo-mechanical characterizations of various wire bonding interconnects illuminated by an electromagnetic pulse," *IEEE Trans. Advanced Packaging*, vol. 33, no. 3, (2010).
- [7] J. Rye and J. Lee, "An integrated antenna-source system of very high ultra wide-band gain for radiating high-power wide-band pulses," *IEEE Trans. Plasma science*, vol. 40, no. 4, pp. 1019-1026, (2012).

# Parallelization of QR Decomposition Algorithm in Multiconductor Transmission Line Equation Based on CUDA

Yao Liu \*, Min Zhou †, Yang Cai †

\* College of Information System and Management, National University of Defense Technology,  
 † College of Science, National University of Defense Technology

## Abstract

In this paper, we consider the general case of lossy conductor and lossy dielectric, and present the parallelization of iterative QR method for a matrix multiplied by the characteristic impedance matrix and admittance matrix based on CUDA. To prove the effectiveness of our method, we evaluate three different types of implementations: traditional single-thread C++, C++ accelerated with OpenMP and Nvidia CUDA. The evaluation result suggests that when the dimensions of problem reaches hundreds, GPU implementation of CUDA is significantly more effective than CPU implementations of single-thread C++ and OpenMP.

**Keywords:** Multiconductor transmission line, iterative QR method, parallelization, CUDA, OpenMP

## 1 Introduction

In this paper, we present a parallel algorithm of QR decomposition to solve the MTL equation. We also provide the comparison of time between parallel and serial algorithms.

Much work has been done to solve the voltage and current wave in multiconductor transmission line. In literature [1], Carl E. Baum, T. K. Liu and F. M. Tesche use an expansion method of eigen modes in positive real matrix and give a solution of lossy conductor and lossy media under normal circumstances, but the specific method of calculation of eigenvalues and eigenvectors was not given. Literature [2] provides a numerical solution of MTL problem. C. R. Paul discussed the solution of MTL equation without external excitation source in different situations in literature [3]. F. M. Tesche, M.V. Ianoz and T. Karlsson also gives the solution of MTL equation for lossless media [4].

Now the most common way to solve the MTL equation is QR algorithm. But it still needs to repeat the multiplication of matrix for millions of or even tens of millions of times, thus, it is necessary to realize the parallelization of QR algorithm to reduce the time of calculation.

## 2 MTL Equation

We consider the lossy conductor and lossy media in  $n$  multiconductor transmission line. Assume that the conductor is

parallel to the  $Z$ -axis. Let  $v_n^{(s)}(z, \omega)$  be the excitation voltage source applied to the  $n$ -th conductor and  $i_n^{(s)}(z, \omega)$  be the excitation current source. Therefore, the voltage and current equation in  $n$  multiconductor transmission line is

$$\frac{d}{dz} i_n(z, \omega) + \sum_{m=1}^N y'_{nm}(\omega) v_m(z, \omega) = i_n^{(s)}(z, \omega), n = 1, 2, 3, \dots, N \quad (2.1)$$

$$\frac{d}{dz} v_n(z, \omega) + \sum_{m=1}^N z'_{nm}(\omega) i_m(z, \omega) = v_n^{(s)}(z, \omega), n = 1, 2, 3, \dots, N \quad (2.2)$$

Among them,  $y'_{nm}(z, \omega)$  is admittance of the  $n$ -th conductor to the  $m$ -th conductor per unit length with the frequency  $\omega$ , which has nothing to do with  $z$ . And  $z'_{nm}(z, \omega)$  is the corresponding characteristic impedance.

After various transformations, we get that if we want to solve the problem, it is essential to realize matrix diagonalization. Thus, our work is change this serial process into parallel algorithm.

## 3 Parallel Implementation of QR Algorithm

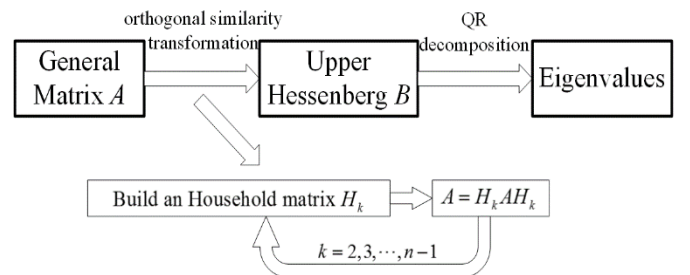


Figure 1: Flow chart for QR algorithm

The QR algorithm can be described as Figure 1. The second part, QR decomposition, is iterative and hard to decouple. Therefore, we choose the first part to realize its parallelism.

In the first part, we can see that matrix multiplication consumes most of the time. And since the parallelism of matrix multiplication is very mellow, we first achieve the parallel multiplication in each multiplication frame. Then the Householder matrix is calculated in corresponding processors.

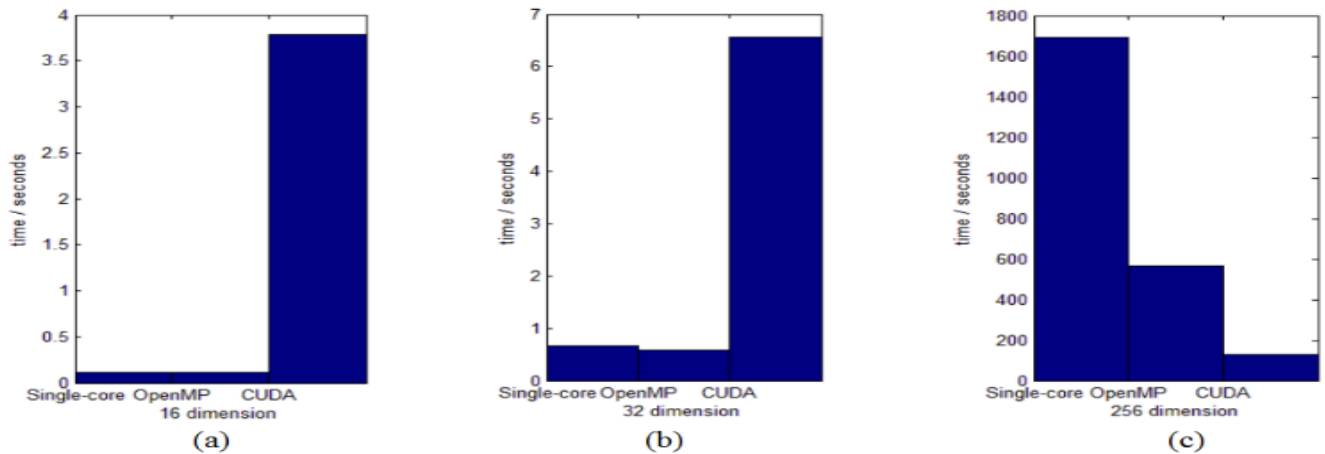


Figure 2: Comparison of three algorithms in three dimensions. We can see that for small dimension problem, CUDA is slower than C++. In fact, parallel implementation such as OpenMP does not benefit much. However, for large-scale problem, parallel implementation significantly accelerate the calculation. And CUDA is the fastest implementation, with a running time less than 10% of that of C++.

That is the way we build a parallel algorithm to change a general matrix into a upper Hessenberg matrix.

## 4 Experiments and Results

We have tried this algorithm in different platforms: serial algorithm in C++ language, parallel algorithm with OpenMP supporting and parallel algorithm on CUDA. Since a cable usually consists of 16 or 32 or 256 wires, so we choose 16 dimensions, 32 dimensions and 256 dimensions matrix to test these algorithm:. The results is shown in the Table 1 and Figure 2.

Table 1: Running time of different algorithm

Matrix Dimension	C++	OpenMP	CUDA
16	0.112s	<b>0.109s</b>	3.785s
32	0.662s	<b>0.582s</b>	6.556s
256	1691.884s	566.767s	<b>128.19s</b>

As the data shown above, we can see that the parallel algorithm has a great advantage over the serial algorithm, especially for the huge matrix. We also get that when the matrix is big enough, CUDA is really time-saving. However CUDA takes much time for data transmission while the matrix is quite medium. At this time, OpenMP is better.

## 5 Conclusion

This paper proposes a parallel implementation of QR algorithm to solve the MTL equation based on CUDA. To prove the effectiveness of our method, we evaluate three different types of implementations: traditional single-thread C++, C++ accelerated with OpenMP and Nvidia CUDA. The evaluation result suggests that when the dimensions of problem reaches hundreds, GPU implementation of CUDA is significantly more effective than CPU implementations of single-thread C++ and OpenMP.

## Acknowledgements

This work is partially supported by the National Natural Science Foundation of China No. 11271370.

## References

- [1] C. E. Baum, T. K. Liu, and F. M. Tesche, On the Analysis of General Multiconductor Transmission Line Networks, Kirtland AFB, Albuquerque, NM, Interaction Note 350, 1978.
- [2] C. E. Baum, T. K. Liu, F. M. Tesche, and S. K. Chang, Numerical Results for Multiconductor Transmission-Line Networks, Interaction Note 322, Air Force Weapons Laboratory, Albuquerque, NM, September 1977.
- [3] D. R. Paul, Analysis of Multicomductor Transmission Lines, New York: Wiley, 1994
- [4] F. M. Tesche, M. V. Ianoz, and T. Karlsson, EMC Analysis Methods and Computational Models, New York: Wiley, 1997
- [5] David R. Kincaid, E. Ward Cheney, Numerical Analysis: Mathematics of Scientific Computing, American Mathematical Society, 2001
- [6] F. M. Tesche, J. Keen, and C. M. Butler, Example of the Use of the BLT Equation for EM Field Propagation and Coupling Calculations, Kirtland AFB, Albuquerque, NM, Interaction Note 591, Aug. 16, 2004.
- [7] L. Paletta, J.-P. Parmantier, F. Issac, P. Dumtas, and J.-C. Alliot, Susceptibility analysis of wiring in a complex system combining a 3-D solver and a transmission-line network simulation, IEEE Transactions on EMC, Vol.44, NO.2, May 2002, pp. 309-317

# A methodology for numerical calculation of isotropic aperture transmission cross section

R Gunnarsson\*, M Bäckström\*

\*Saab Aeronautics, Linköping, Sweden, [ronny.gunnarsson@saabgroup.com](mailto:ronny.gunnarsson@saabgroup.com)

## Abstract

Methodologies for measuring the isotropic transmission cross section of an aperture using a reverberation chamber have previously been developed. A methodology for numerically calculating the isotropic transmission cross section is presented in this paper. Numerical results are presented for the reference case of a circular aperture.

**Keywords:** Isotropic aperture transmission cross section; optical theorem; power integration; finite integration technique, integral equation method.

## 1 Introduction

The electromagnetic environment in an avionics bay is, in engineering practice, well represented by an isotropic environment. This illustrates the need to measure and calculate the isotropic transmission cross section of apertures. Methodologies for measuring the isotropic transmission cross section using a reverberation chamber has previously been developed [1]. A methodology for the numerical calculation of the isotropic transmission cross section is needed as a complement to measurements both for analyses of susceptibility of equipment and systems and in the design of shielded systems. The main challenge in the numerical procedure is how to calculate an average transmission cross section corresponding to the stochastically varying angles of incidence and polarizations that naturally occurs in an overmoded cavity with high Q-value.

## 2 Definitions

Transmission cross section  $\sigma_a$  is a usable way to characterize the power leakage through an aperture, defined as

$$\sigma_a(\theta_{inc}, \phi_{inc}, f, p) = \frac{P_{trans}}{S_{inc}} \quad (1)$$

where  $P_{trans}$  is the (real) power transmitted through the aperture and  $S_{inc}$  is the power density of the external incident field. The transmission cross section is a function of the angle of incidence ( $\theta_{inc}, \phi_{inc}$ ), frequency ( $f$ ) and polarization ( $p$ ). For a plane wave in free-space the power density is given by

$$S_{inc} = \frac{|E_{inc}^{peak}|^2}{2 \cdot Z_0} = \frac{|E_{inc}^{mean}|^2}{Z_0} \quad (2)$$

where  $E_{inc}^{peak}$  is the peak-value and  $E_{inc}^{mean}$  is the RMS-value of the external E-field and  $Z_0$  is the wave-impedance in free space ( $\approx 377\Omega$ ).

## 3 Numerical calculation of aperture transmission cross section

One approach to the numerical calculation of the transmission cross section of an aperture is to use the so-called power integration method. In this approach an integration surface is created on the opposing side of the aperture, in relation to the incident external field. The power transmitted through the aperture is calculated by a numerical integration of the power flow (Poynting vector) through the integration surface according to

$$P_{trans} \cong \frac{1}{2} \iint \text{Re}\{(E \times H^*) \cdot \hat{n}\} dS \quad (3)$$

The benefit of this approach is that it is quite general and applicable also when e.g. the ground plane has a finite thickness. A disadvantage, in comparison to the approach described below, is that it is more time and memory intensive.

Assuming the aperture can be placed in an infinitely thin and perfectly conducting screen an alternative approach can be used. According to Babinet's principle [2] the scattered field from such a screen is identical to the scattered field from the complementary screen, assuming the polarization of the external field is rotated by  $90^\circ$ , see Fig.1. The optical theorem [2] yields the total cross section ( $\sigma_{tot}$ ) of a scatterer as

$$\sigma_{tot} = \frac{4\pi}{k} \cdot \text{im}\{E(0)\} \quad (4)$$

where  $k$  denotes the wavenumber in free-space and  $\text{im}\{E(0)\}$  denotes the imaginary part of the complex forward scattered electric farfield. Note that Equation (4) assumes that the polarization of the forward scattered field and the incident field is the same. The scattering from an aperture in an infinitely thin and perfectly conducting screen is symmetrical, whereby it follows that the transmission cross section is given by  $\sigma_{trans} = \sigma_{total}/2$ . An advantage of using Babinet's principle is that we do not have to model the screen (ground plane), which makes a method-of-moments (MoM) solver suitable since one then only has to mesh (triangulate) the complementary structure. A MoM-solver is also beneficial in some cases since it is better at handling apertures with curved boundaries. The advantage of using the optical theorem is that one only has to calculate the farfield in a single direction.

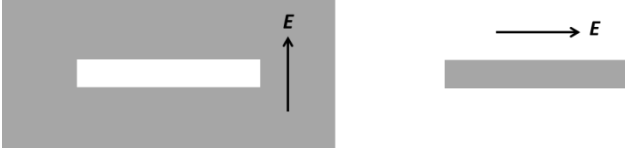


**Figure 1. Equivalent scatterers according to Babinet's principle.**

## 4 Numerical calculation of isotropic aperture transmission cross section

Developing a methodology for the numerical calculation of the isotropic transmission cross section might seem to be a trivial task. However, as illustrated below, if care is not taken one might very well obtain an over-representation of illuminations close to the normal incidence. Two alternative approaches to the calculation of the isotropic transmission cross sections are presented. Note that determining a sufficiently large number of angles of incidence in  $\theta$ - and  $\phi$ -direction ( $N_\theta$  and  $N_\phi$ ) and number of polarizations ( $N_p$ ) is a non-trivial task which will not be discussed here.

### 4.1 Equal surface area distribution

The isotropic transmission cross section can be viewed as the average of the transmission cross section over a large number of stochastically varying angles of incidence and polarizations. One approach to obtain a uniform distribution of illuminations over a half-plane is to divide a half-sphere into a number of surface elements with equal surface area. A simulation is then performed for all  $(\theta, \phi)$  each corresponding to a surface elements. An example of a subdivision of a half-sphere is shown in Fig.2.

Since the half-sphere is circular symmetric in  $\phi$ -direction one should have a linear distribution of the  $\phi$ -angles. Assume we have determined that, apart from the pole, we require  $N_\theta$  and  $N_\phi$  angles of incidence. The  $\theta$ -angles defining the horizontal boundaries of the surface elements in Fig.3 are then given by

$$\theta_1 = \arccos\left(\frac{N_\phi N_\theta}{N_\phi N_\theta + 1}\right) \quad (5)$$

$$\theta_{n+1} = \arccos\left(\cos\theta_n - \frac{N_\phi}{N_\phi N_\theta + 1}\right) \quad n = 1, \dots, N_\theta \quad (6)$$

For the distribution of the  $\theta$ -angles used in the numerical simulations we propose that one uses the average of the values  $\theta_n$  given by Equation (5) and (6). For this distribution the isotropic transmission cross section is given by

$$\sigma_{\text{mean}} = \frac{\sum_{p=1}^{N_p} (\sigma_1(p) + \sum_{n=2}^{N_\theta+1} \sum_{m=1}^{N_\phi} \sigma_{n,m}(p))}{N_p \cdot (N_\phi N_\theta + 1)} \quad (7)$$

where  $\sigma_j(p)$  denotes the transmission cross section for normal incidence and polarization  $p$  and  $\sigma_{n,m}(p)$  denotes the transmission cross section for  $\theta = \theta_n$ ,  $\phi = \phi_m$ .

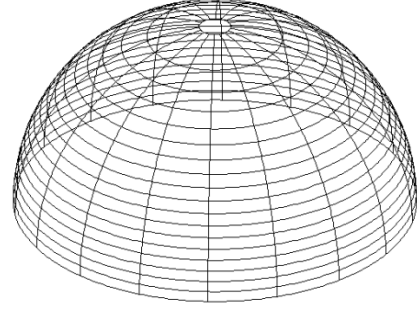


**Figure 2. Subdivision of a half-sphere into surface elements with an equal surface area distribution.**

### 4.2 Linear distribution of $\theta$ - and $\phi$ -angles

An alternative to the approach described in section 4.1 could be to use a linear distribution of both the  $\phi$ - and  $\theta$ -angles and use the Jacobian ( $\sin\theta$ ) to de-emphasize illuminations from angles of incidence close to the pole of the half-sphere. For this distribution the isotropic transmission cross section is given by

$$\sigma_{\text{mean}} = \frac{\pi/2}{N_p N_\theta N_\phi} \sum_{p=1}^{N_p} \sum_{n=1}^{N_\theta} \sum_{m=1}^{N_\phi} \sigma(\theta_n, \phi_m, p) \sin\theta_n \quad (8)$$

## 5 Reference case

As a reference case for the methodology described we selected a circular aperture with radius  $r = 15$  mm placed in a perfectly conducting and infinite ground plane. The number of angles of incidence and polarizations were chosen to be  $N_\theta = 18$ ,  $N_\phi = 72$  and  $N_p = 2$ . Due to symmetry, numerical calculations were only performed in a single  $\phi$ -cut. All results presented were obtained using CST Studio Suite 2014 [3].

### 5.1 Ground plane with zero thickness

For the case of a ground plane with zero thickness we used the integral equation solver and studied the complementary case of a circular disc and the transmission cross section was calculated using the optical theorem. Isotropic transmission cross sections were calculated both for the equal surface area distribution as well as for the linear distribution of  $\theta$ - and  $\phi$ -angles. A comparison of the transmission cross section for normal incidence and the isotropic transmission cross section is shown in Fig.3. The maximum deviation between the isotropic transmission cross section calculated for the equal surface area distribution, averaged according to Equation (7), and the linear angular distribution, averaged according to Equation (8), is only 0.15 dB over 0.5 – 36 GHz.

The ratio of the transmission cross section for normal incidence and the isotropic transmission cross sections are shown in Fig.4. A very good agreement is obtained between the isotropic transmission cross sections calculated using an equal surface area distribution and non-weighted averaging and the linear angular distribution and weighted averaging. Note that a linear angular distribution with non-weighted

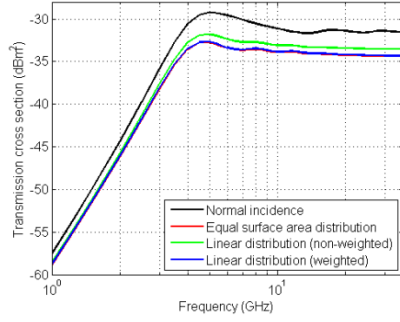


**Figure 3.** Transmission cross section ( $\text{dBm}^2$ ) for normal incidence (black). Isotropic results for equal surface area distribution (red) and non-weighted (green) and weighted (blue) averaging for linear angular distribution.  $t = 0$  mm.

averaging results in considerably higher average transmission cross section. Note also that the ratio for the correctly calculated isotropic transmission cross sections tends to  $4/3$  at low frequencies and  $2$  at high frequencies, which agrees with the analytical results given in [4].

## 5.2 Ground plane with finite thickness

For the case of a ground plane with finite thickness ( $t = 2$  mm) the transmission cross section for the ground plane aperture was calculated using a time-domain solver and the power integration method. Here we only performed simulations for the case of an equal surface area distribution. The ratio of the transmission cross section for normal incidence and the isotropic transmission cross section is shown in Fig.5. The isotropic transmission cross section again tends to the expected low and high frequency limits, see [4].

Visual inspection of the results reveals that the relation between the transmission cross section for  $t = 0$  mm and  $t = 2$  mm for normal incidence is very similar to the corresponding relation between the isotropic transmission cross sections for normal incidence. It therefore follows that  $\sigma_{\text{test}}$ , given by Equation (9), should provide a good approximation to the isotropic transmission cross section for the case of finite ground plane thickness, see Fig.6. In particular, the approximation works very well below the first resonance frequency of the aperture. The benefit of this approach is that one can perform the major part of simulations studying the complementary structure and using the optical theorem, thereby reducing the time and memory requirements.

$$\sigma_{\text{test}} = \sigma_{\text{mean}}^{t=0\text{mm}} \cdot \frac{\sigma_0^{d=2\text{mm}}}{\sigma_0^{d=0\text{mm}}} \cong \sigma_{\text{mean}}^{t=2\text{mm}} \quad (9)$$

## 6 Conclusions

A methodology for the numerical calculation of isotropic aperture transmission cross section has been proposed. Presented numerically calculated isotropic transmission cross sections for the reference case of a circular aperture has been presented and shown to be in excellent agreement with previously reported analytical results.

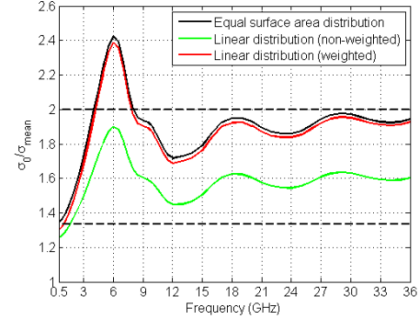


**Figure 4.** Ratio of the transmission cross section for normal incidence ( $\sigma_0$ ) and isotropic transmission cross section ( $\sigma_{\text{mean}}$ ) for an equal surface area distribution (black) and linear angular distribution and non-weighted (green) and weighted (red) averaging.  $t = 0$  mm.

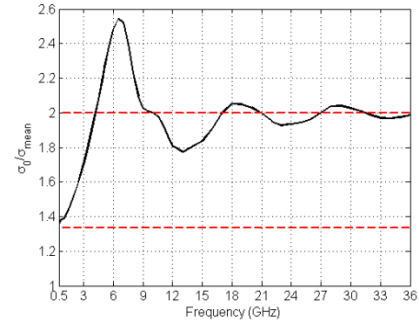


**Figure 5.** Ratio of transmission cross section for normal incidence ( $\sigma_0$ ) and isotropic transmission cross section ( $\sigma_{\text{mean}}$ ) for an equal surface area distribution.  $t = 2$  mm.

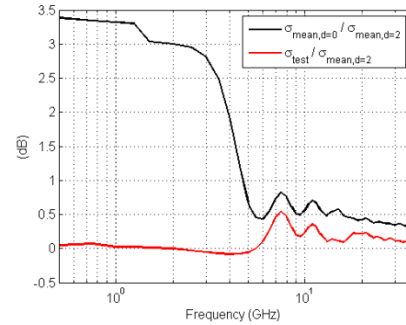


**Figure 6.** Ratio (dB) of  $\sigma_{\text{mean}}^{t=0\text{mm}}$  and  $\sigma_{\text{mean}}^{t=2\text{mm}}$  (black) and of  $\sigma_{\text{test}}$  and  $\sigma_{\text{mean}}^{t=2\text{mm}}$  (red).

## References

- [1] M. Bäckström, T. Nilsson, and B. Vallhagen, "Guideline for HPM protection and verification based on the method of power balance", *EMC Europe 2014*, Gothenburg, Sweden, 1 – 4 September 2014.
- [2] John David Jackson, *Classical electrodynamics*, Third edition, John Wiley & Sons, Inc., New York, 1998.
- [3] <https://www.cst.com/Products/CSTS2>
- [4] D. A. Hill, "Electromagnetic fields in cavities", The IEEE Press Series on Electromagnetic Wave Theory, John Wiley & Sons, Inc., 2009.

# Time Marching Method Instability: a Deconvolution Approach

Juan Miguel David Becerra Tobar<sup>1</sup>, Jose Félix Vega Stravo<sup>2</sup>, John Jairo Pantoja Acosta<sup>3</sup>

<sup>1</sup>Dept. Electric and Electronic Engineering Universidad Nacional de Colombia, Colombia, jmbecerrat@unal.edu.co

<sup>2</sup>Dept. Electric and Electronic Engineering Universidad Nacional de Colombia, Colombia, jfvegas @unal.edu.co

<sup>3</sup>Dept. Electric and Electronic Engineering Universidad Nacional de Colombia, Colombia, jjpantojaa @unal.edu.co

## Abstract

**Time marching is a method for calculating the response of different systems in the time domain. In circuit theory and transmission lines theory, it allows to include nonlinear and frequency dependent devices. However, this method presents some instability problems, which currently do not have a proper explanation. In this paper the similitudes between direct deconvolution and time marching are utilized for explaining the instability problems. This analysis is performed by using the Z transform.**

**Keyword:** Time marching, instability, direct deconvolution.

## 1 Introduction

Time marching (TM) allows calculating the response of systems with integro-differential transfer functions including nonlinear and frequency dependent elements in time domain [1], [2]. Nonetheless, this method does not always yields realistic values and an exponential growth is seen in the variables of interest without any reasonable explanation. This kind of solutions are named instable.

This problem is well known by the scientific community. Common stability strategies involve restricting element values [3], modifying step time, simulation length or other simulation parameters [4], and averaging in time the variables of interest [5].

This work aims to explain one instability cause related with the calculation of variables operated in a convolution by using the Z transform. The process is the same to the one used to explain instability for the direct deconvolution method [6]. Tests on linear circuits were used to show the application of the analysis, and finally some solutions are suggested.

The results of this work can be applied in propagation signal problems that include non-linear devices; for example, propagation in power line communications (PLC), electromagnetic coupling in transmission lines of power systems, or electromagnetic interference in communication networks.

The remainder of this paper is organized as follows: section II explains briefly the time marching method and provides an unstable case, section III shows the analysis of TM with Z transform and its implications, section IV a solution to the instability problem is proposed, and section V presents a result discussion. Finally, the conclusions are presented in section VI.

## 2 Time Marching algorithm

TM algorithm is based in representing the system response in discrete time domain equations and calculating one variable at time using past values of the others are considered constant and this process is repeated iteratively until the simulation is finished. In the following example, this algorithm is applied and the method instability is shown.

### 2.1 Instability example

Consider the circuit shown in Figure 1 that includes a source, three ideal resistors, and a transmission line (TL).  $z_1(t)$  represents the impulse response of the TL's input impedance. The circuit is described by equations (1) and (2) in continuous time domain, which contain the variables of interest,  $i_1(t)$  and  $i_2(t)$ .

$$V_S(t) = R_S \cdot (i_2(t) + i_1(t)) + i_1(t) * z_1(t) \quad (1)$$

$$i_2(t) = \frac{i_1(t) * z_1(t)}{R_2} \quad (2)$$

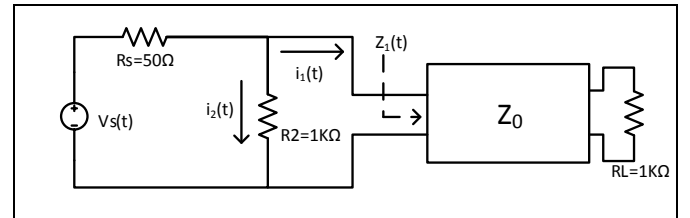


**Figure 1. Linear circuit used as example**

From equations (1) and (2), the variables of interest are found and discretized. These expressions are shown in equations (3) and (4), where  $t_i$  represents the discrete time and  $i_1(t_i)$  and  $i_2(t_i)$  are the value of variables  $i_1$  and  $i_2$  evaluated at time  $t_i$ .

$$i_1(t_i) = \frac{V_S(t_i) - R_S \cdot i_2(t_i) - \Delta t \sum_{k=0}^{i-1} i_1(t_k) z_1(t_{i-k})}{z_1(t_0) \Delta t + R_S} \quad (3)$$

$$i_2(t_i) = \frac{\Delta t \sum_{k=0}^i i_1(t_k) z_1(t_{i-k})}{R_2} \quad (4)$$

Equation (3) is used to calculate  $i_1(t_i)$  when index  $i$  is even with the assumption that  $i_2(t_i) = i_2(t_{i-1})$ . In order of calculating  $i_2(t_i)$ , the equation (4) is utilized when index  $i$  is odd with the assumption  $i_1(t_i) = i_1(t_{i-1})$ . These calculations are repeated until the maximum simulation time is reached.

The following simulation parameters were used as example. The voltage source is represented by sinusoidal signal 5 volts peak at 1MHz, sample frequency of 100MHz and 4μs

simulation time. The transmission line had a characteristic impedance of 50 ohms, 1 meter length and propagation velocity equal to the speed of light.

For obtaining  $z_1(t)$ , the TL's input impedance discretization was performed in the Fourier domain, and the impulse response was calculated by using the IFFT algorithm.

In order to compare the results, the frequency response was calculated Analytically by using ABCD parameters [7]. The results of the TM are shown in Figure 2, it can be seen that  $i_1(t)$  calculated by TM is unstable. Consequently,  $i_2(t)$  and other variables of interest are unstable.

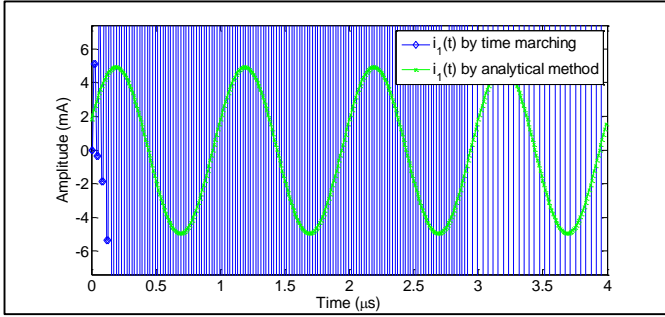


**Figure 2: Current  $i_1(t)$  calculated using TM and ABCD parameters for an unstable case.**

The instability appears in  $i_2(t)$  and  $i_1(t)$  if  $Rs$  is chosen less or equal than  $73\Omega$ .

### 3 Time marching analysis with Z transform

Direct deconvolution is a process used in acoustic and image processing for recovering information that has been modified by a system, and the stability analysis of the obtained results is performed by using the Z transform [6]. The same approach is used here for TM equations that find the value of convolved variables.

First, consider each variable from equation (3) as a time series, and then the Z transform is applied and  $I_1(z)$  is found as shown in equation (5). Thus,  $i_1(t_i)$  can be found by taking the inverse of  $I_1(z)$  and due to the significance of the variable, the causal inverse is desired.

$$I_1(z) = \frac{Vs(z)}{\underbrace{Z_1(z) + Rs}_{\text{known term}}} - \frac{I_2(z) \cdot Rs}{\underbrace{Z_1(z) + Rs}_{\text{unknown term}}} \quad (5)$$

In equation (5),  $I_1(z)$  is expressed as the addition of two terms: one whose components are *known* from the simulation beginning, while the term with the variable  $I_2(z)$  is *unknown* because it is calculated during the TM run. Since  $i_1(t_i) = \mathcal{Z}^{-1}\{I_1(z)\}$ , it can be seen that if one of the terms is unstable,  $i_1(t_i)$  is unstable in general. Besides, due to the TM algorithm  $i_2(t_i)$  is a function of  $i_1(t_i)$ , it is expected that the whole simulation acquires an unstable behavior. Hence, the *known term* is more important than the *unknown term*.

The *known term* instability is related with the zeros of its denominator,  $(Z_1(z) + Rs)$ . For zeros inside the unit circle, the resultant time series is causal and stable, which is the desirable

case. However, for zeros outside the unit circle, the causal time series is unstable.

It is important to notice that in equation (3), the causality of  $i_1(t_i)$  is forced. Thus, if  $(Z_1(z) + Rs)$  has at least one zero outside the unit circle, the TM results will grow exponentially. In order to test this affirmation, the pole-zero plot of the example shown in the previous section was used and it is shown in Figure 3. It is clear that there is a zero of  $(Z_1(z) + Rs)$  far from the unit circle, as expected.

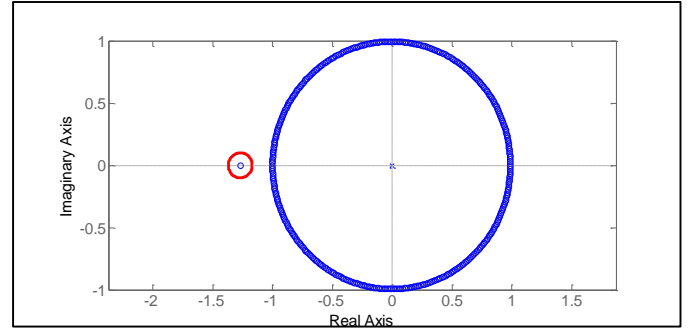


**Figure 3: Zeros of  $Z_1(z) + Rs$ , unstable zeros are marked in red.**

In summary, the first condition that any circuit or system must fulfill in order to obtain stable responses by the TM method is that every deconvolution equation needed to calculate a variable must have their poles inside the unit circle in the known term.

### 4 Time marching instability fixing

In discrete simulation, there are two necessary conditions for accurate results [8]: the signal of interest must decay enough at the end of simulation time, and the transfer function should be significantly attenuated prior the limit frequency, which is known as band-limiting requirement. We proposed to force the accomplishment of the second condition in TM for unstable cases.

The method is composed by the following steps. First, the transmission line impedance, represented by  $Z_1(f)$ , is multiplied by a function  $FIX(f)$  that ensures high attenuation below the limit frequency, which is considered a convolution in time domain, as shown in (6). Second, the IFFT is applied to this product. Third, for recovering the original function, a deconvolution is used as shown in (7), where  $*^{-1}$  represents the deconvolution operation and  $fix(t)$  is the Fourier inverse of  $FIX(f)$ .

$$\mathcal{F}^{-1}\{Z_1(f) \cdot FIX(f)\} = z_1(t) * fix(t) = z_{conv}(t) \quad (6)$$

$$z_{fix}(t) = z_{conv}(t) *^{-1} fix(t) \quad (7)$$

In order to select the fix function, two requirements were stated for obtaining real signals in time domain. First, the conjugated symmetry between positive and negative spectrum of  $Z_1(f)$  must be preserved. Second, the resulting time series from this function must have its zeros inside the unit circle for making the direct deconvolution possible. It is important to

notice that the last condition only can be tested once an IFFT is applied to the fix function spectrum.

A function of the form  $e^{-\alpha f^2}$  fulfill all the previous restrictions, where alpha is a constant. In equation (8) a complete expression for  $FIX(f)$  is shown. The parameter  $k$  allows selecting the desirable attenuation at limit frequency, which is equal to a half of sampling frequency. The Fourier inverse transform of the function  $FIX(f)$  is shown in (9).

$$FIX(f) = e^{-\frac{4k}{F_s^2}f^2} \quad (8)$$

$$\mathcal{F}^{-1}\{FIX(f)\} = \frac{F_s}{4\sqrt{\pi k}} \cdot e^{-\frac{F_s^2}{16k}t^2} \quad (9)$$

For the simulation's parameters used in the previous section and  $k = 10$ , the fix function fulfill the second selection condition. The result of the fix application over the zeros of  $(Z_1(z) + Rs)$  are shown in Figure 4. Since all zeros are inside the unit circle, the TM will yield a stable response as shown in Figure 5. It can be seen that the response is stable, but there is magnitude error in  $i_1(t_i)$ .

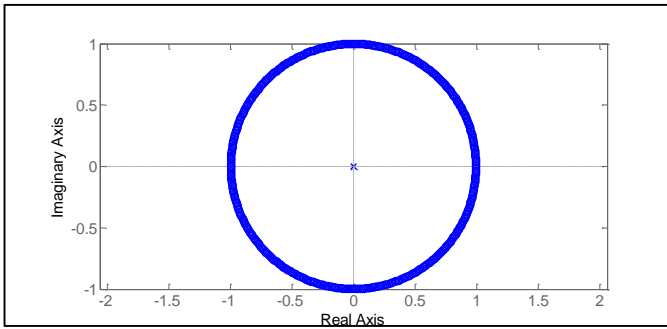


**Figure 4: zeros of fixed  $Z_1(z) + Rs$**

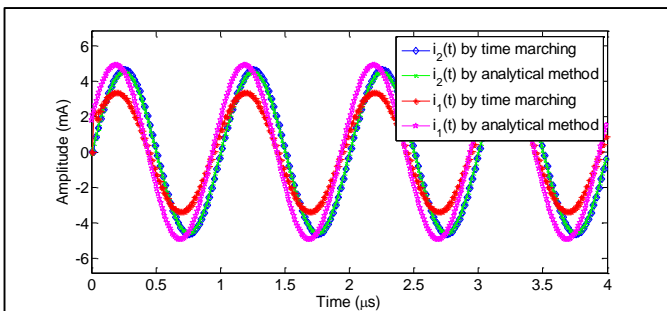


**Figure 5: TM results for fixed impulse response**

Low values of  $k$  will produce high frequency oscillations in the early response. In our tests, a minimum value of five was found to be effective against instability.

## 5 Results discussion

The method proposed here solves the TM unstable behavior, with a magnitude error, which is a good start for solving the instability problem. However, some comments about this solution are relevant.

The known term unstable poles are related to the transfer functions impulse responses used in the deconvolution

equations, but what cause them during the discretization process is unknown. Thus, the relationship between the band limiting condition and the apparition of unstable poles in  $z$  domain is hard to determine, which also hampers finding a solution for the magnitude error.

## 6 Conclusions

The application of  $Z$  transform stability criterion over the deconvolution equations needed in the TM helps to develop a solution for the instability problem of TM. In summary, any method, that introduces the known term poles inside the unit circle can solve this problem.

The proposed fixing method aims to force high attenuation on the transfer function prior half of the sampling frequency in order to fulfill the band-limiting requirement in discrete simulations.

The method for fixing the instability presented here accomplish its objective but it produces error in magnitude.

## 7 References

- [1] J. F. Vega Stavro, "Analytical Methods for the Study and Design of Integrated Switched Oscillators and Antennas for Mesoband Radiation," EPFL, Lausanne, 2013.
- [2] F. M. Tesche, "On the Analysis of a Transmission Line With Nonlinear Terminations Using the Time-Dependent BLT Equation," *IEEE Transactions on Electromagnetic Compatibility*, vol. 49, no. 2, pp. 427–433, May 2007.
- [3] P. J. Davies, "On the stability of time-marching schemes for the general surface electric-field integral equation," *IEEE Transactions on Antennas and Propagation*, vol. 44, no. 11, pp. 1467–1473, Nov. 1996.
- [4] S. E. Bayer and A. A. A. Ergin, "A Stable Marching on Time scheme for Wire Scatterers Using a Newmark-Beta Formulation," *Progress In Electromagnetics Research B*, vol. 6, pp. 337–360, 2008.
- [5] S. M. Rao, *Time Domain Electromagnetics*. Academic Press, 1999.
- [6] J. E. Michaels, "Fundamentals of deconvolution with applications to ultrasonics and acoustic emission," Cornell, 1982.
- [7] R. E. Collin, *Foundations for Microwave Engineering, 2nd Edition - Robert E. Collin*. Wiley-IEEE Press.
- [8] P. J. Pupalais, "The Relationship Between Discrete-Frequency S-parameters and Continuous-Frequency Responses," in *DesignCon*, Santa Clara, CA, 2012, pp. 1–28.

# Development of the HEMP Propagation Analysis and Optimal Hardening Shelter Design, Simulation Tool "KTI HEMP CORD"

† GyungChan, Min, YeongKwan, Jung

Korea Technology Institute Co. Ltd.  
58-10, Sagisogil, Dochuckmyeon,  
Gwangju, Gyeonggi-do, Korea(ROK). [minkti@naver.com](mailto:minkti@naver.com)

## Abstract

High Altitudes Electro-Magnetic Pulse (HEMP) caused by nuclear bomb explosion had been tested during last 1960-1975 by the USA, Russia and other countries. But all of related simulation tools, documents are strongly classified and impossible to use it even, thus IEC and ITU had published the related standards and recommended its protection against HEMP and HPEM. Also, Middle East countries and Far East countries including South Korea are directly vulnerable against HEMP threat. Now we, KTI had developed the HEMP simulation and optimal shelter design tool named by "KTI HEMP CORD"

### Keywords;

High Altitudes Electro-Magnetic Pulse(HEMP), High Power Electro-Magnetic(HPEM), Height of Blast(HOB), Ground Zero(GZ), Shielding Effectiveness(SE)

## 1 Introduction

The HEMP threat<sup>[1]</sup> may have acquired new, urgent and relevance as the proliferation of nuclear weapons and missile technology accelerates of the North Korea, for example, is assessed as already having developed few atomic weapons, and is on the verge of North Korea already has missiles capable of delivering a nuclear warhead over the South Korea. ITU K.78, K81 and IEC recommended its counter-measuring for the industrial facilities. HEMP test and estimation must only be done by the computer simulation which was studied on the 1960-1990 years USA/AFWL papers. This result has significant activities to the South Korea, Japan and China being under the North Korea nuclear bomb threat because all of HEMP related products was strongly limited for export. This KTI newly developed HEMP cord included the HEMP generation & propagation analysis, optimal shelter design tool, essential EM energy attenuation in multi-layered various soils and rocks with HEMP filter design tool of considering the high frequency equivalent circuits. Specially, this study adapted the least square fitting method for the EM energy attenuation in the soils and rocks because it has a various characteristics so, it based on many times field test reports. This paper were proven with the EXEMP CORD developed at 1992 by K.D. Leuthäuser<sup>[2]</sup> and other verification test done by our self and developed the HEMP filters.

## 2. General of the developing procedure

### 2.1 HEMP generation and propagation.

This study needs a variety of HEMP test report with theories<sup>[2],[3],[4],[5],[6]</sup> and papers to understand the HEMP generation, propagation and the coupling mechanism analysis. Specially, we had fallen in difficulties and muddle through the bitters on the unit unification of the mathematical formulas from the atom engineering, physics, aerologic, electron mobility, earth magnetic field, vector direction to the Maxwell equations.

HEMP generation and propagation theories were based on the Ref. [2] –[6] and HEMP wave form adapted DEXP. Simulation and analysis were done by a formal theory and practice.

### 2.2 Analysis of the EM energy attenuation in the multilayer soils and rocks<sup>[7],[8]</sup>

It has a following functions and applied theory;

- Computer simulation of EM energy attenuation in the multilayer soils and rocks.
- Very high accuracy for computer simulation using the statistical least square methods.

### 2.3 HEMP Hardening Shelter Design Tool

This simulation tool can calculate the effective shield effectiveness based on the following algorithms;

- Shielding effectiveness calculation without slots and holes for the welding type shielding cavity using pure material constants
- Shielding effectiveness calculation with gap for the PAN and panel type shielding cavity.
- Shielding effectiveness calculation with various waveguides and pin holes on the shielding wall considering the filter attenuation characteristics.
- Considering the shielding cavity resonant.

### 2.4 HEMP filter design tool

Basically, we adapted the normal low pass filter design concepts even, thus it has specialties to consider a contact resistance, stray capacitance, stray inductance and the conductivity of inductor of a high frequency equivalent circuit.

## 3. Related theories

### 3.1. Brief theory of the E<sub>1</sub> generation, smile diagram.

According to the Karzas-Latter-Longmire theory and K.D. Leuthäuser, gamma ( $\gamma$ ) ray be assumed to be produced at

approximately an exponentially increasing rate after the course of the nuclear explosion.

When a gamma ray of energy  $E_\gamma$  emitted by nuclear burst interacts with an electron of the air molecules in a Compton collision, Compton recoil electrons is created at an angle  $\theta$  with respect to the direction of the incident gamma ray. So we called the  $E_1$  field for the first electrons creation,  $E_2$  field created by the gamma ray  $n^{\text{th}}$  scattering collision and  $E_3$  field created by the geomagnetic field stabilization which was disturbed by  $E_1$  and  $E_2$ . If  $t = 0$  is the time at which the explosion starts, then the number of gamma rays produced up to time  $t$  which is given by  $e^{\alpha t}$ , where  $\alpha$  called by a shake is about  $10^{-9}$  sec. If gamma ray reaches to maximum, it decreases to zero exponentially as a slower rate than starting built up,  $\sigma\beta e^{-\beta(t-T)+\sigma T}$  on condition ( $\alpha \gg \beta, \sigma \lesssim 1$ ). HEMP pulse waveform was defined on the IEC 61000-2-13 and MIL STD 188-125.

Gamma rays have an average energy of about 1MeV, and there are  $7.5 \times 10^{21}$  gamma rays produced per kiloton ( $4 \times 10^{19}$  ergs) of yield.

$$(1 + \sigma)e^{\alpha T} = 7.5 \times 10^{21} Y \quad (1)$$

Here,  $Y$ = Total yield of the explosion in the form of gamma rays expressed in kTon,  $E$  is the mean gamma rays and  $f(t)$  is a expression the time variation of the gamma rays.

According to the Ref.[4], the number of gamma rays emitted by a nuclear explosion per unite time is

$$\dot{N}(t) = \frac{Y}{E} \cdot f(t) \quad (2)$$

If we normalized expression of the  $f(t)$

$$\int_{-\infty}^{\infty} f(t) dt = 1$$

The rate at which primary Compton recoils electrons are produced at a distance  $r$  in direction  $\theta, \phi$  from the explosion is

$$\dot{n}_{pri}(r, t) = g(r) \cdot f(t - \frac{r}{c}) \quad (3)$$

Term of  $\tau = t - \frac{r}{c}$  is known as a retarded time and it is related with the electron traveled time since the creation of the Compton electron. Understanding of the retarded time from the source to observer locations described more details on Ref.[6] using the Jefimenko equation[6].

Here, new important function  $g(r)$  is a number of gammas which interact to produce Compton electrons,

$$g(r) = \frac{Y}{E} \cdot \frac{\exp[-\int_0^r \frac{dr'}{\lambda(r')}]}{4\pi r'^2 \lambda(r')} \quad (4)$$

Where,  $\lambda(r)$  is the mean free paths of gamma rays to produce Compton electrons,  $Y$  has a actual meaning, the gamma yield of the weapon in electron volt (eV),  $E$  is the mean gamma energy in eV and  $c$  is light velocity.

Equation (4) may also be called the radial distribution function or an attenuation function for interacting gamma rays. The  $\frac{Y}{E}$  term is the total number of gamma rays available from the nuclear burst.

$4\pi r'^2$  term accounts for the divergence of the gamma rays as the radius  $r$  is increased while the remaining term account for the reduction in gammas due to the air absorption in the atmosphere based on the mean free path.

Applying a small angle approximation by the Taylor series expansion;  $\sin \omega\tau = \omega\tau$ ,  $\cos \omega\tau = 1 - \frac{\omega^2\tau^2}{2}$  and high frequency condition, then we could find a simplified equation. Also we could get the electric field strength from the relation between current

density and medium conductivity of the air density in the height of the atmospheres. Our basic model of the analysis underlying on the Karzas-Latter-Longmire theory and K.D. Leuth user's EXEMP. There are many limitations to describe on these papers for all of them, so refer to the references for the more detailed theories. Finally, we calculate the electric field strength at the observer location as a following procedure in order to find out the field distribution on the earth without HEMP test.

- 1) Generation of the Compton recoil electrons and propagation analysis

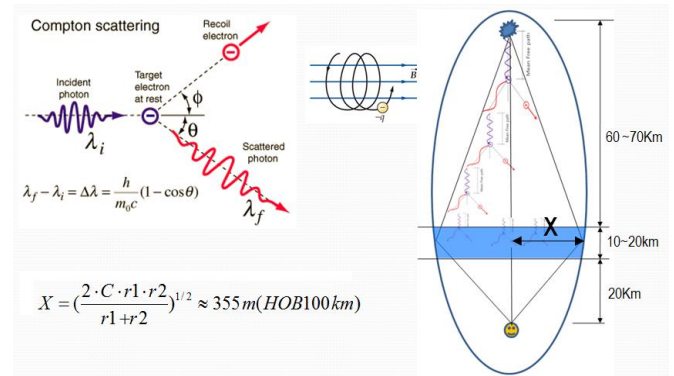


Figure 1. Gamma rays scattering and the elliptic analysis of the source range

- 2) Coordinate system change from the spherical coordinates to rectangular of the earth surface and atmosphere.

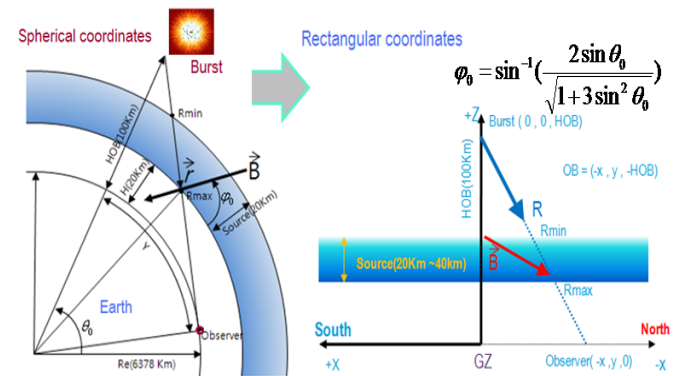
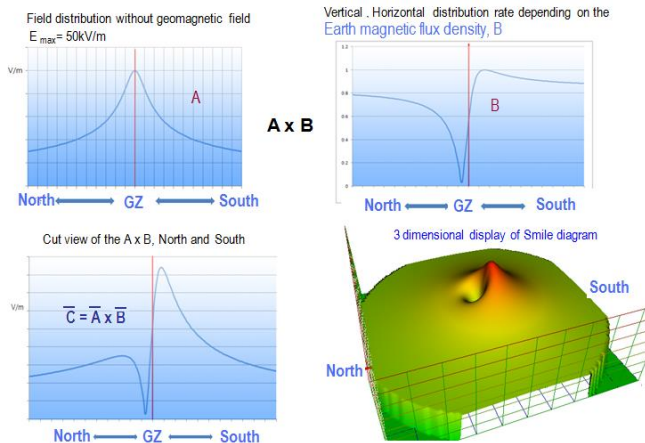


Figure 2. Coordinate system conversion and Earth magnetic field calculation at some location.

- 3) Survival probability of the one gamma ray and electrons distributions depend on the height from the sea level.
- 4) Wave polarization
- 5) Contour plot of the electromagnetic magnitudes on the map.

### 3.2. Brief analysis algorithm of the EM energy attenuation into the soils and rocks

We need to simulate the natural attenuation in the multi-layered soils and rocks when HEMP shelter is installed in the underground tunnel. In this case, finding the ideal material constants of the soils and rock are very important to reduce the uncertainty because these



**Figure 3. The electromagnetic field distribution on the earth.**

materials has a various characteristics. So, this tool optimized its effectiveness using a least square method from the much field test result of the electromagnetic power attenuation in soils and rocks.

### 3.3 Shielding effectiveness estimations of the HEMP shelter and HEMP filter design tool

Shielding effectiveness could be calculated if material constants was given as the well known theory but theoretically calculated result has not corresponded to the shielding effectiveness test on the site. So, this study proposed the ideal estimated solutions for the HEMP shelter design and construction by way of adapting a effective permeability, conductivity and a number of wave guides.

## 4. Verifications

### 4.1 HEMP simulation tool<sup>[9]</sup>

Our simulation results come to have an exact consistency with the EXEMP CORD at the same geometric condition. Our main goal to develop the electric field distribution, smile diagram is just to know the field strength without actual HEMP test used for the optimal shelter design and provided the enough margins between HEMP field strength and EM sensitive system. The contour plot of peak E-field are simulated and compared with EXEMP results when burst at GZ N37.56, E126.97 (Seoul, Gwoang whoa mum) and 10kt, HOB 75km. It's results are well corresponding to the EXEP results. We could get a field strength 2.60kV/m at Seoul, 48.22kV/m at Whoa sung, 28.82kV/m at Pyongyang, 17.74kV/m at Shanghai in China and 21.20kV/m at Hiroshima in Japan. Therefore, we realized that all of main cities in the Far East Asia should be under the threaten if North Korea carries out the HEMP test over the Korea peninsula.

Here, HEMP is defined as nuclear bomb busted in the higher height than minimum 40km.

### 4.2 Estimation of the EM energy attenuation in the multilayer soils and rocks<sup>[9],[10]</sup>

### 4.3 HEMP shelter Design Tool<sup>[10],[11]</sup>

On the view of our experience, the shield effectiveness written on the text formulas are not corresponding to the hardening shelter on site SE test. Our developed simulation tool come to the well corresponding result between the simulation and site SE test when

we considered an effective material constants variation, shelter mechanical slots and wave guide physical dimensions.

### 4.4 HEMP filter design tool<sup>[9]</sup>

A simulation results when  $\pi$  type filter consist of 500uH inductor with stray capacitance 0.1pF, the feed through capacitor 2 uF with the stray inductance 0.1pH and load resistance is a 2 $\Omega$ . This tool is very useful to confirm an important of the contact resistance, stray capacitance and inductance, load impedance and to choose the optimal LPF components.

## 5. Conclusion

This tool provided the estimation of the HEMP field distribution on the earth, analysis of the EM energy attenuation in the multilayer soils and rocks, optimal HEMP hardening shelter and filter design in accordance with the commercial standard ITU, IEC recommendation and MIL STD 188-125. All of the simulation cord and tools related to HEMP are strongly classified by HEMP technology advanced countries that already had high altitude test experiences. Also, very limited papers are available in the open literature to the 3<sup>rd</sup> countries.

Now, we are getting in the new nuclear cold threat since North Korea has successes to develop the nuclear bomb and long distant missile over the Far East Asia and Middle East area. So, we are looking forward to using this study result for the improving the nuclear hazards without classified notice in future.

### References

- [1] Clay Wilson " High altitude electromagnetic (HEMP) and high power microwave (HPM) devices: Threat assessments", CRS report for congress, July 21, 2008.
- [2] K.D Leuthäusser "A complete EMP environment generated by high altitude nuclear bursts",TN 363 10.1992.
- [3] Louis W. Seiler, Jr "A calculation model for high altitude EMP", Air force institute of technology, Mar. 1975.
- [4] W.J. Karzas and Richard Latter "Electromagnetic radiation from a nuclear explosion in space" The Physical Review, Vol. 126, No 6, June. 15, 1962.
- [5] W.J. Karzas and Richard Latter "Detection of the electromagnetic radiation from nuclear explosions in space", TN 40, Oct. 1964.
- [6] Chester D. Eng, "The development of the time dependence of the nuclear EMP electric field" LLNL-TR-420285. Nov. 16. 2009
- [7] John O. Curtis, "Electromagnetic power attenuation in soils", Environment laboratory U.S army engineer research and development center. ERDC/EL TR-05-5, August 2005.
- [8] Smith, S. S. and Arunlanandan, K. "Relationship of electrical dispersion to soil properties", Journal of the geotechnical engineering division, proceedings of the American society of civil engineers GT5, 591-604. 1981.
- [9] G.C. Min " IWIT 2011 HEMP Workshop" Mar. 10, 2011
- [10]G.C. Min, D.I. Kim "Design tool development of the effective HEMP hardening shelter" Institute of Webcasting Internet and Telecommunication" Vol. 10(4). pp.121-126. Sep. 2010
- [11] G.C. Min "Development of the HEMP hardening technology". Weekly Technical Trends" No.1491, Focus, April. 15, 2012

# Electromagnetic Simulation Models for Wideband Pulse Generators Driven By a High-voltage Spark-gap Switch

Jiheon Ryu\*, Jaimin Lee\*, Jin Soo Choi\*, Sung-Hyun Baek\*, Jin Kyung Jung\*

\*Agency for Defense Development, Daejeon, Republic of Korea

## Abstract

Electromagnetic simulation models (ESMs) for wideband pulse generators (WPGs) driven by a spark gap switch (SGS) are useful to design and analyse high power wideband radiators by allowing numerical simulations to be applied. This paper presents a method to convert the WPGs into the equivalent ESMs by separating the WPG into a static simulation model and a transient simulation model. A single pulse forming line was simulated, fabricated and tested to validate the proposed method. The measured results were in good agreement with the simulation.

**Keywords:** Electromagnetic simulation model, wideband pulse generator, spark-gap switch, pulse forming line.

## 1 Introduction

High-voltage spark gap switches (SGSs) that are capable of producing high-power transient electromagnetic fields have been widely used in wideband (WB) radiators including ultra-wideband (UWB) radiators [1]. Numerical electromagnetic simulation programs can be useful to design and analyse high-power wideband pulse generators (WPGs) driven by a nanosecond or sub-nanosecond spark gap switch (SGS). However, these programs do not allow the SGSs to be directly modelled.

In this paper, we present a powerful method to obtain electromagnetic simulation models (ESMs) of the WPGs integrated with a SGS by division of the WPGs into a static simulation model and a transient simulation model. We can calculate the fields and waves in the WPGs by superposition of the simulation results of the two models. A single pulse forming line (SPFL) was simulated, manufactured and tested. The simulation was in good agreement with the measurement [2].

## 2 Electromagnetic simulation model

Fig. 1 shows the procedure to convert a WPG driven by a high-voltage SGS into two simulation models that are able to be calculated by numerical electromagnetic simulation programs. The circuit in Fig. 1(a) is equivalent to the circuit in Fig. 1(b) that have two voltage sources of opposite polarity. The circuit in Fig. 1(b) is the same as the superposition of the circuit in Fig. 1(c) and Fig. 1(d). Because the circuit in Fig.

1(c) does not give rise to transients, it is a static simulation model. The circuit in Fig. 1(d) is a transient simulation model that has a step voltage source. We model the step voltage source by using the discharge properties including the breakdown voltage and rise time. The intact simulation results are obtained by superposing two simulation results for the circuits in Fig. 1(c), (d).

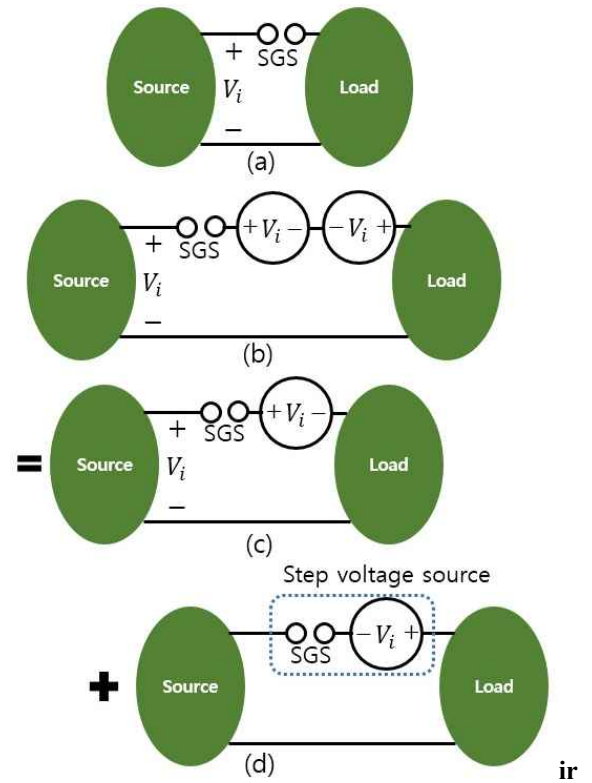


**Figure 1. Conversion of the WPG integrated with a high-voltage SGS.**

Fig. 2 shows a photograph of the 1-ns SPFL fabricated to apply the proposed ESM. The SGS is filled with the Nitrogen gas. Here, the static breakdown voltage  $V_b$  is calculated by

$$V_b(kV) = 6.72(pd)^{1/2} + 24.36(pd), \quad (1)$$

where  $p$  is the pressure in units of bars, and  $d$  is the gap distance in units of centimeters. The breakdown voltage calculated by (1) is 19.8 kV when the gap distance and

pressure of the spark-gap switch are 0.2 mm and 30 bar, respectively. The rise time  $t_r$  is computed by

$$t_r = \frac{88}{Z^{1/3} E^{4/3}} \left(\frac{\rho}{\rho_0}\right)^{1/2} \text{ ns}, \quad (2)$$

where  $E$  is the electric field strength in units of kilovolts per millimeter,  $\rho / \rho_0$  is the ratio of the density of the gas to air under standard temperature and pressure, and  $Z$  is the impedance of the generator driving the breakdown channel in ohms[3].

The simulated and measured waveforms nearly overlap for the major parts of the rectangular pulse, as shown Fig. 3. The measured and simulated full widths at half maximum are approximately 1.2 ns. The measured and simulated amplitude are approximately 7.4 V and 7.8 V, respectively by using a capacitive voltage divider. These voltages correspond to 9.76 kV and 10.3 kV. Although the breakdown voltage in the experiment is slightly higher than that in the simulation, the measured amplitude is smaller because all of the materials are lossless in the simulation. However, the error is only 5.5%. The simulation is in good agreement with the measurement. Therefore, it is concluded from these results that the proposed simulation method is valid.



Figure 2. Manufactured SPFL.

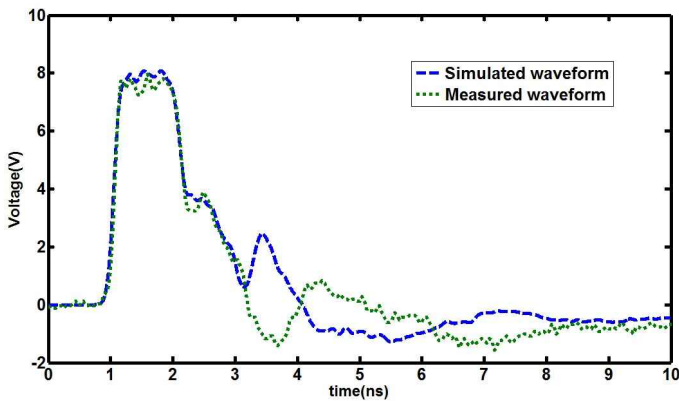


Figure 3. Voltages waveforms induced at the capacitive voltage divider inside the SPFL (simulation and measurement).

### 3 Conclusion

In this paper, an ESM to simulate the WPG driven by a high-voltage SGS was proposed. When we applied the ESM to the SPFL, good agreement between the simulated waveform and

the measured waveform was demonstrated. Because of this simulation method, we have more easily designed and analysed many complicated WB and UWB radiators driven by a high-voltage SGS.

### References

- [1] J. Ryu, J. Lee, H. Chin, J.-H. Yeom, H.-T. Kim, H.-O. Kwon, S. H. Han, and J. S. Choi, "A high directive paraboloidal reflector antenna for high far voltage in an ultra wideband source system," *IEEE Trans. Plasma Sci.*, vol. 41, no. 8, pp. 2283–2290, Aug. 2013.
- [2] J. Ryu, "Electromagnetic transient simulation of spark-gap switched pulse generators for predicting pulse waveforms," *IEEE Trans. Plasma Sci.*, vol. 42, no. 9, pp. 2193–2197, Sep. 2014.
- [3] J. C. Martin, "Solid, liquid and gaseous switches," in *Pulsed Power Lecture Series*, Issue 30, Lubbock, TX: Department of Electrical Engineering, Texas Technical University, 1978.

# Particle Simulation of Coaxial VIRCATOR

*S H Han\**, *J S Choi\**, *S H Baek\**, *T Hurtig*<sup>†</sup>

*\*Agency for Defense Development, Republic of Korea, <sup>†</sup> Swedish Defense Research Agency, Sweden*

## Abstract

**It is important to analyze numerically particle and field of microwave generator to develop the narrowband high power electromagnetic pulse generator. To design the coaxial virtual cathode oscillator we are running the particle simulation analysis with CST<sup>®</sup> Particle Studio Particle-in-Cell code. We have benchmarked the computerized analysis of coaxial VIRCATOR with MAGIC PIC code to verify availability with the help of FOI.**

**Keywords:** coaxial VIRCATOR, MAGIC, CST particle studio.

## 1 Introduction

We have developed the Ultra wideband (UWB) high power electromagnetic (HPEM) pulse generator with compact Marx high voltage generator, pulse forming line and integrated antenna source system (IAS). In addition, narrowband HPEM pulse generators have been researched, which have features of low output EM field efficiency and high susceptibility. A coaxial VIRCATOR has an advantage that it can be made compact.

We have analyzed numerically that high power electromagnetic pulse waves are generated from a coaxial VIRCATOR in order to design by a 3 dimensional particle-in-cell (PIC) code, called CST<sup>®</sup> particle studio (PS).

## 2 Coaxial VIRCATOR simulation

We have designed the coaxial VIRCATOR to radiate in S-band microwave and deliver a MW power in TE<sub>11</sub> mode. Since we have large experience using CST<sup>®</sup> microwave studio (MWS) to design various UWB HPEM pulse generator, we can easily apply CST<sup>®</sup> particle studio (PS) code to simulate electron emission at the cathode and wave conversion because of similar user interface. In addition, it is possible to be numerically analyze the whole coaxial VIRCATOR system such as, Marx high voltage generator operation and pulse forming in conjugate with MWS code.

To verify availability of the numerical analysis by CST<sup>®</sup> PS code, it is necessary to benchmark the computational simulation of a coaxial VIRCATOR by MAGIC PIC code in cooperation with FOI [1]. The geometry of Coaxial VIRCATOR and input pulse wave form was set in the same way as MAGIC PIC code, we have compared the simulation results of CST<sup>®</sup> PS code such as the electron emission current, AK voltage and radiated EM power.

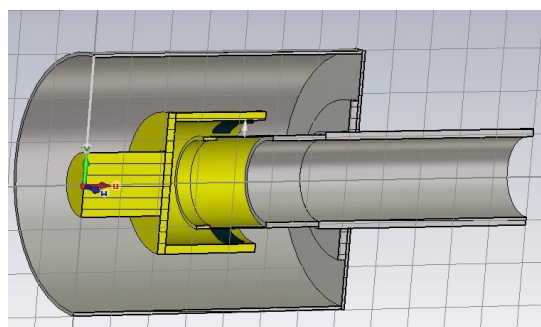


**Figure 1. The coaxial VIRCATOR simulation configuration of CST<sup>®</sup> PS PIC code.**

## 3 Conclusion

Compared with the coaxial VIRCATOR simulation by MAGIC<sup>®</sup> PIC code, CST<sup>®</sup> PS code have produced relatively same simulation result. Under the same input pulse, the diode voltage and current as a function of time have showed a similar trend between MAGIC and CST<sup>®</sup> PS code. The output electromagnetic field power of two codes was similar too. We concluded that CST<sup>®</sup> PS code can be used to design the coaxial VIRCATOR.

## References

- [1] C. Moeller. "Numerical Simulations of direct excitation of the TE<sub>11</sub> mode in a coaxial vircator", IEEJ Trans. FM, Vol. 127, pp. 687-692, Nov 2007.

# Prediction of EMP Coupling to Multi-conductor Transmission Lines by Using Different Iteration Methods.

Jun Guo, Yan-zhao Xie

State Key laboratory of Electrical Insulation and Power Equipment  
Electrical Engineering College, Xi'an Jiaotong University  
Xi'an, Shannxi, China  
gjgjgj@stu.xjtu.edu.cn, yzxie@mail.xjtu.edu.cn

## Abstract

The distributed analytical representation and iterative technique (DARIT) has been proposed for the calculation of electromagnetic pulse (EMP) radiated field coupling to multi-conductor transmission lines (MTLs). At first, this technique adopts the Jacobi iteration scheme (Jacobi-DARIT-field) or the Gauss-Seidel iteration scheme (Seidel-DARIT-field). More recently, based on these two methods, the JOR-DARIT-field and SOR-DARIT-field methods have been developed as well. This paper compares these four methods from the points of view of the accuracy and convergence speed, etc.

**Keywords:** analytical solution; electromagnetic pulse; iterative method; transient analysis; transmission line modeling; waveform relaxation.

## 1 Introduction

To predict the effects of EMP coupling to multi-conductor transmission lines (MTLs), many researchers have proposed the method of modeling of EMP coupling to MTLs [1]-[2]. To increase the computational speed, an approach using the distributed analytical representation and Jacobi iterative technique method which is based on the Waveform Relaxation and Transverse Partitioning (WR-TP) for the response computation between multi-conductor transmission lines illuminated by the incident EMP field (Jacobi-DARIT-field) [3] was proposed. The algorithm can avoid the need for inverting the matrix when solving MTLs equations and leading to high computational efficiency. To increase the convergence rate, another DARIT-field method employing the Gauss-Seidel Iteration Algorithm (Seidel-DARIT-field) has been developed [4].

As we know, the Jacobi iteration and the Gauss-Seidel iteration are the special case of JOR and SOR, respectively. This paper aims to compare the performance between the different iterative methods.

## 2 Outline of the methods

By applying waveform relaxation techniques [3] to the Telegrapher's equations, a recursive set of decoupled differential equations was obtained:

$$\frac{dv_i^{(r+1)}(x, s)}{dx} + z_{ii}(\omega)i_i^{(r+1)}(x) = - \sum_{j=1, j \neq i}^N z_{ij}i_j^{(r+1)}(x, s) + V_i'(x, s)$$

$$\frac{di_i^{(r+1)}(x, s)}{dx} + y_{ii}(\omega)v_i^{(r+1)}(x) = - \sum_{j=1, j \neq i}^N y_{ij}v_j^{(r+1)}(x, s) + I_i'(x, s)$$

The Jacobi iteration and Gauss-Seidel iteration schemes are shown in [3]-[4] in detail. The JOR iteration method and SOR iteration method are extended from the Jacobi iteration and Gauss-Seidel iteration, respectively. The iteration schemes are as follow:

$$v_{JOR,i}^{(r+1)}(x, s) = \omega_{JOR}v_{J,i}^{(r+1)}(x, s) + (1 - \omega_{JOR})v_{J,i}^{(r)}(x, s)$$

$$i_{JOR,i}^{(r+1)}(x, s) = \omega_{JOR}i_{J,i}^{(r+1)}(x, s) + (1 - \omega_{JOR})i_{J,i}^{(r)}(x, s)$$

$$v_{SOR,i}^{(r+1)}(x, s) = \omega_{SOR}v_{GS,i}^{(r+1)}(x, s) + (1 - \omega_{SOR})v_{GS,i}^{(r)}(x, s)$$

$$i_{SOR,i}^{(r+1)}(x, s) = \omega_{SOR}i_{GS,i}^{(r+1)}(x, s) + (1 - \omega_{SOR})i_{GS,i}^{(r)}(x, s)$$

where the  $v_{j,i}$  and  $i_{j,i}$  are the voltage response and current response of line  $i$  by Jacobi method,  $\omega_{JOR}$  is the relaxation factor (RF) for JOR method, the  $v_{GS,i}$  and  $i_{GS,i}$  are the voltage response and current response of line  $i$  by Gauss-Seidel method,  $\omega_{SOR}$  is the RF for SOR method.

The algorithms of iteration 1 of the four methods are the same, it only takes the illuminating EMP wave into account. At iteration 2, each line is excited not only by the incoming EMP wave but also by the coupling effects of all the other adjacent lines. The details of the Jacobi method and Seidel method are proposed in [3]-[4].

## 3 Validation of the proposed algorithm

A validation example is proposed to give a comparison between the four methods. In the example, a symmetrical and lossy three wires with the length of 50 cm, height of 1 cm, diameter of 1 mm and distances between lines of 1 cm which above the lossy ground is considered. The loads on both sides are 50  $\Omega$ . Fig. 1 shows the response of wire #1 obtained with the conventional method (Chain Parameters Matrix method) and with the four methods with the RF for JOR method and SOR method equal to 0.52 and 0.8, respectively. The results of the relative errors  $\varepsilon$  are presented in Table I. It can be seen

that the results from JOR and SOR methods are more accurate than the Jacobi and Gauss-Seidel method with the proper RF.

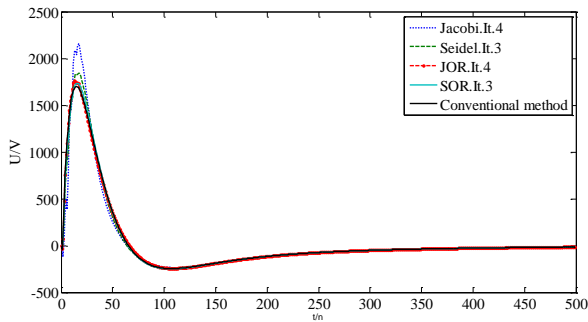


**Figure 1. The far-end response of wire 1 with different coupling factors.**

Table 1. Relative errors of the each method

$\varepsilon$ (%)			
<i>Jacobi.It.4</i>	<i>Seidel.It.3</i>	<i>JOR.It.4</i>	<i>SOR.It.3</i>
0.152	0.053	0.034	0.021

### 3 Conclusion

The validation result shows that JOR-DARIT-field and SOR-DARIT-field methods have faster convergence speed than Jacobi-DARIT-field and Seidel-DARIT-field method. However, it is worthy to note that the performances of JOR method and SOR method are quite depends on the RF, therefore, how to choose an optimal RF is still an open problem.

### References

[1] Paul, CR. Analysis of Multiconductor Transmission Lines, Second Edition. 2008, New York: John Wiley & Sons.  
 [2] Paul, CR. Solution of the Transmission-Line Equations Under the Weak-coupling Assumption. *IEEE Trans. Electromagnetic Compatibility*, 2002, 44( 3): 413—423.  
 [3] Y. Z. Xie, J. Guo and F. Canavero, "Analytic iterative solution of electromagnetic pulse coupling to multiconductor transmission lines," *IEEE Transactions on Electromagnetic Compatibility*, vol.55, no.3, pp.451-466, June 2013.  
 [4] J. Guo, Y. Z. Xie and F. Canavero, "Gauss-Seidel Iterative Solution of Electromagnetic Pulse Coupling to 3-Conductor Transmission Lines," *IEEE Transactions on Electromagnetic Compatibility*.

# Propagation Characteristics of the UWB EM Wave in Soil Media and its Influence on the Detection of Buried Unexploded Ordnance

S . Vijayakumar<sup>1</sup> and M. Joy Thomas<sup>2</sup>

Pulsed Power and EMC Lab, Dept. of Electrical Engineering,  
Indian Institute of Science, Bangalore, India

<sup>1</sup>s.vijayakumar@ee.iisc.ernet.in, <sup>2</sup>jtm@ee.iisc.ernet.in

## Abstract

Threat posed by the Unexploded Ordnance (UXO) is well known and is felt across all the conflict affected countries. At present there exists no equipment/system to detect the unexploded buried ordnance (UXO), which satisfies United Nations Main Action Standard (UNMAS) for the safe removal and disposal of such UXO. Considerable research work is carried out on the Ultra-Wide Band (short pulse) ground penetrating imaging of buried mine. This paper deals with the influence of the soil medium and the incident Electromagnetic (EM) wave frequencies on the landmine detection range and its resolution. Studies were carried out for different soil type as well as varying moisture content. Raleigh criterion minimum resolvable time is calculated for different buried soil depth and soil moisture for various incident EM wave bandwidths. For a moist soil, it is found that incident EM wave of 3 to 5 GHz is having a better range and resolution. One dimensional Finite Difference Time Domain (FDTD) method with piecewise linear recursive convolution (PLRC) technique is used to study the EM wave propagation in the soil media.

**Keywords:** Unexploded Ordnance (UXO), Ultra-wide Band (UWB), Ground Penetrating Radar (GPR), Electromagnetic (EM) wave.

## 1 Introduction

Past conflicts have left behind around 160 million landmines buried in the ground, killing or injuring more than 4,000 people every year. Geneva International Centre for Humanitarian Demining (GICHD) in its report on mine action equipment has commented on the lack of R&D in landmine detection technology. The report also provides important capability area, which can significantly improve the detection of buried landmines. GICHD has identified that improvements in close in detection and detecting outer edge of the landmine leads to more than 10% improvement in landmine detection. This calls for a better theoretical understanding of every important element in the detection system.

### 1.1 UWB GPR Imaging of Buried Landmine

To achieve the stringent UN requirement of 99.96% landmine detection, advanced detection systems with capability of target identification and classification is required. Buried landmines are detected based on reflected EM wave due to

difference in the permittivity of the landmine and its host soil medium. It is shown that GPR using EM wave of frequency spectrum up to 2GHz has very low depth resolution, but offer better detection range. Remote sensing satellites operating in Ku, K and Ka band incident EM wave offer better depth resolution but have very low detection range and are mainly used for earth surface imaging. Many works have been carried out to use frequency spectrum in-between normal GPR and UWB imaging GPR, which has a range of around 15-20 cm to detect the anti-personal mines. To arrive at an optimum frequency for all weather buried landmine detection system, detailed study of the soil medium is required. Estimation of soil depth at which landmine is buried is really difficult due to the variability of the soil media. This paper deals with the resolution involved in estimating the depth of burial of landmine. Selection of incident EM wave parameters like bandwidth, field intensity, polarization, incident angle are very important to achieve the required range and depth resolution. In this work, computer simulation has been carried out to study the EM wave propagation in the soil medium and the influence of incident EM wave bandwidth and its magnitude on the detection range and resolution.

## 2. Electrical Properties of the Soil

In-depth knowledge of electrical and physical property of the soil medium is very important for the design of land mine detection system. Soil is a multi-phase medium with the significant moisture content. Important electrical properties of the soil include DC conductivity ( $\sigma$ ) and the complex dielectric permittivity ( $\epsilon^*$ ). Effect of DC conductivity on EM wave attenuation is negligible at higher frequencies, but for a soil with the nominal moisture content and for the conductivity above 6mS/m, considerable attenuation is observed for frequencies in the range of 300MHz to 5GHz.

### 2.1 Electromagnetic Modelling of the Soil

Many researchers have attempted to find a suitable dielectric model for the soil, considering its texture, temperature, moisture content and organic materials. Deloor [1] has shown that, it is impossible to find an exact dielectric model for the soil and proposes bounds for dielectric permittivity of the soil. Available theoretical mixing model of the soil is very difficult to implement in FDTD method. Also exact mixing models for the frequency of interest are not available. In this paper Double Debye model [2] as given in eq.1 with six unknown parameters namely static permittivity ( $\epsilon_s$ ), high frequency

permittivity ( $\epsilon_\infty$ ), two relaxation times ( $\tau_1, \tau_2$ ), high frequency conductivity ( $\sigma_{model}$ ) and interpolation constant (C) are used to model the soil. Weighted least square method (WLS) is used to find the above unknown parameters in the Double Debye model of the soil using experimental results available in the literature [3-5].

$$\epsilon^* = \epsilon_\infty + \frac{(\epsilon_s - \epsilon_\infty)C}{1 + j\omega\tau_1} + \frac{(\epsilon_s - \epsilon_\infty)(1-C)}{1 + j\omega\tau_2} + j \frac{\sigma_{model}}{\omega\epsilon_0} \quad (1)$$

Table 1: Soil details and its various unknown parameters estimated using WLS method from the experimental data, for all soils,  $\sigma_{model} = 0$

Soil Name	Soil Texture	Moisture Content%	$\epsilon_\infty$	$\epsilon_s$	C	$\tau_1$	$\tau_2$
Soil-1	Clay	7.5	3.53	5.66	0.01	2.0E-9	5.81E-11
Soil-2	Clay	14	5.82	11.15	0.57	1.04E-10	1.14E-10
Soil-3	Silty Clay	15	5.53	14	0.01	2.0E-9	1.03E-10

### 3. FDTD Formulation of the EM Wave Propagation in Soil

One dimensional (1D) simulation offers an initial estimate of the required bandwidth of the incident EM wave and also provides a better insight into the influence of incident EM wave frequencies on the depth of the soil penetration for different soil media. Dispersive characteristics of the soil medium is implemented by using Piecewise linear recursive convolution technique [6] (PLRC). Many one dimensional simulations of the sub surface detection of target have been reported in the literature [7], but all those lack in-depth analysis of the soil characteristics and depth resolution. Dielectric property of the soil is modeled by Double Debye (contains two relaxation time) relaxation model. Scattered field/Total field (SF/TF) method is used to inject the incident EM plane wave. Uni-axial perfectly matched layer (UPML) with polynomial conductivity profile is used to truncate the domain at either ends. A block diagram of the one dimensional simulation model of the landmine detection system, where a landmine of permittivity  $\epsilon_r = 3.5$  is buried under the soil medium is shown in the fig.1.



Fig.1. 1D- Simulation domain of landmine detection system

Sinc function time domain EM wave represented by eq.2 of varying maximum frequency ( $f_{max}$ ) is used as incident EM source due to its simple low pass frequency characteristics

$$E(t) = \frac{\sin(2\pi f_{max}t)}{2\pi Bt} \quad (2)$$

### 4. EM Wave Propagation in Soil Medium

Soil relaxation and DC conductivity ( $\sigma$ ) causes attenuation in the incident EM wave leading to the magnitude of the transmitted signal getting decreased exponentially. Fig. 2 shows the cut off frequency of different soil. It is found that

for a soil with medium moisture content and for a soil depth beyond 2cm, maximum frequency that can propagate is independent of the incident EM wave bandwidth. So for detection of targets buried beyond 5 cm, using higher bandwidth offers not much improvement in the detection.

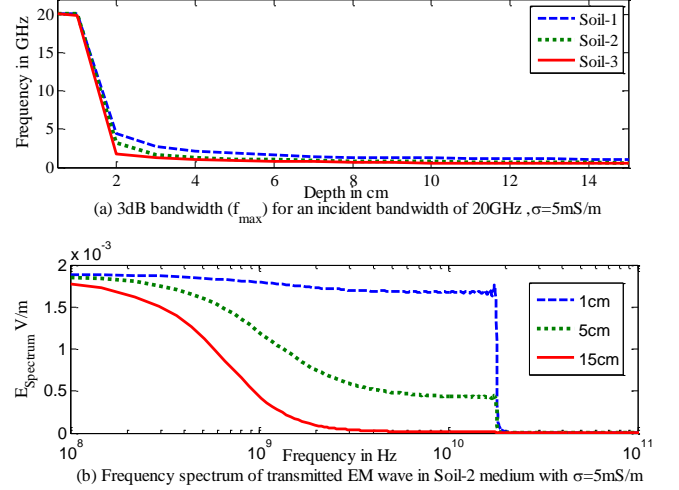


Fig.2. Propagated EM wave frequency characteristics and its maximum frequency in Soil-2,  $\sigma = 5\text{mS/m}$

### 5. Depth Resolution in Landmine Detection.

Simulations were carried out to study the soil depth resolution in the region between the air and the landmine top interface. Raleigh resolution criterion is used to set the resolution time threshold. Resolution time ( $t_{res}$ ) is defined as the time difference between the peaks of the reflected wave from air-soil ( $E_{a-s}$ ) interface and soil-landmine top interface ( $E_{s-m}$ ) as shown in the fig. 3. Resolution time threshold ( $t_{hw}$ ) is taken to be maximum of falling half time width of air-soil clutter and rising half time of soil-landmine reflected signal. The reflected signal from landmine is broader than the air clutter. As shown in the fig. 3 rising half time of landmine reflected signal is taken as the resolution threshold. Though higher bandwidth offers better resolution, it reduces the detection range.

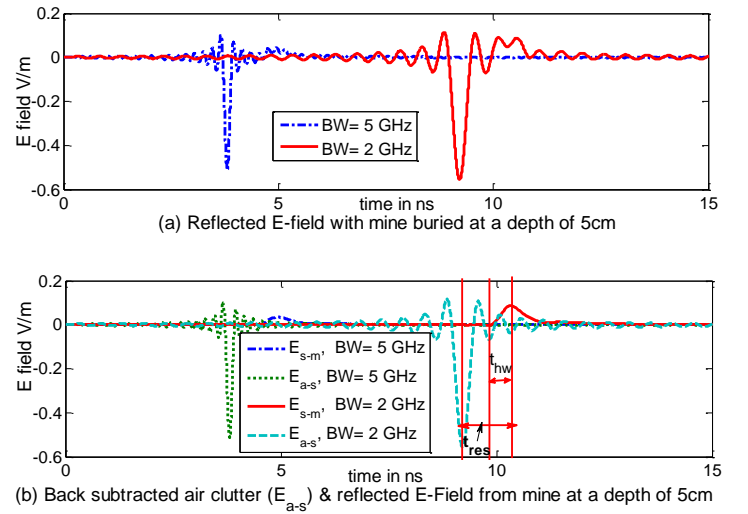


Fig.3. Reflected EM wave in the Soil-3 with  $\sigma = 5\text{mS/m}$

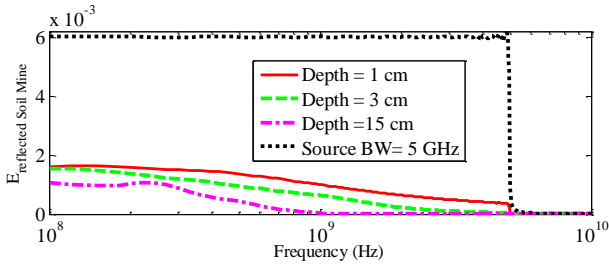
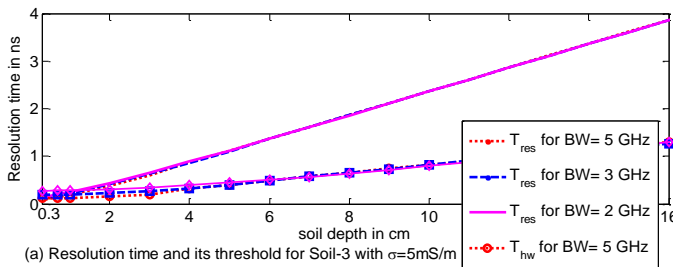
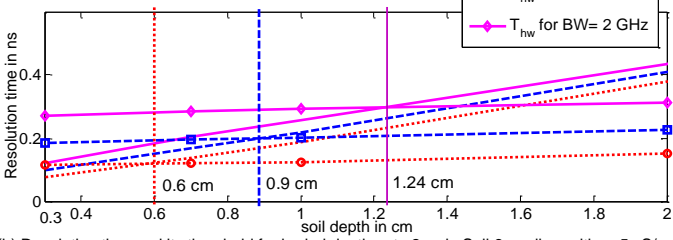


Fig.4 Frequency Spectrum of reflected signal from landmine buried in Soil-3 with  $\sigma = 5\text{mS/m}$

Fig. 4 shows that the frequency spectrum of the reflected wave from the landmine buried at a depth greater than 3cm will have the same frequency content. As the Fig. 5, shows that in a medium moist soil for a depth greater than 3cm, the resolution time is independent of the incident EM wave bandwidth due to high frequency attenuation.

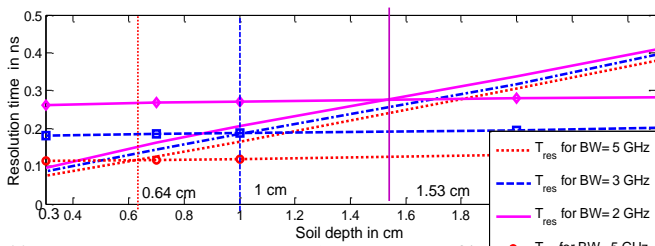


(a) Resolution time and its threshold for Soil-3 with  $\sigma=5\text{mS/m}$

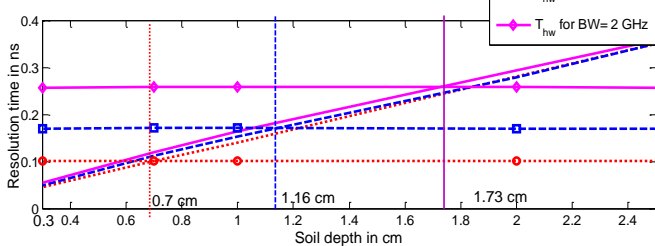


(b) Resolution time and its threshold for buried depth upto 2cm in Soil-3 medium with  $\sigma=5\text{mS/m}$

Fig. 5. Resolution time ( $t_{res}$ ) and its Raleigh Threshold ( $t_{hw}$ ) in Soil-3 with  $\sigma = 5\text{mS/m}$ .



(a) Resolution time  $t_{res}$  and its threshold  $t_{hw}$  for soil-1 with  $\sigma=5\text{mS/m}$



(b) Resolution time  $t_{res}$  and its threshold  $t_{hw}$  for dry soil with constant  $\epsilon_r=4.5$  &  $\sigma=5\text{mS/m}$

Fig. 6. Resolution time ( $t_{res}$ ) and its Raleigh Threshold ( $t_{hw}$ ) in Soil-1 & Dry soil with  $\sigma = 5\text{mS/m}$ .

Target can be assumed to be resolvable, if resolution time is greater than the resolution threshold. Figure 5 and 6 show that high moist content soil has better depth resolution than the low moist soil, higher moisture in soil offer better threshold but it also limits the magnitude of E field peak and signal to noise ratio. Fig. 7 shows the proportion of the reflected E-field with respect to the peak of air soil clutter. For a given incident wave bandwidth, dry soil offer low resolution. So to achieve higher resolution in dry soil, incident wave bandwidth have to be increased, but it reduces the signal to noise ratio in the moist soil. High power incident EM wave with ultra wide bandwidth have to be used to achieve better resolution ( $<1\text{cm}$ ) in both dry and moist soil. Therefore for moist soil, using the very high frequency beyond 5GHz is not advisable for subsurface detection of mines buried more than 5cm below the soil surface.

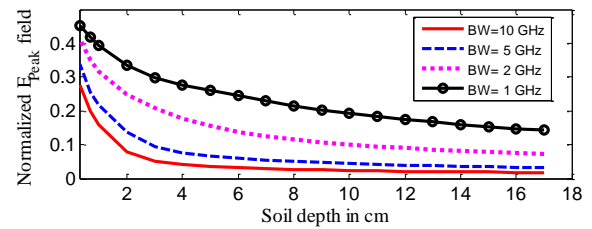


Fig. 7. Peak reflected E-field normalized to peak of air soil clutter for Soil-3 with  $\sigma = 5\text{mS/m}$

## 6. Conclusion

One dimensional FDTD simulation provides wide range of information on incident wave bandwidth and its magnitude. For a soil with the medium moisture content, frequency spectrum of the propagated EM wave in the soil medium beyond 2cm is independent of the incident wave bandwidth and incident EM wave bandwidth from 3GHz to 5GHz offers better trade of between range and its resolution. High power incident EM wave scales the magnitude of the required signal and offers better signal to noise ratio. DC conductivity more than 5mS/m, has significant impact on the attenuation of frequency of interest to find the resolution.

## References

- [1] De Loor, *The Dielectric Properties of Wet Materials*, IEEE Trans. on Geoscience and Remote sensing, Vol GE-21, No-3, pp. 364-369, 1983
- [2] Bhagat, P. K., Kadaba, P.K., *Relaxation Models for Moist Soils Suitable at Microwave Frequencies*, Material Science and Engineering, Elsevier Sequoia S.A. Vol. 28, pp. 47-51, 1977.
- [3] Hoekstra P. and Delaney, A., Dielectric Properties of Soils at UHF and Microwave Frequencies, Journal of Geophysical research, Vol. 79, pp 25-34, No. 11, 1974.
- [4] Hallikainen, M. T., et all, *Microwave Dielectric Behavior of Wet Soil Part I: Empirical Models and Experimental Observations*, IEEE Proc. Geoscience and Remote Sensing, Vol. GE-23, No.1, pp. 25-34, 1985.
- [5] John O.Curtis, Charles A. Weiss, Jr., Joel B. Everett, *Effect of Soil Composition on Complex dielectric Properties*, US Army Corps of Engineers, Technical Report EL-95-34, December 1995.
- [6] Taflov A., Hagness S.C., *Computational Electrodynamics: The Finite-Difference Time-Domain Method, second Edition*, Artech House, 2000.
- [7] Thomas P. Montoya, Glenn S. Smith, *Land Mine Detection Using a Ground-Penetrating Radar Based on Resistively Loaded Vee Dipoles*, IEEE Trans. on Geoscience and Remote sensing, Vol 47, No-12, pp. 1795-1806, 1999

# Recent Research Activities to Investigate the Interaction of Electromagnetic Waves and Cells of the Haematopoietic System

*Lars Ole Fichte, Marcus Stiemer*

*Helmut Schmidt University, Faculty of Electrical Engineering, Hamburg, Germany*

## Abstract

Investigations of the reaction of biologic tissue to external electromagnetic fields is becoming more and more important in modern day signal environment with its evergrowing number of electromagnetic emissions, both intended (i.e. cellphones, WLAN-routers, microwave transmission lines) and unintended (i.e. power leakage from apertures in computer casing, magnetic fields from power lines, stray fields from inductive battery charging stations). However, fundamental properties of cell tissue combined with the characteristics of electromagnetic waves make experiments rather difficult, since a large variety of different test setups with a large number of samples have to be taken into consideration. This paper discusses recent approaches to investigate the interactions between electromagnetic waves and cell of the haematopoietic system, which is believed to be easily exposed to external field. Ongoing tests are discussed with a focus on test setups, as well as intermediate results.

**Keywords:** Cell Damages, Haematopoietic System, Terahertz waves, GSM signal, Microwaves.

## 1 Introduction

The effects of external stress on biological tissue by any kind of external phenomena (be electric, magnetic, electromagnetic, radiating or toxic) is usually investigated by setting up a rigid test, i.e. by defining an environment with fixed conditions for all parameters. For all phenomena mentioned

1. temperature,
2. (relative) humidity (and, sometimes, barometric pressure),
3. dimensions of the test setup (including if any physical boundaries exists with the surroundings),
4. magnitude of the external stress on the tissue under test.

In case the tissue exposed to an external electromagnetic wave, we must add three parameters which make a complete test rather difficult:

1. frequency of the electromagnetic field,
2. direction of the electromagnetic wave,
3. polarization of the electromagnetic wave.

These parameters must be give extra thought, because biological tissue has a permittivity which is depending on the frequency [1] and has been found to show anisotropic characteristics [2].

## 2 Possible test setups

The complicated nature of the "devices" under test (i.e. the biological samples) leave a multitude of possibilities to setup an exposure test. The most common way is to use a test device which allows to generate an electromagnetic field with well defined parameters. This approach is very demanding to the scientist and will result in a experimental setup with a very small test volume (i.e. the volume in which the electromagnetic field has the specified parameters). The reasons for both difficulties is that the wavelength for signals in the RF range is quite small and defined field magnitude can be guaranteed only in a small volume. Primary setup for the tests will use a  $\mu$ TEM cell

Another possibility is the use of an electromagnetic reverberation chamber. An reverberation chamber is an overmoded resonator with a metallic stirrer inside, which is turned (continuously or stepwise; stepwise has become standard in the last years) to effect the field inside the resonator. If the stirrer is efficient enough and an sufficient number of stirrer positions were chosen, the electric field in circa 10 percent of the volume of the resonator (called the test volume) shows three properties which can be used for testing (both electric devices and biological tissue):

- The expectancy of the mean of the magnitude of the field when averaged over the stirrer positions is constant.
- The direction of the electromagnetic wave is homogenously distributed.
- The polarization of the electromagnetic wave is homogenously distributed.

These characteristics apply for all frequencies above a minimum frequency, which is called lowest usable frequency (LUF) and which is near the frequency of the 60-th eigenmode of the resonator. If those conditions are met, an MSC provides a very large test volume at for comparatively low efforts.

## 3 Assessment of cellular damage

Cell culture is understood as a complex process, by which cells of different origin (for example multi-cellular eukaryotes, especially animal cells but also plants, fungi and microbes) are grown under controlled conditions, generally outside of their natural environment. different cell culture techniques (especially the advancement of culture medium, appropriate temperatures and gas mixtures for growing in a cell incubator)

are available to support research and to assess the damages of cell cycle by different effects.

As cells become damaged by different effects (for example radiation) or are no longer needed, they undergo apoptosis or programmed cell death, a normal physiological process that occurs during embryonic development and tissue homeostasis maintenance. Apoptosis is understood as an organized process that signal cells to destruct themselves in order to control the death of damaged cells. With the help of Annexin V it is possible to label cells. By multicolor flow cytometry one can separate apoptotic and undamaged cells. Cells are incubated with FITC Annexin V in a buffer containing propidium iodide (PI) and analyzed by flow cytometry. Untreated cells were primarily FITC Annexin V and PI negative, indicating that they were viable and not undergoing apoptosis.

Further evaluations are planned with the use of gel electrophoresis, utilizing the Comet assay to look for spindle disturbances (e.g. multiple kernels, DNA breaks or else).

In a last step, the exposed samples will be analysed for genetic damages by gene expression profiling. A collection of microscopic DNA spots attached to a solid surface, the complimentary DNA sequences are isolated and tagged with fluorescent materials, which can be detected. The reaction of the DNA will give hints on the effects of electromagnetic radiation and will determine if a tissue reaction is of a thermals nature or not [4].

### 3 Assessment of cellular damage

When the examination of tissue samples is done, special care must be applied to exclude possible external influences. The mandatory actions required to achieve valid results include

- shielding of the setup from external electromagnetic signals, e.g. cell phones or radio stations after a measurement of the field magnitude in the laboratory,
- recording of the environmental parameters during the exposition: temperature, humidity, air pressure and CO<sub>2</sub> level,
- recording of the power generated by the RF Source.

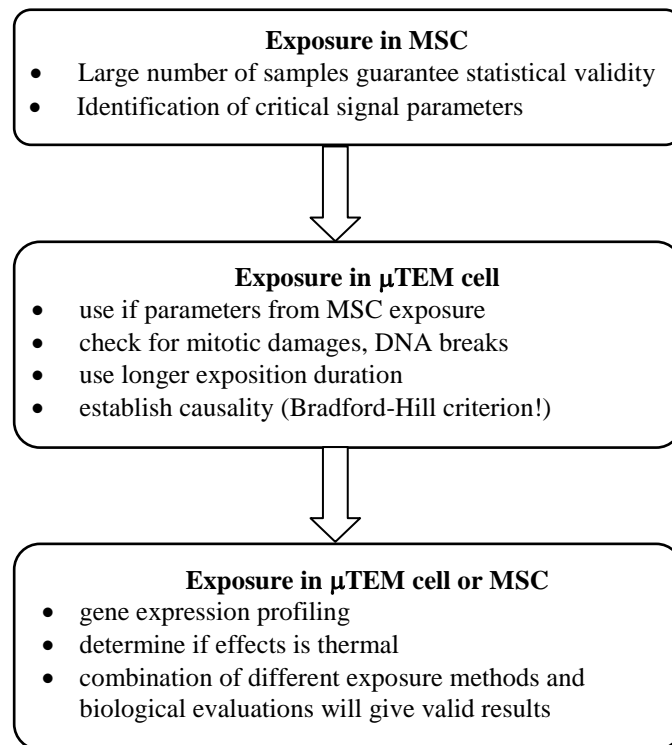
To cope with the fact that the tissue sample consist of living matter and display a variability of damage rates, a sufficiently high number of sample that are submitted to sham exposure (like in the real test, but with an inactive RF source) must be provided, plus negative and positive test samples.

Additionally, to counter the human bias, all tests should be performed randomized and double blind, i.e. controlled by a computer in a way that the lab personnel will perform the biological tests without prior knowledge about the exposure parameters.

A final assessment of the result can only be done after several repetitions of any result, and a causal link between electromagnetic cause and biological effects must be reviewed with the Bradford-Hill [3] criteria in mind.

### 4 Proposed test plan for future Research

The process of the planned tests is displayed below:



### Acknowledgements

We wish to thank your partners for their valuable support:

1. Bundeswehr Research Institute for Protective Technologjes - NBC-Protection, Munster, Germany
2. German Military Medical Service, Munich, Germany,
3. Bundeswehr Institute of Radiobiology, aff. to the Univ. of Ulm, Germany.

### References

- [1] Gabriel, C. und Gabriel, S.: Compilation of the *Dielectric Properties of Body Tissues at RF and Microwave Frequencies*, <http://niremf.ifac.cnr.it/docs/DIELECTRIC/Report.html>.
- [2] Burger, H.C. und van Dongen, R: *Specific Electric Resistance of Body Tissues* Phys. Med. Biol. 5 431, 1961 , doi:10.1088/0031-9155/5/4/304.
- [3] Bradford Hill, A.: *The Environment and Disease: Association or Causation?*, Proceedings of the Royal Society of Medicine, 58 (1965), 295-300.
- [4] Bellossi, A. and Dubost, G.: *Thermal and non thermal effects of electromagnetic fields on bio-systems*. Lulu book on demand ID No. 12433369. 2012.
- [5] Hintzsche, H.; Jastrow, C.; Kleine-Ostmann, T.; Schrader, T. and Stopper, H.: *900 MHz radiation does not induce micronucleus formation in different cell types* Mutagenesis pp. 1–7, 2012. doi:10.1093/mutage/ges007

# The effect of standard cell culture environment on cellular electromagnetic effects study

Wen-yu Peng\*, Jian-gang Ma\*, Xiao-yun LU\*, Yan-zhao XIE †

\* Xi'an Jiaotong University, School of Life Science and Technology, Xi'an 710049, Shaanxi, China.

† Xi'an Jiaotong University, School of Electrical Engineering, Xi'an 710049, Shaanxi, China.

## Abstract

Biological effects of electromagnetic radiation are drawing increasing attentions nowadays. To facilitate the cell based molecular mechanism study of EMF bio-effects, an integrated system combined a cell incubator with a TEM-cell was developed which shows a very good performance. In this study, the cell viability, ROS production and mitochondrial membrane potential of PC3 cells with or without EMP treatment were determined and the results demonstrated the cell responses to EMP radiation were different in the TEM cell combined-incubator or in the open area. Therefore, it's necessary to standardize the culture condition coordinate with the EMP intervention to illustrate the bioeffects from solo EMP radiation without the interference from other environmental factors.

**Keywords:** incubator with TEM-cell, cell viability, ROS, mitochondrial membrane potential

## 1 Introduction

Nowadays, the biological effects of electromagnetic radiation draw more and more attentions from both physicists and biologists. Many studies have been carried out to investigate the cellular response to various electromagnetic radiations. While *in vitro* cell cultivation requires standard culture conditions such as temperature of 37 °C and 95% humidified environment with 5% CO<sub>2</sub> [1]. Change of the temperature or the pH of medium could activate or inhibit many cell signaling pathway and result in the cell behavior alternation. Therefore, maintain the standard cultivation environment during EMF treatment is of great importance to obtain the precise results for cell based study.

In our previous study, an incubator combined with TEM-cell has been constructed to establish the identical cell culture condition with electromagnetic radiation [2]. In this study, we compared the cell response to EMP stimulation in the standard culture condition with that in the open area and reveal that the culture environment during EMP treatment could result in

significant difference of some biological analysis and therefore could led to controversial data. This study demonstrate that for the bioelectromagnetic effects study in cell-based level, it's necessary to carry out the electromagnetic radiation under the standard cell culture condition to coordinate with biological analysis.

## 2 Material and method

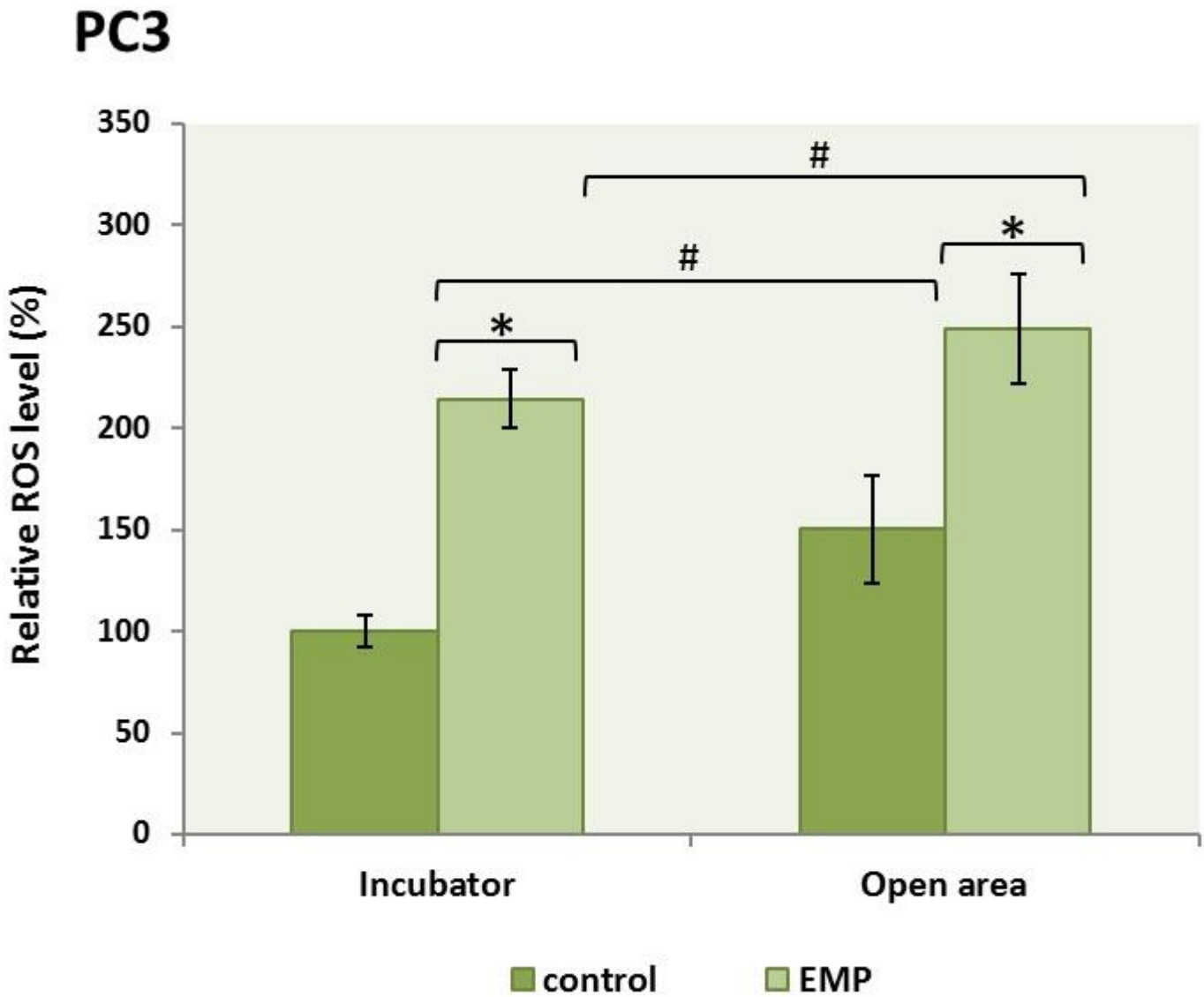
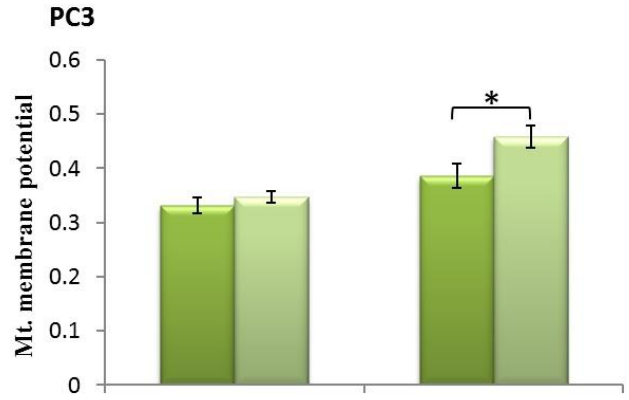
Human prostate cancer cell line PC3 was used to evaluate the cell response to EMP treatment in the open area and in the incubator. PC3 cells were maintained in RPMI 1640 which was supplemented with 10% fetal bovine serum (Gibico) and 1% penicillin-streptomycin in humidified environment of 5% CO<sub>2</sub>. Cells were seeded in triplicate at  $1 \times 10^4$  cells/well in 96-well culture plates and treated under pulsed EMF (30kV/m, 25 pulse/min) for 1.5h at open area and in the incubator, respectively. Cell viability was quantified by cell counting kit-8 (CCK-8) assay and the intracellular reactive oxygen species (ROS) level was determined by fluorescence analysis with dichlorodihydrofluorescein diacetate (H<sub>2</sub>DCFDA) as the indicator. JC-1 staining method was used to reveal the mitochondrial membrane potential. Relative cell viability, ROS production and mitochondrial membrane potential were calculated with regard to that of the control group at 37 °C in the incubator, which was set to 100% viability.

## 3 Result

EMP radiation decreased the PC3 cell viability when cells were treated in the open area. But when cells received the EMP radiation inside the incubator, the effect of electromagnetic treatment on the cell viability was not significant. Although the EMP radiation increased the ROS production no matter cells were treated inside the incubator or in the open area (Fig. 2), but the degree of variations were 2.48 times and 1.44 times in the incubator and in the open area, respectively. For the mitochondrial membrane potential analysis, there was no significant difference between the EMP treated and non-treated

group in the incubator, but slight decrease of mitochondrial membrane potential could be detected when cells were treated in the open area. These results demonstrated that the cell responses to EMP radiation were not coordinated, which might due to the changing of the culture condition during EMP treatment. For the groups treated in the open area, cell activity was changed because the alternation of growth environment (in this case mainly the temperature). After leaving at the open area for 1.5h with or without EMP radiation, cells were incubated again in the incubator for cell viability assay, ROS determination and mitochondrial membrane potential analysis for another period. During this time, response to the alternation of the culture condition again, cells might undergo an adaptation for recovery from the open area stress. Therefore, cell behavior might alter

**Figure 2. The effect of EMP radiation and treating condition on ROS level**  
 \*: compare between the groups with the same treating condition.



of  
Y  
s.  
s  
h  
P  
d

# Examples of the Power Wave Theory of Antennas

*E. G. Farr*

*Farr Fields, LC, 1801 Count Fleet St, Albuquerque, NM, USA, egfarr@gmail.com*

## Abstract

Power wave theory provides a complete and simple description of antenna performance in both the frequency and time domains. To clarify its usefulness, we provide here a number of examples. First, we show how the theory can be used to describe the performance of electrically small electric and magnetic dipoles; the so-called D-dot and B-dot sensors. We calculate the antenna transfer function, and then provide standard antenna parameters, including gain, realized gain, effective length, and effective area. Second, we show how a matching circuit can be combined with an antenna to form a combined Generalized Antenna Scattering Matrix. With this, we show how two common matching circuits affect antenna performance.

**Keywords:** Power wave theory of antennas, electrically small electric and magnetic dipoles, D-dot and B-dot antennas, matching circuit, generalized antenna scattering matrix.

## 1 Introduction

In our papers on the power wave theory of antennas [1, 2], we showed a complete description of antenna performance in both the frequency and time domains. This fills a gap in current antenna theory by providing the simplest possible description of antenna performance in the time domain. It also fills a gap in the frequency domain, since neither antenna gain nor radar cross section include phase information.

Some reviewers of [1, 2] have requested examples of power waves applied to common antennas. We therefore provide here a series of examples that expand upon these ideas. First, we review the definitions of terms. Next, we show how the theory of power waves applies to electrically small electric and magnetic dipoles; or D-dot and B-dot sensors. Third, we show how to add a matching circuit to an antenna, and incorporate its scattering parameters into the Generalized Antenna Scattering Matrix. Finally, we show how some common matching circuits affect antenna performance. We begin now with a review of the definitions. This paper is a summary of material covered in [3].

## 2 Review of Power Waves Applied to Antennas

We summarize here the power wave theory of antennas [1, 2]. In those two papers, we argued that an antenna can be reduced to a 3-port network. One port is the antenna port, and

the second and third ports are the  $\theta$ - and  $\phi$ -polarizations of the incident and scattered fields. We define the following parameters relating to far-field performance as

$$\begin{array}{ll}
 \text{Source Power Wave} & \text{Received power wave} \\
 \tilde{\Pi}_{src} = \frac{\tilde{V}_{src}}{\sqrt{Z_{o1}}} & \tilde{\Pi}_{rec} = \frac{\tilde{V}_{rec}}{\sqrt{Z_{o1}}} \\
 \text{Incident power flux density wave, } \theta \text{ \& } \phi \text{ polarizations} & . (1) \\
 \tilde{\Sigma}_{\theta,inc} = \frac{\tilde{E}_{\theta,inc}}{\sqrt{Z_{o2}}} & \tilde{\Sigma}_{\phi,inc} = \frac{\tilde{E}_{\phi,inc}}{\sqrt{Z_{o2}}} \\
 \text{Radiated radiation intensity wave, } \theta \text{ \& } \phi \text{ polarizations} \\
 \tilde{Y}_{\theta,rad} = \frac{r \tilde{E}_{\theta,rad}}{\sqrt{Z_{o2}}} e^{jr} & \tilde{Y}_{\phi,rad} = \frac{r \tilde{E}_{\phi,rad}}{\sqrt{Z_{o2}}} e^{jr}
 \end{array}$$

Here,  $\tilde{E}_{rad}$  is the radiated far field,  $\gamma = s/v = jk$ ,  $s = j\omega$ , and  $k = \omega/v = 2\pi f/v$  is the propagation constant in the surrounding medium. Furthermore,  $v$  is the velocity of propagation in the surrounding medium, and  $r$  is the distance from the antenna to the observation point in the far field. In addition,  $Z_{o1}$  and  $Z_{o2}$  are the real reference impedances associated with the antenna port and the surrounding medium – most commonly,  $Z_{o1} = 50 \Omega$  and  $Z_{o2} = 120 \pi \Omega$ . The tilde indicates that we are operating in the Laplace domain.

The symbols  $\Pi$ ,  $Y$ , and  $\Sigma$  are Greek versions of  $P$ ,  $U$ , and  $S$ , which are the commonly used symbols for power, radiation intensity, and power flux density, respectively. Thus, to convert the symbol for a “power” quantity to that of a “power wave” quantity, we make the symbol Greek.

The above quantities are assembled into the antenna equation, which is a 3x3 matrix equation. We can express these two different ways, leading to

$$\begin{bmatrix} \tilde{\Pi}_{rec} \\ \tilde{Y}_{\theta,rad} \\ \tilde{Y}_{\phi,rad} \end{bmatrix} = \begin{bmatrix} \tilde{\Gamma} & \tilde{h}_{\theta} & \tilde{h}_{\phi} \\ s \tilde{h}_{\theta} / (2\pi v) & \tilde{\ell}_{\theta\theta} & \tilde{\ell}_{\theta\phi} \\ s \tilde{h}_{\phi} / (2\pi v) & \tilde{\ell}_{\phi\theta} & \tilde{\ell}_{\phi\phi} \end{bmatrix} \begin{bmatrix} \tilde{\Pi}_{src} \\ \tilde{\Sigma}_{\theta,inc} \\ \tilde{\Sigma}_{\phi,inc} \end{bmatrix}, \quad (2)$$

where  $\tilde{\Gamma}$  is the reflection coefficient looking into the antenna port, the two components of  $\tilde{h}$  represent the vector transfer function, and the four components of  $\tilde{\ell}$  represent the dyadic scattering coefficient.

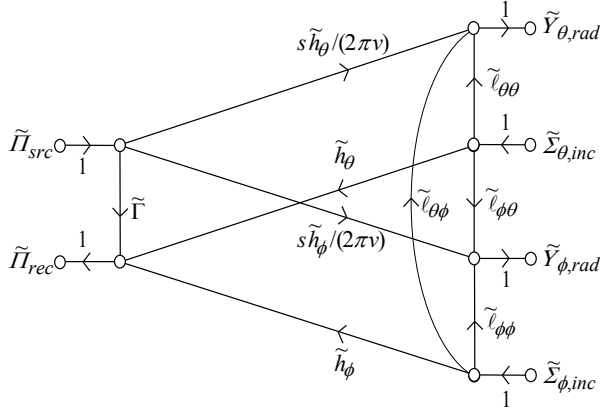


**Figure 1. Signal flow graph of the antenna equation.**

From the transfer function one can calculate antenna gain, realized gain, effective area, and effective length. From the scattering coefficient one can calculate radar cross section or scattering cross section of the antenna.

A signal flow graph of this equation is shown in Fig. 1. We will add a matching circuit to this in Section 4.

### 3 D-dot and B-dot Antennas

For our first examples, we calculate the various antenna parameters of D-dot and B-dot sensors.

We begin with the D-dot sensor, which is an electrically small electric dipole driving a resistive load of  $Z_{o1}$ . The received voltage across the load in both the time and frequency domains is [4, p. 86]

$$\begin{aligned}\tilde{V}_{rec} &= A_{eq} Z_{o1} s \tilde{D}_{inc} = \varepsilon A_{eq} Z_{o1} s \tilde{E}_{inc} \\ V_{rec}(t) &= \varepsilon A_{eq} Z_{o1} \frac{d E_{inc}(t)}{dt}\end{aligned}\quad (3)$$

where  $\varepsilon$  is the permittivity of the surrounding medium. We are restricting the treatment for now to dominant polarization at an angle of maximum coupling. We generalize to an arbitrary angle of incidence at the end of this subsection. The expression for antenna transfer function and impulse response are obtained from [1, 2, Equations (2.11) and (2.15)] as

$$\begin{aligned}\frac{\tilde{V}_{rec}}{\sqrt{Z_{o1}}} &= \tilde{h} \frac{\tilde{E}_{inc}}{\sqrt{Z_{o2}}} \\ \frac{V_{rec}(t)}{\sqrt{Z_{o1}}} &= h(t) * \frac{E_{inc}(t)}{\sqrt{Z_{o2}}}\end{aligned}\quad (4)$$

where “ $*$ ” is the convolution operator and  $Z_{o2}$  is the impedance of the surrounding medium. The surrounding medium is normally free space, for which  $Z_{o2} = 120\pi\Omega$ . Comparing Equations (3) and (4), we find the transfer function and impulse response of the D-dot sensor as

$$\tilde{h} = \varepsilon A_{eq} \sqrt{Z_{o1} Z_{o2}} s = \frac{A_{eq}}{v} \sqrt{\frac{Z_{o1}}{Z_{o2}}} s \quad , \quad (5)$$

$$h(t) = \varepsilon A_{eq} \sqrt{Z_{o1} Z_{o2}} \delta'(t) = \frac{A_{eq}}{v} \sqrt{\frac{Z_{o1}}{Z_{o2}}} \delta'(t)$$

where  $\delta'(t)$  is the time derivative of the Dirac delta function, and we have used  $\varepsilon = 1/(Z_{o2} v)$ . Looking into the port, the input impedance looks like a capacitor of value  $C$ . The reflection coefficient looking into the port is therefore

$$\tilde{\Gamma} = \frac{1/(sC) - Z_{o1}}{1/(sC) + Z_{o1}} = \frac{1 - s\tau_e}{1 + s\tau_e} \quad , \quad \tau_e = Z_{o1}C \quad . \quad (6)$$

With these parameters defined, we can now calculate all the common antenna parameters listed in Section IV of [1, 2]. From Equation (4.4) of [1, 2], realized gain is

$$G_r(s) = \frac{4\pi}{\lambda^2} |\tilde{h}|^2 = \frac{4\pi}{\lambda^2} \frac{A_{eq}^2}{v^2} \frac{Z_{o1}}{Z_{o2}} |s|^2 \quad . \quad (7)$$

For the usual case where  $s = j2\pi f$ , and noting that  $f = v/\lambda$ , this simplifies to

$$G_r(f) = 16\pi^3 A_{eq}^2 \frac{Z_{o1}}{Z_{o2}} \frac{f^4}{v^4} = 16\pi^3 A_{eq}^2 \frac{Z_{o1}}{Z_{o2}} \frac{1}{\lambda^4} \quad . \quad (8)$$

Next, gain can be found from Equation (4.8) in [1, 2],

$$G(s) = \frac{G_r(s)}{1 - |\tilde{\Gamma}|^2} \quad . \quad (9)$$

The effective length is calculated from Equation (4.11) in [1, 2] as

$$\tilde{h}_V = \frac{\tilde{Z}_{in} + Z_{o1}}{Z_{o1}} \sqrt{\frac{Z_{o1}}{Z_{o2}}} \tilde{h} = \frac{1 + s\tau_e}{s\tau_e} \frac{Z_{o1}}{Z_{o2}} \frac{A_{eq}}{v} s \quad . \quad (10)$$

The effective area of the D-dot sensor is now calculated from Equation (4.14) of [1, 2] as

$$\begin{aligned}A_e(s) &= \frac{|\tilde{h}|^2}{1 - |\tilde{\Gamma}|^2} = \frac{1}{1 - |\tilde{\Gamma}|^2} \frac{A_{eq}^2}{v^2} \frac{Z_{o1}}{Z_{o2}} |s|^2 \\ A_e(f) &= \frac{4\pi^2 A_{eq}^2}{1 - |\tilde{\Gamma}|^2} \frac{Z_{o1}}{Z_{o2}} \frac{f^2}{v^2} = \frac{4\pi^2 A_{eq}^2}{1 - |\tilde{\Gamma}|^2} \frac{Z_{o1}}{Z_{o2}} \frac{1}{\lambda^2}\end{aligned}\quad (11)$$

This completes the calculation of the various parameters of a D-dot sensor. A similar treatment of the B-dot sensor is provided in [3].

Note that Equation (11) contains both effective area,  $A_e$ , and equivalent area,  $A_{eq}$ . It should be clear that these are two very

different quantities that both just happen to have dimensions of meters squared.

To generalize the above to arbitrary angles of incidence, one multiplies the transfer function and impulse response by  $\cos(\theta)$ , where  $\theta$  is the angle between the angle of incidence and the angle of maximum coupling. One would then modify the subsequent formulas accordingly.

#### 4 Adding a Matching Circuit to an Antenna

Next, we modify the Generalized Antenna Scattering Matrix to include a matching circuit. The antenna is still described by a 3x3 matrix, but it becomes more complicated due to the presence of the matching circuit.

We begin with a signal flow graph of the antenna, slightly modified from Fig. 1, shown in Fig. 2. The subscript  $a$  indicates that these are S-parameters of the antenna. Recall that these S-parameters are not unitless, as would normally be the case.

The matching circuit is expressed in terms of S-parameters, and its signal flow graph is shown in Fig. 3. The subscript  $m$  indicates that these are parameters of the matching circuit. Note that the two real reference impedances,  $Z_{m01}$  and  $Z_{m02}$ , may be different, which is consistent with the theory of generalized S-parameters. The only constraint is that the reference impedance at port 2 of the matching network must match the reference impedance at the input port of the antenna. We now cascade the above two signal flow graphs to get the signal flow graph of the combined circuit, shown in Fig. 4.

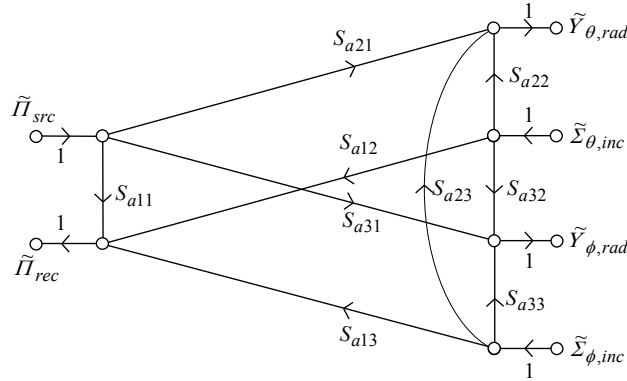


Figure 2. Signal flow graph of the antenna.

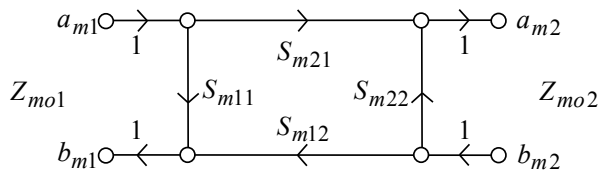


Figure 3. Signal flow graph of the matching circuit.

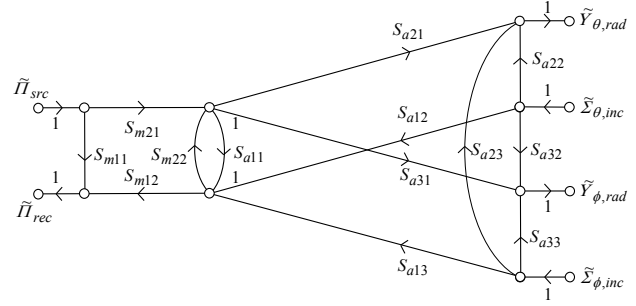


Figure 4. Signal flow graph of the antenna with a matching circuit added.

We now have to simplify this to a standard 3x3 matrix of the form

$$\begin{bmatrix} \tilde{\Pi}_{rec} \\ \tilde{Y}_{\theta,rad} \\ \tilde{Y}_{\phi,rad} \end{bmatrix} = \begin{bmatrix} S_{c11} & S_{c12} & S_{c13} \\ S_{c21} & S_{c22} & S_{c23} \\ S_{c31} & S_{c32} & S_{c33} \end{bmatrix} \begin{bmatrix} \tilde{\Pi}_{src} \\ \tilde{\Sigma}_{\theta,inc} \\ \tilde{\Sigma}_{\phi,inc} \end{bmatrix} \quad (12)$$

where the subscript  $c$  refers to the combined antenna and matching network.

In the presented paper we provide the details of the simplification. We also apply the result to two typical impedance matching networks; a splitter balun for an Impulse Radiating Antenna, and a quarter-wave matching network.

#### 5 Conclusions

We have provided here a few examples of how the theory of power waves clarifies antenna performance. We have shown how to calculate the transfer function and impulse response of D-dot and B-dot sensors. This led to calculations of the gain, realized gain, effective length, and effective area of the sensors. We have also shown how to add a matching circuit to the Generalized Antenna Scattering Matrix. This set of examples demonstrates the usefulness and flexibility of the power wave theory. We encourage the antenna community to add the various terms associated with power wave theory to the next revision of the antenna definitions standards [5].

#### References

- [1] E. G. Farr, "A Power Wave Theory of Antennas, Fourth Revision" Sensor and Simulation Note 564, (2014).
- [2] E. G. Farr, "A Power Wave Theory of Antennas," published in FERMAT e-magazine, www.e-fermat.org, Vol. 7, (2015).
- [3] E. G. Farr, Examples of the Power Wave Theory of Antennas, Sensor and Simulation Note 569, (2014).
- [4] C. E. Baum, "Electromagnetic Sensors and Measurement Techniques," pp. 73-144 in J. E. Thompson and L. H. Lewison (editors), *Fast Electrical and Optical Measurements*, Martinus Nijhoff Publishers, (1986).
- [5] IEEE, *IEEE Standard for Definitions of Terms for Antennas*, IEEE Std. 145-2013, Institute for Electrical and Electronics Engineering, Inc., (2013).

# Radiation characteristics of a high-power ultrawideband pulse radiating antenna

Jae Sik Kim\*, Young Joong Yoon\*, Jiheon Ryu<sup>†</sup>, Jin Soo Choi<sup>†</sup>

\* Department of Electrical and Electronic Engineering, Yonsei University, Seoul, Republic of Korea

<sup>†</sup> Agency for Defense Development, Daejeon, Republic of Korea

## Abstract

In this paper, we present radiation characteristics of a compact high-power ultrawideband pulse antenna. The antenna has dimensions of  $300 \text{ mm} \times 300 \text{ mm} \times 260 \text{ mm}$  ( $0.2\lambda_L \times 0.2\lambda_L \times 0.173\lambda_L$ ), where  $\lambda_L$  corresponds to the lowest frequency of the operating bandwidth. The antenna consists of a modified biconical radiator, loops, a feedthrough insulator, and a coaxial cable. The fabricated antenna realizes a far-voltage / peak input voltage of 1.68 when 1.3 nanosecond pulse width bipolar pulse is excited, and directive radiation.

**Keywords:** Directive antennas, high power radiation, ultrawideband antennas.

## 1 Introduction

To transmit a high-power ultrawideband (UWB) pulse to a target efficiently, a radiator is highly recommended to realize a directive radiation, wide bandwidth, and high electrical capability [1].

In case of a UWB pulse radiating antenna, time-domain analysis is advantageous due to the wide spectrum range of a UWB pulse on a frequency domain [2]. To analyze radiation characteristics of a high-power UWB pulse radiating antenna in time-domain, a far-voltage ( $= V_f$ ) and transient radiation patterns are widely used [3].

In our previous work, a design procedure of a compact high-power UWB pulse radiator is presented [4]. In this paper, we present measurement results of a  $V_f$  at boresight and transient radiation patterns on E and H-planes of the antenna. The results show that the antenna satisfies the recommendations of a high-power UWB pulse radiator.

## 2 Radiation characteristics

The antenna is composed of a modified biconical radiator, loops, feedthrough insulator, and coaxial cable, as shown in Fig. 1 [4]. The configuration of the modified biconical radiator is determined to achieve a compact size (especially for a length dimension) and directive radiation. The loops and feedthrough insulator (PET-100) are inserted to improve an impedance matching characteristic at low frequency region

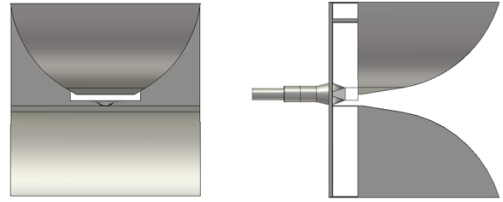


Figure 1. Configuration of the antenna.

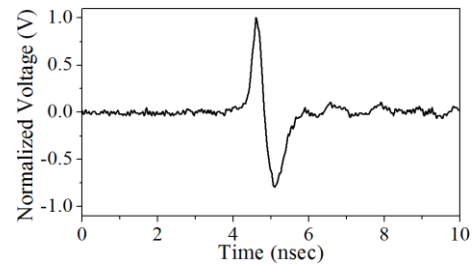


Figure 2. Normalized input pulse of the antenna ( $V_p = 1\text{V}$ ).

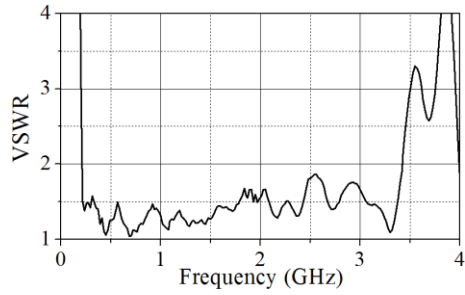
and enhance electrical capability at the end of the feeding section where the highest electric field occurs, respectively [5].

Fig. 2 depicts the normalized input bipolar pulse of the antenna, which is generated from a high-power UWB nanosecond bipolar pulse generator [6]. The pulse width is 1.3 nanosecond.

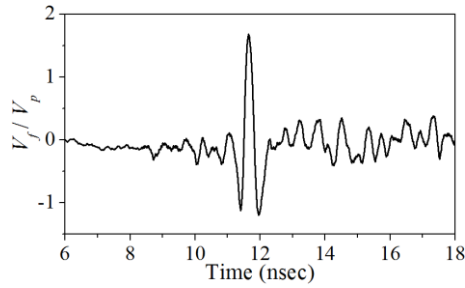
Fig. 3 shows measurement results of the antenna. To measure the characteristics, we used a network analyzer (Agilent technologies E5071C), digitizing oscilloscope (Tektronic DPO 71254), and a D-dot sensor (Model AD-80D [7]) with a matched balun (Model BIB-100G [7]). The measured bandwidth is from 0.2 GHz to 3.44 GHz (17.2:1) which satisfies a wide band condition. The measured peak  $V_f / V_p$  at boresight is 1.68 where  $V_p$  is peak voltage of the input pulse. The transient radiation patterns show that the antenna realizes directive radiation.

## 3 Conclusion

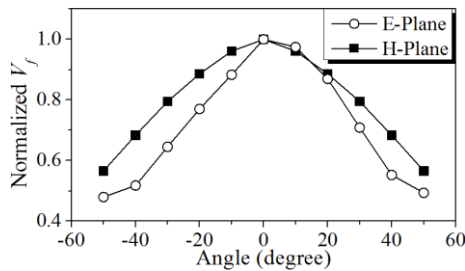
In this paper, radiation characteristics of a compact high-power UWB pulse radiator are presented. The measurement results show that the antenna achieves a directive radiation, compact dimensions, and wide bandwidth characteristics.



(a)



(b)



(c)

- [6] FID GmbH, FPG-N Nanosecond Pulsers, Burbach, Germany.  
[Online]. Available: <http://www.fidtechnology.com>
- [7] PROLYN, Electric Field (D-dot), Albuquerque, NM, USA.  
[Online]. Available: <http://www.prodyntech.com>

**Figure 3. Measurement results of (a) VSWR, (b)  $V_f / V_p$  at boresight, and (c) transient radiation patterns on E and H-planes.**

## References

- [1] L. Desrumaux, A. Godard, M. Lalande, V. Bertrand, Andrieu, and B. Jecko, "An original antenna for transient high power UWB arrays: The shark antenna," *IEEE Trans. Antennas Propag.*, vol. 58, no. 8, (2010).
- [2] A. Shlivinski, E. Heyman, and R. Kastner, "Antenna Characterization in the Time Domain," *IEEE Trans. Antennas Propag.*, vol. 45, no. 7, (1997).
- [3] J. Benford, J. A. Swegle, and E. Schamiloglu, *High Power Microwaves*. New York, NY, USA: Taylor & Francis, (2007).
- [4] J. S. Kim, Y. J. Yoon, and J. Ryu, "A compact high-power antenna for ultrawideband nanosecond bipolar pulse," *Microwave Opt. Technol. Lett.*, Accepted, (2015).
- [5] Y. A. Andreev, Y. I. Buyanov, and V. Koshelev. "Combined antennas for high-power ultra wideband pulse radiation," 14th International Symposium on High Current Electronics, (2006).

# On the characteristic impedance of parallel-plate transmission line with plates of unequal breadths

Wang Shaofei, Xie Yanzhao, Du Leiming, Li Kejie

State Key Laboratory of Electrical Insulation and Power Equipment,  
School of Electrical Engineering, Xi'an Jiaotong University, Xi'an China

## Abstract

With the method of Time Domain Reflection (TDR), simulation models for parallel-plate transmission line with plates of unequal breadths are established to compute accurate value of its characteristic impedance. Based on the results, a new formula for the characteristic impedance is proposed by least square fitting. The proposed formula is well consistent with simulation results, and it could be used to calculate characteristic impedance of parallel-plate transmission line with plates of equal and unequal breadth.

**Keywords:** Parallel-plate transmission line; Unequal breadth; Characteristic impedance

## 1 Introduction

Parallel-plate transmission line is a kind of common structure in the field of microwave transmission, and characteristic impedance is one of its critical parameters. As for the calculation of characteristic impedance, there are many formulas based on microstrip model and Conformal Mapping Method [3, 4, 5, 6]. These formulas themselves exhibit inconsistency to some extent. Moreover, when it comes to the parallel-plate transmission line with plates of unequal breadth, which is common in the structure of bounded-wave EMP simulator and TEM cell, etc., little research has been conducted. Dr. Carlisle proposed a method with Conformal Mapping [1]. However the tremendous complexity limits its application in engineering design. In this paper, TDR method is adopted to calculate the accurate value of the impedance, based on which, a relatively convenient formula is proposed to calculate the characteristic impedance of parallel-plate transmission line with plates of equal and unequal breadths.

## 2 Compute of the characteristic impedance

The characteristic impedance of parallel-plate transmission line is computed with the method of TDR. Model of TDR theory is shown as Fig.1. If step voltage is applied as the source  $V_S$ , by monitoring the waveform of voltage on the transmission line, both incident and reflect voltage could be obtained. Thus the reflection coefficient would be figured out. Then, together with the internal resistance of source  $Z_S$  and the load resistance  $Z_L$ , impedance of transmission line could

be obtained. Such models of parallel-plate line with various parameters are built to compute their impedance. The results are shown as Fig.3.

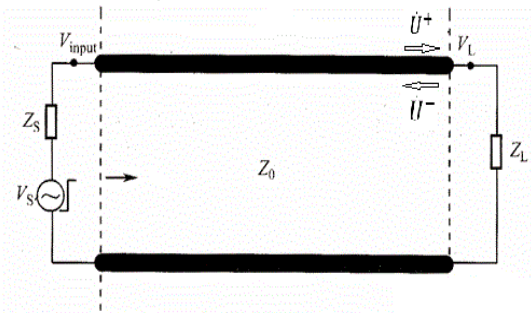


Fig. 1. The TDR model for transmission line

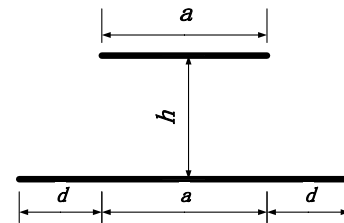


Fig.2 The cross section of parallel-plate transmission line with plates of unequal breadth

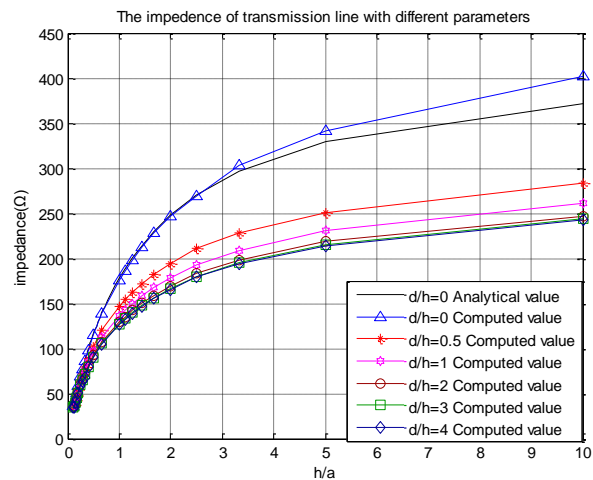


Fig.3 The impedance of transmission line with different parameters

The analytical value is given by Equation (1) [6]. It can be seen from Fig.3 that broadening of the bottom plate has a

remarkable effect on the impedance. Based on Equation (1), together with the computed results, a new formula is proposed as Equation (2).

$$Z_C = \frac{Z_0}{a/h + 1/\pi (1 + \ln(a/h + 5.9))} \quad (1)$$

$$Z_C = \begin{cases} Z_0 \frac{1 - 0.8087d/h}{0.9158a/h + 1/\pi (1.638 + \ln(a/h + 2.349))}, & 0 \leq d \leq 0.1 \\ Z_0 \frac{0.7356 - 0.2419e^{(-0.2419h/d)}}{0.5117a/h + 1/\pi (1 + \ln(a/h + 3))}, & d > 0.1 \end{cases} \quad (2)$$

where  $Z_0$  is the wave impedance in vacuum. The numerator part could be viewed as the modifying factors caused by the broadening of the bottom plate.

### 3 Assessment of the proposed formula

In order to confirm the fitting formula, it is compared with the simulation results, which is shown in Fig. 4.

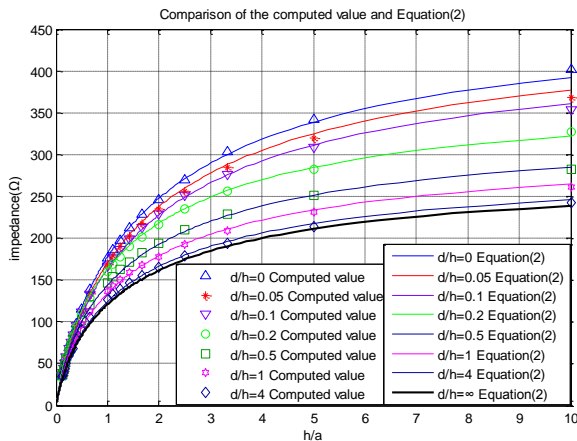


**Fig. 4 Comparison of the computed value and Equation (2)**

As is shown in Fig. 4, Equation (2) is well consistent with simulation results for  $d/h$  from 0 to 4. The impedance decreases with the increase of  $d/h$ . And when  $d/h$  becomes infinity, the impedance reaches its limitation which is approximate to it when  $d/h$  is 4. Dr. Carlisle's formula [1] based on conformal mapping shows the similar tendency, which means that Equation (2) could be applied to calculate the impedance of parallel-plate transmission line with plates of unequal breadths with  $d/h$  from 0 to infinity.

### 4 Conclusion

Based on TDR theory, a new method with which to compute the characteristic impedance of parallel-plate transmission line is proposed. And a relatively simple and direct formula for the impedance of parallel-plate transmission line with plates of equal and unequal breadths is concluded as Equation (2). With the support of the theory of Conformal Mapping from reference [1], the serviceable range of the formula is expanded to parallel-plate transmission line with infinite bottom plate.

### References

- [1] G. W. Carlisle. "Impedance and Fields of Two Parallel Plates of Unequal Breadths", *Sensor and Simulator Notes*, **Note 340**, pp. 1-20, (1969).
- [2] A. E. H. Love. "Some Electrostatic Distributions in Two Dimensions" *Proc. London Math. Soc.* 22, pp. 337-369, (1923).
- [3] Wang Xinwen. "Complex Analytical Conforming Mapping Application in Electromagnetic Engineering", Xidian University, 2011.
- [4] A. P. Lambert, S. M. Booker, P. D. Smith. "Calculation Of The Characteristic Impedance Of Tem Horn Antennas Using The Conformal Mapping Approach" *Antennas and Propagation*, IEEE Transactions on 43.1:47 – 53, (1995).
- [5] R. T. Lee, G. S. Smith. "On the Characteristic impedance of the TEM horn antenna", *Antennas and Propagation*, IEEE Transactions on 52.1:315 – 318, (2004).
- [6] Huang Zhixun, "Theory of Microwave Transmission Line and Practical Technology", Science Press, 1996.

# Modified two-element TEM horn array for radiating UWB electromagnetic pulses

Chunming Tian, Peiwu Qiao, Yanzhao Xie and Juan Chen

School of Electronic and Information Engineering, Xi'an Jiaotong University, Xi'an 710049, China  
tianchm@mail.xjtu.edu.cn

## Abstract

In this paper we have investigated the modified two-element TEM horn antenna array for radiating ultra-wideband electromagnetic pulses. This array is composed of two exponential horn sections, and the configuration of this antenna array is optimized using modelling and simulations in the CST Microwave Studio. Antenna patterns, radiated fields, and the return losses are presented and discussed.

**Keywords:** antenna array, horn Antenna, Radiation Pattern

## 1 Introduction

The techniques of an ultra-wideband (UWB) electromagnetic pulse have been quickly developed due to its being widely applied to ground-penetrating radar systems, ultra-wideband radar systems, and the generation of high-intensity electromagnetic pulses [1-3]. One of the important problems associated with UWB's applications is to use a proper antenna to efficiently radiate the UWB signal. The TEM horn antenna has been extensively studied in the last years and described by many authors [4-6] because of its advantages such as broad band frequency spectrum, good direction, small size and the large effective experimental area, etc.

In this paper we present a modified two-element antenna array which is composed of two exponential TEM horn sections. The behavior of the antennas is simulated and discussed by utilizing the commercial software CST Microwave Studio [7].

## 2 Antenna design

The modified two-element array design is based on a TEM horn antenna construction for broadband applications proposed in paper [4]. The configuration of this array is shown in Fig. 1. It is composed of two exponential horn sections that geometric and impedance tapering is used to improve its matching with free space. Antenna is fed by a parallel-plate. The line impedance of antenna is set in accordance with the following exponential function:

$$Z(z) = Z_0 \exp(\alpha z) \quad \alpha = \frac{1}{L} \ln\left(\frac{\eta}{Z_0}\right) \quad (1)$$

where  $Z$  is the characteristic impedance of the feed line,  $Z_0$  is the impedance of the free space ( $120\pi \Omega$ ), and  $L$  is the length of horn antenna.

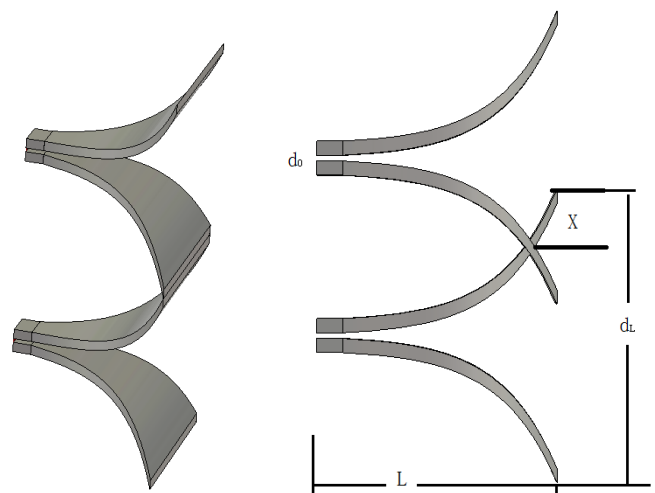


Figure 1. Modified two-element TEM horn array.

## 3 Numerical results

In this section, we will use the CST Microwave Studio to simulate and optimize the array above.

When simulating, the impedance of antenna with Equation (1) is from  $50 \Omega$  of the feed line to  $377 \Omega$  of the free space. For a single horn antenna, the start and finish separation distance between the plates are  $d_0=1.6$  cm,  $d_L=74$  cm. The antenna length is  $L=60$  cm. The optimized parameter  $X$  (shown in Fig. 1) of two-element array is designed for two aims: One is to get better radiating performance, the other is to obtain compact structure as far as possible.

In Fig. 2, the radiation pattern of the two-element array is shown when parameter  $X$  is changed. In this figure, only maximum value of pattern at 1.05 GHz is shown. From here it can be seen that at first radiation pattern decreases while parameter  $X$  increases, when parameter  $X = 10$  cm, the minimum value of pattern is obtained and equal to 12.4dB, then increases with parameter  $X$  and reaches a maximum value at 14.5dB when parameter  $X=17$ cm, and then decreases gradually again. The maximum of far field at 600cm shifted from the aperture is shown in figure 3. It is clear that E-field

varies directly as parameter X when  $X > 7\text{cm}$ . So, from fig. 2 and fig.3, when parameter  $X=17\text{cm}$ , an optimal value of radiation pattern  $14.5\text{dB}$  is reached, better value of E-field is gotten, and at the same time the size of antenna array is reduced  $34\text{cm}$ .

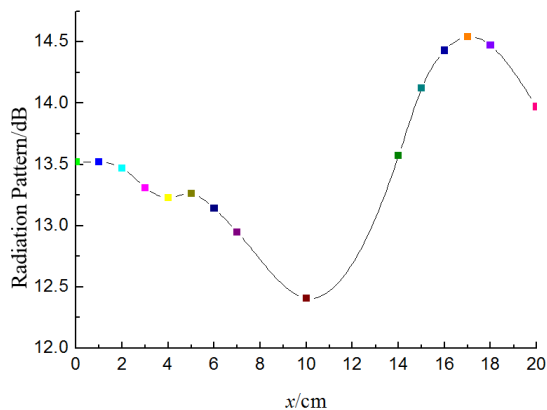


Figure 2. Radiation pattern versus parameter X.

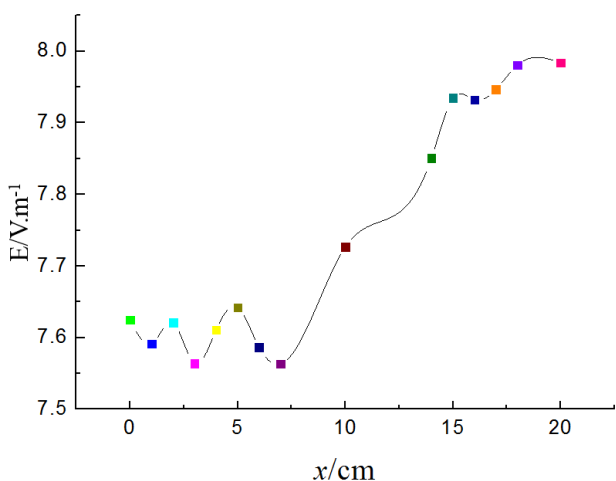


Figure 3. Electric field versus parameter X.

Finally, we simulate the two-element horn array and get the return loss coefficient  $S_{11}$  when parameter  $X=17\text{cm}$ . In the fig. 4, it is shown that  $S_{11}$  is below the desired level of  $-10\text{dB}$  as frequency from  $0.25\text{GHz}$  to  $2\text{GHz}$ , which represents a good reflection characteristic over the previous design.

#### 4 Conclusion

In this paper, the modified two-element TEM horn array is presented and analysed. It is revealed that better radiating performance of antenna array can be obtained by adjusting parameter X, which includes the optimal pattern, better electric field and smaller size.

The antenna array will be further optimized not only with respect to its reflections and antenna pattern in the desired

frequency band but also with more attention to be paid to the pulse distribution in space near the antenna in the future.

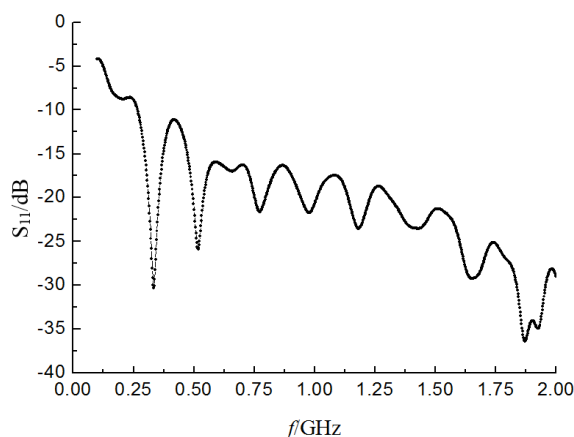


Figure 4. Return loss in X=17cm.

#### Acknowledgements

The described research was supported by the Fundamental Research Funds for the Central Universities.

#### References

- [1] B. Cadilhon, B. Cassany, P. Modin, and etc., “Ultra Wideband Antennas for High Pulsed Power Applications”, *Ultra Wideband Communications: Novel Trends – Antennas and Propagation*, (2011).
- [2] A. A. Jamali and R. Marklein, “Design and Optimization of Ultra-Wideband TEM Horn Antennas for GPR Applications”, *IEEE*, (2001).
- [3] Y. Wang, Y. G. Chen, Q. G. Wang, “Application of TEM horn antenna in radiating NEMP simulator” *7th International Conference on Applied Electrostatics*, (2012).
- [4] A. R. Mallahzadeh, F. Karshenas. “Modified TEM Horn Antenna for Broadband Applications”, *Progress in Electromagnetic Research*, vol. 90, pp. 105-119, (2009).
- [5] M. Khorshidi, M. Kamyab, “New exponential TEM horn antenna with binomial impedance taper”, *Int. J. Electron. Commun.*, vol. 64, pp. 1073–1077, (2010).
- [6] J. G. Wang, C. M. Tian, G. X. Luo, Y. S. Chen, and D. B. Ge, “Four-Element TEM Horn Array for Radiating Ultra-Wideband Electromagnetic Pulses”, *Microwave and Optical Technology Letters*, vol. 31, pp.190-194, (2001).
- [7] CST MICROWAVE STUDIO: 3D EM simulation software. Available from: <http://www.cst.com/Content/Products/MWS/Overview.aspx>

# Optimization of HEMP Simulator Antenna for Improving Test Area Field Distribution

Zheng Sheng-quan<sup>12</sup> Deng Feng<sup>12</sup> Wang Dong-dong<sup>12</sup> Hou Dong-yun<sup>12</sup>

Science and Technology on Electromagnetic Compatibility Laboratory<sup>1</sup>  
China Ship Development and Design Center<sup>2</sup>, Wuhan, China  
E-mail: zhengshengquan@hotmail.com

**Abstract** —Horizontal dipole and headstand cone are two types of HEMP Simulator Antenna, which radiate horizontal and vertical polarization pulse electric field separately. Radiation field distribution of arc horizontal dipoles with different bend radius and conic monopoles with different slope angle are simulated in this paper, and an optimized project of simulator antenna is investigated to improve test area peak field strength or uniformity.

**Keywords:** HEMP simulator, arc horizontal dipole, sloping conic monopole, radiation field

## I. INTRODUCTION

HEMP simulators are applied to generate pulse electric field which simulates the early nucleus explosion radiation. As HEMP has wide frequency spectrum, the field generating devices should have excellent wide frequency characteristic<sup>[1-2]</sup>. The peak field strength and waveshape and uniformity of the field in test area should suffice the requirements of test.

There are several types of HEMP field generating devices as wave guide, horizontal dipole, vertical monopole and hybride. Wave guide and hybride are convenient to be loaded by resistors to implement wide frequency characteristic, but the field generated by these two types of structure is mainly restricted inside or under them, so that the test volume is limited. Gnerally horizontal dipole and vertical monopole are applied to big system under test or what can not be moved to the volume inside or under the structure. Because the field generated by horizontal dipole or vertical monopole is open field, the uniformity becomes beter with the increasing distance, but the field strength reduce. Consequently, the field uniformity of test area should be improved as possible while the field magnitude satisfied the test requirement to reduce test uncertainty<sup>[3]</sup>. On the other hand, adjusting the antenna radiation characteristic could increase the field strength in test area while the voltage of simulator is not sufficient.

## II. MODELING AND SIMULATION FOR TWOTYPES OF RADIATION ANTENNA

Symmetry dipole and its coordinate are presented in figure 1. The radiation field of symmetry dipole is generated by currents on two

arms. The electric field component on  $\hat{r}$  and  $\hat{\theta}$  direction are presented as formula (1).

$$\begin{cases} d\hat{E}_{r_1} = \frac{Z_0 I(z) dz}{2\pi r_1^2} \cos \theta_1 \left(1 + \frac{1}{jkr_1}\right) e^{-jkr_1} \hat{r}_1 \\ d\hat{E}_{r_2} = \frac{Z_0 I(-z) dz}{2\pi r_2^2} \cos \theta_2 \left(1 + \frac{1}{jkr_2}\right) e^{-jkr_2} \hat{r}_2 \\ d\hat{E}_{\theta_1} = j \frac{Z_0 I(z) dz}{2\lambda r_1} \sin \theta_1 \left[1 + \frac{1}{jkr_1} + \frac{1}{(jkr_1)^2}\right] e^{-jkr_1} \hat{\theta}_1 \\ d\hat{E}_{\theta_2} = j \frac{Z_0 I(-z) dz}{2\lambda r_2} \sin \theta_2 \left[1 + \frac{1}{jkr_2} + \frac{1}{(jkr_2)^2}\right] e^{-jkr_2} \hat{\theta}_2 \end{cases} \quad (1)$$

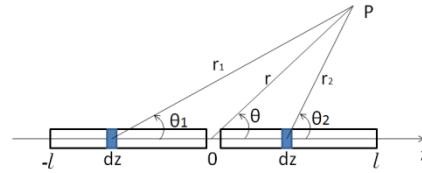


Fig.1 Symmetry dipole and its coordinate

The transient radiation field of symmetry dipole is presented as formula (2).

$$\begin{cases} I(z, t) = I_0 \left(t - \frac{|z|}{c}\right) \\ E(r, t) = \frac{Z_0}{4\pi r} \left[ \frac{2}{\sin^2 \theta} I_0 \left(t - \frac{r}{c}\right) - \frac{1}{1 + \cos \theta} I_0 \left(t - \frac{l}{c} - \frac{r + l \cos \theta}{c}\right) - \frac{1}{1 - \cos \theta} I_0 \left(t - l - r - l \cos \theta\right) \right] \end{cases} \quad (2)$$

The radiation field of grounding monopole standing on the ideal conductor plane is similar to which generated by symmetry dipole in free space. While the diameter of arm is too thick to simply describe the current by  $I_0$  as the current distribution on the surface of armes, both distance and azimuth from current units on different position around the section of pole to space espiial point have difference. Consequently, geometry model of antennas should be constitute to calculate the radiation field by numerical simulation<sup>[4-5]</sup>.

The electromagnetic pulse radiation field characteristic of optimized horizontal dipole and vertical conic monopole which have definite diameter are investigated as follow. The length of horizontal dipole is 250m, pole diameter is 9m, the height is 20m from the ideal ground plane. The dipole is stimulated by 4MV peak voltage duple exponential pulse. The radiation field distribution characteristic of four different cases, which including linear horizontal dipole, arc horizontal dipoles with 200m-bend-radius, arc horizontal dipoles with 150m-bend-radius and arc horizontal dipoles with 100m-bend-radius, are simulated as illustrated in figure 2 to figure 5. Affected by the countercurrent of mirror image from conductor ground plane, the radiation

efficiency of dipole on the ground is relatively low.

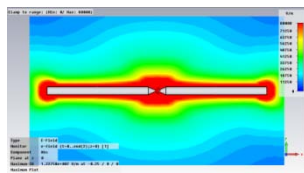


Fig.2 Radiation field distribution characteristic of linear horizontal dipole

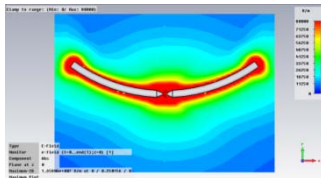


Fig.3 Radiation field distribution characteristic of arc horizontal dipoles with 200m-bend-radius

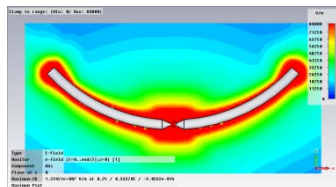


Fig.4 Radiation field distribution characteristic of arc horizontal dipoles with 150m-bend-radius

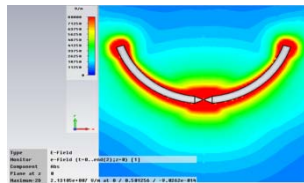


Fig.5 Radiation field distribution characteristic of arc horizontal dipoles with 100m-bend-radius

Height of the conic monopole is 44m, diameter of the cone top is 30m, the ground is infinity ideal conductor plane, The conic monopole is stimulated by 4MV peak voltage double exponential pulse like the dipole. The radiation field distribution characteristic of three different cases, which including upright conic monopole, conic monopoles with 10-degree-slope-angle and conic monopoles with 20-degree-slope-angle at  $x=0$  plane, are simulated as illustrated in figure 6 to figure 8. Affected by the same-direction-current of mirror image from conductor ground plane, the radiation efficiency of upright conic monopole on the ground is obviously higher than that of horizontal dipole.



Fig.6 Radiation field distribution characteristic of upright conic monopole



Fig.7 Radiation field distribution characteristic of conic monopoles with 10-degree-slope-angle

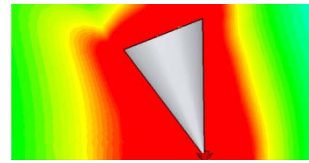


Fig.8 Radiation field distribution characteristic of conic monopoles with 10-degree-slope-angle

### III. RESULT AND ANALYSIS

The radiation field curve at positions  $Y=+84m$  (front side) of feed point of three arc horizontal dipoles with different bend-radius as well as that of linear horizontal dipole are presented as figure 9. From the figure we can see that the uniform test area at same distance from dipole feed point increasing with the radius of arc bend. The field strength at test area decreasing with the distance increasing from the feed point. Therefore, it is required to design the bend radius of arc dipole in reason based on the test field strength magnitude and the size of object under test. For 150m-long test object, it is appropriate that the bend radius get 150m while the test field strength is required not below 25kV/m, as illustrated in figure 10.

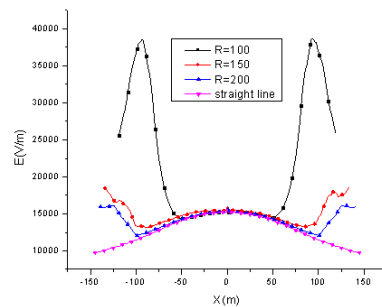


Fig.9 Field curves at the positions 84m front side from feed point of arc horizontal dipoles with three different bend-radii as well as that of linear horizontal dipole

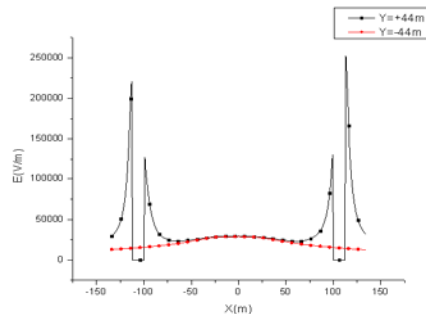


Fig.10 Field curves at the positions 84m front side and backside from feed point of arc horizontal dipole with 150m-bend-radius

The radiation field curves of upright conic monopole, conic monopoles with 10-degree-slope-angle and conic monopoles with 20-degree-slope-angle at  $x=0$  plane, the height of 2m, 5m, 10m and 20m are presented as figure 11 to figure 14. Comparing curves of these figures, we can see that the field strength at slope side of the cone is obviously higher than that at reverse side of the cone while the conic antenna slope to a definite angle. The radiation field strength increase at slope side of 20-degree-slope-angle is more than that of 10-degree-slope-angle. The simulated peak field strength at slope side of conic antennas with different slope angles, 50m from the feed point and different height, are presented as table 1. From table 1 we can see that the uniformities of peak field at height from 2m to 20m are fairly good. Comparing with upright case, the field strength increase about 14%~19% for 10-degree-slope-angle cone, and 40%~46% for 20-degree-slope-angle cone at slope side, as presented in table 2. Considering the height of objects under test, the slope angle should not be too big.

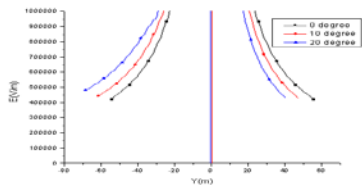


Fig.11 Field curves at the height of 2m, front side and backside from feed point of conic monopoles with different slope-angle

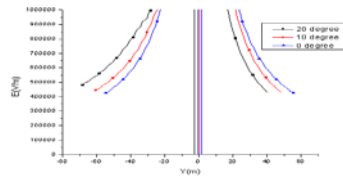


Fig.12 Field curves at the height of 5m, front side and backside from feed point of conic monopoles with different slope-angle

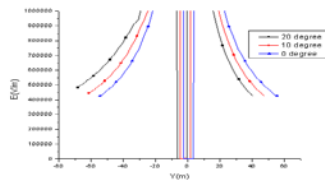


Fig.13 Field curves at the height of 10m, front side and backside from feed point of conic monopoles with different slope-angle

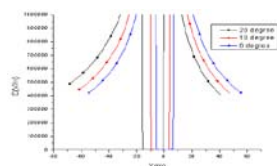


Fig.14 Field curves at the height of 20m, front side and backside from feed point of conic monopoles with different slope-angle

Table 1: Simulated peak fields of conic monopoles with different slope-angle on slope side at 50m from the feed point, at different height (kV/m)

Height(m)	0-degree slope	10-degree slope	20-degree slope
2	466	550	655
5	469	535	657
10	468	548	656
20	459	547	672

Table 2: Field increase percent of conic monopoles with three different slope-angle on slope side at 50m from the feed point, at different height

Height(m)	0-degree slope	10-degree slope	20-degree slope
2	0	+18%	+40%
5	0	+14%	+40%
10	0	+17%	+40%
20	0	+19%	+46%

#### IV. CONCLUSION

Large size horizontal dipole and vertical conic monopole which applied to HEMP simulators could be improved on their radiation fields at test area by changing shape or installation angle properly. Arc shaping horizontal dipole may improve the field uniformity at test area, and the field strength magnitude increase slightly. Sloping conic monopole may obviously increase the field strength at test area on the side of slope, what improves the efficiency of simulator.

#### REFERENCE

- [1] *Electromagnetic compatibility (EMC) –Part 2-9: Environment-Description of HEMP Environment –Radiated Disturbance.*
- [2] W. D. Prather, C.E. Baum, R.J. Torres, F. Sabath, and D. Nitsch, "Survey of worldwide high-power wideband capabilities", *IEEE Trans. Electromagn. Compat.*, vol.46, pp.335-344, Aug. 2004.
- [3] Zheng sheng-quan, Hou Dong-yun, Wang Dong-dong, Deng Feng, "Electromagnetic Pulse Protection Requirements and Test Methods for Systems", ISAPE 2012: pp.857-860.
- [4] H. Wong, K. M. Mak, and K. M. Luk, "Wideband shorted bowtie patch antenna with electric dipole," *IEEE Trans. Antenna Propagat.*, vol. 56, no.7, pp.2098-2101, Jul. 2008.
- [5] K. L. Lau, P. Li and K. M. Luk, "A monopolar patch antenna with very wide impedance bandwidth," *IEEE Trans. Antennas Propagat.*, vol. 53, no. 2, pp. 655-661, 2005.

# Miniaturized COBRA for HPEM System

Jihwan Ahn and Young Joong Yoon

Department of Electrical & Electronic Engineering  
Yonsei University  
Seoul, Korea

## Abstract

In this paper, the miniaturized COBRA is proposed. The proposed miniaturization technique is achieved by dielectric lens antenna theory. The electrical path length is increased by the lens medium in dielectric lens. Therefore the phase error at the aperture of horn can be compensated by shaping dielectric lens which is combined with COBRA lens. The gain of the proposed COBRA is 26.2 dBi which exceeds the gain of conventional COBRA, 23.9 dBi, despite of the size reduction.

**Keywords:** miniaturization, COBRA, dielectric lens, phase error

## 1 Introduction

Generally, narrowband HPEM (high power electromagnetic) sources use an azimuthally symmetric output mode such as the  $TM_{01}$  circular waveguide or the coaxial TEM mode for the reason of source structure and power capacity [1~3]. COBRA (coaxial beam-rotating antenna) is designed to radiate these modes directly from antenna [4,5].

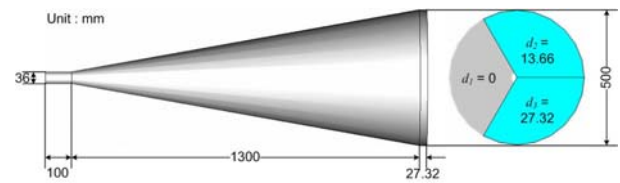
The length of horn is the only factor which can be controlled for minimized HPEM system, since the size of aperture cannot be reduced because of breakdown. But the shortened length with fixed aperture size of horn leads rapid increase of the phase error which causes the gain reduction and pattern distortion [6].

In this paper, miniaturized design of COBRA is introduced. To miniaturize COBRA without gain reduction, the increase of phase error must be suppressed. This can be achieved by modified COBRA lens using principle of lens antenna. The characteristics of COBRA can be improved by this technique despite the length of COBRA lens horn is shortened.

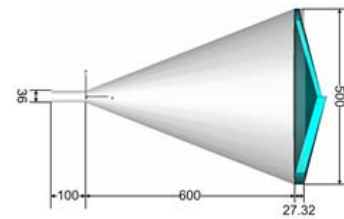
## 2 Antenna Design

The conventional COBRA lens horn design is shown in Fig. 1(a). To get the circular polarization and minimize the thickness of lens,  $N=3$  COBRA lens is designed. The lens material is polycarbonate (PC) with dielectric constant of 3. The length of horn body is 1300 mm and the diameter of aperture is 500 mm.

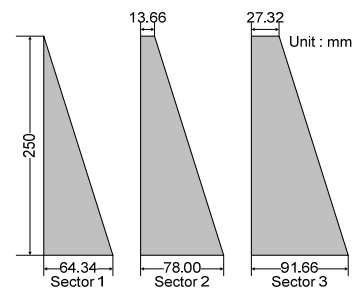
Fig. 1(b) shows the proposed COBRA lens horn structure. The thickness of center part of lens is thicker than that of edge part of lens as shown in Fig. 1(c). This structure is designed to compensate the phase error at the aperture of horn. The length of horn body is 600 mm but the diameter of aperture is same as the conventional COBRA.



(a) Conventional COBRA



(b) Proposed COBRA



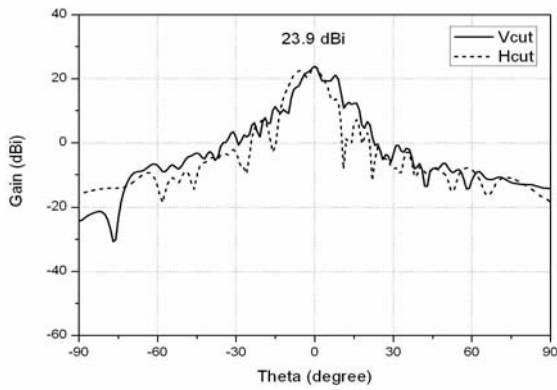
(c) Cross sections of proposed COBRA lens

Figure 1. Geometry of two antennas

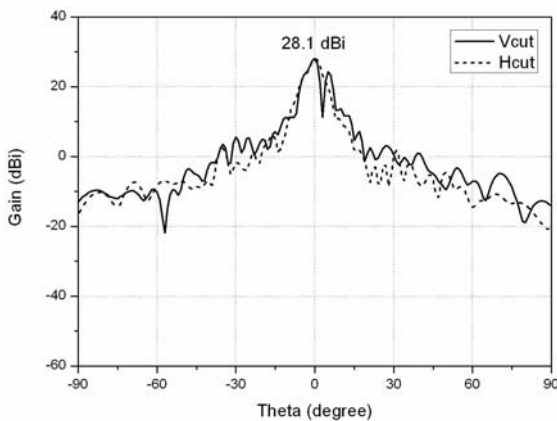
## 3 Results

Fig. 2 presents the simulated radiation pattern of two COBRA lens horn antennas. The gain of conventional COBRA is 23.9 dBi while that of proposed one is 28.1 dBi. As shown in Fig. 1, the proposed structure has shorter body length about half but has higher gain about 4.2 dB compared with the body length of conventional COBRA.

These results are due to that the proposed COBRA lens compensates the phase error at the aperture of horn.



(a) Conventional COBRA



(b) Proposed COBRA

**Figure 2. Radiation pattern of two antennas**

## 4 Conclusion

In this paper, COBRA lens horn design for miniaturized HPEM system is proposed. To compensate the phase error at the aperture of COBRA horn due to the shortened length, modified lens is combined with the conventional COBRA lens. As the result, the gain enhancement of about 4 dB and the size reduction of about 50% can be achieved.

From these results, it might be surely expected that proposed COBRA is appropriate to HPEM generator and proposed miniaturized design of COBRA can be widely used in designing antennas for HPEM generator.

## References

- [1] Clifton C. Courtney and Carl E. Baum, "The Coaxial Beam-Rotating Antenna (COBRA): Theory of Operation and Measured Performance," *IEEE Transactions on Antennas and Propagation*, vol. 48, no. 2, pp. 299-309, Feb. 2000.
- [2] Clifton C. Courtney and Carl E. Baum, "Coaxial Beam-Rotating Antenna (COBRA) Concepts," *Sensor and Simulation Note 395*, April 1996.
- [3] C. C. Courtney, C. E. Baum, W. D. Prather, et al., "Design and Numerical Simulation of the Response of a Coaxial Beam Rotating Antenna (COBRA) Lens," *SSN 449*, August 2000.
- [4] R. A. Koslover, C. D. Cremer, W. P. Geren, D. E. Voss, and L. M. Miner, "Circular TM<sub>01</sub> to TE<sub>11</sub> waveguide mode converter," U.S. Patent 4 999 591.
- [5] Shiwen Yang and Hongfu Li, "Numerical modeling of 8mm TM<sub>01</sub>-TE<sub>11</sub> mode converter," *International Journal of Infrared and Millimeter Waves*, vol. 16, no. 11, 1995.
- [6] A. P. King, "The Radiation Characteristics of Conical Horn Antennas," *Proceedings of the I.R.E.*, vol. 38, pp. 249-251, March 1950.

# Optimization of Offset Parabolic Antennas based on Genetic Algorithm

Junggeun Park\*, Young-seek Chung\*, Wonjune Kang\*, Kang-in Lee\*, Hojun Yoon\*

\*Department of Wireless Communications Engineering,  
Kwangwoon University, Seoul, Korea  
[jungkn@kw.ac.kr](mailto:jungkn@kw.ac.kr)

## Abstract

In this Paper, we apply a genetic algorithm for optimal design techniques for improve the performance of offset parabolic antennas

We use a physical optics to calculate the beam pattern from the surface current of the reflector in order to reduce the computation time in the process of optimization design.

Moreover, we applied the Bezier surfaces to form a reduced and smooth surface of the design variables.

In the process to set the control points of the Bezier surface as a design variable, and we design the optimal antennas to satisfy the objective function

**Keywords:** Offset Parabolic Antenna, Physical Optics, Genetic Algorithm, Bezier Surfaces

## 1 Introduction

Parabolic antenna of high gain and efficiency characteristics are widely used in the military, satellite field. In general, it is composed of the feed antenna and parabolic reflector. The reflector serves to reflect the electromagnetic waves from the primary feed antenna to the free space [1,2].

However, in parabolic antenna structure, the electromagnetic wave which is reflected by the reflector is affect to the primary feed antenna. As a result, it degrade the performance of the antenna. Also, the size of the reflector is designed with an electrical model size that is large compared to the wavelength. So it consume many computation time to analysis by using the full wave analysis.

In this paper, to solve this disadvantage, it analyse the offset parabolic antennas that has low blockage effect using Physical Optics. Consequentially, it Reduce analysis time and derive accurate analysis results. Using genetic algorithms, we propose an optimal shape design techniques.

In this case, we introduced a Bezier surface to generate of a smooth reflective surface and reduce the design variables. In view of the antenna gain and beam width, set the objective function, we optimize the reflector shape that satisfies this function.

## 2 Optimization Techniques of Offset Parabolic Antenna

Figure 1 is the overall structure of Offset Parabolic antenna that is composed of the reflector and primary feed rotated by  $\phi_0$ ,  $\psi_0$  degrees. As a result, the advantage of offsetting the feed is that it eliminates aperture blockage caused by the Primary feed [3,4].

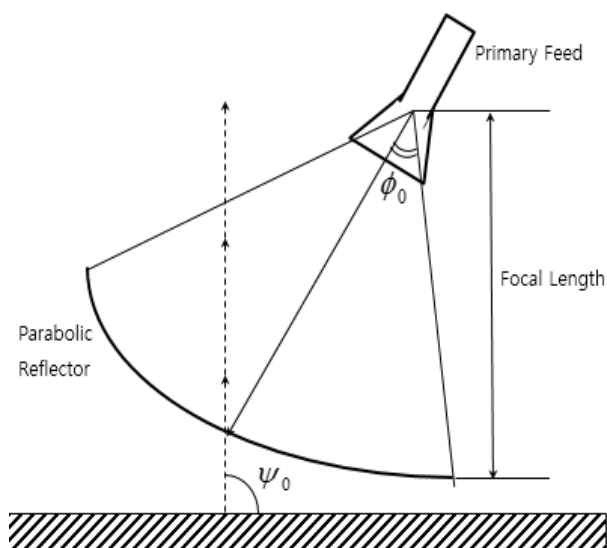


**Figure 1. Offset Parabolic Antennas cross section**

Prior to the optimal design, first for accurate and fast analysis of a parabolic antenna, the electromagnetic field in Aperture area of the Primary Feed assume a Gaussian distribution. And then calculated the beam pattern of the antenna by calculating the surface current in each position of the reflector using PO techniques.

$$\vec{J}_s = \begin{cases} 2\hat{n} \times \vec{H}_i & , \text{Reflection region} \\ 0 & , \text{Shadow region} \end{cases} \quad (1)$$

$$\vec{H}_s = \int_s \vec{J}_a(\vec{r}') \times \nabla G_0(\vec{r} - \vec{r}') ds' + \frac{1}{jk\eta} \nabla \times \int_s \nabla \times (\vec{M}_a(\vec{r}') \times \hat{G}\hat{R}) ds' \quad (2)$$

Based on these antennas Analysis and using the Genetic Algorithm conducted an optimal design of Offset Parabolic Antenna [5]. At this time, the characteristics of the feed

antenna is fixed, and design the antenna of high performance by modifying the shape of the reflector. In addition, the shape of each reflecting plate is shaped using a Bezier surface for reduction of the design variables. The following is an equation of the  $N \times N$  Bezier surface and 3x3 Bezier surface and figure 2 of 3x3 Bezier surface.

$$P(x, y) = \sum_{i=0}^n \sum_{j=0}^m P_{ji} B_{i,n}(x) B_{j,m}(y), \quad 0 \leq x \leq 1, \quad 0 \leq y \leq 1 \quad (3)$$

$$B_{i,n}(x) = \binom{n}{i} x^i (1-x)^{n-i}$$

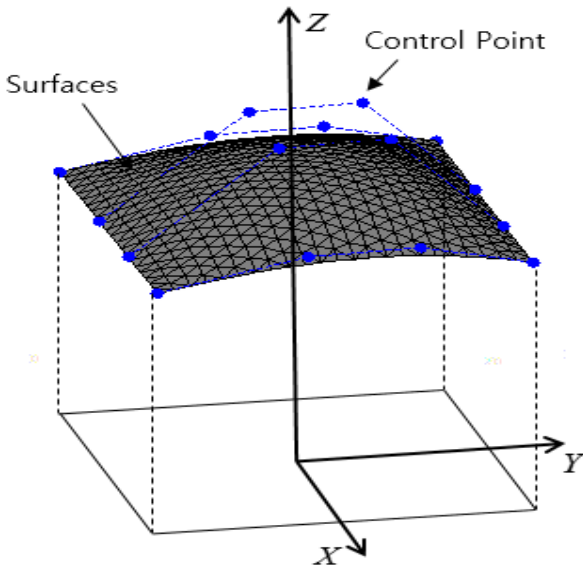


Figure 2. The concept of the Bezier surfaces

The above equation,  $P_{ji}$  are control points of the Bezier surfaces, denoted by 'o' at figure 2. By adjusting the position of these control points can determine the desired reflector shape.

### 3 Genetic Algorithms

The genetic algorithm is a group of genes with a theory of heredity based on the principles of natural evolution that Darwin's theory of evolution, depending on the generation. It was a lot of progress since starting to be introduced in 1970.[6]

The following figure shows a typical genetic algorithms flowchart.

First, we give the fitness of each individual, depending on the degree of violation of objective function and constraints to the distribution of a large number of objects in the design area.

The fitness evaluation of the properties of the parent after Crossover and mutation operation is performed to transfer to the next generation.

While repeating this process, it is possible to obtain a better chromosome.

We use the control points of the Bezier curve as a design variable and real coding Genetic Algorithms.[7]

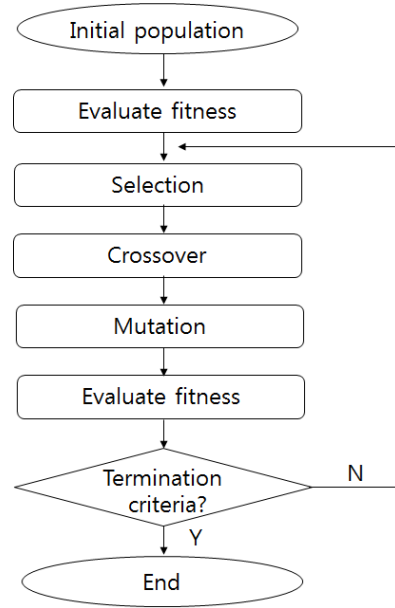


Figure 3. Flow chart of Genetic Algorithms

### 4 Analysis results and discussion

Primary Feed antenna is fixed, and the optimization process by using the 3x3 Bezier surface shape of the reflector. At this time, the design parameters are set a total of 12 variables, and the Z-axis coordinate of the control point except the starting point of the Bezier surface. Then reflection plate shape having a maximum gain that satisfies the following objective function is designed

$$F = |Gain_{des} - Gain_{cal}|^2 \quad (4)$$

Figure 4, 5 antenna shape and beam pattern is derived by the optimization process based on the table 1 design conditions. As a result the performance of the antenna is Gain-35.64dB, 3dB beam width 3.8, side lobe levels -22.7dB

Table 1: Sizes of the vehicle model

Parameter	
Frequency	95 [GHz]
Reflector Size	$20\lambda \times 30\lambda$
Feed Aperture radius	$5\lambda$
Variable	Z Axis [-10 : 40]
Generation	500
Population	50

Figure 6 is shows the average value and the minimum value of the fitness of the design process.

It can be seen that most of the genetic information at 20 generation to have similar properties.

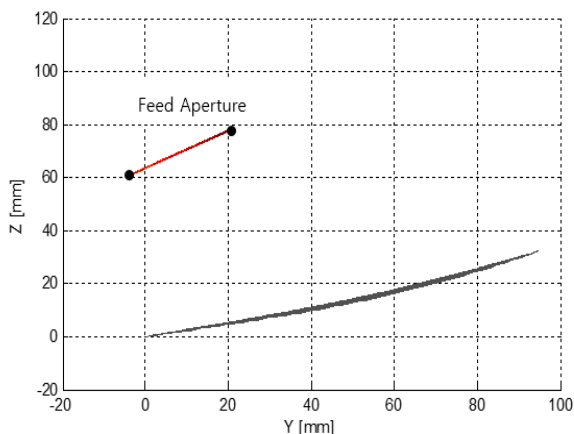


Figure 4. Designed antenna cross section

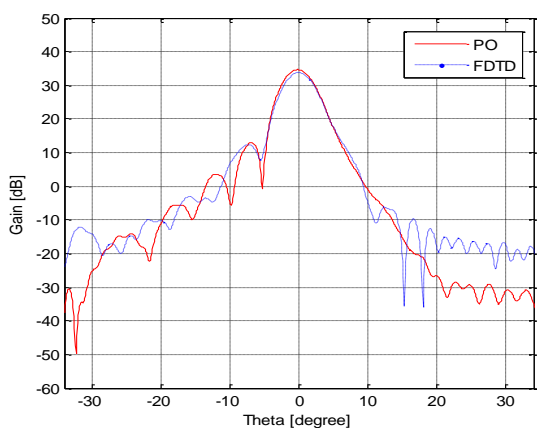


Figure 5. Antenna beam pattern comparison (E-Plane)

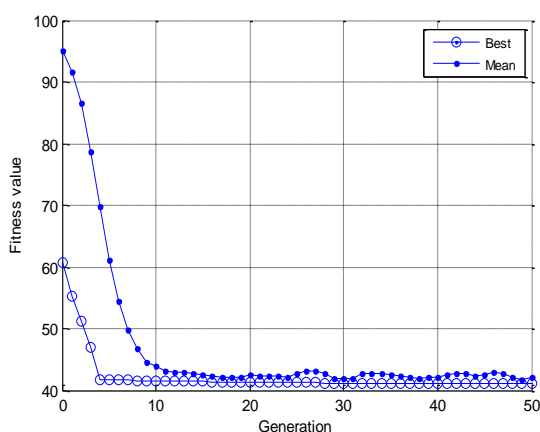


Figure 6. Change of fitness value

## 5 Results

In this paper, we propose a design technique using genetic algorithms and Physical Optics method.

And parametric design method using Bezier surfaces in consideration of the manufacture of the design shape. The control points of Bezier surfaces is set to the design variables minimizing the number of design variables, and reduced the optimization time.

Also, PO method may be to obtain a fast analysis result is compared with the Full-wave-analysis techniques in calculating the electromagnetic problem of large models. So it can apply efficiently with Optimization design that require many iterations. And analysis results also show high accuracy. However, when interference and multiple reflection model is complicated by such analysis requires further research for the error occurring.

## References

- [1] C. A. Balanis, *Antenna Theory Analysis and Design*, McGraw-Hill, 1949.
- [2] R. E. Collin, *Antenna theory-part2*, McGraw-Hill, 1969.
- [3] P. J. B. Clarricoats, A. D. Olver, "Corrugated Horns for Microwave Antennas", London, *IEEE Electromagnetic Wave Series18*, 1984.
- [4] Jose A. Martinez Lorenzo, A. G. pino "Induced- Current Analysis of Reflector Antennas" *IEEE Antennas and Propagation Magazine*, **volume**. 47, No. 2, pp. 92-100, Apr. 2005.
- [5] M. Wong, A. R. Sebak and T. A. Denidni "Wideband Bezier curve shaped microstrip to H-guide transition", *Electronics Letters*, **volume**. 45, No. 24, pp. 1250-1252, Nov. 2009.
- [6] R. L. Hauptm, S. E. Haupt,, *Practical Genetic Algorithms*, Wiley-Interscience, 2004.
- [7] S. L. Avila, W. P. Carpes, Jr., and J. A. Vasconcelos, "Optimization of an offset Reflector Antenna Using Genetic Algorithms", *IEEE Transactions On Magnetics*, **volume** 40, No. 2, pp. 1256-1259, Apr. 2005

# Experimental Verification of a Wideband Patch Antenna for Application to High-power Wideband Radiators

Taehyun Lim\*, Haeok Kwon\*, Jiheon Ryu<sup>†</sup>, Dong Woo Yim<sup>†</sup>, Jin Soo Choi<sup>†</sup>

\*Hanwha Corporation, Republic of Korea <sup>†</sup>Agency for Defense Development, Republic of Korea

## Abstract

We present experimental verifications of a wideband patch antenna for applying to high-power wideband radiators. This antenna was fabricated and tested. We measured the radiation patterns of the patch antenna. We tested DC breakdown of the patch antenna. We estimated pulse breakdown voltage for high-power wideband pulses by using the test results and the previous study on the pulse breakdown

**Keywords:** Wideband patch antenna, DC breakdown, Damped sinusoidal pulse, High-power wideband radiator.

## 1. Introduction

High-power wideband antennas has been test for High Power Electromagnetics effect test [1]. We studied wideband patch antennas (WPAs) since it is compact, lightweight and easy to produce arrays. Among many kinds of patch antennas, we chose E-shaped patch antennas because it has a broad bandwidth [2].

We designed the E-shape patch antenna using CST microwave studio [3]. We measured the E-plane and H-plane radiation patterns at 1GHz, prior to apply to High-power wideband sources. Plus, we tested DC breakdown of the patch antenna to estimate the pulse breakdown voltage for high-power wideband pulses.

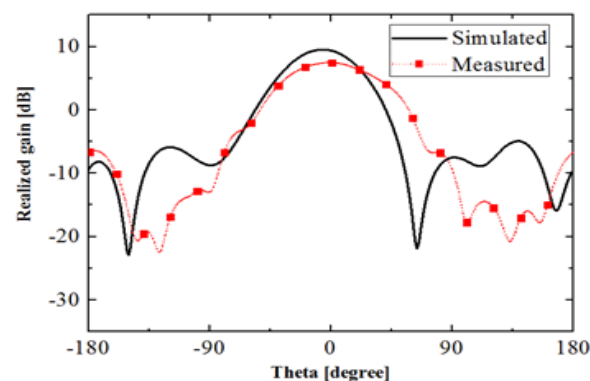
## 2. Beam patterns of the WPA

We determined the width and length of the E-shaped patch antenna [4]. The width and length of the antenna are 140mm and 110 mm, respectively. Fig. 1 shows the fabricated antenna. In the measured radiation patterns shown in Fig. 2, the gains of the E-plane and H-plane are 7.4dB and 7.2dB, respectively. The beam widths of the E-plane and H-plane are 38° and 42°, respectively.



Figure 1. Fabricated E-shape patch antenna

### E-Plane



### H-Plane

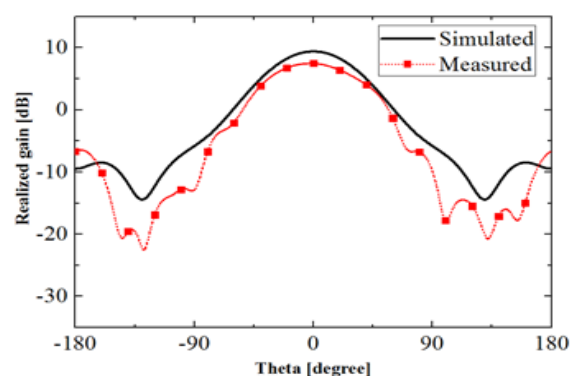


Figure 2. Simulated and measured radiation patterns at 1GHz

## 3. Estimate of pulse breakdown

As shown in Fig. 3, we tested DC breakdown by supplying high-voltage to the WPA using a DC power supply. DC breakdown occurred at the voltage amplitude of 25kV.



**Fig. 3. Experiment setup of the DC breakdown**

According to [5], we can estimate pulse breakdown voltage in air-filled. The product of the pressure and the pulse width is

$$p\tau \approx \frac{0.6}{\frac{E_e}{p}(\frac{E_e}{p}-26)^2}, \quad (1)$$

where  $p$  is the pressure,  $\tau$  is the pulse width and  $E_e$  is the electric field. According to [6], [7], we can estimate the pulse width of the 1-GHz wideband pulses with damped sinusoidal shapes. If we assumed that the quality factor of the pulses is 10, the pulse width of 3.18ns is calculated by

$$\tau = \frac{QT}{\pi}, \quad (2)$$

where  $Q$  is the quality factor and  $T$  is the period of one cycle.

By using the Eqn. (1), (2) and the DC breakdown test, the pulse breakdown voltage of 154.5kV is calculated. It is concluded from these results that this antenna is appropriate for the high-power wideband radiator to be applied.

#### 4. Conclusion

Radiation patterns and DC breakdown voltage of a WPA is measured, prior to apply to High-power wideband sources. The gains of the E-plane and H-plane at 1GHz are 7.4dB and 7.2dB, respectively. The beam widths of the E-plane and H-plane are 38° and 42°, respectively. The DC breakdown of the WPA is 25kV. The pulse breakdown voltage of 154.5kV is calculated. It is concluded from these results that this antenna is appropriate for the high-power wideband radiator to be applied.

#### References

[1] Dave Giri "High-Power Electromagnetic Environments", 15th Annual Directed Energy Professional Society

(DEPS) Symposium, Albuquerque, 26-30 November 2012.

[2] Yuehe, "Ge A compact E-shaped patch antenna with corrugated wings", Antennas and Propagation, IEEE, 2006.

[3] CST Studio Suite™ 2013.

[4] <http://www.rfdh.com/design/patch>.

[5] D. Anderson and M. Lisak, "Breakdown in air-filled microwave waveguides during pulsed operation", American Institute of Physics, 1984.

[6] D.V. Giri, "Switched Oscillators and Their Integration into Helical Antennas", with F. M. Tesche, M. D. Abdalla, M. C. Skipper and M. Nyffeler, Circuit and Electromagnetic System design Note 58, 4 July 2009.

[7] Lausanne, "System design and assessment notes", Study and classification of potential IEMI source, pp. 8-9, 2014.

# Low-Frequency-Compensated Horn Antenna: for the Simulation of HEMP

Shaofei Wang, Yanzhao Xie

State Key Laboratory of Power Equipment and Electric Insulation  
School of Electric Engineering, Xi'an Jiaotong University  
Xi'an, China  
wsf2013@stu.xjtu.edu.cn

**Abstract**—A kind of low-frequency-compensated TEM horn antenna is proposed to simulate High-altitude Electromagnetic Pulse (HEMP). With CST Microwave Studio, simulation model is created to analyze the performance of the antenna. According to the results, the antenna exhibits a cardioid pattern and low VSWR in frequency. Waveforms of electric field on the boresight about 0.4-0.9 meters from the aperture measure up the HEMP radiation environment defined in IEC 61000-2-9 [1].

**Keywords**—low-frequency-compensated; horn antenna; HEMP directivity; waveform

## I. INTRODUCTION

Since electromagnetic pulse created by a nuclear detonation at high altitude (HEMP) severely threatens the survivability of electronic systems [2], many large test facilities have been established to simulate the threat during the past five decades. However these simulators can hardly move. In addition, the radiating-wave simulator almost omnidirectional, which would leads to low efficiency and huge waste of space.

In this paper, a novel simulator based on low-frequency-compensated horn antenna is proposed, which exhibits well directivity, and standard HEMP waveform could be obtained near the aperture of the antenna. In addition, it is of relatively small size, which can be loaded in a truck.

## II. DESIGN PRINCIPLE

The TEM horn can be used to radiate fast electromagnetic transients. However it is capacitive in low frequency regime, and even open-circuited when frequency goes down to zero. Therefore, it could not be applied to radiate HEMP which contains abundant low frequency components. In order to improve the low frequency antenna performance, resistive termination is adopted to connect the two horn conductors. Thus, the low-frequency component form a current loop along the antenna and terminating route, which makes a magnetic dipole. If the terminating route is on the back of the antenna, the combination of magnetic and electric dipole would radiate at the same direction as the high-frequency radiation [3]. This is the so-called low-frequency-compensation. Topology of the low-frequency-compensated horn antenna is shown as fig. 1.

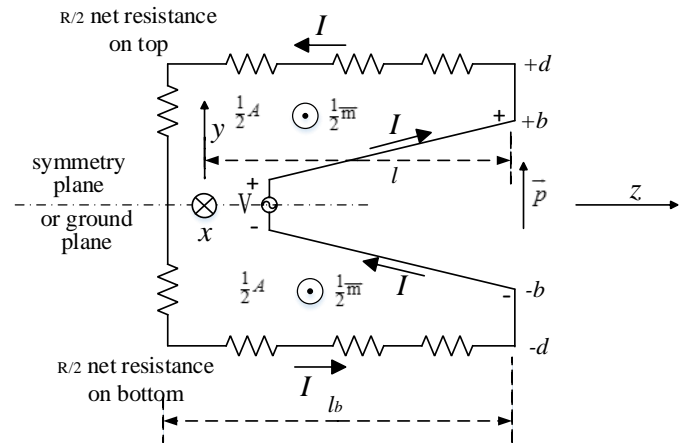


Fig. 1 Topology of the low-frequency-compensated horn antenna

Where  $R$  denotes the total terminating resistance,  $m$  the magnetic dipole moment and  $p$  the electric dipole moment.  $R$  is selected to match the impedance of the horn antenna, in order to eliminate reflection. If the relationship between  $m$  and  $p$  meets (1),

$$\frac{m}{p} = c \quad (1)$$

where  $c$  is the velocity of light in vacuum, fields will be completely transverse with the primary components  $E_\theta$  and  $H_\phi$  enhanced on the boresight (i.e.  $+x$  direction) and null in the opposite direction (i.e.  $-x$  direction). Furthermore, on the boresight, the wave impedance equals to the impedance of vacuum [4].

## III. DESIGN AND PERFORMANCE

### A. Design of the Low-Frequency-Compensated Horn Antenna

Since the antenna is symmetrical in the vertical direction (as shown in fig. 1), in order to be loaded in the truck conveniently, a ground plane is introduced at the symmetry plane. Thus the antenna is designed as fig. 2.

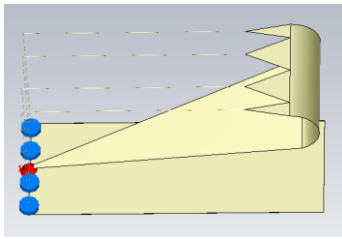


Fig. 2 Simulation model of the antenna

Four resistor chains are adopted as the termination, and the current of each is of the same value [5]. In order to eliminate the reflection, an arc transition is introduced to connect the upper conductor of the horn and the loading route.

### B. Performance of the Low-Frequency-Compensated Horn Antenna

For the purpose of performance evaluation, simulation model is established with CST Microwave Studio. The simulation results show that the antenna has a cardioid pattern even when the frequency is very low such as 1MHz and 10MHz. as is shown in fig. 3.

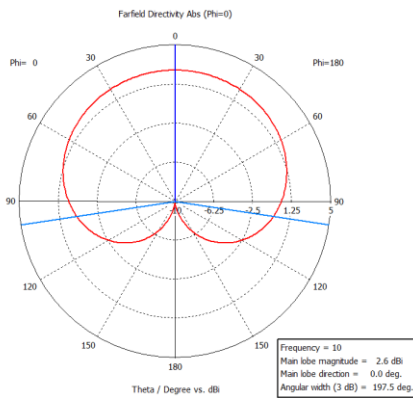


Fig. 3 The pattern of

As for the VSWR (Voltage Standing Wave Ratio), in the frequency band considered, i.e. 0-200MHz, it is 2 around, except for the frequency near 10MHz, as is shown in fig. 4. It means that the antenna has well performance in frequency from DC to 200MHz [6].

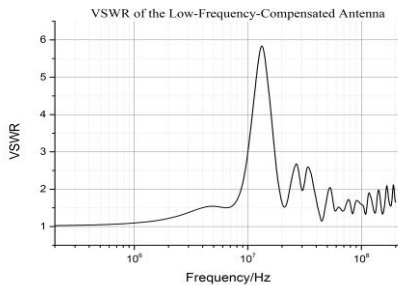


Fig. 4 VSWR of the antenna

The waveform of the source and E-field near the aperture (in the near field zone) is shown in fig. 5. The waveform parameter of electric field on the boresight within 1 m from the aperture is shown in Table 1. Thus, from 0.4-0.9m, the

waveforms of electric field measure up the HEMP radiation environment defined in IEC 61000-2-9.

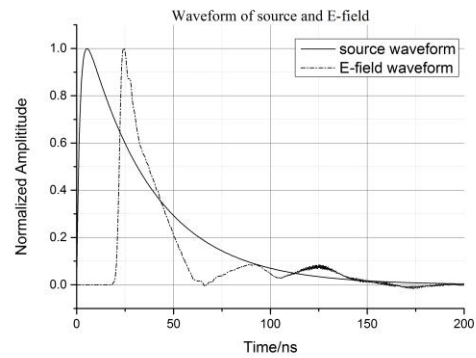


Fig. 5 Waveform of E-field near the aperture

Table 1 Waveform parameter

Distance/m	Rise Time/ns	Pulse Width/ns
0	3.01	34.1
0.1	2.99	31.8
0.2	2.98	30.7
0.3	2.84	30.0
0.4	2.79	28.6
0.5	2.88	27.5
0.6	2.73	24.0
0.7	2.71	23.5
0.8	2.56	21.3
0.9	2.60	18.1
1.0	2.51	15.1

## IV. CONCLUSION

A novel simulator based on low-frequency-compensated horn antenna is proposed. It has a cardioid pattern, which means that it is of well directivity; it has low VSWR, namely it is well performed in the frequency concerned; and waveforms of electric field on the boresight about 0.4-0.9 meters from the aperture measure up the HEMP radiation environment defined in IEC 61000-2-9.

## REFERENCES

- [1] IEC 61000-2-9 Electromagnetic compatibility (EMC) - Part 2: Environment - Section 9: Description of HEMP environment – Radiated disturbance. Basic EMC publication
- [2] J. C. Giles and W. D. Prather, "Worldwide High-Altitude Nuclear Electromagnetic Pulse Simulators," *Electromagnetic Compatibility, IEEE Transactions on*, vol. 55, pp. 475-483, 2013-01.
- [3] C. Baum, "Low-Frequency-Compensated Horn Antenna," *Sensor and Simulator Notes* 377, 1995.
- [4] F. M. Tesche and Y. E. Adamian, "Note 407\_The PxM Antenna and Applications to Radiated Field Testing of Electrical Systems Part-1 - Theory and Numerical Simulations," *Sensor and Simulator Notes*, 407, 1997.
- [5] D. V. Giri, "Design Guidelines for Flat-Plate Conical Guided-Wave EMP Simulators With Distributed Terminators," *Sensor and Simulator Notes*, 407, 1996.
- [6] C. A. Balanis, *Antenna Theory Analysis and Design*, 3rd ed. Hoboken, New Jersey: John Wiley & Sons, Inc., 2005.

# Analysis of the Induced Electromagnetic Field in the Surroundings of a NEMP Simulator

B. Daout<sup>†</sup>, N. Mora\*, M. Sallin<sup>†</sup>, C. Romero<sup>†</sup>, F. Vega<sup>§</sup>, F. Rachidi\*

<sup>†</sup> Montena Technology, Switzerland, bertrand.daout@montena.com

<sup>§</sup> EMC Laboratory, Universidad Nacional de Colombia, Colombia, jfvegas@unal.edu.co

\*EMC Laboratory, Swiss Federal Institute of Technology (EPFL), Switzerland, nicolas.mora@epfl.ch

## Abstract

We present an analysis of the electromagnetic field distribution around a Nuclear Electromagnetic Pulse (NEMP) test installation. We are interested in bounding the exposure levels for the personnel working around the facility and evaluating the likelihood of relevant electromagnetic interferences in the neighboring equipment due to coupling to the wirings.

**Keywords:** NEMP simulator, TEM horn antenna

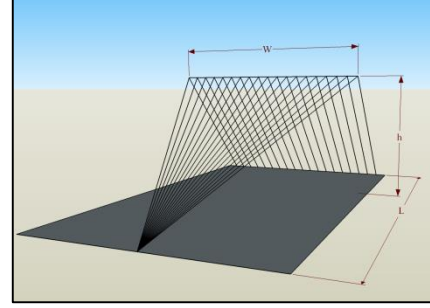


**Fig. 1** Schematic diagram of the structure under study

## 1 Introduction

Previous works [1, 2] on the calculation of the electromagnetic (EM) fields in the working volume of Nuclear Electromagnetic Pulse (NEMP) simulators have shown that they can be determined by assuming the energy to be concentrated in the transverse electromagnetic (TEM) propagation. There are concerns about the exposure of human beings and equipment to radiated EM fields away from the simulator working volume. This has led to the interest in calculating the generated fields in the surroundings of the NEMP generators.

In this work, we discuss the numerical prediction of the induced EM in the surroundings of a NEMP simulator. The transmission line theory can be used to predict the simulator current distribution and the radiated field using the approximated solution of Sommerfeld's integrals derived by Norton [3-5]. The prediction of the near fields, on the other hand, requires a full wave solution. In order to validate the numerical models, full wave simulations of a NEMP simulator by using NEC4 will be presented and compared with experimental results on a test site.

## 2 Structure under study

A schematic diagram illustrating the NEMP simulator under study is presented in Fig. 1. The simulator is composed of a wired conical transmission line [2] terminated in a distributed resistive loading. The line height  $h=5.4$  m and width  $W=8$  m are chosen to obtain a desired characteristic impedance  $Z_c=110$  ohm that will be matched with the resistive termination. The total horizontal length  $L$  from the apex of the conical transmission line up to the end termination lines is 35 m.

Notice that the metallic ground plane (8 x 35 m) has comparable dimensions with respect to  $L$  and  $W$ . The entire structure is located above a lossy ground characterized by a conductivity  $\sigma$  and a relative permittivity  $\epsilon_r$ .

## 3 Prediction of the far fields

In order to calculate the far fields around the structure, the procedure presented in [3] has been used. In a first step, the currents generated in the surface of the conical transmission line due to a voltage excitation at the apex of the line were evaluated by using the transmission line theory [3]. In a second step, the total field is recovered as the superposition of the dyadic Green's functions of the space wave and the surface wave around the source [5]. The dyadic functions presented in [3] relate the electric field  $\vec{E}$  at a distance  $\vec{r}$ , due to a vertical and horizontal current element at position  $\vec{r}'$ :

$$\vec{E}(\vec{r}) = \int_{\text{conductors}} \vec{\Gamma}(\vec{r}; \vec{r}') \cdot \hat{\xi} I(\xi) d\xi \quad (1)$$

Close to the ground, the far fields are governed by the surface wave. On the other hand, at several meters above the ground, the space wave dominates the response. Both the space wave and the surface wave will be affected by the properties of the lossy ground.

## 4 Prediction of the near fields

Due to the complexity of the calculation of the Green's functions close to the current elements, the near fields around the structure can be evaluated by a full wave solution. In this work we have used NEC4 in order to calculate the total field by considering the presence of both space and surface waves.

A schematic diagram illustrating the simulation domain in NEC 4 is presented in Fig. 2. The conical transmission line was approximated by 10 wires. The termination wires were simulated as resistively loaded wires of the same radius of the conical transmission line wires. The wires were discretized with uniform segments with length  $\Delta = \lambda_{\min} / 10$ ; where  $\lambda_{\min}$  is the wavelength at the maximum simulation frequency (100 MHz in this case). The ground plane was modeled as a square grid of size  $\lambda_{\min} / 10$ .

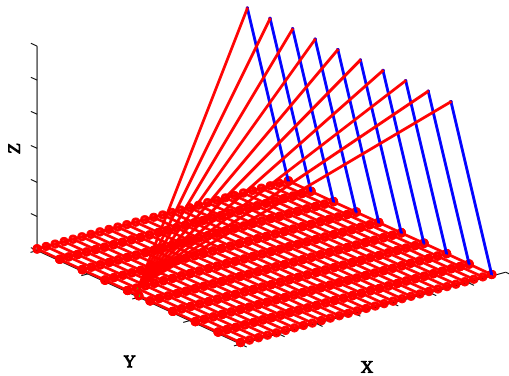


Fig. 2 Schematic diagram of the structure under study

## 5 Experimental results

Measurements of a real facility were performed to validate the calculations and simulations. The field around an outdoor Montena Technology RS105 NEMP simulator was measured at different positions outside the working volume. The vertical electric field was measured with a chain composed of a D-dot free-field electric field sensor, a balun, attenuators, an analog fiber-optic link and a computer controlled high-speed oscilloscope. In order to check the repeatability of the source, the pulsed E-field at the output of the generator was recorded by a reference sensor. The whole measurement chain is designed to acquire standard NEMP pulses showing a peak electric field of about 50 kV/m, a rise-time between 1.8 and 2.8 ns, and an FWHM between 18 and 28 ns.

A comparison of the numerically predicted and measured electric fields at 40 m in the Y direction from the working volume (see Fig. 2) is presented in Fig. 3.

The measurement and numerical prediction of the near vertical electric field are in good agreement. A comparison of the results obtained in the far field region will be shown in the final presentation.

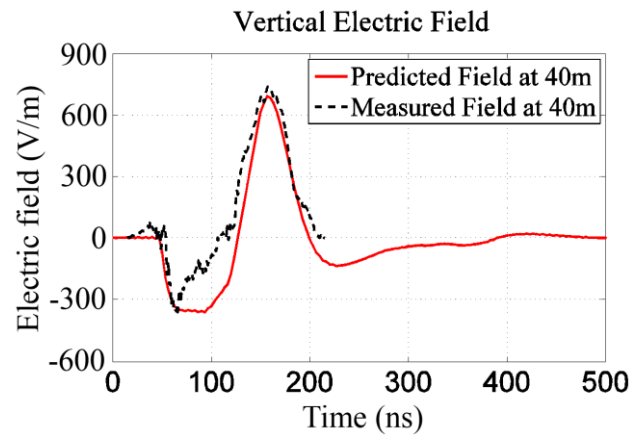


Fig. 3 Comparison of the measured and simulated E-field waveform at 40 m from the center (outside) of the working volume

## 7 References

- [1] C. E. Baum, "Impedances and Field Distributions for Parallel Plate Transmission Line Simulators", *Sensor and Simulation Notes*, vol. 21, 6 June 1966.
- [2] C. E. Baum, "The Conical Transmission Line as a Wave Launcher and Terminator for a Cylindrical Transmission Line", *Sensor and Simulation Notes*, vol. 31, 16 January 1967.
- [3] F. M. Tesche, C. Mo, and R. W. Shoup, "Determination of the electromagnetic fields radiated from the ARES EMP simulator", *Electromagnetic Compatibility, IEEE Transactions on*, vol. 36, pp. 331-341, 1994.
- [4] K. Norton, "The physical reality of space and surface waves in the radiation field of radio antennas", *Radio Engineers, Proceedings of the Institute of*, vol. 25, pp. 1192-1202, 1937.
- [5] E. C. Jordan and K. G. Balmain, *Electromagnetic waves and radiating systems, vol. 4*, Prentice-Hall Englewood Cliffs, NJ, 1968.

# Detection of metal objects by ultrawideband pulses with different polarization

*V.I. Koshelev, E.V. Balzovsky, Yu.I. Buyanov, E.S. Nekrasov,*

*A.A. Petkun and V.M. Tarnovsky*

*Institute of High Current Electronics SB RAS  
2/3, Akademicheskoy Ave., Tomsk 634055, Russia  
koshelev@lhfe.hcei.tsc.ru*

## Abstract

The paper presents the results of the investigations on metal object detection under two different conditions united by a general approach to use ultrawideband (UWB) pulses with different polarization. In the first task, using the developed computer code, a possibility to detect an ideally conducting cross-shaped object located over a randomly nonuniform surface of the dielectric medium, when sounding by two orthogonally polarized UWB pulses, has been investigated. In the second task, as applied to the radar through a wall, a polarization structure of the pulses reflected from metal plates when sounding the objects by UWB pulses with linear and elliptical polarization has been studied.

**Keywords:** Ultrawideband radiation, detection, polarization structure.

## 1 Introduction

In recent years, investigations of possibility to detect the objects located near a randomly nonuniform reflecting surface using UWB electromagnetic radiation have been carried out. To increase the effectiveness, the successive sounding by the orthogonally polarized radiation pulses is used as a rule. Previously [1], a high-power UWB radiation source has been developed. In the source two orthogonally polarized pulses were radiated by the antenna array excited from one generator. It was interesting to consider a possibility to use the similar pulses for the metal object detection against the background of a randomly nonuniform ground surface. For this purpose, we used the numerical simulation methods.

Presently, intensive investigations of the object detection behind the optically opaque obstacles are conducted using short UWB electromagnetic pulses. The essential informative feature for recognition of the sounding objects is a polarization structure (PS) of the reflected pulses [2]. To investigate the PS of the pulses reflected from metal objects, we have developed a receiving antenna array. The array provides recording two orthogonal components of the scattered field from seven horizontal fixed directions in the range of  $\pm 40^\circ$ .

## 2 Object detection over a randomly nonuniform surface

To investigate the UWB pulse reflections from a randomly nonuniform medium surface having fixed electrical properties and containing metal objects, a computer code has been developed. The code is based on the finite-difference time-domain method for Maxwell equations. The geometry of the problem presents a three-dimensional parallelepiped partially filled with the medium having the conductance  $\sigma$  and relative dielectric permeability  $\epsilon$ . Parameters of the dry ( $\epsilon = 4$ ,  $\sigma = 0.002$  Sm/m) and moist ( $\epsilon = 10$ ,  $\sigma = 0.07$  Sm/m) sandy ground have been chosen for the dielectric medium. A plane wave is incident normally on the surface from free space. A cross-shaped object was located near the dielectric medium having a randomly nonuniform surface. The reflected signal accumulated in 25 receiving points located as a  $5 \times 5$ -array opposite the metal object at a distance of  $6.5 \tau_p c$ , where  $\tau_p$  is the sounding pulse length, and  $c$  is the velocity of light. The root-mean-square deviation of the surface from the

mean level  $\sigma_s$  is equal to  $0.14 \tau_{pc}$ . The distance between the object and the mean level of the surface is  $0.75 \tau_{pc}$ . The arm lengths of the object varied in the limits of  $L = (1-4) \tau_{pc}$ .

In the model, the sounding pulses are two three-lobe UWB pulses of a linearly-polarized plane leading-edge electromagnetic field. The pulses were radiated one after another without delay with orthogonal polarizations. To investigate the metal object detection, the computations were performed with the object and without the one. The cross-correlation function of the received orthogonally-polarized signals in each receiving point was calculated for each case. To increase the probability of object detection, a mutual correlation between distributions of the maxima of the received signals at the orthogonal polarizations was calculated as well. The results were averaged by 10 realizations of a randomly nonuniform surface.

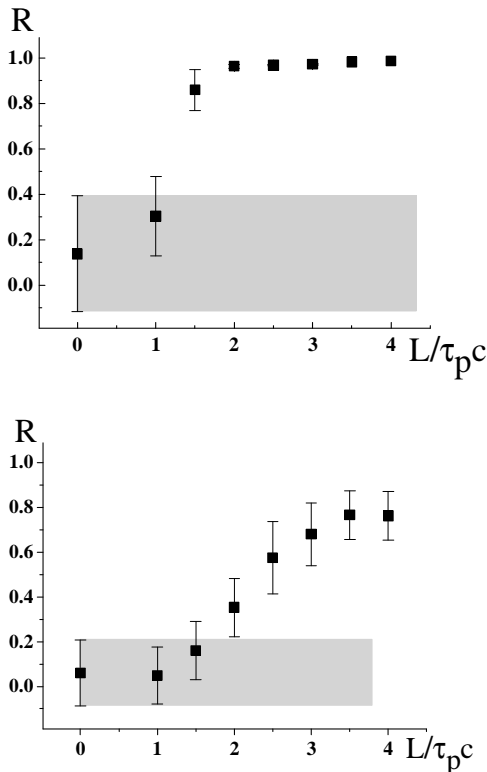


**Figure 1. Mutual correlation between distributions of the maxima of the received signals at the orthogonal polarizations for the dry (upper) and moist (bottom) sand**

By the results of numerical simulation, the average values of the cross-correlation function maxima of the orthogonally-polarized reflected signals versus the metal object dimension have been obtained. At such signal processing, the detection is possible only for dry sand at the object dimensions  $L/\tau_{pc} > 2$ . For the second method of signal processing, the object detection is possible at  $L/\tau_{pc} > 1$  and at  $L/\tau_{pc} > 2$  over the dry and moist surfaces, respectively (Fig. 1).

### 3 Investigation of polarization structure of the reflected pulse field

The investigation of the reflected pulse field PS was carried out in the absence of a dielectric barrier between a transceiver and metal objects. The distance between the centers of the transmitting and receiving antennas was 0.5 m. The objects were located at a 2.3-3.5-m distance. To decrease the mutual influence, the space between the receiving and transmitting antennas was filled with an absorber. The pulse reflected from the object was calculated as the difference of the signals recorded in the presence and absence of the object. Measurement results were averaged by 40 pulses.

To generate a linearly polarized radiation pulse, a  $2 \times 2$  array of combined antennas was used. The antennas were optimized to be excited by a 0.5-ns length bipolar voltage pulse [3]. To obtain an elliptically polarized UWB pulse, a cylindrical helical antenna was used with the matching band of 1.45-2.9 GHz. A 0.5-ns bipolar voltage pulse was applied to the input of this antenna as well.

In the experiments, the metal plates of different sizes were used. The plates were located in the plane normally to the pulse propagation direction with capability to be rotated in this plane.

Initially, measurements of the PS radiation scattered by a  $180 \times 30$ -mm plate sounded by the pulses with vertical linear polarization were made. Inclination of the plate from vertical position leads to the appearance of a cross-polarized component in the reflected field. This results in the change of the electric field hodograph. The inclination of the

hodograph corresponds to the plate inclination at the angles  $\alpha = \pm 45^\circ$ .

Measurement results of the PS radiation scattered by the plates of equal length (275 mm) but different width sounded by the elliptically polarized pulses have been obtained. It was found out that there is an angle  $\delta$  between the plate inclination and a large axis of the reflected pulse hodograph. The value of this angle has no dependence on the angle of the plate inclination  $\alpha$  in the limits of the measurement error. Figure 2 presents the hodographs of the pulses reflected from the plates of the width  $d = 10$  mm (1) and 30 mm (2) with different inclination of  $\alpha$ .

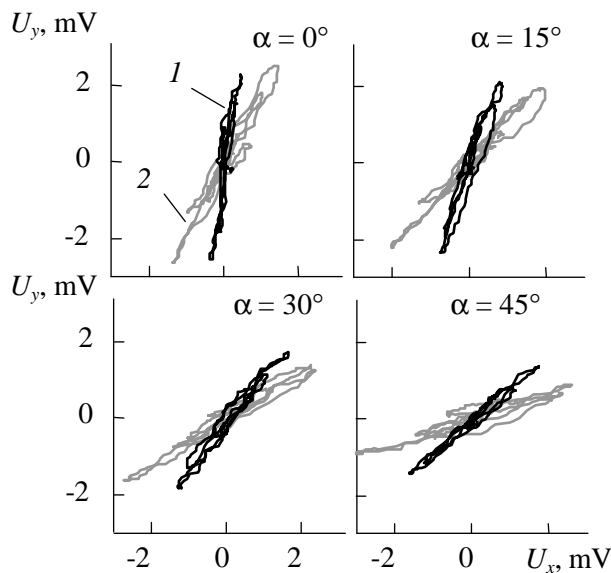


**Figure 2. Polarization structure of the pulses reflected from the metal plates sounded by elliptically polarized pulses**

For the narrow plates with the relative width  $d/\lambda_0 < 0.15$ , the reflected field has almost linear polarization at any positions of the plates. Here,  $\lambda_0$  equals to 15 cm and corresponds to the wavelength at the central spectrum frequency of the voltage pulse exciting the antenna. For wider plates, the reflected field polarization differs from the linear one. For the plates with  $d/\lambda_0 > 0.5$  it tends to the circular one. The experiments have shown that the angle  $\delta$  increases with the enlargement of the plate width (Fig. 3). Thus, successive sounding of the plate by UWB pulses with linear and elliptical polarizations allows

estimating the inclination angle of the plate and its width.

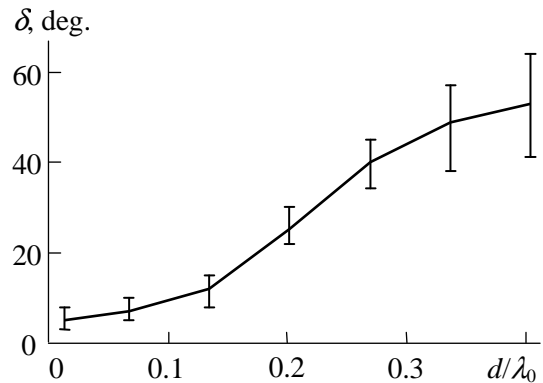


**Figure 3. The difference between the angle of the large axis of the reflected pulse hodograph and inclination angle of the metal plate versus the width of the plate**

#### Acknowledgements

The work was supported by the Basic Research Program of Physical Sciences Division of RAS “Radioelectronic methods in research of the natural environment and human subject”.

#### References

- [1] A.M. Efremov, V.I. Koshelev, B.M. Kovalchuk, V.V. Plisko, and K.N. Sukhushin. “Generation and radiation of high-power ultrawideband nanosecond pulses”, *J. Commun. Technol. Electron.*, **52**, pp. 756-764, (2007).
- [2] V.I. Koshelev, E.V. Balzovsky, Yu.I. Buyanov, P.A. Konkov, V.T. Sarychev, and S.E. Shipilov. “Radar signal polarization structure investigation for object recognition”, *Ultra-Wideband, Short-Pulse Electromagnetics 7*, pp. 707-714, (2007).
- [3] A.M. Efremov, V.I. Koshelev, B.M. Kovalchuk, V.V. Plisko, and K.N. Sukhushin. “High-power sources of ultra-wideband radiation with subnanosecond pulse lengths”, *Instrum. Exp. Tech.*, **54**, pp. 70-76, (2011).

# Pulse Compression for OFDM based Ground Penetrating Radar

Shi Zheng\*<sup>†</sup>, Wen Huang\*, Xuehan Pan\*, Anxue Zhang\*

\*School of Electronic and Information, Xi'an Jiaotong University, Xi'an, China, [anxuezhang@mail.xjtu.edu.cn](mailto:anxuezhang@mail.xjtu.edu.cn);

<sup>†</sup>Academy of Space Electronic Information Technology, Xi'an, China;

## Abstract

Ground penetrating radar (GPR) is a special radar technique that detects motionless subsurface targets. Pulse compression for Line Frequency Modulation (LFM) radar signal is an important technique for improve both range resolution and average transmitted power. We propose another scheme for pulse compression. An Orthogonal Frequency Division Multiplexing (OFDM) signal is transmitted as the radar signal in a GPR system. The implement for OFDM based GPR is simple and the simulation results show the scheme can provide both high average transmitted power and high range resolution.

**Keywords:** Ground Penetrating Radar; Orthogonal Frequency Division Multiplexing; Pulse Compression.

## 1 Introduction

Ground penetrating radar (GPR) detects arbitrary underground low loss dielectric materials and targets by transmitting radio waves [1, 2]. Detection depth and range resolution are the most concerned qualification of a GPR system. Long detection depth requires high transmitted power, while high range resolution has a demand of wide bandwidth. Line Frequency Modulation (LFM) signals can provide both high average transmitted power and wide bandwidth since the time-bandwidth products are much larger than common pulses. Pulse compression is an important technique that greatly compresses the pulse width and obtains high resolution corresponding to the short pulse.

We propose another scheme for pulse compression. An Orthogonal Frequency Division Multiplexing (OFDM) signal is transmitted as the radar signal in a GPR system. OFDM is a recently applied technique in [3] and its mainly advantage is high resolution and flexible signal form. In 2000 Levanon introduced OFDM to radar application by proposing a multi-frequency complementary phase coded radar signal and comparing OFDM signal over other known radar signals[3]. Feasibility studies about system simulation and imaging for OFDM synthetic aperture radar (SAR) were discussed by many authors in the following years [4-8]. In 2010, Qiwei Z. applied the general OFDM signal to ground penetrating radar and estimated the channel response accurately[9]. These studies show that applying OFDM to radar is a feasible approach to achieve better detection. The implement for an OFDM based GPR is simple and the simulation results show

the pulse compression can provide both high average transmitted power and high range resolution.

## 2 Pulse Compression for OFDM Signals

Orthogonal frequency division multiplexing (OFDM) is a special form of multicarrier modulation where its carrier spacing is carefully selected so that each subcarrier is orthogonal to the other subcarriers.

Consider an OFDM signal with the following parameters: subcarrier number  $N$ , bandwidth  $B$ .  $\Delta f = B/N$  is the subcarrier spacing. All the subcarriers are orthogonal in the time duration  $T = 1/\Delta f$ . The OFDM signal can be expressed as

$$s(t) = \sum_{k=0}^{N-1} a_k e^{j2\pi k \Delta f t}, 0 \leq t < T, \quad (1)$$

where  $a_k$  is the complex modulating weight of the  $k$ th subcarrier  $e^{j2\pi k \Delta f t}, 0 \leq t < T$ . The discrete form of the OFDM signal in the sample rate of  $T/N$  is

$$s(n) = \sum_{k=0}^{N-1} a_k e^{j2\pi n k / N}, n = 0, 1, \dots, N-1. \quad (2)$$

Compared with the Inverse Discrete Fourier Transform (IDFT),  $\{s(n)\}$  is the IDFT of  $\{a_k\}$ . Hence, OFDM modulation can be achieved by Inverse Fast Fourier Transform (IFFT).

Transmit the OFDM signal  $s(t)$  to the underground scene, and the radar received signals are recorded as  $r(t)$ . The pulse compression of  $r(t)$  can be realized by correlation processing as following

$$r_c(t) = r(t) * s^*(-t), \quad (3)$$

where  $*$  denotes the convolution operation and  $*$  represents the conjugate symbol. Actually,  $r_c(t)$  is the correlation result of  $r(t)$  and  $s(t)$ .

## 3 Simulation Results

To verify the feasibility of the pulse compression for OFDM based GPR, a simulation is conducted and the results are presents in this section. Consider an OFDM GPR system with the following configurations: bandwidth  $B = 300\text{MHz}$ , number of subcarriers  $N = 64$ . The modulating weights at

each subcarrier  $a_k, k=0,1,\dots,N-1$  are obtained as the QPSK symbols of a random binary code stream. Generate the OFDM signal  $s(t)$  using (1) and the result is shown in Figure. 1(a). It can be seen that the radar signal  $s(t)$  has a long time width. The auto correlation of  $s(t)$  is shown in Figure.1(b) where the main lobe is narrow. Comparison between the two subfigures verifies that the pulse compression for OFDM signal can decrease the pulse width greatly.

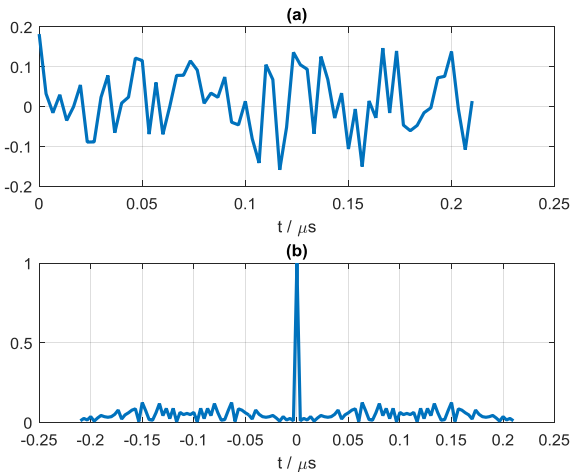


**Figure 1. (a) OFDM signal  $s(t)$ ; (b) Auto correlation of  $s(t)$ .**

We then simulate the propagation of the radar signal in an underground scene, which is modeled as a channel with the impulse response

$$h(t) = \delta(t-0.03) + 0.6\delta(t-0.08) + 0.4\delta(t-0.1567)(\mu\text{s}).$$

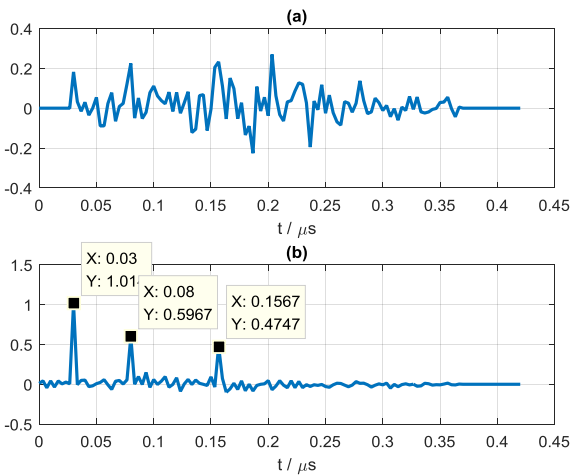


**Figure 2. (a) GPR received signal  $r(t)$ ; (b) Pulse compression result of  $r(t)$ .**

The received signal in the system receiver is shown in Figure.2 (a). It is obvious that the three reflected echoes are overlapped. The corresponding pulse compression result is

shown in Figure. 2 (b), where the three echoes are clearly to distinguished. Comparison between the two subfigures verifies that the pulse compression for OFDM received signal can improve the range resolution in a large degree.

## 4 Conclusion

We propose a new scheme for pulse compression. An OFDM signal is transmitted as the radar signal in a GPR system. The implement for OFDM based GPR is simple and the simulation results show the scheme can provide both high average transmitted power and high range resolution.

## Acknowledgements

The authors are grateful to the supports from the National Natural Science Foundation of China under Grant Nos. 61331005 and 61001039.

## References

- [1] H. M. Jol, *Ground Penetrating Radar Theory and Applications*: Elsevier Science, 2009.
- [2] D. J. Daniels, *Ground Penetrating Radar*, The Institution of Electrical Engineers ed. London, United Kingdom: The Institution of Engineering and Technology, 2004.
- [3] N. Levanon, "Multifrequency complementary phase-coded radar signal," *IEE Proceedings Radar Sonar and Navigation*, vol. 147, pp. 276-284, Dec. 2000.
- [4] D. Garmatyuk, J. Schuenger, Y. T. Morton, K. Binns, M. Durbin, and J. Kimani, "Feasibility study of a multi-carrier dual-use imaging radar and communication system," 2007, pp. 194-197.
- [5] D. Garmatyuk and M. Brennehan, "Adaptive Multicarrier OFDM SAR Signal Processing," *Synthetic Aperture Radar (EUSAR), 2010 8th European Conference on*, pp. 1-4, 0007-10-20 2010.
- [6] R. Mohseni, A. Sheikhi, and M. A. Masnadi-shirazi, "Efficient compression of wavelet packet OFDM radar signals," *IET International Radar Conference 2009*, pp. 5 pp.-5 pp., 01 2009.
- [7] S. Sen and A. Nehorai, "Adaptive OFDM Radar for Target Detection in Multipath Scenarios," *IEEE Transactions on Signal Processing*, vol. 59, pp. 78-90, 2011-01-01 2011.
- [8] S. Sen and A. Nehorai, "Adaptive Design of OFDM Radar Signal With Improved Wideband Ambiguity Function," *IEEE Transactions on Signal Processing*, vol. 58, pp. 928-933, Feb. 2010.
- [9] Z. Qiwei, S. Pennock, M. Redfern, and A. Naji, "A novel OFDM based ground penetrating radar," in *2010 13th International Conference on Ground Penetrating Radar (GPR)*, 2010, pp. 1-6.

# A Valentine Antenna Working in 150 MHz – 350 MHz Band for UWB Application

Xuehan Pan\*, Shi Zheng\*, Anxue Zhang\*

\*School of Electronic and Information, Xi'an Jiaotong University, Xi'an, China, [anxuezhang@mail.xjtu.edu.cn](mailto:anxuezhang@mail.xjtu.edu.cn):

## Abstract

In this paper, we propose a Valentine antenna working in frequency band 150 MHz to 350 MHz. The proposed antenna is designed for UWB applications, which is a part of a Ground-Penetrating-Radar (GPR) system. The antenna, which is composed of metallic strips, radiates pulses in the frequency band 150 MHz – 350 MHz with low dispersion, a high gain and a low cross-polarization in the axial direction. This paper describes the structure of the Valentine antenna and its radiation characteristics that we simulated.

**Keywords:** Valentine antenna, ultra-wideband (UWB), Ground Penetrating Radar (GPR)

## 1 Introduction

Ultra-Wideband (UWB) pulse owns extremely wide band in frequency domain and very narrow pulse width in time domain, these feature endows UWB pulse with very high resolving ability and very high instant power[1]. UWB antenna is used widely in fields like communication, target identification, and radar system. However, due to its extremely wide spectrum, UWB pulse can not be radiated effectively by conventional time-harmonic antennas. The design of UWB antenna (time domain antenna) that can radiate UWB pulse effectively is an important technique in UWB technology[2].

Valentine antenna has been used in UWB applications since 2007[3]. The Valentine antenna we propose has many advantages in the use of the GPR system: it is light and compact in H-plane, and also radiates with low dispersion, a high gain and a low cross-polarization in the axial direction.

## 2 Valentine Antenna

The Valentine antenna is composed of a TEM horn with constant width, which makes the antenna light and compact in H-plane, and a return back in the end of the horn, shown in Figure. 1. The Valentine antenna is a pair of brass strip which has the same width. After a 50Ω input, the strips flare according to an exponential profile to provide the TEM horn. The horn is the main part of the antenna, for the exponential profile guarantees wideband characteristic in the frequency domain[4]. The expression of the strip is

$$0.01 \times e^{(3 \times t)} \quad (1)$$

Then the strips flare according to circular form to make up the return back part. This part is designed to decrease the current reflections from the end of the horn and also increase gain of low frequency.

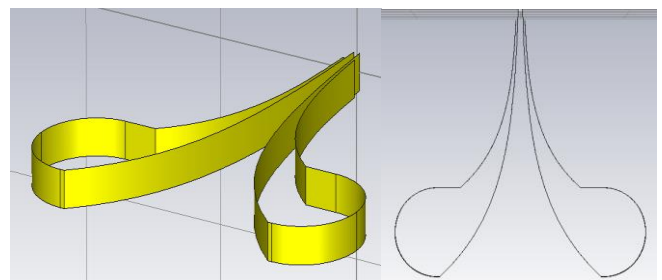


Figure 1. Structure of Valentine antenna.

The dimension of the antenna is 120\*10\*113.6 cm.

## 3 Simulation Results

In this paper, we simulate and optimize the Valentine antenna by CST Microwave Studio. The results show that the proposed antenna has good performance.

The simulated reflection coefficient ( $S_{11}$ ) is shown in Figure 2. In the wide band 150 MHz to 350 MHz,  $S_{11}$  is mainly below -10dB. Figure 3 shows the gain of proposed antenna. The gain is above 2.7 dB in low frequency and increases with the frequency growing. In the frequency 350 MHz, the gain reaches 7 dB.

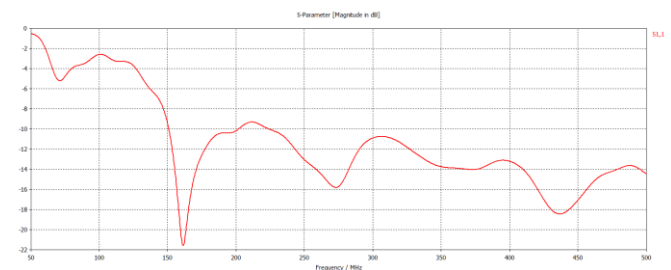
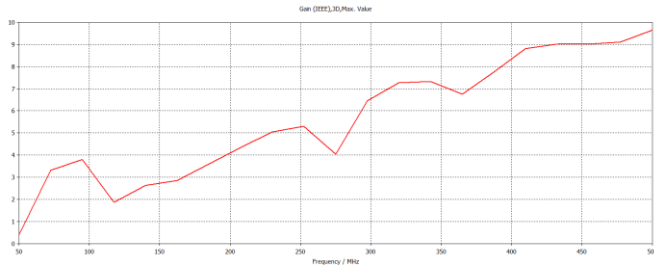


Figure 2. Reflection coefficient of the proposed antenna



**Figure 3. Gain of the proposed antenna**

## 4 Conclusion

We propose a Valentine antenna, which is designed as an UWB antenna, working in the frequency band 150 MHz to 350 MHz. Simulation results show that the proposed antenna has some advantages and is very fit for UWB applications such as GPR.

## Acknowledgements

The authors are grateful to the supports from the National Natural Science Foundation of China under Grant Nos. 61331005 and 61001039.

## References

- [1] H. M. Jol, *Ground penetrating radar theory and applications*: Elsevier, 2008.
- [2] A. Shlivinski, E. Heyman, and R. Kastner, "Antenna characterization in the time domain," *Antennas and Propagation, IEEE Transactions on*, vol. 45, pp. 1140-1149, 1997.
- [3] J.-C. Diot, P. Delmote, J. Andrieu, M. Lalande, V. Bertrand, B. Jecko, *et al.*, "A novel antenna for transient applications in the frequency band 300 MHz–3 GHz: the Valentine antenna," *Antennas and Propagation, IEEE Transactions on*, vol. 55, pp. 987-990, 2007.
- [4] K. Chung, S. Pyun, and J. Choi, "Design of an ultrawide-band TEM horn antenna with a microstrip-type balun," *Antennas and Propagation, IEEE Transactions on*, vol. 53, pp. 3410-3413, 2005.

# A new design of TEM UWB antenna for ISAR imaging

Shitao Zhu\*, Anxue Zhang\*, Zhuo Xu\*, Xiaoli Dong<sup>†</sup>

\* School of Electronic and Information Engineering, Xi'an Jiaotong University, Xi'an, China, 710049, <sup>†</sup> School of Telecommunication and Information Engineering, Xi'an University of Posts & Telecommunications, Xi'an, China, 710121

## Abstract

A pair of transverse electromagnetic (TEM) horn UWB antenna is designed and realized using tapered conductor for developing the ISAR imaging system. The newly developed TEM horn UWB antennas, which are filled with dielectric and have a specific structure design at the end of the horn, possesses much better properties, such as high gain, low input reflection, and signal-ringing levels over the wide operational bands. To analysis the TEM horn UWB antennas performance, firstly, Finite Integration Technology (FIT) is used to calculate S-parameters on feeding port, radiation impulse wave and transmitter/receiver (T/R) antenna coupling. Then, experimental setup, which is consists of a network analyzer and a T/R antenna shielded box, is designed to measure antennas S-parameters and radiation wave. Simulation and experimental results show that low ring radiation impulse and high feeding efficiency are attainable, which indicates that this horn antenna is fit for ISAR imaging system.

**Keywords:** UWB antenna, ISAR imaging system.

## 1 Introduction

The Inverse Synthetic Aperture Radar (ISAR) is widely used in rescue and target recognition, such as Through-Wall detection, Ground Penetrating, Medical imaging, breathing people detection [1-4]. High resolution is a prominent feature for ISAR imaging system for short range targets when the ultra-wideband (UWB) signal is used directly. The UWB antenna is a key device that make the ISAR system more effective.

The central frequency and bandwidth of UWB signals are the key factors for the ISAR imaging system performance. Higher frequencies are needed for better precision and the lower bands decide the target shape. Thus, the ISAR imaging system that transmits short time impulse signals is usually used so as to benefit from both low and high frequencies. So, the antennas must have flat and high directivity gain, narrow beam, and low side-lobe and input-reflection levels over the operational frequency band for the largest dynamic range, best focused illumination area, lowest T/R antenna coupling, reduced ringing, and uniformly shaped impulse radiation [5, 6]. The reduction of direct coupling between the transmitting and receiving antennas is an important issue, as it results in the better detection of imaging targets [7].

In this paper, the special design of TEM UWB antenna which let the antenna have better characteristic in time domain is investigated. The coupling between transmitter and receiver (T/R) antennas is effectually reduced by wave-absorbing and the antenna system is fit for the ISAR imaging system.

## 2 Antenna design and manufacture

### 2.1 Theory

The TEM horn UWB antenna is an end-fire, traveling-wave structure that consists of two conducting plates. To match from  $50 \Omega$  at the feed point to  $377 \Omega$  at the aperture, its aperture angle and plate width must be properly chosen [5]. In order to reduce the length of antenna, make the better matching we design special modeling on the aperture. Generally we can get the input impedance ( $Z_{in}$ ) using equation (1).

$$Z_{in}^i = Z_0 \frac{Z_{in}^{i+1} + jZ_0^i \tan \beta_i l_i}{Z_0^i + jZ_{in}^{i+1} \tan \beta_i l_i} \quad i = 0, 1, 2, \dots, N, \quad (1)$$

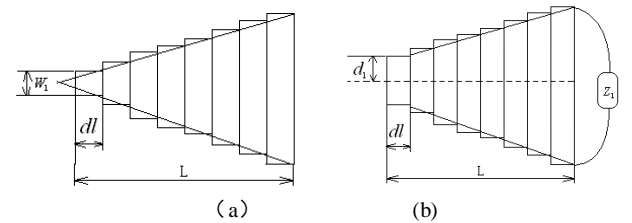


Fig. 1 Staircase modelling of the TEM antenna (a) top face (b) side face

And so,

$$Z_0^i = \begin{cases} 138 \sqrt{\frac{\mu_r^i}{\epsilon_r^i}} \log \frac{8}{(w_i / d_i)}, & (w_i / d_i) \leq 1 \\ Z_{in}^{i+1} [(w_i / d_i) + 2]^{-1}, & (w_i / d_i) \geq 1 \end{cases} \quad i = 0, 1, 2, \dots, N \quad (2)$$

Where

$$Z_{in}^{N+1} = Z_l // Z_0 = \frac{Z_l \cdot Z_0}{Z_l + Z_0}, \quad \beta_i = (2\pi f) / (c) \sqrt{\mu_r^i \epsilon_r^i},$$

$Z_0^i$  is the characteristic impedance of  $i$  number cells,  $Z_l$  is the equivalent impedance of the loaded parts and  $L$  is the length of the antenna,  $N$  is the segment number, as shown in Fig.1 and  $Z_0 = 377 \Omega$ .

$Z_l$  is simulated using Finite Integration Technology (FIT) and the numerical value displays in Fig. 2.

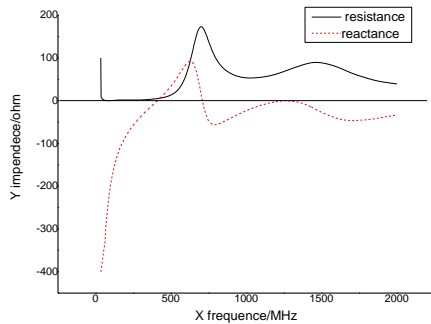


Figure 2 Numerical value of  $Z_l$

Solid line= real component. Dotted line = imaginary component

### 2.2 Antenna design

The antenna is manufactured using the parameter from computation and simulation as shown in figure 3. The motherboard material is polyethylene  $\epsilon_r = 2.25$  and the conducting plates material is copper ( $\sigma = 5.81 \times 10^7$  [S/m]). The antenna length is 210 mm with the center frequency about 1000 MHz and the antenna is fed with the SMA connector. The parallel plate part of the feeding point has the dimension of  $17 \times 6$  mm with 10-mm length as shown in Fig.3.



Figure 3 the antenna

The  $S_{11}$  of the antenna are measured by the AV3618A integrative net analyzer. Fig.4(a) shows the measured reflection coefficient characteristic of the TEM horn UWB antenna in the frequency band of 400MHz to 2000MHz for the  $S_{11}$  less then -10dB.

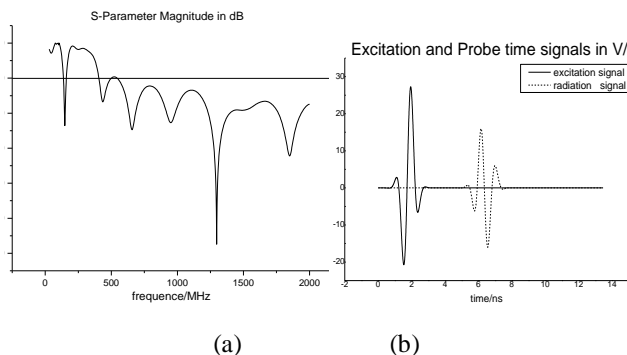


Fig. 4 measured parameter of the antenna, (a)  $S_{11}$ ,(b) Wave shape of the antenna in free space,Solid line=excitation signal. Dotted line = radiation signal

Fig. 4(b) illuminates that the TEM horn antenna has low signal-ringing characteristic and uniformly shaped impulse radiation in time domain and high feeding efficiency in the feeding port.

### 2.3 R/T array design

The simulation modeling, which composed of transmitter and receiver (T&R) antennas in shielded box, is shown in Fig.5(a) and Fig.5(b) interprets low mutual coupling characteristic of the T&R antennas system.

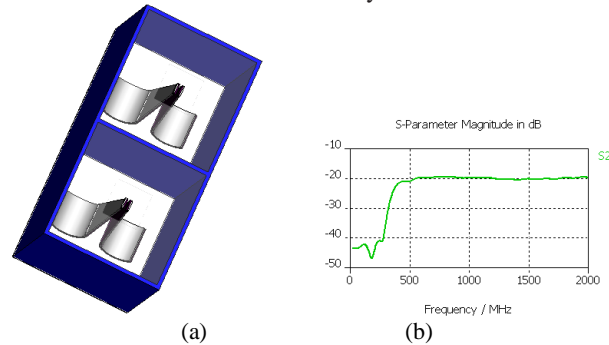


Fig. 5 the Simulation of the (T&R) antennas, (a) Simulation model, (b) the  $S_{21}$

## 3 Experiments

The experiment setting is shown in Fig.6. the transmitting antenna and the receiving antenna is deployed as shown in Fig.5.

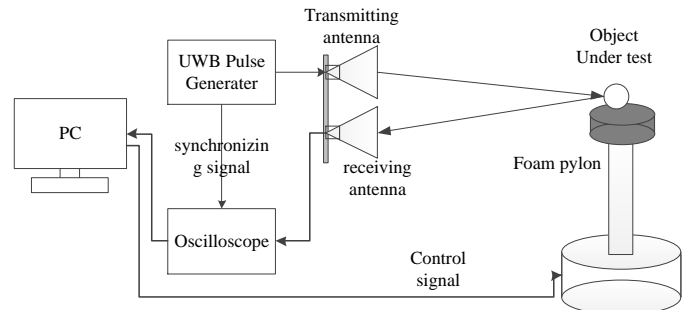


Fig.6 The basic architecture of UWB measurement system

A triple of identical metal rods separated by 20cm and 5cm, respectively, are tested in the UWB ISAR imaging system. The reconstructed images using the method in [8] and the antenna proposed in this paper are shown in Fig.7. The super-resolution image are well reconstructed.

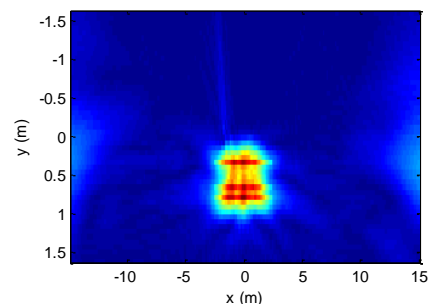


Fig.7 the reconstructed image

### 3 Conclusion

Special design for the TEM horn antenna and coupling simulation are presented in this paper. The VSWR and wave shape measurements have proved that the proposed design technique is successful. This addition tapered structure improves the impedance characteristics of the antenna, enlarges the bandwidth and reduces ring radiation impulse. The coupling characteristic of T&R antennas and the performance of the TRM antenna in time domain tell us the antenna system is fit for the GPR detection system.

### Acknowledgements

The authors are grateful to the supports from the National Natural Science Foundation of China under Grant Nos. 61331005 and 61001039.

### References

- [1] Rovnakova J and Kocur D., "UWB radar signal processing for through wall tracking of multiple moving targets," European Radar conference, Paris, France, Sept. 30-Oct. 1, 2010, pp. 372-375.
- [2] Immoreev I.m "Practical application of ultra-wideband radars," The Third International Conference on Ultra-wideband and Ultra-short Impulse Signals, Sevastopol, Ukraine, Sept. 18-22, 2006, pp. 44-49.
- [3] Sakkila L, Rivenq A, and Tatkeu C, "Methods of target recognition for UWB radar," IEEE Intelligent Vehicles Symposium, San Diego, CA, June 21-24, 2010, pp. 949-954.
- [4] Egor Z., "UWB radar for detection and localization of trapped people," International Radar Symposium, Vilnius, Lithuania, June 16-18, 2010, pp. 1-4.
- [5] D.J. Daniels, Surface penetrating radar, IEE, London, 1996.
- [6] A.S. Turk, Ultra-wideband TEM horn design for ground-penetrating impulse radar systems, *Microwave Opt Technol Lett* 41 (2004), 333-336.
- [7] Dong I. Yang, Hyo J. Eom, and Jung W. Ra, *Microwave and Optical Technology Letters*, *Microwave Opt Technol Lett* 36 (2003): 285-289.
- [8] Shitao Zhu, Anxue Zhang, Zhuo Xu, Xiaoli Dong, UWB ISAR high resolution imaging using near field for rotating target, *Antennas and Propagation (APCAP), 2014 3rd Asia-Pacific Conference on*, 2014.7.26-2016.7.29.

# Active Detection of Fissile Materials via Laser-Induced Ionization-Seeded Plasmas

Geehyun Kim\*, Mark Hammig †

\*Department of Nuclear Engineering, Sejong University, South Korea, email: [gkim01@sejong.ac.kr](mailto:gkim01@sejong.ac.kr)

†Department of Nuclear Engineering and Radiological Sciences, University of Michigan – Ann Arbor, USA, email: [hammig@umich.edu](mailto:hammig@umich.edu)

## Abstract

This work is to develop a method to detect special nuclear materials at long stand-off distances, that do not depend on directly sensing the gamma-ray and neutron radiation emitted by the source. The excitation of electrons and the secondary ionization in the air that surrounds the radioactive materials were studied as an indirect measure of their presence. The fast electrons and ions facilitate the formation of the weak plasma, the density of which increases when radiation-induced tracks are present, compared to their formation in the pristine or polluted air. We established the conditions under which it is feasible to detect SNM at long range, and we conducted experiments to probe the ionization environment. Various probe-and-detect modalities, in which high electric fields are delivered at long range to enhance the ionization signal, were investigated, and the method using fast laser pulses to induce intensely bright plasma sparks detectable at long range were attempted. The presence and properties of the signal showed evidences of ionization in the air, which implies the existence of ionizing sources in vicinity.

**Keywords:** Laser-induced plasma, ionization-seeded, special nuclear materials (SNM), nuclear safeguards, long-range detection

## 1 Introduction

The challenge of highly specific long-range detection of special nuclear materials (SNM) requires the development of alternative technologies to those typically deployed in the nuclear radiation detection field. The standard method of sensing nuclear materials is to detect the ionizing nuclear emissions from the source. However, the direct detection of gamma rays and neutrons is infeasible not only for the geometric attenuation at long range, but also for the scatter attenuation, which markedly reduces the transmitted flux. Instead, one can probe the effect of those emissions in order to assay a larger volumetric region of space, as will be reported in following sections. In this study, we attempted to detect the sources of ionizing radiation via the air ionization created in the surrounding air. Experiments were conducted to study the viability of deriving the signature from the ionized space about the SNM.

## 2 Methods and Experiments

The ionization of the air around a radioactive source increases as has been previously studied [1]. One can further enhance the signal-to-noise ratio of the SNM detection by creating an electron avalanche, or cascade, which is enabled by applying a large electric field in order to activate a few electrons which are then accelerated by the electric field.

With the extra energy imparted to a few free electrons they will soon impact upon other atoms and molecules to knock off more electrons. These secondary events are sufficient even if there is only a small number of free electrons since these can liberate new electrons after being accelerated by the field. In this way, the electron multiplication proceeds in a geometrical progression, and the radiation-induced plasma is constantly replenished by the radiation from the SNM [2], [3]. In order to cause the avalanche, we employed an ultrafast pulsed laser interrogation system to induce the formation of enhanced air ionization when there are free electrons present – such as those that accompany the air surrounding SNM, but to not induce photon-induced ionization, thereby creating a probe that is selective to ionization sources. The theoretical calculations showed that the onset of collisional cascading (i.e. forming an avalanche from an existing electron density) requires an order of magnitude or more less power density than does photoionization. The breakdown behavior at the vicinity of known radiation source was studied and compared with results obtained without the source.

A schematic of the experimental setup using the pulsed laser was shown in Fig. 1. The beam was focused with either a 10 or 30 cm focal length to increase the probability of intersection between radiation-induced tracks and the high-field region. As shown from the source-beam arrangement schematic in Fig. 1, disk sources of alphas ( $^{241}\text{Am}$ ,  $^{210}\text{Po}$ ), betas ( $^{90}\text{Sr}$ ,  $^{36}\text{Cl}$ ), and gamma-rays ( $^{133}\text{Ba}$ ,  $^{60}\text{Co}$ ,  $^{137}\text{Cs}$ ) were placed (nominally) less than 1 cm away from the laser focal spot. We also employed both photodiode-based measures and spectral measurements of the optical output in order to more sensitively detect the presence of the plasma. Visually brighter plasma sparks were observed (or as buzzing) when radiation is present and the secondary ionization intersects the confocal length. In addition, the spectra obtained from the plasma discharge spark showed differences depending on the source existence.

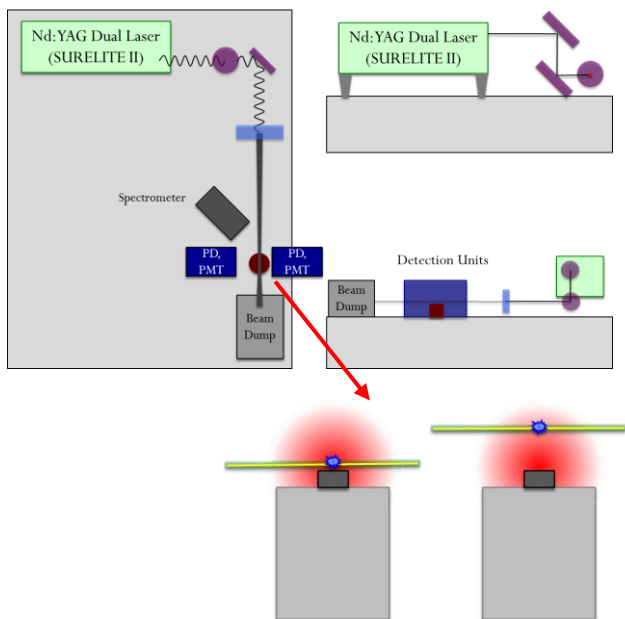


Fig. 1. A Schematic of laser-induced stimulation of ionization-seeded plasma at the vicinity of the radioactive material.

When an alpha or beta source was arranged such that its track intersected (at random time intervals) the confocal length, the spark would get more frequent and much brighter, and it would extend in length, producing stretched shape of spark streaks. If the source was shifted slightly off-axis, then the count rate of sparks, which can be readily detected with standard optical sensors. This confirms that the plasma electrons (due to radiation) present when an alpha source is brought near the beam, collisionally cascading to produce the filaments.

### 3 Conclusion

The goal of the experiment was to a) confirm that the electron density from a radiation source can impact the formation of optical filaments (concentrated air-plasmas), and b) confirm that this selectivity can be achieved so that operationally, one would gimbal the laser beam through the environment and map the regions in which optical filaments are formed, either through radar or optical methods. In this work, we analyzed and validated optical enhancement, the results showing that it is feasible to enhance the signal from the air region about SNM sources, by impinging the ionization cloud by fast laser pulses. As both theoretically and experimentally determined, the focal region of a 10-100 ns pulsed laser can be used as a radiation detector which produces a bright plasma spark when it is intersected by the impinging radiation-induced charge track. We confirmed the ambient electron density can impact the plasma formation, and the signature is strong enough that the both strong and weak emitters can be detected, in spite of the noise competition provided by the solar based airglow.

### Acknowledgements

This work was supported by DTRA Basic Research Program (Grant #: HDTRA1-12-1-0038) and the Nuclear Safety Research Program (Grant No. 20140884) through the Korea Radiation Safety Foundation (KORSAFe) and the Nuclear Safety and Security Commission (NSSC).

### References

- [1] A. J. Peurrung, "On the long-range detection of radioactivity using electromagnetic radiation", *Nucl. Inst. and Meth. A* **481** pp. 731 (2002).
- [2] P. Woskoboinikow *et al.*, "Submillimeter-Laser-Induced air breakdown," *Appl. Phys. Lett.* **32** (1978).
- [3] G. Kim, S. Ramadoss, R. Stevenson, and M. D. Hammig, "SNM Detection via Electron Excitation in the Air that Surrounds the Source," *Proceedings of the INMM Annual Meeting #282* (2013).

# The effect of ANFO on the Complex Resonance Frequencies of an IED

*S A Gutierrez\**, *E Neira<sup>§</sup>*, *J J Pantoja<sup>£</sup>*, *F Vega<sup>†</sup>*

*\*<sup>§</sup> Doctoral student at Universidad Nacional de Colombia, Bogotá \*sagutierrezd@unal.edu.co, <sup>§</sup> eneirac@unal.edu.co, \*<sup>£</sup> <sup>†</sup> Researcher at EMC-UN, Universidad Nacional de Colombia Bogotá jjpantojaa@unal.edu.co, <sup>†</sup> Professor at Universidad Nacional de Colombia, Bogotá jfvegas@unal.edu.co*

## Abstract

**This paper is focused on describing how the resonance poles of an IED are modified by the dielectric constant of the explosive material used as main charge. Additionally, the extraction of complex resonance poles is used to evaluate the electromagnetic response of an electro explosive device (EED) inside of an explosive charge such as ammonium nitrate and fuel-oil (ANFO).**

**Keywords:** Improvised explosive device, Backscattering, Resonance poles, ANFO, Electro explosive device.

## 1 Introduction

Antipersonnel landmines problem in Colombia is the result of armed internal conflict. The integral action program against the antipersonnel landmines PAICMA (by the Spanish: Programa de Acción Integral Contra las Minas Antipersonal) reported nearly of 11043 victims since 1990 until February of 2015. However not all victims report the landmines accidents. Therefore, actual victim's numbers are difficult to be established. Additionally, PAICMA show that 31 of 32 Colombian departments have had events associated to improvised explosive devices (IEDs) or unexploded ordnance (UXO) in the same time period [1].

Colombia's illegal groups built and bury different models of IEDs. Usually these explosive devices act as a personal landmine. Their design was made to hurt, delay military action and take control of territories considered strategic zones. Nevertheless, civilians have been affected with injuries, deaths and forced displacement [1].

A typical IED is composed of a main explosive, an electric detonator, a switch (victim activated or remotely controlled) a casing (that can be a plastic pipe, a wooden case, a glass bottle or a plastic can). Additionally, these devices can have significant amounts of dielectric material, such as plastic beads, stones, bamboo, glass and other nonmetallic parts used as shrapnel.

The randomness of the IED's made demining process a difficult task. Additionally, Colombian soils have high ferrous content. Therefore, detection systems based on metal detector have high rates of false alarm and the demining effectiveness

and its performance can vary with the deminer's expertise. In that way, metal detectors are not a useful tool to recognize if a buried object is hazardous or safely [2].

Related with landmine's activation mechanism, reports of demining activities, news and military information show that IED activation mechanism used by illegal groups in Colombia can vary between electronic, chemical and non-electric activation mechanism. Researchers have found that electro explosive device (EED) is a common element in the IED activation mechanism and the IED's main charge usually is ammonium nitrate and fuel-oil ANFO [1,2].

EED activation is based on the current flow through a bridge-wire that increases its temperature until a critical value to triggering the explosive inside the EED and the main IED's explosive charge. The feeding current is produced when anyone, usually the victim, closes the circuit that is connected to a battery placed near to the IED [3].

In Colombia there are a huge variability on IED's shapes, materials and triggering methods. However, most of IEDs have two common factors: ANFO used as the main explosive charge and EED used as trigger of the IED. Therefore, backscattering signals analyses using the above cited characteristics are a useful way to understand the electromagnetic behavior of these explosive devices.

Since IEDs have a complex structure and they have many composition materials, it is required full-wave simulations in order to model and understand the Colombian IED's backscattering. In this paper, an analysis of the electromagnetic plane wave's propagation in media with different permittivities is carried out with CST Microwave Studio and the resonance frequencies are calculated for the IED's elements.

## 2 IED model

The IED model used in here is based on a small common explosive artifact, M type, as shown in Fig 1. The M type name is due to the IED's switch surface shape.

Usually IEDs battery is interchangeable and it is placed close to the explosive device. So, EED's wires are connected to the mechanical switch and to the battery in an open circuit. This circuit is closed when the victim activate the M type switch.

Information provided by MARTE army Colombian demining group.

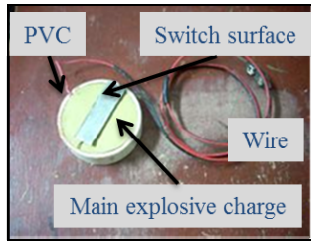


Figure 1. M type IED. Source MARTE army group.

This IED was modeled using its common elements such as: 1) PVC casing with 5cm/3cm in diameter/height respectively; 2) ANFO as main charge; 3) EED as activation mechanism, with 0.3cm/4cm in its diameter/length; 4) two wires AWG22 connected to the IED and coming out of it, its lengths are 4cm and 8cm, Fig 2. About the EED, Its typical components are listed in Table 1 and Fig3. It was modeled based on [4,5].

2.1 Simulation parameters

To obtain the backscattering response of the IED and their parts in a wide frequency range, a time domain simulation was performed in CST Microwave Studio. The simulation was configured to have an incident plane wave over the IED. Absorbing Boundary Conditions (open boundary) were used as boundaries. The excitation signal used was Gaussian pulse with amplitude of 1 V/m and frequency range between 0.5 to 5 Ghz. In order to register the backscattering, a field sensor probe was placed 12 cm from the device under test.

The simulation time was limited to 10 ns in order to reduce the computation time and have all resonances of the IED's parts. Also, this simulation time was useful to avoid reflections when the IED was buried in a homogeneous material.

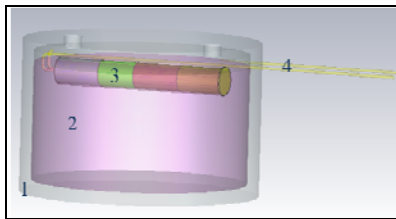


Figure 2. IED model.

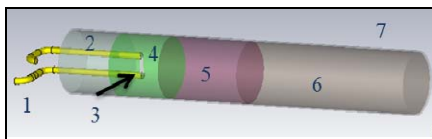


Figure 3. EED model.

Table 1: Parts of an electrical detonator.

Part	Name
1	Copper wires feeders
2	Isolator $\epsilon_r = 2.1$
3	Hot-wire
4	Primary explosive $\epsilon_r = 3$ ,
5	Explosive $\epsilon_r = 2.9$
6	Explosive $\epsilon_r = 3.3$
7	Aluminum casing

2.2 Backscattering of the IED

Each part of the IED was simulated alone in free space and the backscattering responses are shown in Figs 4-6. Next, the main explosive charge and IED parts were assembled in order to have the hold response in time and frequency domain. Fig 7-8

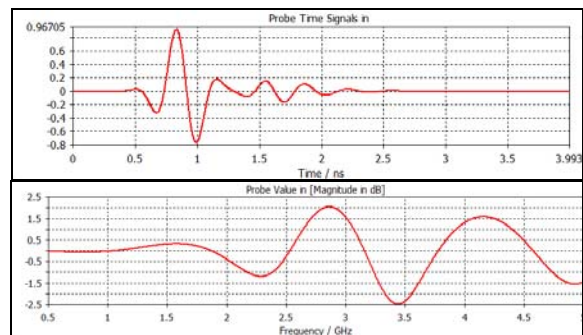


Figure 4. EED Backscattered electric field and frequency response.

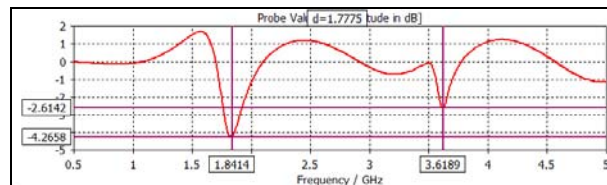


Figure 5. Wires Backscattered electric field.

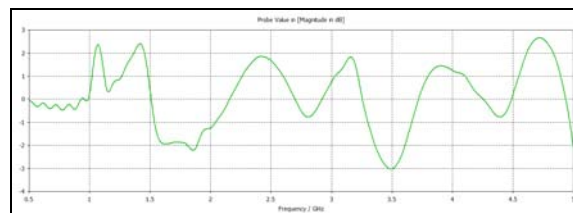


Figure 6. IED response in free space.

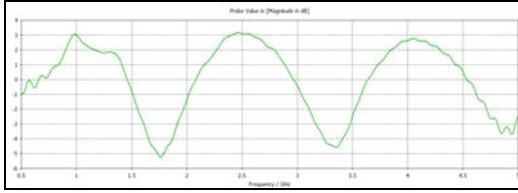


Figure 7. IED surrounded with sand soil.

### 2.3 Resonance frequency

The complex resonance poles were extracted of the backscattering signals applying the algorithm proposed in [6,7]. Due to the resonances poles that appear in the resonance region or late time, the backscattering signal should be truncated in early time response and late time response [6].

Additionally, the resonance frequency could be verified using

$$L \approx \frac{c}{2F_d} \quad (1)$$

Where  $c$  is the light speed and  $F_d$  is the frequency of resonance and  $L$  is the length of the resonance object. Thus, the length  $L$  calculated for EED was 5.06 cm and the two wires have 8.69 cm and 3.56 cm. Its values are too close to the length calculated using the information of Fig 4 and Fig 5. Resonance frequency of an IED without ANFO placed in free space and an IED buried in sandy soil was calculated too, Fig 8. There are similarities between the resonance poles simulated and calculated for each IED; however, these poles appear attenuated due to the explosive dielectric material and their resonance frequency change slightly.

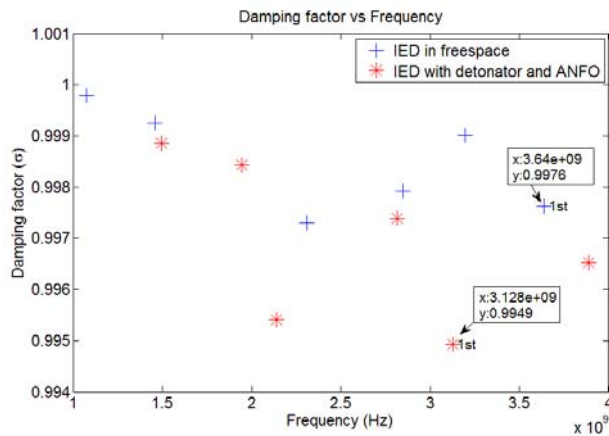


Figure 8. Resonance poles with IED in free space without explosive (plus). IED resonance poles with the EED inside ANFO and bottom of the PVC casing (asterisk).

### 3 Conclusions

The complex resonance poles could be a useful feature to identify the EED inside the IEDs or buried in the soil.

Using full-wave simulations, it was verified that the electrical length of the EED is modified when it is buried on a material such as ANFO. However more work needs to be done and a broader range of scenarios should be simulated in order to draw clearer conclusions of the extracted EED resonance poles and knowing if other resonant parts of the IED hide the EED response.

### References

- [1] PAICMA. (2015, February) Víctimas de minas antipersonal. [Online]. Available: <http://www.accioncontraminas.gov.co/estadisticas/Paginas/-victimas-minas-antipersonal.aspx>
- [2] J. M. H. Hendrickx, A. Molina, D. Diaz, M. Grasmueck, H. A. Moreno, and R. D. Hernández, "Humanitarian ied clearance in colombia," *Proc. SPIE*, vol. 6953, pp. 69530C–69530C–9, 2008. [Online]. Available: <http://dx.doi.org/10.1117/12.782303>
- [3] J. Pantoja, N. Pena, F. Rachidi, F. Vega, and F. Roman, "Characterization, modeling, and statistical analysis of the electromagnetic response of inert improvised explosive devices," *Electromagnetic Compatibility, IEEE Transactions on*, vol. 56, no. 2, pp. 393–403, April 2014.
- [4] J. J. Pantoja, N. Pena, F. Rachidi, F. Vega, and F. Roman, "Susceptibility of electro-explosive devices to microwave interference," *Defence Science Journal*, vol. 63, no. 4, pp. 386–392, 2013.
- [5] M. R. Lambrecht, K. L. Cartwright, C. E. Baum, and E. Schamiloglu, "Electromagnetic modeling of hot-wire detonators," *Microwave Theory and Techniques, IEEE Transactions on*, vol. 57, no. 7, pp. 1707–1713, 2009.
- [6] J. Chauveau, N. De Beauhoudrey, and J. Saillard, "Selection of contributing natural poles for the characterization of perfectly conducting targets in resonance region," *Antennas and Propagation, IEEE Transactions on*, vol. 55, no. 9, pp. 2610–2617, Sept 2007.
- [7] W. Lee, T. K. Sarkar, H. Moon, and M. Salazar-Palma, "Computation of the natural poles of an object in the frequency domain using the cauchy method," *Antennas and Wireless Propagation Letters, IEEE*, vol. 11, pp. 1137–1140, 2012.

# Study on Statistical Characteristic of Transient Disturbances and Correlation with Immunity Waveform

Zhang Weidong\*, Zhang Xiaoli †, Luo Guangxiao\*

\*Beijing Key Lab of High Voltage and Electromagnetic Compatibility, North China Electric Power University, Beijing 102206, China. zwd@ncepu.edu.cn; †China Electric Power Research Institute, Beijing 100192, China, zhangxl@epri.sgcc.com.cn

## Abstract

In order to get the statistical characteristic of transient disturbances while the measured data number is small, two small sample statistical methods are introduced and applied in this paper. The correlation theory was used to express the consistency about the immunity test waveform and measured waveform quantitatively.

**Keywords:** transient disturbances, statistical characteristic, correlation theory, immunity test

## 1 Introduction

Recently, more and more electronics equipments were used in electric power system for relay protection, control systems and communications. These systems may be interfered by many transient disturbances such as lightning, switch operation, short-circuit faults and other EMP [1]. Because the randomness of the transient phenomenon and the number of the measured data is limited, we use small sample statistic method to get the statistical characteristic of the transient disturbances [2]. At present, there is no explicit standard for immunity test of the electronics equipment. In order to estimate the relevancy between actual disturbance characteristics and existed standard, the correlation theory was used to express the consistency about the immunity test waveform and measured waveform quantitatively. The analysis results can be used to modify and add existed standards or develop more suitable standards [3].

## 2 Two small sample statistic methods

The Bayes bootstrap method and stochastic weighted method were more widely applied in dealing with small sample statistical issues. Its basic idea is using the statistic characteristics of experimental data instead of the fact [4].

### 2.1 Basic principle

We suppose that:  $(X_1, X_2, \dots, X_n)$  is the sample,  $X_i \sim F(x)$ . The  $\theta = \theta(F)$  is the unknown number of population distribution.  $F_n$  is the sampling distribution function of  $(X_1, X_2, \dots, X_n)$ ,  $\hat{\theta} = \hat{\theta}(F_n)$ ,  $\hat{\theta}$  is the estimator of  $\theta$ ,

$T_n = \hat{\theta}(F_n) - \theta(F)$ . Sampling from  $(X_1, X_2, \dots, X_n)$ , we can get regeneration sample  $X^* = (X_1^*, X_2^*, \dots, X_n^*)$ .  $F_n^*$  is the sampling distribution function of regeneration sample,  $\hat{\theta}(F_n^*)$  is also the estimator of  $\theta$ ,  $R_n^* = \hat{\theta}(F_n^*) - \hat{\theta}(F_n)$ . Using the distribution of  $R_n^*$  to approximate  $T_n$  is the central idea of bootstrap and stochastic weighted method.

We can make the regeneration samples repeatedly and get

$$X^{*(j)} \triangleq (X_1^{*(j)}, X_2^{*(j)}, \dots, X_n^{*(j)}), (j=1, \dots, N) \quad (1)$$

$$R_n^{*(j)} = \hat{\theta}(F_n^{*(j)}) - \hat{\theta}(F_n), (j=1, \dots, N) \quad (2)$$

Finally we can get

$$\hat{\theta}^{(j)}(F) = \hat{\theta}(F_n) - T_n \approx \hat{\theta}(F_n) - R_n^{*(j)} = 2\hat{\theta}(F_n) - \hat{\theta}(F_n^{*(j)}) \quad (3)$$

Gain  $N$  possible values of  $\theta(F)$  by (3), make them as the samples, which we can use to get the sampling distribution  $F^*(\theta)$  of  $\theta(F)$ . Thus we can make statistical inference about  $\theta$ .

### 2.2 Basic characteristics calculation

The characteristics of the transient disturbances are mainly included: rise time, duration, peak to peak value, energy, rising rate, DC component, the mean square value of AC, bandwidth and dominant frequency.

Take the substation transient measurement as an example. We can get its basic characteristics in Table 1.

### 2.3 Statistical characteristics calculation

Statistic analysis has important meaning in evaluating general level of transient electromagnetic disturbance in substation. Apply the stochastic weighted method on basic characteristics to getting statistical characteristics in Table 2.

## 3 Waveform consistency

We supposed that test waveform is  $x_1(t)$ , the measured waveform is  $x_2(t)$ , the expression of correlation coefficient is [5]

$$\rho_{12} = \frac{\langle x_1(t), x_2(t) \rangle}{\|x_1(t)\|_2 \|x_2(t)\|_2} = \frac{\int_{-\infty}^{\infty} x_1(t)x_2(t)dt}{\left[ \int_{-\infty}^{\infty} x_1^2(t)dt \int_{-\infty}^{\infty} x_2^2(t)dt \right]^{1/2}} \quad (4)$$

Table 1: Basic characteristics

No.	Rise time ( $\mu s$ )	Duration ( $\mu s$ )	Peak to peak value (V)	Energy ( $V^2 \cdot \mu s$ )	Rising rate ( $kV / \mu s$ )	DC component (V)	Mean square value of AC (V)
0	0.0178	15.46	19.2	174.96	4.494	0.018	3.499
1	0.0246	15.46	21.8	200	3.902	0.021	4.000
2	0.0272	24.02	43.2	315.83	6.765	0.051	6.317
...	...	...	...	...	...	...	...
66	0.069	39.7	53.6	702.49	3.107	0.184	14.050
69	0.0383	45.04	32.8	165.15	3.676	-0.029	3.303
70	0.0301	49.34	27.2	139.99	4.040	0.501	2.800

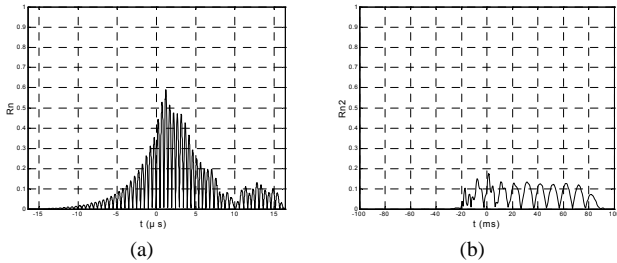
Table 2: Statistical characteristics

	$\mu$		$\sigma$	
Rise time ( $\mu s$ )	0.0236	0.0169, 0.0257	0.0165	0.0134, 0.0218
Duration ( $\mu s$ )	21.281	17.64, 24.692	18.451	16.3797, 19.2984
Peak to peak value (V)	18.38	14.4556, 22.3050	16.581	14.2315, 19.8676
Energy ( $V^2 \mu s$ )	166.74	165.79, 166.85	297.73	282.54, 306.92
Rising rate ( $kV / \mu s$ )	6.566	6.518, 6.584	14.43	14.369, 14.541
DC component (V)	0.0225	0.2223, 0.2228	0.1115	0.1110, 0.1118
Mean square value of AC (V)	3.436	3.422, 3.45	5.990	5.966, 6.034

In Equation (4),  $\langle \bullet \rangle$  is for inner product,  $\|\bullet\|$  is for norm. If the waveforms are same or converse, the value of  $\rho_{12}$  is +1 or -1, else its value is between +1 and -1.

In order to keep the objectivity of  $\rho_{12}$ , it is necessary to calculate the correlation function with time-variation

$$R_{12}(t) = \int_{-\infty}^{\infty} x_1(\tau)x_2(\tau-t)d\tau \quad (5)$$



(a) Measured transient magnetic field with IEC61000-4-10 test waveform  
(b) Measured transient voltage with IEC61000-4-11 test waveform  
Fig.1. Normalized correlation function

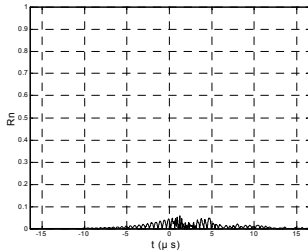


Fig.2. Normalized correlation function of measured transient voltage with IEC61000-4-12 test waveform

In the Fig.1 (a), the maximum of  $\rho_{12}$  is 0.59. In the Fig.1 (b), the maximum of  $\rho_{12}$  is 0.17. In the Fig.2, the maximum of  $\rho_{12}$  is 0.06. It is seen that the consistency of the immunity test waveform and measured waveform is highest for magnetic field and lowest for the transient voltage.

## 4 Conclusion

The Bayes bootstrap was used to analyze the statistical characteristics of transient electromagnetic disturbance due to switching operation in substations. The characteristics parameters were obtained based on the small sample statistical methods from 70 samples. The consistency of the immunity test waveform and measured waveform was analyzed using correlation analysis method. The result shows that the correlation factor of transient magnetic field is higher than transient voltage.

## Acknowledgement

This paper is supported by State Grid Corporation project No. DZ71-12-19.

## References

- [1] Wu Wen, Jun Jia, "Overview of electromagnetic compatibility in electric power system," *Journal of Changsha University of Electric Power*, vol. 18, pp. 42-46, 2003.
- [2] Haijun Deng, Yabing Zha, "A research on the application of bootstrap method and its application in the accuracy assessment," *Journal of Spacecraft TT&C Technology*, vol. 24, no.1, pp. 59-63, 2005.
- [3] Yufeng Wang, Jiyan Zou, Minfu Liao, "EMC Prediction and Analysis in Power System Based on Data Mining Technology," *High Voltage Apparatus*, Vol.43, No.3, pp.183-185, 2007.
- [4] B. Efron, "The bootstrap and modern statistics," *Journal of the American Statistical Association*, vol. 95, no. 452, pp. 1293-1296, 2000.
- [5] Junli Zheng, Qiheng Ying, Weili Yang, *Signal and System*, 2nd ed., Beijing: Higher Education Press, 2000.

# Modelling and analyzing of HEMP coupling to overhead multiconductor transmission lines

Ni LI\*, Jun GUO †, Jian-gong ZHANG\*, Qing LIU †, Yan-zhao XIE †

\*China Electric Power Research Institute, China, lini000@163.com, †School of Electrical Engineering, Xi'an Jiaotong University, China

## Abstract

This paper mainly studies the modelling effects of HEMP coupling to the multiconductor transmission lines. The 110 kV lines are modelled with Chain Parameters Matrix Method. The incident angles  $\psi$ , the conductivity of ground  $\sigma_g$ , and the voltage and current responses of the line are calculated. The results show that the voltage and current responses of the line will augment then diminish with the increase of the incident angles, and the peak values appear at  $\psi = 1^\circ \sim 5^\circ$ . When the line's length is relatively shorter, the response amplitudes will increase with the increase of the length, but as the length reaches a certain value, the responses will no longer augment accordingly.

**Keywords:** HEMP, field-to-wire coupling, multiconductor transmission line.

## 1 Introduction

In recent years, Researchers have also performed studies on modeling of EMP coupling to overhead multiconductor transmission lines in China [1-4]. However, the researches on the impact of EMP on power grid are in the initial stage. The only study is the EMP effect on long cables. This paper applied frequency chain parameter matrix method in the modeling of overhead multiconductor transmission lines, calculated different HEMP incident angle and HEMP coupling under conditions of different ground conductivities and cable lengths, and summarized the rules.

## 2 Modelling of coupling to multiconductor transmission lines

Use frequency chain parameter matrix method in the modelling of 110 kV transmission line structure. The terminal load of transmission lines is equivalent to port capacitance.

### 2.1 Chain parameter matrix method

The structure of HEMP pulsed irradiation on  $N$  pieces of cables is as shown in Fig. 1. In the figure, "x" is the direction along the cables, and "z" is the direction perpendicular to the ground, and "y" is the horizontal direction, which is perpendicular to the cables.  $Z_1$  and  $Z_2$  denote the loads at two ends of the cable, and  $L$  denotes the cable length.

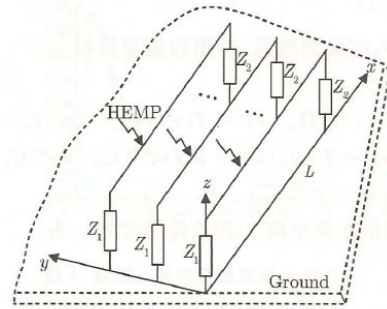


Figure 1. Structure of multiconductor transmission line.

Under the condition of lossy ground, the telegraph equation of multiconductor transmission lines can be expressed in the form of matrix:

$$\frac{d}{dx} \begin{pmatrix} \mathbf{V}(x) \\ \mathbf{I}(x) \end{pmatrix} = \begin{pmatrix} 0 & -\mathbf{Z}' \\ -\mathbf{Y}' & 0 \end{pmatrix} \begin{pmatrix} \mathbf{V}(x) \\ \mathbf{I}(x) \end{pmatrix} + \begin{pmatrix} \mathbf{V}_s'(x) \\ \mathbf{I}_s'(x) \end{pmatrix} \quad (1)$$

The simultaneous differential equations have  $2N$  equations. Use phase-mode transformation method to solve the equation.

Then the voltage and current of load end are:

$$\begin{cases} \mathbf{V}(0) = \mathbf{Z}_c \mathbf{T} (\mathbf{C}_m^+ + \mathbf{C}_m^-) \\ \mathbf{V}(L) = \mathbf{V}_{sT}(L) + \mathbf{Z}_c \mathbf{T} (e^{-\gamma L} \mathbf{C}_m^+ + e^{\gamma L} \mathbf{C}_m^-) \end{cases} \quad (2)$$

$$\begin{cases} \mathbf{I}(0) = \mathbf{T} (\mathbf{C}_m^+ - \mathbf{C}_m^-) \\ \mathbf{I}(L) = \mathbf{I}_{sT}(L) + \mathbf{T} (e^{-\gamma L} \mathbf{C}_m^+ - e^{\gamma L} \mathbf{C}_m^-) \end{cases} \quad (3)$$

### 2.2 Port load equivalent

Before modelling of transmission line, perform modeling of the ports of such terminal equipment. The simple terminal equivalent circuit is as shown in Fig.2. Because capacitive impedance is the major part of impedance, all the above equipment can be treated as capacitors.

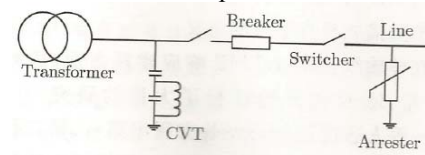


Figure 2. Equivalent circuit of terminal line.

### 3 HEMP coupling to overhead transmission line under condition of different parameters

Take the structure of 110 kV line as an example, and the incident waveform applies IEC standard HEMP waveform, the polarizing angle  $\alpha = 0^\circ$ , and the azimuth angle  $\varphi = 0^\circ$ . Same loads are connected to the two ends of the line in the model, as shown in Fig. 3. The equivalent impedances at two ends of the line are as calculated in the port impedance structure of Fig. 2.

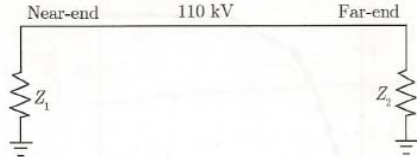


Figure 3. Model of line.

#### 3.1 Relationship between incident angle $\psi$ and coupling to transmission line

Fig. 4 indicates that when the incident angle is  $0^\circ \sim 90^\circ$ , the pulse of line end lasts for 0 ns to 10  $\mu$ s. The response amplitude increases and then decreases. When incident angle is around  $10^\circ$ , the response is the maximum.

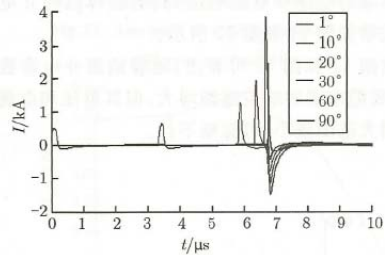


Figure 4. Current responses under different incident angles.

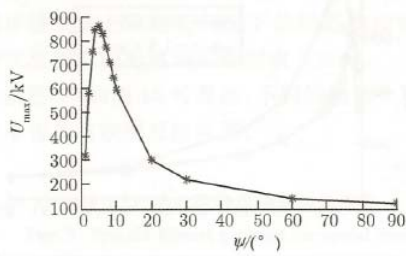


Figure 5. Peak of voltage response under different incident angles ( $\sigma_g = 0.01 \text{ s} \cdot \text{m}^{-1}$ ).

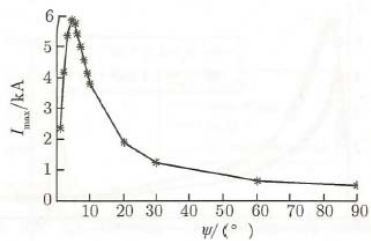


Figure 6. Peak of current response under different incident angles ( $\sigma_g = 0.01 \text{ s} \cdot \text{m}^{-1}$ ).

Fig.5 and Fig.6 indicate that, as mentioned above, when the incident angle increases from  $1^\circ$  to  $90^\circ$ , the voltage or current

response at end of power line increases and then decreases. When  $\psi = 4^\circ \sim 5^\circ$ , the maximum value appears. The maximum value is nearly 50% larger than the response when  $\psi = 10^\circ$ .

Fig.7 and Fig.8 indicate that when the ground conductivity is in the range of actual ground conductivity, the response of power line increases and then decreases as the incident angle increases. Under different ground conductivities, the maximum response appears at different incident angle. In the range of common ground conductivity, the maximum response appears when the incident angle is  $1^\circ \sim 5^\circ$ .

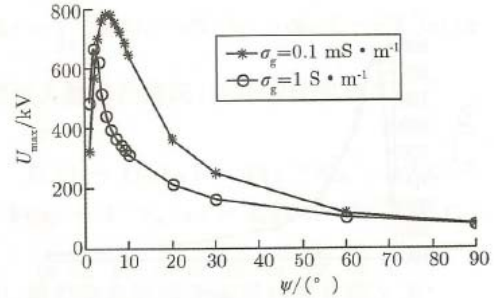


Figure 7. Peak of voltage response under different incident angles ( $\sigma_g = 0.1 \text{ ms} \cdot \text{m}^{-1}, 1 \text{ s} \cdot \text{m}^{-1}$ ).

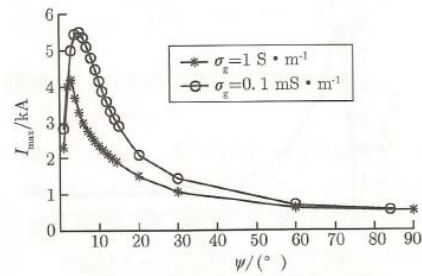


Figure 8. Peak of current response under different incident angles ( $\sigma_g = 0.1 \text{ ms} \cdot \text{m}^{-1}, 1 \text{ s} \cdot \text{m}^{-1}$ ).

#### 3.2 Relationship between line length L and response

Fig.9 and Fig.10 indicate that when the line length is short, as the line length increases, the peak voltage and peak current at ends of power lines increase. When the line length is larger than a certain value, as the line length increases, the peak voltage and peak current at ends of power lines do not increase any more. The critical length is about 2 km.

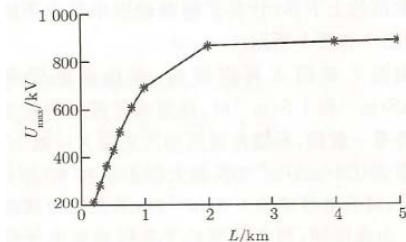


Figure 9. Peak of voltage response under different line lengths.

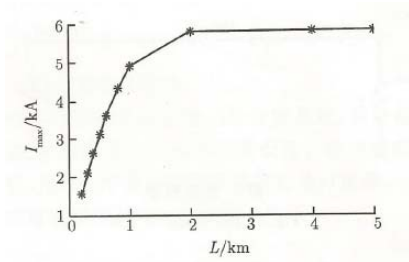


Figure 10. Peak of current response under different line lengths.

### 3.3 The relationship between ground parameters and coupling to power line

Fig.11 and Fig.12 indicate that when ground dielectric constant increases, the response at ends of line increases, but the growths of peak voltage and peak current are negligible.

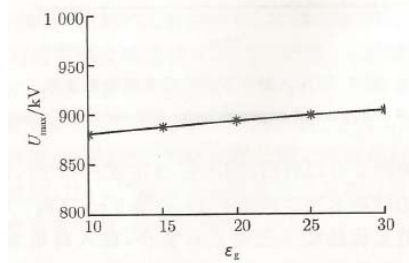


Figure 11. Peak of voltage response under different relative dielectric constants.

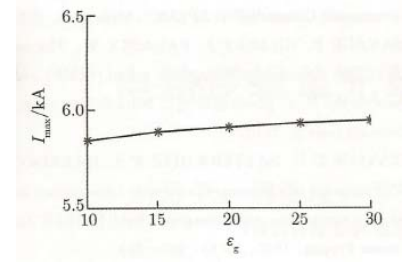


Figure 12. Amplitude of current responses under different relative dielectric constants.

Fig.13 and Fig.14 indicate that when ground conductivity is 0.0001, 0.001 and 0.01  $\text{s}\cdot\text{m}^{-1}$ , the change of response at ends of power line is not big. But when the ground conductivity is 0.1 and 1  $\text{s}\cdot\text{m}^{-1}$ , the voltage and current responses at ends of power line decrease dramatically.

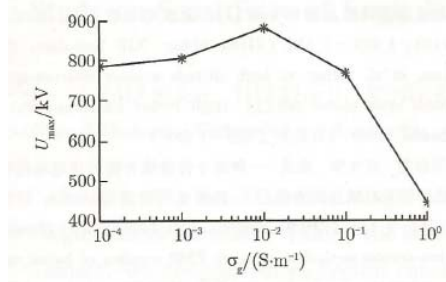


Figure 13. Peak of voltage response under different conductivities.

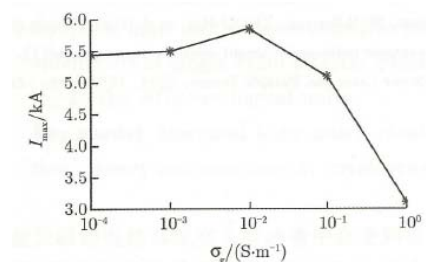


Figure 14. Peak of current response under different conductivities.

Fig.15 indicates that different ground conditions have obvious influence on response waveform.

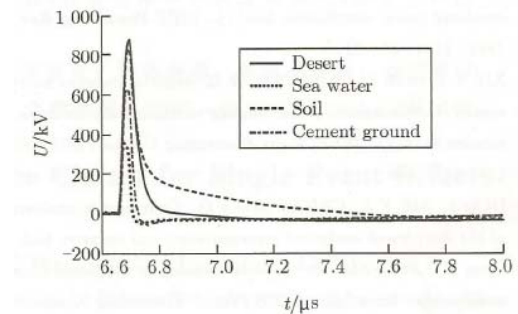


Figure 15. Voltage responses under different ground parameters.

## 4 Conclusions

Based on modelling of an 110 kV power line, the results indicate that as the incident angle increases, the response amplitudes at ends of power lines increase and then decrease, and reach the maximum value when  $\psi = 1^\circ \sim 5^\circ$ . When the line length is relatively shorter, the response amplitudes will increase with the increase of line length, but when the length exceeds a certain value, the responses will no longer augment accordingly. Parameters of ground conditions can also have significant influence on the responses.

## References

- [1] XIE Y Z, GUO J. "Analytical approach for the prediction of EMP coupling to multiconductor transmission lines" [C]//Asia-Pacific International Symposium and Exhibition on Electromagnetic Compatibility (APEMC), Melbourne, 2013.
- [2] ZHAI Ai-bin, XIE Yan-zhao, HAN Jun et al. Effect of high altitude nuclear electromagnetic pulse upon phone call [J]. High Power Laser and Particle Beams, 2009, 21(10): 1529-1533.
- [3] ZHOU Ying-hui, SHI Li-hua, GAO Cheng. A time-domain method to calculate EMP coupling of buried cables based on transmission line model [J]. High Power Laser and Particle Beams, 2006, 18(7): 1163-1166.
- [4] XIE Yan-zhao, SUN Bei-yun, ZHOU Hui, et al. High altitude electromagnetic pulse environment over the lossy ground [J]. High Power Laser and Particle Beams, 2003, 15(7): 680-684.

# Simulation Research of Offshore Wind Farm Lightning Intruding Overvoltage Based on ATP/EMTP

XU Yang<sup>1</sup>, LIU Wenbo, WANG Yu, LAN Lei, ZHU Sheng

1. School of Electrical Engineering, Wuhan University, Wuhan430072, Hubei Province, China  
e-mail: xuyang\_0502@sina.com

## Abstract

This paper analysed the lightning intruding overvoltage of offshore wind power farm by ATP/EMTP. By establishing the submarine cable model, a comparison of three-core XLPE cable with single-core XLPE cable was made, as well as the effect of length of cables and grounding resistance of tower on the overvoltage was studied. The result shows that, by using submarine cable as transmission line, lightning intruding overvoltage of substation could be suppressed. Three-core cable has lower zero-sequence capacity than single-core cable, while its zero-sequence inductance is much higher. Thus the wave impedance of single-core cable is minor than that of three-core cable. And the longer the cables are, the lower the lightning intruding overvoltage of substation would be. What's more, the reduction of grounding resistance of tower could lead to lower overvoltage.

**Keywords:** Offshore wind power, Lightning intruding overvoltage, submarine cable, ATP/EMTP.

## 1 Introduction

As energy-saving and emission reduction becomes a global trend, the research on offshore wind power turns to be a hotspot in every country<sup>[1]</sup>. Earlier studies were mainly concerned on machine modelling, grid-connection as well as optimal designing<sup>[2,3]</sup>. While the environment of offshore wind power farm could be quite harsh, lightning stroking affairs were taking into consideration extensively<sup>[4,5]</sup>. To make a connection with the grid, long submarine cables were adopted. And this could lead to the occurring of power frequency overvoltage in a way<sup>[6-9]</sup>. At the meantime, it was obvious that the lightning intruding overvoltage of offshore power system would be quite different from onshore power system. By using ATP/EMTP, submarine cable, as well as offshore substation and overhead line were modelled, and research on the lightning intruding overvoltage of offshore wind power farm when the lightning stroked the overhead line was carried out.

## 2 Simulation Models and Parameters

### 2.1 System Scheme

The offshore wind power farm is connected to the Onshore Centralized Control Centre by submarine cables, and

then accessed to 220kV system through overhead lines. Two MOAs are considered while simulating. As shown in Fig.1.

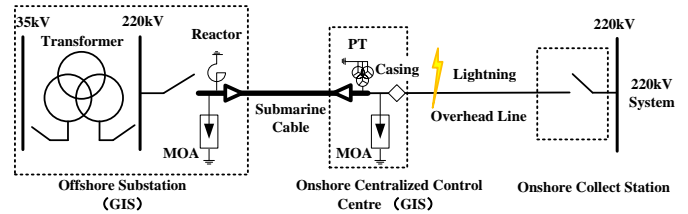


Fig. 1 Scheme of 220kV Offshore Wind Power System

### 2.2 Submarine Cables

The submarine cables used in this project were copper XLPE with cross-sections of  $1 \times 1600\text{mm}^2$  and  $3 \times 500\text{mm}^2$ . By setting parameters of the core, sheath and armour, the models of submarine cables were established, as shown in Fig.2. Reference [10] gave a brief introduction of parameters correction for submarine cables. And Table 1 showed the electrical parameters calculated by ATP-Verify. The resistivity of sea water was taken as  $0.3\Omega\cdot\text{m}$ , and cables were buried 1.2m deep with both-end bonded.

As shown in table, single-core cable has larger zero-sequence capacity while minor zero-sequence inductance than three-core cable. That's to say, the wave impedance of single-core cable ( $Z_S$ ) is minor than three-core cable ( $Z_T$ ).

Table 1: Electrical Parameters of Cables

Type	$R_0(\Omega/\text{km})$	$X_0(\Omega/\text{km})$	$R_1(\Omega/\text{km})$	$X_1(\Omega/\text{km})$	$C_0(\mu\text{F}/\text{km})$	$C_1(\mu\text{F}/\text{km})$
Single-core	0.1593	0.6399	0.04522	0.4826	0.105	0.105
Three-core	0.1789	1.32	0.04277	0.1301	0.071	0.101

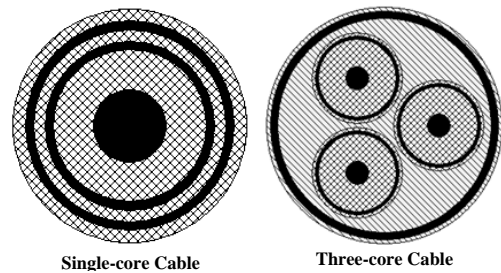


Fig. 2 Models of Single-core Cable and Three-core Cable in ATP

### 2.3 Lightning Current Model

Surge type was adopted in this simulation, whose waveform could be described by the double exponential function. The formula can be expressed as:

$$i=I_0(e^{-\alpha t}-e^{-\beta t}) \quad (1)$$

Where  $\alpha=-1/T_1$ ,  $\beta=-1/T_2$ .  $T_1$ ,  $T_2$  are time to half value and frond time of lighting impulse, which decide the rise time and decay time of the lightning current.

### 2.4 Other Parameters

The equivalent entrance capacitances of equipment were selected referring to Reference [11]. MOAs used were of 216kV rated voltage<sup>[12]</sup>.

## 3 Results and Analyses

The lightning current waveform used for the calculations conformed to the international standard, whose waveform was 2.6/50 $\mu$ s, while amplitude was 170kA.

### 3.1 Analysis of reflection and refraction course

To analyse the reflection and refraction course in this system, we can simplify Fig.1 as Fig.3. In this figure,  $(Z_1, v_1)$ ,  $(Z_2, v_2)$ ,  $(Z_3, v_3)$  are wave impedance and wave velocity of overhead line, GIS, submarine cable, while  $Z_1 \gg Z_2 > Z_3$ .

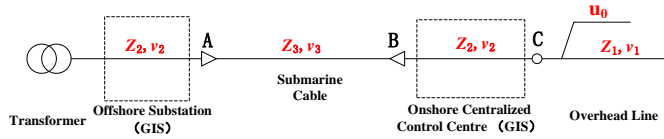


Fig.3 Simplification of 220kV Offshore Wind Power System

Multiple reflections and refractions between nodes A, B, C will occur. Meanwhile, as the length of overhead line and submarine cable are both much longer than that of the GIS pipeline, the GIS pipeline of onshore centralized control centre could be deemed as short-circuit, thus :

$$u_C = u_B = \frac{2Z_3}{Z_1 + Z_3} u_0 \quad (1)$$

As  $Z_1 \gg Z_3$ , it can easily get that  $u_C = u_B \ll u_0$ . That to say, the use of submarine cable could lead to lower overvoltage in this system. As shown in Fig.4.

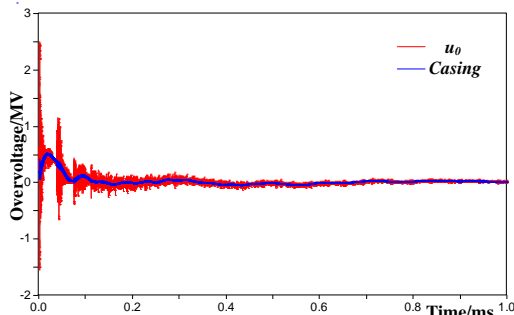


Fig.4 The Waveform of Lightning Intruding Overvoltage

### 3.2 Comparison on Single-core and Three-core Cable

The spacing among three phases of single-core cables is value 20m. And the length of cables are 26km, the grounding resistance of tower is 10 $\Omega$ . The lightning intruding overvoltage of equipment is given in Table2.

Table 2: Overvoltage of Equipment(kV)

Type	Transformer	PT	Cable			Casing
			Head	Middle	End	
Single-core	441.9	648.44	641.56	372.55	441.89	657.78
Three-core	375.15	676.2	672.96	338.97	375.17	680.77

As casing is nearest to the lightning strike point, its overvoltage is the highest. And overvoltage of casing is almost equal to that of the cable head. The lightning intruding overvoltage is greatly suppressed after the wave travelling through the submarine cable. What's more, overvoltage of transformer is lower in three-core cable system than in single-core cable system, while the overvoltage of casing and PT are just on the contrary.

The waveforms of the overvoltage in cables are observed, shown as Fig.5 and Fig.6. The velocity in single-core cable and three-core cable is both about 130m/ $\mu$ s. As the capacity of the cable is much higher than that of the overhead line, it could act as a capacitor in this system. Thus the wave front is smoothed.

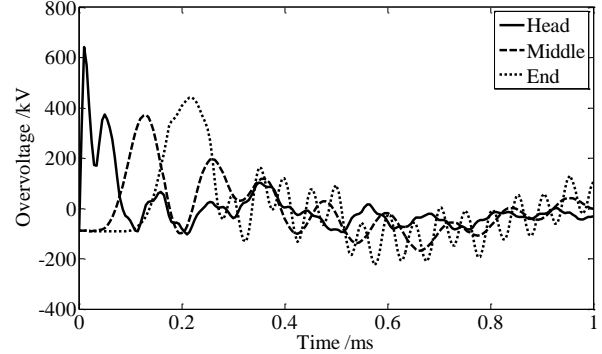


Fig.5 The Waveform of Lightning Intruding Overvoltage in Single-core Cable

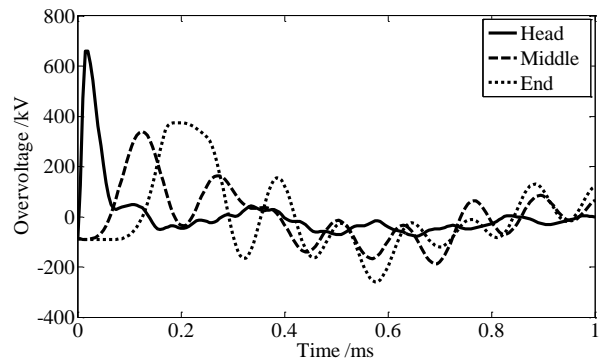


Fig.6 The Waveform of Lightning Intruding Overvoltage in Three-core Cable

What's more, as  $Z_S$  is minor than  $Z_T$ , while both minor than the wave impedance of GIS<sup>[11]</sup>( $Z_G$ ). An even higher reflected wave might stack at the end of cable, causing the overvoltage increasing in end of the cable.

### 3.2 Length of Cable

MATLAB was used to analyse the effect of cable length on lightning intruding overvoltage. Taking both three-core and single-core cables into consideration. Fig.7 give the tendency of overvoltage with different cable length.

It shows that, with the increase of cable length, the overvoltage on transformer both decrease.

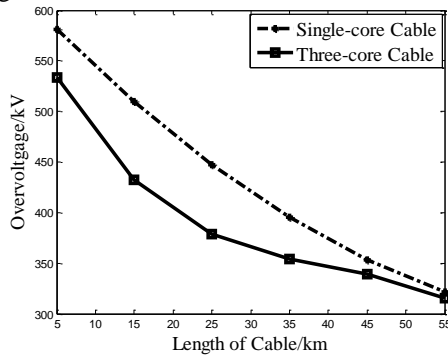


Fig.7 The Effect of Cable Length on Overvoltage of Transformer

### 3.3 Grounding Resistance of Tower

The length of the cable is 26km, while the grounding resistance of tower ranges from 5Ω to 20Ω. The results are given in Fig.8.

It shows that, with the increase of the grounding resistance of tower, the overvoltage on transformer and casing both increase. While the increasing rate of overvoltage on transformer in single core cable system is much higher than three-core cable system.

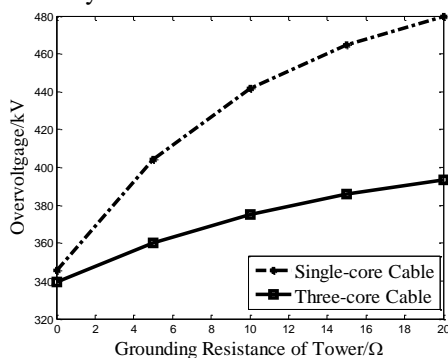


Fig.8 The Effect of Grounding Resistance of Tower on Overvoltage of Transformer

## 4. Conclusion

(1)The lightning intruding overvoltage is suppressed and the wave front is smoothed when the intruding wave travelled through submarine cable.

(2)With the increase of cable length, the overvoltage on transformer decrease.

(3)With the increase of grounding resistance of tower, the overvoltage on transformer increase.

(4) Lightning intruding overvoltage on casing in single-core cable system is higher than in three-core cable system,

while lightning intruding overvoltage on transformer is just the opposite.

## References

- [1] Huang Lingling, Cao Jialin, Fu Yang. Review of electrical systems for offshore wind farms[J]. Power System Protection and Control, 2008, 08: 77-81.
- [2] Liu Jian, Tian Wei, Lu Bin, et al. Design of offshore wind turbine electric pitch system based on supercapacitor[J]. Renewable Energy Resources, 2014,10:1474-1478.
- [3] Wang Zhixin, Wu Jie, Xu Lie, et al. Key Technologies of Large Offshore Wind Farm VSC-HVDC Converters for Grid Integration[J]. Proceedings of the CSEE,2013,19:14-27.
- [4] Rodrigues R B, Mendes V M F, Catalão J P S. Electromagnetic transients due to lightning strikes on wind turbines: A case study[C]//MELECON 2010-2010 15th IEEE Mediterranean Electrotechnical Conference. IEEE, 2010: 1417-1422.
- [5] Rodrigues R B, Mendes V M F, Catalão J P S. Indirect effects of lightning on wind turbines using EMTP-RV[C]//Power Engineering, Energy and Electrical Drives (POWERENG), 2011 International Conference on. IEEE, 2011: 1-5.
- [6] Huang Hui , Zheng Ming , Lan Jinbiao, et al.Simulation Analysis of the Electro-Magnetic Transient on High Voltage Submarine Cable of the Offshore Wind Farms[J]. Power System and Clean Energy,2012,11:72-76+81.
- [7] Wang Xiaotong , Lin Jiming , Chen Gesong, et al. Electromagnetic Transient Analysis of 500 kV Submarine Cable Transmission System From Guangdong to Hainan[J]. Power System Technology,2008,12:6-11.
- [8] Chen Zheng , Kang Yi , Ma Yiqing. Analysis on Reactive Compensation and Electromagnetic Transient in 500 kV Sea Trails Interconnection Project for Hainan and Guangdong Power Grids[J]. Power System Technology,2009,19:143-147.
- [9] Li Jianwei. Research and Simulation of Transient Phenomena of High Voltage AC Submarine Cable Grid Based on ATP-EMTP[J]. North China Electric Power, 2014,04:20-24+34.
- [10] Da Silva F M F. Analysis and simulation of electromagnetic transients in HVAC cable transmission grids[D]. Videnbasen for Aalborg UniversitetVBN, Aalborg UniversitetAalborg University, Det Teknisk-Naturvidenskabelige FakultetThe Faculty of Engineering and Science, Elektriske anlægElectric Power Systems, 2011.
- [11] JIANG Rihong, ZHANG Bing, LUO Xiaoyu. Lightning protection and application example on substation and power station[M]. Beijing, China: China Electric Power Press,2005.
- [12] 2000 G B. Metal-oxide surge arresters without gaps for a.c. systems [S][D].

# Calculation and Analysis on Transient Induced Voltage of Multiple Parallel UHV Transmission Lines

ZHANG Gongda<sup>1</sup>, ZHOU Peihong<sup>2</sup>, ZHANG Xiaoqing<sup>2</sup>, YUE Lingping<sup>3</sup>

1. School of Electrical Engineering, Wuhan University, China, Email: zhanggongda@whu.edu.cn  
2. State Grid Electric Power Research Institute, China 3. State Grid Huzhou Power Supply Company, China

## Abstract

It has transient electromagnetic induction between parallel lines as coupling effects. The magnitude and characteristics of induced voltage on sound circuits is worth studying for improving system operation and insulation configuration. In this paper, the simulate models of six parallel circuits in one corridor around HuZhou city were set up in power system electromagnetic transient program to calculate the coupling effects. The magnitude and distribution of switching induced voltage caused by permanent single phase grounding fault in UHVAC system and monopolar grounding fault in UHVDC system was calculated. The characteristics of induced voltage on sound circuits nearby fault circuit were analysed. The results show that maximum transient induced voltage caused by UHVAC fault on UHVDC sound circuits is lower than it caused by UHVDC fault. The most serious induced voltage caused by monopolar grounding fault is still on the antipode circuit. The magnitude of induced voltage caused by both AC and DC switching overvoltage does not pose risks to the people on line working comply with the current standard.

**Keywords:** multi-parallel, UHV, switching overvoltage, transient induction.

## 1 Introduction

The transient induced voltage on low-medium voltage transmission lines, or communication lines is an inducement of network instability and device damage. The interactions caused by the transient electromagnetic induction on several nearby parallel overhead lines may cause some significant problems to the operation and maintenance especially in the UHV(Ultra High Voltage) / EHV(Extra High Voltage) system.<sup>[1-4]</sup>

The space of lines corridor has become valuable more and more in the eastern china, the phenomenon of several AC/DC transmission lines erected in one corridor has become widespread. Under extremely circumstance, six transmission circuits parallel with each other adjacently in HuZhou city, Zhejiang province. The magnitude and characteristics of transient induced voltage generated by switching overvoltage

on sound circuits is worth studying for improving system operation and insulation configuration of UHV/EHV lines.

## 2 Parameters of multiple parallel lines

### 2.1 Overview of parallel lines

1000kV HuaiShang line is a dual circuit in same tower system, the length is 656km.  $\pm 800$ kV JinSu project has 2100km bipolar line, and 7200MW transmission power.  $\pm 800$ kV FuFeng project has 1906km bipolar line, and 6400MW transmission power.  $\pm 500$ kV GeNan/LinFeng project has two bipolar lines and  $2 \times 3000$ MW transmission power, GeNan line 1114km, LinFeng line 976km.

The route map of these parallel lines in HuZhou city is shown in Fig. 1. The arrangement of four circuits in one corridor west of ZheBei station is shown in Fig. 2, the arrangement of six circuits in one corridor east of ZheBei station is shown in Fig. 3. The segment of HuaiShang west of ZheBei station is called WanZhe line; the segment east of ZheBei station is called ZheHu line.

### 2.2 Coupling parameters for simulation

For considering the electromagnetic coupling effect, the parallel spacing of four whole lines was measured and classified by using tower's GPS coordinate, thus the coupling lines models were built. Around HuZhou, the segment data points were also established for getting the information of induced voltage along this several parallel circuits corridor. The length of this corridor in HuZhou is about 263km, including UHV four circuits coupling segment 124km, UHV/EHV six circuits coupling segment 72km, and UHV three circuits coupling segment 67km<sup>[5]</sup>. The spacing of parallel lines distance between the centres of tower is about 70m to 80m. The sketch of parallel relationship and data points is shown in Fig. 4.

The rule of HVDC system operation which is constant current control of converter, constant voltage control of inverter was adopted in the simulation. It has DC voltage drop about 6% of rated voltage on the side of inverter.

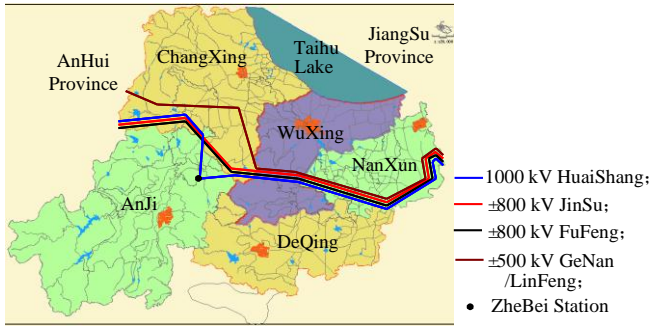


Figure 1. Route map of EHV/UHV lines in HuZhou.

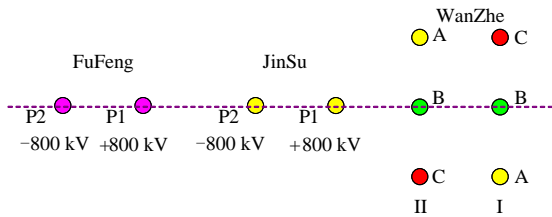


Figure 2. Arrangement diagram of four circuits in same corridor.

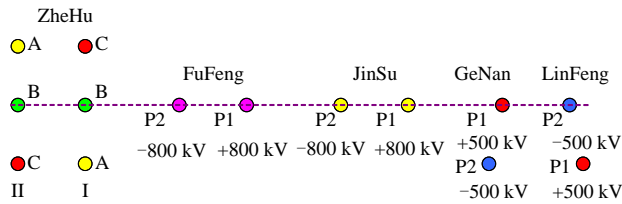


Figure 3. Arrangement diagram of six circuits in same corridor.

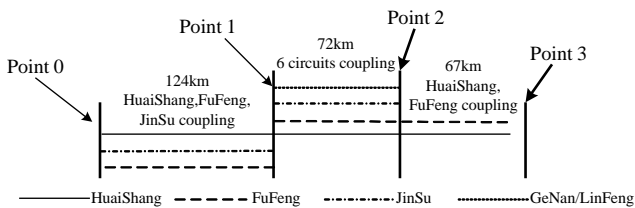


Figure 4. Parallel relationship and induced voltage data points of six circuits.

### 3 Simulation Results

#### 3.1 Induced voltage caused by AC switching overvoltage

According to the previous AC overvoltage studies [6-7], the magnitude of switching overvoltage due to the permanent single phase grounding fault is more than the line energizing overvoltage and single-phase automatic reclosing overvoltage. And then the transient induced voltage on the sound phases is stimulated more severely.

The maximum transient voltage in AC system caused by permanent single phase grounding fault on WanZhe II circuit is 1480kV be equal to 1.65 p.u.(1 p.u.=816kV). The transient induced voltage on the JinSu positive circuit which is closest to WanZhe II circuit is 883kV (1.08 p.u.), but the highest induced voltage is 889kV (1.09 p.u.) on the FuFeng negative circuit. The refraction, reflection and addition of travelling wave induced on FuFeng negative circuit is a reason for the phenomenon. As the permanent single phase grounding fault occurring on ZheHu I circuit, the highest induced voltage is 889kV (1.09 p.u.) on the FuFeng negative circuit which is closest to ZheHu I circuit. The calculation results of transient induced voltage on each DC circuits are shown in Table 1 and Table 2 (P1 stands for positive circuit, P2 stands for negative circuit).

Table 1: Induced voltage on DC circuits under the permanent single phase grounding fault of WanZhe II circuit (kV)

Data Point	JinSu		FuFeng		GeNan		LinFeng	
	P1	P2	P1	P2	P1	P2	P1	P2
Point 0	883	873	881	889	-	-	-	-
Point 1	843	831	873	873	506	489	490	499
Point 2	822	801	837	847	506	480	490	487
Point 3	821	800	832	845	-	-	-	-
Maximum	883	873	881	889	506	489	490	499

Table 2: Induced voltage on DC circuits under the permanent single phase grounding fault of ZheHu I circuit (kV)

Data Point	JinSu		FuFeng		GeNan		LinFeng	
	P1	P2	P1	P2	P1	P2	P1	P2
Point 0	838	826	876	872	-	-	-	-
Point 1	843	834	876	889	511	491	501	503
Point 2	814	804	835	851	517	483	503	489
Point 3	805	801	869	846	-	-	-	-
Maximum	843	834	876	889	517	491	503	503

#### 3.2 Induced voltage caused by DC switching overvoltage

Previous studies indicated that monopolar grounding fault at the middle of whole line is a major cause of most serious switching overvoltage that is on the antipode circuit around fault point. The transfer overvoltage on the parts of four DC lines in HuZhou city far away from the middle of whole line is much lower than occurring local monopolar grounding fault. In the simulation, local fault at the point 0 was set up to analyse the characteristics of maximum induced voltage.

As JinSu monopolar grounding, calculation results of transient induced voltage on each DC circuits are shown in Table 3 and Table 4. The induced voltage 1078kV (1.32 p.u.) on sound circuit is higher than on each other parallel circuits. Occurring monopolar grounding fault on JinSu P1, the induced voltage on FuFeng P1 is higher than on FuFeng P2, the induced voltage on ±500kV negative circuits such as GeNan P2, LinFeng P2, is higher than on their antipode circuits (GeNan P1, LinFeng P1). As FuFeng monopolar

grounding, the situation of induced voltage on circuits is similar to which caused by JinSu monopolar grounding.

Table 3: Induced voltage on DC circuits under JinSu positive circuit grounding fault (kV)

Data Point	JinSu		FuFeng		GeNan		LinFeng	
	P1	P2	P1	P2	P1	P2	P1	P2
Point 0	0	1078	906	872	-	-	-	-
Point 1	287	984	872	851	501	522	496	552
Point 2	195	937	875	838	512	490	514	504
Point 3	-	-	861	833	-	-	-	-
Maximum	287	1078	906	872	512	522	514	552

Table 4: Induced voltage on DC circuits under JinSu negative circuit grounding fault (kV)

Data Point	JinSu		FuFeng		GeNan		LinFeng	
	P1	P2	P1	P2	P1	P2	P1	P2
Point 0	1078	0	890	910	-	-	-	-
Point 1	984	294	878	881	523	479	528	494
Point 2	937	190	865	871	493	485	486	491
Point 3	-	-	846	865	-	-	-	-
Maximum	1078	294	890	910	523	485	528	494

#### 4 Influence on live working

The minimum approach distance for live working includes the minimum electric clearance and human activity area. According to the IEC standard, the minimum electric clearance refers to the minimum clearance distance avoiding electric breakdown at the working points during live working. The level of switching overvoltage on working lines is relate to the value of minimum approach distance, and to the safety of workers.

According to the China national standards<sup>[8-9]</sup>, the design value of minimum approach distance on DC transmission line can be calculated by the maximum switching overvoltage on the whole line, and the design maximum switching overvoltage factor for JinSu project is 1.6 p.u., for FuFeng is 1.7 p.u. The maximum induced voltage 1078kV (1.32 p.u.) on UHVDC circuit in the parallel corridor is lower than the design maximum value. The existing rules for operation and maintenance is unaffected, the live working workers is safe.

#### 5 Conclusion

In this paper, the simulation models of several parallel transmission lines considering electromagnetic coupling effect were built for studying the characteristics of switching induced voltage. The object line segments of this study are situated near the side of inverter, the characteristics of transient induced voltage caused by AC system switching overvoltage are different from that cases caused by DC system fault. The maximum transient induced voltage caused

by the permanent single phase grounding fault of 1000kV line on UHVDC sound circuits is lower than it caused by UHVDC monopolar grounding fault. The most serious induced voltage caused by UHVDC monopolar grounding fault is still on the antipode circuit. The magnitude of transient induced voltage caused by both AC and DC switching overvoltage does not pose risks to the people working comply with the current standard.

#### Acknowledgements

The authors would like to express their thanks for great help provided by the colleagues of Wuhan University, State Grid Electric Power Research Institute and HuZhou Power Supply Company.

#### References

- [1] T. Imamura, A. Ametani. "Investigation of transient induced voltage to a communication line from an overhead power transmission line", *IEE Proceedings*, **Vol.137**, pp. 129-139, (1990).
- [2] M. S. Rahimian, S. H. H. Sadeghi, "LEMP coupling with medium voltage overhead lines and its effects on low voltage", *Electromagnetic Compatibility, 2002 3rd International Symposium on*, pp. 115-118 (2002).
- [3] Chamni Jaipradidtham, Artiwat Naksuriyavong. "Research on the effect of induced voltages in transient stability for multi circuit modeling on 500 kV EHV parallel transmission lines using a modified genetic algorithm", *Proceedings of the International Electrical Engineering Congress 2014*, pp. 1-4, (2014).
- [4] Zhou Peihong, Xiu Muhong. "The influence between AC and DC transmission line built in same corridor". *High Voltage Engineering*, **Vol.29**, pp. 5-7, (2003).
- [5] ZHANG Wenjie, ZHANG Gongda. "Calculation and analysis on steady-state induced voltage during maintenance operation of multi parallel circuits of EHV/UHVDC/UHVAC transmission lines", *Power System Technology*, **Vol.38**, pp. 2310-2314, (2014).
- [6] Jeong-Boo Kim, Eung-Bo Shim. "Switching overvoltage analysis and air clearance design on the kepc0 765 kV double circuit transmission system". *IEEE Transactions On Power Delivery*, **Vol.15**, pp. 381-386, (2000).
- [7] T. Keokhoungning, S. Premrudeepreechacharn. "Evaluation of switching overvoltage in 500 kV transmission line interconnection nam theun 2 power plant to roi et 2 substation", *Power and Energy Engineering Conference, Asia-Pacific*, pp. 1-4, (2009).
- [8] China Electricity Council. "GB 50790 Code for designing of  $\pm 800$ kV DC overhead transmission line", *National Standard of the People's Republic of China*, (2013).
- [9] China Electricity Council. "DL/T 876 Guide of insulation co-ordination for live working", *Electric power industry standard of the people's Republic of China*, (2004).

# Study of Influence Factors of Transient Enclosure Voltages in GIS

CHEN Shu, GUO Jie , LI Kelun

Department of electrical engineering, Xi'an Jiaotong University, Xi'an 710049, China  
chenshu1992221@126.com

## Abstract

Transient enclosure voltages, one special case of very fast transient over voltages, are common electromagnetic transient phenomena in Gas Insulated Substation caused by the operation of disconnect switch or fault to ground. A new simulation model combined the idea of three transmission lines model with the impact of changeable frequency and soil resistivity is proposed in this paper. EMTP-ATP software is employed to study the effect of different influence factors such as number of grounding points, length of ground lead and geometric dimensions of GIS enclosure to the peak value of transient enclosure voltages in this paper. The results of the new simulation model is more convincing and may provide useful reference for the suppression of transient enclosure voltages.

**Keywords:** Transient Enclosure Voltage, Gas Insulated System, Very Fast Transient Over Voltages, Grounding, Enclosure, EMTP-ATP.

## 1 Introduction

Gas Insulated Substations (GIS) have been widespread used in power grid over 110kV level due to the advantages of high reliability, convenient operation, less occupied area, less disturbance from environment and easier maintenance than open-type substation. Transient enclosure voltage (TEV) is a special case of very fast transient over voltage (VFTO) [1]. Because of the special structure of GIS, the operations of disconnect switch or ground faults will cause electromagnetic wave with very steep wave front, propagating along GIS core wires with a lot of reflections and refractions when the waves meet each different surge impedance. On account of skin effect [2], the high frequency current travelling waves only flow along the surface of core wires and the inner surface of the enclosure of GIS, so that TEV generated within the GIS do not appear on the exterior surface of the enclosure until discontinuities in the enclosure are encountered like bushing, potential transformer etc [3].

TEV represents the voltage of grounded enclosure rises rapidly in nanoseconds rise time. It is a kind of special VFTO transient phenomenon with high amplitude, MHz frequency, nanoseconds rise time, microseconds last time and fast attenuation. These high potentials cause breakdowns between the GIS enclosures and other nearby grounded components, and have resulted in protection and control wiring failures and

personnel shocks [4]. Researchers have already done a lot of work on this area. A simple three transmission lines theoretical model has been proposed in 1982 [3]. However the model is not very practical and comprehensive in high frequency and there is not much about the propagating characteristic on GIS enclosure. In this paper, a new model improved from former models considering the cause of TEV and the propagation characteristics along the enclosure has been established to study the influence factors of TEV to provide directions on reducing TEV.

## 2 Simulation model

Air/SF<sub>6</sub> termination is modelled as a junction of three transmission lines, first proposed by E.P.Dick in paper [3]. The theoretical model is widely employed in calculating TEV in the past years. The configuration is showed in Fig.1.

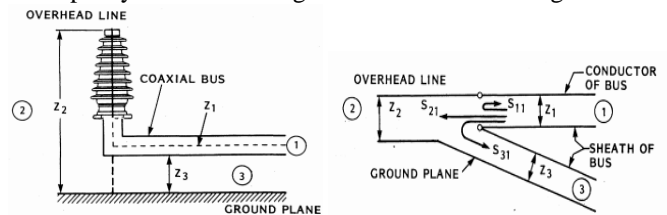


Figure.1 Air/SF<sub>6</sub> termination modelled as a junction of three transmission lines [3]

Z<sub>1</sub> is the impedance of the internal coaxial GIS core wire, Z<sub>2</sub> is the impedance of overhead line-to-ground transmission line, Z<sub>3</sub> is the impedance of bus enclosure to ground transmission line. Scattering coefficient S<sub>31</sub>, the refraction of wave from the core wire to the enclosure, can be calculated by using equation (1).

$$S_{31} = -\frac{2Z_3}{Z_1 + Z_2 + Z_3} \quad (1)$$

According to a practical 220kV GIS, the exterior diameter of GIS enclosure is 346mm, the inner diameter is 330mm, and the height to ground is 1m. Using the idea of three transmission lines model, an ideal slope source is treated as a VFTO wave from the inner layer of GIS enclosure and transmission line model LCC as the outer layer of GIS enclosure which is divided into several segments in cascade in case to measure voltages at different points of GIS enclosure, considering earth resistivity and the influence of high frequency which are not taken into account in other simulation models. The simulation model of each electrical components are shown in table.1. The simulation model has been set up like fig.2 and there are 5 probes, measuring the voltages of different points of the enclosure. For each interval is 5m. Fig.3 shows the waveforms of each measuring point

and the maximum amplitudes are listed in table.2. All the five waveforms have similar shapes but different amplitudes. The

first probe close to the source has maximum peak value among the five.

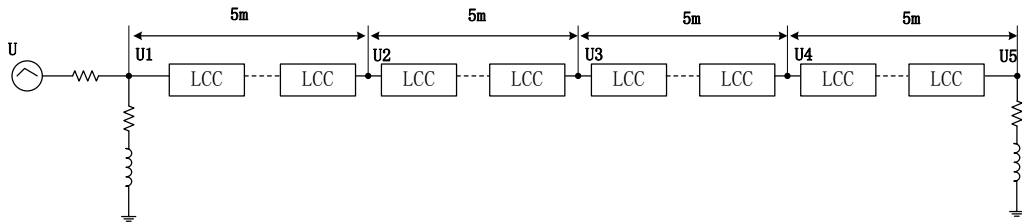


Figure 2. Simulation model to calculate TEV's

Table 1. Electrical equivalent circuit components

Components	Equivalent Model and Value
GIS Enclosure of Bus Bar	Distributed line LCC model with Semlyen method l=20m, impedance is $Z_3$
Ground Lead	$L_0=1\mu\text{H/m}$
Ground Resistance	$R=0.5\ \Omega$
Earth Resistivity	$\rho=300\ \Omega\cdot\text{m}$
VFTO Source	Slope source with 10ns rise time

Table 2. Maximum amplitudes of TEV's measured by five probes

nodes	$U_1$	$U_2$	$U_3$	$U_4$	$U_5$
$U_m/\text{kV}$	24.885	19.705	17.368	15.698	17.995

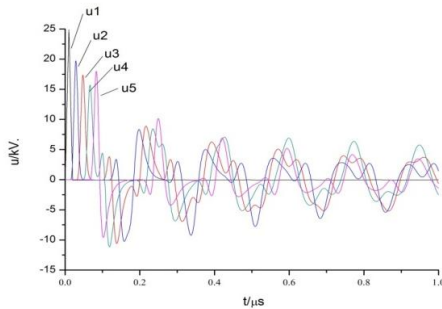


Figure 3. Waveforms of each measuring point (the interval between two grounding lead is 20m)

### 3 Influence factors of TEV

The TEV is calculated in a segment length of 20m GIS bus bar, changing the number of grounding points, length of ground lead, and geometric dimension of GIS enclosure to analyze their influence to TEV by EMTP software.

#### 3.1 The number of grounding points

As it is shown in Fig.2, only two grounding points are installed. Considering if adding more grounding points is

useful to limit TEV's, we can change the number of grounding points and assume all the grounding points are arranged with uniform distance. Table.3 shows the results of changing the number of grounding points.

Table 3. The influence of changing the number of grounding points to the peak values of TEV

Number of grounding points	$U_1/\text{kV}$	$U_2/\text{kV}$	$U_3/\text{kV}$	$U_4/\text{kV}$	$U_5/\text{kV}$
2	24.885	19.705	17.368	15.698	17.995
3	24.885	19.663	13.932	12.321	14.276
5	24.885	16.248	11.344	7.960	13.856
21	24.885	9.320	6.327	4.664	6.375

From table.3, adding the number of grounding points can decrease the peak value of TEV because of the shunting effect of ground lead except first node which is directly fixed by the source.

#### 2.2 The length of ground lead

Since TEV has tens MHz frequency range, ground lead can be presented as a vertical cylinder with a radius of  $r_g$  divided into several different surge impedances changing with height. For example, if the average height of one segment of grounding lead is  $h_g$ , the surge impedance  $Z_g$  of this segment can be calculated as equation (2).

$$Z_g = 60 \ln \left( \frac{2\sqrt{2}h_g}{r_g} \right) \quad (2)$$

The junction of ground lead and GIS enclosure can be depicted as Fig.4 and its equivalent circuit as Fig.5.

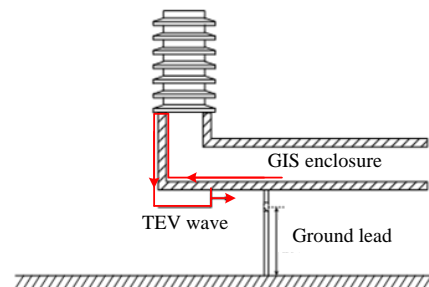
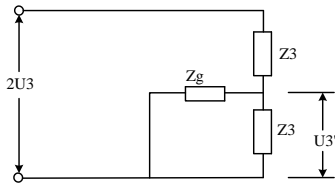


Figure 4. Structure diagram of grounding lead on the GIS enclosure



**Figure 5.** Equivalent circuit of grounding lead and enclosure

$U_3$  is the value of TEV at grounding point, so the TEV with a grounding lead  $U_3'$  can be calculated as equation (3).

$$U_3' = \frac{\frac{Z_3 Z_g}{Z_3 + Z_g}}{Z_3 + \frac{Z_3 Z_g}{Z_3 + Z_g}} \times 2U_3 = \frac{2Z_g}{Z_3 + 2Z_g} U_3 \quad (3)$$

From the equation (2), we can figure out the relationship between  $Z_g$  and  $h_g$  is proportional. From equation (3),  $Z_g$  and  $U_3'$  is proportional. From theoretical point of view, increasing the length of ground lead means increasing the average height  $h_g$  of ground lead, as a result the TEV should be larger.

We calculate the TEV's with different length of ground lead, the results are shown in table.4.

**Table 4.** The influence of changing the length of ground lead to the peak values of TEV

Length of ground lead/m	$U_1$ /kV	$U_2$ /kV	$U_3$ /kV	$U_4$ /kV	$U_5$ /kV
0.5	24.793	19.613	17.277	15.609	8.112
1	24.854	19.674	17.337	15.669	12.932
2	24.885	19.705	17.368	15.698	17.995
10	24.910	19.729	17.392	15.722	25.830

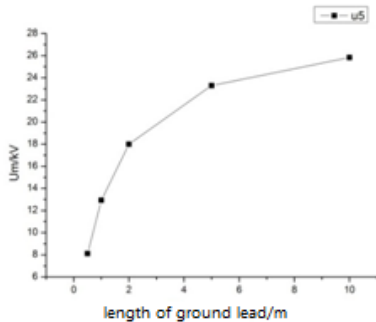


**Figure 6.** the peak values of TEV at  $U_5$  point with different length of ground lead

The length of ground lead has an important role on TEV particularly at node 5, and the relationship between the length of ground lead and the peak value of TEV is proportional from table.4 and fig.6, the same result as theoretical analysis. In order to suppress TEV, decreasing the length of ground lead is one solution.

### 2.3 The radius of GIS enclosure

To study the influence of radius of GIS enclosure, the radius is changed from 17.3cm to 50cm, to calculate the peak value of TEV's as table.5 showing.

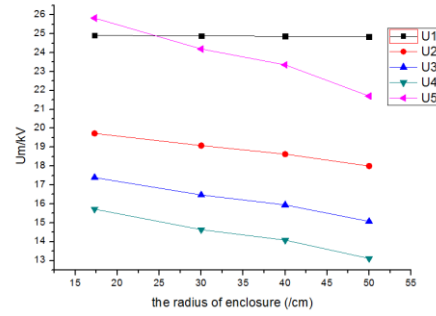


**Figure 7.** The peak values of TEV with different radius of enclosure

From fig.7, with the increase of the radius of GIS enclosure, the peak values of TEV decrease. The impedance of enclosure to ground  $Z_3$  changes with the radius like equation (4).

$$Z_3 \approx 60 \ln \left( \frac{2H}{r_o} \right) \quad (4)$$

As a result, the radius is inversely proportional to  $Z_3$  and also proportional to  $S_{31}$  because of equation (1). It is the same conclusion as simulation results.

## 4 Conclusion

A new ideal simulation model of one segment of GIS bus bar considering the propagation characteristics of high frequency surge wave in GIS with a transient slope source and soil resistivity in EMTP-ATP software is employed to analysis the influence factors of TEV. The study shows the number of grounding points, the length of ground lead, and the radius of GIS enclosure all have an impact on TEV especially the number of grounding points. It is concluded that more grounding points, less length of ground lead and less radius of GIS enclosure can decrease the peak value of TEV.

## Acknowledgements

Authors would like to thank Chen Jie, Jiao Lixin and Yang Hao, colleagues in department of electrical engineering, Xi'an Jiaotong University, for providing valuable suggestions for this paper.

## References

- [1] Kriti Chandrakar, R.S. Gorayan. "Analysis and Control of Transient Enclosure Voltages in GIS", *annual IEEE India Conferenc*, (2013).
- [2] G.L. Ford, S.A. Boggs. "Transient Ground Rise in SF6 Substation Investigated", *Transmission & Distribution*, volume 31, No 8, Aug (1979).
- [3] N. Fujimoto, E.P. Dick. "Transient Ground Potential Rise in Gas Insulated Substations – Experimental Studies", *IEEE Transactions on Power Apparatus and System*, volume PAS-101, No 10, October (1982).
- [4] G.L. Ford, L.A. Geddes. "Transient Ground Potential Rise in Gas Insulated Substations – Assessment of Shock Hazard", *IEEE Transactions on Power Apparatus and System*, volume 101(10) pp.3620-3629, October (1982).

# Characteristics Analysis of Metal Oxide Arresters in GIS Excited by Very Fast Impulse

Jie Chen\*, Jie Guo, Ai-ci Qiu,

\* School of Electrical Engineering , Xi'an Jiaotong University, Xi'an 710049, China

## Abstract

With the development of the UHV and EHV electric power industry in China, GIS is applied widely. VFTO caused by disconnector operations in GIS may damage the insulation of equipment for its high frequency and great amplitude. As one of the main overvoltage protective equipment, the protection characteristic of surge arresters has received attention widely.

In this paper, a GIS model was set up to simulated the source of very fast impulse. Typical waveforms of current and voltage for MOA was measured and processed in to the frequency domain. Results present that the maximum VFTO of different measurement points in GIS decreased to some extent after installation of MOA. In addition, the VFTO reduction of point DS1 is slightly smaller than point MOA when the MOA was installed at the branch terminal. That is, the inhibition behavior of MOA under very fast impulse has a certain range. Very fast impulse is decreased with MOA in the circuit for both closing and opening operation.

**Keywords:** Metal Oxide Arrester, Very Fast Impulse, Voltage-Current Characteristics, Modelling

## 1 Introduction

In recent years, with the fast development of Ultra-High Voltage (UHV) and Extra-High Voltage (EHV) power system in China, GIS has been widely adopted and applied. The operations of disconnectors in gas insulated switchgears (GIS) will generate very fast transient overvoltage (VFTO) with frequencies ranging from 30kHz to 100 MHz and maximum amplitude up to 2.5 per unit [1- 3]. VFTO may damage the insulation of gas insulated equipment and transformers [4]. Metal oxide surge arrester (surge arrester) is one of the main overvoltage protective equipment in power system, of which the voltage-current characteristic under the voltage pulse with a front time of several non-seconds have been of great concern.

Researchers have done meaningful experiments of metal oxide arrester blocks or surge arresters for lightning impulse. Agreements have already been reached that it is essential to considerate dynamic characteristic in study for LI and other fast-front surges.[4] As the IEC standard suggested, the residual voltage of surge arrester in the conventional model should be increased approximately 5%~10% for overvoltage verification

under lightning impulse voltage (LI) [5].

Also, researchers have done some experiment of metal oxide arrester block under very fast impulse. Schmidt et al investigated the influence of arrester block shape (with or without whole in the center) on the V-I characteristics using a rectangular current impulse with a front time of 20ns [6]. However, the dynamic voltage-current characteristic of arrester block for very fast impulse and the difference of the response characteristics under very fast impulse and LI still need further research.

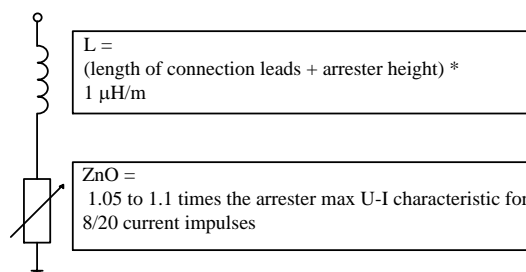


Figure 1. MOA Model for Fast Front Impulse

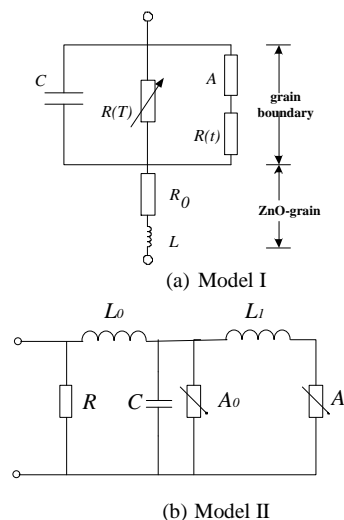


Figure 2. MOA Model for Very Fast Impulse

In this paper, a GIS model was set up to simulated the source of very fast impulse. Typical waveforms of current and voltage for MOA was measured and processed in to the frequency domain. Results present that the maximum VFTO of different measurement points in GIS decreased to some extent after installation of MOA. In addition, the VFTO reduction of point No.1 is slightly smaller than point No. 5 when the MOA was installed at the branch terminal. That is, the protection of MOA under very fast impulse has a certain range. VFTO is decreased with MOA in the circuit for both closing and opening operation.

## 2 GIS Modelling For Very Fast Impulse

The circuit and measuring point for the characteristic analysis of MOA under very fast impulse was presented in Fig.3. Both the closing and opening operation of disconnection No. 2 (DS2) was simulated on the platform. And the GIS MOA was installed at the bus branch terminal shown in Fig.3.

Table 1 presents the equivalent circuit which may be used to represent components. Most of the information included in this table has been taken from Reference [8].

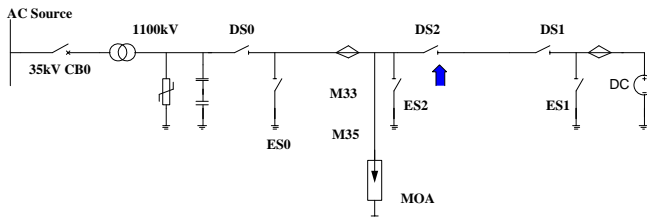


Figure 3. Schematic Diagram of Experimental Installation of Very Fast Impulse

Table 1 Components Modelling for Very Fast Impulse

Components	Equivalent	Notes
Bus duct	Loss-free distributed parameter transmission line	Propagation velocity taking into account the effect of spacers is close to 0.95 of the speed of light in vacuum
Open switch, open breaker	<ul style="list-style-type: none"> <li>The breaker is divided into as many sections as there are interrupters, all connected by the grading capacitors.</li> <li>Two equal lengths of bus connected by a capacitor equivalent to the series combination of all the grading capacitors.</li> </ul>	The parameters of the sections are calculated from the physical dimensions of the breaker.
Open disconnector	A capacitor	
Bushing	A capacitor	
Power transformer (termination)	An equivalent network whose parameters are evaluated from the frequency response of the transformer	

The lossless propagation lines of the table take into account the internal mode (conductor enclosure) and do not take into account the external mode (enclosure-ground), supposing the enclosure perfectly earthed. If transient enclosure voltages have to be considered the external mode has to be taken into account because at high frequencies grounding connections may have significant impedance. Because duration time of this kind of overvoltage is very short, components that influence this kind of overvoltage are those of substations. Outgoing transmission lines act only as surge impedances.

MOV Experimental results show that the arrester block residual voltage under very fast impulse increases approximately from 14.7% to 18.2% than under LI. [7] The capacitance  $C_0$  of arrester block can be affected by the steepness of the applied transient and was measured that the higher the steepness of the applied transient current, the smaller the capacitance  $C_0$  is measured. For air insulation substation usage, the inductance  $L_l$  could take the

value of  $1\mu\text{H/m}$  electrical height of MOV. For gas insulation substation usage, the inductance  $L_l$  could take the value of  $0.33\mu\text{H/m}$  electrical height of MOV.

In this paper, the MOA model was presented in Fig. 4, considering the dynamic voltage-current characteristics of MOV under very fast impulse. In Fig. 4,  $C_s$  is equal to the stray capacitance of MOA, while  $L_s$  expresses the inductance of leading lines. For air insulation substation usage, the inductance  $L_s$  could take the common value of  $1\mu\text{H/m}$  electrical height. And for gas insulation substation usage, the inductance  $L_s$  could take the value of  $0.33\mu\text{H/m}$  electrical height.

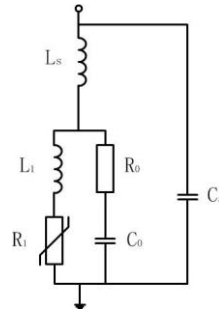


Figure 4 MOA Model for Very Fast Impulse

## 4 Inhibition Characteristic under Very Fast Impulse

The simulation results of inhibition characteristic for MOA under very fast impulse were presented in table 2. The simulation of very fast impulse in GIS with or without MOA was presented in Fig. 5, and the frequency analysis results were presented in Fig.6. The simulation results present that the maximum VFTO of different measurement points in GIS decreased to some extent after installation of MOA. In addition, the VFTO reduction of point DS1 is slightly smaller than point MOA when the MOA was installed at the branch terminal. That is, the inhibition behavior of MOA under VFTO has a certain range. VFTO is decreased with MOA in the circuit for both closing and opening operation.

The typical current waveform of MOA under very fast impulse was presented in Fig. 7. It is clear that the current peak value of MOA is approximately 4.447kA.

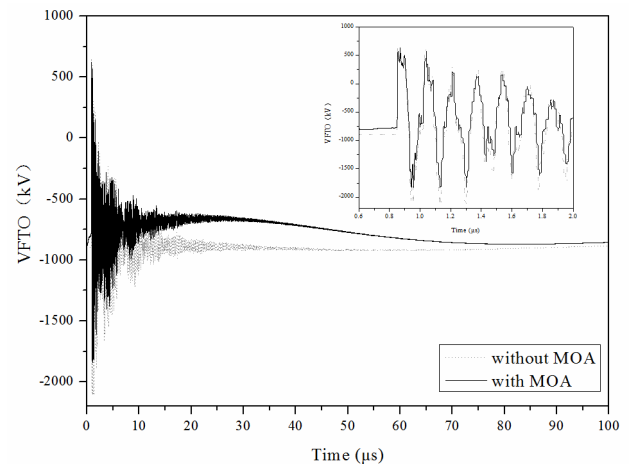


Figure 5. Typical Waveform of MOA for Very Fast Impulse

Table 2 Comparison of Very Fast Impulse with or without MOA

Measuring Point	Without MOA	With MOA	Reduction
MOA	2.351	2.052	12.7%
M33	1.565	1.365	12.8%
M35	2.127	1.872	12.0%
DS2	2.091	1.848	11.6%
DS1	2.352	2.101	10.7%

Compared the frequency spectogram of VFTO with and without MOA at the bus branch terminal, the high frequency in VFTO waveform was decreased to some extent presented in Fig.6. As for the frequency spectogram of the current waveform for MOA, it is a little bit richer than that of the voltage waveform.

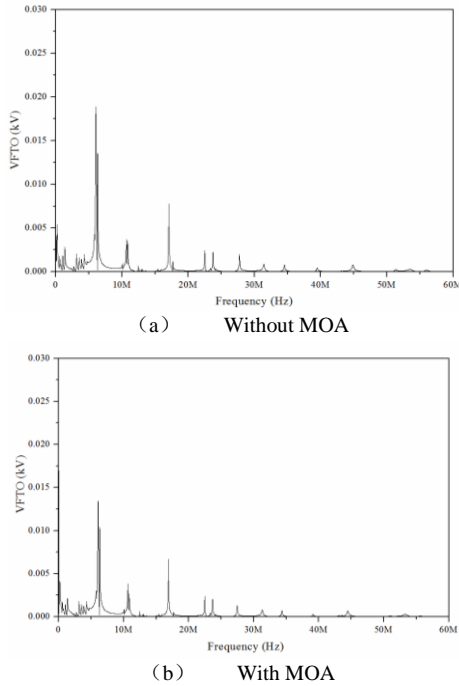


Figure 6. Frequency spectogram of MOA for Very Fast Impulse

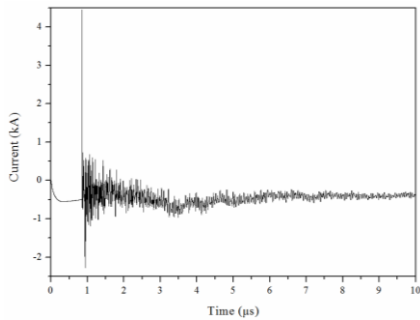


Figure 7. Typical Current Waveform of MOA for Very Fast Impulse

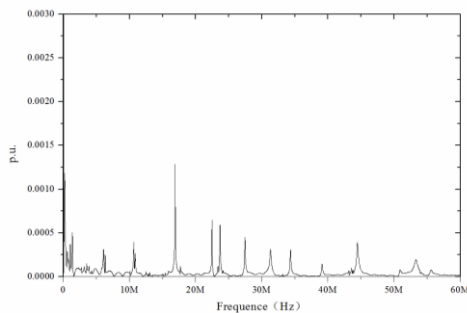


Figure 8. Frequency Spectrogram of Current for MOA (1.0 p.u.= 4.447 kA)

## 5 Conclusion

In this paper, the modeling of metal oxide arrester and the response of MOA when excited by very fast impulse are investigated respectively, based on the experimental result of MOV behavior under very fast impulse. The results could provide not only the basis of very fast impulse simulation and insulation co-ordination but also the theoretical foundation for metal oxide arrester designing in GIS. The main conclusions can be drawn as follows:

- 1) Both simulation and experimental results present that the maximum VFTO of different measurement points in GIS decreased to some extent after installation of MOA.
- 2) In addition, the VFTO reduction of point DS1 is slightly smaller than point MOA when the MOA was installed at the branch terminal. That is, the inhibition behavior of MOA under VFTO has a certain range.
- 3) VFTO is decreased with MOA in the circuit for both closing and opening operation.

## Acknowledgements

Financial support by the National Basic Research Program of China (973 Program) (No. 2011CB209405) is gratefully acknowledged.

## References

- [1] Y. Li, Y. Shang, L. Zhang, et al. "Analysis of very fast transient overvoltage ( VFTO ) from onsite measurements on 800 kV GIS". *IEEE Trans. Dielectrics and Electrical Insulation*, 19(6), pp. 2102-2110. (2012).
- [2] Y. Shu, W. Chen, Z. Li, et al. "Experimental Research on Very-Fast Transient Overvoltage in 1100-kV Gas-Insulated Switchgear". *IEEE Trans. Power Delivery*, 28(1), pp. 458-466. Jan. (2013)
- [3] IEEE Working Group 3.4.11. "Modeling of metal oxide surge arresters". *IEEE Trans. Power Delivery*, 10(2), pp. 778-785. (1995).
- [4] J. A. Martinez, D. W. Durbak. "Parameter determination for modeling systems transients—Part V: surge arresters". *IEEE Trans. Power Delivery*, 20(3), pp. 2073-2078. (2005).
- [5] IEC. IEC60099-4—2006, "Surge arresters – Part 4: Metal-oxide surge arresters without gaps for AC systems"[S]. Gevena, Switzerland: IEC, (2006).
- [6] Z. Li, H. Wang, X. Yan, et al. "Analysis of Test and Model for Metal Oxide Arrester Under Steep-front Wave" (in Chinese). *High Voltage Engineering*, 31 (10), pp. 18-20. (2012).
- [7] J. Chen, J. Guo, A. Qiu, et al. "Experimental Research on V-I Characteristics of Metal Oxide Varistors under Very Fast Wave" (in Chinese) . *Journal of Xi'an Jiaotong University*, 48(10), pp. 54-59. 2014
- [8] "Very fast transient phenomena associated with gas insulated substations", CIGRE paper.33/13-09, (1988)

# Influence of Ground Wires on Ion Flow Field around HVDC Transmission Lines

Bo Zhang, Jinliang He

State Key Lab of Power Systems, Dept. of Electrical Engineering, Tsinghua University, Beijing 100084, China

## Abstract

The electric field is one of the most important factors to be considered in the design of a transmission line. Due to corona, there are ions in the space around HVDC transmission lines, which makes the electric field more complex. The ground wires of the transmission line will enhance the corona on the conductors but will absorb more ions from the space at the same time. In this paper, the ion flow fields are simulated by a numerical method. The influence of the height and the number of the ground wires on the ion flow field around HVDC transmission lines is also discussed.

**Keywords:** Corona, electric field, ions, HVDC Transmission Lines.

## 1 Introduction

There are space charges around HVDC transmission lines due to corona discharge which forms ion flow field. The ion flow field on the ground is one of the special parameters compared with the HVAC transmission lines. The total electric field in the ion flow field is composed of two parts. One is that from the charged transmission line itself. The other is that from the space charge. As the space charge will move with the electric field, the ion flow field is nonlinear.

There have already been some methods to evaluate the ion flow field near the transmission lines, such as the analytic methods, semi-analytical methods, and numerical methods. Sometimes, some methods do not take the ground wires into account. However, on one hand, the ground wires of the transmission line will increase the electric field on the surface of the conductors, and then enhance the corona discharge, which will increase the ions in the space. On the other hand, the ground wires can absorb the space charges. Thus, whether the ground wires will increase or decrease the electric field on the ground is an interesting problem.

In this paper, the ion flow fields are simulated by a numerical method. The influence of the height and the number of the ground wires on the ion flow field around HVDC transmission lines is also discussed. The results would be useful for design of HVDC transmission lines.

## 2 Numerical Method

The equations which rule the bipolar ion field are [1]:

$$\nabla \cdot \mathbf{E} = (\rho^- - \rho^+) / \varepsilon_0 \quad (1)$$

$$\mathbf{J}^+ = \rho^+ (k^+ \mathbf{E} + \mathbf{W}), \quad \mathbf{J}^- = \rho^- (k^- \mathbf{E} - \mathbf{W}), \quad (2)$$

$$\nabla \cdot \mathbf{J}^+ = -R\rho^+ \rho^- / e, \quad \nabla \cdot \mathbf{J}^- = R\rho^+ \rho^- / e, \quad (3)$$

where  $\mathbf{J}$ ,  $\rho$ ,  $k$ ,  $R$ ,  $e$ , and  $\mathbf{W}$  are ion current density, ion density, ion mobility, ion recombination coefficient, electron charge, and wind velocity respectively. Superscripts “+” and “-” indicate that corresponding variables are for positive or negative ion. Because the electric fields and the ions affect each other naturally, iterative method is used. The main process of the method in this paper is as follows:

- 1) Simulating charges in the conductors are calculated based on the applied voltages at conductor surfaces and ground by ignoring the existence of the ions in the air. The region of interest is subdivided in to small triangular elements. The iterative process is started by assigning initial values to  $\rho^+$  and  $\rho^-$  around the grid nodes.
- 2) The electric fields at the middle points of the sides of triangular elements are calculated based on the Gauss’ law.
- 3) The equations for calculating the ion densities around the grid nodes are set up based on the integral form of the current continuity equation.
- 4) Step 2 and step 3 will be repeated until the ion densities obtained in two consecutive iterations differ from each other by amounts smaller than specified tolerances.

The ground wires can be regarded as special conductors on which the potential is zero. And then, they can be taken into account by above method.

## 3 Influence of the Position and the Number of the Ground Wires

In order to obtain the effect of the ground wires on the ion flow field on the ground, the ion flow fields near the  $\pm 800$ -kV

bipolar HVDC transmission line shown in Figure 1 are calculated with the help of the above method. Figure 2 shows the influence of heights of the ground wires on the ion flow fields, and Figure 3 shows the influence of number of the ground wires.

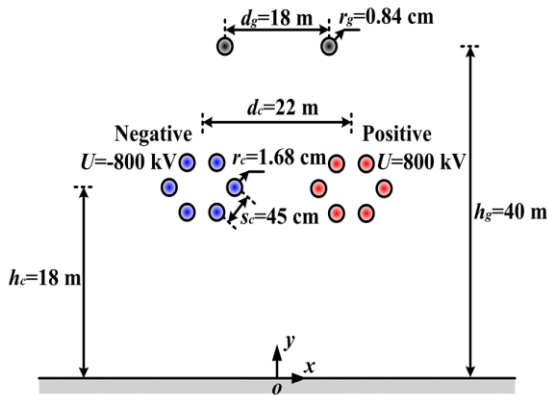
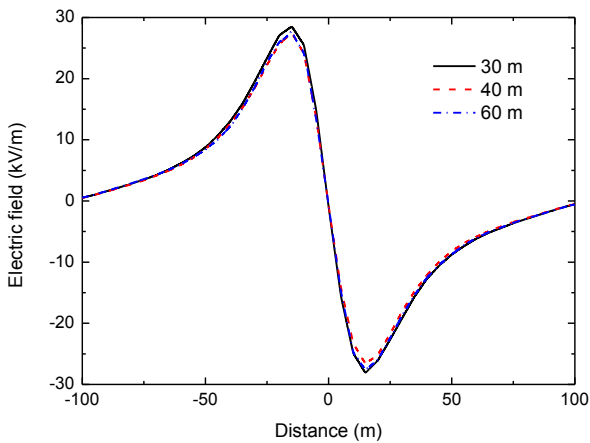
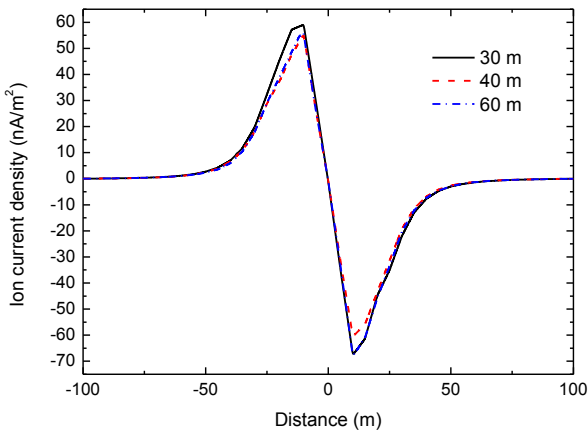


**Figure 1. Cross-section of a ±800-kV bipolar HVDC transmission lines.**

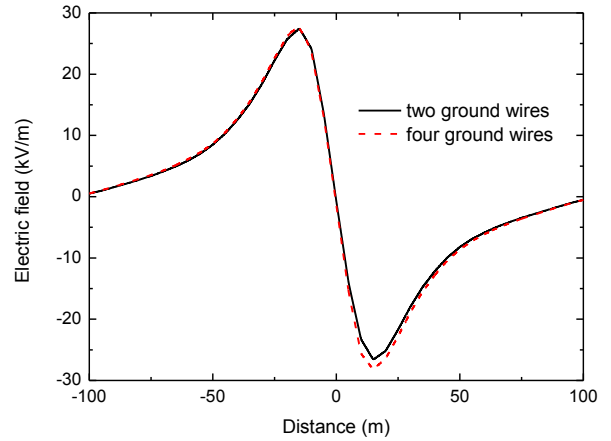


(a) Total electric field

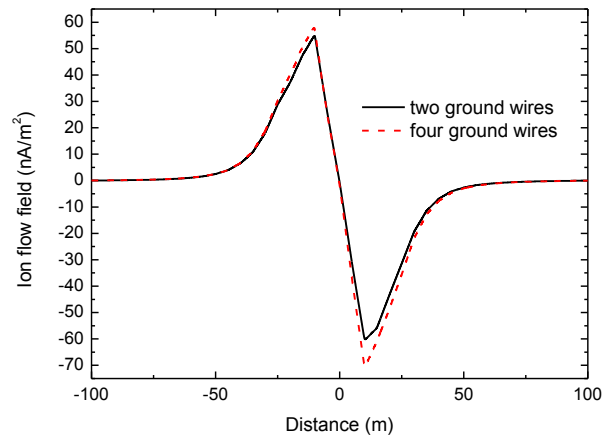


(b) Ion current density

**Figure 2. Influence of position of the Ground Wires on ion flow fields**



(a) Total electric field



(b) Ion current density

**Figure 3. Influence of number of the Ground Wires on ion flow fields**

It can be seen from Figure 2 that on one side when the ground wires are so high that they are far from the conductors, the ion flow fields on the ground is strong, on the other side when the ground wires are so low that they are close to the conductors, the ion flow fields on the ground is also strong. The smallest ion flow field appears when the height of the ground wires is 40 m. This may be because the ground wires of the transmission line will not only enhance the corona on the conductors but will also absorb ions from the space. When the ground wires are close to the conductors, the corona on the conductors will be so strong that the ion flow fields on the ground will be great. When the ground wires are far from the conductors, few ions in the space can be absorbed by the ground wires, they can only move to the ground, which makes the ion flow fields on the ground great also.

From Figure 3 it can be seen that the increasing the number of the ground wires will also enhance the corona on the conductors, and then make the ion flow fields on the ground great.

However, no matter what mechanism the influence is, for the parameters used in the paper, the influence of the ground wires on the ion flow fields on the ground is small.

#### **4. Conclusion**

In this paper, the influence of the height and the number of the ground wires on the ion flow field around HVDC transmission lines is discussed. The ground wires of the transmission line will not only enhance the corona on the conductors but will also absorb ions from the space. However, no matter what mechanism the influence is, the influence of the ground wires on the ion flow fields on the ground is small.

#### **Acknowledgements**

This work was supported in part by the National Natural Science Foundations of China under Grant 51322703, and in part by the Basic Research Program of China National Basic Research Program of China (973 Program) under Grant 2011CB2094-01.

#### **References**

- [1] Bo Zhang, Jinliang He, Rong Zeng, et al., "Calculation of ion flow field under HVdc bipolar transmission lines by integral equation method," *IEEE Transactions on Magnetics*, Vol. 43, No. 4, pp. 1237–1240, July 2007.

# Transient Electric Field Caused by High-voltage Circuit Breaker's Switching Operation

*Xu Kong, Yan-zhao Xie, Qing Liu, Shao-Fei Wang, Xue-mei Sun and Yu-Hao Chen*

*State Key Laboratory of Electrical Insulation and Power Equipment, School of Electrical Engineering, Xi'an Jiaotong University, Xi'an 710049, China (kongxu@stu.xjtu.edu.cn)*

## Abstract

During the switching operation of the high-voltage circuit breaker, transient electric field (E-field) pulses can be generated and radiated outside the breaker. As the breaker's secondary control circuit is vulnerable under the effect of the switching E-field pulse, it is important to study the characteristics of the pulse. So, in this paper, the switching E-field pulses excited in breaker's synthetic test are measured and their basic characteristics are studied and summarized.

**Keywords:** Circuit Breaker; Switching E-field Pulse; Measurement.

## 1 Introduction

Transient electromagnetic pulses during breakers' switching operation have electro-magnetic interference (EMI) effect on secondary electronic equipment [1]-[6]. Many substation faults in China are suspected to be caused by switching electro-magnetic pulses. So, this kind of EMI effect draws more and more attentions. However, it is difficult to do switching E-field pulse measurement in substations and the breakers installed in substations rarely operate. According to IEC standard 62271-101 [7], high-voltage circuit breaker need to do synthetic test to examine its performance. During the synthetic test various failures, even catastrophic failures, have been found due to the generated transient electromagnetic field. And the most frequently malfunction is happened within the breaker's control circuit which can couple with the transient electromagnetic field through its power cord and telecommunication lines. Fig.1 shows a damaged one whose AC power port has breakdown.

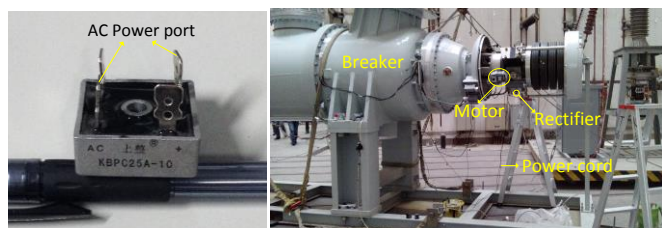


Fig.1 One damaged rectifier and its power cord

So, in this paper, the switching E-field pulses excited in breaker's synthetic test are measured and their basic characteristics are summarized.

## 2 Typical waveform of the switching E-field pulse in synthetic test

Different test method can generate switching E-field pulses with different waveform. Fig.2 shows the schematic of the opening capacitive load test circuit and Fig.3 gives the typical E-field pulse waveform generated by this kind of test. This kind of E-field pulse usually has a high frequency damped oscillation part at the beginning of the pulse and followed by a lower frequency damped oscillation. The dominant resonant frequency is 135 kHz.

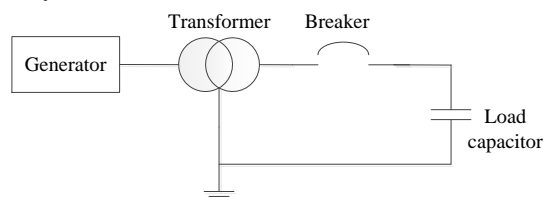


Fig.2 Schematic of the opening capacitive load test circuit

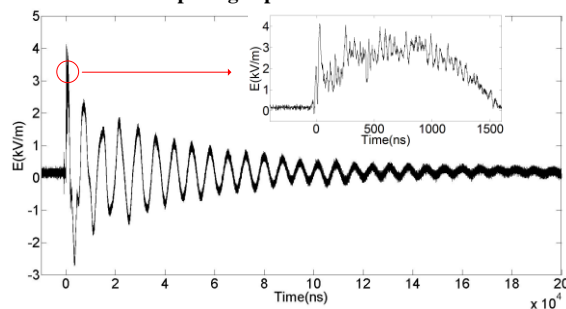
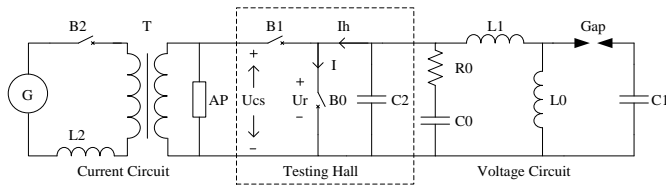


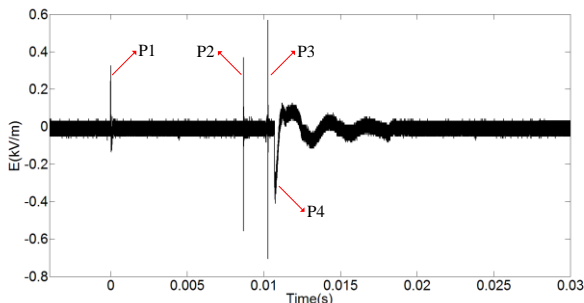
Fig.3 Typical E-field pulse waveform when opening capacitive load

Fig.4 shows the schematic of the synthetic test circuit and Fig.5 gives the typical E-field pulse waveform generated by this kind of test. Each test can generate four pulses  $P_1 \sim P_4$ .  $P_1$  is caused by application of arc prolonging circuit  $AP$ .  $P_2$  is caused by switching of voltage circuit.  $P_3$  is caused by extinguishing of the arcs in  $B_1$ .  $P_4$  is caused by extinguishing of the arcs in  $B_0$ .



**Fig.4 Schematic of the synthetic test circuit**

- $G$  – Short circuit generator
- $T$  – Transformer
- $B_0$  – Test breaker
- $B_1$  – Auxiliary breaker
- $B_2$  – Protective breaker
- $AP$  – Arc prolonging circuit
- $Gap$  – Igniting gap
- $R_0$  – Damping resistance
- $L$  – Inductance
- $C$  – Capacitance



**Fig.5 Typical E-field pulse waveform of synthetic test**

The detailed characteristics of these four pulses including duration time, amplitude and waveform feature are listed in Table I.

**TABLE I  
DETAILED CHARACTERISTICS OF THESE FOUR PULSES**

Pulse	Duration time	Amplitude	Waveform feature
$P_1$	$150 \mu S$	0.33 kV/m	Approximately positive polarity pulse with fast rising edge and relatively slow falling edge
$P_2$	$30 \mu S$	0.57 kV/m	Bipolar pulse with high frequency damped oscillation
$P_3$	$30 \mu S$	0.78 kV/m	Bipolar pulse with high frequency damped oscillation
$P_4$	$4 ms$	0.42 kV/m	Approximately negative polarity pulse with fast rising edge and slow falling edge followed by very low frequency damped oscillation

### 3 Basic characteristic of the switching E-field pulse in synthetic test

The transient E-field pulses during switching operation in synthetic test depends on many factors including the breaker's mechanical structure, synthetic test circuit component values, length of the wire, power-frequency recovery voltage and interrupting current. The transient E-field pulse usually contains first a period of fast rising edge or high-frequency oscillation pulses, followed by a later period of slow falling edge or low-frequency resonance waveform. The maximum amplitude of each test is illustrated in table II.

**TABEL II  
TRANSIENT E-FIELD PULSES AMPLITUDE**

Photo					
V	208 kV	189 kV	280 kV	208 kV	310 kV
I	252 A	50 kA	38 kA	45 A	63 kA
E-field Amplitude	4 kV/m	25 kV/m	0.75 kV/m	14 kV/m	0.78 kV/m

### 4 Conclusion

By doing measurement experiment, it is found that the switching operation in synthetic test can generate E-field pulses outside the breaker. The wave feature of the E-field pulse changed remarkably with test configuration. Generally speaking, the transient E-field pulse contains first a period of fast rising edge or high-frequency oscillation pulses, followed by a later period of slow falling edge or low-frequency resonance waveform. One test can generate multiple pulses and their wave characteristics are different from each other.

In order to provide a standard waveform of the switching E-field pulse, we will do more measurement experiment in the future and summarize the statistic characteristics of the switching E-field pulse.

### References

- [1] M.M. Rao, M.J. Thomas and B.P. Singh, "Transients Induced on Control Cables and Secondary Circuit of Instrument Transformers in a GIS During Switching Operations," *IEEE Trans. Power Del.*, vol. 22, no. 3, pp. 1505-1513, July. 2007.
- [2] Amir Mansour Mire and Zlatan Stojkovic, "Transient electromagnetic phenomena in the secondary circuits of voltage and current

- transformers in GIS (measurements and calculations)," *IEEE Trans. Power Del.*, vol. 16, no. 4, pp. 571-575, Oct. 2001.
- [3] Qi Huang, Xiao-hua Wang, Wei Zhen and Philip W. T. Pong, "Broadband point measurement of transient magnetic interference in substations with magnetoresistive sensors," *IEEE Trans. Magn.*, vol. 50, no. 7, pp. 1-5, July. 2014.
- [4] Jin-liang He, Zhan-qing Yu, Rong Zeng, Bo Zhang Shui-ming Chen and Jun Hu, "Power-Frequency Voltage Withstand Characteristics of Insulations of Substation Secondary Systems," *IEEE Trans. Power Del.*, vol. 25, no. 2, pp. 734-746, Apr. 2010.
- [5] Y. V. Parfenov, L. N. Zdoukhov, A. V. Shurupov and A. V. Kozlov, "Research of Flashover of Power Line Insulators Due to High-Voltage Pulses With Power ON and Power OFF," *IEEE Trans. Electromagn. Compat.*, vol. 55, no. 3, pp. 467-474, June. 2013.
- [6] C.M. Wiggins and S.E. Wright, "Switching transient fields in substations", *IEEE Trans. Power Del.*, vol. 6, no. 2, pp. 591-600, Apr. 1991.
- [7] *High-voltage switchgear and controlgear – Part 101: Synthetic testing*, IEC Standard 62271-101, 2012.

# Characterization of Limiters for HPM and UWB Front-Door Protection

*T Nilsson\**, *M Bäckström†*

\* Saab Aeronautics, Sweden, [tony.nilsson@saabgroup.com](mailto:tony.nilsson@saabgroup.com) † Saab Aeronautics, Sweden, [mats.backstrom@saabgroup.com](mailto:mats.backstrom@saabgroup.com)

## Abstract

An extensive study of front-door protection devices i.e. limiters has been made. This paper contains results from both HPM- and UWB-measurements done on various limiters, in order to characterize them. The measurements show that some limiters are not suitable as protection against HPM- and UWB-pulses. The limiters that were found to provide the best protection are limiters based on diode technologies. PIN- and Schottky-diodes generally shows very good performance and they fulfil many parameters that have been set by FOI. To obtain a full protection it is presumably necessary to use two or more limiters in combination, which complement each other.

**Keywords:** HPM, UWB, Limiter, Front-door protection.

## 1 Introduction

The threat from high power microwave (HPM) weapons is steadily gaining importance and has since a couple of years entered MIL-STD 464C. Both civilian and military electronic equipment are vulnerable to this threat. A typical component that needs to be protected is a front-end receiver.

Depending on the level of threat and the damage level of the receiver different types of protection circuits can be used to limit the power delivered to the sensitive circuitry. The growing use of array antennas (AESA) has also increased the demands on miniaturization of the protection devices. We present pulsed power measurements on several types of commercial limiters and ESD/NEMP, protection devices as well as in-house designed MMIC limiter circuits, see [3]. The study was done at The Swedish Defence Research Agency (FOI), during the years 2003 to 2006, see [1] and [2].

## 2 HPM and UWB Measurement Setups

Two different measurements setups were used for HPM- and UWB-measurements respectively, in order to characterize the protection devices.

The HPM- setup is based on synthesized sweeper, which is triggered by a pulse generator. The microwave pulse is then propagated through internal switches before it reaches one of the four power amplifiers and then injected in the device under test (DUT). Injected, transmitted and reflected power is measured. The HPM-measurements was typically done at the

frequencies of 2.4 or 6.0 GHz. The PRF (Pulse Repetition Frequency) was 1 kHz, the rise time and pulse width was 10 ns and 100 ns respectively.

The UWB-measurements setup consists of a pulse source capable of delivering pulses (uni-polar) up to 400 Volt with a rise time of about 300 ps and a pulse width of about 1 ns into a 50Ω load. Special attenuators are used before and after the DUT to regulate the power delivered to the DUT. A fast sampling oscilloscope is used to measure injected and transmitted pulse.

## 3 Test Objects

A large variety of different protection devices are available on the market. The tested devices presented in this paper are samples of what was available at the time during 2003 to 2006. Many different technologies have been investigated, of which some are not intended to be used for HPM- or UWB-protections. The technologies range from PCB mounted protection devices such metal oxide varistors (MOV) and gas discharge tubes (GDT) to on-chip and coaxially mounted diode based devices. Some examples are seen in Fig. 1.



**Figure 1. Integrated circuit microwave limiter (to the left) and coaxially mounted limiter (to the right) [1].**

About ten different types of protection devices were investigated. Also the susceptibility of receiver circuits was also investigated, see [4]. Results from some of the protection devices are presented here. During the last ten years, advances in the development of protection devices have been made, but, to our knowledge, not many results have been published. Advances in development of Gallium Nitride (GaN) semiconductors for microwave application have also decreased the susceptibility of front-end components, which can be used in AESA systems. This might have changed some limiter requirements.

## 4 Measurement Results. Examples

Both HPM and UWB measurements were done in order to characterize different parameters. Example results, for one and the same diode limiter, are seen in Fig.2 and Fig.3.

The HPM-measurements was done starting at a low power levels and was step wised increased, with increments of 1 dB to 33 dBm. The pluses were injected with bursts of 32 pulses, with 1 kHz PRF.

UWB measurements are useful for characterizing the general response to fast pulses and to investigate the possible spike leakage. Measurements were done starting at low levels, and were step wised increased by changing to a lower attenuator level before the DUT. In the measurements a 33 Hz PRF was used.

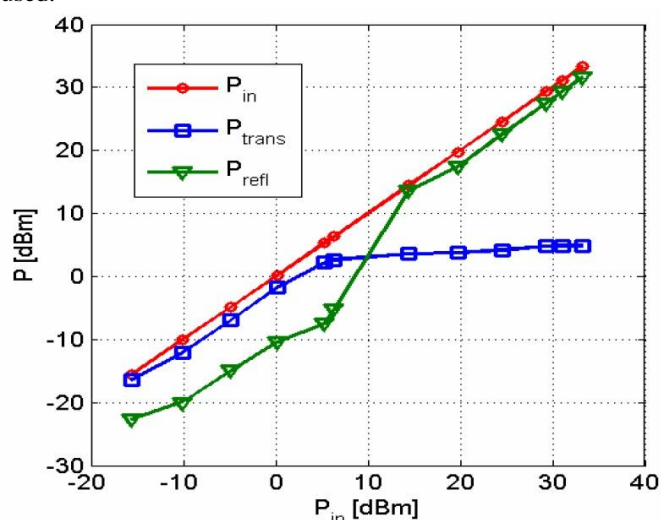


Figure 2. Coaxial diode limiter subjected to HPM pulses, input, transmitted and reflected power [1].

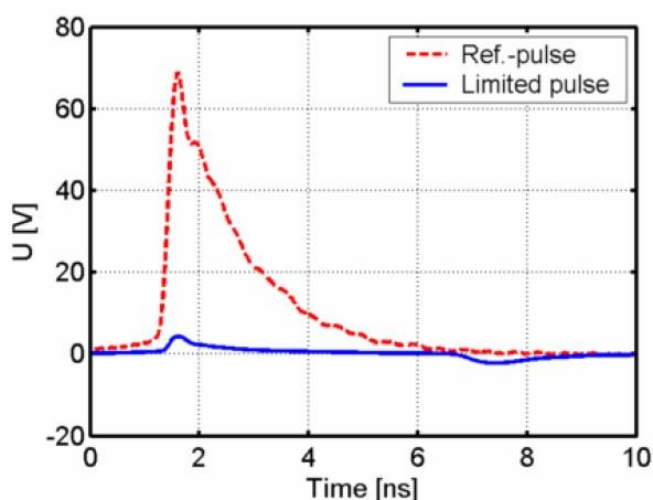


Figure 3. Coaxial diode limiter subjected to UWB pulse, the dashed line is the injected pulse (Ref. pulse) and the solid line it the transmitted pulse (limited pulse) [1].

## 5 Conclusions

The results show that some of the tested devices are not suitable as front-door protection against HPM- and UWB-pulses. Other devices have showed to provide quit good protection against both HPM- and UWB-pulses.

The diode-based limiters have in general showed a good capability to protect from both HPM- and UWB-pulses. They are in fast acting devices with short response - and recovery-time. They are also able to withstand moderate CW and peak pulse power/energy levels. They also introduce relatively small insertion loss and are able to work for broad frequency bands, up to tens of GHz. The diode limiters are also small in size, which makes them an attractive alternative for integration with array antennas and other applications where the size is critical.

If the power/energy levels are higher, the diode limiters might suffer burnout, due to their lack of high power/energy handling capabilities. In this case other types of protection devices are required, which can handle higher power/energy levels. GDT and MOV are protection devices which have better power/energy handling capabilities. Measurements on these devices have however showed rather poor results. The results from the GDT and the MOV showed only a small response to the input pulses, but they might have been triggered if the input power levels were higher.

A combination of different technologies integrated into one limiter, i.e. a hybrid-circuit would be ideal. The combination of two different technologies, where the first stage takes care of high power/energy pulses and were a second stage the cleans up the remaining power/energy and the fast transients of the pulses. For high frequency limiters it is also important to have a low capacitance in order to minimize the insertion loss and noise figure, otherwise the overall system performance will be seriously degraded.

## Acknowledgements

This work was financially supported by The Swedish Defence Research Agency (FOI).

## References

- [1] T. Nilsson, "Investigation of Limiters For HPM and UWB Front-door Protection", LITH-ISY-EX--06/3716--SE, (2006).
- [2] T. Nilsson, R. Jonsson, "Investigation of Limiters for HPM Front Door Protection", Book of Abstracts EuroEM 2004, pp. 29-30, (2004).
- [3] T. Nilsson, R. Jonsson, "HPM Front-door Coupling and Protections Progress Report 2003", FOI-R--1020--SE, (2003).
- [4] T. Nilsson and R. Jonsson, "Investigation of HPM Front-door Protection Devices and Component Susceptibility", FOI-R--1772--SE, (2005).

# Low Insertion Loss Energy Sensitive Bandpass Filter to Protect Ku-Band Receivers from HPEM Threats

W A Arriola\*, T H Jang<sup>†</sup>, J Y Ahn\*, and I S Kim\*

\*Kyung Hee University, South Korea and I S Kim(ihnikim@khu.ac.kr), <sup>†</sup>Korea Testing Laboratory, South Korea and T H Jang(thjang1@naver.com)

## Abstract

This paper introduces a low insertion loss (IL) energy sensitive bandpass filter (ESBPF) to protect Ku-band receivers from high power electromagnetic (HPEM) threats. Two anti-parallel Schottky Barrier diodes mounted on two layered split ring resonator (CSRR) structures in a WR-75 waveguide function as an ESBPF. The ESBPF operates as a BPF at a power level below the maximum permissible power level (MPPL) of the LNAs. The ESBPF provides a better IL compared with those of the previous limiters. 0.39 dB IL improvement from 1.27 dB to 0.88 dB has been measured at the power level lower than -27 dBm for the frequency range from 12.25 GHz to 12.75 GHz. Furthermore at the centre frequency of 12.5 GHz, 0.723dB IL has been obtained. At the power level higher than -2 dBm, the circuit provides different levels of attenuation depending on the input power within the identical frequency band. The ILs have been measured up to 5 dBm, which provides isolation characteristic larger than -7.5 dB.

**Keywords:** ESBPF, Energy Sensitive Bandpass Filter, HPEM.

## 1. Introduction

Front door coupling of high power electromagnetic signal at high frequencies above 10 GHz is one of the dangerous factors for receivers using waveguide structures since a very sensitive LNAs are located right after antennas. The waveguide transmission media are usually used due to its low insertion loss property compared with another transmission media in terms of conduction of weak information signals. However the waveguide transmission media can afford to couple very high power signals. Any protective device has not been used since any insertion loss (IL) of the protective device can deteriorate receiver sensitivity. Thus, a low insertion loss device to protect receivers, especially in front of LNAs, has been required.

In [1], an energy sensitive bandpass filter (ESBPF) in waveguide was introduced. Its IL was 1.27 dB which could affect the sensitivities of LNAs seriously. An ESBPF with a very low insertion loss has to be designed. Several research works on waveguide filter using complementary split ring resonator (CSRR) structures have been published [2]-[5]. In

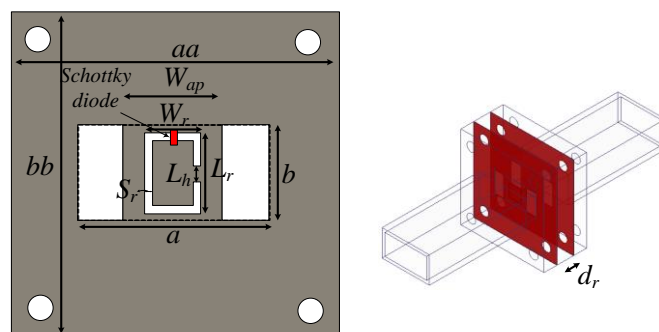


Figure 1. Energy sensitive bandpass filter (ESBPF) structure. (a) Circuit structure on a layer. (b) Two layer structure.  $aa = bb = 38\text{mm}$ ,  $a = 19.05\text{ mm}$  and  $b = 9.525\text{ mm}$ .

[2], the CSRR structure was analysed for planar circuit applications in 2005. At the almost same time, the identical structure of the CSRR analysed by [3] was tried to show some possibility for waveguide filter applications based on an aluminium sheet of 1.5 mm thickness. 5dB insertion loss and 0.73% fractional bandwidth were measured. In [4], various structures of split ring resonators and CSRRs had been investigated for waveguide band pass/stop filters by only simulation and the circular structure showed the lowest insertion loss among all the simulated ones.

A narrowband waveguide BPF using an array of a rectangular CSRR like frequency selective surface (FSS) was introduced by [5] where the circuit changed the resonant frequency due to the addition of capacitances across the upper and bottom slot gaps and no bias or energy sensitive characteristics were presented. Furthermore, important design and measurement information were not included. After this work, CSRR was used for FSS applications in [6]. The structure presented by [6] showed switching characteristics based on the application of bias to PIN diodes mounted across the upper slot gap of the periodic CSRR.

In this paper, to obtain a low insertion loss characteristic, a low insertion loss bandpass filter structure has been developed based on complementary split ring resonator (CSRR) and a self-activated antiparallel Schottky Barrier diodes have been mounted on the filter circuit to provide energy sensitive properties.

In Section 2, a CSRR with low loss characteristic will be introduced with an aluminium sheet in a WR-75 waveguide. In Section 3, the resonator will be modified to add energy

sensitive characteristics as a bandpass limiter with low IL and high isolation suitable to protect a Ku-band LNAs in microwave receivers. An ESBPF with a low loss resonator will be optimized, simulated, fabricated, and measured to verify the characteristics of our proposed design. In Section 4 the conclusion of this work is presented.

## 2. Low insertion loss waveguide ESBPF

To use the CSRR as an efficient resonator for waveguide filter element in front of LNA, IL must be minimized. We propose the structure in Fig. 1 as a low insertion loss ESBPF. And a bridge is placed at the center of the right vertical slot on the CSRR to hold the island inside a square slot. Antiparallel Schottky Barrier diodes have been mounted at the center of the upper slot of the CSRR to provide switching characteristics as shown in Fig. 1. For a fast switching, the MADS – 101318 - 1197HP: anti-parallel Schottky Barrier diode model has been used.

Fig. 1(a) shows the CSRR structure. To study the IL of the resonator, the structure has been simulated by HFSS with the dimensions of  $L_r = 8.7\text{mm}$ ,  $W_r = 5.9\text{mm}$ ,  $S_r = 0.4\text{mm}$ ,  $L_h = 1.5\text{mm}$  and  $W_{ap} = 10\text{mm}$ . The simulated S-parameters for the single layer of the CSRR without diodes are shown in Fig. 2

The S-parameters of the structure shown in Fig. 1 have been simulated by using the lumped equivalent circuit model of the diode shown in Fig. 3(a) and by using the equivalent model for HFSS shown in Fig. 3(b). The simulation results are shown in Fig. 4. The dimensions of the structure were optimized to include the diode function. The dimensions adopted are,  $L_r = W_r = 5.9\text{mm}$ ,  $S_r = 0.3\text{mm}$ ,  $L_h = 1.5\text{mm}$ ,  $d_r = 7.35\text{mm}$ , and  $W_{ap} = 10\text{mm}$ .

## 3. Measurement results

To verify the previous simulations, an ESBPF with the center frequency  $f_0 = 12.5\text{GHz}$  has been fabricated. Two layers have been used and an optimized distance of  $d_r = 5.47\text{mm}$  between the two is shown in Fig. 1(b). The dimensions were identical to the ones simulated in Section II for the ESBPF.

The fabricated circuit is shown in Fig. 5. The measured S-parameters are shown in Fig. 6 for different power levels. The measurement results in Fig. 6 shows that while the transmission characteristics are changed by different input power levels between  $-27\text{dBm}$  and  $5\text{dBm}$ , the filtering characteristics are not changed very much. The dynamic range of the ESBPF is shown in Fig. 7.

For the ESBPF using two layers, the measurement result show an insertion loss lower than  $0.88\text{dB}$  for the frequency band from  $12.25\text{GHz}$  to  $12.75\text{GHz}$ .

## 4 Conclusion

In this paper a new circuit design reducing IL of the ESBPF based on antiparallel configuration of Schottky Barrier diodes

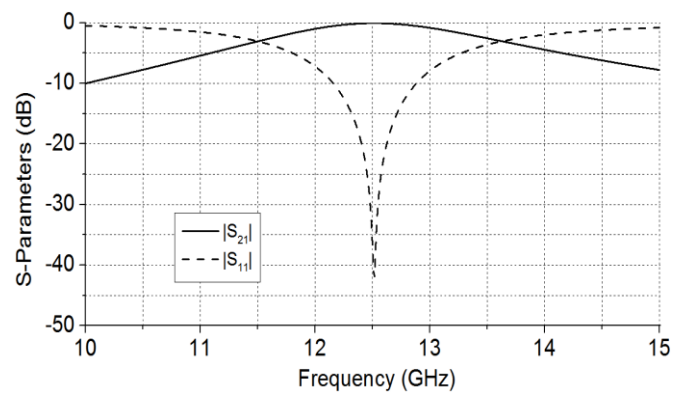


Figure 2. Simulation results for a single layer CSRR without diodes at the center frequency of 12.5 GHz.

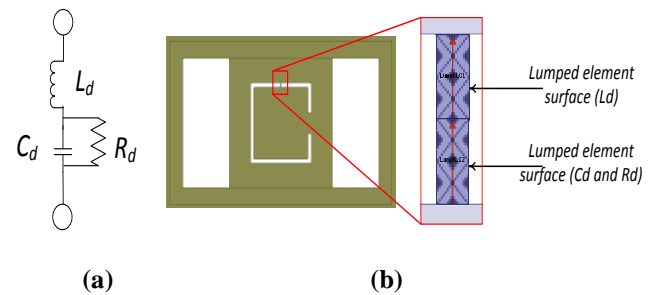


Figure 3. Equivalent circuit models for the diode. (a) Lumped element circuit model. (b) Lumped element circuit model used for HFSS.  $C_d = 0.085\text{pF}$ ,  $L_d = 0.7\text{nH}$  and  $R_d = 3\text{M}\Omega$ .

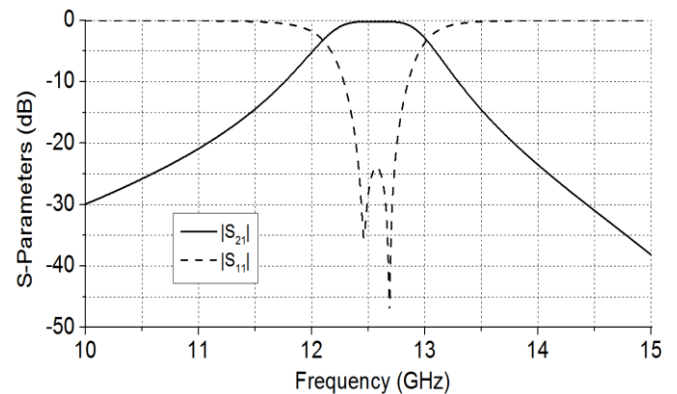
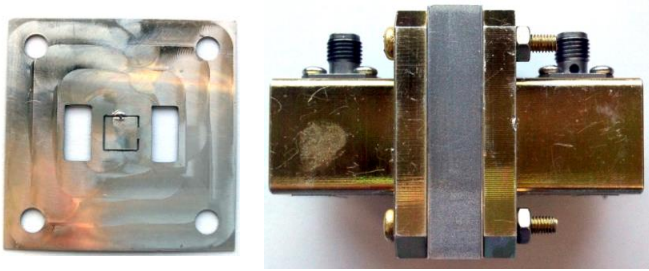
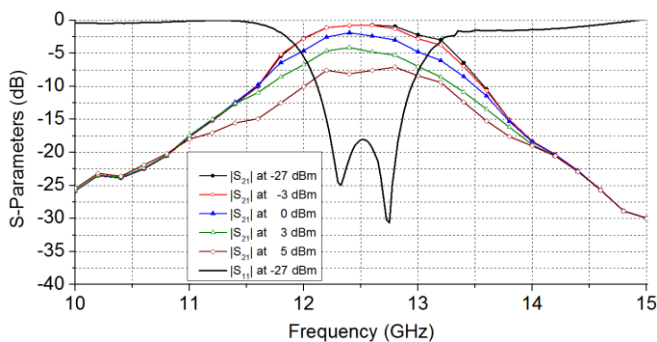


Figure 4. Simulation results for a two layered CSRR with diodes mounted as shown in Fig. 1(a) based on the model shown in Fig. 3(b).

has been introduced to protect Ku-band microwave receivers from HPEM and to reduce the out of band noise/interference. The CSRR circuit has been modified to mount the diode to



**Figure 5. Photos for the fabricated two layers ESBPF. (a) ESBPF layer. (b) Two layers ESBPF.**



**Figure 6. Measurement results for the attenuation and filter characteristics of the ESBPF under different power levels.**

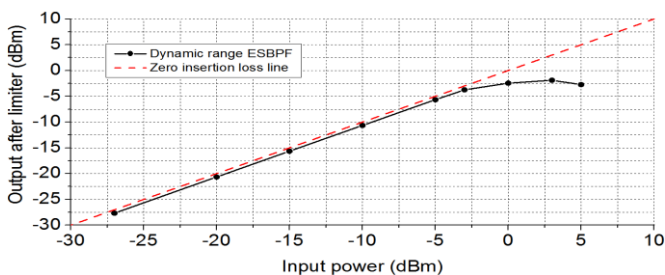


**Figure 7. Measurement results for the dynamic range of the ESBPF.**

provide energy sensitive characteristics. And to increase power rejection and selectivity, another layer has been added. The bridge connected to the internal conductor island to the outer conductor plane did not give any influence for the self activation of the diodes. This work has achieved bandpass characteristics with low ILs at input power levels below -3 dBm, and limiting 7.5 dB at 5 dBm input signals to protect Ku-band LNAs. Also variable attenuation characteristics have been shown at different input power levels.

## References

- [1] T. H. Jang, S. I. Yang, W. A. Arriola, K. H. Kim, J. W. Lee, and I. S. Kim "Energy sensitive bandpass filter to protect Ku-band LNAs from HPEM threats", *Microwave and Wireless Components Letters*, Vol. 25, No. 1, pp.67-69, January 2015.
- [2] J. D. Baena, J. Bonache, F. Martin, and R. M. Sillero, "Equivalent-circuit models for split-ring resonators and complementary split-ring resonators coupled to planar transmissions lines", *IEEE Microwave Theory and Tech.*, Vol. 53, No. 4, pp. 1451-1461, April 2005.
- [3] N. Ortiz, J. D. Baena, M. Berute, F. Falcone. M. A. G. Laso, T. Lopetegi, R. Marques, F. Martin, J. G. Garcia, and M. Sorolla "Complementary split-ring resonator for compact waveguide filter design", *Microwave and Optical Technology Letters*, Vol. 46, No. 1, pp.88-92, July 2005.
- [4] A. Bage, and S. Das, "Studies of some non conventional split ring and complementary split ring resonators for waveguide band stop & band pass filter application", *2013 IEEE Int. Microwave and Photonics Conference*, pp. 1-5, December 2013.
- [5] S. M. Amjadi, and M. Soleimani, "Narrow band-pass waveguide filter using frequency selective surfaces loaded with surface mount capacitors", *2007 IEEE International Conference on Electromagnetics in Advanced Applications*, pp.173-176, September 2007.
- [6] K. Chang, S. I. Kwak, and Y. J. Yoon, "Equivalent circuit modeling of active frequency selective surfaces", *2008 IEEE Radio and Wireless Symposium*, pp. 663-666, January 2008.

# Reliable HEMP Protective Devices for the Power Line

Joon-Hyuck Kwon<sup>\*†</sup>, Ki-Hwan Song<sup>\*</sup>, Jong-Gwan Yook<sup>†</sup>

<sup>\*</sup>Agency for Defense Development, Republic of KOREA,

<sup>†</sup>Yonsei University, Republic of KOREA

jhkwon@add.re.kr, yosonggi@add.re.kr, jgyook@yonsei.ac.kr

## Abstract

This paper introduces the reliable HEMP protective devices for the AC power line. Two types of devices are designed, the first device utilizes CM inductor-based circuit and the second device utilizes DM inductor-based circuit. The results of reliability test and MIL-188-125-1 PCI test for the proposed devices are discussed.

**Keywords:** Power line, Protective device, Reliability, PCI.

## 1 Introduction

High-altitude electromagnetic pulse (HEMP) is generated by a nuclear burst above the atmosphere which produces coverage over large areas and can affect electric/electronic systems. The HEMP-induced current may flow into internal portions of a system by the direct conduction on the electrical wiring which penetrates the external structure, and can damage PCB boards and electric circuits in a system. To protect equipment and/or systems against the HEMP-induced current, protective devices installed at the point of entry (POE) must limit residual current and transient pulse energy. In general, the pulsed current injection (PCI) test based on MIL-STD-188-125-1/2 is carried out to evaluate performances of the protective devices. This paper introduces two types of reliable HEMP protective devices for the power line. The first one is the device utilizing common mode (CM) inductor-based circuit and the second one is the device utilizing the differential mode (DM) inductor-based circuit. The proposed devices comply with the reliability standard as well as MIL-STD-188-125-1 PCI standard [1-2].

## 2 Protective circuit design

In this paper, two types of protective devices for the AC power line are introduced.

### 2.1 CM inductor circuit-based device

CM inductor arranges the lines to share the core to remove common mode signals. It makes high inductance value so that low value capacitors can be mounted in the device. As the result, the size of the device is smaller than the DM inductor circuit-based device [3]. However, because all the lines share one inductor core, it is hard to apply this type of device to high current applications. So this device is suitable for the

low current power line. Figure 1 shows the circuit diagram of the proposed protective device based on the CM inductor to apply low current power line (< 100A).

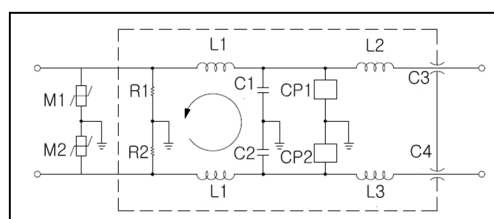


**Figure 1. Circuit diagram of the protective device based on CM inductor.**

### 2.2 DM inductor circuit-based device

Each line has individual inductor cores in this device. Also higher capacitors are installed to have higher insertion loss characteristics. Generally, the size of the DM inductor-based device is larger than that of CM inductor-based device [3]. But manufacturing DM inductor-based device, especially in the high current applications, is simpler than that of CM inductor-based device because each line in the DM inductor circuit is independent to be made. Figure 2 shows the circuit diagram of the proposed protective device based on DM inductor elements for the high current power line application ( $\geq 100A$ ).

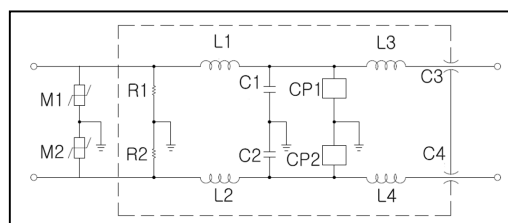


**Figure zing 2. Circuit diagram of the protective device based on DM inductors.**

### 2.3 Considerations for the reliability

Protective circuits and components were designed to be satisfied with the PCI test criteria on the short pulse and intermediate pulse in MIL-STD-188-125-1. Moreover, the reliability standard was applied to the proposed devices to have the proper performances even under the rough conditions [2].

This standard classifies three categories consisting of the

performance, environment, and life time test. Each category is presented in Table 1 in detail. Only the case that five samples of each device have no failure is in conformity with the reliability criteria.

Table 1: Test conditions and criteria for the power line protective devices [2].

Categories	Test items	Test conditions	Pass/Fail criteria
Performance test	PCI	MIL-STD-188-125-1	MIL-STD-188-125-1
	Insertion loss	MIL-STD-220C	Refer Figure 3 (red line)
	Voltage drop	50% of maximum load or 100A, whichever is lower	$\leq 2\%$ @ rated current $\leq 50A$ device, $\leq 3\%$ @ rated current 100-200A device
	Leakage current	Rated Voltage	$< 1.8A$ @ rated current $\leq 50A$ device $< 6A$ @ rated current 100-200A device
Environment test	Low Temp.	Storage : $-40^{\circ}C$ , 16hr Operating: $-40^{\circ}C$ , 2hr	During testing : voltage drop and rated current
	High Temp.	Storage : $+85^{\circ}C$ , 16hr Operating: $+50^{\circ}C$ , 2hr	After testing : PCI, insertion loss and voltage drop
	Thermal Shock	$-40^{\circ}C \sim +85^{\circ}C$ , 5 cycles	After testing : PCI, insertion loss and voltage drop
	Overload	140% of rated current, 15 minute	
Life time test	Accelerated-life	$(85 \pm 2)^{\circ}C$ , 1000hr	After testing : PCI, insertion loss and voltage drop
	Pulse repetition	Short pulse : 2,500A, 40 pulses Intermediate pulse: 250A, 203 pulses	

The components such as GDTs, MOVs, inductors, and capacitors in the protective device were selected and designed to guarantee those performances under reliability test conditions. The MTBF (Mean Time Between Failure) for the devices was calculated at 228,000 hours.

### 3 Test results and conclusion

Two types of HEMP protective devices (CM inductor circuit for 50A, DM inductor circuit for 200A) were evaluated in accordance with PCI and relevant reliability standard. The test results of PCI and performance are shown in Table 2 and those of insertion loss are shown in Figure 3 and 4, respectively. It is shown that proposed protective devices comply with PCI and performance requirements. Also proposed devices were fully satisfied with all environment and life time criteria.

Table 2: Typical PCI and performance test results

Test items	Norms	Criteria	Measured values
PCI Short pulse	Peak current(A)	$\leq 10$	$\leq 1.95$ @50A device $\leq 2.42$ @200A device
	Peak rate of rise (A/s)	$\leq 1 \times 10^7$	$\leq 6.45 \times 10^4$ @50A device $\leq 1.20 \times 10^5$ @200A device
	Root action (A- $\sqrt{s}$ )	$\leq 1.6 \times 10^{-1}$	$\leq 1.58 \times 10^{-2}$ @50A device $\leq 2.05 \times 10^{-2}$ @200A device
PCI Intermediate pulse	No damage or performance degradation (Measured MOV voltage before testing : 558~682V)	No damage or performance degradation (MOV voltage after testing : 654~665V)	
Voltage drop	$\leq 5V$ @ 50A device $\leq 7.5V$ @ 200A device	$\leq 0.3V$ @ 50A device $\leq 1.4V$ @ 200A device	
Leakage current	$\leq 1.8A$ @ 50A device $\leq 6A$ @ 200A device	$\leq 1.47A$ @ 50A device $\leq 1.45A$ @ 200A device	

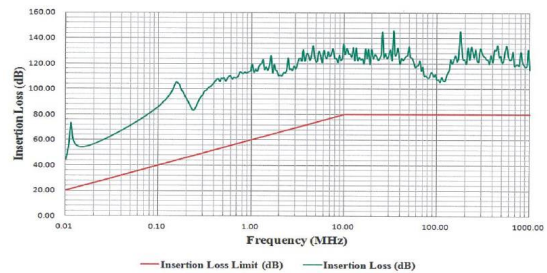


Figure 3. Measured insertion loss for 50A device.

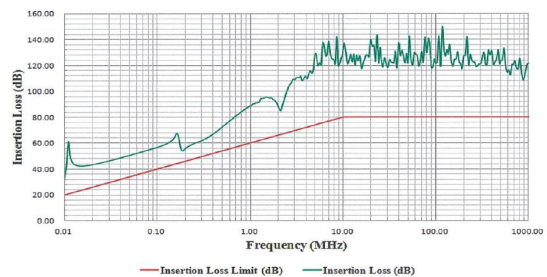


Figure 4. Measured insertion loss for 200A device.

### References

- [1] MIL-STD-188-125-1, "High-altitude electromagnetic pulse (HEMP) protection for ground-based C4I facilities performing critical, time urgent missions, Part 1, Fixed facilities", 17 July 1998.
- [2] RS-KTL-2012-0018 "Reliability assessment specification for HEMP protection filter", Korea Testing Laboratory, 28 December 2012.
- [3] www.incompliancemag.com, "Facility power filters: Symmetric vs. asymmetric performance", September 2013.

# Key Design Technologies of RF Front-end Protection Module with Ultra-low Limited Output Power

Dongdong Wang<sup>1,2</sup>, Lan Gao<sup>2</sup>, Shengquan Zheng<sup>1,2</sup>, Feng Deng<sup>1,2</sup>, and Dongyun Hou<sup>1,2</sup>

<sup>1</sup>Science and Technology on Electromagnetic Compatibility Laboratory

<sup>2</sup>China Ship Development and Design Center

Wuhan, China

dongdong\_wang@me.com

**Abstract**—Existing technologies employed by RF limiters played the role of preventing physical damage to RF front-end circuits caused by HIRF and EMP radiation. However, saturation of the receiving channel in the presence of HIRF or EMP was always ignored and few researches were made. In this paper, the design methods and tested results of a kind of RF front-end protection module with ultra-low limited output power were presented. The module consisted of an active biasing circuit and a passive limiter circuit, and it featured rather low on-state impedance and high isolation degree in comparison with commonly utilized passive limiter. The output power of the module was generally less than 0 dBm, which was smaller than the saturation threshold power of sensitive amplifying devices in the receiving channel.

**Keywords**- RF front end, Biasing circuit, Limiter circuit

## I. INTRODUCTION

Although physical damage of transceiver RF front-end circuits caused by HIRF (high-intensity radiation field) and EMP (Electromagnetic Pulse) radiation has been widely reported and investigated, another important phenomenon, i.e., saturation of the receiving channel, was always ignored and few researches were made [1]. Experimental results obtained from typical RF receiving channels tests showed that if the amplitude of the input EMP power reached 0 dBm or larger, and its duration was at the level of tens of nanoseconds, LNAs (low noise amplifiers) in the receiver would be in saturation state about hundreds of microseconds, and that would decrease the channel gain and resulted in disfunction in amplifying normal injected signals. If the P.R.F (pulse repetition frequency) of the EMP were as high as several kilohertz, serious suppression effects would be induced. It is thus necessary to design RF front-end protection module with output limiting power level less than 0 dBm to prevent the receiver from entering deep saturation status.

## II. TECHNICAL INDEXES OF THE LIMITER

The limiter's technical indexes were as follows:

a) Maximum input power, 30 dBm. According to the HIRF and EMP protection requirements of vulnerable RF electronic systems, the functional orientation of the anti-saturation limiting module was as the second-stage protective measure. The leakage power of the first-stage module was generally no more than 30 dBm.

b) output power: less than 0 dBm while the input was 30 dBm. The above demand was based on the fact that if the output power was higher than 0 dBm, the receiver would be saturated.

c) input limiting threshold: less than 0dBm. If the module did not play its limiting role when the input RF signal power was higher than 0 dBm, the receiver would be saturated.

d) spike leakage energy: less than 10 nanojoule. GaAs MOSFET was as the first-stage active amplifying device in the front-end LNA, and the MOSFET's damage energy threshold in adiabatic state was at the range of 50~100 nanojoule. Considering that the volume of GaAs MOSFET would be smaller in the future as improvement of the fabrication technology, the damage threshold would further decrease, so that the spike leakage energy was demanded to be no more than 10 nanojoule [2-4].

## III. TECHNICAL DESIGN OF THE PROTECTION MODULE

### 1) General design method

The protection module consisted of two parts, the active biasing circuit and the passive limiting circuit. The active was composed of a peak value detector and a high-speed comparator, while the passive contained multi-stage pin diodes. The input RF signal was first injected into the active circuit through a directional RF coupler, and its output was then transformed into video signal by Schottky-diode peak value detector. If the amplitude of the detected video signal exceeded the comparator's threshold value set in advance, the comparator's output would be the high value, which drove the passive limiting circuit into low-impedance state.

For the realization of the above demanded technical indexes, it was necessary to analyze the main influencing factors related with each parameter.

a) Maximum input power: It depended on the width of the intrinsic layer the first-stage PIN diodes.

b) output power: It was determined by the on-state impedance of the limiter at certain input power level. To be specific, the on-sate impedance was related with several factors, including the number of stages of the limiter, the value of the distributed inductance, width of the diodes' intrinsic layers, as well as the current value provided by the active biasing circuit.

c) input limiting threshold: It depended on the input threshold value of the high-speed comparator.

d) spike leakage energy: it was related with the start-up delay of the active biasing circuit and the intrinsic layers' width.

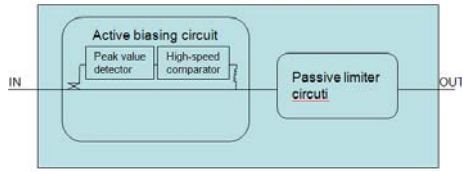


Figure 1. Block diagram of the RF front-end protection module.

### 2) Design methods of the active biasing circuit

One important parameter associated with of the active biasing circuit was its response time, which relied on the performance of the peak value detector and the high-speed comparator. If the response time was pretty short, for example, less than 10 nanoseconds, the leakage energy of the limiter would be rather small so as to prevent transferring strong interference to LNA.

For the purpose of shortening the response time, highly integrated IC consisting of the detector and comparator was employed. The volume of the IC was less than 3mm (length)×3mm (width)×0.5mm (height), and that promised extraordinarily small distributed inductance and strayed capacitance. The input start-up threshold power of the comparator was set to -20 dBm, which was equal to the output power value of the RF directional coupler in the condition that the injected signal power was 0 dBm.

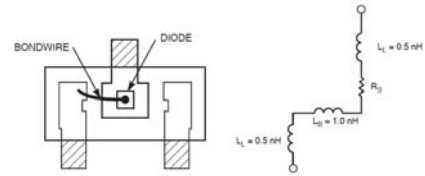
### 3) Design methods of the passive limiting circuit

The processing technique of the passive limiting circuit had great influences on its time-domain and frequency-domain performances. SOT package was always utilized in limiters for the reason that being easy to be soldered on PCB and low cost. However, semiconductor device packaged in SOT featured with relatively large strayed inductance and parasitic capacitance. As shown in Figure 2(a) was the general structure of PIN diodes packaged in SOT-23, of which the inductance of the bonding wire was about 1 nanohenry ( $L_B=1.0$  nH), and two bend leads 0.5 nanohenry ( $L_s=0.5$  nH each) creating a total inductance 2 nH. If the applied frequency was 1 GHz, the series impedance of the diode was  $12.6\Omega$ , generally much higher than the on-state impedance of the PIN diodes ( $1\sim 2\Omega$  in most cases).

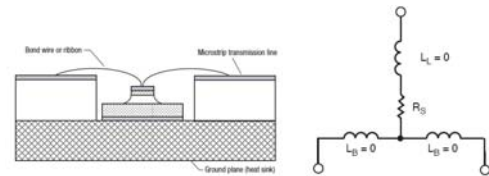
For the purpose of lowering the on-state impedance of the diodes and improving the circuit's applied frequency, PIN diodes with die package were used as the basic limiting elements as illustrated in Figure 2(b). The two bonding wires starting from the diode's anode was in series connection with the central conductor of the limiter circuit's  $50\ \Omega$  microstrip, and that structure enabled opposite current flow directions in the two bonding wires. The distance between the wires was so short that the magnetic fields arising from the oppositely flowing current canceled each other, and that led to the result

that the total inductance of the two bonding wires was approximately zero.

To further improve the performance, 3 limiting stages were employed in the circuit. The on-state impedance can be decreased to 1/3 of single stage and the limiter's isolation can be increased to being 9.5 dB more than single stage in ideal condition.



(a) Structure and the equivalent circuit of the SOT-packaged PIN diode [5].



(b) Structure and the equivalent circuit of the dice-packaged PIN diode [6].

Figure 2. Contrast between the SOT-packaged and dice-packaged PIN diodes.

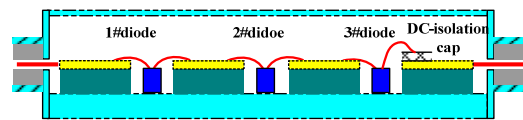


Figure 3. Interior structure of the passive limiter circuit.

## IV. TEST VERIFICATION

### 1) Test results of the active biasing circuit

Figure 4 was the test waveforms of the active biasing circuit's input RF signals and the comparator's output signals. It verified the design parameters that the start-up threshold power was as low as -10 dBm, the dynamic range of the input was larger than 35 dBm, and the response time was shorter than 10 ns (typical values 7-9 ns). The amplitude of the output biasing voltage signal was about 600 mV when terminated with  $50\text{-}\Omega$  load.

### 2) Test results of the passive limiter circuit

The test results showed that passive limiter circuit based on dice-packaged PIN diodes featured lower insertion loss and limiting threshold level in comparison with SOT-packaged PIN diodes, as illustrated in Figure 6 and 7. At the condition of the same input RF signal power, the output power of the circuit equipped with dice-packaged PIN diodes was 6-dB lower than the circuit equipped with SOT-packaged PIN.

### 3) Test results of the portection module

The protection module consisted of the active biasing circuit and the passive limiter circuit and the above two circuits were in series connection. Test results were illustrated

in Figure 8 and 9. It showed that the power amplitude of the output RF signal was less than -15 dBm when the input signal power was 27 dBm, and that index was much smaller than the general level of currently available limiter modules, which was about 5-7 dBm. It can be calculated that the on-state impedance of the anti-saturation module was about  $0.2 \Omega$  as the isolation was 42 dB when 27-dBm RF signals was injected.

Figure 9 showed the comparison results of the input-output power curves between the passive limiter circuit and the anti-saturation protection circuit. It was clear that the output power of the anti-saturation circuit was generally 15-30 dB smaller than the passive limiter circuit.

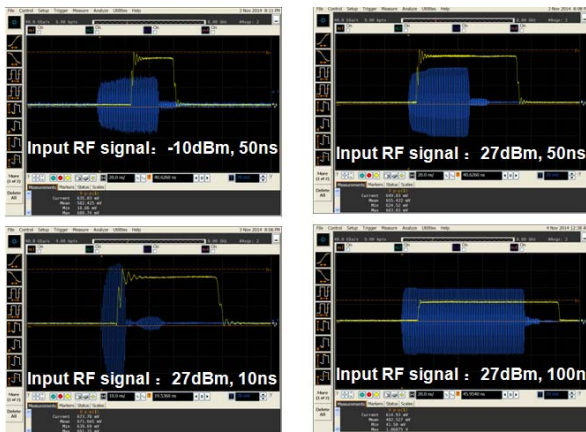


Figure 4. Experimental tests waveforms of the input RF signals and output biasing signals of the active circuit. (Blue lines, input RF signals; yellow lines, output biasing signals. Vertical, voltage, V; horizontal, time, 20 ns/div).

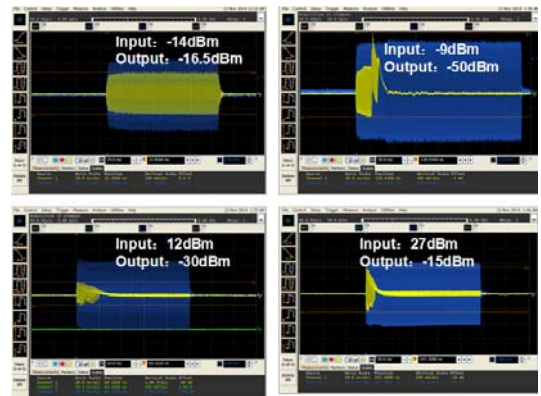


Figure 8. Experimental tests waveforms of the input and output RF signals of the protection module. (Blue lines, the input RF signals; yellow lines, the output biasing signals. (Vertical, voltage, V; horizontal, time, 20 ns/div).

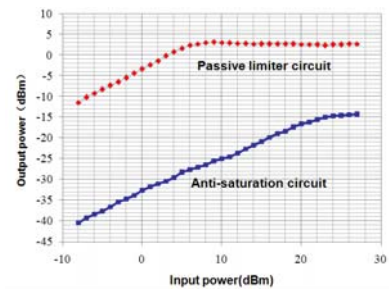


Figure 9. The input-output power curves of the passive limiter circuit and the anti-saturation protection circuit

## V. CONCLUSION

The established indexes at the beginning were verified by the experiments made on the protection module, as illustrated in the following table.

TABLE I. COMPARISON BETWEEN THE REQUIRED AND THE TESTED RESULTS OF THE PERFORMANCE INDEXES OF THE PROTECTION MODULE

Index	Required Value	Tested Result
<i>Maximum input power</i>	no less than 30 dBm	>30 dBm
<i>output power</i>	0 dBm (@27 dBm in)	-15dBm (@ 27dBm in)
<i>input limiting threshold</i>	0 dBm	-10 dBm
<i>spike leakage energy</i>	no larger than 10 nJ	~1 nJ

## REFERENCES

- [1] D. Wang, F. Deng, S. Zheng, et al. Experimental Investigation on the EMP damage characteristics of PIN diode limiter[J]. Chinese Journal of Ship Research, 2015, 10(2): 65-69.
- [2] J. J. Whalen, "The RF pulse susceptibility of UHF transistors," IEEE Trans. electromagnetic compatibility, vol. EMC-17, no. 4, pp. 220-225, Nov. 1975.
- [3] S. Kuboyama, T. Suzuki, T. Hirao, and S. Matsuda, "Mechanism for single-event burnout of bipolar transistors," IEEE Trans. nuclear science, vol. 47, no. 6, pp. 2634-2639, Dec. 2000.
- [4] P. Li, G. Liu, W. Huang, and L. Wang, "The mechanism of HPM pulse-duration damage effect on semiconductor component," High Power Laser and Particle Beams, vol. 13, no. 3, pp. 353-356, May 2001
- [5] Application note, "PIN Limiter Diodes in Receiver Protectors," Skyworks Solutions, Inc., 2008
- [6] Application note, "Low Cost Surface Mount Power Limiters," Avago Technologies, 2010

Figure 6. Test results of the passive limiter circuit based on SOT-packaged PIN diodes. Left, S21 (Vertical, insertion loss, 2 dB/div; horizontal, frequency, 800 MHz/div). Right, input and output signals (Blue lines, input signal; yellow lines, output signal. Vertical, voltage, V; horizontal, time, 50 ns/div).

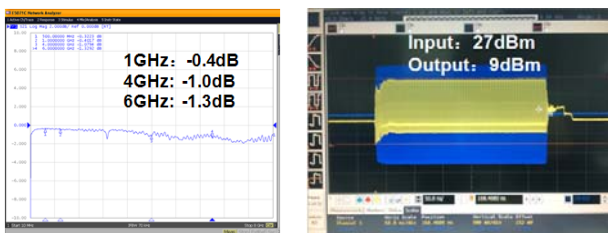
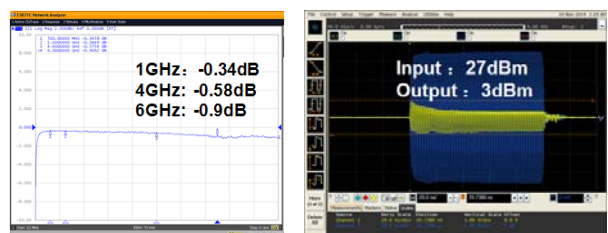


Figure 7. Test results of the passive limiter circuit based on dice-packaged PIN diodes. Left, S21 (Vertical, insertion loss, 2 dB/div; horizontal, frequency, 800 MHz/div). Right, input and output signals (Blue lines, input signal; yellow lines, output signal. Vertical, voltage, V; horizontal, time, 20 ns/div).



# Simple printed structures for low-cost and effective protection against UWB pulses

A.T. Gazizov

\*Department of Integrated Computer Control Systems, \*\*Television and Control Department  
\*National Research Tomsk Polytechnic University, \*\*TUSUR University  
Tomsk, Russia  
gazizov@tpu.ru

## Abstract

The paper describes new principles of design of simple printed structures aimed at low-cost and effective protection against UWB pulses. The structure of asymmetrical modal filter without resistors is considered, and the possibility of the 20 times attenuation is shown. Another structure - a turn of a meander line - is described, and the possibility of the 2.5 times attenuation is shown. New devices based on the described principles will be reliable, cheap and radiation-resistant due to the absence of any component.

**Keywords:** coupled lines, meander line, modal filter, protection, UWB pulse

## 1 Introduction

Nowadays, there is an increasing threat of deliberate electromagnetic impact on electronics [1]. Such an impact can result in malfunction or failure of electronic equipment. Ultra-wideband (UWB) pulses impact is especially dangerous, because existing surge protectors do not protect against it [2]. There are only known some industrial devices that protect against UWB pulses but have large dimensions and a high cost. Thus, currently there is no both low-cost and effective protection against UWB pulses. However, the increasing role of electronics in our life makes this protection essential. Therefore, a search for new design principles of the protection is important.

The idea of modal filtration has been suggested [3] and several devices based on modal filtration principle have been developed. Among them there are symmetrical structures of modal filters (MF) for Fast Ethernet network [4], for lightning [5] and electrostatic discharge [6] protection. The physical principle of their operation is based on the phenomenon of UWB pulse decomposition to modes with different propagation delays in the coupled line. So, the difference between these delays can be longer than the duration of the interference pulse if there is nonhomogeneous dielectric filling in the cross section of the line. Then, one pulse, applied between active and the reference conductors at the near end of the line, will be decomposed into two pulses at the far end of the line.

The asymmetrical MF based on PCB technology has been considered recently, and it has been shown, that the MF with special resistors can attenuate the UWB pulse by 7 times [7]. However, it is important to investigate the structures without resistors in order to reduce cost of the device and to make a protective structure in itself a thin strip of foiled fiberglass that can decompose dangerous pulses. The aim of this paper is to present new design principles of protective structures without resistors, that provide with a better attenuation coefficient.

## 2 Simulation method and structure parameters

The simulation of the UWB pulse propagation is carried out by a quasi-static analysis based on fast and accurate models [8] implemented in the available TALGAT system. A base of proposed structures is coupled line (defined by **L**, **C**, **R**, **G** parameters) having cross section (Fig. 1) with optimal parameters for power network [7]: separation of conductors  $s=15$  mm; width of conductors  $w=15$  mm; dielectric thickness  $h=0.5$  mm; conductor thickness  $t=105$   $\mu$ m; distance between the edge of the structure and the conductor  $d=w$ ; relative permittivity  $\epsilon_r=4$ . Pulse signal is excited between the active (A) and reference (R) conductors (Fig. 1). E.m.f. source parameters: rise, top and fall times  $t_r=t_t=t_d=1$  ns, while the magnitude is 2 kV.

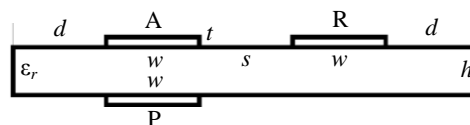
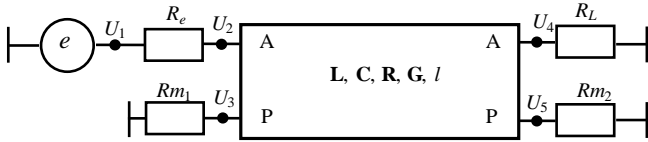


Figure 1. Cross section of proposed structures

## 3 Asymmetrical MF without resistors

The MF circuit diagram is shown in Fig. 2: length  $l=1$  m;  $U_1-U_5$  – nodes;  $R_e$  – e.m.f. source resistance;  $R_L$  – load resistance;  $Rm_{1,2}$  – MF resistances; A-A – active conductor, P-P – passive conductor. In general it is supposed that the magnitudes of the decomposed pulses are at a minimum when all the resistances are equal to geometric mean of the even and odd modes impedances (“matched” case) [9]. This condition makes the magnitudes to be equal and also decreases reflections. In this case  $R_e=R_L=Rm_{1,2}=R=36.515$   $\Omega$ .



**Figure 2. Circuit diagram of MF**

The output ( $U_4$  in Fig. 2) waveform of the MF for the “matched” case is shown in Fig. 3. The maximum magnitude is 0.14 kV and attenuation coefficient is 7 (relative to 1 kV).

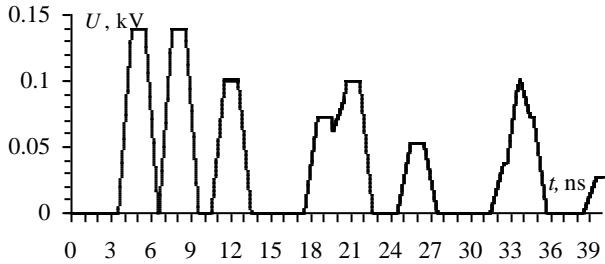


**Figure 3. Output waveform of MF for “matched” case**

In order to simulate the MF without resistors,  $R_{m1}$  and  $R_{m2}$  should have limit in values corresponding to the open-circuit and the short-circuit modes. Waveforms at the output of the MF were calculated for different combinations of limit  $R_{m1}$  and  $R_{m2}$  values. The highest attenuation coefficient was obtained in the case when one of the resistors simulated open-circuit mode and another – short-circuit. It was revealed that the order of resistors does not influence the output waveform. Waveform at the output of MF with  $R_{m1}=1000R$  and  $R_{m2}=0.001R$  is shown in Fig. 4. The obtained waveform shows that the maximum magnitude is 0.084 kV and attenuation coefficient is 12.

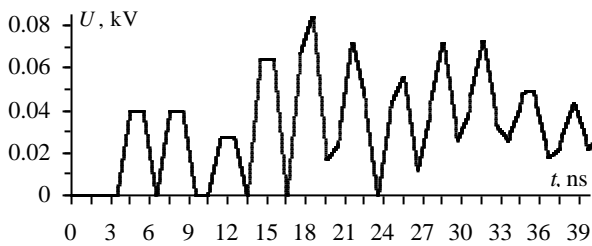


**Figure 4. Output waveform of MF without resistors**

It is worth noting that in Fig. 4 the maximum magnitude is defined not by the first two pulses, as in Fig. 3, but by the fifth pulse. It also can be seen that the fifth pulse in Fig. 4 is a superposition of two pulses, so its magnitude can be reduced by changing the parameters of the structure. For example, we can increase the length of the MF in order to increase the time interval between pulses. Output waveform of the MF with increased length ( $l=2.5$  m) is shown in Fig. 5. Note that the magnitude of the fifth pulse (the maximum magnitude) decreased down to 0.062 kV (attenuation coefficient increased up to 16), because the fifth pulse is no longer a complete superposition of the two pulses.

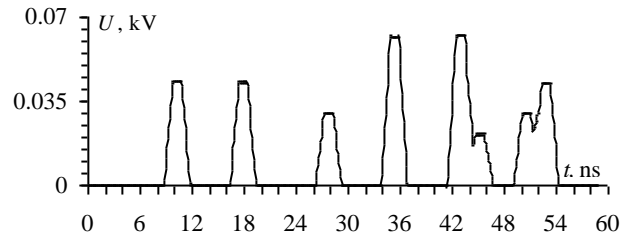


**Figure 5. Output waveform of MF ( $l=2.5$  m) without resistors**

However, the maximum magnitude can be further decreased by increasing the  $\epsilon_r$  value which previously was equal to 4 according to the dielectric substrate material (cheap and widely used FR-4). Output waveform of MF, with increased  $l$  and  $\epsilon_r$  values, is shown in Fig. 6. It can be seen that the maximum magnitude decreased down to 0.05 kV (attenuation coefficient increased up to 20).

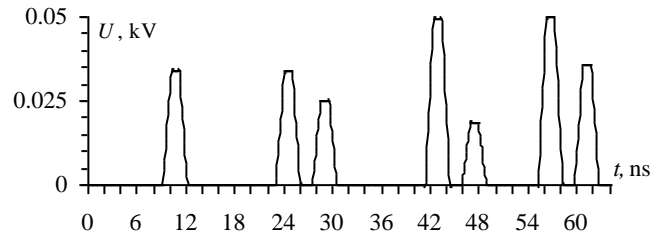


**Figure 6. Output waveform of MF ( $l=2.5$  m,  $\epsilon_r=8$ ) without resistors**

## 4 Turn of meander line

Consider the structure having the same cross section (Fig. 1) but another circuit diagram, which is shown in Fig. 7. Essentially, it is a turn of a meander line (ML) but here it represents another approach to UWB pulses protection. The output of the structure corresponds to the  $U_3$  node.

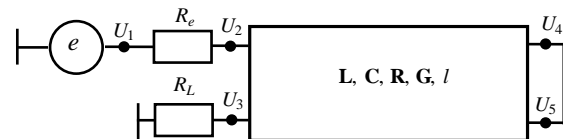


**Figure 7. Circuit diagram of ML**

Output waveform of the ML with initial parameters of the cross section ( $s=15$  mm,  $h=0.5$  mm,  $\epsilon_r=4$ ,  $l=1$  m) is shown in Fig. 8a. The obtained waveform is a sum of the signal itself, passed along the first and the second half-turns of ML, and the crosstalk from the signal rise and fall at the input of the ML. Initial  $s$  and  $h$  values provide a close coupling and that is why the maximum magnitude at the output (0.85 kV) is close to the input pulse magnitude (1 kV). In order to reduce the coupling we can increase the  $h$  value and decrease the  $s$  value. For example, output waveform of the ML with changed parameters ( $s=1$  mm,  $h=6$  mm) is shown in Fig. 8b.

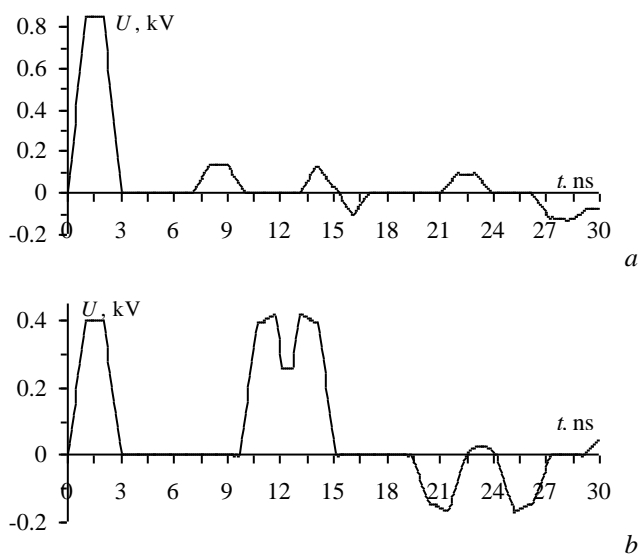


**Figure 8. Output waveform of ML:**  
**a)  $s=15$  mm,  $h=0.5$  mm; b)  $s=1$  mm,  $h=6$  mm**

Although the reduction of the coupling leads to the decrease of the crosstalk magnitude, it also leads to the increase of the delayed pulses magnitude. The optimal case is when these magnitudes are equal as can be seen in Fig. 8b. In this case the maximum magnitude is 0.4 kV and the attenuation coefficient is 2.5.

## 5 Conclusion

In this paper new principles of design of simple structures for low-cost and effective protection against UWB pulses are described. For the first time it was obtained that asymmetrical MF without resistors can have attenuation coefficient 70% higher (12 compared to 7) than MF with resistors with the same parameters of the cross section. It is shown that changing of the cross section parameters and length of the MF without resistors may increase the attenuation coefficient up to 20. Another principle of UWB pulse decomposition based on widely used ML is shown for the same cross section. For this approach the attenuation coefficient 2.5 is obtained. Despite that it is much less than that of the MF, the ML can be much shorter than the MF. Moreover, the use of cascaded connection of the MF and the ML structures is possible and can be convenient and effective due to the same cross section used.

The influence of the proposed structures on the wanted signal is the question of a separate research. Here we note only that this influence depends on the type of protected circuit (type of the wanted signal) and it is different for MF and ML: MF has a lowpass amplitude frequency characteristic, and MF bandwidth can be adjusted by the choice of its parameters, whereas the characteristic of ML has allpass character.

In this paper only numerical lossless simulation was used to demonstrate the essence of the proposed design principles. However, due to the simplicity of the considered cross section and structures, the analytical expressions to calculate coupled

line parameters and waveforms can be used. Use of these expressions will allow to obtain analytically the optimal parameters giving the best characteristics of protective structures under design constrains.

Results of this paper will contribute to a significant reduction of the MF cost and to the implementation of the new filtering principles. New devices based on the described principles will be reliable, cheap and radiation-resistant due to the absence of any component.

## Acknowledgements

Development of necessary software was supported by the state contract 8.1802.2014/K of the Russian Ministry of Education and Science, modeling of coupled lines was supported by RFBR grant 14-29-09254, simulation of waveforms was carried out at the expense of RSF grant 14-19-01232 in TUSUR University.

The author thanks the reviewers for their valuable comments.

## References

- [1] E. Genender, H. Garbe, F. Sabath, "Probabilistic Risk Analysis Technique of Intentional Electromagnetic Interference at System Level", *IEEE Trans. on Electromagn. Compat.*, vol. 56, pp. 200–207, (2014).
- [2] A.M. Zabolotsky, T.R. Gazizov, A.G. Bova, W.A. Radasky, "Dangerous pulse excitation of coupled lines", *17-th Int. Zurich Symp. on Electromagnetic Compatibility. EMC-Zurich 2006*, pp. 164–167, (2006).
- [3] T.R. Gazizov, A.M. Zabolotsky, I.E. Samotin, "Modal Decomposition of UWB Pulse in Power Cable Structures: Simple Experiment Showing Useful Possible Applications", *Book of abstracts EUROEM 2008*, p. 62.
- [4] T.R. Gazizov, I.E. Samotin, A.M. Zabolotsky, A.O. Melkozerov, "Design of printed modal filters for computer network protection", *Proc. of 30-th Int. conf. on lightning protection*, pp. 1246-1–1246-3, (2010).
- [5] T.R. Gazizov, A.M. Zabolotsky, A.O. Melkozerov, E.S. Dolganov, P.E. Orlov, "Improved design of modal filter for electronics protection", *Proc. of 31-st Int. conf. on lightning protection*, pp. 1–4, (2012).
- [6] T.R. Gazizov, A.M. Zabolotsky, E.S. Dolganov, "Modal filter as a device for electrostatic discharge protection of onboard computers and control units of space vehicles", *Russian Physics Journal*, vol. 55, pp. 282–286, (2012).
- [7] A.M. Zabolotsky, A.T. Gazizov, "Simulation of ultra-wide band pulse propagation in asymmetrical modal filter for power network protection", *Int. Journal of Circuits, Syst. and Signal Proces.*, vol. 9, pp. 68–74 (2015).
- [8] T.R. Gazizov, "Analytic expressions for Mom calculation of capacitance matrix of two dimensional system of conductors and dielectrics having arbitrary oriented boundaries", *Proc. of the 2001 IEEE EMC Symp.*, pp. 151–155, (2001).
- [9] I.E. Samotin, "Alignment condition of the pulse magnitudes on the output of the modal filter", *Tehnologii EMS*, vol. 35, pp. 31–34, in Russian, (2010).

# Overview of test methods for HEMP protective filters in Korea

Tae Heon Jang\*, Hyo Sik Choi\*, Won Seo Cho\*

\* RF Application Technology Center, Korea Testing Laboratory, 516 Haean-ro, Sa-dong, Sangnok-gu, Ansan-si, Gyeonggi-do, South Korea 326-901, thjang@ktl.re.kr, chs3040@ktl.re.kr, wscho@ktl.re.kr

## Abstract

For the protection of the installation or enclosure from the conducted HEMP (high altitude electromagnetic pulse) disturbance, HEMP protection filters are used. This paper describes the overview of test methods for the performance and reliability of HEMP protection filters. Mil-std-188-125-1, IEC 61000-4-24 and RS-KTL-2012-0018 are introduced: Mil-std-188-125-1 contains minimum performance requirements and minimum testing requirements for HEMP protection of ground-based systems and facilities. IEC 61000-4-24 deals with methods for testing protective devices for HEMP conducted disturbance. Recently IEC SC 77C is in preparation of FDIS of IEC 61000-4-24 Ed. 2.0. The FDIS includes the new sub-clause 5, Annex A and Annex B as significant technical changes with respect to the previous edition. RS-KTL-2012-0018 is a reliability assessment specification for HEMP protection filter in Korea. This specification defines reliability tests of HEMP filters with current ratings less than and equal to 200 A.

**Keywords:** HEMP, conducted disturbances, protection, filter, performance test, reliability test.

## 1 Introduction

High altitude electromagnetic pulse (HEMP) occurs when a nuclear explosion is higher than an approximate altitude of 30 km above the earth's surface. A high-altitude nuclear burst produces three types of electromagnetic pulses which are observed on the earth's surface: early-time HEMP (fast), intermediate-time HEMP (medium) and late-time HEMP (slow). This classification of the HEMP environment is based on the description of the electromagnetic environment prevailing at typical locations within a system of installation. For components, devices, equipment, subsystems or systems located within an installation, the conducted and radiated environment incident at their locations are determined by the amount of protection provided by EM shields and/or conductive point of entry (POE) elements present in the installation or enclosure.

For the protection of the installation or enclosure from the conducted HEMP disturbance, HEMP protection filters are used to power lines, signal lines and telecommunication. This paper describes the overview of test methods for the performance and reliability of HEMP protection filters. Mil-std-188-125-1, IEC 61000-4-24 and RS-KTL-2012-0018 are introduced in this paper: Mil-std-188-125-1 contains technical

requirements for high altitude electromagnetic pulse (HEMP) protection of ground-based systems and facilities for performing critical and time-urgent command, control, communications, computer, and intelligence (C4I) missions. IEC 61000-4-24 deals with methods for testing protective devices for HEMP conducted disturbance. Recently IEC SC 77C is in preparation of FDIS of IEC 61000-4-24 Ed. 2.0, which includes the new sub-clause 5 (Measurement method for HEMP combination filters), Annex A (Investigation for the establishment of a measurement setup) and Annex B (Test method for the quantitative determination of the direct response behaviours of a coaxial surge protector) as significant technical changes with respect to the previous edition. RS-KTL-2012-0018 is a reliability assessment specification for HEMP protection filter in Korea which is published by Korea Testing Laboratory. This specification defines reliability tests of HEMP filters for power lines, audio/data lines and control/signal lines with current ratings less than and equal to 200 A.

## 2 Requirements of Mil-std-188-125-1

Table 1 shows three pulses for the pulsed current injection test of installed HEMP protection filters and Table 2 is requirement for the residual current of the filters.

Table 1 - Pulsed current injection requirements

	Short pulse (E1)	Intermediate pulse (E2)	Long pulse (E3)
Rise time	≤ 20 ns	≤ 1 μs	≤ 0.2 s
FWHM	500-550 ns	3 ms - 5 ms	20 - 25 s
Amplitude	2 500 A	250 A	1 000 A

Table 2 - Residual internal stress limits for classes of electrical POEs

Class of electrical POE	Peak residual current A	Peak rate of rise A/s	Root action $A\sqrt{s}$
Commercial power lines			
Short pulse	≤ 10	≤ 10 <sup>7</sup>	≤ 1,6×10 <sup>-1</sup>
Intermediate pulse	No damage or performance degradation		
Long pulse	No damage or performance degradation		
Audio/data lines			
Short pulse	≤ 0,1	≤ 10 <sup>7</sup>	≤ 1,6×10 <sup>-3</sup>
Intermediate pulse	No damage or performance degradation		
Long pulse	No damage or performance degradation		
Control/signal lines, low-voltage lines (< 90 V)			
Short pulse	≤ 0,1	≤ 10 <sup>7</sup>	≤ 1,6×10 <sup>-3</sup>
Control/signal lines, high-voltage lines (≥ 90 V)			
Short pulse	≤ 1,0	≤ 10 <sup>7</sup>	≤ 1,6×10 <sup>-2</sup>

### 3 IEC 61000-4-24: setup and requirements

Figure 4 shows a typical measurement setup using shielded enclosures included in FDIS for IEC 61000-4-24 Ed.2.0. The required performance criteria are given in Table 3 to Table 5 for the early-time HEMP test.

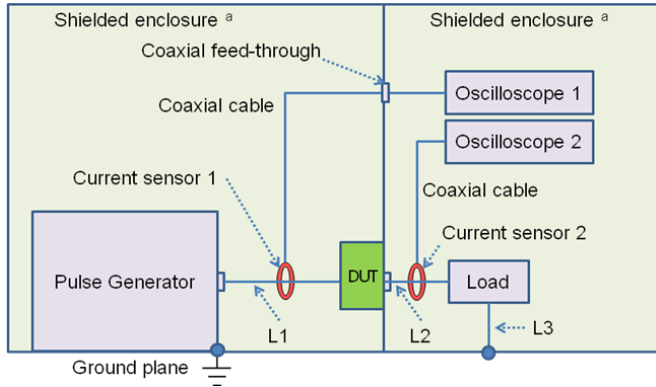


Figure 1 – Example of test setup using shielded enclosures

Table 3 – Performance criteria of filter against early-time HEMP, AC power port with nominal load  $2 \Omega$

Severity Level	Protection Concepts	Peak residual current or voltage		Peak rate of rise $A/s$	Root action $A\sqrt{s}$
		$I_{Load}, A$	$U_{Load}, V$		
Level 1	IEC 61000-6-2 (industrial)	$U_{Load} / R_{Load}$	$2 \cdot \hat{U}_{Nom}$	$2 \times 10^8$	3,2
Level 2	Critical infrastructures	50	100	$5 \times 10^7$	$8,0 \times 10^{-1}$
Level 3	Special case (Mil-Std-188-125)	10	20	$10^7$	$1,6 \times 10^{-1}$
Level X	User defined	UD	UD	UD	UD

Table 4 – Performance criteria of filter against early-time HEMP, DC power port with nominal load  $2 \Omega$

Severity Level	Protection Concepts	Peak residual current or voltage		Peak rate of rise $A/s$	Root action $A\sqrt{s}$
		$I_{Load}, A$	$U_{Load}, V$		
Level 1	IEC 61000-6-2 (industrial)	$U_{Load} / R_{Load}$	$\hat{U}_{Nom}$	$2 \times 10^8$	3,2
Level 2	Critical infrastructures	50	100	$5 \times 10^7$	$8,0 \times 10^{-1}$
Level 3	Special case (Mil-Std-188-125)	Not defined			
Level X	User defined	UD	UD	UD	UD

Table 5 – Performance criteria of filter against early-time HEMP, Signal, data and control port with nominal load  $50 \Omega$

Severity Level	Protection Concepts	Peak residual current or voltage		Peak rate of rise $A/s$	Root action $A\sqrt{s}$
		$I_{Load}, A$	$U_{Load}, V$		
Level 1	IEC 61000-6-2 (industrial)	$U_{Load} / R_{Load}$	$\hat{U}_{Nom}$	$2 \times 10^8$	3,2
Level 2	Critical infrastructures	1	50	$5 \times 10^7$	$8,0 \times 10^{-1}$
Level 3	Special case (Mil-Std-188-125)	$0,1^a$ $1^b$	$5^a$ $50^b$	$10^7$	$1,6 \times 10^{-3 a}$ $1,6 \times 10^{-2 b}$
Level X	User defined	UD	UD	UD	UD

<sup>a</sup> applies to the device with operating voltage less than 90 V

<sup>b</sup> applies to the device with operating voltage of 90 V and greater.

### 4 Reliability tests by RS-KTL-2012-0018:2012

RS-KTL-2012-0018 is a reliability assessment specification for HEMP filter and contains performance tests, environmental tests and lift tests as shown in Table 6 to Table 8. This specification is used to R-mark certification for HEMP protection filters in Korea as a reference specification.

Table 6 – Performance tests and criteria

Performance tests	Test condition	Criteria
Insertion loss	10 kHz to 10 MHz	$20\log(f)-60$ , in dB
	10 MHz to 1 GHz	80, in dB
PCI test	Mil-Std-188-125-1	Mil-Std-188-125-1
Voltage drop	50 % of rated load, or 100 A (the less)	If $\leq 50A, \leq 2 \%$
		If $> 50A, \leq 3 \%$
Leakage current	With rated voltages	Manufacturer Spec.

Table 7 – Environmental tests and performance criteria

Test items	Test condition	Criteria
Low temperature	Storage : $-40^\circ C$ , 16H	Voltage drop, rating currents and operation during the test
	Operating: $-40^\circ C$ , 2H	
High temperature	Storage : $+85^\circ C$ , 16H	After the test, Table 6
	Operating: $+50^\circ C$ , 2H	
Thermal shock	$-40^\circ C \sim 85^\circ C$ , rapid Repeat 5 cycles	After the test, Table 6
Over loads	140 % of the rated, 15M	

Table 8 – Life tests and performance criteria

Test items	Test condition	Criteria
High temperature	For three test samples operating, $+85^\circ C \pm 2^\circ C$ Test time: 1 000 H	After the test, Table 6
PCI Test	Audio/data	$203 \times E2$ 250 A
	Control/signal	$196 \times E1$ 2500 A

### References

- [1] Mil-Std-188-125-1, "High-Altitude Electromagnetic Pulse (HEMP) protection for ground-based c4i facilities performing critical, time-urgent missions, Part I - fixed facilities"(2005).
- [2] IEC 61000-4-24, Electromagnetic compatibility (EMC)-Part 4: Testing and measurement techniques-Section 24: Test methods for protective devices for HEMP conducted disturbance (1997).
- [3] Tae Heon Jang, "Analysis of PCI Cable Effects in HEMP Conducted Disturbance", The Journal of KIEES. 2013 Aug. (2013)
- [4] RS-KTL-2012-0018, "Reliability assessment specification for HEMP Protection Filter" (2012)
- [5] Jin ho Lee, Gi Hwan Song, Hyo Sik Choi and Tae Heon Jang, "Performance verification of HEMP protection devices using the Reliability assessment specification for HEMP protection filters", The conference of the Korean Reliability Society (2013)

# Laboratory test of the IEMI vulnerability of a security surveillance camera

*E B Savage\*<sup>1</sup> and W A Radasky\*<sup>2</sup>*

*\*Metatech Corporation, Goleta, California, USA, <sup>1</sup>savagee@cox.net, <sup>2</sup>wradasky@aol.com*

## Abstract

Surveillance cameras are a very important part of physical security, such as for monitoring and recording any activities outside a facility. Being outside, and possibility mounted close to the facility boundary, such cameras might be vulnerable to IEMI attacks – either an IEMI attack on the overall facility, or an IEMI attack specifically aimed at the surveillance cameras themselves. In this paper we report on the results of laboratory tests that simulated IEMI attacks on a sample network-connected surveillance camera.

**Keywords:** IEMI vulnerability, video camera, radiated IEMI.

## 1 Introduction

A facility in which IEMI might be a concern would undoubtedly also have physical security systems, including surveillance cameras, especially if the facility is unmanned or large. If the facility comes under IEMI attack, such cameras can help to quickly search for the source of the attack, such as a van parked nearby, and look to see if other adverse activities occur, beyond just the EM attack. However, as an electronic device, placed outdoors, possibly close to the boundary fences, and with part of its case plastic (transparent, for the optical view), and also if using a network cable for control and sending the video stream, there can be a concern about IEMI effects on the camera and its cable. Thus in the tests reported here we performed IEMI simulation tests of a sample surveillance camera. Two types of tests were done – radiated and conducted IEMI simulation.

## 2 Test Device

The particular camera appeared to be well constructed. It had an aluminum case, with rubber gaskets to seal against bad weather. It used a shielded network cable, with PoE (power over Ethernet), so this was its only attached cable. For our tests, power was supplied by a “midspan” unit from the same manufacturer. A segment of network line was used to keep this unit (which itself only appeared to have a plastic case) away from the IEMI environment (since power would probably be provided from inside the facility). The camera was exercised by monitoring its video stream on a PC, which was not exposed to the IEMI attack. Thus, the tests simulated IEMI environments in the camera itself, and on some of its attached network cable.

## 3 Radiated IEMI Tests

For the radiated tests a screened room was used, with a pulser connected to a wide band antenna. The pulser had a 3-nanosecond pulse width, and a fixed peak output level of 6.8 kilovolts. Fig.1 shows a sample test setup. The antenna was moved backwards or forwards to adjust the incident field level. The camera (on a cardboard box in the photo) was kept in the center of the antenna’s beam pattern, and the network cable ran off to the side – thus only a very limited part of the cable was exposed to the highest field levels. The cable ran to the back of the screened room, out through a feedthru, through the midspan (power supply), and then to the video monitoring PC.

Not shown in the photo is a current probe that monitors the current on the network cable a short distance below the view in the photo. This was connected to a 1 GHz oscilloscope (barely fast enough for this fast pulse); Fig. 2 shows a sample current measurement.

Using the antenna separation distance, the field level at the camera was varied from 2 kV/m to about 13.8 kV/m, and the camera was oriented either horizontally or vertically. The pulse repetition rate was also varied, from a single shot up to 100 pulses per second.

No permanent damage was found during testing, but there were upsets. It was common for the video display to become



**Figure 1. Photo of one of the radiated tests. (Here the cable is looped to increase exposure.)**

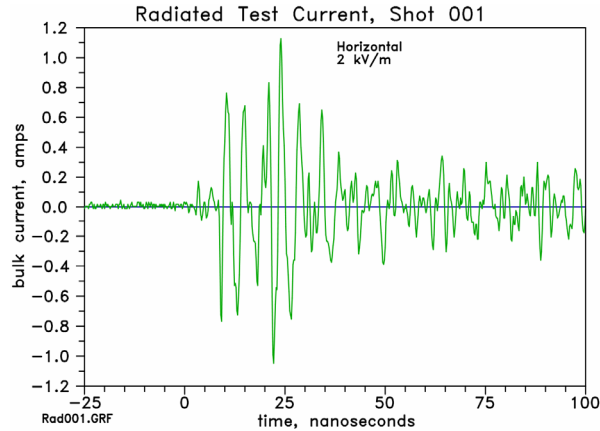


Figure 2. Sample of the network cable bulk current.

“choppy” – as if it was running at a very low frame rate (such as about 1 frame per second). In a few cases the video monitoring software completely froze – no longer updating the video scene. Sometimes there were also messages from Windows that the network was not performing well. It is likely that transient noise was being induced in the network signals by the pulses, causing the network error detection to reject network packets. If there are overwhelming network failures, then the channel throughput can be degraded below what is necessary for a live stream. Generally the live stream returned once the disruption stopped, although this can take some time. The upset level was about 5 kV/m when the cable was looped slightly in front of the camera, as shown in Fig. 1.

#### 4 Injection Tests

Note that the antenna was generally much closer to the camera than might be typical for an actual IEMI attack. This was necessary because the pulser has a relatively low output (and the screened room size also sets a limit). Of course it is much harder and more expensive to have a fully realistic test – if a very high level pulser was available, a suitable location, far away from anything else, or within an extremely large screened room, would have to be used. The small antenna-camera distance means the cable itself is not as exposed as might happen in a real situation. For this reason we also performed pulse injection tests.

Fig. 3 shows the test setup. An “EFT” pulser (5 nanoseconds rise, 50 nanoseconds width) was connected to a capacitive coupling clamp, through which the camera’s network cable ran. This induced a bulk current on the cable (which is shielded). A current probe recorded this current, and Fig. 4 shows a sample recorded waveform.

In the tests we varied the pulser charge level, from 0.5 kV to 7.3 kV, and also the repetition rate of the EFT spikes (up to 10 kHz). As for the radiated tests, we did not cause damage, but we could affect the video stream, causing video frames to be lost, so the video appeared choppy, as if we were getting much less than the 30 frames per second under normal conditions. The upset level (where we could tell that frames



Figure 3. View of the injection test setup.

were being lost) was somewhere between the 2 and 4 kV pulser charge level.

#### 5 Conclusions

This particular model of camera is a quality product, and we could not cause damage up to the highest levels of our radiated and conducted IEMI simulation tests. We could upset the camera – disrupting its video stream, and freezing the video in some cases (in some cases without any indication that the frame was frozen). It appears likely that these problems were due to the disruption of the network traffic due to coupling to the network cable.

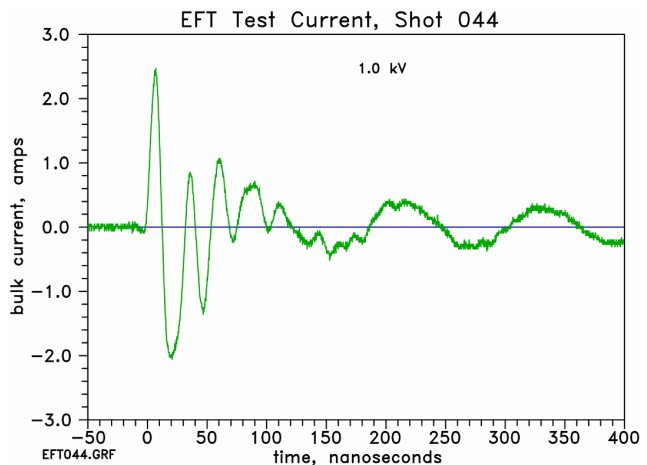


Figure 4. Sample bulk current measurement from the injection tests.

# Laboratory tests of the IEMI/HEMP vulnerability of some low power switched-mode power supplies (SMPS)

*E B Savage\*<sup>1</sup> and W A Radasky\*<sup>2</sup>*

*\*Metatech Corporation, Goleta, California, USA, <sup>1</sup>savagee@cox.net, <sup>2</sup>wradasky@aol.com*

## Abstract

**Much of modern low-power equipment uses switch mode power supplies (SMPS) to convert AC to DC. This paper reports on simulated IEMI (Intentional Electromagnetic Interference) tests of samples of such supplies. The tests consisted of IEMI injection of interference into the mains AC port.**

**Keywords:** IEMI, SMPS, EFT, CWG, harmonics.

## 1 Introduction

SMPS are used extensively in modern electronic equipment, because of their efficiency, utility, and versatility. Thus, it would be useful to perform IEMI simulation tests of SMPS samples, as reported in this paper. The test samples are shown in Fig. 1, and consisted of:

1. Network router (3 samples; it has an internal SMPS).
2. Laptop charger (2 samples).
3. Cell phone USB charger (3 samples).
4. Wall wart (plugs directly into wall AC outlet; 6 samples).

The first three each consisted of several samples of the same model, while the last, wall warts (a “black bump” on the wall), had five different models. All of the tests were for injection of interference into the AC power line of the equipment. This consisted of high level transient pulses, either fast (EFT) or slower (CWG) pulses or harmonic distortion of the AC power. For the stand-alone power supplies (all but #1), the tests did not include any of the equipment that would normally be attached and powered by the supply – resistive loads were used instead (except for the network router, which was run in a 2-PC network).



Figure 1. Tested samples.

In the EFT tests there was some upset and damage; in the harmonics test there was one upset and no damage. The CWG pulses damaged many of the samples. The network routers did not suffer any adverse effects in any of the tests – all the other equipment was damaged by one of the three types of IEMI.

## 2 EFT (Fast Pulses: 5 ns rise, 50 ns wide)

A standard pulser (see the sample test setup, for a wall wart, in Fig. 2) was used. Internally the pulser couples the pulses onto the isolated AC line used to power the test device. This pulser produces pulses with a 5 nanosecond rise time and a 50 nanoseconds pulse width. We set the pulser to deliver 150,000 pulses over a 5 minute test time. Four measurements were recorded on an oscilloscope: the voltage and current on the AC input line and on the DC output line. A single test, for a particular test device and configuration, consisted of 5 minutes of pulses, and then the charge voltage was stepped up, and this would be repeated – up to the maximum charge voltage of 4.5 kV. The two configurations tried were pulsing the “line” or the “neutral” wire of the AC power (the wall warts and USB phone chargers do not have a ground wire).

In these tests we watched the DC output – damage would be seen in the permanent failure of the DC, upset would mean temporary loss of DC output. We also looked at the leakage – the level of fast transient that got through to the DC output; the worse case was at about 550 volts peak for 4.5 kV pulser charge (with coupling and loading, typically about 2 kV peak was measured on the AC input).

EFT alone often does not cause damage, as it does not have

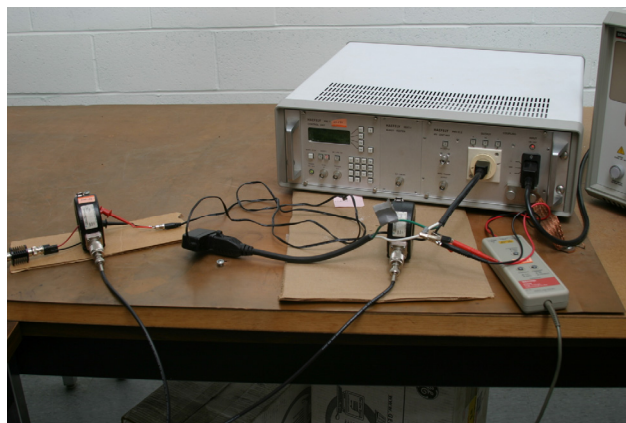


Figure 2. EFT test setup for a wall wart.

much energy. But with equipment powered up, EFT can also trigger the dumping of system power, and this causes damage – so this can be a concern with AC line injection. Throughout the tests small “tinking” sounds could be heard in test devices, but only two were damaged – both at the highest charge levels. Both were generic USB phone chargers – one was under “line” drive and the other under “neutral” drive, and both had mild “explosions” several minutes into the 5 minute pulse series. Upsets were also found for the laptop chargers, also at the highest pulser charge level. The charger output turned off, but was restored by a power down/up cycle (unplug/plug). The pulses may have triggered some internal protection circuit, such as overload protection.

### 3 CWG (Surge - slower: 1.2 $\mu$ s rise, 50 $\mu$ s wide)

These were similar to the EFT pulse tests, except a different pulser was used (wider, and so more energy). Its output had a 1.2 microsecond rise time and a 50 microsecond pulse width. These tests were actually done last, because often CWG pulses can cause damage, and once a device is damaged, it can no longer be tested further (2 cell phone USB chargers had been eliminated in EFT testing at this point). Fig. 3 shows one of the test setups (the pulser is not seen – it is off to the right), and sample waveforms are shown in Fig. 4. The pulser internally couples the pulse onto the AC mains line. A single test consisted for 30 pulses over 5 minutes.

We did not notice any upsets during the tests (we watched the DC output voltage on a meter), but we had damage – all units were killed except for the network routers. The cell phone USB charger died at a pulser charge level of 1 kV. All six wall warts died, at levels of 1.5 kV to 3.2 kV. The two laptop computer chargers died at charge levels of 3.3 and 3.4 kV. Many of the deaths occurred on the first shot in a 5 minute test; only two (wall warts) lasted more than a few shots into the 30 shot test sequence (this may depend on how big the pulser charge voltage increments were, and how far the test shot was above the device’s actual damage level).

### 4 AC Harmonics

Before the (damaging) CWG tests, we subjected the test devices to harmonic distortion tests. The test setup was

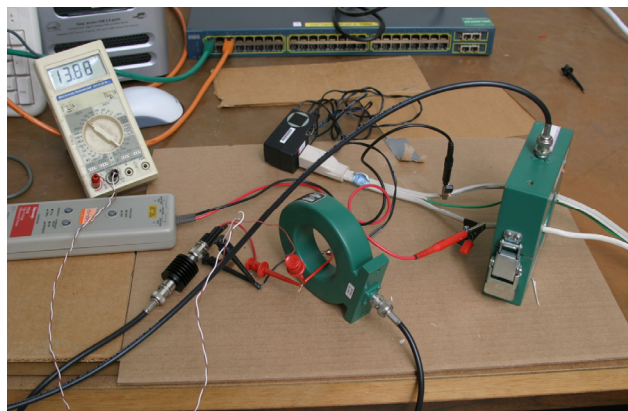


Figure 3. Typical CWG test setup (for a wall wart).

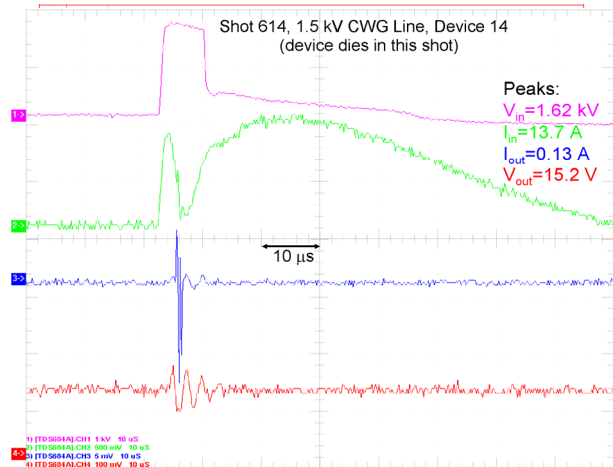


Figure 4. Sample CWG test waveforms.

similar to the other two tests – an interface source (AC waveform generator) powered the test devices, while we looked for DC output failures or device damage. Resistors were put on the DC outputs for loads. In this case, for test efficiency, we drove multiple test devices at once, as shown in the setup in Fig. 5. Of the infinite number of possible distortion waveforms (harmonic amplitude and phase values) we arbitrarily picked four, all single harmonic. We applied the distortion for 5 minutes, watching the DC output on a meter (and occasionally watching the DC output waveform on an oscilloscope). The test level parameter was the percent distortion; we started at a low level, and incrementally stepped this up if there was no damage after 5 minutes.

The results were that no device was damaged, and with one exception, all also continued to supply well-regulated DC output. In fact, typically the SMPS’s tested did not care about the quality of their input AC power.

### 5 Conclusions

SMPS’s are not very vulnerable to harmonic distortion, but if powered up, might be upset or damaged by fast pulses, and wider pulses can be damaging. The network routers were impervious to our IEMI simulated attacks – the reason for this was not investigated.



Figure 5. One of the harmonics test setups.

# IEMI laboratory tests of network line protectors: vulnerability and protection ability

*E B Savage\*<sup>1</sup> and W A Radasky\*<sup>2</sup>*

*\*Metatech Corporation, Goleta, California, USA, <sup>1</sup>savagee@cox.net, <sup>2</sup>wradasky@aol.com*

## Abstract

An important response mode for an IEMI attack on a facility is coupling into network cables, with resulting damage to the network equipment. Thus, a possible IEMI defense is the use of pulse suppression devices on the network cables. In this paper we look at the vulnerability and protection performance of some network cable protectors. We performed laboratory tests on eight samples (all from the same manufacturer) with surge protection, and on one sample (much more expensive) that includes additional protection features. Tests were done with standard high-level pulses: EFT (50 nanoseconds wide) and Telecom (700 microseconds wide).

**Keywords:** Network vulnerability, surge protectors, TPD.

## 1 Introduction

In this paper we are concerned with an IEMI (Intentional Electromagnetic Interference) attack on a modern facility – one with an important function performed using modern electronics. For many cases, such a facility is highly dependent on internal data communication over standard network cabling. EM assaults, such as IEMI, or the similar attack of HEMP (high-altitude electromagnetic pulse), involve the coupling of transient signals (“pulses”) into such cabling, and then those signals propagate along the wires and into equipment, where they may cause damage or upset – see Fig. 1. Various approaches may be used in “hardening” a facility (building in protection) against such attacks. One

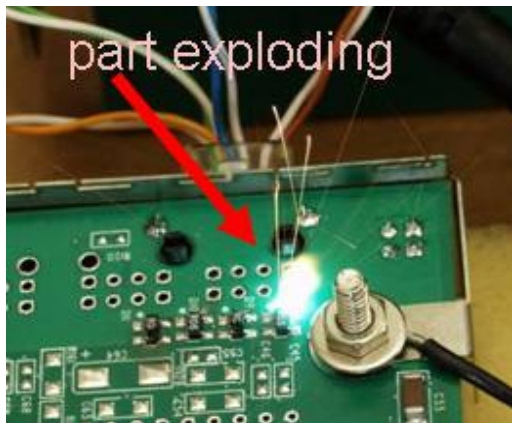


Figure 1. Damage occurring from high-level pulse injection into the network interface of power substation

very standard approach is to use what might be generically called TPDs (terminal protection devices) or specially SPDs (surge protection devices) where nonlinearity characteristics limit high-level pulses, to prevent transient pulses on the cables from getting into the vulnerable attached equipment.

SPDs have been used for a very long time (lightning arrestors are a type of such devices), but their protective behavior can vary significantly. It is not common to find such devices built specifically for IEMI protection. Some protective devices do advertise protection against EMP, or fast turn-on times, and thus possibly might have some usefulness for IEMI. Generally sufficient information is not provided to evaluate such devices as IEMI protectors, and instead laboratory tests must be used to evaluate their performance. Two input features are looked for in such tests. First, for nonlinear surge protection devices, the devices must turn on (generally shorting the line to ground) fast when the voltage starts to get high, so the high level surge is prevented from getting to the protected equipment. Secondly, the protective device should not itself be damaged by the pulse (and if it is damaged, it should be left shorted to ground, to prevent further pulses from getting past). Here we report on pulse response tests on six types of protective devices (see Fig. 2), in which we looked for such adverse effects.

## 2 Experiments

The experimental setup consisted of feeding the pulser output into the input side of the protective device, with a resistive load on the output side. An oscilloscope was used to record the voltages and currents on both sides of the protector. Fig. 3 shows a typical result for the fast pulse (5 ns rise, 50 ns

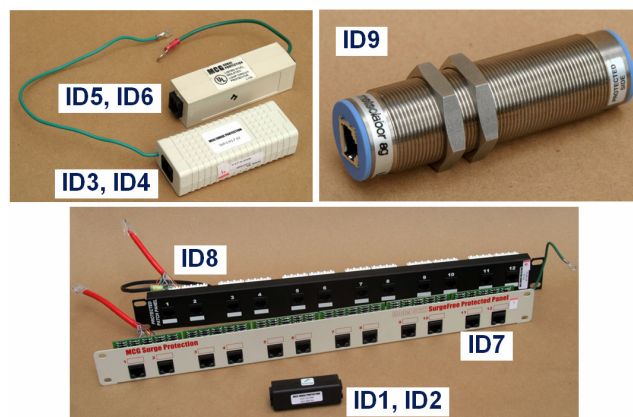


Figure 2. The devices tested.

width). The blue line is the input current, and with minor differences, represents the normal waveshape of the pulser's output (into a purely resistive load); this is approximately the short circuit current. The red line is the input voltage (and also the output voltage if the protective device is only a shunt transient limiter). Generally network protectors have a turn-on voltage on the order of about 100 volts. This input voltage peak is much higher than this (3.6 kV), indicating that the protection turns on much too slowly for this case. The green line is the current on the output side; it is much lower (14.5 amps) than the input current (123 amps), but still very high compared to normal network signal levels.

For each device (some of the test devices actually consisted of multiple copies of the same protective devices, such as to be used for a router, with many network lines, and for these there were many samples of the same device for testing) we started testing at low levels (e.g. 1 kV charge level) and gradually moved up in charge level with each successive test – up to the maximum charge level (8 kV, but actually through some problem in our pulser, above 7 kV the pulse level does not go to the full charge, but rather 7.3 kV is the upper level). Fig. 4 summarizes how much of the incident pulse voltage gets through the protector, and certainly some protection is being provided. However, these peaks appear to be linear (except at 8 kV, due to the pulser problem noted above). That there does not appear to be any nonlinearity in the peak behavior indicates that it is probably the quickness (or better, slowness) of the protection turn-on that governs the peak level, not the turn-on voltage of the protective device. However none of the protective devices were damaged by these fast pulses.

Tests were also performed with wider pulses (CWG, 50 microseconds wide, and Telecom, 700 microseconds wide). With wider pulses the slow turn-on was not an issue, and the residuals (pulse level that leaks past the protector) were lower. However, some of the protective devices could be damaged with these wider, more energetic, pulses.

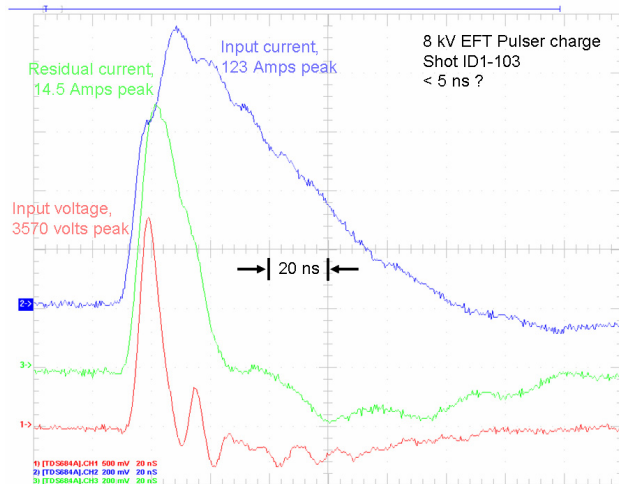


Figure 3. Sample measurement with EFT pulse (5 nanoseconds rise, 50 nanoseconds width).

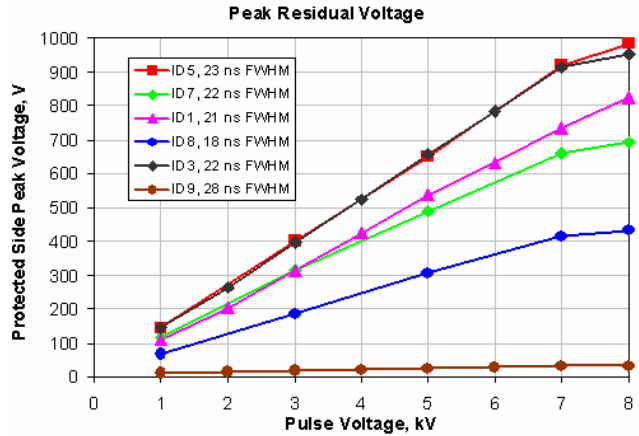


Figure 4. Summary of peak residual (protected side) voltage for the EFT pulse tests.

### 3 Conclusions

The more expensive protector (ID9) provided good protection, and was not damaged in the tests; conclusions for the other devices are as follows. The EFT pulser (up to 7.3 kV) could not damage any of the protectors, but they did not turn on fast enough to limit the residuals to a low level. We did not see any differences between devices that advertised <5 ns turn-on and ones that claimed <1 ns turn-on. Wide pulses (and up to about 4.3 kV, see Fig. 5) also could not damage the devices that used diodes, but the ones with integrated circuit packaged devices were damaged (at charging levels of 1 to 3 kV), although for these slow pulses the residuals were low. Damage was not a simple failure – random series of full, partial, or no functionality can result at any point in a shot series, even at the same charge voltage, after an initial damage shot.

Note that for IEMI the pulses may rise even much faster than for our fastest pulse (or may be sinusoidal, also with extremely fast “rise” times).

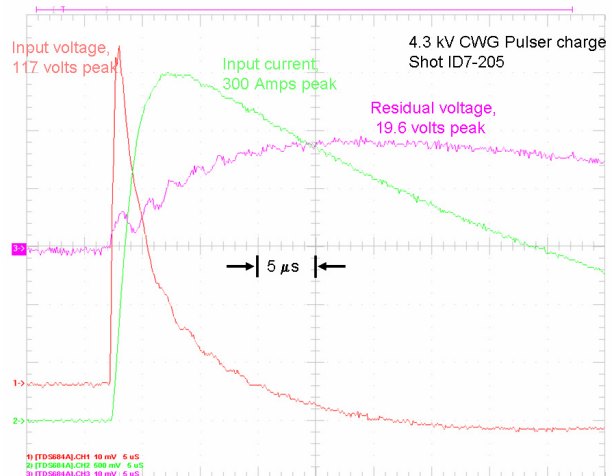


Figure 5. Sample waveforms from a CWG shot.

# Study of the Propagation of IEMI Signals along Power and Communication Lines

*N. Mora\**, *G. Lugrin\**, *F. Rachidi\**, *M. Nyffeler<sup>†</sup>*, *P. Bertholet<sup>†</sup>*, *M. Rubinstein<sup>+</sup>*

*\*EMC Laboratory, Swiss Federal Institute of Technology (EPFL), Switzerland, nicolas.mora@epfl.ch*

*<sup>†</sup>HPE Laboratory, Federal Department of Defence – Armasuisse, Switzerland*

*+ University of Applied Sciences of Western Switzerland, Yverdon, Switzerland*

## Abstract

**This work studies the propagation of IEMI (Intentional Electromagnetic Interference) signals along power/communication cables. Specifically, the attenuation and distortion of the IEMI signals resulting from conductive and dielectric losses are studied.**

**Keywords:** Intentional electromagnetic interferences (IEMI), field coupling into transmission lines, power lines, communication lines

## 1 Introduction

This work deals with the evaluation of voltages and currents at equipment terminals that are sensitive to an IEMI attack [1]. IEMI stresses on a system can be applied either through conducted coupling or radiated electromagnetic coupling [2]. In both cases, interferences (either induced or directly injected) will reach the sensitive devices through connected cables.

This work studies the attenuation and distortion of IEMI signals along power and communication cables. The analysis is based on the Transmission Line (TL) theory [3].

## 2 Modeling considerations

The propagation of IEMI signals along power and communication lines will be affected by (i) conductive losses and dielectric losses, and (ii) radiation losses. The distorted transmission will result in the modification of the amplitudes and the rise time of the original induced waveform.

In this study, we assess the attenuation and distortion of the signals through a simplified TL analysis considering uniform lines with conductive and dielectric losses. The radiation losses and reflection due to non-uniformities will not be considered in this work.

Consider the coupling of an electromagnetic disturbance onto a lossy uniform transmission line of finite length  $L$ . The electromagnetic disturbance is represented as an equivalent lumped source at a given position along the line. In order to simplify the analysis, we will assume that the line is matched at both ends and an equivalent voltage source is used to excite the line at one of the ends, as schematically shown in Fig. 1.

The transmission line is characterized by its characteristic impedance  $Z_0$  and its complex propagation constant  $\gamma$ . The

propagation transfer function  $H$  relating the voltages at both ends of the line can be expressed as:

$$H = \frac{V(L)}{V(0)} = e^{-\gamma L} = e^{-\alpha L} e^{-j\beta L} \quad (1)$$

where the complex propagation constant  $\gamma$  has been decomposed into the attenuation constant  $\alpha$  and the phase constant  $\beta$ .

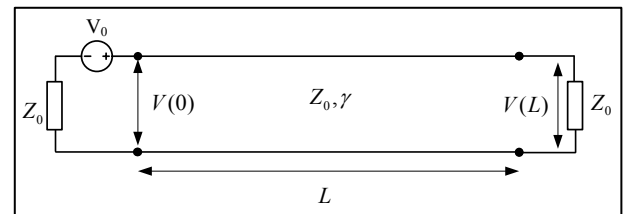


Fig. 1 Schematic diagram of a uniform two-wire transmission line excited by an equivalent voltage source representing the field-to-wire coupling from an external source.

The complex propagation constant of a transmission line can be calculated from its per-unit-length RLGC parameters as [3]:

$$\gamma = j\omega\sqrt{LC} \sqrt{\left(1 - \frac{R'G'}{\omega^2 LC}\right) - j\left(\frac{R'}{\omega L} + \frac{G'}{\omega C}\right)} \quad (2)$$

For lines using good conductors such as copper or aluminium (as in communication and power cables), the attenuation should be governed by the conductance of the line, which is directly related to the dielectric losses. However, for lines with very small cross-section, the skin effect plays an important role in the attenuation of the signals.

## 4 Overview of the parametric analysis and results

The per-unit-length parameters of several power and communication lines were extracted in order to assess the significance of the conductive and dielectric losses at the expected frequencies of IEMI perturbations. The p.u.l. parameters of each of the lines were calculated by considering a finite conductivity of the conductors and the presence of a dielectric with known complex permittivity (assuming a constant tangent loss of the dielectric). The p.u.l. resistance of

the lines was calculated by including the frequency variation due to the skin effect.

The results for a 10-m low voltage power cable are presented in Fig. 2. The top plot shows the injected signal (black line) which is representative of a hyperband IEMI waveform with a risetime of 229 ps. The lower panel presents the propagated signals at the other end of the line. The blue curve corresponds to the calculated signal when no losses are included. If the conductive losses are included (green curve), there is an attenuation of about 10% for the peak amplitude, and an increase in the signal risetime.

On the other hand, if only the dielectric losses are considered (cyan curve), the peak attenuation is about 40% and a more significant increase is observed for the risetime. Finally, the red curve shows the results obtained when both losses are included. In this case, the overall peak attenuation is about 50% and the obtained risetime is comparable to the one obtained if only dielectric losses are included.

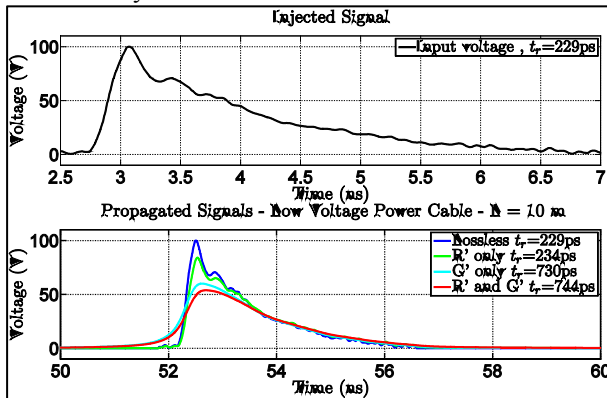


Fig. 2 Propagation along a 10-m long low voltage power cable. (a) Injected signal. (b) Propagated signal at the right end of the line.

A similar study was carried out considering a network cable (Cat 5). The simulation results are shown in Fig. 3. Unlike the case of the power cable for which the dielectric losses were predominant, in this case, the conductive losses prevail. This is essentially due to (i) smaller cross section, and (ii) thinner dielectric coating, of the twisted wires in the network cable in comparison with the power cable.

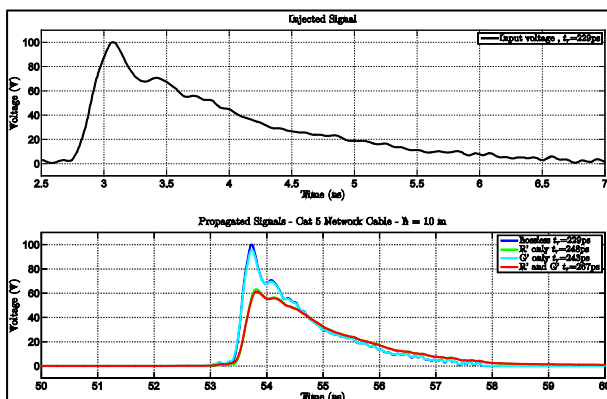


Fig. 3 Propagation along a 10-m long network (Cat 5) twisted pair. (a) Injected signal. (b) Propagated signal at the right end of the line.

## 5 Conclusions

The differential mode propagation of very fast injected transients can be significantly affected by the presence of losses in power and communication lines, resulting in an attenuation of the peak and an increase of the risetime. Similar results were obtained in [4-7] where the propagation of IEMI signals in low voltage power networks was assessed from experimental point of view.

Traditional surge protection devices (SPDs) are used to protect from overvoltages and overcurrents originated by signals that are slower than the expected IEMI signals (e.g., those originated from ESD, NEMP, or lightning). The presented analysis allows the evaluation of the required propagation distance at which the attenuation and distortion of IEMI signals are such that traditional SPDs can be effectively used to protect sensitive devices connected at the end of the lines.

## Acknowledgements

This study was financed by the Armasuisse Science and Technology (Contract Nr. 8003504623).

## References

- [1] W. A. Radasky, C. E. Baum, and M. W. Wik, "Introduction to the special issue on high-power electromagnetics (HPEM) and intentional electromagnetic interference (IEMI)," *Electromagnetic Compatibility, IEEE Transactions on*, vol. 46, pp. 314-321, 2004.
- [2] D. V. Giri and F. M. Tesche, "Classification of intentional electromagnetic environments (IEME)," *Electromagnetic Compatibility, IEEE Transactions on*, vol. 46, pp. 322-328, 2004.
- [3] C. R. Paul, *Analysis of multiconductor transmission lines*. Hoboken, N.J.: Wiley-Interscience : IEEE Press, 2008.
- [4] D. Mansson, T. Nilsson, R. Thottappillil, and M. Backstrom, "Propagation of UWB Transients in Low-Voltage Installation Power Cables," *Electromagnetic Compatibility, IEEE Transactions on*, vol. 49, pp. 585-592, 2007.
- [5] D. Mansson, R. Thottappillil, and M. Backstrom, "Propagation of UWB Transients in Low-Voltage Power Installation Networks," *Electromagnetic Compatibility, IEEE Transactions on*, vol. 50, pp. 619-629, 2008.
- [6] N. Mora, C. Kasmi, F. Rachidi, M. Darces, and M. Helier, "Modeling of the propagation along low voltage power networks for IEMI studies," in *Electromagnetics in Advanced Applications (ICEAA), 2013 International Conference on*, 2013, pp. 436-439.
- [7] N. Mora, C. Kasmi, F. Rachidi, M. Darces, M. Hélier, and M. Rubinstein, "Analysis of the Propagation of High Frequency Disturbances along Low-Voltage Test Raceway," presented at the American Electromagnetics International Symposium (AMEREM), Albuquerque, New Mexico, USA, 2014.

# Effect of the Penetration through a Concrete Wall on the Propagation of Common Mode IEMI Signals

N. Mora\*, G. Lugrin\*, F. Rachidi\*, M. Nyffeler†, P. Bertholet†, M. Rubinstein‡

\*EMC Laboratory, Swiss Federal Institute of Technology (EPFL), Switzerland, nicolas.mora@epfl.ch

†HPE Laboratory, Federal Department of Defence – Armasuisse, Switzerland

‡University of Applied Sciences of Western Switzerland, Yverdon, Switzerland

## Abstract

We present a study on the effect of the penetration of transmission lines through concrete walls on the attenuation and distortion of common mode IEMI signals. The propagation of high frequency signals along a transmission line passing through a concrete wall is analyzed as a function of the concrete electrical parameters, thickness of the wall and the frequency of the signal.

**Keywords:** Intentional Electromagnetic Interference (IEMI), Transmission lines, Debye model

## 1 Introduction

This work deals with the evaluation of voltages and currents at equipment terminals that are sensitive to an IEMI attack [1] [2]. Outdoor power or communication cables, on which disturbance signals could be injected or induced, pass through concrete walls. It can be expected that the concrete structure of the wall has a beneficial effect on the attenuation of propagating signals.

In this work, we present a study of the effect of the penetration of transmission lines through concrete walls on the propagation of common mode IEMI signals. The propagation of high frequency signals along a transmission line will be analyzed as a function of the electrical parameters of the concrete, the thickness of the wall and the frequency of the signal. The study will be based on the Transmission Line (TL) theory.

## 2 Modeling considerations

### 2.1 TL equivalent

We will model the penetration of the conductor into a concrete slab as a transmission line surrounded by a homogeneous lossy dielectric. Consider the propagation of a signal along a transmission line composed of a single bare wire located at a height  $h$  above a ground plane that penetrates a concrete wall of thickness  $L$  as schematically shown in Fig. 1.

The voltage source at the input of the line represents the injection or coupling of a common mode signal onto the outdoor cabling that will propagate to the interior of a

building passing across the wall. The penetration of the wire into the concrete wall will introduce a discontinuity in the propagation of the signal in free space and it can be represented as a separate transmission line cascaded with the outdoor and indoor portions of the line.

The cross sections of the outdoor and indoor transmission line sections are shown at the bottom left and right panels of Fig. 1. The outdoor and indoor portions of the line are assumed to be in free space. On the other hand, the cross section of the portion of the line inside the concrete wall is shown in the bottom-middle panel of Fig. 1. The transmission line inside the wall is assumed to be surrounded by a homogeneous dielectric characterized by its relative permittivity  $\epsilon_r$  and the loss tangent  $\tan \delta$ . Notice that for the considered example, the line is a bare wire (no dielectric coating) and is in direct contact with the concrete.

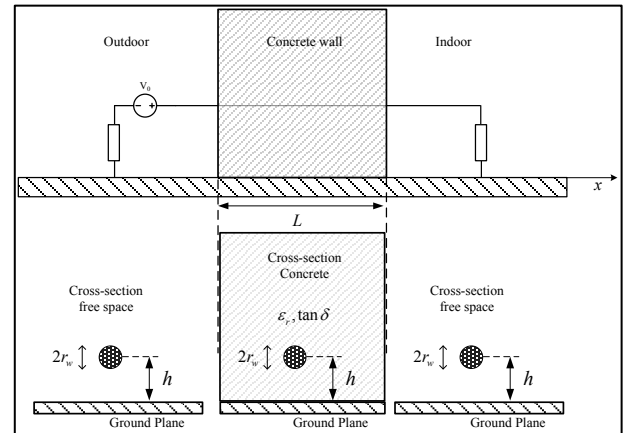


Fig. 1 Schematic diagram of a transmission line penetrating a concrete wall

### 2.2 Two-port network representation of the wall

A two-port network representation of the concrete transmission line can be used in order to calculate the reflected and transmitted signals at the line interface (see Fig. 2). The transmission matrix (ABCD parameters) of the two-port network relates the input and output voltages and currents as [3]:

$$\begin{bmatrix} V_1 \\ I_1 \end{bmatrix} = \begin{bmatrix} A & B \\ C & D \end{bmatrix} \begin{bmatrix} V_2 \\ I_2 \end{bmatrix} \quad (1)$$

It can be shown that the transfer function between the output voltage and the injected signal  $H_w$  can be calculated with [4]:

$$H_w = \frac{V_2}{V_0} = \frac{Z_0}{AZ_0 + B + CZ_0^2 + D} \quad (2)$$

where  $Z_0$  is the characteristic impedance of the transmission line in free space.

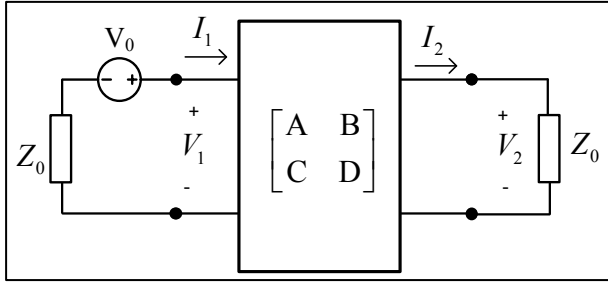


Fig. 2 Two-port network representation of the transmission line section through the concrete wall.

The transmission matrix of the line can be estimated as [3]:

$$\begin{bmatrix} A & B \\ C & D \end{bmatrix} = \begin{bmatrix} \cosh(\gamma_w L) & Z_{0-w} \sinh(\gamma_w L) \\ \frac{1}{Z_{0-w}} \sinh(\gamma_w L) & \cosh(\gamma_w L) \end{bmatrix} \quad (3)$$

with:

$$\begin{aligned} \gamma_w &= \sqrt{(R'_w + j\omega L'_w)(G'_w + j\omega C'_w)} \\ Z_{0-w} &= \sqrt{\frac{R'_w + j\omega L'_w}{G'_w + j\omega C'_w}} \end{aligned} \quad (4)$$

where  $R'_w, G'_w, L'_w, C'_w$  are the per-unit-length parameters of the transmission line section through the concrete wall.

### 2.3 Complex permittivity of concrete

A Debye model for calculating the effective conductivity and relative permittivity of concrete has been proposed in [4]. The complex dielectric constant is calculated as a function of the DC conductivity  $\sigma_0$  and the relative HF permittivity  $\epsilon_\infty$  of the wall as:

$$\begin{aligned} \hat{\epsilon}_w &= \epsilon_0 \epsilon_r (1 - j \tan \delta) \\ \tan \delta &= \frac{\sigma_{\text{eff}}}{\omega \epsilon_0 \epsilon_r} \\ \epsilon_r \epsilon_0 &= \epsilon_\infty \epsilon_0 + \sqrt{\frac{2\sigma_0 \epsilon_\infty \epsilon_0}{\omega}} \\ \sigma_{\text{eff}} &= \sigma_0 + \sqrt{2\omega \sigma_0 \epsilon_\infty \epsilon_0} \end{aligned} \quad (5)$$

The values of  $\epsilon_\infty$  and  $\sigma_0$  have been derived in [4], by fitting the wall attenuation measurements for different water contents of the concrete.

## 3 Simulation results

In order to assess the attenuation provided by the wall for different values of the concrete humidity, a transmission line with  $r_w = 5$  mm,  $h = 10$  cm was simulated for different wall lengths. The transmission line sections before and after the concrete wall are assumed to be ideal transmission lines.

The line was excited with a double exponential pulse characterized by a risetime of 364 ps. The results for a 10-cm thick concrete wall are presented in Fig. 4. The top plot shows the waveforms of the injected (in black) and transmitted pulses, computed for different water contents ( $W=1\%$ ,  $W=10\%$ ,  $W=30\%$ , and  $W=100\%$ ). The bottom panel presents the magnitude of the transfer function between the injected signal and the transmitted signals, for the considered values of the concrete water content.

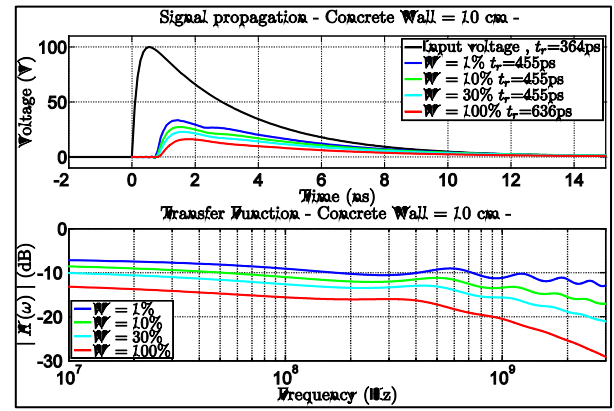


Fig. 3 Study of the propagation of an impulse through a 10-cm thick concrete wall. Top: injected and transmitted signals for different water contents of the wall. Bottom: Magnitude of the transfer functions between the injected signal and the transmitted signal.

As can be seen from the simulation results, the transmitted signals are attenuated by traveling through the concrete wall.

## 5 Conclusions

The presented study showed that common-mode IEMI signals along a transmission line suffer attenuation passing through a concrete wall. Attenuation levels of more than 60% of the peak amplitude are obtained for the adopted line configuration and excitation impulse.

## Acknowledgements

This study was financed by the Armatisuisse Science and Technology (Contract Nr. 8003504623).

## References

- [1] W. A. Radasky, C. E. Baum, and M. W. Wik, "Introduction to the special issue on high-power electromagnetics (HPEM) and intentional

- electromagnetic interference (IEMI)," *Electromagnetic Compatibility, IEEE Transactions on*, vol. 46, pp. 314-321, 2004.
- [2] D. V. Giri and F. M. Tesche, "Classification of intentional electromagnetic environments (IEME)," *Electromagnetic Compatibility, IEEE Transactions on*, vol. 46, pp. 322-328, 2004.
- [3] D. M. Pozar, *Microwave engineering*. Hoboken, NJ: Wiley, 2012.
- [4] D. V. Giri and F. M. Tesche, "Modeling of Propagation Losses in Common Residential and Commercial Building Walls," *Interaction Notes*, vol. 624, 2013.

# Application of varistor for RF protection of semiconductor bridge

Bin Zhou\*, Jun Wang<sup>†</sup> Pei-kang Du<sup>†</sup> Yong Li<sup>†</sup>

\*School of Chemical Engineering, Nanjing University of Science and Technology, Nanjing 210094, Jiangsu, CHINA.  
(e-mail:zhoubinnust@126.com)

## Abstract

The principle of varistor which was used in radio frequency (RF) protection of semiconductor bridge (SCB) was investigated in this paper. According to the RF injection experiment, electro-explosive performances of SCB with or without varistor were studied. The results showed that the ability of SCB to anti-RF had dramatically improved by varistor and there was no significant difference of SCB performances which was protected by varistor after 20W RF injection experiment. Therefore, the varistor had no influences on electro-explosive of SCB and could provide RF protection to SCB when in parallel with SCB.

**Keywords:** initiator, semiconductor bridge, radio frequency protection.

## 1 Introduction

Semiconductor bridge (SCB) is a kind of electro-explosive device which use it semiconductor film to ignite primary explosive. It has advantages of small, safety, ESD and RF tolerant. At the same time, it can operate at low energies and function very quickly. However, the electromagnetic environment is becoming more and more complex with the use of radar and other electromagnetic weapons. So there is a demand for ammunition to anti-RF. The electromagnetic environmental compatibility of initiator catches much attention for its characteristic of sensitive. Although SCB is insensitive to RF, but we still need to strengthen its ability of anti-RF.

The researchers had provide many ways to strengthen SCB, like changing the structure of SCB or adding external components. Ensign-Bickford company designed a new SCB structure that added a layer of dielectric material to top and bottom of SCB. There was no current in SCB when the voltage of SCB below the threshold voltage of dielectric material. But the dielectric material would be breakdown in nanosecond when giving the SCB all-fire voltage, the SCB would fire at the same time. The capacitor that formed by dielectric material could shunt high-frequency AC and suppressed voltage caused by ESD. This structure had a good performance of immunity to ESD and RF hazards[1]. L. Dow Robert added ferrite element to EED to absorb energy on bridgewire caused by RF. It could withstand high RF power levels or electromagnetic pulse by radar.[2] Re-Long Chiu provided a new kind of explosive device initiator. They

designed a multilayer semiconductor structure and supplied a MOS capacitor on the substrate. This structure could use the chemical reaction between metal and silicon to generate plasma. It showed excellent no-fire levels.[3] John H Henderson mounted the filter and EED on the same substrate. The filter was made of one capacitor and two ferrite beads.[4] Thomas A baginski designed a semiconductor junction igniter which had characteristics of immunity to ESD and RF.[5] Fei Chen[6] investigated the damage mechanism of SCB under RF and set up mathematical model and physical model under RF. In this paper, the mechanism of SCB that protected by varistor was studied by theoretical analysis and experiments.

## 2 The principle of varistor for RF protection

Generally, the SMD varistor is mounted in parallel with other device. The varistor will show open state with 100 M $\Omega$  resistance when there is no voltage coupled into the device, therefore it has no influence on the normal function of device. But the resistance of SMD varistor will change from 100M $\Omega$  to 100m $\Omega$  in nanosecond (<0.5 nS) when coupled into any power. So the voltage of the device can be controlled in a low level. Thus the varistor protects the device from voltage pulse by absorb the large energy that flow through itself. However, the resistance of varistor will return back after the voltage disappearing. The capacitance of varistor can reach 1000pF for its multilayer structure. When in low-frequency RF environment, the SMD varistor shows open state and has no influence on the normal operate of device. While in high-frequency RF environment, the SMD varistor forms a low-impedence bypass in nanosecond to shunt induced current to protect the device form the impact of electromagnetic radiation.

The equivalent circuit model of SMD varistor that used to protect SCB initiator was shown in Fig. 1. In this paper, we chose A-type SMD varistor with 8V breakdown voltage and the actual picture was shown in Fig 2.

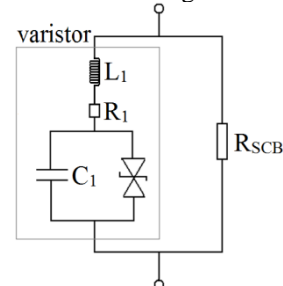


Figure 1. The equivalent model of varistor with SCB



**Figure 2. Photography of varistor**

Under the condition of high RF, the varistor shows a conducting state. The equivalent series resistance( $R_s$ ) and inductance( $L_s$ ) also exist in the circuit, thus the actual situation can be expressed as Equation (1).

$$Z = R + j \left( 2\pi fL - \frac{1}{2\pi fC} \right) \quad (1)$$

$f < \frac{1}{2\pi\sqrt{LC}}$ , the impedance will decrease with the increasing frequency.

$f = \frac{1}{2\pi\sqrt{LC}}$ , the impedance reaches minimum. The frequency is the resonant frequency and the resistance value of varistor is the parasitic resistance.

$f > \frac{1}{2\pi\sqrt{LC}}$ , the impedance will increase with the increasing frequency.

So the dynamic impedance of varistor is much less than SCB's. The capacitance can shunt current caused by high frequency for low impedance. Thus, the current that flows through SCB will decrease. The capacitance will not dissipate the energy, so most coupling energy will be absorbed by resistance. Meanwhile the parasitic resistance is very small and the area of SCB is large, the Joule heat caused by current can be dissipated soon. So it protects SCB from high RF.

### 3 Samples and experiment devices

#### 3.1 Samples

SCB chip is the most crucial element in SCB initiator. Fig. 3 is the structure of heavily doped polysilicon SCB (H shape). Between the silicon substrate and Aluminum pad is the heavily doped polysilicon and the doping concentration is  $7 \times 10^{19}$  atoms/cm<sup>3</sup>. We have two kinds of chips that one is D-type with the size of  $400\mu\text{m}(\text{L}) \times 100\mu\text{m}(\text{W}) \times 2\mu\text{m}(\text{T})$  and another is X-type with  $80\mu\text{m}(\text{L}) \times 20\mu\text{m}(\text{W}) \times 2\mu\text{m}(\text{T})$ . The resistance and all-fire energy of D-type is  $1.0\Omega$  and 10mJ, while X-type is  $1.3\sim 1.7\Omega$  and 3mJ.

The chip was packaged in ceramic plug as is shown in Fig. 4. The chip was adhered to ceramic plug with 4.5mm diameter by epoxy. Bonding the pins and chip with Si-Al wire and coating the Lead styphnate (LTNR) to the top of chip. While

the varistor was assembled on the bottom of ceramic plug and electric contracted to pins which meant in parallel with SCB chip. The experiment samples were shown in Table 1.

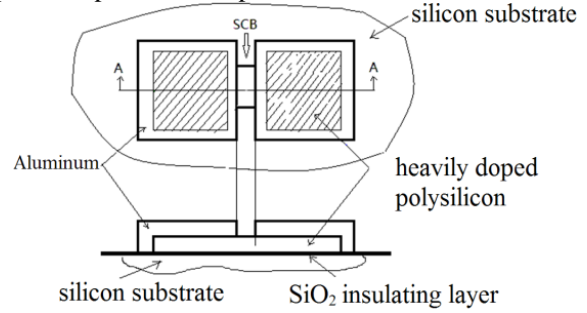


**Figure 3. SCB chip**

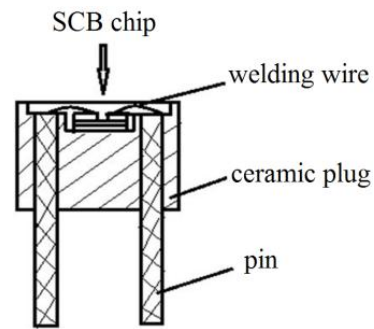


**Figure 4. Ceramic plug package structure**

Table 1: experiment samples

sample	State of sample
D-type	D-type SCB initiator without any protection
A-D-type	D-type SCB initiator being protected by A-type varistor
X-type	X-type SCB initiator without any protection
A-X-type	X-type SCB initiator being protected by A-type varistor

#### 3.2 The principle of capacitor discharge experiment

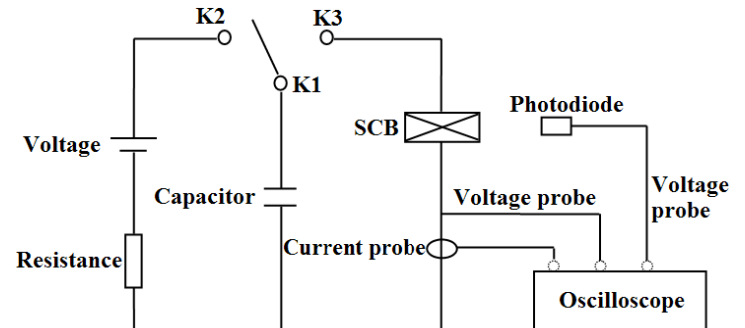


**Figure 5. Schematic of capacitor discharge experiment**

Capacitor discharge experiment was adopted to test the SCB initiator and the schematic diagram was shown in Fig. 5. We

used the oscilloscope to record the voltage and current of circuit during the experiment.

### 3.3 The principle of RF sensitivity experiment

In shielded room, the RF power was applied into SCB by a frequency and output power adjustable RF source through a matching device. The firing sensitivity under different RF frequency and the firing power under certain frequency were obtained by RF sensitivity test. The schematic of RF experiment was shown in Fig.6.

Equipment: Agilent 8257D RF resource, HP 436A、HP437B power meter, Agilent 8481A、Agilent 8481B、Agilent 8481H power sensor, AR DC3002 double directional coupling meter, TL16G-TP1 matching device and so on.

Experiment conditions: Ambient temperature was 20 °C ; Relative humidity was no more than 45%; RF energy was input through two pins with 10s injection time and recorded the result.

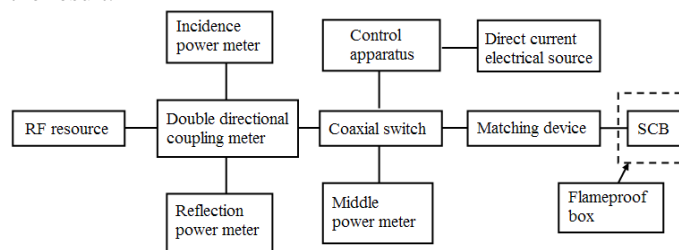


Figure 6. The schematic of RF experiment

## 4 The impact of varistor to RF sensitivity of SCB

To study the performances of RF protection capability of SCB initiator, two kinds of samples were tested by RF injection. The anti-RF ability was judged by percentage of firing, firing power, firing time and electro-explosive performance of SCB initiator.

### 4.1 The result of RF sensitivity experiment

According to RF injection experiment, we could test D-type and X-type SCB initiator which was out of protection. The Langlie procedure was adopted and set the test frequency 400MHz (the energy that coupled into the device was maximum under this condition). RF residence time was 10s and the test result was listed in Table 2

Table 2: RF sensitivity of SCB initiator

sample	50% firing power/W	Standard deviation/W	99.9% firing power/W
X-type	8.01	0.56	9.74
D-type	11.78	0.77	14.15

The results of SCB initiator without protection in experiment were as followed: 50% and 99.9% firing RF power of D-type

was 11.78W and 14.15W; while the X-type was 7.32W and 9.26W.

To test the function of varistor to SCB initiator, other experiments were carried out under the condition of 50% and 99.9% firing RF power. The result was shown in Table 3.

Table 3: RF injection experiment

sample	amount of samples	power/W	amount of firing samples
D-type	10	11.78	4
D-type	10	14.15	10
A-D-type	10	14.15	0
A-D-type	10	20	0
X-type	10	8.01	5
X-type	10	9.74	10
A-X-type	10	9.74	0
A-X-type	10	20	0

All of D-type SCB initiators without protection were firing under the condition of all-fire power. However, the initiators with varistor protected could keep safety under the same condition. We could get the same result from another type of SCB initiator.

The result showed that SMD varistor which was in parallel with SCB initiator could effectively decrease the RF sensitivity of initiator. Upon the RF resource was applied to SCB initiator, the SMD varistor could form low impedance bypass for its capacitance. Therefore the varistor would shunt most of power and protect the SCB initiator.

### 4.2 The firing experiment of SCB initiator after RF injection

According to firing experiment, we could comparing X-type (without RF experiment) with A-X-type initiator (after 20W RF experiment). Experiment conditions: Capacitor was 22 μF and charging voltage was 9V; Giving the power to the device from pin-to-pin. The typical firing curve and the result was shown in Fig. 7 and Table 4, separately.

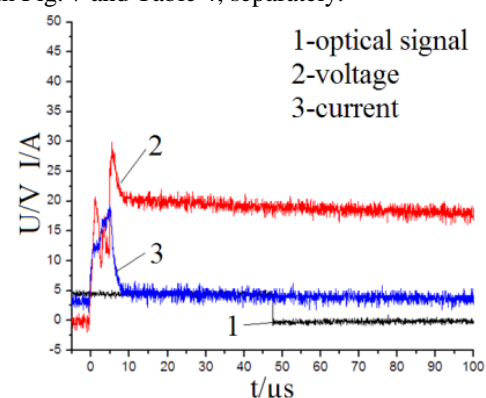


Figure 7. SCB initiator voltage and current signal

Table 4: RF injection experiment

sample	NO.	resistance/ $\Omega$	Burst time/ $\mu$ s	Firing time/ $\mu$ s	Average burst time/ $\mu$ s	Standard deviation/ $\mu$ s	Average firing time/ $\mu$ s	Standard deviation// $\mu$ s
X-type without RF injection	X1	1.60	4.24	80.16	4.1	0.33	95.22	15.18
	X2	1.37	3.88	102.04				
	X3	1.42	3.56	72.6				
	X4	1.64	3.68	104.92				
	X5	1.49	4.04	124.92				
	X6	1.60	4.68	110.84				
	X7	1.35	3.96	78.48				
	X8	1.64	4.20	93.04				
	X9	1.47	4.40	92.72				
	X10	1.56	4.36	92.44				
A-X-type after RF injection	A-X1	1.57	4.80	103.32	4.04	0.28	94.46	13.13
	A-X2	1.46	4.16	81.44				
	A-X3	1.69	3.96	76.52				
	A-X4	1.35	3.72	86.36				
	A-X5	1.41	4.12	85.8				
	A-X6	1.45	3.80	98.96				
	A-X7	1.57	3.88	107.72				
	A-X8	1.50	3.96	80.68				
	A-X9	1.66	3.96	108.76				
	A-X10	1.63	4.00	115.00				

Table 5: t-test result

	Burst time	Firing time
t	0.444	0.114

The t-test was applied to check the experiment results of these two kinds of SCB initiator. From Table 5, we could conclude there was no significant difference between two kinds of SCB initiator in firing time. Therefore, the SCB initiator could keep its nature after RF experiment.

## 5 conclusion

The RF protection principle of SMD varistor which was used in SCB initiator was investigated in this paper. Meanwhile, RF protection capability of SCB with the protection was tested by RF injection experiment at frequency of 400MHz. The influences of SMD varistor to the electro-explosive performance of SCB initiator were also studied. The conclusions were as follows:

- (1) The RF firing sensitivity of D-type and X-type SCB initiator would significantly reduce after being protected by SMD varistor. Both D-type and X-type SCB initiator would fire at their all-fire energy. While they could keep safety at the same condition after being protect by SMD caristor. So SMD caristor could dramatically improve the RF protection capability of SCB.
- (2) The firing performance of X-type initiator which was protected by varistor wouldn't change after 20W RF injection experiment. Thus the varistor could improve RF protection capability without changing the firing performances of SCB initiator.

## References

- [1] D. B. Novotney, B. M. Welch. "Semiconductor bridge development for enhanced ESD and RF immunity", *AIAA99-2417*, (1999).
- [2] R. L. Dom, P. W. Proctor. "Attenuator for protecting an electroexplosive device from inadvertent RF energy or electrostatic energy induced firing", *USP5279225*, (1994).
- [3] Re-Long CHUI. "Silicided MOS capacitor explosive device initiator", *USP2015/0007739*, (2015).
- [4] J. H. Henderson, T. A. Baginski. "An RF-Insensitive Hybrid Electroexplosive Device Incorporating an Integral Filter", *IEEE Transactions on Industry Applications*, 32. 465-470, (1996).
- [5] T. A. Baginski, S. L. Taliaferro. "Novel Electroexplosive Device Incorporating a Reactive Laminated Metallic Bridge", *Journal of propulsion and power*, 17. 184-189, (2001).
- [6] FEI chen. "The research on mechanism of SCB under ESD and RF", *Nanjing university of science and technology*, (2012).

# Simulation of protective effect of several protective devices to sensitive EED under extreme ESD environment

Zhixing Lv\*, Nan Yan \*, Wei Ren †, Yingwei Bai †

\*State Key Laboratory of Explosion Science and Technology, Beijing Institute of Technology, Beijing, 100081, China, yn@bit.edu.cn, †Shanxi Applied Physical Chemistry Research Institute, Xi'an, 710061, China

## Abstract

Pin-pin ESD protection methods of EED were studied due to harmfulness of ESD (Electrostatic Discharge) to EED (Electrical Explosive Device). TVS (Transient Voltage Suppressor), varistors, semiconductor arrester and shunt capacitance were simulated by Pspice software respectively. Results showed that TVS and varistors could be used for pin-pin ESD protection to EED; semiconductor arrester and shunt capacitor were not suitable for pin-pin ESD protection to EED. The pin-pin ESD protective effect of TVS and varistors to EED were studied by experiments. Results showed that when human body's electrostatic voltage is 50kV, EED was not fired protected by TVS and electrostatic protection capability increased by more than 90%, while the protection capability only increased by 3.1% when varistors were used.

**Keywords:** Sensitive EED, ESD, electrostatic protection

## 1 Introduction

Bridgewire EED is the most widely used in EED [1]. Because the input electrical energy is used as the excitation energy, it is susceptible to all kinds of electromagnetic environment [2, 3]. The static security of pyrotechnics is the most critical performance indicators in safety evaluation of EED use [4, 5]. Liu Shanghe academician suggested that the body static voltage could reach up to 50kV [6]. Chen Fei, etc. used varistors in the ESD protection to SCB. But SCB are insensitive pyrotechnics [7], the protection of sensitive EED under extreme ESD environment have not been reported.

The way to improve the pin-pin antistatic ability can be divided into two categories: one is to improve the threshold of EED firing, so there is not enough ESD energy to make ignition composition firing or injury; one is to shunt the electrostatic energy and reduce the energy injected into the bridgewire by the use of electronic components, etc. [8]

## 2 The characteristics and simulation analysis of ESD protection device

### 2.1 Simulation of protective effect of TVS to pin-pin ESD

The EED bridgewire material is nickel-chromium alloy; diameter is 9 $\mu$ m; bridge resistance is 6.5 $\Omega$ ; safe current is 50mA; the electrostatic voltage is 50kV. The ESD current flowing through the bridge is calculated with PSPICE simulation model and shown in FIG 2 of the red curve.

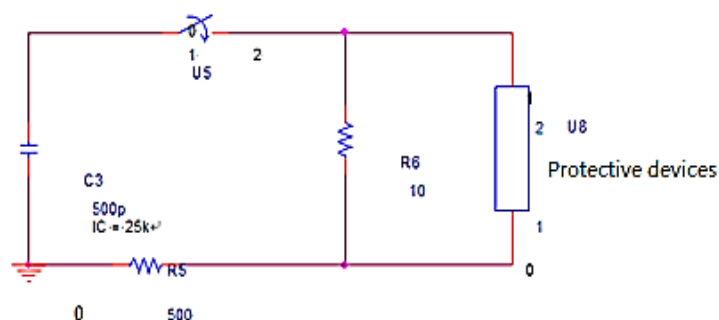
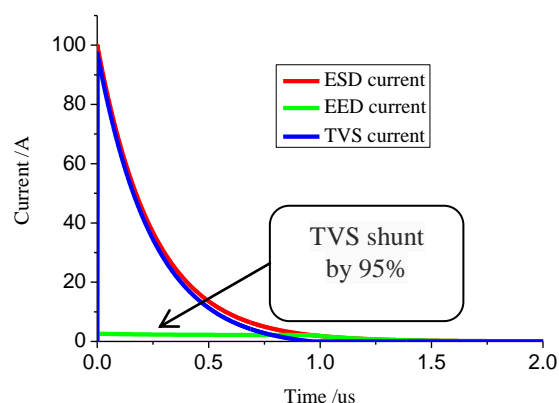


Figure 1 Parallel circuit model of protective device

Bidirectional TVS (Type SMDJ12CA) is selected as a protective device. The maximum reverse work voltage  $V_{RWM}$  is 12V. Use Orcad/Pspice to simulate protective effect of TVS to ESD which are shown in Figure 2.



Current-time curve

Figure 2 The protective effect of SMDJ12CA TVS under voltage 50kV

We can see that for static voltage 50kV, static current peak is 100A, and EED current peak is only 5A, namely TVS diversion 95% of the current. ESD energy of EED reduces from 8mJ to 0.035mJ, which is only 1/200 of ESD energy flows into the EED bridgewire. The protective effect of TVS is very significant by theoretical calculations.

### 2.2 Simulation of protective effect of varistors to pin-pin ESD

When electrostatic voltage is 50kV, the ESD current peak in the total circuit is 100A, and the EED current peak is only 10A, namely varistors diversion 90% of the current. The ESD energy flows into the EED bridgewire reduced from 8mJ to 0.245mJ which is one thirty of the unprotected.

### 2.3 Simulation of protective effect of semiconductor arrester to pin-pin ESD

We can see that when electrostatic voltage is 50kV, the ESD current peak in the total circuit is 100A, and the EED current peak is 80A, namely semiconductor discharge diversion 20% of the current. The ESD energy flows into the EED bridgewire reduced from 8mJ to 2.25mJ. The protective effect of semiconductor discharge is poor by theoretical calculations.

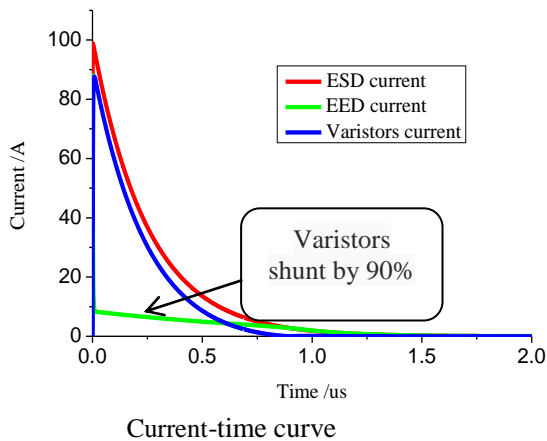


Figure 3 The protective effect of Varistor under voltage 50kV

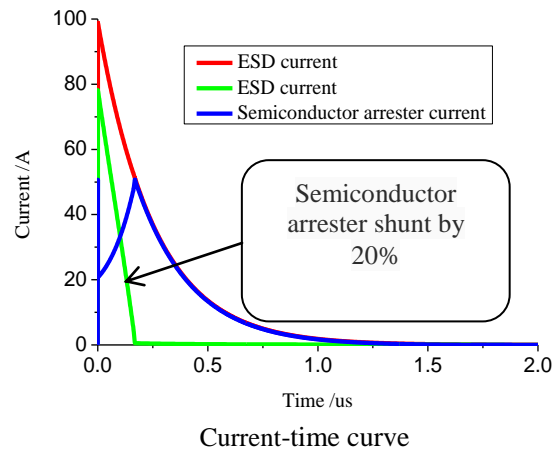


Figure 4 The protective effect of Semiconductor arrester under voltage 50kV

### 2.4 Simulation of protective effect of shunt capacitance to pin-pin ESD

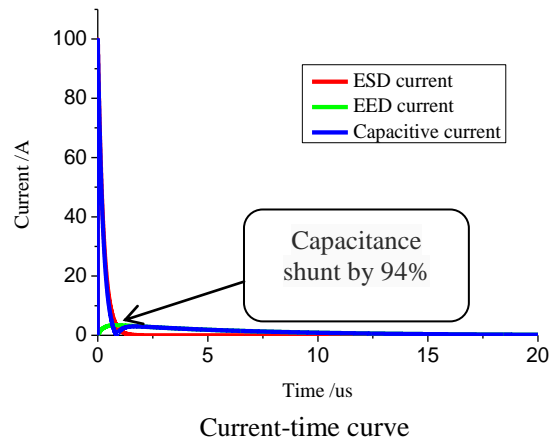


Figure 5 The protective effect of 1μF capacitance under voltage 50kV

As shown in Figure 5, after paralleling 1μF capacitor, when voltage is 50kV, the EED current peak reduces from 72A to 4A94.4%, but the duration of the discharge is longer. From the energy-time curve we can see that the ESD energy flows into the EED bridgewire reduced from 8mJ to 0.31mJ. But the effect lasts more than ten microseconds which is two orders of magnitude larger than other protective devices (hundreds of nanoseconds). Therefore shunt capacitance is not suitable for ESD protection to sensitive EED.

## 3 Experimental study on pin-pin electrostatic protection

According to the simulation analysis of various components above, the protective effects of semiconductor arrester and

shunt capacitance to pin-pin ESD were not ideal. So experimental verifications were taken by varistors and TVS.

### 3.1 experimental verification by varistors

The experimental verifications were taken by varistors. (Type TG0402ML240K).

The model (single RC series 5kΩ) were taken as test conditions. After static test, the measured critical ignition condenser discharge voltage is 27.11 kV.

By analyzing the test results, we can see that current can not shunt quickly because of the short response time of varistors, which resulted in the sample fire. Compared with the simulation results above, we can see that the effect difference between the protected and unprotected is about 20%. Therefore the protective effect of varistors is ineffective.

### 3.2 experimental verification by TVS

The experimental verifications were taken by TVS. (Type P6KE12CA and ESD12V32D-C).

We can see from table 2 that the sample is not fried under the extreme 50 kV voltage by TVS protection. This suggests that product is safe under 50 kV ESD by TVS protection, which fully shows protective effect of TVS is ideal.

We can get the conclusions from Figure 6 in the following:

(1) The protective effect of ESD of the TVS is significantly better than the varistors'.

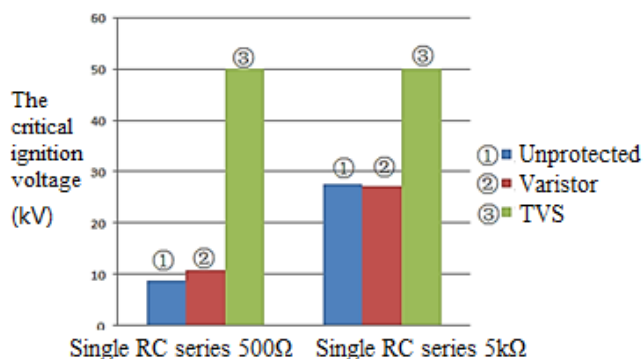


**Figure 6 Results of electrostatic sensitivity test of different protective devices**

(2) For sample 12 diameter bridgewire, the electrostatic critical ignition voltage is 26.30kV. When varistors are used, electrostatic voltage increased to 27.11kV only and electrostatic protection capability is increased by 3.1% only. When TVS are used, electrostatic voltage reaches up to 50kV or more. Compared with the simulation results, electrostatic protective capacity increases by more than 90%. According to the results we can see that the response time of TVS ( $10^{-12}$  seconds) was faster (four orders of magnitude faster) than the varistor' ( $10^{-8}$  seconds). Therefore the protective effect of ESD of the TVS is significantly better than the varistors'.

## 4 Conclusion

(1) TVS, varistors, semiconductor arrester and shunt capacitance were simulated by Pspice software respectively. Results showed that TVS and varistors could be used for pin-pin electrostatic protection of EED; semiconductor arrester and shunt capacitor were not suitable for pin-pin electrostatic protection of EED.

(2) The pin-pin high pressure static tests have been taken by varistors and TVS respectively on sample. Results showed that the varistors was not reliable for protection in the static environment, while TVS can still effectively protect the pin-pin on sample when extreme high pressure is 50kV. Therefore the protective effect of ESD of the TVS is significantly better than the varistors'.

## References

- [1] Cai Ruijiao. "The design sensitivity principle", China, Beijing institute of technology press, 1, (1999).
- [2] GJB 736.11-1990. "EED electrostatic sensitivity test", China, National defense science and technology commission.
- [3] GBT8031-2005. "Industrial electric detonator", China, Standardization Administration of China.
- [4] MIL-DTL-23659F-2010. "Electric detonators universal design specification", USA, US Department of Defense Department of the Navy.
- [5] ZHANG Chuang. "Electrostatic Harzard and Protection of Initiating Explosive Device during Production", EQUIPMENT ENVIRONMENTAL ENGINEERING, 10, pp. 121-124, (2013).
- [6] Liu Shanghe, Tan Zhiliang, Wu Zhancheng. "The Development in Electrostatic Protection Engineering", Engineering Science, 2, pp. 17-23, (2000).
- [7] Chen Fei, Zhou Bin , Qin Zhichun. "Anti-electrostatic and Anti-RF Technology of Semiconductor Bridge Explosive Devices", Explosive Materials, 39, pp. 32-36, (2010).
- [8] Lanrin J, Zaky G, Keith G B. "On the prediction of digital circuit susceptibility to radiated EMI", IEEE Trans. on EMC, 37, pp. 528-535, (1995).

# Wideband Differential Technique to Measure the Input Impedance of Electro-Explosive Devices

John J. Pantoja\*<sup>1</sup>, Néstor Peñã\*, Ernesto Neira<sup>1</sup>, Félix Vega<sup>1</sup>, Francisco Roman<sup>1</sup>

\*Electronics and Systems of Telecommunications Group (GEST), Universidad de los Andes, Bogotá, Colombia

<sup>1</sup>Electromagnetic Compatibility Group (EMC-UN), Universidad Nacional de Colombia, Bogotá, Colombia  
jjpantojaa@unal.edu.co

## Abstract

A procedure to characterize the differential-mode input impedance of electro-explosive devices (EED) in a wide frequency band is described in this document. The differential measurement is obtained from the device's mixed-mode S parameters. Measurements are performed with a differential probe to connect the differential port, formed by the EEDs' two lead-in wires, and the single-ended ports of a vector network analyser. Experimental results are compared with an EED analytical model based in transmission lines in cascade, obtaining a good agreement.

**Keywords-** Electro-explosive device (EED), Mixed-mode S parameters, differential measurement, balanced devices..

## 1 Introduction

The wideband characterization of differential devices, such as dipole antennas, transmission lines, and electro-explosive devices, shows some challenges because the measuring instruments usually present unbalanced ports. An alternative to performing this measurement using a balun is the use of the mixed-mode S parameters of a differential port conformed by two single-ended ports in a vector network analyser (VNA). Improvements in the accuracy and the frequency range with this technique are directly achieved.

Although new balun designs provide interesting wideband responses [1], the direct characterization based on the mixed-mode S parameters offers an attractive alternative since the accuracy and frequency band depend on the VNA and connecting devices characteristics and the de-embedding process. In [2], this technique is used to measure the input impedance of critical equipment with multiple and non-standard microwave ports. In [3], the same technique is proposed to characterize the receiving properties (i.e. gain and input impedance) of differential antennas. In this document, the procedure presented in [3] is used to measure the differential input impedance of hot-wire based electro-explosive devices (EEDs) and the results are compared with an analytical model based on the EED's transmission line model proposed in [4].

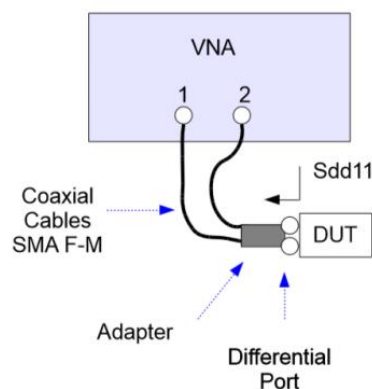


Figure 1. Differential measurement using two common-mode ports of a vector network analyzer

## 2 Differential Measurement

The differential mode input impedance can be calculated as [3]

$$Z_{in} = Z_{0diff} \frac{1+S_{dd}}{1-S_{dd}} \quad (1)$$

where  $Z_{0diff}$  is the VNA differential impedance and  $S_{dd}$  is the de-embedded differential reflection S parameter. The differential S-parameter can be obtained using a conventional VNA as

$$S_{dd} = \frac{1}{2}(S_{11} - S_{21} - S_{12} + S_{22}) \quad (2)$$

where  $S_{11}$ ,  $S_{21}$ ,  $S_{12}$ , and  $S_{22}$  are the conventional single-ended S parameters. The measurement setup to obtain the differential impedance of any device under test (DUT) is shown in Fig 1.

Since the EED has not a standard port for microwave measurements, an adapter is required. Depending on the adapter, a de-embedding process should be performed. In this case, the same adapter and de-embedding method presented in [3] was performed. Fig. 2 shows the detail of the EED connection to the differential adapter.

The measurement procedure includes the VNA calibration with standard calibration kit at the end of the coaxial cables and the adapter de-embedding. Due to the adapter simplicity (i.e. it is composed by two coaxial cables and a section of a parallel wire transmission line), the de-embedding can be performed by modeling the adapter with a two-port network of transmission lines in cascade and good results are obtained

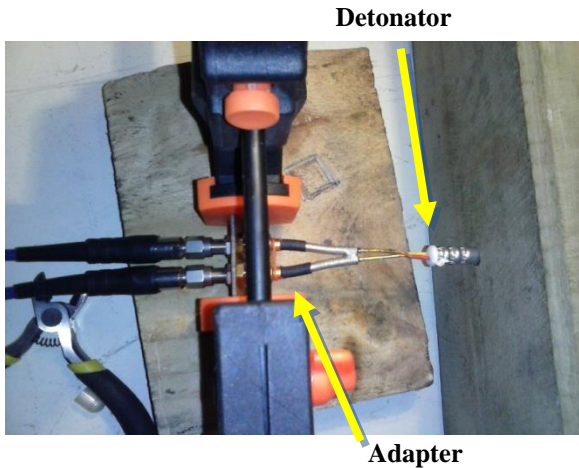


Figure 2. Experimental setup.

up to 3 GHz [3]. To assure an adequate electrical connection between the adapter and the EEDs without soldering, a pressure system was used. The EED lead-in wires were introduced in SMA internal pins and they were squeezed by using tiny screws.

### 3 Safety Measures

Since the devices under test are explosive devices, special safety measures should be considered. First, the VNA output power must not exceed the EED's No-Fire Threshold (NFT) [5]. This parameter is around 0.25 A for low energy EEDs. In addition, the test should be performed in a site with controlled environmental conditions. Basic safety measures for explosive handle are presented in [6]. In particular, the test site should be:

- Fresh and dry
- Well-ventilated
- Without direct solar exposure
- Without excessive vibration

In addition, since EEDs are susceptible to electromagnetic fields, they should not be exposed to radiofrequency disturbances. Therefore, to avoid the initiation risk due to electromagnetic signals, EEDs should be carried in a metallic closed box and the test should be performed in a shielded room.

### 4 Results

The differential impedance measurement of different filled and unfilled EEDs between 100 MHz to 3 GHz was performed. To illustrate the technique, Fig. 3 shows the comparison between an inert-EED impedance measurement and the results of the transmission line model described in [4]. The figure shows that a good agreement is obtained. Fig. 4 presents the transmission line parameters used in the analytical model, which were calculated based in the actual EED dimensions and the fillers' electrical characteristics. Dielectric losses and permittivity were based on typical values in the microwave range.

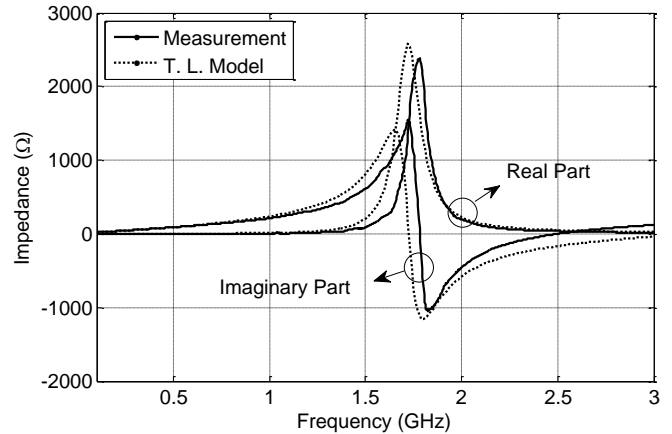


Figure 3. Measured inert-EED impedance compared to the calculated from the transmission line model.

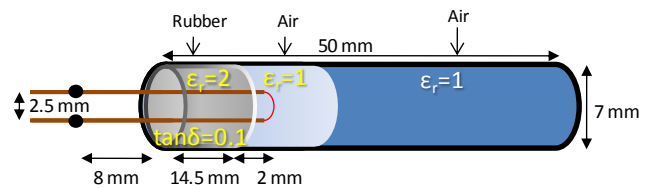


Figure 4. Diagram of an inert EED with dimensions and fillers' electrical properties.

### 5 Conclusion

A technique to experimentally characterize the input impedance of EEDs, based on the differential reflection S parameter, was presented. It was shown that this technique produces stable and accurate measurements of the input impedance of EEDs in the microwave range. These experimental results were compared with an analytical model based in transmission lines, obtaining a good agreement between measurements and calculations.

### References

- [1] B. Baker, "A Wideband Balun for HF, VHF, and UHF Applications," *Microwave Magazine, IEEE*, vol. 15, pp. 86-91, 2014.
- [2] N. Mora, M. J. Salvatierra, C. Romero, F. Rachidi, and M. Rubinstein, "Critical equipment input impedance measurement for IEMI calculations," in *Electromagnetic Compatibility (EMC), 2013 IEEE International Symposium on*, 2013, pp. 416-422.
- [3] J. J. Pantoja, N. Peñã, F. Román, F. Vega, and F. Rachidi, "Wideband Experimental Characterization of Differential Antennas," in *Proc. of the Sixth European Conf. on Antennas and Propagation EuCAP 2012 Prague*, 2012.
- [4] M. R. Lambrecht, K. L. Cartwright, C. E. Baum, and E. Schamiloglu, "Electromagnetic Modeling of Hot-Wire Detonators," *IEEE Trans. Microw. Theory Tech.*, vol. 57, pp. 1707-1713, 2009.

- [5] *Ministry of Defence Explosives Regulations (JSP 482), Chapter 24*, Ministry of Defence, UK Government, DSEA-DOSR-Policy, Edition 4, 2013.
- [6] United Nations Mine Action Office, "National Technical Standards and Guidelines Sudan," in *Part 1, Chapter 12*, ed, 2007.

# Research on Induction Current of Bridge Wire of Industrial Electric Caps using FDTD Arithmetic

DU Bin\*, Luan Ying<sup>†</sup>

(\*Department of Chemical Engineering, Anhui University of Science and Technology, Huainan Anhui 232001;

<sup>†</sup> Xi'an Jiaotong University, Xi'an, 710061)

## Abstract

**This paper introduces the principles and characteristics of the electromagnetic FDTD method. It has, based on the orthogonal FDTD arithmetic, deduced the non-orthogonal algorithm in arbitrary medium, and calculated the induced current of industrial electric detonator in continuous electromagnetic radiation. The results show that the industrial electric detonator could be probably ignited by induction current flowing through the bridge wire under continuous electromagnetic radiation.**

**Keywords:** stability conditions; industrial electric detonator; induction current; electromagnetic radiation

## 1 Introduction

With an increasingly expanded application of FDTD arithmetic, various types of unconventional FDTD arithmetics are gradually developed. Wherein, the arithmetic in different coordinate systems and the arithmetic by adopting different grid sizes are included. When the studied object or medium has the curved surface (circular wave guide, and surface of aircraft, etc.), the “ladder” boundary is formed if the traditional rectangular grid cell is used to fit the surface, and the use of the “ladder” boundary will not only stimulate the transmission of surface wave and arouse the additional numerical dispersion, but also need reducing the size of grid cell and correspondingly reducing the time step, and thereby greatly increasing the computational storage content and lengthening the computation time, so as to fit

the medium interface in small curvature radius or the multi-layer medium interface. For the purpose of overcoming the problem aroused by the “ladder” surface, the better method is to use the common curvilinear coordinate system, making the coordinate line fit the geometrical surface of the medium. Thus, Holland puts forward FDTD arithmetic in the common curvilinear coordinate system<sup>[1]</sup>, and Jin-Fa Lee improves the discrete iterative equations<sup>[2-6]</sup> to be more intuitive and easier to programme on the basis of Holland's research. Whereas, discrete iterative equations given by them all direct at the single medium. This paper deduces the non-orthogonal FDTD arithmetic suitable for arbitrary medium and tries to apply the arithmetic to the calculation of the induction current of bridge wire of industrial electric detonator on the basis of reference of predecessors' related literatures.

## 2. Analysis of the radiation current of bridge wire of the industrial electric detonator

Due to the geometric structure and the complexity of the selected materials of the industrial electric detonator, there are many factors influencing the electromagnetic compatibility. It is very hard to conduct the overall modeling analysis on the industrial electric detonator with the current calculation method and the computer level. So, some simplified treatments have to be conducted when analyzing the electromagnetic compatibility of the industrial electric detonator. Based on the simplification, safety criteria are proposed to make it possible for the analysis and calculations.

The ideal simplified model of the industrial electric detonator is shown in Figure 1. The shield and attenuation effects of the case of the industrial electric detonator are ignored in the analysis. Only the worst electromagnetic radiation is considered in such treatment.

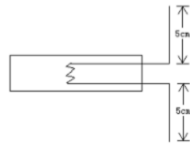


Fig.1 Simplified model of the industrial electric detonator of bridge wire  
Generally, the resistance of the bridge

wire is about  $2\Omega$ . The resistance of the bridge wire can be very small comparing with the resistance of the lead, so it can be ignored. The lead of the bridge wire is 10 cm with the diameter of 1 mm.

Under the exposure of the outer-electromagnetic field, the industrial electric detonator can produce the electromagnetic scattering as well as induction current in the bridge wire. In order to guarantee that the calculation of values is conducted in the finite region, the corresponding absorption boundary conditions must be adopted on the truncated boundary. PML absorption boundary condition is adopted in this calculation.

The sine electromagnetic wave of the high power microwave under the gauss impulse modulation undergoes approximate treatment, and the electric field of the incident wave is

$$E^{inc} = E_0 \sin(2\pi f_0 t) \exp\left[-\frac{(t-t_0)^2}{T_0^2}\right] \quad (1)$$

Wherein: the direction of

$$E_0 = 1.0 \times 10^5 V/m, f_0 = 6GHz, t_0 = 2ns, T_0 = 0.6ns, E^{inc}(t)$$

is parallel with the axis of the bridge wire.

The large-equivalent nuclear explosion in high altitude can produce very strong electromagnetic impulse. When the electromagnetic impulse spreading to the ground is simplified to one plane wave, the normalized nuclear electromagnetic impulse in high altitude can be approximately described by a double-index single impulse.

$$E(t) = 5.25 \times 10^4 \left[ \exp(-4 \times 10^6 t) - \exp(-4.67 \times 10^8 t) \right] \quad (2)$$

In the equation, E(t) is the intensity of the electric field (v/m) and t is the time s.

The induction current of the bridge wire can be gotten by Equation (3). The integral path can be the circle around the bridge wire.

$$I = \oint_C H \cdot dl \quad (3)$$

Results of the induction current flowing through the bridge wire under the radiation of the high-power microwave and the nuclear electromagnetic impulse calculated by Feko software are respectively shown in Figure 2 and Figure 5

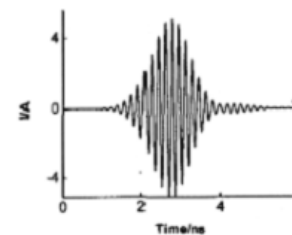


Fig.2 Induction current of the bridge wire under the radiation of the high power microwave

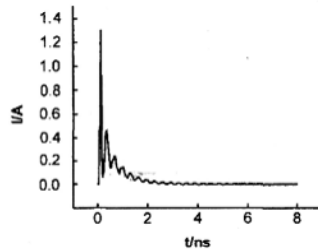


Fig.3 Induction current of the bridge wire under the radiation of the nuclear electromagnetic impulse

Seeing from Figure 2, we can know that the incident wave used for numerical calculation has impact on the wave form of the induction current in the conditions of frequency  $f_0$  or field strength (or power), but has a little impact on the peak value of the current. In addition, seen from Figure 2 and Figure 3, peak values of the induction current are about 5A and 1.4A, far higher than the striking current of the industrial electric detonator. So it is confirmed that the industrial electric detonator can be detonated by the induction current flowing through the bridge wire under the continual radiation of the high power microwave or the nuclear electromagnetic impulse.

### 3. Conclusions

This paper firstly introduces the principles and characteristics of the electromagnetic FDTD method. Then, it has, based on the orthogonal FDTD arithmetic, deduced the non-orthogonal algorithm in arbitrary medium, and discussed the stability conditions for calculation of values. Thereafter, this paper calculates the induced current of industrial electric detonator in continuous electromagnetic radiation and comes to the conclusion theoretically that the industrial electric detonator could be probably ignited by induction current flowing through

the bridge wire under continuous electromagnetic radiation.

### Bibliographies

1. [1]K. S. Yee, "Numerical Solution of initial Boundary Value Problems Involving Maxwell's Equation in Isotropic Media", IEEE Trans. OD AP. VOLAP-14 1966, PP302-307.
2. [2]Gao Benqing, "FDTD Method", National Defense Industry Press,1995.3.
- 3.[3] Wang Changqing, Zhu Xili, FDTD Method to Calculate Electromagnetic Field, Peking University Press, 2014.
- 4.[4] Jia-Ying Wang. Ben-Qing Gao. "A Method of Sub-region Connection in FDTD Algorithm,"Microwave &Optical Tech. Leters Vol. 19, No.3. Oct. 1998
- 5.[5]A Taflove, M.E.Brodwin. "Numerical Solution of Steady State Electromagnetic Scatering ProblemsUsing the Time Domain Maxwell's Equations," IEEE Trans. on MTT,1975,23(8), pp623-630.
- 6.[6] G.Mur, "Absorbing Boundary Conditions for the Finite-Diference Approximation of Time Domain Electromagnetic Field Equations."IEEE Trans. on EMC. Vol.23. pp.377-382, Nov. 1981.
- [7]Jia Ying, "Time Domain Electromagnetic Field Calculation Technology and its Application", Ph.D. and other doctoral theses of Beijing Institute of Technology, 1998.12

# Application of the Random Coupling Model to Statistical Properties of Complex Enclosures

*Bo Xiao\**, *Thomas Antonsen\**, *Edward Ott\**, *Steven M. Anlage\**

\* *Department of Physics and Department of Electrical and Computer Engineering at the University of Maryland, College Park, MD, USA 20742-4111, [anlage@umd.edu](mailto:anlage@umd.edu), <http://anlage.umd.edu>*

## Abstract

**The effectiveness of the Random Coupling Model (RCM) in predicting electromagnetic wave coupling to electronic components within a complex enclosure is examined. In the short wavelength limit with respect to the characteristic length of the enclosure, electromagnetic wave propagation within a large enclosure is sensitive to small changes to the interior, or to the boundaries of the enclosure. Such changes can reduce or invalidate the applicability of deterministic predictions of the electromagnetic fields at radiofrequencies (RF) in large enclosures. Under such circumstances, a statistical approach is needed to provide a better understanding of RF coupling to components within large enclosures. In this contribution, we experimentally demonstrate the applicability of the RCM to estimate the probabilistic magnitudes of RF fields on a variety of components that are partially shielded within a complex, three-dimensional enclosure.**

**Keywords:** Overmoded enclosures, statistical electromagnetism, electromagnetic compatibility, Random Coupling Model, wave scattering.

## 1 Introduction

There is practical interest in the statistics of electromagnetic radiation affecting sensitive electronics that are shielded within a large enclosure, especially for electromagnetic compatibility (EMC) [1-3]. The radiofrequency (RF) coupling to electronics within a large enclosure can be studied by considering a wave scattering problem in the short wavelength limit. While the applied wavelength is short with respect to the characteristic length of the wave enclosure, electromagnetic field distributions in electrically large enclosures can vary dramatically even with a small rearrangement of the internal objects, a small change in the enclosure boundaries, or a change in frequency of the excitation waveform. Coupling of electromagnetic fields to a component, such as a conductor or an electronic device, in one enclosure may be quite different in another nearly identical enclosure. Therefore, deterministic calculations are valid only for the particular situation modeled. Under such circumstances, analysis of the statistical properties of

electromagnetic fields in these complex environments is necessary, and the statistical predictions can better represent the properties of complex enclosures.

In this work, the statistical treatment we employ is the Random Coupling Model (RCM) which is based on wave chaos and has been successfully applied to describe the statistics of many wave scattering properties [4-8]. In a wave chaotic system, the statistical features of the scattering or impedance matrix has a universal fluctuating part and a system-specific deterministic part. The universal fluctuation part is well predicted by Random Matrix Theory (RMT) [7], and the Random Coupling Model combines the system-specific deterministic part with the universal fluctuation part in an impedance approach [4-8].

## 2 Experiment

We test the application of the RCM in modeling the wave coupling to electronic components within a complex enclosure (see Fig. 1). The complex enclosure is a reverberation chamber (rectangular aluminum box with dimensions of 1.22 m  $\times$  1.27 m  $\times$  0.65 m) with internal stirrers. We consider 2-port systems in which one port acts as a source of radiation (which can include, for example, open apertures on the wall of the enclosure), and the second port is considered a target and can take the form of a monopole or electrically-large object (such as a wire bundle). We measure the scattering matrix between these two ports as a function of frequency and configuration details of the box (typically many stirrer locations).

We treat the data statistically according to the RCM prescription as,

$$Z_{cav} = j \text{Im}[\langle Z_{cav} \rangle] + \text{Re}[\langle Z_{cav} \rangle]^{1/2} z \text{Re}[\langle Z_{cav} \rangle]^{1/2}, \quad (1)$$

where  $z$  is the normalized (universally fluctuating) impedance matrix (predicted by RMT and the losses in the system),  $Z_{cav}$  is the cavity impedance matrix, and  $\langle Z_{cav} \rangle$  is the ensemble and/or frequency averaged cavity impedance matrix. An example of the use of this equation to extract the universally fluctuating impedance for a 1-port system is shown in Fig. 2 [4].

We present data on induced-voltage pdfs for target ports in complex enclosures which are illuminated either internally or through an open aperture. The RCM predictions are found to

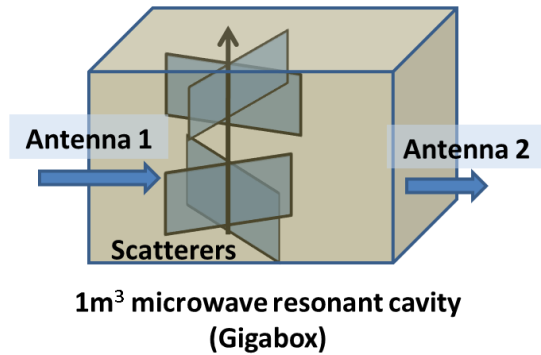


**Figure 1.** Schematic diagram of the two-port complex enclosure used for tests of the random coupling model.

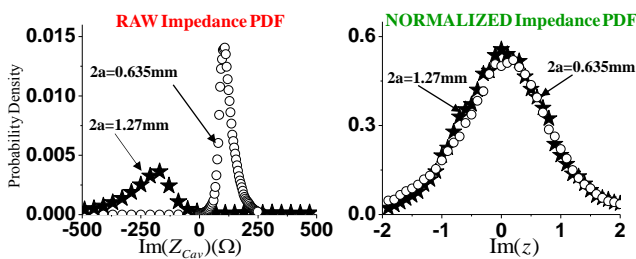


**Figure 2.** (Left) probability distribution function (pdf) of raw cavity impedance data measured with antennas of different diameters, as indicated. (Right) plot of normalized impedance pdf after the system-specific antenna effects have been removed, revealing the universal underlying impedance fluctuations described by Random Matrix Theory.

be in excellent agreement with the measured results. We comment on the extension of the RCM to increasingly complex scenarios including chains of connected enclosures, systems with mixed regular and chaotic ray dynamics, and the statistics of evanescent coupling between enclosures through apertures and waveguides that are below cutoff.

## Acknowledgements

This work was supported by the Air Force Office of Scientific Research FA95501010106, and the Office of Naval Research N00014-13-1-0474 and the Center for Nanophysics and Advanced Materials (CNAM).

## References

- [1] D. A. Hill, *Electromagnetic Fields in Cavities: Deterministic and Statistical Theories*, New York: Wiley-IEEE Press, 2009.
- [2] D. Fedeli, G. Gradoni, V. M. Primiani and F. Moglie, "Accurate Analysis of Reverberation Field Penetration Into an Equipment-Level Enclosure," *IEEE Transactions on Electromagnetic Compatibility*, vol. 51, no. 2, pp. 170-180, May 2009.
- [3] G. B. Tait, R. E. Richardson, M. B. Slocum, M. O. Hatfield and M. J. Rodriguez, "Reverberant Microwave Propagation in Coupled Complex Cavities," *IEEE Transactions on Electromagnetic Compatibility*, vol. 53, no. 1, pp. 229-232, Feb. 2011.
- [4] S. Hemmady, "A Wave-Chaotic Approach to Predicting and Measuring Electromagnetic Field Quantities in Complicated Enclosures (PhD Thesis)," 2006. [Online]. Available: <http://hdl.handle.net/1903/3979>.
- [5] S. Hemmady, X. Zheng, H. Hart, T. M. A. Jr., E. Ott and S. M. Anlage, "Universal Properties of Two-Port Scattering, Impedance, and Admittance Matrices of Wave-Chaotic Systems," *Physical Review E* vol. 74, 036213, 2006.
- [6] S. Hemmady, T. M. Antonsen, E. Ott and S. M. Anlage, "Statistical Prediction and Measurement of Induced Voltages on Components Within Complicated Enclosures: A Wave-Chaotic Approach," *IEEE Transactions on Electromagnetic Compatibility*, vol. 54, no. 4, pp. 758-771, 2012.
- [7] G. Gradoni, J.-H. Yeh, B. Xiao, T. M. Antonsen, S. M. Anlage and E. Ott, "Predicting the statistics of wave transport through chaotic cavities by the Random Coupling Model: a review and recent progress," *Wave Motion* vol. 51, pp. 606-621, 2014.
- [8] Zachary B. Drikas, Jesus Gil Gil, Hai V. Tran, Sun K. Hong, Tim D. Andreadis, Jen-Hao Yeh, Biniyam T. Taddese and Steven M. Anlage, "Application of the Random Coupling Model to Electromagnetic Statistics in Complex Enclosures," *IEEE Transactions on Electromagnetic Compatibility*, vol. 56, no. 6, pp. 1480-1487, 2014.

# Real-Time Radiated tests optimization using a bootstrap module

C. Kasmi\*, S. Lalléchère#, S. Girard#, P. Bonnet#, F. Paladian#

\*Wireless Security Lab, French Network and Information Security Agency, 51 bvd de la Tour Maubourg, 75007 Paris, France

#Université Clermont Auvergne, Université Blaise Pascal, Institut Pascal, CNRS UMR 6602, 63178 Aubière, France

## Abstract

Recent studies have shown a high interest in statistical methods dedicated to the prediction of the maximum confidence in simulation and measurements for Electromagnetic Compatibility. In particular, it has been shown that one of the main issues remains the access to a number of samples allowing estimating the risks in regards to test set-up random variables. In this paper it is argued that a real-time bootstrapping module enables to optimize the number of experiments while estimating the maximum confidence level of the accessible samples.

**Keywords:** Reverberating cavities, Statistics, Immunity.

## 1 Introduction

Several studies [1-6] have demonstrated that electronic devices are susceptible to intentional electromagnetic interferences (IEMI). In order to reduce the threat of IEMI to tolerable levels, adequate protective devices can be involved. Their design relies on an accurate estimation of the risk levels which is crucial for critical applications. Recently, the Electromagnetic Compatibility (EMC) community has shown a high interest in the estimation of the maximum confidence in simulation and measurement results as it may introduce a significant risk for the safety and security of critical infrastructures.

Meanwhile, extreme values theory [7-8] and reliability analysis methods [9-10] have recently been proposed to overcome worst case challenges in EMC. Nevertheless, due to their complexity and the required number of experiments, the use of the mean contributions and safe margins are still recommended. In this context, the estimation improvement of the mean contributions of a physical quantity and their related maximum confidence levels become naturally important.

During EMC analysis, it is commonly accepted that only a reduced number of experiments or measurements from the so called population are accessible due to cost and computation constraints in regards of numerous random parameters. Thus, one of the important aspects, depicted in Fig. 1, is the available set of measurements (later called sample). A statistical study of the sample (stochastic process) is required so that the mean contributions can be assessed.

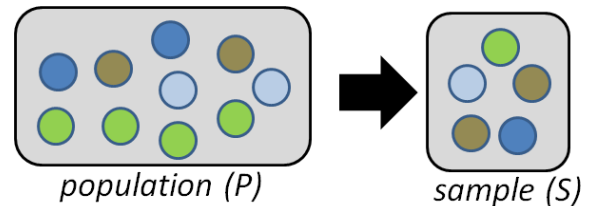


**Figure 1:** Schematic of the accessible set of sample  $S$  of a population  $P$ .

In 1979, Elfron came up with the bootstrapping procedure [11] allowing the estimation of the maximum confidence of samples in regards of a population. A first attempt dealing with the analysis of the conducted propagation of IEMI along the power network was proposed in [12]. As it was considered as a specific test case, this paper contains complementary details about the classical bootstrapping procedure and, as a key contribution, it will be demonstrated the benefit of a potential real-time bootstrapping module for EMC testing optimization integrated into the instrumentation of the test set-up.

The paper is organized as follows: in Section 2, the main lines of the three-step bootstrapping procedure are given. In Section 3, the benefit of the bootstrapping for the optimization of EMC radiated tests is demonstrated through a test case.

## 2 Bootstrapping theory

The bootstrapping procedure [11-16], introduced in 1979 by Elfron [11], is based on the derivation of *new observations* obtained by randomly taking a set of the original data (*sampling with replacement*). It can be mentioned that these methods are based on stochastic process, such as Monte-Carlo, and do not require any additional information. The principle is based on a three-step procedure defined by:

1. *New observations* obtained by randomly taking a set of the original data  $S$  (*sampling with replacement*); The first step is to randomly generate with replacement new samples  $S_i$  of size  $m$  from  $S$  considering each element of  $S$  with the same probability ( $1/m$ ) in order to estimate the reliability of the sub-set  $S$  in regards of the population  $P$  statistic while obtaining their confidence level;
2. The second step of the proposed approach refers to the definition of the statistical observable of the physical quantity; the statistical observable will be defined as the

mean  $\mu$  and the standard deviation  $\sigma$  of the set  $S_i$  of independent and identically distributed (IID) values;

- In order to perform such a task, we focus on the statistical observations convergence of the  $s$  sub-system of the set of samples  $S_i$ . After defining the observable, such as the statistical moments of the observations, the procedure is replicated  $s$  ( $s = 1000$  as recommended in [16]) times so that the representativeness of the measured samples by the  $s$  bootstrapped sets of samples can be studied.

In the next section, the benefit of the method is demonstrated through an immunity test case.

### 3 EMC radiated tests

This contribution relies on measurements achieved in Mode Stirred Reverberation Chamber (MSRC) from Institut Pascal embedded with a cabinet designed [17] from scratch. The goal was to manufacture a device allowing a precise control of several typical EMC parameters: slot, sizes of enclosures, location of subsystems (Fig. 2). As depicted in Fig. 2, a metallic enclosed box ( $2.1 \text{ m}^3$ ) was achieved with a  $0.2 \times 0.8 \text{ m}^2$  rectangular aperture at upper side. The developed moving systems allow moving an external trap (T), or an inner plate (P) jointly with a rotating unit (stirrer S) with high levels of precision ( $\pm 0.02 \text{ mm}$  and  $\pm 0.004^\circ$  repeatability respectively for trap / plate and stirrer).

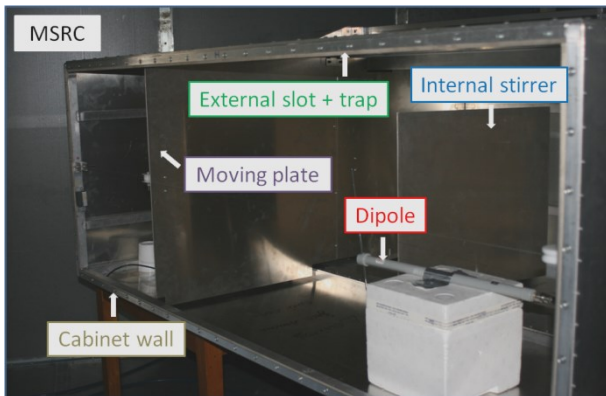


Figure 2: Inner view of the experimental cabinet including external slot, moving plate and internal stirrer [17].

The aim of this paper is to focus on the measurement of the mean power ( $P_r$ ) received by a dipole (ETS Lindgren Model 3121C) inside the cabinet (slot entirely opened) with a spectrum analyzer ANRITSU MS2663C (9 kHz - 8.1 GHz) at frequency  $f = 778.5 \text{ MHz}$ . A given power is injected in Reverberation Chamber (RC) via log-periodic antenna (ETS Lindgren Model 3144), the stirrer remaining in its initial position.

Thanks to the automation of the whole process (geometrical moving and power measurements) thousands of data sets can be obtained. Despite all, the entire time dedicated to measurements may increase quickly due, for instance, to the standards requirements [18] for MSRC testing. In the following, 1000 measurements ( $m = 1000$ ) will be considered, modelling a variation  $\pm 10 \text{ mm}$  of the moving plate (P)

around its initial location. This may stand for intrinsic uncertainties of the enclosed system (cabinet) under environmental constraints (thermal, mechanical) during its normal operation.

#### 3.1 Classical application

Table I gives an overview of the mean contributions obtained from straightforward Monte-Carlo (MC) computations.

TABLE I. MC RESULTS

Statistics	Received Power (MC) in mW
Mean	10.251
Std	4.192

Table II is obtained by applying the three step procedure to the measurements. It shows good agreement between bootstrapped mean and standard deviation obtained with  $m = 1000$  comparatively to the MC mean and standard deviation. The coefficient of variation (rate between standard deviation and mean) derived from Table II validates the good convergence of the results for both for the mean and standard deviation of the received power (respectively around 1.2 % and 1.4 %).

TABLE II. RESULTS FOR BOOTSTRAP ( $m=1000$ ) IN MW

Statistics	Received Power (Bootstrap) in mW	
	Mean ( $s = 1000$ )	Std ( $s = 1000$ )
Mean	10.258	4.189
Quantile 0.05	10.052	4.091
Quantile 0.95	10.474	4.289

Useful information about the confidence intervals, given by applying the bootstrap, are summarized in Table II. The 0.05 and 0.95 quantiles' assessment of the bootstrapped mean and standard-deviation which show the confidence levels given from bootstrapped data (highlighted with a red frame).

In supplement, the bootstrapping procedure enables to enhance the statistical study of the mean contributions. In the next Section, we seek to define the confidence interval as an alternative stop condition to the classical MC method.

#### 3.2 Real-time bootstrap module

During classical EMC analysis, the number of experiments either simulated or measurements are known to be a challenge for computation and time costs. Classical approaches impose the estimation of the statistical moments convergence based on MC experiments. Nevertheless, it is argued hereafter that the measurements could be stopped as soon as a sufficient confidence level of the mean contributions or a quantile has been reached.

In order to estimate the pertinence of the proposed approach, the convergence of the bootstrapping means and standard-deviations are analysed for each new value in the original set of parameters. Thus, the length of the bootstrapped samples is

taken in  $\{1, 2, \dots, m = 1,000\}$  where  $m$  denotes the length of the dataset (the number of samples involved in the re-sampling process). Defining a constraint confidence level, the need of an additional experiment is iteratively and in real-time estimated.

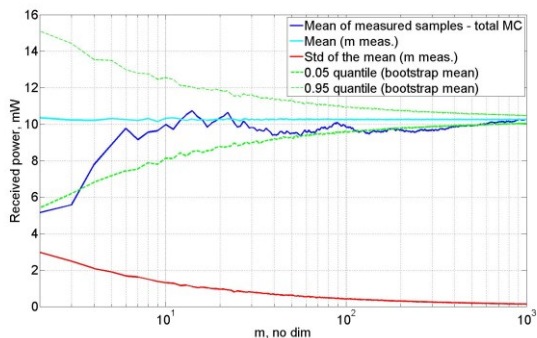


**Figure 3: Mean, standard deviation and maximum confidence levels for the bootstrapped means.**

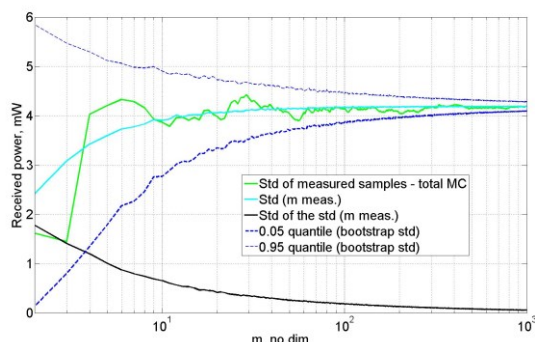


**Figure 4: Mean, standard deviation and maximum confidence levels for the bootstrapped standard deviations.**

Figures 3 and 4 provide an overview of this potential iterative and real-time assessment applied to the standard deviation. Indeed, the mean behaviour computed from bootstrapped is provided in Figure 3. First, it is shown a quick convergence:  $m = 3$  gives an accurate assessment of mean received power. Comparatively to MC convergence, 0.05 and 0.95 quantiles from bootstrapped standard-deviations offer a realistic view of the data set dispersion. Given particular assumptions about the authorized margins (standards [18-19] for instance), bootstrapping allows a precise optimization of the number of measured samples required with high confidence levels. Computation of standard deviation in Figure 4 validates the quick convergence relatively to parameter  $m$  ( $m = 20$ ).

## 4 Conclusion

This contribution addressed the use of bootstrap process for EMC radiated tests optimization. The use of a dedicated and embedded system jointly with a bootstrap module justified the benefit offered by this technique: precise confidence intervals were provided with a limited number of experiments (e.g. decreasing the experimental time and costs). The device designed in this work is representative of a huge diversity of

EMC protections: the process may be useful for standard [18] assessment of the shielding effectiveness of real systems. Future work will demonstrate the interest of bootstrap for realistic radiated EMC testing [19].

## References

- [1] D. Nitsch, M. Camp, F. Sabath, et al., "Susceptibility of some electronic equipment to HPEM threats", *Electromagnetic Compatibility, IEEE Transactions on*, vol. 46, pp. 380-389, 2004.
- [2] F. Brauer, F. Sabath, and J.L. Haseborg, "Susceptibility of IT network systems to interferences by HPEM", *Electromagnetic Compatibility, IEEE International Symposium on*, pp. 237-242, 2009.
- [3] N. Mora, C. Kasmi, F. Rachidi, M. Hélier, and M. Darces, "Modeling and measurement of the propagation along low voltage power networks for IEMI studies", *Technical report*, February, 2013.
- [4] C. Kasmi, "Application de la topologie électromagnétique à la modélisation du réseau énergétique basse tension : étude statistique des perturbations conduites", *PhD thesis*, UPMC, December, 2013.
- [5] Y. V. Parfenov, L. N. Zdoukhov, W. A. Radasky, and M. Ianoz, "Conducted IEMI threats for commercial buildings", *Electromagnetic Compatibility, IEEE Transactions on*, vol. 46, pp.404-411, 2004.
- [6] D. Mansson, R. Thottappillil, and M. Backstrom, "Propagation of UWB Transients in Low-Voltage Power Installation Networks", *Electromagnetic Compatibility, IEEE Transactions on*, vol. 50, pp.619-629, 2008.
- [7] G. Gradoni and L.R. Arnaut, "Generalized Extreme-Value Distributions of Power Near a Boundary Inside Electromagnetic Reverberation Chambers", *Electromagnetic Compatibility, IEEE Transactions on*, vol.52, no.3, pp.506,515, Aug. 2010.
- [8] C. Kasmi, M. Hélier, M. Darces, and E. Prouff, "Generalised Pareto distribution for extreme value modelling in Electromagnetic Compatibility", *Electronics Letters* 49, Vol. 5, pp. 334-335, 2013.
- [9] M. Larbi, P. Besnier, B. Pecqueux, "Probability of EMC Failure and Sensitivity Analysis With Regard to Uncertain Variables by Reliability Methods", *Electromagnetic Compatibility, IEEE Transactions on*, online early access., Jan. 2015.
- [10] A. Kouassi, J-M. Bourinet, S. Lalléchère, P. Bonnet, and M. Fogli, "Safety assessment of a transmission line with EMC requirements", *XXXIth URSI GASS*, Beijing, China, August 2014.
- [11] B. Efron and R. J. Tibshirani, "An introduction to the bootstrap", *Chapman and Hall*, London, 1993.
- [12] C. Kasmi, M. Hélier, M. Darces, and E. Prouff, "Application of a bootstrapping procedure to the analysis of the conducted propagation of electromagnetic interferences along the power network", *Kleineheubach Tagung*, Miltenberg, Germany, September 2014.
- [13] G. J. Babu and K. Singh, "Inference on means using the bootstrap", *Ann. Stat.* Vol. 11, pp.9 99-1003, New-York, 1983.
- [14] Y. Zhang, D. Hatzinakos, and A.N. Venetsanopoulos, "Bootstrapping techniques in the estimation of higher-order cumulants from short data records", *Acoustics, Speech, and Signal Processing - ICASSP-93, IEEE International Conference on*, vol.4, no., pp.200,203 vol.4, 27-30 April 1993.
- [15] A. Cucchiarelli and P. Velardi, "A statistical technique for bootstrapping available resources for proper nouns classification", *Information Intelligence and Systems*, 1999. *Proceedings of International Conference on*, vol., no., pp.429-435, 1999.
- [16] F. Harrell, "Regression Modeling Strategies: With applications to linear models, logistic regression, and survival analysis", *Springer*, 2001.
- [17] S. Lalléchère, S. Girard, P. Bonnet, and F. Paladian, "Stochastic approaches for ElectroMagnetic Compatibility: a paradigm from complex reverberating enclosures", in *Proc. ESA Workshop on EMC*, Venice, Italy, May 2012.
- [18] International Electrotechnical Commission (IEC), *IEC 61000-4-21, EMC - Part 4-21: Testing and measurement techniques - Reverberation chamber test methods*, 2003.
- [19] IEEE standard method for measuring the shielding effectiveness of enclosures and boxes having all dimensions between 0.1 m and 2 m, 2013.

# Threshold Probability Model for EMP Effects Evaluation

Kejie LI<sup>#1</sup>, Yanzhao XIE<sup>#2</sup>

<sup>#</sup>State Key Laboratory of Electrical Insulation and Power Equipment  
School of Electrical Engineering, Xi'an Jiaotong University  
Xi'an, Shaanxi Province, China  
[1kejie.li@hotmail.com](mailto:kejie.li@hotmail.com), [2yzxie@mail.xjtu.edu.cn](mailto:yzxie@mail.xjtu.edu.cn)

Yury V. Parfenov

Russian Academy of Sciences  
Joint Institute for High Temperatures  
125412 Moscow, Izhorskaya 13, bld.2, Russia  
[lparfenov@ihed.ras.ru](mailto:lparfenov@ihed.ras.ru)

**Abstract**—It has been known that EMP has effects on electronic systems while it is difficult to analyze the whole process directly. For some kind of system effects only relies on its inherent variances, which are called effect thresholds, there are means to evaluate their vulnerability and reliability. Some experiments and calculation have been done to estimate an electronic communication system's effect threshold in this paper.

**Keywords**—Effect Threshold; Probability Model; EMP Experiment; Evaluation Method

## I. INTRODUCTION

High power electromagnetic pulse environment has great effects on electronic devices and systems, under which circumstance the signal might be interrupted, the logic disturbed and synchronization lost. As the pulse power increased, the effects became much more serious, resulting in short-circuit, power supply overloaded and isolation breakdown.

It is difficult to analyze the whole process from the electromagnetic pulse incidence to the effects occurred directly. Usually, we only focus on the relationship between certain interesting factors (e.g. external excitation like incident EMP amplitude, bandwidth, waveform, etc. and inherent characters as system type, status, specified voltage, etc.) and the effects.

## II. THRESHOLD PROBABILITY MODEL

### A. Effect Threshold

For some kinds of device and system to be tested, the occurrence of the effects only relies on the relationship between certain affect factor and system's inherent variances. The effects occur when the affect factor is larger than the system's variance and not the other way. We call the system's variance the effect threshold, written as  $H$ . If the  $H$  is constant, the effect resulting function of the system can be written below

$$y = f(x) = \begin{cases} 0, & \text{if } x < H \\ 1, & \text{if } x \geq H \end{cases}$$

If the  $H$  is a random variable with certain distribution, written as  $H \sim F(\theta)$ , while the  $F$  is the probability function of

$H$  and  $\theta$  is  $F$ 's parameters vector, the effect resulting function remains the same. However, as  $H$  is random, it's impossible to calculate the  $y$  only from the input  $x$ . Assuming the  $y$  is also a random variable with two values: 0 or 1, then

$$P(y = 1|x) = P(x \geq H) = P(H \leq x) = F(\theta)(x)$$

With the definition of  $P(y_i = 1|x_i) = p_i$ , if  $H$  submits to normal distribution with  $\mu$  and  $\sigma$ , we get

$$F(x) = \int_{-\infty}^x \frac{1}{\sqrt{2\pi}\sigma} e^{-\frac{(z-\mu)^2}{2\sigma^2}} dz = 0.5(\operatorname{erf}\left(\frac{x-\mu}{\sqrt{2}\sigma}\right) + 1)$$

where  $\operatorname{erf}(x)$  is error function<sup>[1]</sup>.

### B. Multi-Thresholds Model

Considering a system with more than one threshold, the effects results are divided into  $n+1$  by  $n$  thresholds if results cannot be superposed. Sorting the threshold by  $H_1 < H_2 < \dots < H_n$ , the effect resulting function is:

$$y = f(x) = \begin{cases} 0, & \text{if } x < H_1 \\ 1, & \text{if } x \geq H_1 \text{ and } x < H_2 \\ \dots & \dots \\ n, & \text{if } x \geq H_n \end{cases}$$

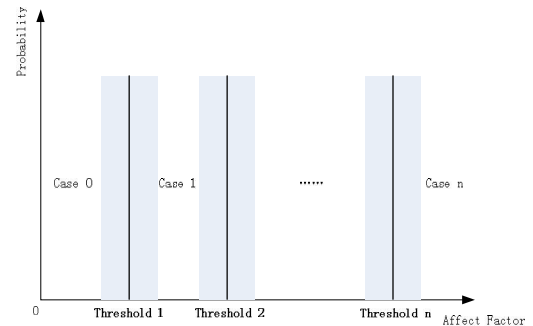


Figure 1. Multi-Threshold Effects Model

### III. EMP EFFECTS EXPERIMENT

Building up some kinds of electronic communication systems as experiment object, the system acted normally, sending and receiving data between each other, before the experiment. Effect results were recorded if having any. E-field amplitude was changed several times for observing different results<sup>[2]</sup>.

A ‘Flag’ was defined to identify the effect results. For each kind of experiment results, the effect was described and an unique flag was given to the effect resulting function.

TABLE I. THE DESCRIPTION OF EFFECTS FOR DIFFERENT CASES

Case	Flag	Effects Description
Case 0	0	Normal.
Case 1	1	Network communication was interrupted.
Case 2	2	Computer restarted automatically.

TABLE II. DATA OF EFFECTS EXPERIMENTS

$x_i$ E/(kV/m)	$y_i$ Effects Flag	$x_i$ E/(kV/m)	$y_i$ Effects Flag	$x_i$ E/(kV/m)	$y_i$ Effects Flag
15.79	0	42.43	0	43.84	2
15.32	0	41.01	0	43.37	2
15.79	0	41.49	1	46.20	2
25.93	0	41.96	0	48.09	2
23.57	0	48.09	2	49.03	2
25.46	0	47.14	2	49.03	2
41.49	1	43.84	1	50.91	2

### IV. EFFECTS THRESHOLD AND RESULT PROBABILITY DISTRIBUTION CALCULATION

Using the following function to split the 3 states process into 2 processes with 2 states, for each the model mentioned before can be easily used.

$$g_1(y) = \begin{cases} 0, & \text{if } y < 1 \\ 1, & \text{if } y \geq 1 \end{cases} \quad g_2(y) = \begin{cases} 0, & \text{if } y < 2 \\ 1, & \text{if } y \geq 2 \end{cases}$$

By regressing each threshold’s distribution function, a likelihood function was made:

$$L(\theta) = \prod_{i=1}^n p_i^{y_i} (1 - p_i)^{1-y_i}$$

As  $F$  was assumed to be normal distribution, i.e.

$$p_i = \Phi\left(\frac{x_i - \mu}{\sigma}\right), \text{ the formula above can be transformed into}$$

$$L(\mu, \sigma) = \prod_{i=1}^n \Phi\left(\frac{x_i - \mu}{\sigma}\right)^{y_i} \left[1 - \Phi\left(\frac{x_i - \mu}{\sigma}\right)\right]^{1-y_i}$$

The maximum likelihood estimation of the  $L$  gave the estimation of parameters  $\mu$  and  $\sigma$ , from which the whole information of  $F$  can be acquired.

TABLE III. THE MEAN AND STANDARD DEVIATION OF THRESHOLD

	Threshold 1	Threshold 2
Mean( $\mu$ )	41.8026	43.5025
Standard Deviation( $\sigma$ )	1.4188	0.8933

### V. CONCLUSION

Based on effect threshold model, the relationship between affect factors and effects results can be acquired through effects experiment and statistical calculation.

Under multi-thresholds situation the model can be extended, each state’s probability is independent after splitting the effect results function.

### REFERENCES

- [1] Parfenov, Y.V., H. Kohlberg and W.A. Radasky, et al. The probabilistic analysis of immunity of a data transmission channel to the influence of periodically repeating voltage pulses. in Electromagnetic Compatibility and 19th International Zurich Symposium on Electromagnetic Compatibility, 2008. APEMC 2008. Asia-Pacific Symposium on. 2008. Singapore.
- [2] Camp, M., H. Gerth and H. Garbe, et al., Predicting the breakdown behavior of microcontrollers under EMP/UWB impact using a statistical analysis. Electromagnetic Compatibility, IEEE Transactions on, 2004. 46(3): p. 368-379.

# On the Statistical Validity of HEMP Field Tests

Lars Ole Fichte\*, Sven Knoth<sup>†</sup>, Marcus Stiemer\*

\*Helmut Schmidt University, Faculty of Electrical Engineering, Hamburg, Germany

<sup>†</sup> Helmut Schmidt University, Faculty of Economics, Hamburg, Germany

## Abstract

Critical electronic devices, i.e. units whose operation is essential, must be able to work even when exposed to extreme electromagnetic signals, such as High Altitude Nuclear Electromagnetic Pulses (HEMP). As a consequence, field tests with HEMP simulators are mandatory.

In this paper, several statistical approaches to assess the quality of HEMP field tests are presented and compared to the test protocol specified by a German standard. The proposed schemes are based on acceptance sampling and confidence intervals and improve the significance of the derived conclusions. In addition, more advanced techniques are discussed.

**Keywords:** HEMP field tests, Statistical Evaluation

## 1 Introduction

Several national and international standards on how to perform HEMP field test exist, and have been reviewed in numerous papers in the past [1]. Yet, employing statistical models can lead to a better understanding of the test's validity.

Since various statistical models will be considered below, some helpful basic facts stemming from statistical risk analysis shall be outlined first.

A device under test (DUT) which fails to pass a HEMP test with a non-zero probability **might**, but **need not** fail in the next test run. If we consider, e.g., a DUT with a probability of failure  $p_{FA} = 0.1$ , and perform a test sequence of five single exposures on it, the probability for at least one failure is  $1 - (1 - 0.1)^5 = 0.41$ , which is remarkably high.

This means that a satisfactory device with a sufficiently small failure probability has a good chance to fail the test. This gives rise to the question how reliable and significant test results are and how they should be validated.

To deal with this problem, limits for 'sturdy' and 'vulnerable' DUTs can be introduced, e.g. a DUT with  $p_{FA}=0.1$  would be classified as sturdy, whereas  $p_{FA}=0.5$  would mean that it is vulnerable. The aim of any statistical method proposed in this paper is to ensure that the chances for misclassification are as small as possible

(i.e., that a vulnerable devices is tested and classified as sturdy, or vice versa).

Tab.~1 shows the four possible combinations. While in the cases marked with 'ok' the test results correctly predict the system vulnerability in the real world, 'case 1' means that a

vulnerable DUT was not detected by the test sequence. This is the worst case from an operational viewpoint. The last combination, 'case 2', is undesirable from an economic viewpoint because 'sturdy' DUTs are falsely rejected.

Table 1: Classification of a DUT after test sequence

	passed	failed
"vulnerable"	Case 1	Ok
"sturdy"	ok	Case 2

## 2 Acceptance testing

Acceptance sampling is a common tool in statistical quality control [6]; here, a randomly selected sample of items (of size  $N$ ) out of a finite lot consisting of  $N$  items is evaluated to make a decision regarding the lot disposition, that is, to accept or to reject the lot. This is usually based on the criterion that the number of items that fail the test does not exceed a predefined level  $c$ . Note that in economical scenarios the test procedures can be very sophisticated and are usually multi-stage procedures; yet we will investigated simple single stage tests in this paper only.

For setting up our procedure, we employ the operation characteristic function -- see, for instance, Section 15.2.2 'The OC Curve' in [6] on page 637 ff.:

$$L(p) = P_p(\sum_{i=1}^N X_i \leq c),$$

which defines the probability of accepting the lot for a given (but unknown) reject rate  $p$ .

This rate  $p$  is added as subscript to the probability measures here, and  $X_i$  indicates that sample  $i$  meets the specification ( $X_i = 0$ ) or not ( $X_i = 1$ ).

The operation characteristic function  $L$  is governed by a hyper geometric distribution but can be approximated by a binomial distribution for  $N \gg N$ , which is met by the HEMP test design through  $N \rightarrow \infty$ . The simple acceptance sampling plan is defined by two numbers  $(N, c)$  ( $N$  is the number of independent tests,  $c$  is the maximum number of allowed rejects within the  $N$  tests for accepting the lot). Using this notation, the test plan given in [2] is characterized by  $(N, I)$ , and the probability for rejecting the DUT can be expressed by the operation characteristic function  $p_{Fail}(p_{FA}) = 1 - L(p_{FA})$ . Now, we apply design ideas known from acceptance sampling to design a better test procedure by using [3].

We choose the two probabilities  $p_{FA}^{good}$  and  $p_{FA}^{bad}$  and define limits for  $L(p)$ :

$$L(p_{FA}^{good}; N, c) \geq 1 - \alpha \text{ and}$$

$$L(p_{FA}^{bad}; N, c) \leq \beta.$$

An exemplary R-Code shows the simple setup of the test:

```
p.good <- 0.1; p.bad <- 0.5
L.good <- 0.95; L.bad <- 0.05

cG <- -1
repeat {
cG <- cG+1
NG <- cG
while ( pbinom(cG, NG, p.bad) > L.bad ) NG <-
NG + 1
if ( pbinom(cG, NG, p.good) >= L.good ) break
```

The function `pbinom(q,N,p)` computes the cumulative distribution function of a binomial distribution.

For the discussed example the result is the following sequence for  $N$ :

```
cG = 0, NG = 5, L.bad = 0.0312, L.good = 0.5905
cG = 1, NG = 8, L.bad = 0.0352, L.good = 0.8131
cG = 2, NG = 11, L.bad = 0.0327, L.good = 0.9104
cG = 3, NG = 13, L.bad = 0.0461, L.good = 0.9658
```

This shows that the test procedure meets the defined criteria and can be used for testing.

### 3 Confidence intervals

Besides the design described in [1,2] and the acceptance sampling approach discussed in the previous section, one could derive design rules based on confidence intervals for success probabilities (or proportions). Essentially we are interested in upper bounds for the unknown probability  $p_{FA}$ . See [4] for a comparison of seven different concepts to construct such an interval. Here we focus on the classic one by [5] and two designs relying on normal approximation (known as Wald and Wilson intervals, respectively). Before we will describe these three approaches in more detail, we recall the framework. We assume that  $N$  HEMP tests were performed and  $0 \leq x \leq N$  failures were registered. Given these two numbers, we determine an upper bound  $\pi^{upper}$  so that

$$P_{\{ p_{FA} \}} (p_{FA} \leq \pi^{upper}) \geq 1 - \alpha.$$

We applied several well known approaches to estimate the confidence intervals, i.e. Clopper-Pearson intervals, Wald interval, Wilson and Agresti-Coell intervals; the results are displayed in fig.1.

The R package `binom` provides functions to calculate the three intervals described above as well as some further constructions of confidence intervals. Besides these three we

consider the Agresti-Coull interval [7] whose performance is in between those of Clopper-Pearson and of Wilson [8].

By calling `binom.confint(x, N, conf.level = 1 - alpha)` we obtain the two bounds for  $N$  trials,  $X=x$  failures and confidence level  $1 - \alpha$ .

In Figure 1 we present the upper bounds  $\pi^{upper}$  for  $N \in \{2,3,\dots,20\}$ ,  $x \in \{0,1\}$  and  $1 - \alpha = 95\%$ .

Obviously the Wald interval is rather useless ( $x=0$  is not defined and for  $x=1$  and  $N \geq 5$  the resulting values are definitely too small).

The other three perform similarly. It is not surprising that the Clopper-Pearson bounds are the largest ones (they comply with the level  $1 - \alpha$  by construction). Wilson- and Agresti-Coull bounds are really close to each other, while Wilson provides always smaller values. For  $x=0$  and  $N > 12$ , Clopper-Pearson and Agresti-Coull bounds are nearly the same. To give a recommendation for the choice of  $N$  we deduce that  $N \approx 10$  provides a reasonable performance. Then, no failure ( $x=0$ ) would yield  $\pi^{upper} \approx 0.2$ , which is a reasonable upper bound for practice. If one would allow  $x=1$  (one failure), then one should use a much larger  $N$  or has to cope with upper bounds of size  $\pi^{upper} > 0.3$ .

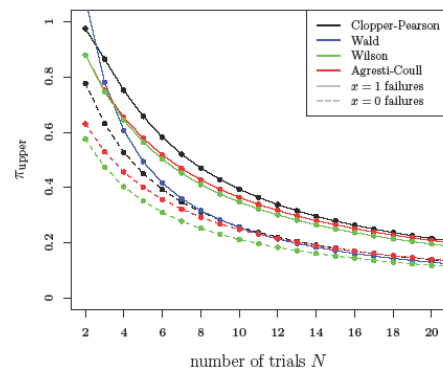


Figure 1 Various confidence intervals for HEMP tests.

### 4 Conclusions

We employed statistical methods to evaluate the HEMP field test procedure in [1] and [2]. As a result, we propose three different ways to determine the number of single tests  $N$  and the corresponding success rates:

1. choosing a test procedure from the Guenther algorithm [3] (acceptance sampling) to determine  $N$  -- here  $X > 1$  may be possible or
2. calculation of  $N$  by evaluating the confidence interval for  $p_{FA}$ , again for  $X=0$ .

The method of generalized linear models (binary regression in particular) will be investigated in our future work, and can probably be employed if certain covariates failure relationships are known for DUTs.

## References

- [1] Sabath, F.; Potthast, S. (2013). "Tolerance Values and the Confidence Level for High-Altitude Electromagnetic Pulse (HEMP) Field Tests". *IEEE Transactions on Electromagnetic Compatibility*, 55(3), pp. 518 - 525.
- [2] VG 96903-50 Beiblatt 1, Normenstelle Elektrotechnik (NE) im DIN (2012). "Nuclear electromagnetic pulse (NEMP) and lightning protection, Test methods, test equipment and limiting values".
- [3] Guenther, W. C. (1977). "Sampling Inspection in Statistical Quality Control", Griffin, London, UK.
- [4] Newcombe, R.G. (1998). "Two-sided confidence intervals for the single proportion: comparison of seven methods". *Statistics in Medicine*, 17(8), pp. 857 - 872.
- [5] Clopper, C.J.; Pearson, E.S. (1934). "The use of confidence or fiducial limits illustrated in the case of the binomial". *Biometrika*, 26(4), pp. 404-413.
- [6] Montgomery, D. C. (2009). "Statistical quality control: A Modern Introduction", 6th ed., John Wiley & Sons (Asia), Pte. Ltd.
- [7] Agresti, A. (2013). "Categorical Data Analysis". Wiley, Hoboken, N. J., 3rd ed.
- [8] Agresti, A.; Coull, B.A. (1998). "Approximate Is Better than `Exact" for Interval Estimation of Binomial Proportions". *The American Statistician*, 52(2), pp. 119.

# Some standardization problems of high power electromagnetic pulses, formed by test facilities

*Yury V. Parfenov<sup>1</sup>, Boris A. Titov<sup>1</sup>, Leonid N. Zdoukhov<sup>1</sup>, William A. Radasky<sup>2</sup>*

<sup>1</sup>*Russian Academy of Sciences, Joint Institute for High Temperatures, 125412 Moscow, Izhorskaya 13, bld.2, Russia, e-mail: [parfenov@ihed.ras.ru](mailto:parfenov@ihed.ras.ru)*

<sup>2</sup>*Metatech, Corp, 358 S. Fairview Ave, Suite E, Goleta, CA, USA, 93117, e-mail: [wradasky@aol.com](mailto:wradasky@aol.com)*

There are two kinds of high power electromagnetic pulses: high altitude electromagnetic pulses (HEMPs) and ultrashort (wideband) electromagnetic pulses (typically hyperband), having peak amplitudes above 100 V/m [1]. It is important to evaluate the immunity of electronic devices to the action of similar pulse test facilities (simulators), which have been created in many countries. Availability of the normative documents containing data on amplitudes and waveforms of reproduced pulses was one of conditions of their creation. The international standards [2, 3] concerned provide this type of information. The first of the named documents is devoted to HEMP and represents it in a form of a unipolar pulse having 10-90% rise time of 2.5 nanoseconds and the duration at 50% of the peak value of 23 nanoseconds. The peak of the standard pulse is equal to 50 kV/m. HEMP standardization in the IEC has collected the developed experimental base [4] used to perform tests of a considerable quantity of objects.

Application of the HEMP simulators has revealed some of their shortcomings. One of the shortcomings is analyzed in [5]. The authors of the paper ascertain that features of the waveforms over the test volumes of HEMP simulators differ from features of the pulse set by the standard [2]. They fear that the noted differences can decrease the reliability of the results of electronic devices tests to their immunity to HEMP fields. To eliminate the possible shortcomings they offer to restrict the deflections of pulsed electromagnetic fields in the test volumes of HEMP simulators from the standard HEMP in the frequency domain (similar restrictions in the time domain already are present in existing standards).

A high-priced modernization will be necessary for realization of these considerations with reference to existing HEMP simulators. Before making a decision about modernization of simulators, it is useful to get the answer to the following question: whether modernization will lead to a real increase of reliability of results of testing electronic devices of immunity to HEMP action? In formulating the answer to this question one must take into account that the reliability of test results depends not only on the degree of conformity of EMPs in test volumes of HEMP simulators to a standard HEMP, but also from degree of conformity of EMPs formed by simulators to real HEMP. It is necessary to say here that the recommended standard [2] HEMP waveform is idealized and differs from forms of real HEMPs (and this is mentioned in [2]). Moreover, the standard HEMP waveform could be not registered from a real high nuclear explosion in principle,

since such pulse is not capable to spread over free space because its spectrum includes the zero frequency.

The next aspect follows from the aforesaid. It is possible that frequencies being minimized in the spectrum of pulses in test volumes of HEMP simulators can be present in spectrum of real HEMPs. Also introduction to the spectrum of the standard HEMP of the zero frequency in some cases can bring about a result, which cannot be observed in reality. Therefore, we plan to analyze the role of the assumptions, which were accepted at the development of the standard HEMP form several dozens years ago. Only after that it will be possible to formulate trends of HEMP simulators modernization. It is also possible that the analysis of these aspects could result in a modification of the IEC HEMP standard waveform [2].

Now the similar problem is also observed in the field of hyperband EMPs. A lot of sources of powerful hyperband EMPs exist in many countries. Examples of such sources are presented in [6]. They radiate their pulses with differing features (pulse peak, spectrum, pulse repetition rate and others). At present standards similar to the standards in the field of HEMP including the standard containing hyperband EMP waveforms has recently been developed [7]. We will present some evaluations of this standard in our report. Perhaps, this analysis will be useful in developing new hyperband sources, as well as at making a decision about the trends of HEMP simulator modernization.

## References

- [1] IEC/TR 61000-1-5 Ed. 1.0 (2004-11): High power electromagnetic (HPEM) effects on civil systems.
- [2] IEC 61000-2-9 Ed. 1.0 (1996-02): Description of HEMP environment - Radiated disturbance.
- [3] IEC 61000-2-13 Ed. 1.0 (2005-03): High-power electromagnetic (HPEM) environments - Radiated and conducted.
- [4] IEC/TR 61000-4-32 Ed. 1.0 (2002-10): HEMP simulator compendium.
- [5] *Giri D.V., Prather W.D.* High-Altitude Electromagnetic Pulse (HEMP) Rise time Evolution of Technology and Standards, IEEE Trans on EMC, Special Issue on HEMP, June 2013.
- [6] IEC/TR 61000-4-35 Ed. 1.0 (2009-07): High power electromagnetic (HPEM) simulator compendium.
- [7] IEC 61000-4-36 Ed. 1.0 (2014-11): IEMI immunity test methods for equipment and systems.

# Overview of HPEM Standards Produced by IEC SC 77C

Richard Hoad\*, William A. Radasky†

\*QinetiQ Ltd., Cody Technology Park, Farnborough, UK, [rhood@qinetiq.com](mailto:rhood@qinetiq.com)

†Metatech Corporation, 358 S. Fairview Ave., Suite E, Goleta, CA 93117 USA, [wradasky@aol.com](mailto:wradasky@aol.com)

## Abstract

This paper provides an overview of the work of IEC SC77C but focusses on recent publications produced by the committee. IEC SC77C is a standards committee that has been developing high-power electromagnetic (HPEM) standards and publications for use in civil applications since 1992. The initial publications dealt with the High-altitude Electromagnetic Pulse (HEMP) phenomenon and in 1999 work began on Intentional Electromagnetic Interference (IEMI).

**Keywords:** High-Power Electromagnetics (HPEM); High-altitude Electromagnetic Pulse (HEMP); Intentional Electromagnetic Interference (IEMI); International Electrotechnical Commission (IEC).

## 1 Introduction

Since 1989 (beginning work as a working group under IEC TC 77: Electromagnetic Compatibility (EMC)) and after the formation of IEC SC 77C in 1992, the subcommittee has been developing standards and publications dealing with the severe electromagnetic environments of HEMP and IEMI. Figure 1 below indicates graphically the development of publications up to the beginning of 2015.

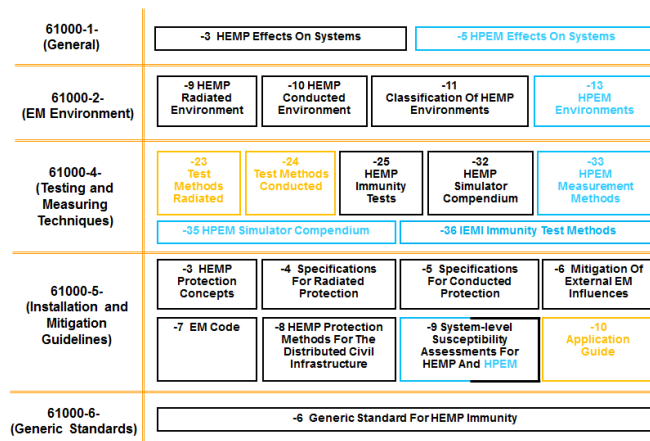


Figure 1. Summary of SC 77C Publications

Published, stable publications dealing with HEMP are shown in black. Publications dealing mainly with IEMI are shown in light blue and publications presently being worked on are shown in orange. Whilst many of the older publications deal specifically with HEMP, and many of the newer publications

deal with IEMI (work began on these publications in 1999), others deal generally with the protection methods available to protect against high-level EM transient fields at frequencies above 10 MHz, which are applicable to both HEMP and IEMI.

## 2 IEC SC 77C Publication Summary

Preparation of SC 77C standards is consistent with the development of EMC standards within the IEC and is therefore structured according to "IEC Publication 61000" which is divided into seven major parts as indicated:

- Part 1: General – 2 SC 77C publications
- Part 2: Environment – 4 SC 77C publications
- Part 3: Limits – no SC 77C publications
- Part 4: Testing and measurement techniques – 7 SC 77C publications
- Part 5: Installation and mitigation guidelines – 7 SC 77C publications
- Part 6: Generic standards – 1 SC 77C publication
- Part 9: Miscellaneous – no SC 77C publications

Each part is further subdivided into several subparts or sections, published either as International Standards, Technical Specifications or Technical Reports.

This paper builds on previous publications [1, 2] and focusses on providing a summary of three publications, which are presently in production by SC 77C. More details of our existing publications will be provided during the conference.

### 2.1 IEC 61000-4-24 Edition 2.0

Electromagnetic compatibility (EMC) – Part 4: Testing and measurement techniques – Section 24: Test methods for protective devices for HEMP conducted disturbance.

This publication is a revision of the published test method to evaluate the performance of surge protective devices used for HEMP conducted environments. New test methods for combination surge arrester/filters that are typically used for commercial power connections to shielded facilities are added. These “filters” have very high input current requirements and very low output residual level requirements to ensure that equipment inside a facility is not damaged. As the threat is in the form of time waveforms, both the test waveforms are defined in the time domain (including time domain norms for the residuals).

The pass/fail requirements for residuals are given for different levels of protection desired including industrial applications, critical infrastructure applications and military applications. The residuals for military applications are based on [3].

## 2.2 IEC 61000-4-23 Edition 2.0

Electromagnetic compatibility (EMC) – Part 4-23: Testing and measurement techniques – Test methods for protective devices for HEMP and other radiated disturbances.

This standard is undergoing a revision to allow the shielding effectiveness of a shielded volume to be evaluated with the transmitter in the inside of the facility in addition to being on the outside. This is due to the fact that some underground facilities do not have much space on the outside for a transmitter. In addition, this standard is being harmonized with IEEE 299-2006 [4] as much as possible, especially with regard to the number of frequencies tested and the separation distances.

## 2.3 New Project IEC 61000-5-10

This is a new project begun at the end of 2014 that is intended to provide guidance for the application of the entire body of IEC SC 77C publications. It is considered that a comprehensive guide to consolidate this work will be of great help to industry.

The publication will include several specific examples of how to apply the publications in the IEC SC 77C series. The sample problems will include:

- 1) Application of a protection and testing scheme for a new facility
- 2) Application of a protection and testing scheme for an existing facility

For both applications, protection and testing schemes need to be identified for three cases: a HEMP environment protection and testing scheme; an IEMI environment protection and testing scheme; and a HEMP+IEMI protection and testing scheme. This means there will be 6 schemes covered in this publication.

## 3 Conclusion

This paper has introduced IEC SC 77C publications that deal with high power transient phenomena. The SC 77C Committee members produce standards and other publications dealing with the protection from severe electromagnetic threats for use in civil applications.

## References

- [1] R. Hoad and W. A. Radasky, "Progress in IEC SC 77C high-power electromagnetics publications in 2009," Asia-Pacific EMC Symposium, 2010, pp. 762-765.
- [2] W. A. Radasky, "Status of IEC SC 77C high-power electromagnetics publications in 2012," 6th Asia

Conference on Environmental Electromagnetics (CEEM), Shanghai, 2012, pp. 1-4.

- [3] MIL-STD-188-125-1, "High-Altitude EMP Protection for Fixed Ground-Based Facilities," Department of Defense, 2005.
- [4] IEEE 299-2006, "IEEE Standard Method for Measuring the Effectiveness of Electromagnetic Shielding Enclosures," February 2007.

# An overview of two recent IEMI publications: IEEE Std 1642 and Cigré Technical Brochure 600

*W A Radasky\**

*\*Metatech Corporation, Goleta, California, USA, wradasky@aol.com*

## Abstract

**In this paper two important and recent IEMI publications are reviewed. One is an IEEE standard practice dealing with the protection of computer systems that are easily accessible to the public. The second is a Cigré Technical Brochure that describes the threat of IEMI to low voltage control electronics found in high voltage power substations throughout the world. Both of these publications were developed with strong reliance on the basic IEMI standards published by the International Electrotechnical Commission (IEC). This paper will review the scope of each document and provide a summary of the content to make the technical community aware of the standardization progress of work in these areas.**

**Keywords:** Intentional Electromagnetic Interference (IEMI), EMC standards, high-power electromagnetic (HPEM) fields, Cigré, IEEE, EMC, IEC

## 1 IEEE Std 1642-2015

IEEE Std 1642-2015, “Recommended Practice for Protecting Public Accessible Computer Systems from Intentional Electromagnetic Interference (IEMI),” January 2015 [1].

### 1.1 Working Group Information:

Chairman of the working group – William Radasky  
Members of the working group – Mats Bäckström, William Croisant, Sven Fisahn, Heyno Garbe, Richard Hoad, Daniel Månsson, Michael McInerney, Yury Parfenov, Frank Sabath, Edward Savage, Kwok Soohoo, Rajeev Thottappillil, Holger Thye, Anthony Wraight, and Perry Wilson.

### 1.2 Scope and Purpose:

This recommended practice establishes appropriate electromagnetic (EM) threat levels, protection methods, monitoring techniques, and test techniques for specific classes of computer equipment. This equipment is expected to be accessible to the public at ranges less than 100 meters, and the loss of operation of the equipment due to intentional electromagnetic interference (IEMI) is expected to cause losses (both financial and of confidence) to businesses

operating computer equipment, which are providing services to the public or to private companies.

The principle class of equipment to be considered in this recommended practice includes fixed (non-mobile) computer equipment. Examples include automated teller machines (ATMs), electronic cash registers at stores, computer equipment in banks and at airports, computer equipment controlling traffic flow, computer equipment controlling communications or allowing Internet access, computer equipment providing police, fire and security services, computer equipment controlling the operation of the power grid (including smart meters), computer equipment operating in hospitals, etc.

The purpose of this document is to provide information for manufacturers and users to specify the EMC requirements for computer equipment and systems that can be used by the public or businesses, which require a high-level of security to prevent intentional electromagnetic fields from interfering with the operation of these computers.

## 2 Cigré TB 600

Cigré (International Council on Large Electric Systems) is an international organization that focuses on the design and protection of high-voltage ( $V > 100$  kV) power grids throughout the world. They produced technical reports that often serve as pre-standards especially due to their close relationship with the International Electrotechnical Commission (IEC). Cigré Study Committee 4 (SC 4) has within its scope work on electromagnetic compatibility (EMC).

Cigré Technical Brochure 600, “Protection of High Voltage Power Network Control Electronics Against Intentional Electromagnetic Interference (IEMI),” prepared by WG C4.206, November 2014 [2].

### 2.1 Working Group Information:

Convener of the working group – William Radasky  
Members of the working group – Mats Bäckström (SE), Haeivelto de Souza Bronzeado (BR), Darren Carpenter (UK), Jinliang He (CN), Richard Hoad (UK), Masaru Ishii (JP), Armin Kälin (CH), Daniel Månsson (SE), Yury Parfenov (RU), Leonid Siniy (RU), Yasunao Suzuki (JP)

Corresponding members of the working group – Hideki Motoyama (JP), Farhad Rachidi (CH), W. H. Siew (UK), Tetsuya Tominaga (JP)

## 2.2 Introduction to the Technical Brochure

Electromagnetic compatibility (EMC) has been a very important aspect of protecting modern electronic equipment from accidental exposure from fixed and mobile transmitters and from the emissions of nearby electronic equipment. Unfortunately with the advancements of solid-state technology (which has allowed the development of small powerful generators), it is possible for hackers, criminals and terrorists to intentionally generate high levels of electromagnetic fields for which commercial equipment is not protected. It is therefore crucial to understand this new threat of intentional electromagnetic interference (IEMI), especially with regard to the critical infrastructures. In particular the electric power grid is one of the most important of the critical infrastructures, as most of the other infrastructures depend on the consistent flow of electrical power.

This technical brochure reviews the threat that electromagnetic (EM) weapons may pose to high voltage substation control electronics. This particular set of electronics is selected as significant levels of power flows through high voltage substations, and over the past 2 decades most of the control electronics used have changed from analog to digital, making them more sensitive to fast transient disturbances. In addition, most substation electronics (e.g., relays) operate automatically without the influence of operators and are hence vulnerable to serious electronic upsets in addition to damage.

This brochure reviews potential electromagnetic threat weapons, the factors that influence the exposure of equipment to high levels of high-frequency fields and induced voltages, the levels of susceptibility of equipment to these types of induced transients, and the protection methods that could be applied to reduce the threat. As part of this work, basic standards produced by IEC SC 77C (EMC: High Power Transient Phenomena) have been referenced. ITU-T has already adapted the IEC basic standards for their application to communications facilities. This brochure specifically adapts the IEC standards to the protection of substation electronics.

## 3 Discussion and Conclusion

This paper will review this new IEEE Standard Practice and will highlight the basic approach for the protection of computer equipment from IEMI.

This paper will also review this new Cigré Technical Brochure and will highlight the basic approach for the protection of substation electronic equipment from IEMI.

## References

- [1] IEEE Std 1642-2015, “Recommended Practice for Protecting Public Accessible Computer Systems from Intentional Electromagnetic Interference (IEMI),” January 2015.
- [2] Cigré Technical Brochure 600, “Protection of High Voltage Power Network Control Electronics Against Intentional Electromagnetic Interference (IEMI),” prepared by WG C4.206, November 2014.

# Field uniformity area assessment using a hyper-band HIRA

Tae Heon Jang\*, Jae Han Cho\*, Won Seo Cho\*

\* RF Application Technology Center, Korea Testing Laboratory, 516 Haean-ro, Sa-dong, Sangnok-gu, Ansan-si, Gyeonggi-do, South Korea 326-901, thjang@ctl.re.kr, [jaehan8919@ctl.re.kr](mailto:jaehan8919@ctl.re.kr), wscho@ctl.re.kr

## Abstract

This paper shows the assessment results of the field uniformity area (FUA) at a distance, radiated from a half impulse radiating antenna (HIRA) driven by a hyper-band pulse source. The FUA assessment methods according to IEC 61000-4-3, IEC 61000-4-20 and RS105 of Mil-Std-461F are analyzed. The assessments are performed at the distance of 3 m, 6 m and 12 m by simulation and measurements. The applied criteria for the amplitudes in time domain is within -0 dB to +6 dB for 75% of the 16 test points on the area of 1.5 m × 1.5 m. The results show that simulation results are very similar as the measurement results.

**Keywords:** half impulse radiating antenna, HIRA, hyper-band, field uniformity area.

## 1 Introduction

In November 2014, IEC SC 77C published IEC 61000-4-36 ed.1.0 which is IEMI immunity test methods for equipment and systems. IEC 61000-4-36 has quite wide scope and it does not provide a detail test procedure for each phenomenon at the moment.

The task force team (TFT) in IEC SC 77C established to study a test procedure for hyper-band transient immunity test methods for equipment and systems. The reason this TFT focuses on hyper-band transient signal is that a hyper-band transient signal has wide frequency spectrum about from 200 MHz to about 2 GHz, it can be repetitive with a rate and hyper-band sources are commercially available and one can make of an effective radiator with an intention of interference. Under such an EM environment, most of telecommunication equipment to be operated within the frequency range and computers are likely to be disturbed or damaged. Therefore it needs a standardized test method to assess the immunity of equipment and systems against hyper-band transient sources.



Figure 1. Conceptual structure of KOHIRA

This paper shows the assessment results of the field uniformity area (FUA) at a distance, radiated from a half impulse radiating antenna driven by a hyper-band pulse source. The FUA assessment methods are analyzed from IEC 61000-4-3, IEC 61000-4-20 and RS105 of Mil-Std-461F.

The test system used for the field uniformity area assessment with hyper-band transient signal was KOHIRA (Korean half impulse radiating antenna), which was introduced in AMEREM 2014. KOHIRA consists of half of a paraboloidal reflector of diameter 1.164 m, fed by two coplanar arms, each at 45 degrees from the vertical. KOHIRA is energized by a transient pulse generator PBG 3 from Kentech in UK. PBG 3 has the maximum peak amplitude 12 kV into a 50 Ω load, full-width to half-maximum (FWHM) time of the pulse about 3 ns and the 10-90 % rise time about 100 ps. KOHIRA is expected to work from about 125 MHz to about 1.75 GHz. The far field of KOHIRA can be defined by (1) and it starts approximately at about 12 m [1].

$$r \geq \frac{D^2}{2ct_r} \quad (1)$$

## 2 Test setup for simulation and measurement

### 2.1 Simulation setup

The FUA assessment by simulation was performed by CST MW Studio. Double exponential waveform source in a waveguide port was applied to the coaxial input of KOHIRA and the amplitude was set to 5.5 kV, rise time 100 ps and FWHM 3 ns. For this simulation, two lumped elements of 200 Ω were used as the terminations of KOHIRA. Figure 2 shows the model of KOHIRA for the simulation.

Figure 3 shows measurement distances from the end of the reflector of KOHIRA: 3 m, 6 m and 12 m. The size of the FUA to be assessed for the cross section at each distance is 1.5 m × 1.5 m and the FUA starts from 0.8 m above ground plane as shown in Figure 4.

Figure 3 shows measurement distances from the end of the reflector of KOHIRA: 3 m, 6 m and 12 m. The size of the FUA to be assessed for the cross section at each distance is 1.5 m × 1.5 m and the FUA starts from 0.8 m above ground plane as shown in Figure 4.

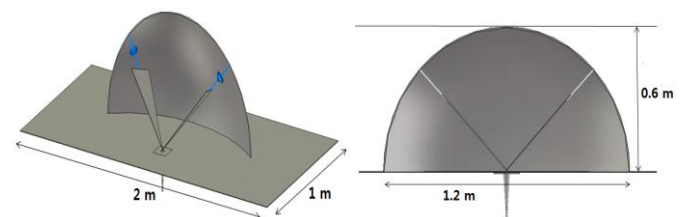


Figure 2. Model of KOHIRA for simulation

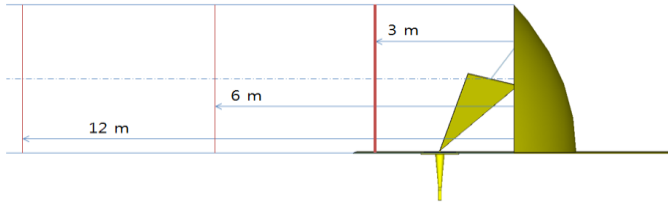


Figure 3. Measurement distances for FUA assessment

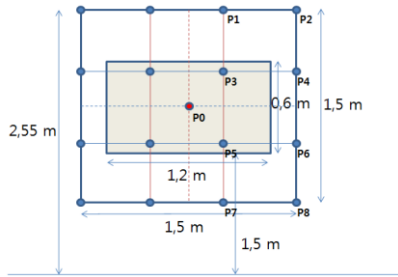


Figure 4. Field uniformity area (FUA), 1.5 m x 1.5 m



Figure 5. Measurement setup in a semi-anechoic room

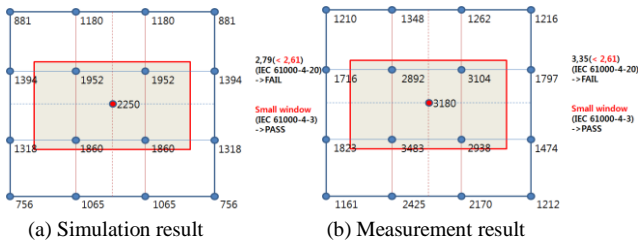


Figure 6. Assessment results at a distance 3 m

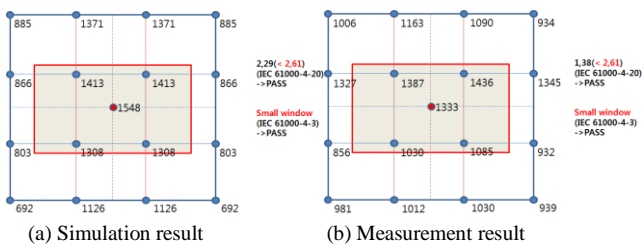


Figure 7. Assessment results at a distance 6 m

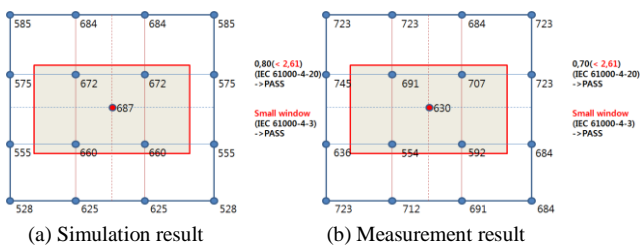


Figure 8. Assessment results at a distance 12 m

The size of FUA 1.5 m x 1.5 m was derived by IEC 61000-4-3 and IEC 61000-4-20. IEC 61000-4-3 and IEC 61000-4-20 describe a concept of field uniformity in frequency domain. IEC 61000-4-20 uses a statistical approach for calculation of 75 % criteria among the measurement points, while IEC 61000-4-3 uses an approach counting the number of measurement points satisfied with the requirement of -0 dB to +6 dB differences. On the other hand, Annex C of IEC 61000-4-20 and RS105 of Mil-std-461F describe a requirement of field uniformity in time domain.

## 2.2 Measurement setup

Figure 5 shows the measurement setup for the FUA assessment with a hyper-band KOHIRA positioned at 1.5 m above the ground plane in a semi-anechoic room. The measurement of electric field at each test point was performed with D-dot sensor, AD-70(R).

## 3 Field uniformity area assessment results

Figure 6 to Figure 8 show measurement results compared to the simulation results of the field distribution of FUA at the distance 3 m, 6 m, and 12 m.

The applied criteria for the amplitudes is within -0 dB to +6 dB for 75 % of the 16 test points on the area of 1.5 m x 1.5 m according to IEC 61000-4-3 and IEC 61000-4-20.

For this criteria, IEC 61000-4-20 statistically requires the standard deviation for 16 points of FUA shall be less than and equal to 2.61. The results show that simulation results are very similar as the measurement results and both results are satisfied with the IEC 61000-4-20 requirement to the amplitude aspect.

## 4 Conclusion

Field uniformity area assessment method for the immunity test method using a hyper-band transient signal can be defined by limiting of the amplitude, rise time and pulse width within certain tolerances in time domain.

Measurement data at 6 m showed the possibility of use an area in the near field area for hyper-band transient immunity test, even though not in far field area.

## References

- [1] Tae Heon Jang, D.V.Giri. "Design aspects of Korean half impulse radiating antenna", *AMEREM 2014*, pp. 003, (2014).
- [2] IEC 61000-4-3, Electromagnetic compatibility (EMC) - Part 4-3: Testing and measurement techniques - Radiated, radio-frequency, electromagnetic field immunity test
- [3] IEC 61000-4-20, Electromagnetic compatibility (EMC) - Part 4-20: Testing and measurement techniques - Emission and immunity testing in transverse electromagnetic (TEM) waveguides
- [4] Mil-std-461F, Department of Defence interface standard - Requirements for the control of electromagnetic interference characteristics of subsystem and equipment

# A brief review of the root action norm for waveform analysis

*E Schamiloglu*

*Department of Electrical and Computer Engineering, University of New Mexico, MSC01 1100  
Albuquerque, NM 87131-0001 USA*

## Abstract

The statistical comparison of stress envelopes to individual waveforms is based on waveform norm attributes. Waveform norm attributes were introduced by Baum and then expanded on by others. This paper provides a brief overview of the root action norm and how it has become one of the standard waveform norms in the EMP community.

**Keywords:** Root action norm, waveform norms, EMP.

## 1 Introduction

The International Electrotechnical Commission's (IEC's) technical committee SC 77C is preparing the second edition of its IEC 61000-4-24: Electromagnetic Compatibility (EMC) - Part 4-24: Testing and measurement techniques - Test methods for protective devices for high-altitude EMP (HEMP) conducted disturbance - Proposed Horizontal Standard. This standard deals with methods for testing protective devices for HEMP conducted disturbance. It includes two-terminal elements, such as gas discharge tubes, varistors, and two-port surge protection devices, such as HEMP combination filters. It covers testing of voltage breakdown and voltage-limiting characteristics but also methods to measure the residual voltage and/or the residual current, peak rate of rise and root action for the case of very fast changes of voltage and current as a function of time. The second edition introduces methods to test HEMP combination filters [1]. During one of the committee meetings held in Thun, Switzerland in 2013 there was some discussion regarding the root action norm. This led the author to research this topic, resulting in this brief overview.

## 2 Waveform Norms

An important portion of EMP testing is the assessment of the effects of an injected waveform on a device under test (DUT). The statistical comparison of stress envelopes to individual waveforms is based on waveform norm attributes. (Norm attributes are scalar quantities that characterize the features of a complicated waveform. Norms typically used as pass/fail criteria for pulsed current injection test residual internal stresses are peak current, peak rate of rise, and root action [1]. These quantities apply to short pulse tests only. The reader is referred to Baum for additional information [2].

There are five waveform norms that are commonly accepted in the EMP community. These are summarized in Table 1. Each of the five norms in Table 1 is considered to provide important statistical insight into the effects on the DUT [3]. The first and the last quantities are perhaps the most useful since they are most closely associated with circuit upset and component failure [4]. Heating effects, including burnout, are directly related to the energy delivered by the injection signal, which is described by the root action integral when the load has a resistive component [5]. In this paper we will focus on the root action norm.

Table 1: Waveform norms commonly adopted in the EMP community [3].

Norm	Equation	Nomenclature
N <sub>1</sub>	$ f(t) _{\max}$	Peak Absolute Amplitude
N <sub>2</sub>	$\left  \frac{df(t)}{dt} \right _{\max}$	Peak Absolute Derivative
N <sub>3</sub>	$\left  \int_0^t f(x) dx \right _{\max}$	Peak Absolute Impulse
N <sub>4</sub>	$\int_0^{\infty}  f(t)  dt$	Rectified Impulse
N <sub>5</sub>	$\sqrt{\int_{t_0}^{t_1}  f(t) ^2 dt}$	Root Action Integral

### 2.1 Square Root of the Action Integral Response

We focus on the root action norm, more commonly implemented as the *square root of the action integral response*, which is the norm of a current waveform  $i(t)$  defined by Equation (1)

$$\sqrt{\int_{t_0}^{t_1} |i(t)|^2 dt} \quad (1)$$

where  $t_0 = 0$  is the start of the pulsed current injection drive pulse;  $t_1$  is typically 5 msec for the early-time HEMP and typically 500 msec for intermediate-time HEMP [1], although these are not necessarily "standard" values.

In physics, the action is a functional  $S$  that takes a function of time and (for fields) space as input and returns a scalar. For the Euler-Lagrange system of equations and adopting

Hamilton's principle, we assume that the Lagrangian  $\mathcal{L}$  (the integrand of the action integral) depends only on the coordinate  $x(t)$  and its time derivative  $dx(t)/dt$ , and may also depend explicitly on time. In that case, the action integral can be written [6]

$$S = \int_{t_1}^{t_2} \mathcal{L}(x, \dot{x}, t) dt \quad (2)$$

For an electrical network comprising inductors and ignoring capacitors, it can be shown that the Lagrangian can be expressed as [7]

$$\mathcal{L} = \frac{1}{2} i^T L i \quad (3)$$

where  $i^T$  is the transpose of the current matrix. Thus the root action integral is a measure of the injected energy in a pulsed current injection experiment. Normalized to inductance it yields the square root of the action integral response, whose dimensions are [Ampere  $\cdot$  sec<sup>1/2</sup>].

Thus the root action integral is directly related to the energy delivered by the injection signal – it is nothing other than the square root of the action integral where the Lagrangian  $\mathcal{L}$  describing the circuit is the integrand.

## References

- [1] High-Altitude Electromagnetic Pulse (HEMP) Protection for Ground-Based C41 Facilities Performing Critical, Time-Urgent Missions Part 1: Fixed Facilities (MIL-STD-188-125-1 Notice 1, 7 April 2005).
- [2] C.E. Baum, "Norms of Time-Domain Functions and Convolution Operators," in H.N. Kritikos and D.L. Jaggard, Eds., *Recent Advances in Electromagnetic Theory* (Springer-Verlag, New York, NY, 1990), Chap. 2, and references therein.
- [3] J. Beilfuss and R. Gray, "Source Selection Techniques for EMP Direct Drive Simulation," *IEEE National Symposium on Electromagnetic Compatibility* (Denver, CO, May 23-25, 1989), pp. 93-96.
- [4] C.E. Baum, "Black Box Bounds," *Interaction Note 429*, 19 May 1983 (available at the Summa Notes website: <http://ece-research.unm.edu/summa/notes/In/0429.pdf>).
- [5] D.V. Giri, *High-Power Electromagnetic Radiators* (Harvard University Press, Cambridge, MA, 2004), p. 73.
- [6] H. Goldstein, *Classical Mechanics* (Addison-Wesley, Reading, MA, 1965).
- [7] L.O. Chua and J.D. McPherson, "Explicit Topological Formulations of Lagrangian and Hamiltonian Equations for Nonlinear Networks," *IEEE Trans. Circuits Syst.* Vol. 21, pp. 277-285 (1974).

# The Discrete Method of BLT Equation on Non-parallel Two-Wire Transmission Line

Mengshi Zhang, Guyan Ni, and Min Zhou

College of Science, National University of Defense Technology, Changsha 410073, China

## Abstract

The terminal response of non-parallel two wire transmission line in frequency domain and time domain can be calculated by the discrete method based on the BLT equation. For the non-parallel two wire transmission line, the frequency-domain discrete formula of the BLT equation is obtained under the distribution source of the Agrawal model. Then the time-domain discrete formulation of the BLT equation is obtained by the inverse Fourier transform. Each section of the transmission line is equivalent to a parallel transmission line, and the terminal response of voltage and current in frequency domain and time domain can be calculated with these two discrete formulas. Finally, numerical examples are presented for the plane wave illumination.

**Keywords:** non-parallel transmission line; BLT equation; terminal response

## 1 Introduction

The BLT equations are often applied to solve the induced voltage and current on terminal impedance of transmission line<sup>[1]</sup>. The distributed source in BLT equation usually has two models: Taylor model<sup>[2]</sup> and Agrawal model<sup>[3]</sup>. The traditional BLT equation can only solve the model of parallel transmission line, while for the non-parallel transmission lines, the traditional BLT equation can not calculate the terminal response.

In this paper, we present the discrete method of BLT equation on non-parallel two wire transmission line. The transmission line is divided into  $n$  sections, and each section is approximated as a parallel transmission line. The frequency domain discretization formulations of the induced voltage and current on terminal impedances of the non-parallel transmission line are obtained by using the distribution vectors of Agrawal model, and then we use the inverse Fourier transform to obtain time domain discretization formulations. Finally, numerical examples are presented for the plane wave illumination.

## 2 The BLT equation for solving the terminal response

There are usually two models of the traditional BLT equations that solve terminal responses of a parallel two wire transmission line: Taylor model and Agrawal model. In fact Taylor model and Agrawal model are two different

descriptions of the same solution, which are equivalent to the calculation<sup>[4]</sup>. In order to facilitate the calculation and to show the consistency of the formulas, each part of this paper use Agrawal model to do the calculation.

The Agrawal model is also called scattered voltage formulation. For the parallel two wire transmission line of length  $L$  with terminal load  $Z_1, Z_2$ , the induced voltages and currents can be expressed in matrix form as<sup>[1,5,6,7]</sup>

$$\begin{pmatrix} V(0) \\ V(L) \end{pmatrix} = \begin{pmatrix} 1+\rho_1 & 0 \\ 0 & 1+\rho_2 \end{pmatrix} \begin{pmatrix} -\rho_1 & e^{\gamma L} \\ e^{\gamma L} & -\rho_2 \end{pmatrix}^{-1} \begin{pmatrix} S_1 \\ S_2 \end{pmatrix} \quad (2.1)$$

$$\begin{pmatrix} I(0) \\ I(L) \end{pmatrix} = \frac{1}{Z_c} \begin{pmatrix} 1+\rho_1 & 0 \\ 0 & 1+\rho_2 \end{pmatrix} \begin{pmatrix} -\rho_1 & e^{\gamma L} \\ e^{\gamma L} & -\rho_2 \end{pmatrix}^{-1} \begin{pmatrix} S_1 \\ S_2 \end{pmatrix} \quad (2.2)$$

Here,  $Z_c$  is the characteristic impedance;  $\gamma$  is the propagation constant;  $\rho_i = \frac{Z_i - Z_c}{Z_i + Z_c}$ ,  $i = 1, 2$ .

The source vector is given by (2.3) as

$$\begin{pmatrix} S_1 \\ S_2 \end{pmatrix} = \begin{pmatrix} \frac{1}{2} \int_0^L e^{\gamma x} V_{s2}(x) dx - \frac{V_1}{2} + \frac{V_2}{2} e^{\gamma L} \\ -\frac{1}{2} \int_0^L e^{\gamma(L-x)} V_{s2}(x) dx - \frac{V_2}{2} + \frac{V_1}{2} e^{\gamma L} \end{pmatrix} \quad (2.3)$$

The distributed voltage source  $V_{s2}$  is expressed as

$$V_{s2}(x) = E_x^{inc}(x, d) - E_x^{inc}(x, 0) \quad (2.4)$$

Two lumped voltage sources  $V_1$  and  $V_2$  in Eq.(2.3) are given by

$$V_1 = \int_0^d E_z^{inc}(0, z) dz, \quad V_2 = -\int_0^d E_z^{inc}(L, z) dz \quad (2.5)$$

## 3 The discrete formulation of BLT equations

### 3.1 The discrete formulation of BLT equations in frequency domain

The non-parallel transmission line is divided into  $n$  sections, as shown in Fig.1. The distance of two wires in the left terminal is  $d_0$ . The radius of the wire is  $a$ . The angle between the wire is  $2\theta$ . The length of  $x$  axis  $L_x = L \sec \theta$ .

Take each section as a parallel transmission line. Parameters of the section  $m$  are as follows. Let  $\Delta x_m = L_x / n$  be the length of the  $m$ th section,  $P_m(x, y, z) = (x_m^c, y_m^c, z_m^c) = ((m-0.5)\Delta x_m, 0, 0)$  be the center point,  $d_m = d_0 + 2x_m^c \tan \theta$  be the distance of two wires,  $R_m = 0$  be the per-unit-length resistance,  $G_m = 0$  be the

per-unit-length conductance,  $L_m = \frac{\mu}{\pi} \ln \frac{d_m}{a}$  be the per-unit-length inductance,  $C_m = \frac{\pi \varepsilon}{\ln \frac{d_m}{a}}$  be the per-unit-length capacitance,  $Z_m = R_m + j\omega L_m$  be the per-unit-length impedance,  $Y_m = G_m + j\omega C_m$  be the per-unit-length admittance,  $Z_{cm} = \sqrt{\frac{Z_m}{Y_m}}$  be the characteristic impedance,  $\gamma_m = \sqrt{Z_m Y_m}$  be the propagation constant,  $\varepsilon$  be the dielectric constant;  $\mu$  be the magnetic permeability.

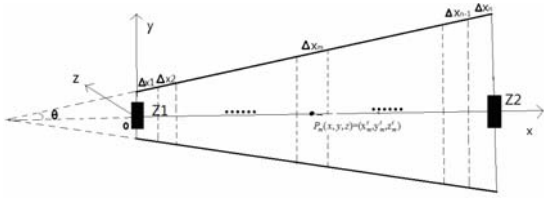


**Fig.1 the discrete model of non-parallel two wire transmission line**

By the definition of integral, integral terms of (2.3) are rewritten as the following sum forms

$$\begin{pmatrix} S_1 \\ S_2 \end{pmatrix} = \begin{pmatrix} \frac{1}{2} \sum_{m=1}^n e^{(m\Delta x_m - \frac{1}{2}\Delta x_m)\gamma_m} V_{s2}(x_m) \Delta x_m - \frac{V_1}{2} + \frac{V_2}{2} e^{j\gamma L_x} \\ -\frac{1}{2} \sum_{m=1}^n e^{(L_x - m\Delta x_m + \frac{1}{2}\Delta x_m)\gamma_m} V_{s2}(x_m) \Delta x_m + \frac{V_1}{2} e^{j\gamma L_x} - \frac{V_2}{2} \end{pmatrix} \quad (3.1)$$

Because of the short distance between the two wires, the distributed voltage source  $V_{s2}$  and the two lumped voltage sources  $V_1$ ,  $V_2$  are as follows

$$V_1 = -E_z^{inc}(0,0,0)d_1, \quad V_2 = -E_z^{inc}(L_x,0,0)d_n \quad (3.2)$$

$$V_{s2}(x_m) = E_x^{inc}(x_m^c,0,\frac{d_m}{2}) - E_x^{inc}(x_m^c,0,-\frac{d_m}{2}) \quad (3.3)$$

Combining formulations (2.1), (2.2) and (3.1), we obtain the discrete numerical solution of the terminal response in frequency-domain for plane-wave illumination.

### 3.2 The discrete formulation of BLT equations in time domain

#### 3.2.1 The calculation of distributed source vector in time domain

By the inverse Fourier transform and (2.3), we have

$$s_1(t) = \frac{1}{2} \frac{L_x}{n} \sum_{m=1}^n v_{s2}(t + \frac{x_m^c}{v}, x_m^c) - \frac{v_1(t)}{2} + \frac{v_2(t + \frac{L_x}{v})}{2} \quad (3.4)$$

$$s_2(t) = -\frac{1}{2} \frac{L_x}{n} \sum_{m=1}^n v_{s2}(t + \frac{(L_x - x_m^c)}{v}, x_m^c) + \frac{v_1(t + \frac{L_x}{v})}{2} - \frac{v_2(t)}{2} \quad (3.5)$$

where

$$v_1(t) = -E_z^{inc}(t,0,0,0)d_1, \quad v_2(t) = -E_z^{inc}(t,L_x,0,0)d_n \quad (3.6)$$

$$v_{s2}(t, x_m^c) = E_x^{inc}(t, x_m^c, 0, \frac{d_m}{2}) - E_x^{inc}(t, x_m^c, 0, -\frac{d_m}{2}) \quad (3.7)$$

#### 3.2.2 The calculation of BLT equation in time domain

By the inverse Fourier transform, the time-domain formulations of  $SS_1(\omega)$  and  $SS_2(\omega)$  are as follows<sup>[8,9,10,11]</sup>

$$\begin{pmatrix} SS_1(t) \\ SS_2(t) \end{pmatrix} = \begin{pmatrix} \sum_{n=0}^{\infty} (\rho_1 \rho_2)^n \left( s_2(t - \frac{(2n+1)L_x}{v}) + \rho_2 s_1(\frac{t - 2(n+1)L_x}{v}) \right) \\ \sum_{n=0}^{\infty} (\rho_1 \rho_2)^n \left( s_1(t - \frac{(2n+1)L_x}{v}) + \rho_1 s_2(\frac{t - 2(n+1)L_x}{v}) \right) \end{pmatrix} \quad (3.8)$$

Then, the discrete solution of the voltage BLT equations in time domain can be written as

$$\begin{bmatrix} v(0,t) \\ v(L,t) \end{bmatrix} = \begin{bmatrix} 1 + \rho_1 & 0 \\ 0 & 1 + \rho_2 \end{bmatrix} \begin{bmatrix} SS_1(t) \\ SS_2(t) \end{bmatrix} \quad (3.9)$$

Similarly we can get the discrete solution of the current BLT equation in time domain as follows

$$\begin{bmatrix} i(0,t) \\ i(L,t) \end{bmatrix} = \frac{1}{Z_c} \begin{bmatrix} 1 - \rho_1 & 0 \\ 0 & 1 - \rho_2 \end{bmatrix} \begin{bmatrix} SS_1(t) \\ SS_2(t) \end{bmatrix} \quad (3.10)$$

## 4 Numerical tests

In order to show how to apply the discrete formulation of BLT equation, and check on its validity, numerical examples have been considered under the plane wave illumination. Respectively we use the discrete formulation and the traditional BLT equation to calculate the terminal induced voltage and current of time domain and frequency domain to make the comparison. The numerical tests involve the following parameters

- line length  $L = 30m$ ;
- wires separation  $d = 0.2m$ ;
- wire radius  $a = 0.0015m$ ;
- load resistance  $Z_1 = Z_2 = 293\Omega$ ;
- incident angles  $\phi = 0, \psi = \pi/3$ ;
- polarization angle  $\alpha = 0$ ;
- The wire is evenly divided into 500 sections.

#### 4.1 The numerical test in frequency domain

The incident E-field : double exponential waveform

$$E^{inc}(\omega) = \frac{1}{2\pi} \left( \frac{1}{4 \times 10^6 + \omega i} - \frac{1}{4.76 \times 10^8 + \omega i} \right).$$

Let the angle of two wires  $2\theta = 0$ . Using Mathematica8.0, we calculate the induced current and voltage in terminal 2 by the analytic solution based on (2.1),(2.2) and discrete numerical solution respectively, as shown in Fig. 2.

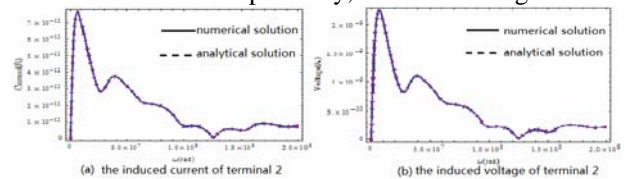


**Fig.2 the frequency-domain response of terminal 2**

Let the angle of two wires  $2\theta = \pi/1800$ . Using Mathematica8.0, we obtain the discrete numerical frequency-domain solutions of two-wire lines with  $2\theta = 0$  and  $2\theta = \pi/1800$ , respectively, as shown in Fig. 3.

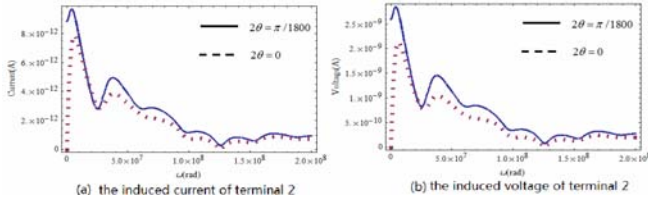


**Fig.3 the frequency -domain response of terminal 2**

Because the angle between the two wires are expanded, the distance of the two wires in terminal 2 will increase, which lead to the induced voltage and current increase. Figure 3 is consistent with our theoretical analysis in frequency domain.

**4.2 The numerical test in time domain**

The expression of excitation source in time domain is as follows

$$E^{inc}(t) = \begin{cases} 1.05(e^{-4 \times 10^6 t} - e^{-4.76 \times 10^8 t}), & t \geq 0 \\ 0, & t < 0 \end{cases}$$

Let the angle of two wires  $2\theta = 0$ . Using Mathematica8.0, we calculate the induced current and voltage in terminal 2 by the analytic solution<sup>[11]</sup> and discrete numerical solution, respectively, as shown in Fig. 4.

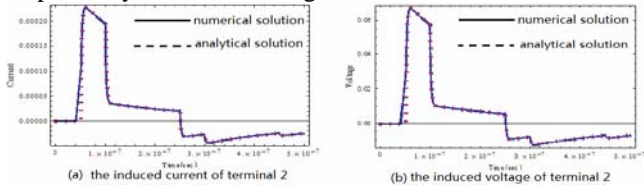


**Fig.4 the time-domain response of terminal 2**

It can be seen in Fig.4 that the image of the numerical solution and the analytical solution of induced current and voltage in terminal 2 in time domain are overlapped, which shows the consistence of the discrete and analytical solution.

Let the angle of two wires  $2\theta = \pi/1800$ . Using Mathematica8.0, we obtain the discrete numerical time-domain solutions of two-wire lines with  $2\theta = 0$  and  $2\theta = \pi/1800$ , respectively, as shown in Fig. 5.

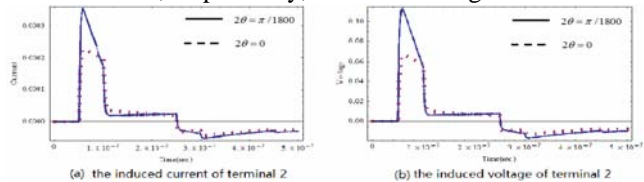


**Fig.5 the time-domain response of terminal 2**

Because the angle between the two wires are expanded, the distance of the two wire in terminal 2 will increase, which lead

to the induced voltage and current increase. Figure 5 is consistent with our theoretical analysis in time domain.

**5 Conclusion**

In this paper we use the discrete numerical method to calculate the terminal load response of non-parallel two wire transmission line, and the discrete formulation of BLT equation in frequency domain and time domain are obtained. Through the numerical test under the plane wave illumination, the discrete method solution and analytical solution are compared. The consistency of the two results shows the validity of this method. This method can also be applied to the model of multi conductor transmission line<sup>[12]</sup> and even more general model.

**Acknowledgements**

Project supported by the Natural Science Foundation of China (Grant No 61171018).

**References**

- [1] Tesche F M, Ianoz M V , Karlsson T. EMC A nalysis Methods and Computational Models[M]. New York: John Wiley & Sons, 1997.
- [2] Taylor C D, Satterwhite R S, and Harrison C W.The Response of a Terminated Two-Wire Transmission Line Excited by a Nonuniform Electromagnetic Field[J]. IEEE Trans. Antennas Propag., 1987, 13(6):987-989.
- [3] Agrawal A K. et al. Transient Response of Multiconductor Transmission Lines Exited by a nonuniform Electromagnetic Field[J]. IEEE Transactions on Electromagnetic Compatibility, 1980, 22(2):119-129.
- [4] Ni G Y, Luo J S, Li C L. Comparison of Taylor and Agrawal Coupling Models and Their Analytic Solutions. High Power Laser and Particle Beams, 2007, 19(9) : 1522-1525.
- [5] Smith A A, Jr. Coupling of External Electromagnetic Field to Transmission Lines[M]. New York: Wiley, 1977.
- [6] Tesche F M. Plane Wave Coupling to Cables, Part II, in Handbook of Electromagnetic Compatibility[M] R. Perez, ed. New York: Academic Press, 1995.
- [7] Ushida H. Fundamentals of Coupled Lines and Multiwire Antennas[M]. Sendi: Sasaki Press, 1967.
- [8] Guo H P, Liu X G, Electromagnetic Field and Electromagnetic Waves, Xian: Xian Electronic Science and Technology University Press, 2003.
- [9] Kong J A, Electromagnetic Wave Theory, Beijing: Electronics Industry Press, 2003.
- [10] Xu L Q, Cao W, The Theory of Electromagnetic Field and Electromagnetic Waves, Beijing: Science Press, 2010.
- [11] Ni G Y, Yan L, Yuan N C. Time-domain analytic solutions of two-wire transmission line excited by a plane-wave field. Chinese Physics B, 2008, 17(10) : 3630-3634.
- [12] Wang Q G, Zhou X, Li X D. BLT Equation Based Time-domain Simulation Method of Transmission-line Networks Responses to Electromagnetic Pulse [J]. High Voltage Engineering, 2012, 38(9): 2205-2212

# The tensor field equation of systematic electromagnetism and its exterior form representation

Shaorong Chen\*, Xiang Li\*, Xishun Liu\*, Jianshu Luo<sup>†</sup>, Zhuangzhuang Tian\*, Jun Zhang\*

\*College of Electronic Science and Engineering, <sup>†</sup>College of Science;  
National University of Defense Technology, Changsha 410073, China.

## Abstract

When the input of system is ‘four-dimensional electromagnetic potential’, the exterior form of tensor field equation of electromagnetic system can be obtained by manipulating the existing theory. The expansion sets of the equation in space contains 8 sub-equations. Four of them have already included in the Maxwell equations set. The fifth is time-varying equation about electric field curl, the sixth is equation about half of magnetic field 6 symmetry tensor (each set contains three components), the other two parts are mutual-dual equations of the charge conservation law that have been known.

**Keywords:** systematic electromagnetism, exterior form, Maxwell equations, magnetic monopole, Yang-Mills field.

## 1 Introduction

Maxwell’s equation are traditionally thought as four independent axioms, but, remarkably, here says that this is not so. They are just explicit expressions in different observation conditions by the same field equation of electromagnetism system, and the coefficients  $\varepsilon$  and  $\mu$  in equations set can just be determined from metric uniformity.

We always think that when more equations set up, the solution is certainly more difficult. But in actuality, the cause of complexity and difficulty is the lack of equations rather than an excess. Maybe solution will be easy when the quantity of equations is enough, and makes varieties and relation complete and systematic. Just like electromagnetism system can be described simply by one field equation, while any combinations of component equations set (including Maxwell equations) are complex.

Making use of some theories about signals and systems (Deducing process is omitted, in other paper later), the tensor field equation of systematic electromagnetism is constructed:

$$x_v'' \left[ (\partial_\mu A_w) dx^\mu dx^w + (\partial'_\mu A'_w) dx'^\mu dx'^w \right] + x_v'' \left[ (\partial_\mu A_w) dx^\mu \wedge dx^w \right] = 0 \quad (0)$$

In the formula,  $v, \mu, w = 0, 1, 2, 3$  and  $\{A_w\}$  is so-called ‘‘4-dimensional electromagnetic potential’’; the superscript ‘‘'’’ and ‘‘''’’ in equation are used for connection<sup>[1][2]</sup>  $\nabla = \nabla_a$ ,

$\nabla' = \nabla_b$ ,  $\nabla'' = \nabla_c$  located in a different position  $a, b, c$  in  $\square^4$  space, i.e.  $A' = \{A'_0, A'_1, A'_2, A'_3\}$  means the descriptions of electromagnetic potential in position  $b$  with variable  $x' = \{x'_0, x'_1, x'_2, x'_3\}$ , and the 1-form base in position  $b$  is  $dx'^\mu$ , etc., the wedge product ‘‘ $\wedge$ ’’ in  $(\partial_\mu A_w) dx^\mu \wedge dx^w$  expanded between  $\nabla_a$  and  $\nabla_b$ .

## 2 Tensor field equation’s expansion sets of electromagnetism system in space.

The deducing process is omitted, and there are 8 equations in total

### 2.1 The condition of field equation’s expansion

**Condition a:** when coordinate connections  $\nabla, \nabla', \nabla''$  are different.

**Condition b:** when  $\nabla''$  is the same with one of  $\nabla$  and  $\nabla'$ , namely there is not third coordinate connection. (Making  $\nabla'' = \nabla'$  means  $\nabla_c = \nabla_b$ )

**Condition c:** when all 3 coordinate connections are same, or there is a mutual translation matrix between them.

### 2.2 Field equation’s expansion sets

2.2.1 Field equation can get  $\frac{\partial F_{\mu w}}{\partial x_v} + \frac{\partial F_{v\mu}}{\partial x_w} + \frac{\partial F_{wv}}{\partial x_\mu} = 0$  after

using ‘‘condition a’’, so deducing:

**a.** Tensor Equation:

$$d_{R^3} (*\beta^2) = d_{R^3} \beta^1 = 0 \quad (1)$$

its vector version is  $\nabla \cdot \vec{B} = 0$

**b.** Tensor Equation:

$$d_{R^3} \xi^2 + d_{x_0} \beta^2 = 0 \quad (2)$$

its vector version is  $\frac{\partial \beta^2}{\partial t} = d_{R^4} d_{R^3} j_{(t)}^1$ .

**c.** Tensor Equation:

$$d_{R^3} (*\xi^2) + d_{x_0} (*\beta^2) = 0 \quad (3)$$

its vector version is  $\nabla \times \vec{E} + \frac{\partial \vec{B}}{\partial t} = 0$ .

d. Tensor Equation:

$$d_{x_0} (*\xi^2)_{\square^4} = 0 \quad (4)$$

its vector version is  $\frac{\partial}{\partial t} \{\nabla \times \vec{E}\} = 0$ .

2.2.2 Field equation can get  $(x_w)^b [F_{ab}] = -(\partial_v A_w) dx^v$  after using “condition b”, so deducing:

e. Tensor Equation:

$$d(*\xi^2) = -\frac{\sigma^3}{\varepsilon} \quad (5)$$

its vector version is  $\nabla \cdot \vec{E} = \frac{\rho \cdot 4\pi}{\varepsilon}$ .

f. Tensor Equation:

$$d_{R^3} \beta^1 = \mu j^2 + \mu \varepsilon \cdot \frac{\partial \vec{E}}{\partial t} \quad (6)$$

its vector version is  $\mu \cdot \vec{J} = \nabla \times \vec{B} - \varepsilon \mu \cdot \frac{\partial \vec{E}}{\partial t}$ .

2.2.3 Field equation can get  $\frac{\partial A_w}{\partial x_\mu} dx^\mu \wedge dx^w = 0$  after using

“condition c”, so deducing:

g. Tensor Equation:

$$d(j^1) = 0 \quad (7)$$

its vector version is  $\nabla \cdot j^1 = -\frac{\partial(\rho_0)}{\partial t}$ .

(In formula  $\rho_0 = \rho v^0$ ,  $v^0$  is 4-dimensional velocity' s component in time axis.)

h. Tensor Equation:

$$d(*j^1) = 0 \quad (8)$$

its vector version is  $\nabla \cdot \vec{J} = \frac{\partial \rho}{\partial t}$ .

### 2.3 Annotation

- a. In above Tensor field equations, “\*” is “Hodge operator”.
- b. Vector expansions of Equation (1) and equation (3) can only be true when they satisfy Abel condition, the complete expansions in vector version are:

$$\nabla \cdot \vec{B} = iq(\vec{A} \cdot \vec{B} - \vec{B} \cdot \vec{A})$$

$$\nabla \times \vec{E} + \frac{\partial \vec{B}}{\partial t} = iq\left\{\left(\vec{A} \times \vec{E} + \vec{E} \times \vec{A}\right) + \left(A_0 \vec{B} - \vec{B} A_0\right)\right\}$$

Namely “magnetism charge density” can naturally exist in Yang-Mills field when it does not satisfy Abel condition, while this is a basic condition hypothesis that Yang ZhenNing and Mills deduced “Yang-Mills action functional”.

## 3 The relations between the expansions and the Maxwell equation

Equation (1),(3), (5) and (6) are Maxwell equations set. They are classified according to the form dimension to further explain their relationship. The red equations shown in Table 1 are new equations, they are not included in Maxwell’s.

Table 1: The exterior form representation from equation (1) to equation (8)

	3-form equation	2-form equation	Annotation
1	$d_{R^3} (*\beta^2) = 0$	$d_{R^3} \beta^1 = 0$ $\nabla \cdot \vec{B} = 0$	Absence of Magnetic Charges
2	$d_{R^3} \xi^2 + d_{x_0} \beta^2 = 0$ $\frac{\partial \beta^2}{\partial t} = d_{R^4} d_{R^3} j_{(\tau)}^1$		May named: Magnetic Charges
3	$d_{R^3} (*\xi^2)$ $+ d_{x_0} (*\beta^2) = 0$	$\nabla \times \vec{E} + \frac{\partial \vec{B}}{\partial t} = 0$	Faraday’s Law
4	$d_{x_0} (*\xi^2)_{\square^4} = 0$ $\frac{\partial}{\partial t} \{\nabla \times \vec{E}\} = 0$		May named: Absence of Electronic Charges
5	$d(*\xi^2) = -\frac{\sigma^3}{\varepsilon}$	$\nabla \cdot \vec{E} = \frac{\rho \cdot 4\pi}{\varepsilon}$	Gauss’s Law
6		$d_{R^3} \beta^1 = \mu j^2 + \mu \varepsilon \cdot \frac{\partial \vec{E}}{\partial t}$ $\mu \vec{J} = \nabla \times \vec{B} - \varepsilon \mu \cdot \frac{\partial \vec{E}}{\partial t}$	Ampere-Maxwell law
7		$d(j^1) = 0$ $\nabla \cdot j^1 = -\frac{\partial(\rho_0)}{\partial t}$	Law of Charge conservation
8		$d(*j^1) = 0$ $\nabla \cdot \vec{J} = \frac{\partial \rho}{\partial t}$	Law of Charge conservation

### 3.1 About the proving experiments

In Table 1, equation (1), (3), (5) and (6) are Maxwell equations set, they are authentic. Equation (2), (4) and (7) are new equations that are waiting to test. Equation (7) can be verified by equation (8), and the meaning of equation (8) is obvious.

Equation (4) can be verified by equation (3). For example, when  $\frac{\partial}{\partial t} \{\nabla \times \vec{E}\} = 0$ , we can get  $\frac{\partial^2 \vec{B}}{\partial t^2} = 0$  after substituting

equation (4) into equation (3).  $\frac{\partial^2 \vec{B}}{\partial t^2} = 0$  means that magnetic

field does not exist “acceleration”. It shows that magnetic field does not exist “acceleration” because of equation (4), instead of the contrary. So we can verify that magnetic field has no “acceleration” to learn that equation (4) is true. We affirm that the none-acceleration phenomenon of magnetic must exist. The current electromagnetism theorem can’t deduce this phenomenon.

Because equation (2) just contain any one of the two equivalence sets of 6 tensor components of magnetic field. Its proving is more complex. We need to comprehend the complexity by the form dimensionality which constitute the equations.

### 3.2 Form dimensionality and the meaning of electromagnetism equation

TABLE 1 shows that equation (1), (3) and (5) are both 2-form equation and 3-form equation, and they are homotopy equality! According to meaning of homotopy equality, homotopy invariant establish whether in high-dimension or low-dimension. It may tell us electromagnetism existential form and the reason of electromagnetism can propagate wirelessly (While putting actual thing  $\square$  in  $M^4$ , according to Hopf map and Hopf fibration, it’s logical to regard  $\{M^4 - \square\}$  as increase or decrease of thing’s dimension).

- a. Equation (1) tells us, pure magnetism in  $\square^3$  space can reside in space and the inner thing. It appears as 2-form quantity in the inner thing, while manifest as 1-form quantity in  $\{M^4 - \square\}$  space.
- b. Equation (3) tells us, electromagnetism can propagate whether in space or the inner thing. It manifest as 2-form quantity in the inner thing, and manifest as 1-form quantity in  $\{M^4 - \square\}$  space.
- c. Equation (5) tells us, electric density can exist in 3-form quantity in the inner thing  $\square$ . It exist in 2-form quantity in  $\{M^4 - \square\}$  space, and manifest as 1-form electric field!  
Consent to item a, b and c, pure 3-form equation (2), (4) and 2-form equation (6), (7), (8) could tell us:
- d. Equation (7) and equation (8) tell us, 2-form electric in the inner thing equal to the form value of mapping 1-form electric current in the same place.
- e. Equation (6) tells us, 1-form electric field and 1-form magnetic field are generated by 2-form electric current in the inner thing  $\square$ . Consenting to item a, b, c, it shows that the oncoming electric field and magnetic field can only exist in space, not the inner thing  $\square$ .
- f. Equation (4) tells us, 2-form electric field is a stable quantity, and 3-form electric field does not exist.
- g. Equation (2) tells us, *2-form magnetism are generated by 1-form electric current with mapping twice, and only exist in the inner thing and cannot propagate in space, which consent to item a, b and c.* And because magnetic monopole just exist in the inner thing, may it be the basic reason why magnetic field in space always appear both south and north poles. It also points out the proving direction of this project, metering “magnetic monopole”

must be in the inner side, while metering process can be got from the deducing process of equation (2).

From above analysis, we work out that electric field and magnetic field existing in space are only 1-form quantity. When transforming into 2-form quantity, they can only be stable and existed in the inner thing!

Equation (1), (3), (4), (5)and(8) are pseudo-form equations (namely their plus-minus relates to coordinate system direction). Equation (2), (6), (7) are truth-form equations. Truth-form equation (2), (6) are pure 2-form or 3-form equations. It means that transformation and mutual influence proceed with the same form dimension. It is their own properties and a stable state. The pseudo-form equation (1),(3),(4),(5) always connect with form quantity of different dimension.

Only equation (7)’s property is very special. From deducing process, we can know that equation (7) is in accord with truth-form’s definition. But, according to pseudo-form definition, equation (7) is also a pseudo-form equation. So equation (7) and (8) are on equal footing, they are equivalent to each other. In fact, they both describe attribute of “Charge conservation”!

## 4 Summary and conclusions

From the existing electromagnetism theory, the viewpoint of deducing Maxwell equations set based on “Law of Charge conservation” seemed to be wrong (there are more basic conditions or postulations, it will be discussed in other paper). Because the result what we got shows that “Law of charge conservation” and Maxwell equations set are equal, not that one is more basic and essential than the other one.

The magnetic field is 2-form quantity in  $\square^3$  space, the electric field is 2-form quantity in  $M^4$ . The Maxwell equations set are incomplete on the fiber bundle  $M^4$ .

Four-dimensional electromagnetic potential  $A_w = j_w$ ,  $j_w$  is 1-form electric current  $j_{(\tau)}$  component on fiber bundle  $M^4 = e^{ict} \times T^3$  ( $T^3$  is the 3-torus) when pseudo-metric  $*1 := \text{vol}^3(\mathbf{R})$  is defined in space  $\square^3$ .

One of new equations may concerns about the generation or excitation equation of “magnetic monopole”, because the equation relates to the covariant component of 4-dimensional electric current. The other one of new equations can give a reason why magnetic field is without “acceleration” (If “acceleration of magnetic field” or definition like this is existing, then the new equation asserts that this phenomenon is existing).

## References

- [1] Theodore Frankel. “The Geometry of Physics: an introduction 2<sup>nd</sup> ed.”, *Cambridge University Press*, (2004).
- [2] John E. Gilbert. “Clifford Algebras and Dirac Operator in Harmonic Analysis”, *Cambridge University Press*, (1991).

# Measurement result and analysis of aeronautical cables at high frequency range

Z L Tong\*, J S Luo\*, H Lei<sup>†</sup>, Y F Liu<sup>†</sup>, X S Liu<sup>‡</sup>, C X Tang<sup>‡</sup>

\* College of Science, National University of Defense Technology, Changsha, China, e-mail:tongzl@nudt.edu.cn

<sup>†</sup> Shenyang Aircraft Design & Reserch Institute, Shenyang, China

<sup>‡</sup> PLA 94452, Henan, China

## Abstract

This paper presents the measurement result of the induced voltage of two type aeronautical cables connected to a short wave radio station at three different frequency ranges. The measurement focuses on the induced voltage only from the cables themselves for testing the sensitivity of these different aeronautical cables under high frequency microwave. In this paper, we compare the quantity of the induced voltage of the two type cables and analyze the relationship between the induced voltage from the cables and the frequency.

**Keywords:** aeronautical cables, high frequency, measurement

## 1 Introduction

In the frame of the HIRF-SE European project [1] which is focused on the modelling of the electromagnetic effects inside an aircraft submitted to an HIRF (High Intensity Radiated Field) environment for HIRF certification analysis, some work on aeronautical cables and aeronautical equipments at low frequency has been completed. A research studied the numerical simulation of aeronautical cable topology and validated the cable model on the low-frequency range 30kHz-400MHz [2], and another research studied the modelling approach of conducted disturbances at the equipment interface due to Back-Door constraints and tested the approach in the 10kHz-400MHz frequency range [3]. In U.S., the National Institute of Standards and technology has completed shielding effectiveness/penetration studies on three different aircraft types for Federal Aviation Administration. The studies are used to understand the cavity coupling characteristics between antennas placed in various compartments inside the aircraft and antennas placed at various angular positions around an aircraft [4].

This paper presents the measurement result of the induced voltage of coaxial cables and the shielded eight-core wire under L-band (1GHz-2GHz), S-band (2GHz-4GHz) and X-band (8GHz-12GHz) plane wave. The purpose of this work is to test the sensitivity of these different aeronautical cables under high frequency plane waves, and the measurement focuses on the induced voltage only from the cables

themselves. In this measurement, the coupling effect from the cables is the most interested, so we measure the induced voltage instead of the induced current to avoid the disturbance from the equipment. The first part of the paper describes the cables and the test setup. The second part describes the various measurement condition and measurement result. Finally, we present some analysis on the measurement result.

## 2 Measurement case description

The cables and the harness considered in this work come from a short wave radio station in an aircraft. The short wave radio station contains a receiver, a sender and an antenna, and there are different cables connecting them. The measurement focuses on the connecting cables and the harness.

### 2.1 Description of cables and harness

The harness contains one antenna, two electronic equipments (receiver and sender) and four cables. The connections in the harness are shown in Fig. 1.

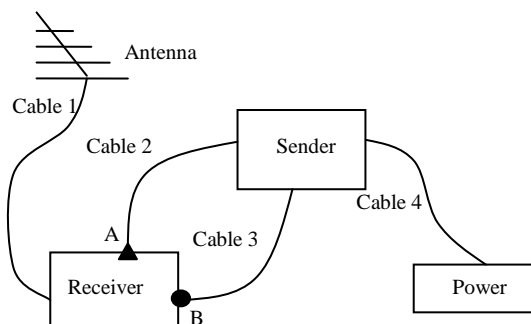


Figure 1. View of the harness

There are two coaxial cables, one shielded eight-core wire and a power wire in the harness. Cable 1 is a coaxial feeder between the antenna and the receiver, Cable 2 is a coaxial cable and Cable 3 is a shielded eight-core cable between the receiver and the sender, Cable 4 is a power wire. All the cables are well connected at the junctions. In the measurement, Cable 2 and Cable 3 are concerned and we use probes to measure the induced voltages of Cable 2 at point A and those of Cable 3 at point B. The reason for the choice of these two points is that these two points share a similar

location at the receiver and it makes the comparison between the induced voltages of those two types of cables reasonable.

Table 1. Definition of each cable

Cable No.	Cable Type	Length (m)
Cable 1	Coaxial cable	2.00
Cable 2	Shielded eight-core wire	1.50
Cable 3	Coaxial cable	1.15
Cable 4	Power wire	-

### 2.2 Description of the measurement setup

In this measurement, the types of measurement equipment are as followed:

- Signal Generator: Agilent 8257D;
- Spectrum Analyzer: Agilent E447;
- Radiating antenna: RGA60;
- Amplifier: L-band use (BONN) BTMA0925-250;  
S-band use (BONN) BTMA2060-100;  
X-band use (BONN) BTMA6018-35.

In this measurement, the equipments have been placed on a metallic ground plane which has a distance 75cm from the floor and well grounded. The dimensions of the metallic ground plane are 250cm×120cm. The harness has been placed at a distance 10cm over the ground plane. The radiating antenna placed in front of the metallic ground plane at a distance of 75cm and from the floor 105cm, where can meet the far field radiation condition of the antenna and produce the needed plane wave in the measurement. An electric field probe is placed at a distance 30cm over the edge of the metallic ground plane where in front of the radiating antenna. The measurement equipments had been placed in the shielded cavity far from the radiating field of the radiating antenna.

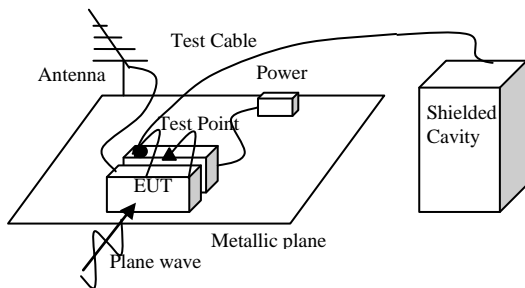


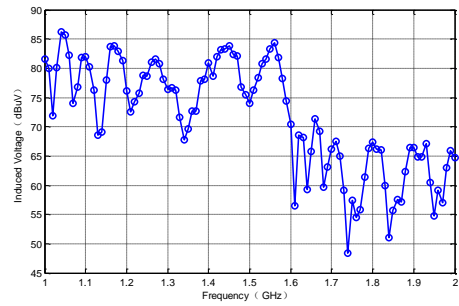
Figure 2. View of the harness in the test configuration

In the measurement, we penetrated the probe in the test point of the under measurement cable and shield the junction well, then measured the induced voltage of the cable at a specific frequency by the spectral analyzer.

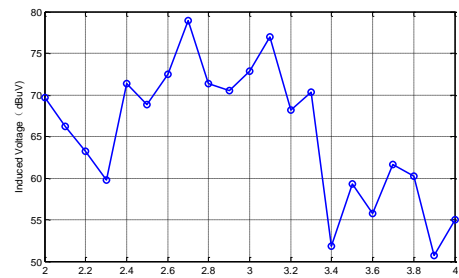
### 3 Measurement result

In this section, the measurement results will be presented.

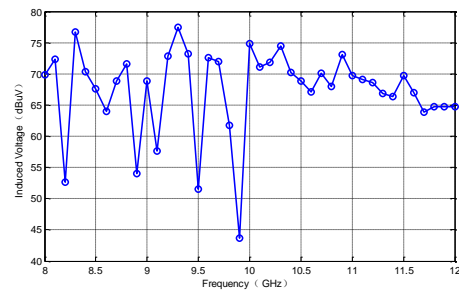
When we measured the induced voltage of Cable 2 at A point, the output power of Signal Generator is -35dBm at L-band and S-band and X-band is -15dBm.



(a) L-band



(b) S-Band



(c) X-band

Figure 3. Induced voltage of shielded eight-core wire

The measurement results in Figure 3 show that the shielded eight-core wire is sensitivity to the external microwave. And with the increasing of frequency, the coupling efficiency of the wire will decrease, it can be figure out as when we measured the induced voltage at X-band reached the similar quantity level it needs much higher output power than L-band and S-band. Besides, Figure 3(a) shows that the induced voltage decreases rapidly when the frequency of plane wave reaches 1.6GHz at L-band. Figure 3(b) shows the point in S-band is 3.4GHz. However, there is not a such point in X-band.

When we measured the induced voltage of Cable 3 at B point, the output power of Signal Generator is -10dBm at L-band, S-band and X-band.

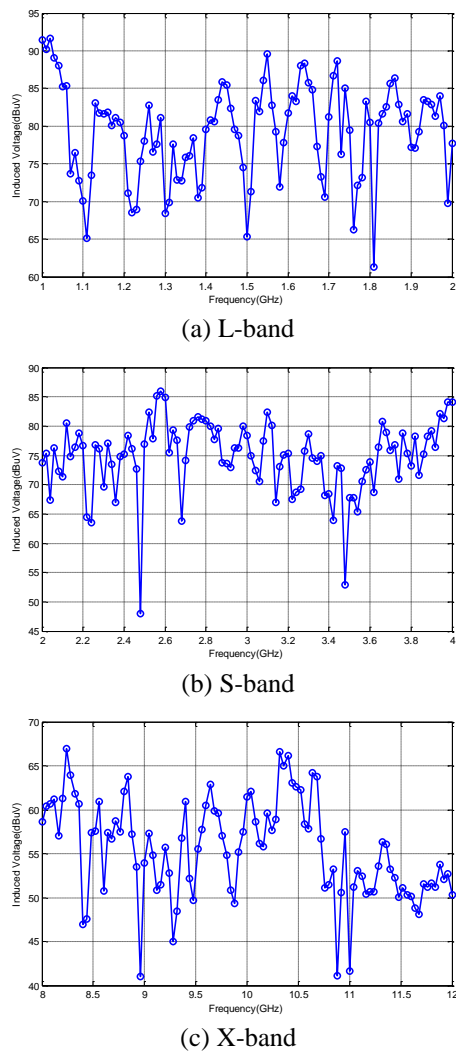


**Figure 4. Induced voltage of coaxial cable**

The measurement results in Figure 4 show that the shielded eight-core wire is more vulnerable than the coaxial cable under high frequency microwave. It should increase about more than 20dB from the output power source to make the induced voltage of coaxial cable at the same quantity with the shielded eight-core wire. And for both the two types of cables, the induced voltages of cables decrease with the increasing of frequency. It means both the two type cables have a low coupling efficiency at high frequency.

## 4 Conclusion

In this paper, the induced voltages of two types of aeronautical cables have been measured under three different frequency ranges of microwave. The measurement results show that both the two types of aeronautical cables are sensitive under high frequency microwave and the shielded eight-core wire is more vulnerable than the coaxial cable. Besides, the coupling efficiency of both the two type cables under high frequency microwave decreases when the frequency of microwave increases.

## Acknowledgements

This work was supported by the National Natural Science Foundation of China (No. 61171018 and No. 11271370).

## References

- [1] HIRF-SE Project, [www.hirf-se.eu](http://www.hirf-se.eu)
- [2] M. Ridel, P. Savi, M. Alberti, J-P. Parmantier, I.A. Maio, F. Nardone. "Numerical Simulation of Aeronautical Cable Topology and Experimental Validation". *Electromagnetic in Advanced Applications (ICEAA)*, pp. 1356-1359, (2011).
- [3] A. Guena, K. Diomande, J-L Braut, M. Ridel, J-P Parmantier, J-L. Vagneur, B. Chatellier. "EMC Modeling of Avionic Equipment at Low Frequency [10kHz-400MHz]", *Proc of the 10<sup>th</sup> Int. Symposium on Electromagnetic Compatibility (EMC Europe 2011 York)*, pp. 198-203, (2011).
- [4] C. Grosventor, D. Novotny, D. Camell, G. Koepke, R.T. Johnk, N. Canales. "Electromagnetic Airframe Penetration Measurements of the FAA's 737-200", *CreateSpace Independent Publishing Platform*, (2014) .

# Crosstalk analysis of PCB traces based on BLT equations and equivalent multi-conductor transmission line model

Y Li\*, G Y Ni\*, X D Chen \*

\* College of Science, National University of Defense Technology, Changsha, Hunan, China, 410073

## Abstract

The crosstalk analysis of PCB traces is an important part of electromagnetic interference analysis of an electronic system. For this purpose, an analytic approach is presented, which allows the crosstalk current and voltage of multiple PCB traces to be calculated with an external electromagnetic field coupling into one trace. The BLT equations for PCB traces are derived by solving the equivalent multi-conductor transmission line equation at two junctions in the electromagnetic topological network, after the excitation field is decomposed into the horizontal and vertical components. Computational example is presented to show crosstalk influence between two PCB traces.

**Keywords:** PCB traces, BLT equations, field decomposition, crosstalk, equivalent multi-conductor transmission line model.

## 1 Introduction

With the development of electronic technology towards high-speed, wideband, high-sensitivity and miniaturization, traces on PCBs become more and more dense and the frequency of clock signal becomes higher. Therefore, the phenomenon of crosstalk among PCB traces becomes more and more serious. PCB traces work under surroundings with much electromagnetic interference, such as the crosstalk from the natural coupling within PCB traces with one of them excited by an external electromagnetic field. The crosstalk from the coupling within PCB traces is undesirable and sometimes very harmful. It even can cause penetration of a signal excited in one trace into another trace. Therefore, PCBs design engineers have to deal with crosstalk problems in order that there are relatively pure signals flowing through the traces.

Although the method of predicting crosstalk under the excitation of the lumped sources had been discussed widely in the previous literature and papers [1-2], how to predict the crosstalk among multiple PCB traces with one of them or some of them excited by the distributed source was few investigated. We notice that the BLT equations can be used to calculate the terminal responses of a multi-conductor transmission line illuminated by an external field [3]. Then, the BLT equations for PCB traces are established and then used to analyze the crosstalk problems of PCB traces under the distributed source.

## 2 Crosstalk response formulations of PCB traces with one of them illuminated by an external field

### 2.1 The Equivalent Multi-conductor Transmission Line Model of PCB Traces

Consider the PCB traces structure with microstrip cross section depicted in Fig. 1, where the  $n$ th trace of  $N$  traces is illuminated by a time-harmonic uniform plane wave  $E^{inc}, H^{inc}$ .

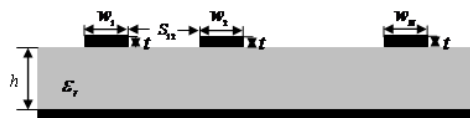


Fig. 1. Cross section of the PCB

Assume that the incident field only excites the quasi-TEM dominant mode in PCB trace. PCB traces support quasi-TEM wave within an approximate frequency limit [4], which is

given by  $f_{c,max} = \frac{21.3}{(w[mm] + 2h[mm])\sqrt{\epsilon_r + 1}}$  [GHz], with strip

width  $w$ , substrate height  $h$ , and relative permittivity  $\epsilon_r$ . For typical cross-sectional dimensions, this frequency limit lies in the range of 1-10GHz [5]. The crosstalk of PCB traces can therefore be treated by using transmission line theory, based on equivalent multi-conductor transmission line model. Within this range, wave propagation along the trace  $n$ th can be described equivalently by the characteristic impedance  $Z_{c,n}$  and the transmission line phase constant  $\beta_n = \omega\sqrt{\mu_0\epsilon_0\epsilon_{r,eff,n}}$  with angular frequency  $\omega$ , vacuum permeability  $\mu_0$ , permittivity  $\epsilon_0$ , and effective relative permittivity  $\epsilon_{r,eff,n}$ . These quantities are given by [6]. Because the propagation characteristic of lossless TEM transmission lines is completely determined by the propagation phase matrix  $\beta$  and the characteristic impedance matrix  $Z_c$ , the equivalent multi-conductor transmission line model as shown

in Fig. 2 is obtained by matching these quantities with respect to the microstrip lines. In the equivalent multi-conductor transmission line model all wires reside in the same effective medium, hence a mean-value effective dielectric constant

$$\varepsilon_{r,eff,mean} = \left( \frac{1}{N} \sum_{n=1}^N \sqrt{\varepsilon_{r,eff,n}} \right)^2$$

is applied to the present case. The

$$\text{equivalent radius } r_{eq,n} = 2h \exp \left( -\frac{Z_{c,n} \sqrt{\varepsilon_{r,eff,mean}}}{60} \right)$$

describes the

equivalent radius of the traces. The characteristic impedance

$$\text{matrix of the equivalent wires is given as } \mathbf{Z}_{c,wires} = \sqrt{\frac{\mu}{\varepsilon \varepsilon_{r,eff,mean}}} \frac{1}{2\pi} \mathbf{F}.$$

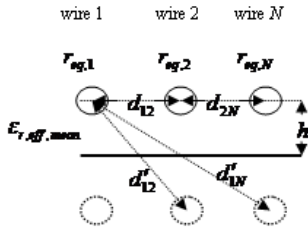


**Fig. 2. The equivalent multi-conductor transmission line model of PCB traces**

## 2.2 Decomposition of the Excitation Field

Suppose that an incident field  $\mathbf{E}^{inc}, \mathbf{H}^{inc}$  is a uniform plane in which the incident electric field is described by amplitude  $E_0$ , polarization angle  $\gamma$ , incidence angle  $\theta$  and azimuth  $\phi$ . The incident electric field can be decomposed into the horizontal component  $\mathbf{E}_h$  and vertical component  $\mathbf{E}_v$  according to the general theory of planar layered media[7]. Hence  $\mathbf{E}_h = E_x \hat{x} + E_y \hat{y}$  and  $\mathbf{E}_v = E_z \hat{z}$ , where

$$E_x(x, y, 0) = E_0 [(1 - R_{12}^{TM}) \cos \phi \cos \gamma \cos \theta + (1 + R_{12}^{TE}) \sin \phi \sin \gamma] e^{-jk_0 \sin \theta (x \cos \phi + y \sin \phi)}, \quad (1)$$

$$E_z(x, y, z) = E_0 \frac{\cos \gamma \sin \theta}{\varepsilon_r} \frac{1 + r_{12}^{TM}}{1 + r_{12}^{TM} e^{-j2k_z h}} [e^{jk_z z} + e^{-jk_z (2h+z)}] e^{-jk_0 \sin \theta (x \cos \phi + y \sin \phi)}, \quad (2)$$

with these quantities given by [5].

## 2.3 The BLT Equations for PCB Traces

By using transmission line concepts, Baum et al. [8] derive a complete solution of Maxwell's equations, known as the BLT equations. The BLT equations are matrix equations describing the behaviour of the voltage and current at all of the junctions of the conductors in the network [3]. These BLT equations become really useful when several transmission lines are connected together.

We consider  $N$  traces on PCB with one of trace illuminated by an external source. PCB traces are equivalent to the multi-conductor transmission line model, based on equivalent principle. Fig. 3 shows an electromagnetic topological network of the equivalent multi-conductor transmission lines for PCB traces that can be analyzed by the BLT equations. In this case, this network contains two junctions and one tube. This tube includes  $N$  transmission lines with the terminating impedances being generalized  $N$ -port loads.

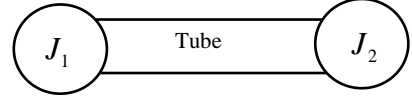


**Fig. 3. The electromagnetic topological network of PCB traces**

The BLT equations for PCB traces can be established in supermatrix form as follows:

$$\begin{bmatrix} \mathbf{V}(0) \\ \mathbf{V}(l) \end{bmatrix} = \begin{bmatrix} \mathbf{U}_N + \rho_1 & 0 \\ 0 & \mathbf{U}_N + \rho_2 \end{bmatrix} \begin{bmatrix} -\rho_1 & \mathbf{Q}^{-1} e^{A} \mathbf{Q} \\ \mathbf{Q}^{-1} e^{A} \mathbf{Q} & -\rho_2 \end{bmatrix} \begin{bmatrix} \mathbf{S}_1 \\ \mathbf{S}_2 \end{bmatrix}$$

$$\begin{bmatrix} \mathbf{I}(0) \\ \mathbf{I}(l) \end{bmatrix} = \mathbf{Z}_{c,wires}^{-1} \begin{bmatrix} \mathbf{U}_N - \rho_1 & 0 \\ 0 & \mathbf{U}_N - \rho_2 \end{bmatrix} \begin{bmatrix} -\rho_1 & \mathbf{Q}^{-1} e^{A} \mathbf{Q} \\ \mathbf{Q}^{-1} e^{A} \mathbf{Q} & -\rho_2 \end{bmatrix} \begin{bmatrix} \mathbf{S}_1 \\ \mathbf{S}_2 \end{bmatrix}$$

$\mathbf{V}(0), \mathbf{V}(l), \mathbf{I}(0), \mathbf{I}(l)$  are the terminal voltage and current response vectors at two terminal loads, respectively. Matrices  $\rho_i$  are the reflection coefficient matrices of equivalent transmission lines of PCB traces at the terminal load  $i$  defined as

$$\rho_i = (\mathbf{Z}_i - \mathbf{Z}_{c,wires}) (\mathbf{Z}_i + \mathbf{Z}_{c,wires})^{-1},$$

which  $\mathbf{Z}_i$  are the terminal load impedance matrices and  $\mathbf{Z}_{c,wires}$  is the characteristic impedance matrix of the equivalent transmission lines of PCB traces. The source supervector is described by

$$\begin{bmatrix} \mathbf{S}_1 \\ \mathbf{S}_2 \end{bmatrix} = \begin{bmatrix} \frac{1}{2} \int_0^l \mathbf{Q}^{-1} e^{A x} \mathbf{Q} \mathbf{V}_s(x_s) dx_s - \frac{\mathbf{V}_1}{2} + \mathbf{Q}^{-1} e^{A} \mathbf{Q} \frac{\mathbf{V}_2}{2} \\ -\frac{1}{2} \int_0^l \mathbf{Q}^{-1} e^{A(l-x_s)} \mathbf{Q} \mathbf{V}_s(x_s) dx_s + \mathbf{Q}^{-1} e^{A} \mathbf{Q} \frac{\mathbf{V}_1}{2} - \frac{\mathbf{V}_2}{2} \end{bmatrix}$$

which

$$\mathbf{V}_s(x) = [0 \quad \cdots \quad E_x(x, y_n, 0) - E_x(x, y_n, -h) \quad \cdots \quad 0]^T$$

with  $E_x(x, y_n, 0), E_x(x, y_n, -h)$  given by (1),

$$\mathbf{V}_1 = [0 \quad \cdots \quad \int_{-h}^0 E_z(0, y_n, z) dz \quad \cdots \quad 0]^T$$

and

$$\mathbf{V}_2 = [0 \quad \cdots \quad \int_{-h}^0 E_z(l, y_n, z) dz \quad \cdots \quad 0]^T$$

with  $E_z(0, y_n, z), E_z(l, y_n, z)$  given by (2).

### 3 Numerical computation

Consider two PCB traces with one of traces excited by a transient field. This incident transient plane wave field with  $\theta = 0, \phi = \pi/2, \gamma = \pi/2$  has a transient Gaussian time waveform. The two strips with the same thickness  $t = 0.5mm$  and the same width  $w = 2mm$  have length  $l = 40mm$  and are also placed on the substrate layer with  $\epsilon_r = 4.7$  and a height  $h = 2mm$ . Two PCB traces are terminated at both ends by two impedance matrixes  $\mathbf{Z}_1 = \mathbf{Z}_2 = \begin{pmatrix} 50 & 0 \\ 0 & 50 \end{pmatrix}$ .

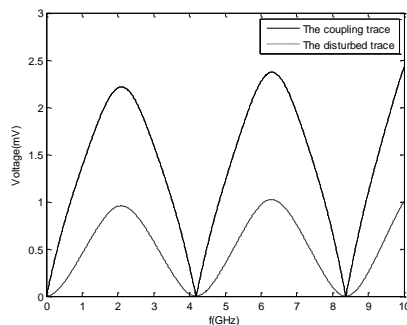


Fig. 4. Crosstalk voltage of two PCB traces for frequency domain

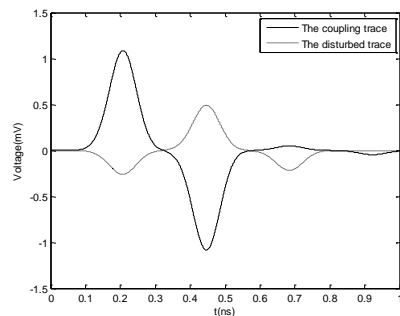


Fig. 5. Crosstalk voltage of two PCB trace for time domain

Fig. 4 and Fig. 5 depict the simulated results in the frequency and time domains for the two traces at junction  $J_2$  due to the Gauss pulse incidence, respectively. These curves show that coupling is always weak at 4.2GHz, 8.4GHz. We also observe that the peak crosstalk voltage of the disturbed trace is less than that of the coupling trace in Fig. 3. Crosstalk voltage time domain waveforms for two PCB traces at node  $J_2$  are reduced with time increasing. There are multiple reflections along the PCB traces with round-trip time intervals of  $T = 2L/c = 0.267ns$ . Time peak response at time 0.2ns and 0.46ns, this corresponds to one round-trip from the node  $J_2$ .

### 4 Conclusion

After the excitation field is decomposed and PCB traces are equivalent to the multi-conductor transmission line model, an analytic method has been presented by establishing the BLT equations for PCB traces that can be derived by solving the equivalent multi-conductor transmission line equation. The

simulated results of two PCB traces show that the crosstalk voltage of the coupling trace is stronger than that of the disturbed trace at the terminal loads.

### Acknowledgments

This work was supported by the National Natural Science Foundation of China (No.61171018 and No.11271370).

### References

- [1] W. T. Huang, C. H. Lu, and D. B. Lin. Suppression of crosstalk using serpentine guard trace vias. Progress in Electromagnetics Research, 109:37-61, (2010).
- [2] K. Lee, H. B. Lee, H. K. Jung, et al. A serpentine guard trace to reduce the far-end crosstalk voltage and the crosstalk induced timing jitter of parallel microstrip lines. IEEE Transactions on Advanced Packaging, 31(4): 809-817, (2008).
- [3] F. M. Tesche, M. V. Ianoz, T. Karlsson. EMC: Analysis methods and computational models. New York: John Wiley & Sons, (1997).
- [4] F. Gardiol. Microstrip circuits. New York: John Wiley & Sons, (1994).
- [5] M. Leone. Radiated susceptibility on the printed-circuit-board level: simulation and measurement. IEEE Transactions on Electromagnetic Compatibility, 47(3):471-478, (2005).
- [6] K. C. Gupta, R. Garg, and R. Chada. Computer-aided design of microwave circuits. Norwood, MA: ARtech House, (1981).
- [7] W. C. Chew. Waves and fields in inhomogeneous media. New York: Van Nostrand Reinhold, (1990).
- [8] C. E. Baum, T. K. Liu, and F. M. Tesche. On the analysis of general multiconductor transmission-line networks. Interaction Note 350:230-331. (1978).

# Electromagnetic topology analysis and Simulation of electromagnetic coupling of cable bundle of aircraft platform system

J S Luo\*, H Wang †

\* College of Science, National University of Defense Technology, Changsha, Hunan 410073, China . Email:jshluo@126.com

† School of Mathematics and Computing Science, Changsha University of Science and Technology, Changsha, Hunan 410114, China. Email:hncswhua@163.com

## Abstract

**This paper studied the electromagnetic coupling of cable bundle of plane platform system by using the method of electromagnetic topology. In this paper, we described the basic ideas and theory of electromagnetic topology and introduced the application of electromagnetic topology in the cable bundle of plane platform system. A simulation on the subsystem of a VHF radio has been completed, and the simulation shows the approving result at low frequency.**

**Keywords:** Electromagnetic topology, BLT equation, electromagnetic coupling

## 1 Introduction

The concept of electromagnetic topology was first proposed by F.M. Tesche [1] in 1978, initially as a method about analyzing the survival rate and vulnerability of electronic system in the internal electromagnetic pulse environment generated by nuclear. Since then, many scientists explored electromagnetic analysis, computational method, experiment and theoretical research based on topological theory, derived a lot response of electronic system in excitation electromagnetic environment [2]. But using the method of topological decomposition, the problem of how to calculate and evaluate cable bundle of electromagnetic coupling of the aircraft platform system is far from being solved.

In 1978, according to topology method, C.E.Baum proposed a network computing model about uniform multi-conductor transmission line interfered by electromagnetic field in complex system, and together with T.K.Liu and F.M.Tesche, derived[2-3] the famous BLT equation of electromagnetic topology theory. But in heterogeneous parallel multi-conductor transmission line network, BLT equation is not adapt. The transmission lines used in actual electronic systems are mostly not parallel, such as stranded cable. Therefore, C.E.Baum proposed how to find out a new computing theory, method and network research theory on uneven non parallel multi-conductor transmission line based on the topology method in [4].

From 1993 to 1996, J.P. Parmantier attended a test on electromagnetic coupling of plane in France, and took charge of developing a calculation software CRIPTE based on

electromagnetic topology. And the software is successfully applied to computing coupling effect of electromagnetic field generated by aircraft, missiles and other electronic system. Recently, he extended the concept of electromagnetic topology to high frequency [6]. In 2007 December, Parmantier made a summary report entitled "numerical coupling model and results of complex system" in the HPE2007International Workshop. In report, Parmantier pointed out the important status of electromagnetic coupling model at present, introduced the design thought and method of the system from a topological point of view, and pointed out that the electromagnetic topological method can provide guidance for analysis the electromagnetic coupling, and protecting electromagnetic in the very poor shield system.

## 2 Simulation model

The simulation model has 12M length, 2.5m maximum height, 1m body diameter, 9.5m span. Simulation of electromagnetic induction effect of cable in the complex electromagnetic environment the model is divided into two parts: First, simulation of electromagnetic induction effect of outside interference source to cables of some subsystem module of radio system in the model; Second, simulation of electromagnetic induction effect of outside interference source to all cables of radio system in the model.

The first part: we study the VHF radio subsystem module of the radio system, it is used for the simulation of device arranged in the equipment cabin and cockpit, mainly including the transmitter, receiver, control box, inverter and rectifier. a transmitter and a receiver are placed in equipment cabin, a control box is placed on the upper of the cockpit, and converter .and rectifier are placed on the lower. There are six cables in devices, each cable has two wires. Connection of VHF radio subsystem and cables are given, as shown in Figure 1.

The source of interference of external electromagnetic field environment is the maximum frequency of 500MHz y to the polarization Gauss pulse, from the model of normal incident.

The purpose of simulation in this part is to calculate the induced current at the port of each cable by using PAM-CEM and CRIPTE software to consider changes of electromagnetic field in aircraft and electromagnetic induction effect of cables

in internal system which influenced by external electromagnetic interference source.

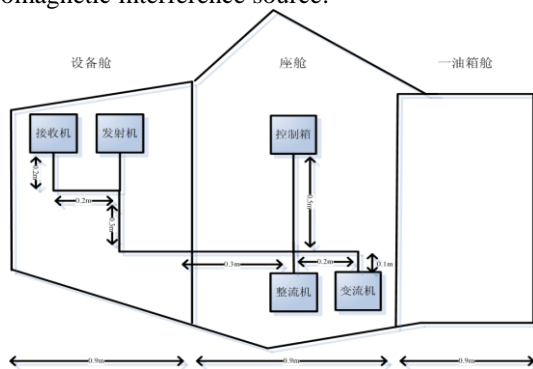


**Figure 1. Schematic diagram of connection on subsystem of VHF radio and cable**

In the second part, we research the electromagnetic induction effect of the entire radio system the model under the influence of outside interference source. And the 21 cables among the radio system equipment of the model were considered, each cable with two wires. Topology map about structure of its system and cable connection are given, as shown in Figure 2.

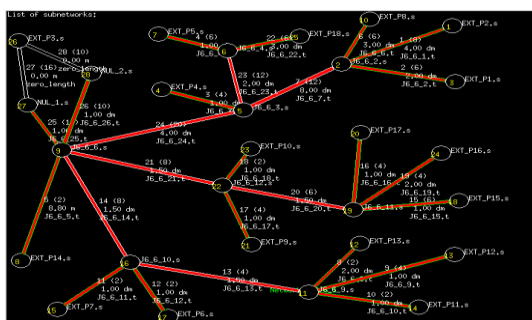


**Figure 2. The topological map of radio system and cable connection**

The source of interference of external electromagnetic field environment is the maximum frequency of 500MHz y to the polarization Gauss pulse, from the model of normal incident.

The purpose of simulation in this part is to calculate the induced current at the port of each cable by using PAM-CEM and CRIPTE software to consider changes of electromagnetic field in aircraft and electromagnetic induction effect of cables in internal system which influenced by external electromagnetic interference source. Compared with the first part of this section, the method used has the same principle, because the cable number increases, the computational complexity is greatly improved.

### 3 Numerical simulation

#### 3.1 Pipeline modelling

Methods for pipeline modelling include experimental and numerical method. The experimental method is that various

electrical parameters, such as, R, L, G, C and other parameters are obtained by the direct use of instrument measuring cable. While the advantages of numerical methods is that consumption is small, large number of the cable parameters can quickly and automatically be handled, but the difficulties are that the exact position of basic wire element of cable bundle is not informed and that section of cable bundle many core line is meshed. In order to avoid the above two disadvantages, ONERA has developed a numerical calculation software, called ALEATUB, which can generate arbitrary cross section of cable bundle. In a calculation, the same cable bundle can be generated several different structure and their R,L,C matrix can be automatically calculated. If the pipe model is used many times in one or several networks, ALEATUB program can generate some different data files of pipeline. As long as we have the following information, numerical method of pipeline modelling will be fast realized.

- (1) The radius of wire and the radius of dielectric insulator. In EMPTAC, the wire with 20AWG specification is most commonly used, but the ground wire with 22AWG specifications is usually used, in addition, for shielding twisted pair, another radius is formulated. The equivalent radius of three different wires are selected.
- (2) The essence of reference conductor (metal layer or shielding layer). If the reference conductor is specified as a shielding layer, the radius of the shielding layer will be automatically calculated to contain all internal conductors. If the reference conductor is specified as a metal plane (for non shield wire cable), the average height of the cable need to be given. The average height is equal to distance between the reference plane and the center of the cable bundle. If the distance is less than the equivalent radius of this bundle conductor, this bundle conductor will be arranged on the reference plane. In fact, this process is also used to describe the cable on the reference plane. For two reference conductors, static resistance is taken as 1.
- (3) The maximum distance between the lines (automatically generated). By the way, the lines are not in contact with each other.
- (4) there is a group of line contact with each other in the cable, inner conductor of each group is assigned a digital recognition.

#### 3.2 Numerical simulation

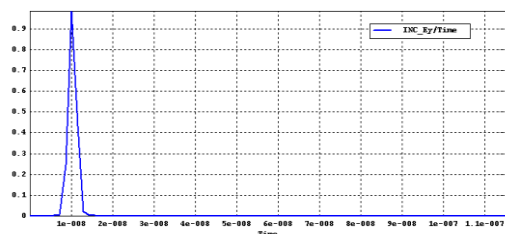


**Figure 3. Signal of Gauss excitation source, the change of Ey with time**

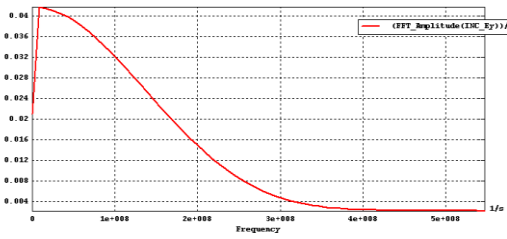


Figure 4. Gauss excitation source, changes of Ey with frequency

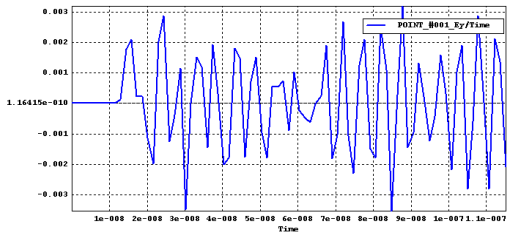


Figure 5 Variation of point 1 Ey with time of the electric field

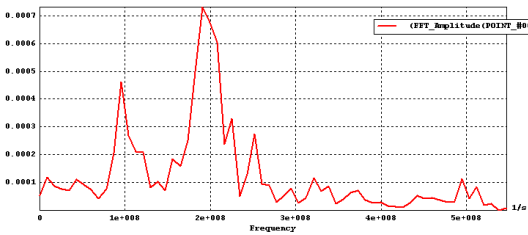


Figure 6 Variation of point 1 Ey with frequency of the electric field

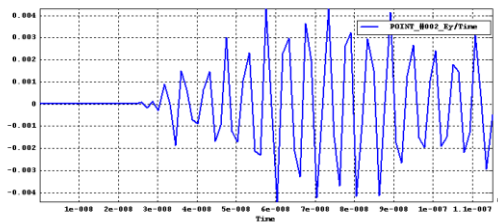


Figure 7 Variation of point 2 Ey with time of the electric field

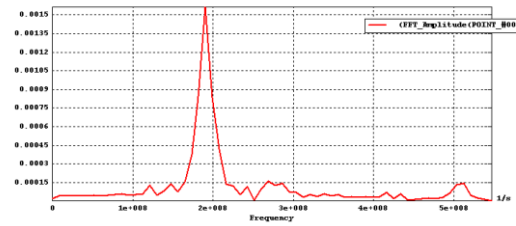


Figure 8 Variation of point 2 Ey with the frequency of the electric field

## 4 Conclusion

Using numerical calculation method, we find out that it is possible to put the method into a large network, and the topology decomposition of network can effectively reduce the computing time and memory space.

The simulation results confirm that the CRIPTE code can give good results at low frequency. But we must remember the fact that all parameters used by codes are selected for a model. While the network meshes are considered, but some errors cannot be excluded from model, hence the simulation must be systematically confirmed through the connection of network model.

## Acknowledgements

This work was supported by the National Natural Science Foundation of China (No. 11271370).

## References

- [1] A. B. Author, C. D. Author. "Title of the article", *The Journal*, **volume**, pp. 110-120, (2000).
- [2] F. M. Tesche. "Topological concepts for internal EMP interaction", *IEEE Trans. Electromagnetic Compatibility*, **volume** 20, pp. 60-64, (1978).
- [3] C. E. Baum, T. K. Liu, and F. M. Tesche. "On the analysis of general multiconductor transmission-line networks". *Interaction Notes* 350, (1978).
- [4] C. E. Baum. "Electromagnetic topology: a formal approach to the analysis and design of complex electronic systems". *Interaction Notes* 400, 1980.
- [5] C. E. Baum. "Application of concepts of advanced mathematics and physics to the Maxwell equations", *Physics Notes* 11, (1999).
- [6] J. P. Parmantier. "Approche Topologique pour l'etude des couplages electromagnetiques", *Ph.D. report*, Lille Flandres Artois University, (1991).

# Iterative QR Method for Multi-conductor Transmission Line Equation

H Wang \*, J S Luo †

\* School of Mathematics and Computing Science, Changsha University of Science and Technology, Changsha, Hunan 410114, China. Email:hncswhua@163.com

† College of Science, National University of Defense Technology, Changsha, Hunan 410073, China. Email:jshluo@126.com

## Abstract

The multi-conductor transmission line equation is obtained based on the development of telegraph equation. While the number and complexity of the wire increase, the characteristic impedance matrix, admittance matrix and the distribution of the source with the external excitation vector dimension become large, which costs the expensive computation and memory when solving the multi-conductor cable transmission line equation. For the general case of lossy conductor and lossy dielectric, an iterative QR method is proposed for solution of eigenvalues and eigenvectors problems of the product of the characteristic impedance and admittance matrices. It can reduce the cost of computation and memory significantly when solving the multi-conductor transmission line equation by comparing with the Gaussian elimination method commonly used. Numerical examples are given to validate the proposed method.

**Keywords:** Multi-conductor transmission line, iterative QR method, numerically stable diagonalization.

## 1 Introduction

The N-line multi-conductor transmission line composed of a parallel with the N conductor and a reference conductor parallel is one of the basic circuit units of complex electronic systems. Many scholars have studied solutions of this multi-conductor transmission line voltage wave and current. Baum, Liu and Tesche [1] gave a solution based on positive real matrix expansion method for lossy conductors and lossy dielectric solution in a general case, but did not give a method to calculate the eigenvalues and eigenvectors. Paul [2] discussed the case without external excitation source for multi-conductor transmission line voltage and current propagation equation in the lossless and lossy conductor, lossless and lossy dielectric, but for a general case of lossy conductors and lossy dielectric, only a special case of symmetric conductor loop is discussed in detail. Tesche, Ianoz and Karlsson [3] introduced a solution for multi-conductor transmission line voltage and current propagation equation in the case of lossless dielectric.

Double line telegraph equation is developed based on multi-conductor transmission line control voltage and current

spread. But there are two differences between the multi-conductor transmission line and two-conductor transmission line: 1. to eliminate the terminal reflection of two-conductor transmission line, only the terminal load impedance equal to the characteristic impedance of the conductor is required. However, in multi-conductor transmission line problem, the characteristic impedance matrix has to be considered, which is general non-diagonal matrix. 2. The capacitance and conductance between the N conductor and reference conductor also form a matrix, so for lossy conductor and lossy dielectric, the admittance matrix is non-diagonal matrix. With the increase in the number of conductors, the characteristic impedance matrix and admittance matrix dimension in multi-conductor transmission line equation becomes large. To solve the multi-conductor transmission line equation, eigenvalues and eigenvectors of the admittance matrix and the characteristic impedance matrix need to be calculated. For production matrix of high-dimensional admittance matrix and impedance matrices, especially for lossy conductors and lossy dielectric, both matrices are complex, and are dependent to the frequency. Therefore, the computational time and memory expense to calculate the eigenvalues and eigenvectors are considerable large, which enlarge the computational time and memory expense to solve voltage wave and current on the cable composed of the multi-conductor transmission line. For the general case of lossy conductor and lossy dielectric, an iterative QR method is proposed for solution of eigenvalues and eigenvectors problems of the product of the characteristic impedance and admittance matrices. It can reduce the cost of computation and memory significantly when solving the multi-conductor transmission line equation by comparing with the Gaussian elimination method commonly used. Numerical examples are given to validate the proposed method.

## 2 Derivation of N line of multi-conductor transmission line equation

For  $N$  – line multi-conductor composed of  $N$  uniform fine conductor and a parallel reference conductor, suppose the conductor is lossy and the dielectric is lossy. Suppose the conductor is parallel to the  $z$ -axis, assume that the plus excitation voltage source of the  $n$  th conductor is  $v_n^{(s)}(z, \omega)$ , the excitation current source is  $i_n^{(s)}(z, s)$ , then, the voltage

and current propagation equations controlled by the  $N$  – line multi-conductor transmission line are

$$\frac{d}{dz} i_n(z, \omega) + \sum_{m=1}^N y'_{nm}(\omega) v_m(z, \omega) = I_n^{(s)'}(z, \omega), n = 1, 2, \dots, N \quad (1)$$

$$\frac{d}{dz} v_n(z, \omega) + \sum_{m=1}^N z'_{nm}(\omega) i_m(z, \omega) = v_n^{(s)'}(z, \omega), n = 1, 2, 3, \dots, N \quad (2)$$

Where,  $y'_{nm}(\omega)$  is the unit length admittance of the  $m$ th

uniform conductor corresponding to the  $n$ th uniform conductor with frequency  $\omega$ , which is independent to  $z$ .

$z'_{nm}(\omega)$  is the corresponding eigen -impedance.

By use of matrix form, the  $N$  – line multi-conductor transmission line equations (1), (2) can be expressed as:

$$\frac{d}{dz} \vec{I}(z, \omega) + Y'(\omega) \vec{V}(z, \omega) = I^{(s)'}(z, \omega) \quad (3)$$

$$\frac{d}{dz} \vec{V}(z, \omega) + Z'(\omega) \vec{I}(z, \omega) = V^{(s)'}(z, \omega) \quad (4)$$

Equations (3), (4) are the general form of  $N$  – line multi-conductor transmission line equations with excitation source, where the excitation source can be divided into the antenna mode and transmission line mode. Due to the antenna mode in the transmission terminal is zero, only the terminal response of transmission line is considered, and the antenna mode is often ignored. Here, sinusoidal excitation source is considered.

To solve equations (3), (4), the coupling between  $I'(z, \omega)$  and  $V'(z, \omega)$  is supposed to be removed. Therefore, equation (3) is left multiplied by non-singular matrix  $T(\omega) = (t_{nm}(\omega))_{N \times N}$  on both sides, and is added by equation (4) on both sides, so

$$\frac{d}{dz} \vec{V}_{T,q}(z, \omega) = -B_q(\omega) \vec{V}_{T,q}(z, \omega) + \vec{V}_{T,q}^{(s)'}(z, \omega) \quad (5)$$

Where,  $q = +1$  corresponds to the wave along a positive direction of the  $z$  axis,  $q = -1$  corresponds to the wave along a negative direction of the  $z$  axis.  $\vec{V}_{T,q}(z, \omega)$ ,  $q = \pm 1$  is called the combination voltage wave. From equation system (5),  $\vec{V}_{T,q}(z, \omega)$ ,  $q = \pm 1$  can be solved, then, from the following equation,  $\vec{I}_q(z, \omega)$  and  $\vec{V}_q(z, \omega)$  can be solved.

$$\vec{I}_q(z, \omega) = T_q^{-1}(\omega) (\vec{V}_{T,q}(z, \omega) - \vec{V}_q(z, \omega)) \quad (6)$$

$$\vec{V}_q(z, \omega) = Z_q(\omega) \vec{I}_q(z, \omega) \quad (7)$$

where

$$Z_q(\omega) = B_q^{-1}(\omega) Z'(\omega) \quad (8)$$

[1] used eigenvector expansion of positive real matrix to discuss the diagonalization problem and the solution of

equation system (5), but did not give method to calculate the eigenvalue and eigenvector of  $Z'(\omega)Y'(\omega)$ . And for lossless dielectric and lossless conductor, and lossy conductor and lossless dielectric, the diagonalization transform matrix of  $Z'(\omega)Y'(\omega)$  is independent of the frequency  $\omega$ , so using eigenvector expansion method increase the computational cost and memory expense.

To reduce the computational and memory expense, we will discuss two cases, lossy conductor and lossless dielectric case, and lossy conductor and lossy dielectric case, to solve the diagonalization of  $Z'(\omega)Y'(\omega)$  and equation system (5) using iterative QR method.

### 3 Iterative QR algorithm for matrix

Denote  $A(\omega) = Z'(\omega)Y'(\omega)$  of degree  $N$ , by Alston

Householder theorem [5], there exist an unitary matrix  $Q(\omega)$  of degree  $N$  and an upper triangular matrices  $R(\omega)$  such that

$$A(\omega) = Q(\omega)R(\omega) \quad (9)$$

Householder transform algorithm is as follows: denote  $A_1$  to be the first column of  $A$

$$\begin{cases} \beta \leftarrow (a_{11}/|a_{11}|) \|A_1\|_2 \\ y \leftarrow A_1 - \beta e^{(1)} \\ \alpha \leftarrow \sqrt{2} / \|y\|_2 \\ v \leftarrow \alpha y \\ Q_1 \leftarrow I_N - vv^* \end{cases}$$

where  $\|A_1\|_2 = \left( \sum_{i=1}^N a_{i1}^2 \right)^{1/2}$ , and so forth, we have

$Q_1, Q_2, \dots, Q_{N-1}$ , denote  $Q = Q_1 \cdots Q_{N-1}$ , then

$$Q^*(\omega)A(\omega) = R(\omega) \quad (10)$$

$R(\omega)$  is an upper triangular matrix. However, the diagonal elements of  $R(\omega)$  are not necessarily the eigenvalues of  $A(\omega)$ .

Francis proposed an iteration algorithm to solve the eigenvalues of  $A(\omega)$  using QR decomposition of  $A(\omega)$  [5]. Without loss of generality, suppose  $R(\omega)$  has non-negative diagonal elements. The algorithm to calculate the eigenvalues of  $A(\omega)$  is as follows:

$$A(w) \leftarrow A(w)$$

For  $k = 1$  to  $M$  do

$$A_k(\omega) = Q_k(\omega)R_k(\omega), Q_k(\omega) \text{ is U matrix, } R_k(\omega)$$

is upper triangular matrix with nonnegative diagonal elements.

$A_{k+1}(\omega) \leftarrow R_k(\omega)Q_k(\omega)$   
end do

To reduce computational time and speed up the convergence rate, Shifted QR algorithm [5] can be employed to calculate the eigenvalues of  $A(\omega)$ .

(1) Use Alston Householder transform  $Q_1, Q_2, \dots, Q_{N-1}$  to get Hessenberg matrix  $H(\omega) = (h_{ij}(\omega))_{N \times N}$ , where  $h_{ij}(\omega) = 0, i > j + 1$ . Let  $A_1(\omega) = H(\omega)$ .

(2) Take the diagonal elements on lower right of  $A_1(\omega)$  as  $z_k$ , and perform QR decomposition on  $A_k(\omega) - z_k I_N$ , we have

$$A_k(\omega) - z_k I_N = Q_k(\omega) R_k(\omega)$$

Denote the last row of  $R_k(\omega)$  to be  $Y_N = (0, 0, \dots, 0, \alpha)^T$ , then  $\alpha$  is an eigenvalue of  $A(\omega)$ .

(3) Assign  $Q_k(\omega)R_k(\omega) + z_k I_N$  to  $A_{k+1}(\omega)$ . The computational procedure is as follows:

$$A_1(\omega) \leftarrow H(\omega)$$

For  $k = 1$  to M do

For  $A_k(\omega)$ , diagonal element of lower right of  $A_k(\omega)$

is chosen as  $z_k$

$$A_k(\omega) - z_k I_N = Q_k(\omega) R_k(\omega)$$

$$A_{k+1}(\omega) \leftarrow Q_k(\omega) R_k(\omega) + z_k I_N$$

end do

## 4 Examples and analysis

Model I: The cables are composed by nine parallel conductors. The center conductor is the reference conductor, and the conductor radius is 0.3cm. The distance between the conductor and the reference conductor is 1cm. The conductors are filled with dielectric material. The lossy conductor and lossy medium are selected, as shown in Fig. 2.

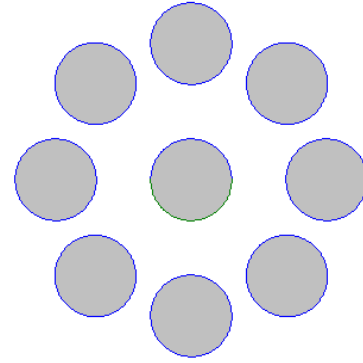


Figure 3 cables composed by nine parallel conductors

The selected parameters:  
 $r = 1$ ; % the distance from the wire to the reference conductor  
 $a = \pi / 4$ ; % the conductor angle difference  
 $d = 0.3$ ; % the conductor radius  
 $l = 10$ ; % the wire length  
 $a1 = 1.5e7$ ; % the conductor conductivity (where the selected conductor material is copper)  
 $a2 = 1$ ; % the conductivity of dielectric materials  
 $b1 = 4 * \pi * 1e-7$ ; % the conductor permeability  
 $c0 = 8.85 * 1e-12$ ; % the vacuum dielectric constant  
 $c1 = 2.3 * c0$ ; % the dielectric permittivity (PE)  
 $w = 1e8$ ; % the frequency

A diagonal matrix is obtained as follows:

$$10^{13} \times \text{diag}\{-0.0128 + 6.3107i, -0.0004 + 0.2165i, -0.0004 + 0.2165i, 0.0002 - 0.0895i, 0.0001 - 0.0693i, 0.0001 - 0.0693i, 0.003i, 0.003i\}$$

## Acknowledgements

This work was supported by the National Natural Science Foundation of China (no. 11271370)

## References

- [1] C. E. Baum, T. K. Liu, F. M. Tesche. "On the Analysis of General Multiconductor Transmission Line Networks", Kirtland AFB, Albuquerque, NM, Interaction Note 350, (1978).
- [2] D. R. Paul. "Analysis of Multicomductor Transmission Lines", New York: Wiley, (1994).
- [3] F. M. Tesche, M. V. Ianoz, T. Karlsson. "EMC Analysis Methods and Computational Models", New York: Wiley, (1997).
- [4] D. R. Kincaid, E. W. Cheney. "Numerical Analysis: Mathematics of Scientific Computing", American Mathematical Society, (2001).
- [5] F. M. Tesche, J. Keen, C. M. Butler. "Example of the Use of the BLT Equation for EM Field Propagation and Coupling Calculations", Kirtland AFB. Albuquerque, NM, Interaction Note 591, (2004).

# Experimental Research on Rod-shaped Triggered Gas Switch

Chen Jingliang, Lei Wanglong, Yao Xueling<sup>†</sup>

State Key Laboratory of Electrical Insulation and Power Equipment, Xi'an Jiaotong University, Xi'an 710049, China  
<sup>†</sup>xlyao@mail.xjtu.edu.cn

## Abstract

The rod-shaped triggered gas switch was designed in the paper, with the two main electrodes are placed in parallel and the trigger electrode is located in the orthogonal plane to the main electrodes and mounted between two main electrodes. The experimental circuit is setup and the trigger characteristics are researched. The experimental results show that when the gap distance is 6.65 mm, the self-breakdown voltage is 14.6 kV, the operating voltage scope of the switch is from 48.0% to 85.7%, and the discharging delay time  $\tau_a$  changes from 21.6  $\mu$ s to 2.66  $\mu$ s and the delay jitter  $\tau_j$  changes from 4.25  $\mu$ s to 0.49  $\mu$ s accordingly. At the same time, the pulse arc running and electrode erosion are also observed. It is found that the electrode erosion tracking is mainly decided by the amplitude of the pulse current, and with the increase of the pulse current, the erosion spots change from round to ellipse and the erosion track gets longer along the inner electrode orientation, and the erosion spots cover the whole electrode surface.

**Keywords:** Rod-shaped gas switch, Self-breakdown voltage, Operating range, Arc running and arc erosion track

## 1 Introduction

Discharging switches were the most important components in pulsed power systems including plasma physics, controlled nuclear fusion, nuclear explosion, electromagnetic pulse, electromagnetic launch and beam of particles. The characteristics of the discharging switch had direct influence on the pulse current waveform. The common discharging switches included ignitron, gas switch, semiconductor switch and magnetic rotating arc switch<sup>[1-4]</sup>.

Triggered gas switches (TGS) were widely used in pulsed power system because of its simple structure and excellent characteristics such as high voltage and high current endurance. The triggering characteristics were the important parameters of the TGS. When the high current passed through, the TGS will cause electrode erosion<sup>[5, 6]</sup>. Electrode erosion was the important factor that impacts the static and dynamic characteristics, which changed the self-breakdown voltage, the jitter and the performance parameters by changing electric field strength near the etch pit<sup>[7-9]</sup>.

In this paper, the TGS with rod-shaped electrodes was designed and the experimental setups of the trigger device were introduced. The trigger characteristics were researched and the cathode erosion spots and anode erosion spots were

observed when the impulse current with different transfer charge passed through TGS.

## 2 The Structure and Experimental Circuit of TGS

### 2.1 The structure of TGS

The spatial layout of the TGS was shown in Fig.1.

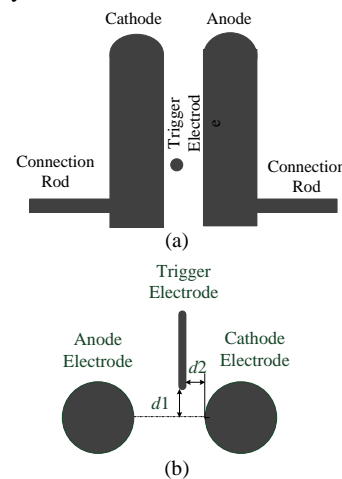


Fig.1 The structure of the triggered gas switch  
 (a) Electrode Front View/Top View, (b) Electrode Top View/Front View/

The TGS consisted of an anode, a cathode and a trigger electrode in the middle. Two main electrodes were all made from copper with a diameter of 40mm and placed in parallel. The trigger electrode, which was also made from copper, has a diameter of 10mm and is placed in the orthogonal plane to the plane of the two main electrodes. The distance between the end of the trigger electrode and the central line of the two main electrodes was  $d_1$ , and the closest distance between the trigger electrode and the cathode was  $d_2$ .

### 2.2 The experimental circuit of TGS

The experimental circuit of the TGS was showed in Fig.2.

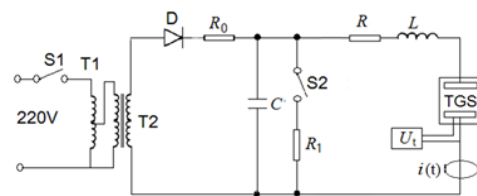


Fig.2 Experimental circuit

where S1 was the control switches, T1 was the voltage regulator, T2 was the transformer, D was rectification diode,  $R_0$  was charging resistance,  $C$  was storage capacitor, resistor

$R_1$  and switch  $S_2$  were grounding protecting circuit.  $S$  was the main switch.  $L$  and  $R$  were equivalent inductance and resistance, respectively. TGS was the tested sample. With  $U_t$  providing the high voltage triggering pulse connected between the trigger electrode and the cathode electrode. The impulse current  $i(t)$  was measured by a Rogowski coil.

$U_t$  was produced by the trigger circuit and the trigger pulse voltage was shown in Fig.3.

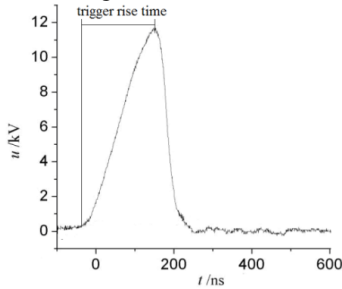


Fig.3 The triggering pulse waveform

For the trigger device to work reliably, the output trigger pulse voltage of the trigger pulse circuit was high enough, with the maximum pulse voltage in the range of 15-20kV.

### 3 Experimental Results and Analysis

#### 3.1 The trigger characteristics of TGS

##### (1) The self-breakdown characteristics

The self-breakdown voltage of TGS was influenced by the position of the trigger electrode, because the position could impacts the electric field distribution between two main electrodes. With  $d_1=1.2$  mm and  $d_2=1$  mm, the self-breakdown characteristics of TGS were shown in Fig.4.

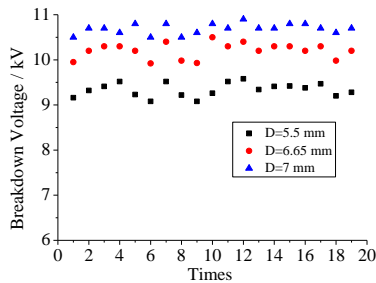


Fig.4 The self-breakdown characteristics

From Fig.4, it could be seen that when TGS operated in self-breakdown state, the breakdown electric field decreased with the increase of the gap distance because the trigger electrode could cause distortion for the electric field between the main electrodes.

##### (2) The trigger characteristics

When trigger pulse voltage was applied, the initial plasma was formed, TGS discharged and the discharging current began to rise. The discharging delay  $\tau_d$  was defined as the time between the point where the triggering pulse begun to drop and the point where discharging current began to rise.

The closing speed of TGS could be characterized by  $\tau_d$ , and the operating stability was characterized by the delay jitter  $\tau_j$ , which was the maximum dispersion of delay (the average of  $\tau_d$  of 20 discharging times). Fig.5 showed the trigger

characteristics as a function of applied voltage for the TGS with the trigger pulse voltage  $U_{tr}=14$  kV.

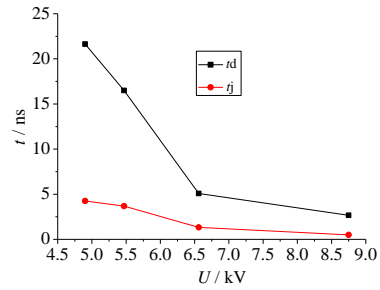


Fig.5 The discharging delay and jitter

Form Fig.5, it could be observed that when the applied voltage of TGS increased,  $\tau_d$  and  $\tau_j$  was shortened. When the applied voltage was 5.5 kV,  $\tau_d$  and  $\tau_j$  were 16.5  $\mu$ s and 3.7  $\mu$ s, respectively. When applied voltage increased to 8.5 kV,  $\tau_d$  and  $\tau_j$  were less than 2.5  $\mu$ s and 0.5  $\mu$ s, respectively. The reasons for these results were as following:

(1) When applied voltage increased, the transient electric field enhanced of TGS, the initial trigger plasma produced by trigger device could be accelerated higher speed.

(2) With the acceleration of the initial trigger plasma, more secondary collision happened, more secondary electrons could be produced and the velocity of electrons could be accelerated as well, such that the discharging delay  $\tau_d$  and  $\tau_j$  were shortened accordingly.

Fig.7 showed the trigger characteristics of TGS with different settings of trigger voltage.

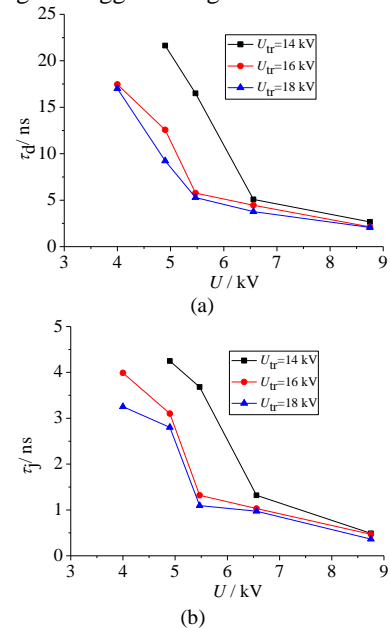


Fig.7 The influence of trigger voltage on discharging delay and jitter

(a) Relation between discharging delay and discharging voltage

(b) Relation between delay jitter and discharging voltage

#### 3.2 The discharging arc spots of TGS

##### (1) The electrode erosion trace

When the main electrodes of TGS were placed vertically and pulse current  $i$  was low, the transfer charge  $Q=\int idt$  was also low, and the electrode erosion trace was only a round

spot. With pulse current or transfer charge increased, the electrode erosion trace become longer, as shown in Fig.8.

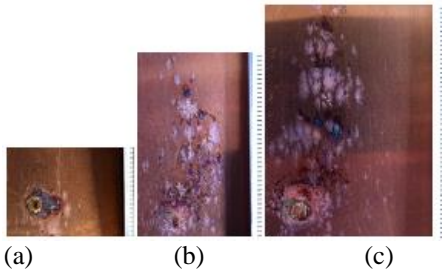


Fig.8 The electrode erosion trace  
(a)  $i=8$  kA,  $Q=1.06$ C (b)  $i=14$  kA,  $Q=1.84$ C, (c)  $i=22$  kA,  $Q=2.89$ C

When impulse current was 14kA and  $Q=1.84$ C, the electrode erosion trace length was 39 mm, but when current was 22kA and  $Q=2.89$ C, the electrode erosion trace length increased to 47 mm.

The electrodes erosion trace was different from that of main electrodes placed vertically, as shown in Fig.9.

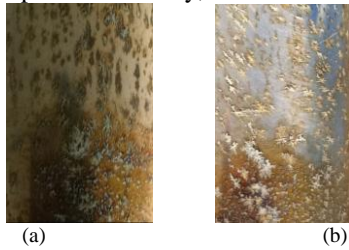


Fig.9 The electrode erosion trace with different place situation  
(a) Vertical placed, (b) horizontal placed

From Fig.9, we observed that when main electrodes were placed vertically, the erosion trace was general parallel, but when electrodes were placed horizontal, the erosion trace had an intersection angle. This was the corporative result of electromagnetic Lorentz force and impulse current arc heating force. They were all produced by impulse current itself. With the increase of current, erosion spots changed from round to ellipse and erosion track gets longer along the direction of the inner electrode.

The electrodes erosion traces overlap and scanning electron microscopy (SEM) images were shown in Fig.10.

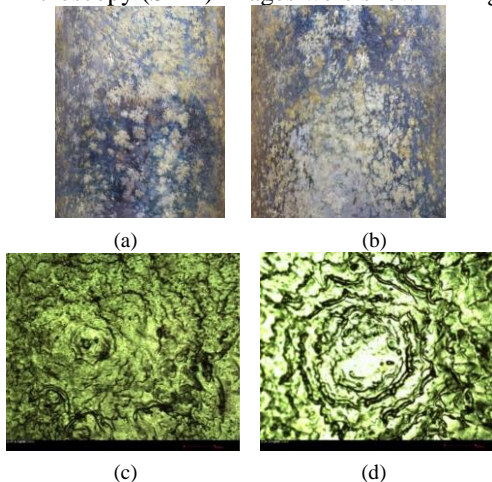


Fig.10 Electrode erosion trace after many times of impulse current applied  
(a) Erosion of cathode, (b) Erosion of anode, (c) SEM of discharging spot of cathode, (d) SEM of discharging spot of anode

## 4 Conclusions

The rod-shaped triggered gas switch was designed and the experimental circuit was set up. The experimental results showed that when gap distance was 6.65 mm, self-breakdown voltage was 10.2 kV. When trigger pulse voltage was 14.6 kV, the operating voltage of the rod-shaped gas switch was from 48.0% to 85.7%, and  $\tau_d$  changed from 21.6  $\mu$ s to 2.66  $\mu$ s and  $\tau_j$  changed from 4.25  $\mu$ s to 0.49  $\mu$ s accordingly. At the same time, it was also found that the electrode erosion trace was mainly decided by the amplitude of pulse current and the transfer charge. With the increase of impulse current, the erosion spots changed from round to ellipse and the erosion track get longer along the direction of the inner electrode. Because of the arc running on the surface of the electrodes, the life time of the designed rod-shaped gas switch can be prolonged significantly.

## Acknowledgements

The study was supported by the National Natural Science Foundation of China (No.51177131, No.51221005) and Technological Innovation Team of Shaanxi Province (No. 2012kct-07).

## References

- [1] Kihara R, Cummings D B. Commercial high current ignitron development[C], 7th International IEEE Pulsed Power conference. Monterey, USA: IEEE, 1989: 18-21
- [2] Bhasavanich D, Hitchcock S S, Creely P M, et al. Development of a compact, high-energy spark gap switch and trigger generator system[C], 8th International Pulsed Power Conference. San Diego, USA: IEEE, 1991:343-345
- [3] Li Huanyang, Yu Yuehui, Hu Qian, et al. Research of applying the switch RSD to pulsed power supply[J]. Proceedings of the CSEE, 2003, 23(11): 23-28(in Chinese)
- [4] Wang Qingling, Guo Liangfu, He Mengbing. et al. Development of rotary arc gap-switch in axial magnetic field[J]. Proceedings of the CSEE, 2006, 26(3): 101-105(in Chinese).
- [5] A. L. Donaldson, M. O. Hagler, M. Kristiansen, G. Jackson, and L. Hatfield, "Electrode erosion phenomena in a high-energy pulsed discharge," IEEE Trans. Plasma Sci., 1984, 12(1): 28-3.
- [6] A. Watson, A. L. Donaldson, K. Ikuta, and M. Kristiansen, "Mechanism of electrode surface damage and material removal in high-current discharges," IEEE Trans. Magn., 1986, 22(6):1799-1803.
- [7] S. J. MacGregor and F. A. Tuema, "Triggered gas switches," in Proc.Inst. Elect. Eng. Colloq. New Develop. Pulsed Power Technol., 1991, 1-4.
- [8] Lehr F M, Smith B D, Donaldson A L, et al. The influence of arc motion on electrode erosion in high current, high energy switches. Proceedings of 6th IEEE International Pulsed Power Conference, Virginia, USA, 1987, 529- 533
- [9] Lehr F M, Kristiansen M.. Electrode erosion from high current moving arcs[J]. IEEE Transactions on Plasma Science, 1989, 17 (5): 811- 817.

# An automatic fragmenting and triggering method for capacitive pulse forming units of the electromagnetic railgun

Xukun Liu, Xinjie Yu, Xiucheng Liu and ZANJI Wang\*

\* State Key Lab of Power System, Department of Electrical Engineering, Tsinghua University, Beijing 10084, China

## Abstract

This paper proposes an automatic fragmenting and triggering calculation method for capacitive pulse forming units (PFUs). As to each segment of PFUs, the triggering time is determined by the time that the rail current decreases to the minimum limit, the number of PFUs is then determined by the maximum possible values of the peak rail current after triggering this segment. Based on a representative example, the validity of this method is proven through comparisons with Simplorer® simulation software.

**Keywords:** automatic fragmenting and triggering, PFU.

## 1 Introduction

Electromagnetic launching technology has been the a research focus in the area of military equipment. With the advantages of low control difficulty and high reliability, capacitive pulsed-power supply (CPPS) has become the most prevailing form of energy storage in the electromagnetic railgun system. In actual railgun systems, however, the peak value of the rail current must be limited below the maximum allowable value in order to prevent the rail from ablation. The demand for higher armature velocity leads to the application of the multiple-triggered system. Previous studies are based mainly on experiments or simulations, both of which consume a large amount of time and effort. Calculation of the automatic fragmenting and triggering strategy is less involved and concerned.

However, this calculation is of great significance. On one hand, it could free us from unwieldy system simulation and inefficient parameter tuning. On the other hand, it could provide solutions to further studies on multiple-triggered systems, such as the optimization of system parameters. This paper fills the blank in the field of multiple-triggered system analysis, by proposing an automatic fragmenting and triggering method.

## 2 Model of the Electromagnetic Railgun System

The analytical model of CPPS-based electromagnetic railgun system is mainly composed of two primary parts, namely CPPS with initial energy storage and the railgun load [1]. The basic module of CPPS is the pulse forming unit (PFU). The topology of PFU is demonstrated in Fig 1.  $C$  is energy storage capacitor,  $L$  is pulse forming inductor,  $R$  is the sum of the inductor resistance and the lead resistance. A cluster of PFUs, which are in parallel and share the same triggering time, compose a segment. A cluster of segments, which are in parallel but hold different triggering time, compose a set of CPPS. The configuration of CPPS is demonstrated in Fig 2.

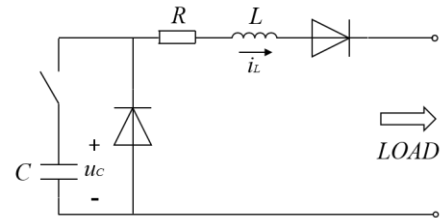


Figure 1. Topology of PFU.

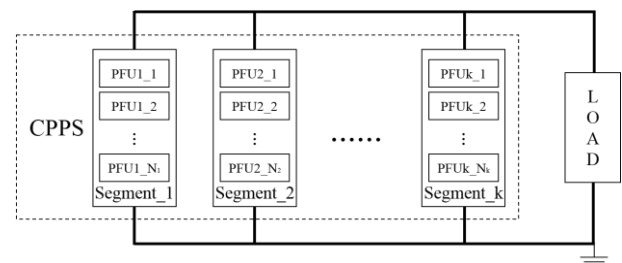


Figure 2. Configuration of CPPS.

Intensive Studies on the railgun model have been conducted [2]. However, in this analytical model, it is more appropriate to simplify the railgun load into a model of constant resistance. The aim of this simplification is to gain wider applicability with an acceptable tolerance of error.

## 3 Method of Automatic Fragmenting and Triggering

This method is a combination of theoretical analysis and numerical computation. Logically, it can be divided into three parts: calculation of PFU state, calculation of load waveforms and calculation of strategy. It is worth mentioning that these parts are closely intertwined and are a whole entity in essence.

### 3.1 Calculation of PFU State

To be convenient for description, PFU State is defined as a joint quantity of inductance current ( $i_L$ ) and capacitor voltage ( $u_C$ ). When the output of a PFU is connected to a constant voltage source, the circuit theoretical analysis is as follows.

- When  $i_L > 0$  and  $u_C > 0$ , the PFU works in the RLC state. The circuit topology is demonstrated in Fig 3. The expressions of  $u_C$  and  $i_L$  are Equation (1) and (2).

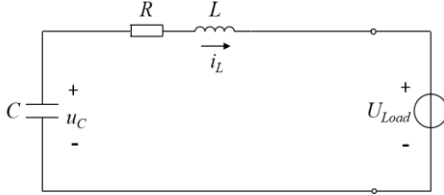


Figure 3. Topology of RLC State.

$$u_C(t) = U_{Load} + (u_C(0) - U_{Load})e^{-\alpha t} \cos \omega t + \frac{1}{\omega} (\alpha(u_C(0) - U_{Load}) - \frac{i_L(0)}{C})e^{-\alpha t} \sin \omega t \quad (1)$$

$$i_L(t) = i_L(0)e^{-\alpha t} \cos \omega t + \frac{1}{\omega} (\frac{u_C(0) - U_{Load}}{L} - \alpha i_L(0))e^{-\alpha t} \sin \omega t \quad (2)$$

where,

$$\alpha = \frac{R}{2L}, \quad (3)$$

$$\omega = \sqrt{\omega_0^2 - \alpha^2} = \sqrt{\frac{1}{LC} - (\frac{R}{2L})^2} \quad (4)$$

- When  $i_L > 0$  and  $u_C = 0$ , the PFU works in RL state. The circuit topology is demonstrated in Fig 4. The expressions of  $u_C$  and  $i_L$  are Equation (5) and (6).

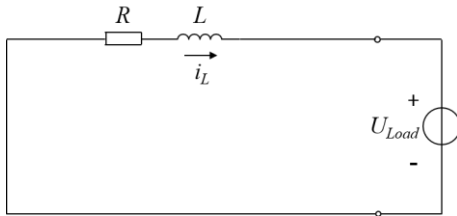


Figure 4. Topology of RL State.

$$u_C(t) = 0 \quad (5)$$

$$i_L(t) = (\frac{U_{Load}}{R} + i_L(0))e^{-\frac{t}{\tau}} - \frac{U_{Load}}{R} \quad (6)$$

where,

$$\tau = \frac{L}{R} \quad (7)$$

- When  $i_L = 0$  and  $u_C = 0$ , the PFU works in the stop state, which means this PFU has already finished the discharge process.

### 3.2 Calculation of Load Waveforms

To be convenient for description, load state is defined as a joint quantity of rail current ( $i_{Rail}$ ), load voltage ( $u_{Load}$ ), armature velocity ( $v_a$ ) and armature displacement ( $s_a$ ). And load waveforms refers to the waveforms of the load state.

Because of the parallel relation, the rail current is the summation of all PFUs' inductance current. However, the

triggering time varies from segment to segment. At one certain moment, PFUs in different segments are in different states, namely, different capacitor voltage and different inductance current. Therefore, it is too complex to derive and solve the full expressions of the rail current and the load voltage. Obviously, the numerical computation is more effective to the multiple-triggered problem. Given fragmenting and triggering strategy, calculation steps for load waveforms are as follows.

- (1) Discretize the time scale into a vast lot of discrete periods;
- (2) As to one specific period, calculate every PFU's inductance current at the end moment of the period; (In this calculation process, the PFU state is given or already calculated, the load voltage can be approximately taken as a constant, circuit principles have been discussed in Section 3.1.)

- (3) Summate all PFUs' inductance current and acquire the rail current;

- (4) Calculate the load voltage, according to the characteristics of the load;

- (5) Calculate the armature acceleration of the period, according to the electromechanical formula Equation (8);

$$F = \frac{1}{2} L' i_{Rail}^2 = m a_a \quad (8)$$

- (6) Calculate the armature velocity and displacement at the end moment of the period, according to the differential formula Equation (9) and Equation (10);

$$v_a(t) - v_a(0) = a_a \Delta t \quad (9)$$

$$s_a(t) - s_a(0) = v_a \Delta t \quad (10)$$

- (7) Repeat Step (2) to Step (6) until all discrete periods are calculated.

(The begin moment of the next period is the very end moment of the previous period.)

### 3.3 Calculation of Strategy

To be convenient for description, strategy is short for fragmenting and triggering strategy which is defined as a joint quantity of triggering time and the number of PFUs. Define  $n_k$  as the number of the PFUs of the Segment k. The calculation of strategy is the solving process of an optimization problem. The constraints are the maximum allowable rail current ( $i_{max}$ ), the preset minimum limit of rail current ( $i_{min}$ ) and the total number of PFUs ( $n_{total}$ ). The target is the maximization of the armature launch velocity. Rail length fixed, the increase of the rail current leads to the increase of the armature acceleration, and leads to the increase of the launch velocity. The optimal target in essence is the maximization of the average rail current. Calculation steps are as follows.

- (1) Find the optimal  $n_1$ .

(The specific meaning of "optimal" is that the peak value of the rail current reaches the maximum under the constraint of  $i_{max}$ . The specific method is traversing  $n$  from 1 to  $n_{total}$  until the optimal value is found.)

- (2) Calculate the load waveforms until the rail current decreases to  $i_{min}$  or the armature launches. Take the time of that moment as the triggering time of the next segment or the terminal of the calculation.

(The calculation method of the load waveforms has been discussed in Section 3.2.)

- (3) Find the optimal  $n$  of the next segment.
- (4) Repeat Step (2) and Step (3) until all PFUs are triggered.

#### 4 A Testing Example

A 3MJ multiple-triggered system is taken as the example to show the performance of this method. The settings of system parameters are shown in Table 1.

Table 1: System Parameters Settings

Parameters	Value
System Initial Energy Storage ( $E_0$ )	3 MJ
Total Number of PFUs ( $n_{total}$ )	30
PFU Capacitance ( $C$ )	2 mF
PFU Capacitor Pre-charged Voltage ( $u_C(0)$ )	10 kV
PFU Inductance ( $L$ )	50 $\mu$ H
PFU Resistance ( $R$ )	20 m $\Omega$
Load Equivalent Resistance ( $R_{Load}$ )	1 m $\Omega$
Armature Mass ( $m$ )	0.05 kg
Rail Length ( $s$ )	6 m
Maximum Limit of Rail Current ( $i_{max}$ )	800 kA
Preset Minimum Limit of Rail Current ( $i_{min}$ )	700 kA

Conduct numerical computation on the platform of MATLAB<sup>®</sup>R2014a, the optimal strategy is shown in Table 2.

Table 2: Optimal Strategy

$t$ (ms)	0	0.61253	1.19071	1.71005
$n$	14	5	5	6

The waveforms of the rail current and the armature velocity from the calculation on MATLAB<sup>®</sup>R2014a and the simulation on Simplorer<sup>®</sup>11 are shown in Fig 5 and Fig 6. To ensure the effectiveness of the comparison, the Simplorer<sup>®</sup> simulation shares the same system parameters and strategy with the MATLAB<sup>®</sup> calculation. Difference exists only in the load model. In Fig. 5 and Fig. 6, red curves are MATLAB<sup>®</sup> calculation results, which use a constant resistance as load; blue curves are Simplorer<sup>®</sup> simulation results, which use the same constant resistance as load; black curves are Simplorer<sup>®</sup> simulation results, which use an actual railgun model as load.

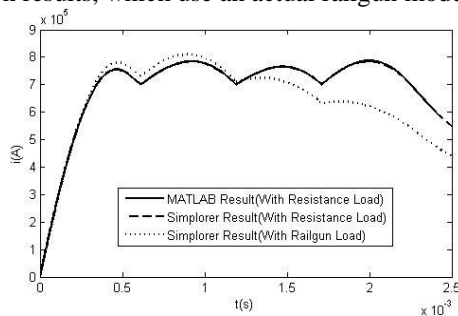


Figure 5. Rail Current Waveform.

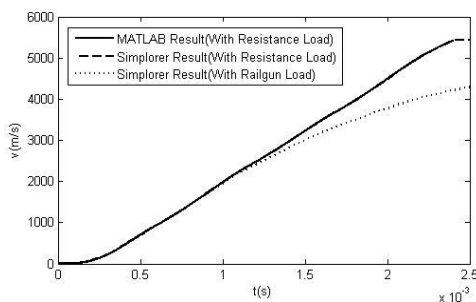


Figure 6. Armature Velocity Waveform.

Comparing red curves and blue curves, conclusions can be drawn that time discretization in the calculation process causes little error, in other words, this method possesses a high computational accuracy. Comparing red curves and black curves, facts have to be admitted that there exist differences between the MATLAB<sup>®</sup> calculation and the actual situation. The cause of the differences is the simplification of the load model. The topology of a relatively accurate railgun load is demonstrated in Fig 7 [2]. All of resistance and inductance are time-varying, which makes the whole system extremely complex to solve.  $L_{Rail}$  is in proportion to the armature displacement. The waveforms of the load resistance is shown in Fig 8.

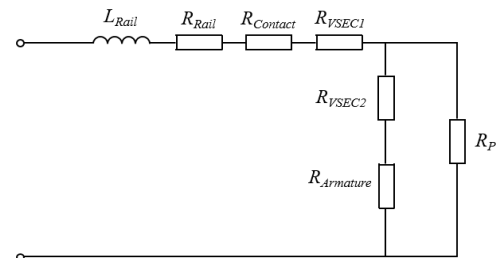


Figure 7. Topology of Relatively Accurate Railgun Load.

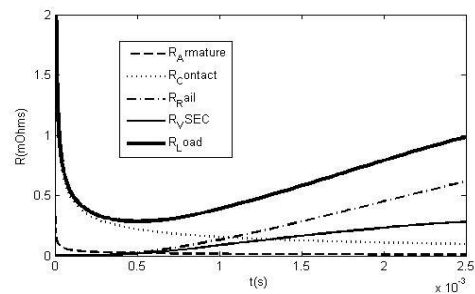


Figure 8. Load Resistance Waveforms.

It is worth stressing that the aim of this simplification is to help us get rid of manual simulation and tuning. At this point, within a rational range, the sacrifice of accuracy is worthy.

#### 5 Conclusion

This paper proposes an automatic fragmenting and triggering method for capacitive pulse forming units of the electromagnetic railgun. Meanwhile, based on a representative example, this paper provides contrastive analysis with Simplorer<sup>®</sup> simulation, to prove the validity of this method.

This paper opens a door to the further study on multiple-triggered systems, such as the optimization of system parameters and the strategy calculation based on fixed launch velocity. These are problems awaiting attentions.

#### References

- [1] Gong, C., Yu, X., & Liu, X. "Study on the system efficiency of the synchronously-triggered capacitive pulsed-power supply in the electromagnetic railgun

system”, *Electromagnetic Launch Technology (EML), 17th International Symposium*, pp. 1-6, (2014).

- [2] Yu X, Fan Z. “Simulation and two-objective optimization of the electromagnetic-railgun model considering VSEC resistance and contact resistance.” *Plasma Science, IEEE Transactions on*, 39(1),pp. 405-410, (2011).

# Transient Analysis Method of Pulsed Power Circuit

Seong-Ho Kim, Young-Hyun Lee, Byungha Lee, Jin Hyuk Chung, Sanghyuk An

Institute of Defense Advanced Technology Research, ADD, Daejeon 305-600, Korea

## Abstract

A method of a transient circuit analysis applicable in the pulsed power circuit containing massive inductors is described. The electromagnetic launcher system consisting of a pulsed power supply and a launcher has many massive inductors in the power supply and an inductive load of rails. Though the system can be analyzed well by using constant resistance  $R$  and inductance  $L$ , another correction method can be employed if the result using constant values is not satisfactory by the magnetic diffusion effect. The method is based on the correction of the voltages obtained from constant  $R$  and  $L$ . When a situation requiring the magnetic diffusion or the skin depth effect arises, this correction method will play a good role to reach the accurate solution.

**Keywords:** transient circuit analysis, skin effect, diffusion, electromagnetic launcher, railgun.

## 1 Introduction

Usually pulsed power supplies delivering a large current of several hundred or MA during a few ms are used for the study of electromagnetic acceleration of a metal armature. In the pulsed power circuit, an inductor is an important component to control the magnitude and shape of the current waveform. In the usual cases, constant resistance and inductance values are employed to describe the inductor. Since discharges of the pulsed power supply are done transiently and the inductors in the power supply or in the launcher are made of massive conductors, it is necessary to consider the diffusion of the electromagnetic fields in the analysis of the circuit.

In the study of electromagnetic launchers, the inductance values calculated by Kerrisk are usually used. [1] Since he calculated them in the condition of the high-frequency limit, the values are good for the inductance gradient values in the force equation of the armature where the skin depth is nearly zero because of the velocity skin effect. However, since the magnetic field and current density continuously diffuse inside the massive inductor, the inductance value derived from usual energy method shows an increasing tendency. [2]

Some authors say time-dependent inductance based on the definition of the inductance from energy or flux method. [2-3] Since the time-dependent values were derived from a particular current waveform, they are not free from the waveform used. The typical example of such application is the use of a resistance value derived from skin depth. [4] The

time-dependence of the resistance is related to a particular waveform derived, e.g. a step-function current waveform.

In this presentation, a method of a transient circuit analysis considering the diffusion effect is described. It can be applicable in the analysis of the pulsed power circuit and electromagnetic launcher.

## 2 Circuit Analysis by Voltage Correction

If an electrical component has well-defined terminals A and B, the difference of the electric scalar potential between point A and point B is obtained by integrating the electric field  $\vec{E}$  and the magnetic vector potential  $\vec{A}$  :

$$V_{AB} = \int_A^B \vec{E} \cdot d\vec{r} + \frac{d}{dt} \int_A^B \vec{A} \cdot d\vec{r} \quad (1)$$

where the first term is a resistive voltage drop  $V_R$ , and the second an inductive voltage drop  $V_L$  along the given path of the integration. An inductive component shows particular responses to a step-function current of 1A from its geometry and material property. The resistive voltage response  $V_{RS}$  and flux response  $\Phi_{LS}$  can be obtained numerically by solving Maxwell equations.

For the current waveform  $I$ ,  $V_R$  and  $V_L$  are obtained by Duhamel's integration  $V_{RS}$  and  $\Phi_{LS}$  :

$$V_R(t) = \int_0^t V_{RS}(\tau) \dot{I}(t-\tau) d\tau \quad (2)$$

$$V_L(t) = \frac{d}{dt} \left[ \int_0^t \Phi_{LS}(\tau) \dot{I}(t-\tau) d\tau \right]. \quad (3)$$

In the Kirchhoff's circuit equations, the voltage of the electrical component is expressed as

$$V = IR + \Delta V_R + L \frac{dI}{dt} + \Delta V_L. \quad (4)$$

where the correction voltages  $\Delta V_R$  and  $\Delta V_L$  are:

$$\Delta V_R = V_R - IR, \quad (5)$$

$$\Delta V_L = V_L - L \frac{dI}{dt}. \quad (6)$$

The circuit equations are solved first by constant  $R$  and  $L$  with zero values of  $\Delta V_R$  and  $\Delta V_L$ . Then, the subsequent calculations including the correction voltages will result more accurate solution close to the measured one.

## 3 Application to a Solenoid Inductor

A solenoid is a typical example of inductor made by winding coils on the tube of a cylindrical geometry. In the case using a filimentary coil, the inductance is well defined for all frequency regions. However, when the cross-sectional area of the coil is large for a low resistance, the inductance varies with the frequency. It is mainly due to the magnetic diffusion effect.

Fig. 1 shows the distribution of the current density of a solenoid coil used in a high current circuit. The width of the winding coil is 4 mm, and the height of the coil is 10 mm. The inner diameter of the solenoid is 80 mm. It consists of 2 layers of 8 turns. The gap between each ring is 1 mm. The current density distribution at 1 kHz is shown in Fig. 1.

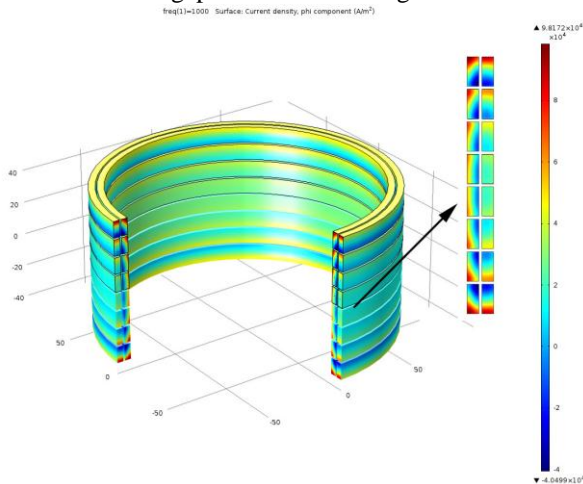


Fig. 1. Current density distribution of a solenoid at 1 kHz current waveform

The inductance of the solenoid at 1 kHz was calculated to be about 38.1  $\mu$ H with a resistance of 11.36 m $\Omega$ . Since the skin depth is 2.1 mm, the current distribution shown in Fig. 1 is not uniform. Those impedance values are also can be used to describe a circuit of transient current pulse of sub-millisecond duration.

To see the details, the current density distribution at 0.4 ms after a step-function current waveform was calculated, and shown in Fig. 2. The upper coils show very non-uniform current distributions.

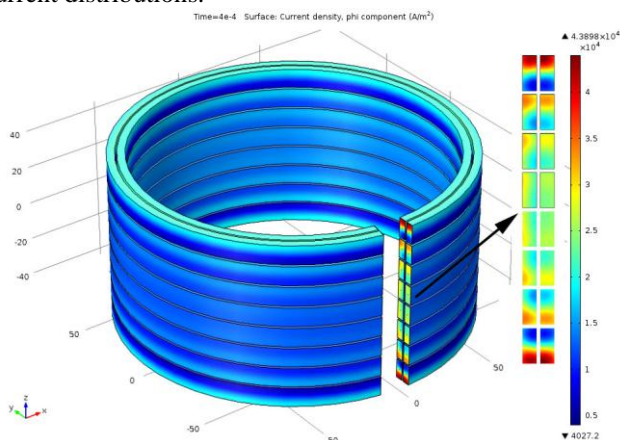


Fig. 2. Current density distribution of a solenoid at 0.4 ms after a step-function current waveform.

By using the finite element method the resistive voltage response  $V_{RS}$  and flux response  $\Phi_{LS}$  along the center line of each coil were calculated.

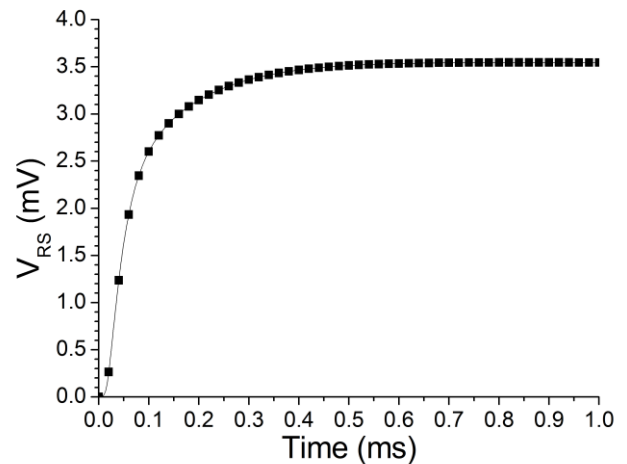


Fig. 3. Resistive voltage response  $V_{RS}$  for the step-function current of 1 A.

Fig. 3 shows the voltage response obtained by integrating the electric field along the center line of the coils. Since initially the electric field cannot penetrate inside the conductor, the voltage starts with a zero value. The later voltage response value 3.54 mV corresponds to the DC resistance value 3.54 m $\Omega$  of the solenoid.

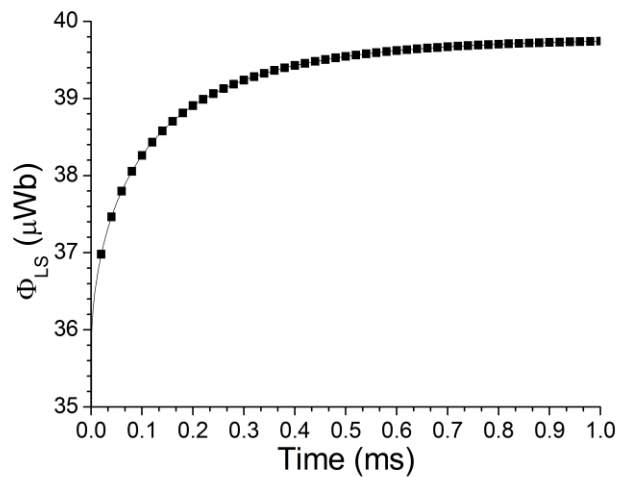


Fig. 4. Magnetic flux response  $\Phi_{LS}$  for the step-function current of 1 A.

Fig. 4. Shows increasing inductance with the magnetic diffusion. The initial flux response value 36  $\mu$ Wb corresponds to the inductance value at high frequency limit 36  $\mu$ H of the solenoid. It also shows a zero penetration depth of magnetic field at starting time. After about 1 ms, the solenoid shows DC behaviour. The inductance at DC reaches 39.7  $\mu$ H, which is 10 % larger than the initial value.

From the temporal behaviour of the response curves shown in Fig. 3 and Fig. 4, the solenoid circuit producing sub-millisecond pulse are more accurately described by the

voltage correction method introduced in Section 2. More detailed example of a calculation compared with the measurement is shown in [5]. The method of transient circuit analysis considering the magnetic diffusion effect was employed successfully in the analysis of the RLC circuit module containing a massive inductor [5], and the rail pair of an electromagnetic launcher system. [6]

## 4 Summary

To explain the voltage correction method, the calculation of the responses for the step-function current in a solenoid inductor was done as an example. In this paper, the increasing duration of the response curves is lower than 1 millisecond. However, if the geometry of the inductor becomes more massive, the temporal duration of the increasing response becomes longer, and may take several milliseconds. When the duration of the transient current is comparable to the increasing duration of the response curves, the voltage correction method describes the circuit behavior more accurately than the method using constant impedances.

## References

- [1] J. F. Kerrisk, "Current Distribution and Inductance Calculations for Rail-gun Conductors," LA-9092-MS, Technical Report, Los Alamos National Lab., NM, USA, (1981).
- [2] J. F. Kerrisk, "Current Diffusion in Rail-gun Conductors," LA-9401-MS, Technical Report, Los Alamos National Lab., NM, USA, (1982).
- [3] K. Moyama and H. Fukumoto, "Evaluation of Railgun Inductance by 2-D Transient FE Analysis," IEEE Trans. on Magn., 33(1), pp. 260 – 265, (1997).
- [4] A. N. Smith, R. L. Ellis, and J. S. Bernardes. "Thermal Management and Resistive Rail Heating of a Large-scale Naval Electromagnetic Launcher," IEEE Trans. on Magn., 41(1), pp. 235-240, (2005).
- [5] Seong-Ho Kim et al., "Transient Analysis of Circuit Containing Massive Conductors," IEEE Trans. on Plasma Sci., 42(3), pp. 853 – 858, (2014).
- [6] Seong-Ho Kim et al., "Modeling and Circuit Analysis of an Electromagnetic Launcher System for a Transient Current," IEEE Trans. on Plasma Sci., published online, (2015).

# Development of small electromagnetic railgun launch device for inductive pulsed power supply

Rui Ban, Xinjie Yu, Zhen Li and Zanji Wang\*

\* State Key Lab of Power System, Department of Electrical Engineering, Tsinghua University, Beijing 100084, China

## Abstract

Inductive electromagnetic railgun has been a hot topic in the field of electromagnetic launch. Recently most researchers focus on inductive pulsed power supply unit and replace railgun with a small L-R load in experiment for convenience. The replacement can simulate part of load features for the unit circuit but cannot be used in large capacity systems, especially when studying system efficiency. In order to promote applicable inductive pulsed power supply research, a small electromagnetic railgun launch device is designed and implemented. Experiment results demonstrate that the designing target has been reached.

**Keywords:** electromagnetic railgun, launch device, inductive pulsed power supply

## 1 Introduction

Compared to traditional gun, the electromagnetic railgun has drawn more attentions for precise control and high speed, which meets the needs for information battle. Researches on electromagnetic railgun have lasted for several decades, key technologies of which are pulsed power supply and launch device [1]. Studies on capacious pulsed power supply and related launch device are becoming mature. Inductive pulsed power supply has been a research hotspot for the energy density of it is much higher than capacious pulsed power supply, which contributes to device miniaturization.

The research on Inductive electromagnetic railgun focuses on inductive power supply. Most laboratories, except for large laboratories, such as IAT, replace railgun with a small L-R load in experiment, because the replacement has little effect on most parameters [2]. With the development of research, a small L-R load cannot meet the demand of research anymore. Real railgun load is essential for the study on some key parameters, such as system launch efficiency. In order to promote applicable inductive pulsed power supply research, we successfully developed a small electromagnetic railgun launch device for inductive pulsed power supply and proposed a regular method to the development.

## 2 Design

The design process contains 4 steps.

### 2.1 Determining demands by power supply

Launch device for laboratory must meet the demands of different power supplies and have the ability to speed up the armature to a significant speed. We proposed the following demands: total inductor of power supply is 2 mH, inductors ratio is 4:1, and the armature's initial speed is less than 100 m/s when the energy of power supply is 10 kJ [3,4].

Fig. 1 reveals the output current waveform of the power supply.

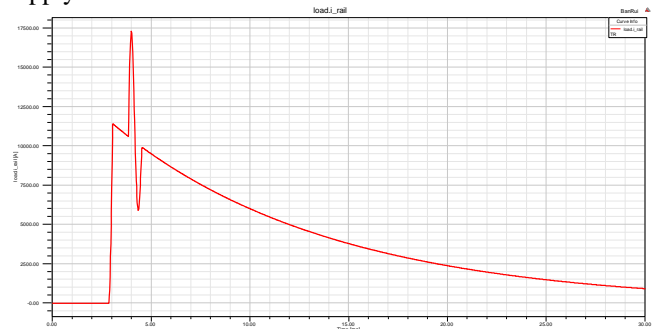


Figure 1. Output current waveform of the power supply

### 2.2 Determining parameters by demands

There are three main parameters to be determined: the length of rail, the distance between rails and the mass of armature. The distance between rails doesn't determine initial speed of armature directly but affects the size of armature. We set the distance between rails at 10 mm. Then we run a simulation in Simpler 11.0. According to the result of simulation showed in Fig. 2, the armature will obtain a speed of 46 m/s when the length of rail is 30 cm and the mass of armature is 3 g, in which condition our demands are satisfied.

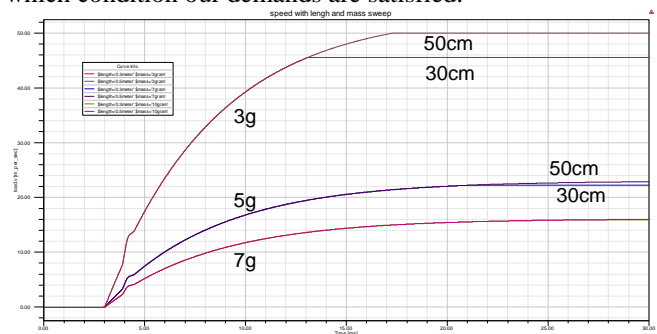


Figure 2. Simulation result

### 2.3 Designing model by parameters

There is no need to consider erosion and machining but the distance between rails must be exactly 10 cm and the whole device need firm fixation. As a result, we designed the model in Fig. 3.

Armature is the core of railgun launch device. The most common design is C-shaped armature, whose tail is slightly wider than the distance between rails [5]. The width should be properly designed to keep a balance between contact resistance and friction. We designed 4 kinds of armatures with different size and each made of pure aluminium and aluminium alloy.

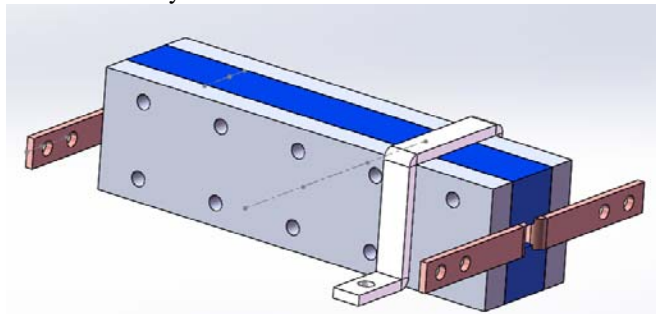


Figure 3. The design of railgun model

### 2.4 Designing speed measurement device

We use optical fiber sensors to measure initial velocity. The armature passes through two sensors successively. The sensor will form a pulse signal when covered. Armature speed can be calculated by measuring the time between two rising edge.

## 3 Implementation

By putting rails, armature, fixed gear and sensors together, a small electromagnetic railgun launch device for inductive pulsed power supply was assembled. Fig. 4 and Fig.5 show the real railgun device and different kinds of armatures.



Figure 4. 4 kinds of armatures



Figure 5. 4 kinds of armatures

## 4 Conclusion and Discussion

A small electromagnetic railgun was developed in order to meet the demands of inductive pulsed power supply. The distance between rails is 10 cm and the length of rail is 30 cm. The mass of armature is about 2.7 g and the expected speed is 46m/s. According to system test results, the designing targets have been reached.

Based on our existing design, more railguns with different length will be developed and experiments with armatures of different materials, sizes and shapes will be finished. Also, a more accurate method to measure speed should be studied as armature speed rising up.

## References

- [1] Fair, H.D., "Guest Editorial The Past, Present, and Future of Electromagnetic Launch Technology and the IEEE International EML Symposia", *IEEE Transactions on Plasma Science*, vol.41, no.5, pp.1024-1027, (2013)
- [2] J. D. Powell and K. A. Jamison, "Analysis of an inverse railgun power source," *IEEE Transactions on Magnetics*, vol. 22, no. 6, pp. 1669-1674, (1986).
- [3] A. Sitzman, D. Surls, and J. Mallick, "Design, Construction, and Testing of an Inductive Pulsed-Power Supply for a Small Railgun", *IEEE Transactions on Magnetics*, vol. 43, no. 1, pp. 270-274, (2007).
- [4] Z. Li, X. Yu, S. Ma, and Y. Sha, "Structural Parameter Optimization of Inductors Used in Inductive Pulse Power Supply," in *Proc.17th IEEE Int. Symp. Electromagnetic Launch (EML)*, San Diego, CA, Jul. 7-11, 2014.
- [5] L. Rip, S. Satapathy, and K.-T. Hsieh, "Effect of geometry change on the current density distribution in C-shaped armatures," *IEEE Transactions on Magnetics*, vol. 39, no. 1, pp. 72-75, (2003).

# Performance Evaluation of an Experimental Railgun

Young-Hyun Lee, Seong-Ho Kim, Byungha Lee, Jin Hyuk Chung, Sanghyuk An

Institute of Defense Advanced Technology Research, ADD, Daejeon 305-600, Korea

## Abstract

An experimental railgun was fabricated to study physical phenomena being developed when accelerating a solid armature by electromagnetic force. Main dimensions of the launcher and the pulse forming network were determined based on the mechanical and electrical analysis to achieve the required muzzle velocity. Experimental tests were carried out to evaluate the railgun performance. In this paper, dynamic characteristics of the railgun are described by comparing the results of analysis and measurements.

**Keywords:** railgun, circuit analysis, rail vibration.

## 1 Introduction

There might be some mechanical and electrical problems during launching an armature in a railgun. It is important to compare and analyse the measured signals and the analysis results to identify the causes of these problems. An experimental railgun was fabricated to study what technologies are required to accelerate an armature safely and what problems are produced. We measured current into the rails, voltage at the breech and muzzle, armature passing time through the specified positions and dynamic strains at the several locations along the rail. The measured current, breech voltage and armature passing time were utilized to evaluate the overall performance of the railgun and to correct the mathematical model developed to predict the launch performance. The muzzle voltage signal was used to investigate contact conditions between the armature and the rails. We could explain the high frequency of rail vibration depending on the armature velocity by comparing the analysis results with the strain signals.

## 2 Modelling for analysis

The capacitor based PFN is connected to the railgun with power cables. An Electrical circuit diagram of the whole system is shown in Fig. 1. We have to establish the motion coupled circuit equations because armature motion depends on current. One dimensional armature motion is assumed. The circuit equation can be written as second-order differential equations of the following matrix form [1]:

$$[M]\{\ddot{V}\} + [D]\{\dot{V}\} + [K]\{V\} = \{0\} \quad (1)$$

where  $\{V\}$  is the voltage on each capacitor [1]. All the constant and time-varying impedance parameters of the PFN and railgun are included in the matrix  $[M]$ ,  $[D]$  and  $[K]$  of Eq. (1). The armature motion governed by current can be described using the following equation:

$$m\ddot{x} = F_p - \mu(F_{N,me} + F_{N,em}) \quad (2)$$

where  $m$ ,  $x$ ,  $\mu$ ,  $F_{N,me}$ , and  $F_{N,em}$  are the armature mass and position, friction coefficient, mechanical normal force, and electromagnetic normal force, respectively [1].

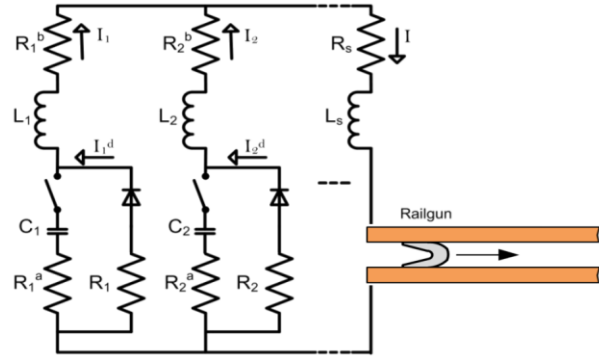


**Figure 1. Circuit diagram of the PFN and railgun.**

We can design the main dimensions of the railgun and the PFN required to satisfy the target performance by solving the coupled Eq (1) and (2).

It is important to consider the rail vibration because armature velocity during launching phase grows up to hypervelocity. Its vibration shapes are strongly dependant on the zones of moving velocities divided by the characteristic velocities of elastic waves. The vibrating structure is simplified as shown Fig. 2. Governing equations based on Timoshenko beam theory are established as Eq. (3) and analysed using the moving repulsive force that can be calculated from above circuit analysis. These vibration analysis can provide deep insight into real vibration induced during firing the railgun.

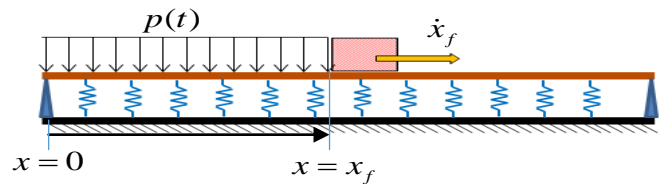


**Figure 2. Simplified vibration model of a railgun.**

$$\rho A \ddot{w} + \kappa GA(\theta' - w'') + kw = p(t)[1 - H(x - x_f)] \quad (3-1)$$

$$\rho I \ddot{\theta} - EI\theta'' - \kappa GA(w' - \theta) = 0 \quad (3-2)$$

where  $w$  is the transverse deflection,  $\theta$  is the bending rotation angle,  $\rho$  is the mass density per unit volume,  $A$  is the cross sectional area,  $\kappa$  is the shear correction factor,  $k$  is the stiffness per unit length of the elastic foundation,  $p(t)$  is a moving force per unit length,  $H$  is a Heaviside step function,  $x_f$  is the armature position. Moreover,  $I$  is the area moment of inertia,  $E$  is Young's modulus, and  $G$  is the shear modulus [2].

### 3 experimental tests

The mathematical models were verified experimentally.

Fig. 3 shows the current, breech voltage, armature position and velocity measured when discharging 24 modules simultaneously at initial time and 2 modules apiece at a specified time of a total 48 capacitive modules of PFN. The armature exits the muzzle at 4.5 ms. It is shown that the calculated current does not match the measured one well from around 3.8 ms. Furthermore there is a spike of breech voltage at that time. These indicate that the transition meaning arcing contact occurs at around 3.8 ms. The breech voltage rises up again because the armature loses the metal contacts with the rails and arc is produced just after the armature departure from the muzzle.

The muzzle velocity is estimated indirectly. Based on the correspondence of the simulated data to measurements on the trajectory and time information of the armature, the muzzle velocity can be calculated.

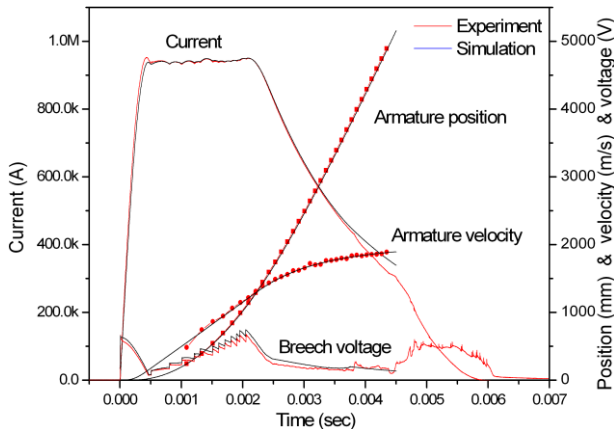


Figure 3. Comparison of experiment and simulation.

Fig. 4 and Fig. 5 show the strains measured at 1.1 m and 3.3 m location from breech end. There is a high amplitude but rapidly decaying motion near the armature passing time as shown in Fig. 4. Fig. 5 shows a small amplitude but high frequency motion propagated forward and backward the armature position. Decaying motion is induced because the armature velocity at 1.1 m is lower than the critical velocity that elastic waves can propagate over. The elastic waves propagate around the armature because the armature velocity goes over the critical velocity at 3.3 m location.

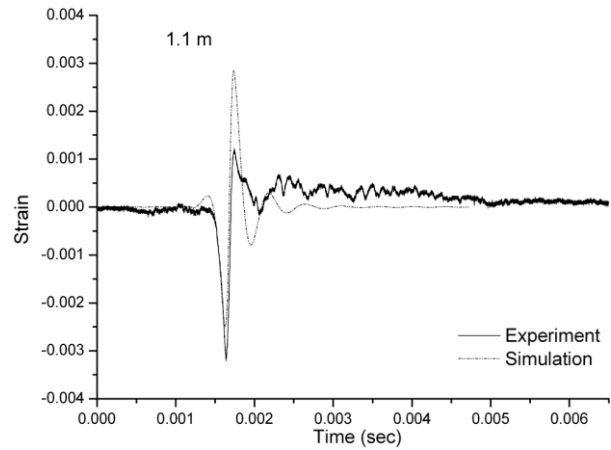


Figure 4. Rail vibration at 1.1 m location.

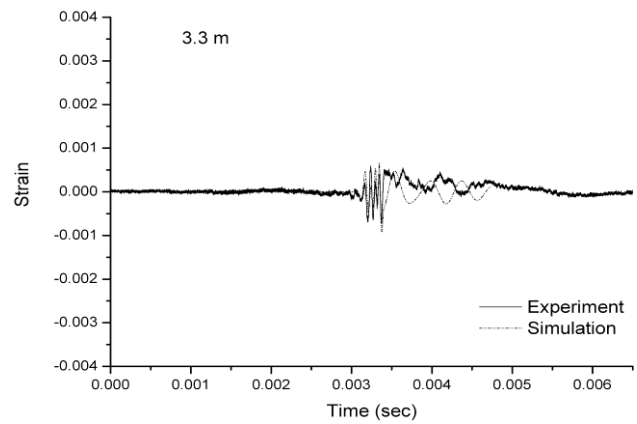


Figure 5. Rail vibration at 3.3 m location.

### 4 Conclusions

The performance of an experimental railgun was evaluated. We verified the design adequacy of the railgun through dynamic measurements. Further researches are required to study hypervelocity contacts engaged under high current. Solving the problems related to such contacts will play a key role to build railguns for practise use.

### References

- [1] Y. H. Lee, S. H. Kim, B. H. Lee, S. An, K. S. Yang. "Experimental Tests of a 25mm Square-bore Railgun", *16<sup>th</sup> International Symposium on Electromagnetic Launch Technology*, (2012).
- [2] Y. H. Lee, S. S. Kim. "Combined analytical and numerical solution for an elastically supported Timoshenko beam to a moving load", *Journal of Mechanical Science and Technology*, **28(7)**, pp. 2549-2559, (2014).

# Saturation of Amorphous-Core Tesla Transformer Applied to Pulsed High-Voltage Generator

C. H. Kim\*, H. O. Kwon<sup>†</sup>, J. S. Choi\*

\*Agency for Defense Development, Republic of Korea, Tel.: +82-42-821-2754, <sup>†</sup> Hanwha Corporation, Republic of Korea

## Abstract

We have designed and tested a pulsed high-voltage generator based on an amorphous-core tesla transformer. Compared with the unsaturated state, inductance and resonant period of the transformer were reduced at the saturated state due to high-current at the 1<sup>st</sup> stage of the transformer. To compensate reduction of the inductance and period, a virtual variable-inductor was introduced into the simplified circuit for PSPICE simulation. Saturation of the core can be estimated from inductance variation of the virtual variable-inductor.

**Keywords:** Tesla transformer, resonance, amorphous, core saturation, inductance reduction

## 1 Introduction

A pulsed high-voltage generator based on an iron-core tesla transformer has some advantages compared with a Marx generator; for pulse repetition, energy efficiency, and compactness, etc. [1]. Thin silicon steel or electrical steel shows good permeability and high-saturation (typically 1.6 ~ 2 T) of magnetic flux density  $B$ . Amorphous-core material, compared with silicon steel, generally has higher permeability, better frequency characteristics and lower energy loss but a little bit lower saturation (typically 1.5 T) of  $B$ . By these overall characteristics, amorphous-core material is increasingly applied to high-power transformers for high-frequency or short pulse application. This paper describes and discusses a peculiarity that caused by the core saturation in our tests about the high-voltage pulse generator which consists of an amorphous-core tesla transformer and peripheral parts.

## 2 Design and test

We have designed and tested a pulsed high-voltage generator based on an amorphous-core tesla transformer to study a pulsed power source which can be applied to a high-power electromagnetic (HP EM) radiator.

### 2.1 Design and fabrication

The designed transformer consists of a pair of magnetic core loops, four parallel coils for the 1<sup>st</sup> stage, and two parallel coils for the 2<sup>nd</sup> stage. This type of transformer was presented

by Pecquois et al. in 2012 [2]. The magnetic core material is 25  $\mu\text{m}$  thick amorphous foil of Metglas<sup>TM</sup> 2605SA1 [3]. To make the magnetic core we stacked layers of the amorphous foil and insulation film by in turn and the lamination (stacking) factor of the core is about 50 %. Total cross section of the core at the centre of the transformer is 38 mm x 30 mm. Fig.1 shows a circuit for PSPICE simulation for the designed generator. The multi coils [2] at the 1<sup>st</sup> and the 2<sup>nd</sup> stages of the transformer were simplified to one coil in each stage to reduce the number of variables in Fig.1. The load voltage resulted from this simplified circuit corresponds just to a half value of the real double-circuit's result. A virtual variable L1 was introduced for PSPICE simulation to predict effects of inductance variation which can be derived by the core's  $B$ - $H$  peculiarity. Fig.2 shows the structure of the designed generator. The generator has 280 mm in diameter ( $\Phi$ ) of inside cylindrical housing and 600 mm in length ( $l$ ) except for the dummy load and the DC charger.

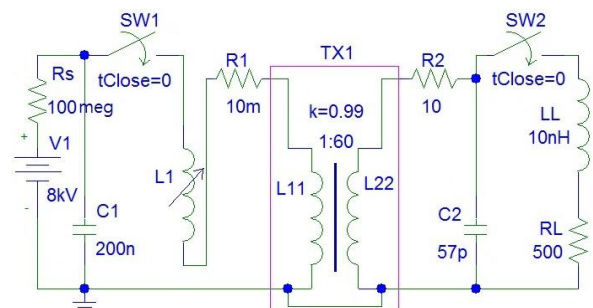


Figure 1. Simplified Simulation Circuit for the Generator

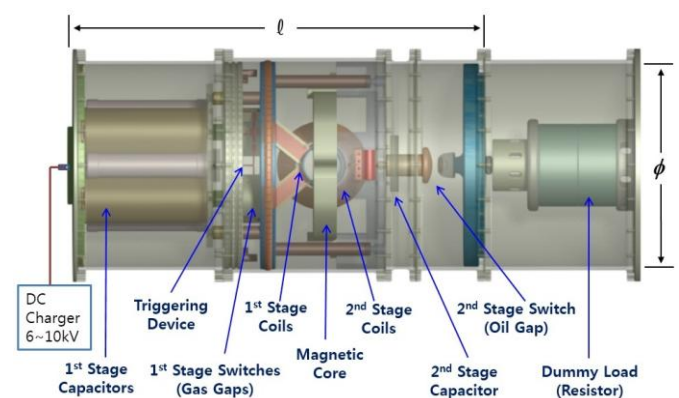
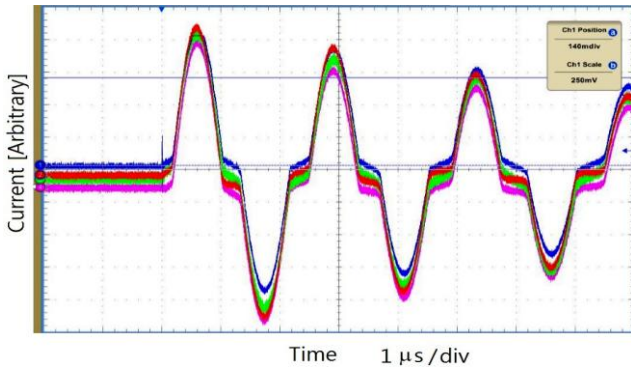


Figure 2. Designed Pulsed High-Voltage Generator

## 2.2 Test and discussion

The L11 and L22 were measured at low current which was supplied from an impedance analyser with a frequency range between kHz and MHz. In this low current, the magnetic core was not saturated. On the other hand, high current of kilo amperes which flows through the 1<sup>st</sup> stage coils can force to saturate the magnetic core. At the low current, C1 = 200 nF, L11 = 1.7  $\mu$ H, C2 = 57 pF, and L22 = 6 mH, respectively.



**Figure 3. Distorted 1<sup>st</sup> Stage Current of the Four Coils of the Transformer at the Saturated State**

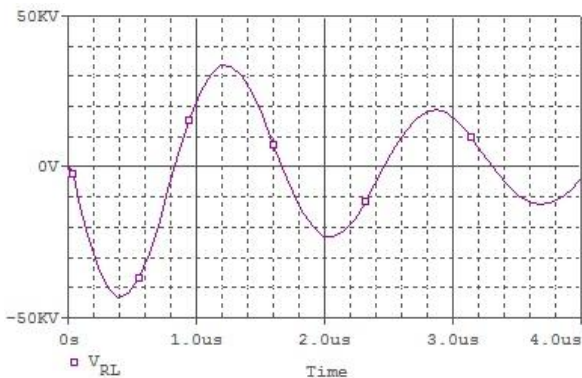


**Figure 4. Load Voltage (a Half Value, not Compensated) by PSPICE Simulation**

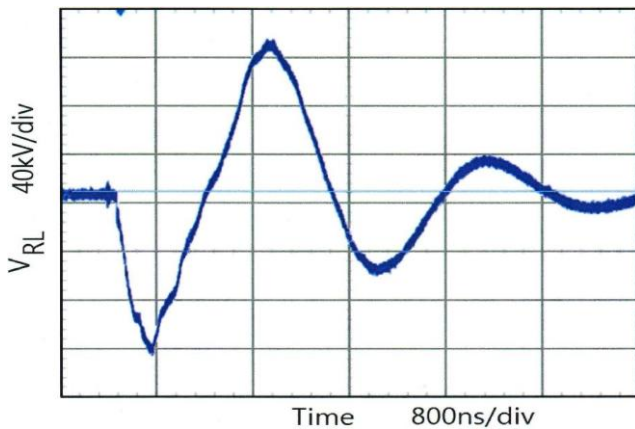


**Figure 5. Load Voltage Acquired from Experiment with At-all-times Closed Oil Gap**

The calculated resonant period of the first and the second stage of the transformer circuit is 3.7  $\mu$ s under the unsaturated state. Once the core was saturated, inductance of the 1<sup>st</sup> coil and period of the 1<sup>st</sup> stage current were reduced. Fig.3 presents experimental 1<sup>st</sup> stage current of the four coils. All four waves are distorted in sinusoidal shape. The reason of this distortion is known by the core saturation. The resonant period at the 1<sup>st</sup> stage of the transformer was 2.3  $\mu$ s which is smaller than the 3.7  $\mu$ s of the unsaturated state.

Although the properly controlled oil gap gives higher voltage peak and oil breakdown strength was observed from 90 kV/mm to 105 kV/mm for microseconds of pulse-width in our former tests, to discuss resonant period without peaking, this paper presents the SW2 closed at-all-times only. Fig.4 and Fig.5 show the load voltages of the generator obtained from simulation and experiment, respectively. When we assumed that the virtual variable-inductor L1 of 1.7  $\mu$ H at the low-current state is decreased to 0.3  $\mu$ H at the high-current state, the period reduction agrees well with the inductance decreasing. The amount of inductance variation stands for the peculiarity of the saturated amorphous core. With the L1 of 0.3  $\mu$ H in Fig.1, the negative load voltage peak by the simulation is -43 kV (compensation, i.e., multiply by two, is necessary and so -86 kV is actually predicted), and the period is 1.6 ~ 1.7  $\mu$ s, as shown in Fig.4. The measured negative load voltage peak is about -130 kV and the period is 1.6 ~ 2.0  $\mu$ s. Voltage difference between Fig. 4 and Fig. 5 is probably caused by the peculiarity of the magnetic core and/or insufficient material parameters for transformer simulation.

## 3 Summary

A peculiarity of an amorphous-core tesla transformer was shown and discussed. Compared with unsaturated condition, resonant period reduction in the current and the voltage waves occurred at the saturated core. The core saturation was caused by the high current of the 1<sup>st</sup> stage of the transformer. The period reduction was analysed by introducing a virtual variable-inductor into the simplified circuit for PSPICE simulation. The period reduction effect corresponds to the inductance decreasing from 1.7  $\mu$ H to 0.3  $\mu$ H. Thus, the peculiarity of the saturated amorphous core can be estimated by the inductance variation of the virtual variable-inductor.

## References

- [1] V.A. Kolchanova, "On Calculation of the Tesla Coil with Iron Core," *Modern Technique and Technologies, IEEE*, pp. 40-41, (2003).
- [2] Romain Pecquois, Laurent Pecastaing, Marc Rivaletto, Antoine Silvestre De Ferron, and Rene Vezinet, "MOUNA: An Autonomous, Compact, High-Power, and Wideband Electromagnetic Source Based on a Novel Resonant Pulsed Transformer," *IEEE Transactions on Plasma Science*, vol. 40, no. 5, pp. 1407-1415, May (2012).
- [3] <http://www.metglas.com>

# Parametric analysis of STRETCH meat grinder circuit based on equivalent induction theory

Jianmin Ding, Xinjie Yu, and Zanji Wang

State Key Lab. of Power System, Dept. of Electrical Engineering, Tsinghua University, Beijing 100084, China, djm13@mails.tsinghua.edu.cn

## Abstract

For parameter and performance analysis of the STRETCH circuit topology, this paper has proposed a theory of equivalent induction which helps to understand the topology from a new angle, and thus obtains analytical expressions of four performance indices, i.e. primary / secondary current multiplication ratio  $m_1 / m_2$ , ratio of the maximum capacitive energy over total inductive energy  $\eta_C$ , maximum voltage across the main switch  $V_{Sopm}$ . Thus, influences of two key parameters charging cut-off current  $I_0$  and inductance ratio  $n_L$  on seven performance indices (four above, and three more indices which are essential but comparatively easier to analyse: charging time / efficiency  $T_0 / \eta$ , muzzle velocity proportional term  $\propto v$ ) are particularly discussed, which are of certain value to the design and operation of inductive pulsed power supply system.

**Keywords:** STRETCH meat grinder, equivalent induction, performance indices, parametric analysis.

## 1 Introduction

Inductive pulsed power supplies (IPPS) have been a research hotspot in the area of electromagnetic launch. The current research is mainly devoted to proposing new (or modified) topologies and setting up experimental systems with higher energy. However, parametric analyses in deep and theoretical methods in detail for the topologies are still lacking.

Based on the basic meat grinder topology, IAT (Institute for Advanced Technology) has proposed a modified topology for IPPS, i.e. STRETCH (Slow Transfer of Energy Through Capacitive Hybrid) meat grinder circuit (as shown in Fig 1). Expression of the maximum voltage across the commutation capacitor  $C_1$  is given [1]. Taking a 2-MJ muzzle energy EM launch system as an example, the effects of battery and inductor parameters on the overall efficiency and system size have been discussed [2]. It's merely conceptual analysis, rather than quantitative analysis.

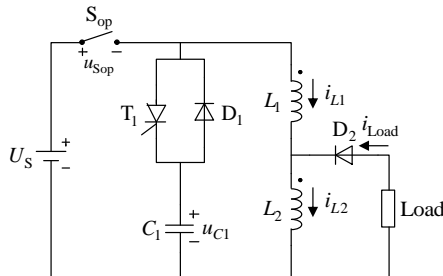


Figure 1. Topology of STRETCH meat grinder

## 2 Selection of key parameters and performance indices

### 2.1 Design and operation parameters

As shown in Fig. 2, the working process of the STRETCH circuit topology can be divided into 5 stages according to the working state transition caused by the switching of the semiconductor devices. (1) Charging Stage: The inductors  $L_1$  and  $L_2$  are charged to the pre-set current  $I_0$  by the primary source  $U_S$ . (2) Discharging Stage I:  $i_{L1}$  reduces to 0,  $i_{L2}$  and  $i_{Load}$  reach the primary current peak  $I_{P1}$ , and  $u_{C1}$  reaches the reverse voltage peak  $U_{C1m}$ . Current multiplication of  $i_{L2}$  and  $i_{Load}$  is based on the principle of magnetic flux compression. The leakage-inductor energy of  $L_1$  is stored into the commutation capacitor  $C_1$  in this stage. (3) Discharging Stage II:  $L_2$  supplies the load current alone, and  $u_{C1}$  keeps the constant negative value  $U_{C1m}$ . (4) Discharging Stage III:  $T_1$  is triggered, and the capacitor  $C_1$  releases the stored energy, thus adjusting the waveform of  $i_{Load}$ .  $i_{Load}$  reaches the secondary current peak  $I_{P2}$  in this stage. The stage ends when  $i_{L1}$  reduces to 0 again. The time delay between the start of Discharging Stage I and the triggering time of the thyristor  $T_1$  is  $t_D$ . (5) Discharging Stage IV:  $L_2$  supplies the load current alone, again.  $u_{C1}$  keeps a constant negative value  $U_{C1end}$ .

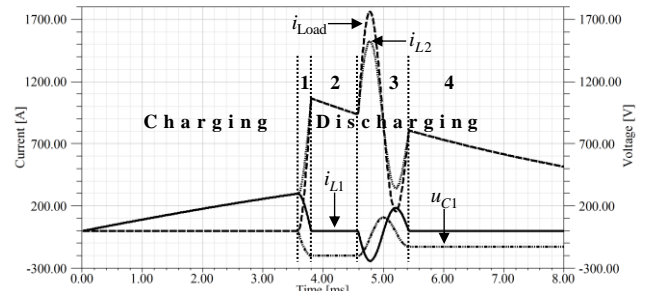


Figure 2. Working stage division of the topology

In IPPS, once the topology is given, system parameters to be determined include component parameters (e.g.  $L_1$ ,  $L_2$ ,  $C_1$ ) and control parameters (e.g.  $I_0$ ,  $t_D$ ). In system design phase, the total energy level (i.e. the initial inductive energy  $E_0$ ) is given, and then the component and control parameters to be determined are called design parameters. In system operation phase, the component parameters are already set, and then the control parameters to be determined are called operation parameters.

This paper selects two key parameters that require attention in system design and operation phase, i.e. the charging cut-off

current  $I_0$ , which is closely related to the energy level, energy loss, efficiency, etc., and inductance ratio  $n_L (=L_1/L_2)$ , which is closely related to the flux compression and current multiplication.  $n_L$  is considered as design parameters, while  $I_0$  is both design and operation parameter.

## 2.2 Performance indices

In order to quantize the influences of parameters on system performance, seven performance indices are proposed.

(1)  $T_0$ : charging time, i.e. the duration time of Charging Stage. (2)  $\eta$ : charging efficiency, i.e. the ratio between the initial inductive energy  $E_0$  and the total energy  $E_S$  supplied by the primary source  $U_S$ . (3)  $m_1$ : primary current multiplication ratio, i.e. the ratio between the primary current peak  $I_{P1}$  and  $I_0$ . (4)  $m_2$ : secondary current multiplication ratio, i.e. the ratio between the secondary current peak  $I_{P2}$  and  $I_0$ . (5)  $\eta_C$ : stored energy ratio, i.e. the ratio between the maximum capacitive energy ( $C_1 U_{C1m}^2/2$ ) and the total inductive energy  $E_0$ . (6)  $V_{Sopm}$ : maximum voltage across the main switch  $S_{op}$ . (7)  $\propto v$ : muzzle velocity proportional term. Motive force in EM launch is proportional to  $i_{Load}^2$ , and the duration time of the launch process is 3~4ms generally. So the integration of  $i_{Load}^2$  within 3.5ms since discharging can roughly reflect the muzzle velocity, for there is an approximate proportional relation between them.

It's worthy of note that, in order to simplify the discussion, a resistance-inductance load (i.e.  $L_L$  and  $R_L$  in series) is used as the load model to take place of the actual railgun load.

## 3 Equivalent induction theory

### 3.1 Derivation for expressions of four performance indices

Ignoring the internal resistances ( $R_{L1}$  and  $R_{L2}$ ) of the inductors and the resistive part of the load, i.e.  $R_{L1} = R_{L2} = R_L = 0$ , the topology in discharging stage can be simplified as shown in Fig. 3(a).

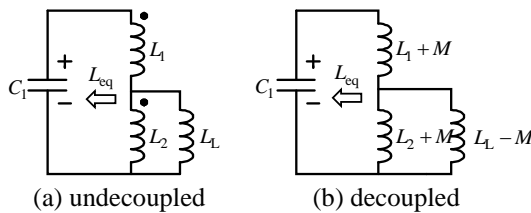


**Figure 3. Simplified topology of discharging stage without considering the resistances**

Focusing on Discharging Stage I, the leakage-inductor energy of  $L_1$  is stored into the capacitor  $C_1$ . On the one hand,  $u_{C1}$  increases from the initial value 0 to the peak value  $U_{C1m}$ . On the other side, considering the current path of  $i_{L1}$ , where  $C_1$  locates as well,  $i_{L1}$  reduces from the initial value  $I_0$  to 0. It can be regarded that, seeing from the commutation capacitor  $C_1$  side, the equivalent inductance  $L_{eq}$  transfers its energy ( $L_{eq} I_0^2/2$ ) to the capacitor  $C_1$ , i.e.

$$C_1 U_{C1m}^2/2 = L_{eq} I_0^2/2 \quad (1)$$

Decouple the mutual induction between the inductors  $L_1$  and

$L_2$  at the junction, as shown in Fig. 3(b), where  $M$  is the mutual inductance. Hence,

$$\begin{aligned} L_{eq} &= L_1 + M + (L_2 + M) // (L_L - M) \\ &= L_1 + M - (M - L_L) \frac{L_2 + M}{L_2 + L_L} \end{aligned} \quad (2)$$

$U_{C1m}$  corresponds exactly to the maximum capacitive energy. Thus, according to Equation (1), the stored energy ratio  $\eta_C$  can be expressed as

$$\eta_C = \frac{C_1 U_{C1m}^2/2}{L_{tot} I_0^2/2} = \frac{L_{eq} I_0^2/2}{L_{tot} I_0^2/2} = \frac{L_{eq}}{L_{tot}} \quad (3)$$

where  $L_{tot}$  is the total inductance, i.e.  $L_{tot} = L_1 + L_2 + 2M$ .

According to Equation (1),  $U_{C1m}$  can be expressed as

$$U_{C1m} = -I_0 \sqrt{L_{eq}/C_1} \quad (4)$$

Maximum voltage across  $S_{op}$ , i.e.  $V_{Sopm}$ , occurs when  $u_{C1}$  reaches its peak  $U_{C1m}$ . Supposing that  $U_{Send}$  is the final voltage value of the primary source,  $V_{Sopm}$  can be expressed as

$$V_{Sopm} = U_{Send} - U_{C1m} = U_{Send} + I_0 \sqrt{L_{eq}/C_1} \quad (5)$$

Consider the initial and final state of Discharging Stage I. Based on energy conservation law,

$$L_{tot} I_0^2/2 = C_1 U_{C1m}^2/2 + (L_2 + L_L) I_{P1}^2/2 \quad (6)$$

Substituting Equation (1) and (2) into Equation (6), the primary current multiplication ratio  $m_1$  can be acquired

$$m_1 = \frac{I_{P1}}{I_0} = \frac{L_2 + M}{L_2 + L_L} \quad (7)$$

Focusing on Discharging Stage III, each inductor's current reaches its peak value at the same time when ignore the resistances. Meanwhile,  $u_{C1}$  reduces from the initial value  $U_{C1m}$  to 0. It can be regarded that, the commutation capacitor  $C_1$  returns its energy  $C_1 U_{C1m}^2/2$  to the equivalent inductance  $L_{eq}$  via the current path of  $i_{L1}$ . Thus, the reverse peak value of  $i_{L1}$  is  $-I_0$ . Suppose the peak value of  $i_{L2}$  is  $I_{P2}$ . Based on KCL,

$$I_{P2} = I_{P2} - (-I_0) = I_{P2} + I_0 \quad (8)$$

Based on energy conservation law,

$$\frac{1}{2} L_{tot} I_0^2 = \frac{1}{2} (L_1 + M) I_0^2 + \frac{1}{2} (L_2 + M) I_{P2}^2 + \frac{1}{2} (L_L - M) I_{P2}^2 \quad (9)$$

Substituting Equation (8) into Equation (9), the secondary current multiplication ratio  $m_2$  can be acquired

$$m_2 = \frac{I_{P2}}{I_0} = 2 \frac{L_2 + M}{L_2 + L_L} = 2m_1 \quad (10)$$

Now, based on the proposed equivalent induction theory when ignore the resistances, analytical expressions of the four performance indices, i.e.  $m_1$ ,  $m_2$ ,  $\eta_C$  and  $V_{Sopm}$ , are obtained, as Equation (7), (10), (3), (5), respectively.

### 3.2 Validity verification

Results of simulation based on Simplorer<sup>®</sup> usually agree well with the experimental results. Take a circuit for example, and the parameters are set as follows,  $L_1$ : 503.5 $\mu$ H,  $L_2$ : 59.8 $\mu$ H,  $k$ : 0.9319,  $L_L$ : 1.4 $\mu$ H,  $C_1$ : 210.87 $\mu$ F,  $U_S$  (a pre-charged capacitor  $C_S$  with internal resistance  $R_S$ ): 51.6mF / 200V / 2m $\Omega$ ,  $I_0$ : 1kA, and  $t_D$ : 0.3ms. Compare the results of the four indices, i.e.  $m_1$ ,  $m_2$ ,  $\eta_C$  and  $V_{Sopm}$ , obtained by simulation and above

mentioned expressions, respectively. As listed in Table 1, the results of theory method are quite close to those of simulation. Slight differences are due to regarding the semiconductor devices as ideal switches without considering the switching losses in the above derivation. Generally speaking, the validity of the proposed theory and expressions of the four indices are confirmed.

There will be analysis deviations caused by ignoring the resistances. However, according to the proposed theory and analytical expressions above, general relationships between the performance indices and system parameters could be obtained directly and clearly. This is of certain value to the design and operation of IPPS.

**Table 1: Results comparison between simulation and theory method**

Indices	$m_1$	$m_2$	$\eta_C$	$V_{Sopm} / V$
Simulation method	3.61	7.07	9.71%	788.6
Theory method	3.62	7.24	9.59%	784.5

## 4 Analysis on design and operation parameters

### 4.1 Influences of operation parameter $I_0$ on indices

As a single-parameter problem, it is easier to discuss. In system operation phase, component and control parameters are determined except  $I_0$ . It's obvious that, the expressions of the indices  $m_1$ ,  $m_2$ , and  $\eta_C$ , are irrelevant with  $I_0$ . So these three indices stay unchanged when the value of operation parameter  $I_0$  varies.

As mentioned above,  $V_{Sopm} = U_{Send} - U_{C1m}$ .  $U_{Send}$  decreases when  $I_0$  increases, due to an increase of  $E_s$ , i.e. energy supplied by the primary source.  $U_{C1m}$  is proportional to  $I_0$ , so it increases in reverse when  $I_0$  increases, which is usually more significant than the reduction of  $U_{Send}$ . Thus,  $V_{Sopm}$  increases on the whole when  $I_0$  increases.

The changing trends of  $T_0$ ,  $\eta$ , and  $\infty v$  with  $I_0$  are easy to analyse, so the influences of operation parameter  $I_0$  on indices are listed directly here in Table 2. According to the results, once the index  $\infty v$  is large enough to meet the requirement of the muzzle velocity, it's not suggested that the system operates at a high level of  $I_0$ .

**Table 2: Influences of operation parameter  $I_0$  on indices**

Indices	$T_0$	$\eta$	$m_1$	$m_2$	$\eta_C$	$V_{Sopm}$	$\infty v$
$I_0 \uparrow$	$\uparrow$	$\downarrow$	-	-	-	$\uparrow$	$\uparrow$
Effect*	$\times$	$\times$	-	-	-	$\times$	$\sqrt$

\*  $\sqrt$ : positive,  $\times$ : negative, -: no influence

### 4.2 Influences of design parameters $I_0$ and $n_L$ on indices

This is a multi-parameter problem. In system design phase, the total energy level  $E_0$  is given, meanwhile, component parameters except the inductors' parameters, and control parameters except  $I_0$ , are already determined. One term of the inductors' parameters, i.e. coupling coefficient  $k$ , is a given constant value. The inductance  $L_1$  and  $L_2$  can be uniquely determined by  $I_0$  and  $n_L$ , as Equation (11)~(13). Now, all the system parameters are already given, or can be determined by

$I_0$  and  $n_L$ .

$$L_{tot} = 2E_0 / I_0^2 \quad (11)$$

$$L_2 = L_{tot} / \left( n_L + 1 + 2k\sqrt{n_L} \right) \quad (12)$$

$$L_1 = n_L L_2 \quad (13)$$

During charging stage, the inductors act as a whole  $L_{tot}$ , which is only related to  $I_0$ . Thus,  $T_0$  and  $\eta$  are independent of  $n_L$ .

$L_{tot}$  and  $L_{eq}$  both decrease when  $I_0$  increases.  $L_{eq}$  increases when  $n_L$  increases. In both cases, the ratio  $L_{eq}/L_{tot}$  increases, so  $\eta_C$  increases, thus  $V_{Sopm}$  increases as well.

The ratio  $(L_2+M)/(L_2+L_L)$  decreases when  $I_0$  increases, so  $m_1$  and  $m_2$  decrease. However, the reference of the multiplication, i.e.  $I_0$  increases, so the total current level rises, thus  $\infty v$  increases. The ratio  $(L_2+M)/(L_2+L_L)$  increases when  $n_L$  increases, so  $m_1$  and  $m_2$  increases. It's obvious that  $I_0$  and  $n_L$  have different influences on  $m_1$  and  $m_2$ , there is a tradeoff between them.

The influences of design parameter  $I_0$  and  $n_L$  on indices are listed in Table 3. The results show that influences of  $I_0$  and  $n_L$  on indices are not always the same. In system design phase, suitable  $I_0$  and  $n_L$  should be selected according to the indices on which your attention is focused.

**Table 3: Influences of design parameters  $I_0$  and  $n_L$  on indices**

Indices	$T_0$	$\eta$	$m_1$	$m_2$	$\eta_C$	$V_{Sopm}$	$\infty v$
$I_0 \uparrow$	$\downarrow$	$\downarrow$	$\downarrow$	$\downarrow$	$\uparrow$	$\uparrow$	$\uparrow$
$n_L \uparrow$	-	-	$\uparrow$	$\uparrow$	$\uparrow$	$\uparrow$	$\uparrow$
Total	$\downarrow$	$\downarrow$	TBD	TBD	$\uparrow$	$\uparrow$	$\uparrow$
Effect*	$\sqrt$	$\times$	TBD	TBD	$\times$	$\times$	$\sqrt$

\*  $\sqrt$ : positive,  $\times$ : negative, -: no influence, TBD: To be determined.

## 5 Conclusions

During parametric analysis, performance indices  $T_0$ ,  $\eta$ , and  $\infty v$  can be analysed intuitively in general, but not the same case with the four indices  $m_1$ ,  $m_2$ ,  $\eta_C$  and  $V_{Sopm}$ . Based on the proposed equivalent induction theory, and concise expressions of these four indices, the above problems are well solved. The theory helps to understand the STRETCH circuit topology from a new point of view as well.

## Acknowledgements

This work is supported in part by the NSFC under Project 51377087 and in part by the Tsinghua University Initiative Scientific Research Program.

## References

- [1] Sitzman A, Surls D, Mallick J. "Stretch meat grinder: a novel circuit topology for reducing opening switch voltage stress", *IEEE Pulsed Power Conference*, pp. 493-496, (2005).
- [2] Dierks E, McNab I R, et al. "Battery-Inductor Parametric System Analysis for Electromagnetic Guns", *IEEE Trans. Plasma Sci.*, 39(1), pp. 268-274, (2011).

**Gold Sponsors:**

**Metatech**

<http://www.metatechcorp.com/>



**montena**

<http://www.montena.com/system/home/>



<http://highpower.co.kr/>



<http://english.hanwhacorp.co.kr/index.jsp>

**Silver Sponsors:**



[http://www.narda-sts.it/narda/default\\_en.asp](http://www.narda-sts.it/narda/default_en.asp)



<http://www.i-spec.co.kr/>



<http://www.ker.ne.kr/>



[www.eretec.com](http://www.eretec.com)

**Exhibitors:**

**EMI Solutions  
Pvt Ltd**

**ETS.LINDGREN  
& GTL(API)**

**OMNI LPS**

**Kapteos**